frontiers | Research Topics

Recent advances in durability improvement and low-carbon strategy of engineering materials and structures

Edited by
Zhongya Zhang, Anbang Li and Zhidong Zhang

Published in
Frontiers in Materials

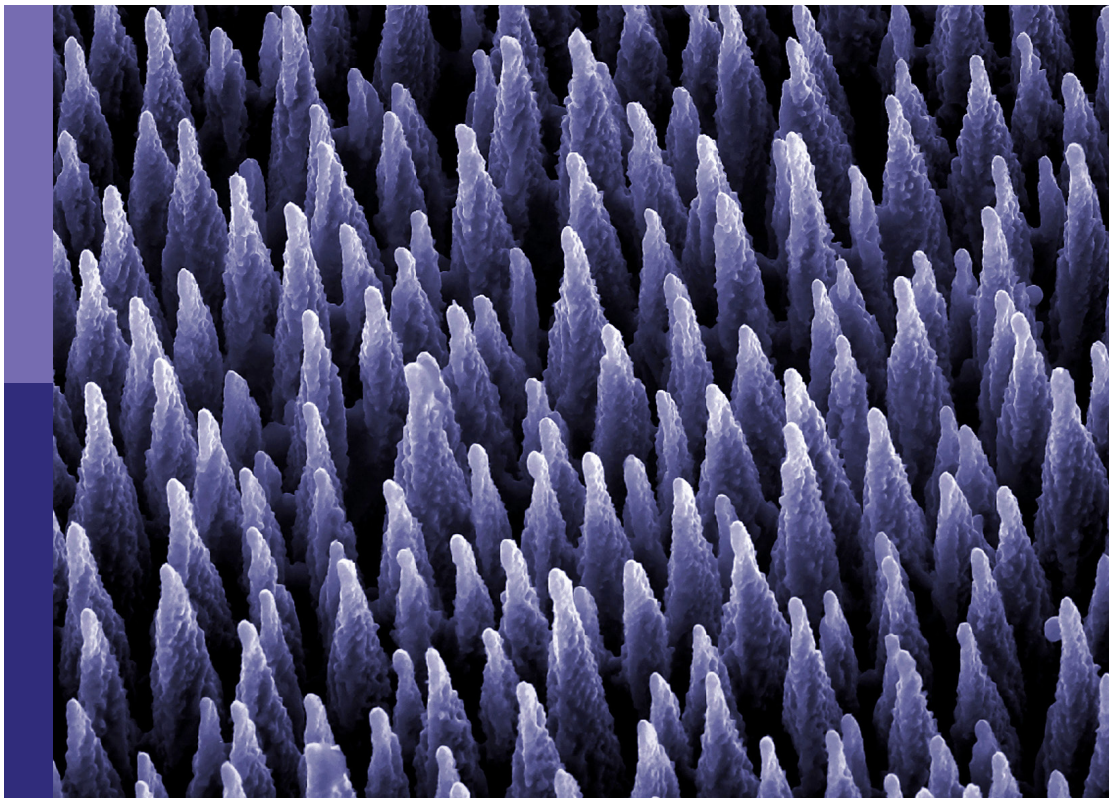

ISSN 1664-8714
ISBN 978-2-8325-5367-1
DOI 10.3389/978-2-8325-5367-1

About Frontiers

Frontiers is more than just an open access publisher of scholarly articles: it is a pioneering approach to the world of academia, radically improving the way scholarly research is managed. The grand vision of Frontiers is a world where all people have an equal opportunity to seek, share and generate knowledge. Frontiers provides immediate and permanent online open access to all its publications, but this alone is not enough to realize our grand goals.

Frontiers journal series

The Frontiers journal series is a multi-tier and interdisciplinary set of open-access, online journals, promising a paradigm shift from the current review, selection and dissemination processes in academic publishing. All Frontiers journals are driven by researchers for researchers; therefore, they constitute a service to the scholarly community. At the same time, the *Frontiers journal series* operates on a revolutionary invention, the tiered publishing system, initially addressing specific communities of scholars, and gradually climbing up to broader public understanding, thus serving the interests of the lay society, too.

Dedication to quality

Each Frontiers article is a landmark of the highest quality, thanks to genuinely collaborative interactions between authors and review editors, who include some of the world's best academicians. Research must be certified by peers before entering a stream of knowledge that may eventually reach the public - and shape society; therefore, Frontiers only applies the most rigorous and unbiased reviews. Frontiers revolutionizes research publishing by freely delivering the most outstanding research, evaluated with no bias from both the academic and social point of view. By applying the most advanced information technologies, Frontiers is catapulting scholarly publishing into a new generation.

What are Frontiers Research Topics?

Frontiers Research Topics are very popular trademarks of the *Frontiers journals series*: they are collections of at least ten articles, all centered on a particular subject. With their unique mix of varied contributions from Original Research to Review Articles, Frontiers Research Topics unify the most influential researchers, the latest key findings and historical advances in a hot research area.

Find out more on how to host your own Frontiers Research Topic or contribute to one as an author by contacting the Frontiers editorial office: frontiersin.org/about/contact

Recent advances in durability improvement and low-carbon strategy of engineering materials and structures

Topic editors

Zhongya Zhang — Chongqing Jiaotong University, China
Anbang Li — Xi'an University of Architecture and Technology, China
Zhidong Zhang — ETH Zürich, Switzerland

Citation

Zhang, Z., Li, A., Zhang, Z., eds. (2024). *Recent advances in durability improvement and low-carbon strategy of engineering materials and structures*. Lausanne: Frontiers Media SA. doi: 10.3389/978-2-8325-5367-1

Table of contents

frontiers | Frontiers in Materials

TYPE Editorial
PUBLISHED 16 April 2024
DOI 10.3389/fmats.2024.1407364

OPEN ACCESS

EDITED AND REVIEWED BY
John L. Provis,
Paul Scherrer Institut, Switzerland

*CORRESPONDENCE
Zhongya Zhang,
zhangzhongya@cqjtu.edu.cn

RECEIVED 26 March 2024
ACCEPTED 03 April 2024
PUBLISHED 16 April 2024

CITATION
Zhang Z, Li A and Zhang Z (2024), Editorial: Recent advances in durability improvement and low-carbon strategy of engineering materials and structures.
Front. Mater. 11:1407364.
doi: 10.3389/fmats.2024.1407364

Editorial: Recent advances in durability improvement and low-carbon strategy of engineering materials and structures

Zhongya Zhang[1,2]*, Anbang Li[3] and Zhidong Zhang[4]

[1]State Key Laboratory of Mountain Bridge and Tunnel Engineering, Chongqing Jiaotong University, Chongqing, China, [2]School of Civil Engineering, Chongqing Jiaotong University, Chongqing, China, [3]Xi'an University of Architecture and Technology, Xi'an, China, [4]ETH Zürich, Zurich, Switzerland

KEYWORDS

durability, concrete, UHPC, low-carbon, performance improvement, composite structure, life-cycle, steel structure

Editorial on the Research Topic
Recent advances in durability improvement and low-carbon strategy of engineering materials and structures

Introduction

The pursuit of low carbon and durable civil engineering materials and structures is a crucial step towards achieving sustainable development in society. Currently, civil engineering faces challenges including high carbon emissions from the production of materials, complex manufacturing and construction processes for structures, and significant life-cycle management and maintenance costs. It is urgent to explore a comprehensive path to sustainability that spans material research and development, structural design, and life-cycle theoretical innovation.

It is a matter of great pride and gratification to come up with the Research Topic for Frontiers in Materials: Recent advances in durability improvement and low-carbon strategy of engineering materials and structures. The papers covering the following topics (but not limited to) were collected and published (after rigorous peer review) for this Research Topic: 1) low carbon, 2) high performance, 3) durability, 4) construction, 5) structure, 6) long-term performance, 7) strengthening, and 8) life-cycle. For low-carbon building materials, the performance of recycled concrete and cement soil was investigated (Zhao et al.; Liu et al.), and the quality grade assessment and fracture failure mechanism were analyzed within a theoretical framework. On the basis of low-carbon materials research, we must innovate current structural forms to match new materials. Therefore, a new bridge structure design method and combined structure connection system based on UHPC are proposed, and their mechanical properties are obtained through a series of well-designed tests (Li et al., Jiang et al.). With the material foundation and structural design established, engineers are increasingly focused on the reliability of health monitoring during both construction and operation. A method was proposed to enhance the longitudinal

thrust stiffness of the buckle tower by leveraging the joint effect of approach bridges, achieving full equilibrium for the horizontal component of the backstay force in cable-stayed arch bridges (Wang et al.). The monitoring method for detecting debonding between concrete beams and reinforced steel plates, based on piezoelectric smart materials, was also updated to improve the construction quality (Wang et al.). Under the long-term effects of harsh service environments, even the most robust structures will suffer performance degradation, such as cracking, spalling, and reduced bearing capacity. Among them, high temperature and salt erosion are common afflictions that can easily degrade the properties of the concrete matrix. It is crucial to understand the deterioration mechanism and design the corresponding countermeasures (Wang et al., Li et al.). At the same time, reinforcing deteriorating structures is often preferred as it is more economical than demolishing and rebuilding them. A new strengthening technique, based on multifaceted wrapping with UHPC, is proposed, and the mechanism by which it enhances damaged structures is studied (Jiang et al.). The influence of various reinforcement methods and interface treatments on the damaged RC beams reinforced with UHPC was analyzed by *in-situ* tests (Song et al.). In addition, some articles provide us with research progress related to the Research Topic, including the performance of new concrete and geomaterials, optimization of new construction machinery and equipment, and the basic performance of structural foundation systems. All the articles on this Research Topic provide reliable theoretical support for the low carbonization and durability optimization of civil engineering materials and structures.

This Research Topic has provided multidisciplinary research opportunity to present the state of the art in the development of durability improvement and low-carbon strategies for engineering materials and structures. Additionally, this platform has played a vital role in connecting prominent scientists, researchers, and scholars from around the globe.

We are quite sure that this book will play a role catalyst to have a more extensive exploration of low-carbon building materials and high-performance durable structures for various technological applications to address unresolved Research Topic in civil engineering, including bridge engineering, tunnel engineering, structural engineering, and geotechnical engineering.

Author contributions

ZZ: Conceptualization, Data curation, Formal Analysis, Funding acquisition, Investigation, Methodology, Project administration, Resources, Software, Supervision, Validation, Visualization, Writing–original draft, Writing–review and editing. AL: Data curation, Formal Analysis, Writing–review and editing. ZZ: Investigation, Software, Supervision, Writing–review and editing.

Funding

The author(s) declare that financial support was received for the research, authorship, and/or publication of this article. This work is financially supported by the National Natural Science Foundation of China (Grant No. 52208302).

Acknowledgments

We sincerely thank frontiers for allowing us to host the Research Topic and publish this book. This Research Topic would not have been possible without the contributions of talented authors, hardworking and professional reviewers, and the dedicated editorial team of Frontiers in Materials. Congratulations to all authors who have contributed to this Research Topic.

Conflict of interest

The authors declare that the research was conducted in the absence of any commercial or financial relationships that could be construed as a potential conflict of interest.

Publisher's note

frontiers | Frontiers in Materials

TYPE Original Research
PUBLISHED 20 September 2023
DOI 10.3389/fmats.2023.1280057

OPEN ACCESS

EDITED BY
Anbang Li,
Xi'an University of Architecture and Technology, China

REVIEWED BY
Peng Xie,
Hainan University, China
Yi-Xiang Song,
Hebei University of Technology, China
Duofeng Cen,
Ningbo University, China

*CORRESPONDENCE
Fei Gan,
1071384683@qq.com

RECEIVED 19 August 2023
ACCEPTED 12 September 2023
PUBLISHED 20 September 2023

CITATION
Li M and Gan F (2023), Experimental study of high temperature on the shear properties of early-age concrete. *Front. Mater.* 10:1280057. doi: 10.3389/fmats.2023.1280057

Experimental study of high temperature on the shear properties of early-age concrete

Meilin Li and Fei Gan*

College of Civil Engineering, Guizhou University, Guiyang, China

Fire accidents happen randomly which may occur in the construction of concrete buildings. In this study, the effects of high temperature and curing ages on shear properties of early-age concrete were experimentally studied. The pore structure of early-age concrete before heating, after heating, and re-curing after heating were examined through nuclear magnetic resonance and scanning electron microscope tests. Experimental results reveal that high temperature treatment of early-age concrete multiplies the number of pores but has little influence on the change of pore size distribution, while the re-curing treatment reduces pore size but has little influence on the change of pore numbers. Under the same exposed temperature, the shear strength of concretes before heating, after heating, and re-curing after heating increases gradually with curing ages. For concretes with certain curing ages, the shear strength increases first and then decreases with the exposed high temperature. While the cohesion and internal friction angle show a negative relationship with elevated temperature. The research can provide base data for buildings encountering fire accidents.

KEYWORDS

early age concrete, thermal effect, shear behavior, NMR, fire

1 Introduction

Fire has been one of the major threats to the safety of buildings. The mechanical properties of concrete after fire have become one of the research hotspots (Nadeem et al., 2014; Khan and Abbas, 2015; Laim et al., 2022). Fire accidents happen randomly and many of them happen during the construction period of concrete buildings. For example, a large fire accident happen in a reinforced concrete building in Wuhan, China only after 3 days of concreting (Wang et al., 2022). The physical-mechanical properties and durability of concrete show significant degradation after exposure to high temperature. Hence, it is crucial to understand the thermal damage behavior of early-age concrete after fire.

The thermal damage behavior of concrete has been widely investigated since the 1940s. The compression strength (Pan et al., 2018; Monte et al., 2019; Zhao et al., 2021a), thermal conductivity (Nguyen et al., 2019), composite behavior (Xotta et al., 2015), dynamic behavior (Bi et al., 2020), and microstructure change (Liu et al., 2018; Jia et al., 2019) of concrete exposed to elevated temperature have been investigated through experimental works. Previous studies have illustrated that the mechanical properties of concrete suffered significant degradation when exposed to high temperature. The degradation mechanism of concrete strength can be attributed to three reasons: 1) incompatibilities between the aggregates and the cement paste (Zhao et al., 2021b); 2) chemical changes (such as siliceous aggregates transforming from α phase to β phase) (Masse et al., 2002); 3) and moisture transport (Lim and Mondal,

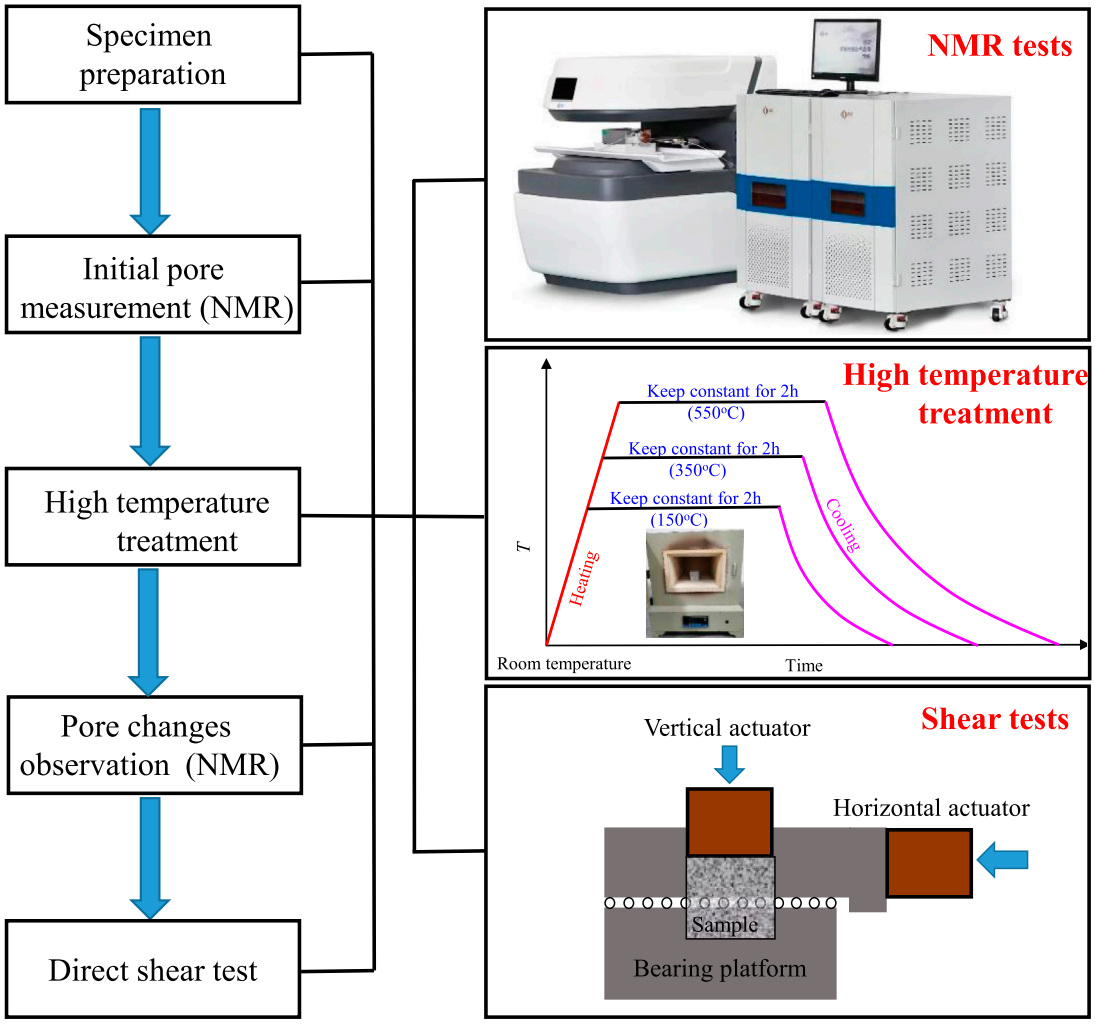

FIGURE 1
Schematic diagram of test procedure (Wang et al., 2022).

2014; Ahn et al., 2016). It should be noted that these experimental works mainly focused on the thermal behavior of in-service concrete. Research on the thermal behavior and mechanical properties of early-age concrete, however, is less studied. It is well known that the microstructure and chemical composition of early-age concrete is quite different from that of concrete in service due to inadequate hydration (Wang et al., 2022). Some scholars have explored the effect of temperature on the mechanical properties of early age concretes. For example, Li et al. (Li et al., 2017) presented a comprehensive experimental study on the degradation of mechanical properties of cement-based materials at their early age after fire. Chen et al. (2009) investigated the splitting tensile strengths of early-age concretes after heating up to 800°C. Yuan et al. (2021) studied the cracking resistance of early-age concrete under elevated temperatures. Shu et al. (2021) analyzed the compressive strength and tensile strength of early-age concrete after high temperature treatment. Previous studies mainly focus on the compression or tension properties of early-age concrete. Research on the shear properties of early-age concrete, however, is very limited, especially under the effect of thermal damage. Shear failure has been detected in many concrete structure engineerings in practice. For example, tunnel lining concrete may suffer shear damage due to the rupture of surrounding rock or the excavation of an adjacent tunnel (Zhang et al., 2018; 2019; Zhao et al., 2020; Zhao et al., 2021a).

In this study, the effect of high temperature on the shear properties of early-age concrete is experimentally studied. Pore structure evolution of early-age concrete before heating, after heating, and re-curing after heating is investigated through NMR and SEM tests.

2 Experimental study

2.1 Specimens preparation

Cement-based materials were used in this study. Cubic specimens were prepared with size of 70 × 70 × 70 mm. They were made of white Portland cement, water, and standard sand.

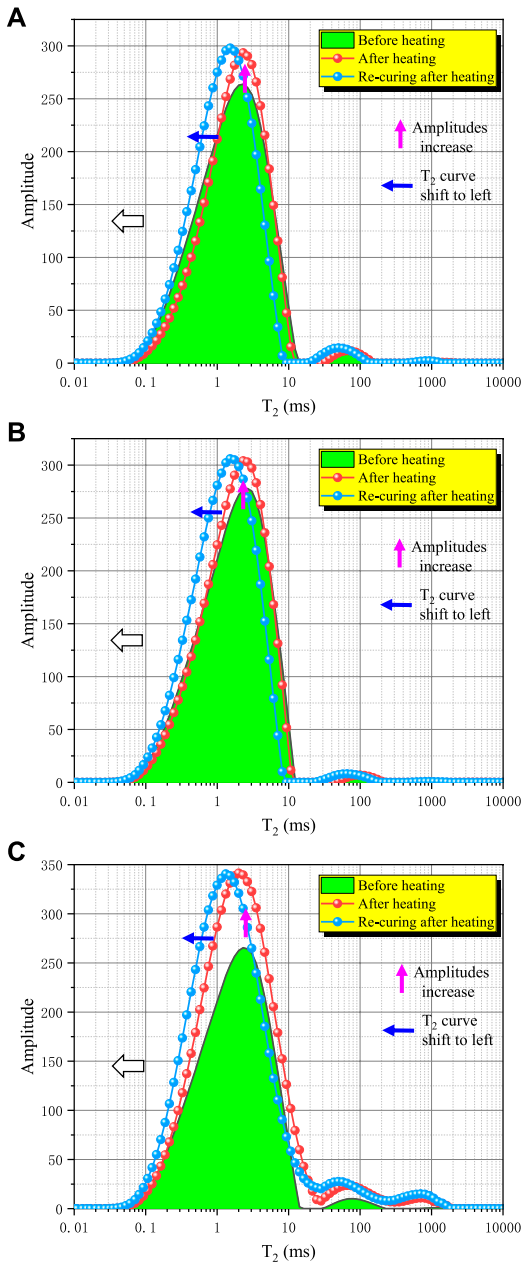

FIGURE 2
T_2 distribution of early-age concretes (14 days curing ages) before heating, after heating, and re-curing after heating **(A)** exposed to high temperature of 150°C; **(B)** exposed to high temperature of 350°C; and **(C)** exposed to high temperature of 550°C.

First, these materials were stirred in a cement mixer and then placed into 70 × 70 × 70 mm molds. After casting for 1 day, the mixtures were demoulded and were placed in a curing room with a constant temperature of 25 °C and humidity of 90%.

After the specimens were cured for certain days, they were exposed to high temperature to simulate fire conditions. To investigate the effects of curing ages on the shear behavior of thermal-damaged concretes, four curing ages (i.e. 3, 7, 14, and 28 days) were designed.

2.2 Test procedure

Figure 1 shows the sketch of the test procedure. After specimens were cured for certain days, NMR tests were first carried out on the early age concrete to obtain the initial pore structure. Then, these early-age concrete specimens were heated through an electrical heating furnace with a heating rate of 5 °C/min. Previous studies suggest that concretes exposed to temperature over 600 °C exhibited serious damage and the mechanical properties were degraded significantly (Li et al., 2017). Therefore, in this study, four groups of temperature (room temperature, 150°C, 350°C, and 550°C) were set. To evaluate the repairability of thermal-damaged concretes, the early-age concretes were re-cured for another 28 days. NMR tests were carried out again to investigate the pore changes induced by thermal damage and the re-curing process. Finally, direct shear tests were conducted on these thermal-damaged concretes.

3 Experimental results and analysis

Figure 2 shows the T_2 distribution of early-age concretes before heating, after heating, and re-curing after heating, respectively. All NMR tests were successively carried out on specimens with different curing ages, with the main results being exemplified by specimens with a curing age of 14 days. As shown in the figure, all T_2 curves exhibited two peaks, which correspond to the micro-pores and macro-pores, respectively. High temperature causes thermal damage to early-age concrete. Compared to the initial curve, the T_2 area is significantly enlarged after exposure to high temperature. Both the two T_2 peaks become higher after the high temperature treatment, while the position of the peaks remains unchanged. Previous studies indicated that the T_2 peak represents the number of pores and the T_2 distribution reflects the form of the pore size distribution (PSD) (Frosch et al., 2000; Weng et al., 2018; Zhao et al., 2022). Therefore, high temperature treatment of early-age concrete multiplies the number of pores but has little influence on the change of PSD. Moreover, the multiple of pores increases with the exposed temperature. For example, for samples heating up to 150°C and 550°C, respectively, the amplitude of the first T_2 curve increased by 29.654 and 78.822 a. u., respectively.

After heating, the early-age concretes were re-cured for another 28 days. The T_2 curve of re-cured concrete after heating is also presented in Figure 2. As shown in the figure, the T_2 curve shits to left on the T_2 relaxation time axis but the amplitude of the T_2 peaks remains nearly unchanged. This indicates that pore size decreased after re-curing but the number of pores kept unchanged.

3.2 Effect of curing ages on shear properties

Figure 3 shows the peak shear strength of tested specimens with varied curing ages. Note that average values are presented from three identical specimens. As expected, the peak shear strength of early-age concrete before heating increases with the curing ages due to the cement hydration reaction. After exposure to different high temperatures, one group of specimens was used to carry out shear tests directly, while the other group was re-cured for another 28 days.

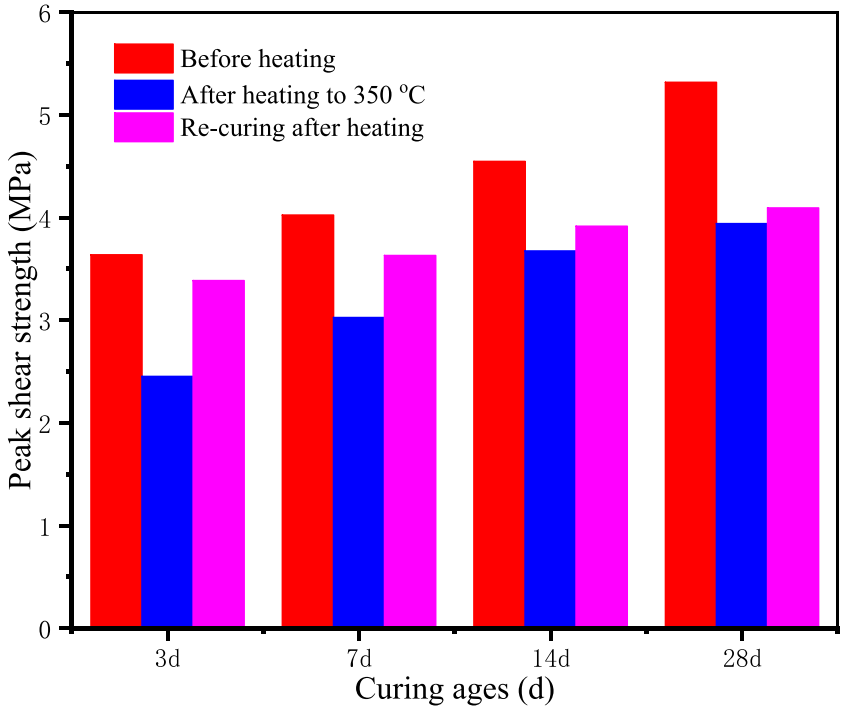

FIGURE 3
Peak shear strength of tested specimens with varied curing ages under.

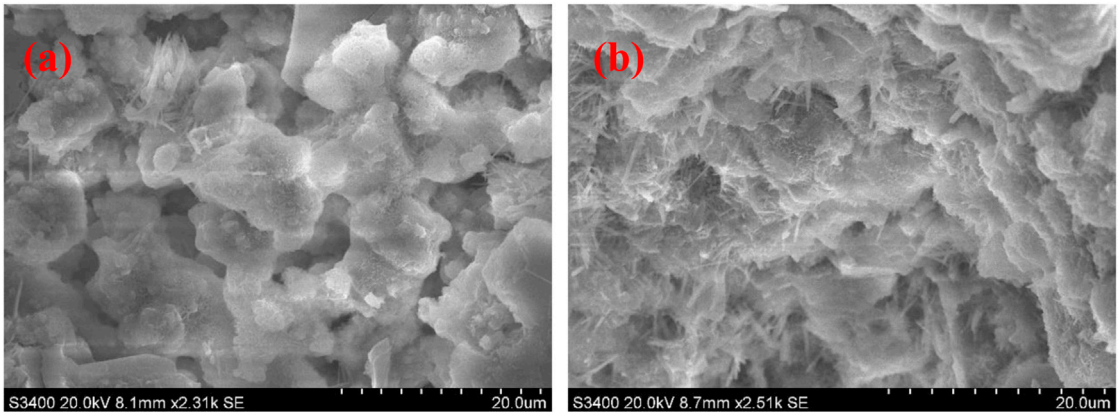

FIGURE 4
SEM images of the concrete before heating with curing ages; **(A)** 3 days and **(B)** 14 days.

The peak shear strength of concretes after heating shows a similar changing trend to that of specimens before heating, i.e., the shear strength increases with curing ages. After re-curing, the peak shear strength increases to a certain level depending on the curing ages. In general, the strength recoverability decreases with the curing ages. For example, in the case of re-cured concretes after exposing to 350°C, the peak shear strength increased by 0.93, 0.6, 0.24, and 0.15 MPa for concretes with 3, 7, 14, and 28 days curing ages, respectively.

To further interpret the test results, SEM tests were carried out on concretes with different curing ages before heating, after heating, and re-curing after heating. Figure 4 shows the SEM images of the concretes before heating. With the increase of curing ages, the hydration products (such as C-S-H, CH) increase gradually, which results in the enhancement of concrete density and integration. For specimens with curing ages of 3 and 7 days, the degree of hydration is very low. There exist a lot of free water and pore voids within the material. Therefore, the flocculent structure of hydration products and the internal structure are loose (Li et al., 2017). While for specimens with curing ages of 14 and 28 days, the degree of hydration is much higher than the one with 3 and 7 days curing ages. A larger number of hydration products are generated

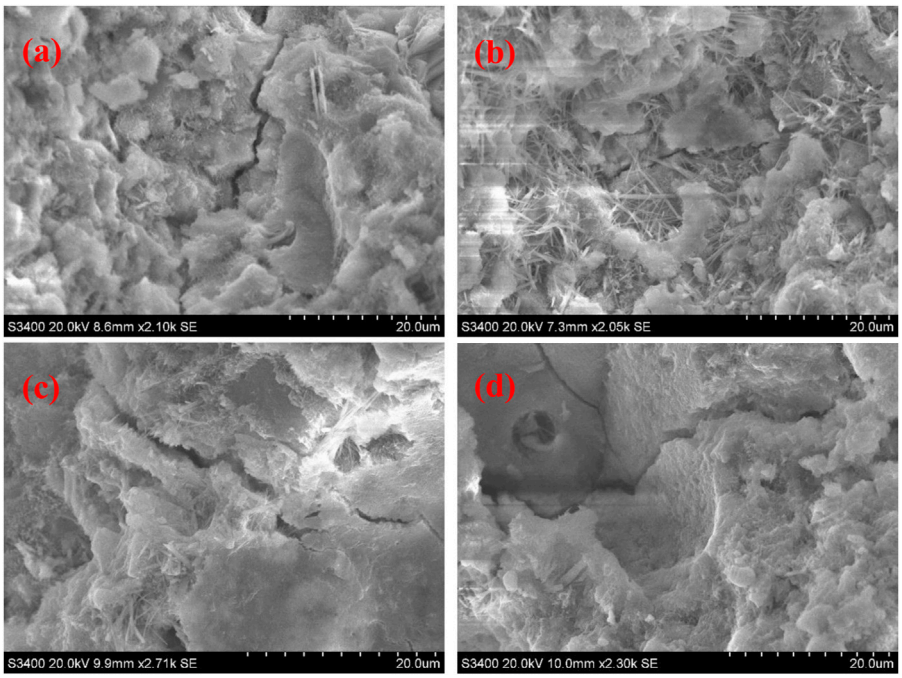

FIGURE 5
SEM images of the concretes after exposure to temperature of 350°C with different curing ages; **(A)** 3 days; **(B)** 7 days; **(C)** 14 days; and **(D)** 28 days.

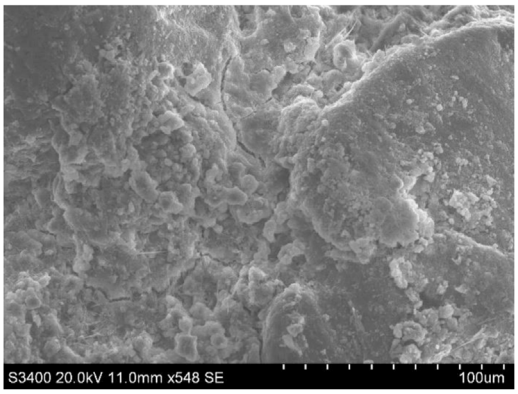

FIGURE 6
SEM image of concrete (curing ages 7d) re-curing after heating.

which results in a decrease in free water and porosity. Hence, the flocculent structure of hydration products and the internal structure become denser. This provides an explanation that the peak shear strength of early-age concrete before heating increases with the curing ages.

Figure 5 shows the SEM images of the concretes after exposure to temperature of 350°C with different curing ages. Thermal-induced cracks are observed at this temperature regardless of curing ages. In the case of concretes with curing ages of 3 and 7 days, thermal-induced cracks were induced because of the loose internal structure. Although the integrity of concretes with 14 and 28 days curing ages are denser, the free water and crystal water were difficult to release when subjected to high temperature, leading to high water vapor pressure inside the specimen. As a result, thermal-induced cracks were also observed in concretes with 14 and 28 days curing ages.

Figure 6 shows the SEM image of the concretes (curing ages 7 days) re-curing after heating to 350°C. By detail examining the SEM image of the specimen, there are many remnants of hydration products within concretes after re-curing. For the specimens with curing ages less than 28 days, the degree of hydration is low. The less the curing ages before heating, the less the hydration products. After re-curing, many remnants of hydration products were generated, especially for specimens with low hydration degrees. As shown in Figure 6, these remnants of hydration products can fill the voids or cracks induced by thermal damage, hence improving the specimen strength. Since the specimen with 3 days curing ages before heating had the largest cement continuing to hydrate, the shear strength increment after re-curing was the largest compared to the concretes with other curing ages.

3.3 Effect of high temperature on shear properties

3.3.1 Peak shear strength

Figure 7 shows the peak shear strength of early-age concretes under different temperature treatments. Under the same curing ages, the peak shear strength of early-age concretes increases first and then decreases with the exposed high temperature. For example, the peak shear strength of concretes at curing ages of 14 days is 4.55 MPa before heating, which increased to 4.79 MPa when heating

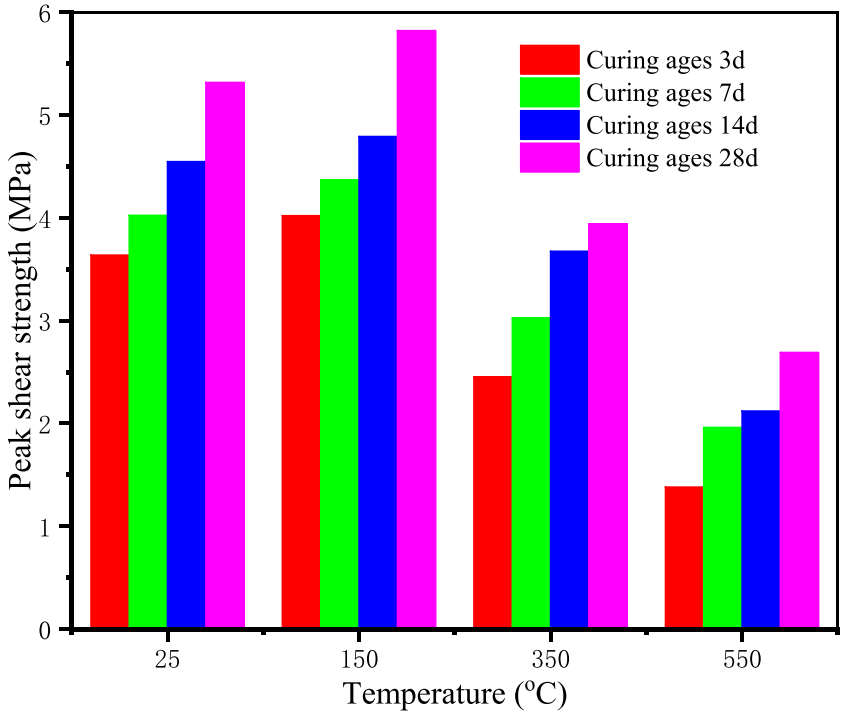

FIGURE 7
The peak shear stresses of early-age concrete under different temperature treatments.

FIGURE 8
Early-age concretes (14d) after high temperature treatment.

to 150°C. While exposed to temperature of 350°C and 550°C, the peak shear strength of early-age concretes decreased to 3.67 and 2.12 MPa, respectively.

The main characteristic of early-age concrete is inadequate hydration reaction. The effect of high temperature on the early-age concrete is twofold. On the one hand, high temperature treatment can accelerate the hydration process. Meanwhile, the evaporation of free water may dehydrated the C-S-H gel, which results in the hardening of the cement slurry, and an increase in the chemical bonding forces (Kocak and Nas, 2014; Li et al., 2021). These factors cause an increase in the peak shear strength. On the other hand, thermal damage occurs in concrete when exposed to high temperatures. High temperature can cause microstructural changes in cement pastes, and produce thermal stress which induces micro-cracking in concrete. As a result, the strength of thermal damaged concretes is less than that of unheated concretes.

In the case of early-age concretes exposed to 150°C, the thermal damage to the concrete can be ignored. As shown in Figure 8, no obvious cracks are observed on the concrete surface. While the hydration reaction is promoted and the chemical bonding forces is strengthened, leading to an increase in shear strength. In the case of early-age concretes exposed to 350°C, part of the chemical-bound water is removed. Several micro-cracks are observed on the crack surface due to high temperature. Although the accelerated hydration of cement improves the shear strength, the damage to concretes is more significant due to the thermal cracking. Therefore, the peak shear strength of early-age concrete exposed to 350°C is lower than

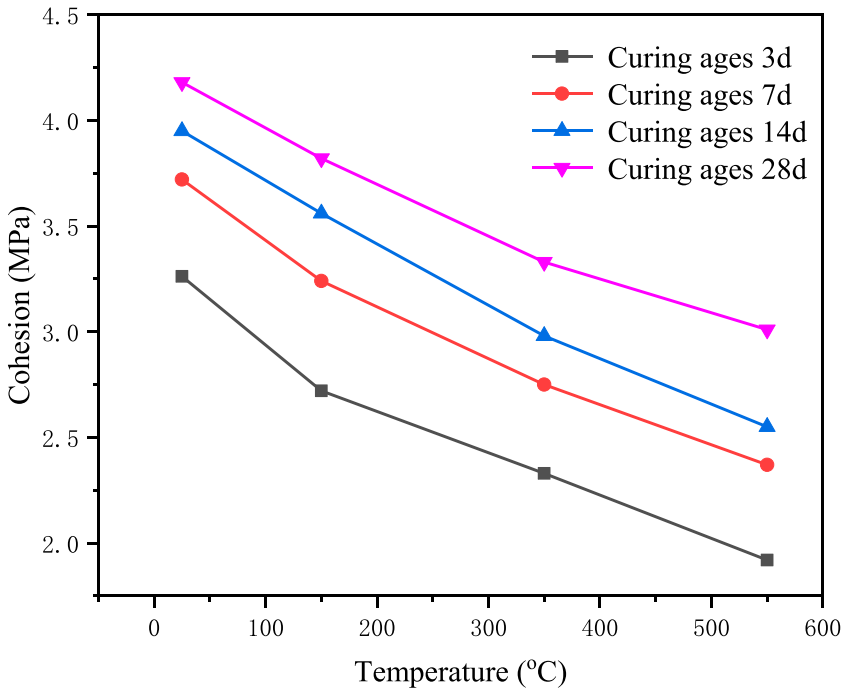

FIGURE 9
Cohesion of early-age concrete (14d) under different temperature treatments.

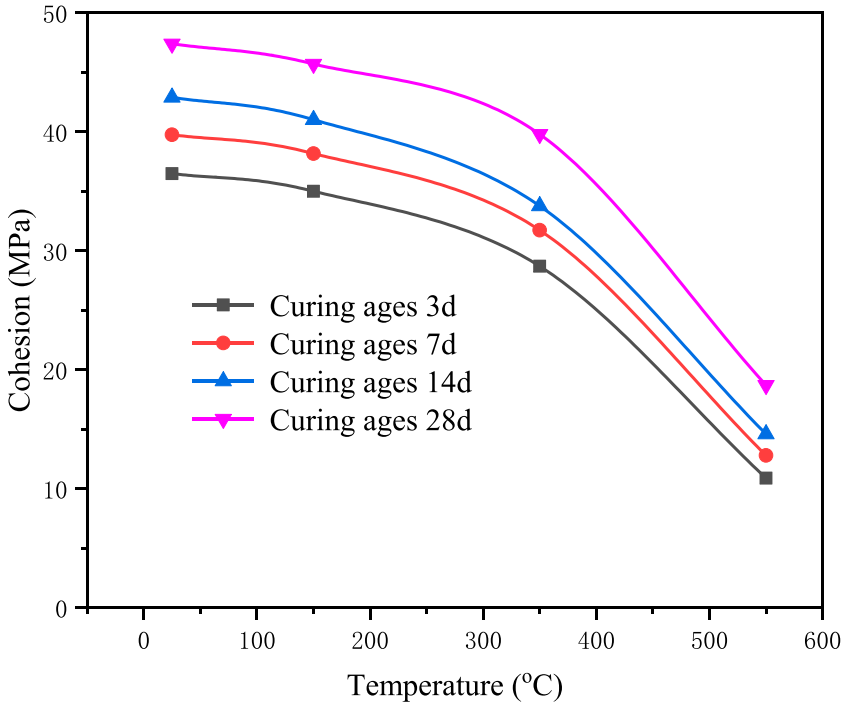

FIGURE 10
Internal friction angle of early-age concrete (14d) under different temperature treatments.

that of unheated specimens. After exposure to 550°C, both physical and chemical bond water are released completely. Thermal-induced micro-cracks increase considerably causing macroscopic damages in early-age concretes. As shown in Figure 8, a large number of cracks are observed on the concrete surface. These cracks coalesced causing a rapid decrease in shear strength.

3.3.2 Shear strength parameters

To obtain the shear strength parameters, additional shear tests were conducted under different normal stresses. Previous studies have indicated that normal stress can considerably enhance the shear resistance of concretes (Zhang et al., 2019; Zhang et al., 2020). Experimental results show that with the increase of normal stress, the peak strength of specimens for the same temperature treatments increases linearly. The Mohr-Coulomb criterion can be used to describe the relationship.

$$\tau_f = c + \sigma_N \times \tan(\varphi) \quad (1)$$

where τ_f and σ_N represent the peak shear stress and normal stress, respectively, c and φ are the cohesion and internal friction angle, respectively.

Figure 9 shows the evolution of cohesion c with exposed temperature. With the increase of exposed temperature, cohesion c decreases linearly. Meanwhile, concretes with less curing ages exhibited more reduction of cohesion under the same thermal treatment conditions. However, this tendency was not found in the evolution of internal friction angle with exposed temperature. As shown in Figure 10, the internal friction angle decreased nonlinearly with temperature. For example, the internal friction angle decreased by 4.38%, 17.67%, and 65.9% for specimens with 14 days curing ages when the specimens were heated to 150 °C, 350 °C, and 350 °C, respectively. In general, both the nominal cohesion and internal friction angle were reduced after high temperature treatments. Therefore, thermal damage can result in deterioration of shear resistance of concrete, especially for concretes with less curing ages.

The cohesion of concretes consists of two parts: 1) interlock between cement and aggregate; 2) adhesion between the cementitious pastes and the aggregates (Zhang et al., 2019). Previous studies show that temperature below 550°C removes the physical and chemical water which mainly causes the damage of cement pastes but has little influence on the aggregates (Zhao et al., 2021a). The thermal damage destroys the cementations matrix leading to the weakening of the cement-aggregate interlock and adhesion. Hence, the concrete cohesion decreases linearly with the exposed temperature.

Internal friction angle includes two portions: contact friction and shear dilation (Wong et al., 2007). After high temperature treatment, the pore structures become loose due to the removal of physical and chemical bound water. This change of microstructure may result in a decrease in shear dilation angle and friction resistance of concrete. Such reduction increases with the exposed temperature. Hence, the concrete internal friction angle decreases non-linearly with the exposed temperature.

4 Conclusion

In this paper, a comprehensive experimental study on shear properties of early-age concretes under elevated temperature is presented. Microstructure characteristic of early-age concretes before heating, after heating, and re-curing after heating is analyzed through NMR and SEM tests. The following conclusions can be drawn.

(1) NMR test results show that the peaks of the T_2 curve become higher after the high temperature treatment, but the position of the peaks remains unchanged. This indicates that high temperature treatment of early-age concrete multiplies the number of pores but has little influence on the change of pore size distribution. After re-curing, the T_2 curve shits to left but the amplitude of the T_2 peaks remains nearly unchanged, indicating that re-curing treatment reduces pore size of concretes but has little influence on pore numbers.
(2) Under the same exposed temperature, the shear strength of concretes before heating, after heating, and re-curing after heating increases gradually with curing ages. The peak shear strength of early-age concrete before and after heating increases with the curing ages due to the cement hydration reaction. After re-curing, many remnants of hydration products were generated, which fill the voids or cracks induced by thermal damage, hence improving the specimen strength.
(3) High temperature treatment can accelerate the hydration process but also cause thermal damage occurs in concrete. Therefore, the peak shear strength of early-age concretes increases first and then decreases with the exposed high temperature.
(4) Cohesion and international friction angle were altered due to thermal damage. Both of them decreased over exposed temperature. This can be attributed to that thermal damage destroying the cementations matrix leading to the weakening of the cement-aggregate interlock and adhesion.

Data availability statement

The raw data supporting the conclusion of this article will be made available by the authors, without undue reservation.

Author contributions

ML: Writing–original draft. FG: Conceptualization, Supervision, Writing–review and editing.

Funding

The authors declare financial support was received for the research, authorship, and/or publication of this article. This research was supported by the Guizhou Provincial Science and Technology Foundation (Nos[2021]292 and [2021]N404).

Conflict of interest

The authors declare that the research was conducted in the absence of any commercial or financial relationships that could be construed as a potential conflict of interest.

Publisher's note

References

Ahn, Y. B., Jang, J. G., and Lee, H. K. (2016). Mechanical properties of lightweight concrete made with coal ashes after exposure to elevated temperatures. *Cem. Concr. Compos.* 72, 27–38. doi:10.1016/j.cemconcomp.2016.05.028

Bi, J., Liu, P., and Gan, F. (2020). Effects of the cooling treatment on the dynamic behavior of ordinary concrete exposed to high temperatures. *Constr. Build. Mater.* 248, 118688. doi:10.1016/j.conbuildmat.2020.118688

Chen, B., Li, C. L., and Chen, L. Z. (2009). Experimental study of mechanical properties of normal-strength concrete exposed to high temperatures at an early age. *Fire Saf. J.* 44, 997–1002. doi:10.1016/j.firesaf.2009.06.007

Frosch, G. P., Tillich, J. E., Haselmeier, R., Holz, M., and Althaus, E. (2000). Probing the pore space of geothermal reservoir sandstones by Nuclear Magnetic Resonance. *Geothermics* 29, 671–687. doi:10.1016/s0375-6505(00)00031-6

Jia, Z., Chen, C., Shi, J., Zhang, Y., Sun, Z., and Zhang, P. (2019). The microstructural change of C-S-H at elevated temperature in Portland cement/GGBFS blended system. *Cem. Concr. Res.* 123, 105773. doi:10.1016/j.cemconres.2019.05.018

Khan, M. S., and Abbas, H. (2015). Effect of elevated temperature on the behavior of high volume fly ash concrete. *Struct. Eng.* 19 (6), 1825–1831. doi:10.1007/s12205-014-1092-z

Kocak, Y., and Nas, S. (2014). The effect of using fly ash on the strength and hydration characteristics of blended cements. *Constr. Build. Mater* 73, 25–32. doi:10.1016/j.conbuildmat.2014.09.048

Laim, L., Santiago, A., Caetano, H., Craveiro, H. D., and Shahbazian, A. (2022). Numerical analysis and structural fire design of protected SHS steel columns with thermally enhanced gypsum-based mortars. *J. Build. Eng.* 54, 104629. doi:10.1016/j.jobe.2022.104629

Li, Q., Liu, L., Huang, Z., and Yuan, G. (2017). Residual compressive strength of cement-based grouting material with early ages after fire. *Constr. Build. Mater.* 138, 316–325. doi:10.1016/j.conbuildmat.2017.02.025

Li, Q., Lu, L., Yuan, G., and Doh, J. H. (2021). Influence of curing age on the mechanical properties of fly ash concrete exposed to elevated temperature. *Struct. Concr.* 22, E868–E883. doi:10.1002/suco.202000155

Lim, S., and Mondal, P. (2014). Micro- and nano-scale characterization to study the thermal degradation of cement-based materials. *Mater. Char.* 92, 15–25. doi:10.1016/j.matchar.2014.02.010

Liu, Y., Jin, B., Huo, J., and Li, Z. (2018). Effect of microstructure evolution on mechanical behaviour of concrete after high temperatures. *Mag. Concr. Res.* 70 (15), 770–784. doi:10.1680/jmacr.17.00197

Masse, S., Vetter, G., Boch, P., and Haehnel, C. (2002). Elastic modulus changes in cementitious materials submitted to thermal treatments up to 1000°C. *Adv. Cem. Res.* 14, 169–177. doi:10.1680/adcr.2002.14.4.169

Monte, F. L., Felicetti, R., and Miah, M. J. (2019). The influence of pore pressure on fracture behaviour of Normal-Strength and High-Performance Concretes at high temperature. *Cem. Concr. Comp.* 104, 103388. doi:10.1016/j.cemconcomp.2019.103388

Nadeem, A., Memon, S. A., and Lo, T. Y. (2014). The performance of fly ash and metakaolin concrete at elevated temperatures. *Constr. Build. Mater.* 62, 67–76. doi:10.1016/j.conbuildmat.2014.02.073

Nguyen, T. D., Pham, D. T., and Vu, M. N. (2019). Thermo-mechanically-induced thermal conductivity change and its effect on the behaviour of concrete. *Constr. Build. Mater.* 198, 98–105. doi:10.1016/j.conbuildmat.2018.11.146

Pan, Z., Tao, Z., Cao, Y. F., Wuhrer, R., and Murphy, T. (2018). Compressive strength and microstructure of alkali-activated fly ash/slag binders at high temperature. *Cem. Concr. Comp.* 86, 9–18. doi:10.1016/j.cemconcomp.2017.09.011

Shu, Q. J., Lu, L. M., Yuan, G. L., Zhong, C. S., and Xu, B. (2021). Experimental investigation on the mechanical properties of early-age concrete after heating up to 550 °C. *Eur. J. Environ. Civ. En.* 25 (8), 1364–1378. doi:10.1080/19648189.2019.1578269

Wang, C., Zhao, H., Zhao, Y., and Bi, J. (2022). Thermal characteristics and recoverability of early-age mortar consisting of a flame retardant $Mg(OH)_2$. *J. Build. Eng.* 57, 104897. doi:10.1016/j.jobe.2022.104897

Weng, L., Wu, Z., and Li, X. (2018). Mesodamage characteristics of rock with a pre-cut opening under combined static–dynamic loads: A nuclear magnetic resonance (NMR) investigation (NMR). *Investig. Rock Mech. Rock Eng.* 51, 2339–2354. doi:10.1007/s00603-018-1483-4

Wong, R. C. K., Ma, S. K. Y., Wong, R. H. C., and Chau, K. T. (2007). Shear strength components of concrete under direct shearing. *Cem. Concr. Res.* 37 (8), 1248–1256. doi:10.1016/j.cemconres.2007.02.021

Xotta, G., Mazzucco, G., Salomoni, V. A., Majorana, C. E., and Willam, K. J. (2015). Composite behavior of concrete materials under high temperatures. *Int. J. Solids Struct.* 64–65, 86–99. doi:10.1016/j.ijsolstr.2015.03.016

Yuan, M., Qiang, S., Xu, Y., Li, Y., and Xu, W. (2021). Research on cracking mechanism of early-age restrained concrete under high-temperature and low-humidity environment. *Materials* 14, 4084. doi:10.3390/ma14154084

Zhang, Z. Y., Jin, X. G., Lin, S. Z., and Bi, J. (2019). Direct shear behavior of sulfate-exposed shotcrete: experimental and modelling research. *Constr. Build. Mater.* 210, 607–619. doi:10.1016/j.conbuildmat.2019.03.229

Zhang, Z. Y., Jin, X. G., and Luo, W. (2018). Mechanical responses of shotcrete specimens in direct shear tests. *Constr. Build. Mater.* 188, 305–313. doi:10.1016/j.conbuildmat.2018.08.097

Zhang, Z. Y., Zhou, J. T., Zou, Y., Yang, J., and Bi, J. (2020). Change on shear strength of concrete fully immersed in sulfate solutions. *Constr. Build. Mater.* 235, 117463. doi:10.1016/j.conbuildmat.2019.117463

Zhao, Y., Ding, D., Bi, J., Wang, C., and Liu, P. (2021a). Experimental study on mechanical properties of precast cracked concrete under different cooling methods. *Constr. Build. Mater.* 301, 124141. doi:10.1016/j.conbuildmat.2021.124141

Zhao, Y., Wang, C., and Bi, J. (2020). Analysis of fractured rock permeability evolution under unloading conditions by the model of elastoplastic contact between rough surfaces. *Rock Mech. Rock Eng.* 53, 5795–5808. doi:10.1007/s00603-020-02224-x

Zhao, Y., Wang, C., Ning, L., Zhao, H. F., and Bi, J. (2022). Pore and fracture development in coal under stress conditions based on nuclear magnetic resonance and fractal theory. *Fuel* 309, 122112. doi:10.1016/j.fuel.2021.122112

Zhao, Y., Wang, C., Teng, M., and Bi, J. (2021b). Observation on microstructure and shear behavior of mortar due to thermal shock. *Cem. Concr. Comp.* 121, 104106. doi:10.1016/j.cemconcomp.2021.104106

frontiers | Frontiers in Materials

TYPE Original Research
PUBLISHED 12 October 2023
DOI 10.3389/fmats.2023.1276118

OPEN ACCESS

EDITED BY
Zhongya Zhang,
Chongqing Jiaotong University, China

REVIEWED BY
Jianan Qi,
Southeast University, China
Jiale Zhou,
Dongguan University of Technology, China
Binglin Lai,
Southeast University, China
Yang Zhang,
Hunan University, China

*CORRESPONDENCE
Yongsi Li,
2110391046@st.gxu.edu.cn

RECEIVED 11 August 2023
ACCEPTED 19 September 2023
PUBLISHED 12 October 2023

CITATION
Li B, Li Y, Liu X, Liu X, Zhu S and Ke L (2023), Section optimization design of UHPC beam bridges based on improved particle swarm optimization.
Front. Mater. 10:1276118.
doi: 10.3389/fmats.2023.1276118

Section optimization design of UHPC beam bridges based on improved particle swarm optimization

Beian Li[1], Yongsi Li[2]*, Xiang Liu[1], Xianlin Liu[1], Siwen Zhu[2] and Lu Ke[2]

[1]Guangxi Xinxiang Expressway Co., Ltd., Nanning, China, [2]School of Civil Engineering and Architecture, Guangxi University, Nanning, China

Ultra-high performance concrete has excellent mechanical properties such as ultra-high strength and high durability, and has a broad application prospect in the field of bridge engineering. To make full use of the superior mechanical properties of UHPC and reduce the cost of the bridge, the particle swarm optimization algorithm is used to optimize the structural design of the UHPC beam bridge; Aiming at the problem that the traditional particle swarm optimization algorithm is easy to fall into local optimum, the nonlinear adaptive weight update method is used to improve the particle swarm optimization algorithm. Based on the above-mentioned improved particle swarm optimization algorithm, the optimal design method of ordinary reinforced UHPC beams and prestressed UHPC beams with commonly used highway spans is studied. The reliability of the optimized structural limit state is analyzed by Monte Carlo (MC) importance sampling method. The results show that compared with the traditional particle swarm optimization algorithm, the improved particle swarm optimization algorithm has higher convergence speed and convergence accuracy. The optimal height-span ratio of ordinary reinforced UHPC beams decreases with the increase of the span, and the construction cost gradually increases; The optimal height-span ratio of the prestressed beam decreases first and then increases with the increase of the span, and the construction cost gradually increases. The calculation results of load capacity reliability indexes of optimization results are all higher than the target reliability indexes of similar components stipulated in China's "Uniform Standard for Structural Reliability Design of Highway Engineering".

KEYWORDS

ultra-high performance concrete, simply supported beam bridge, optimization design, improved particle swarm optimization, reliability

1 Introduction

Compared with conventional concrete, UHPC, designed based on particle packing theory, has excellent durability and significant compressive strength (Zhou et al., 2022; Ke et al., 2023a; Zhou et al., 2023). And UHPC can be combined with carbon fiber-reinforced polymer for high load or corrosive environments (Ke et al., 2023b; Ke et al., 2023c). Incorporating UHPC materials into bridge engineering structures can effectively reduce the structural weight and improve durability, and has broad application prospects (Zhou et al.,

2018; Xue et al., 2020). To make full use of the excellent performance of UHPC and minimize the cost, it is necessary to optimize the design of UHPC simply supported beam bridges.

At present, a lot of research has been carried out on the optimal design of concrete beams at home and abroad. Giuseppe et al. (Quaranta et al., 2014) used a special technique based on differential evolution to minimize the cost of prestressed concrete beams. Guo and Zhang (2022) proposed a multi-objective model for the optimal design of reinforced concrete beams, where the optimal solution involves a trade-off between cost and deflection. Zekeriya et al. (Aydın and Ayvaz, 2013) optimized the overall cost of prestressed concrete bridges based on an improved hybrid genetic algorithm, considering working stress, ultimate strength, ductility limit, deflection, and geometric constraints. Akintunde (2021) carried out cost optimization of tension reinforcement in structural members by artificial neural networks. The results show that artificial neural network (ANN) can be used to design single-reinforced rectangular beams that minimize the cost of reinforced concrete beams while meeting code requirements. Although there are many methods for the optimal design of simply supported concrete beam bridges, most of them have the disadvantages of complex algorithms, large amounts of calculation, and difficulty in determining parameters.

Particle Swarm Optimization (PSO) is a concept of swarm intelligence that draws inspiration from neuroscience, cognitive psychology, social behavior, and behavioral science research (Wang et al., 2021). It is mainly used in the field of optimization (Jain et al., 2018; Aje and Josephat, 2020). In recent years, the PSO has been gradually applied in the field of civil engineering. For example, Wei et al. (2022) solved the reasonable main cable curve of the suspension bridge through the improved particle swarm optimization, and compared it with the N-R iterative method and the finite element method. The results show that the proposed improved particle swarm optimization method has high accuracy and fast calculation speed. Khajehzadeh et al. (2011) developed an improved particle swarm optimization method to optimize the design of the extended foundation and retaining wall so that the total cost is the lowest under the constraint conditions. Luh and Lin (2011) proposed a two-stage PSO-based optimization scheme for truss structures. Although PSO algorithms have been applied to the field of structural engineering, there is limited literature on the optimization of UHPC simply-supported beams.

In this article, based on the improved particle swarm optimization, the optimal design of the UHPC simply supported beam bridge is carried out with the lowest cost of the main beam of the superstructure as the objective function. Ordinary reinforced UHPC beams with spans of 10, 13, 16, 20, 25, and 30 m and prestressed UHPC beams with spans of 20, 25, 30, 35, 40, and 50 m were studied. The influence of the bridge span and the height of the main beam on the cost is respectively analyzed in this paper. Finally, The Monte Carlo importance sampling method is used to analyze the reliability of the limit state of the load-carrying capacity and the serviceability limit state of the optimization results and compare the reliability levels of structures with different spans and different height-span ratios.

2 Particle swarm optimization

Each particle in the particle swarm optimization algorithm represents a point in the d-dimensional space, and each particle has its own speed and position, as well as the fitness value of the corresponding objective function. Assuming that each particle is a small bird in a flock of birds, the position and speed of each bird are different. To achieve the purpose of finding food, each small bird constantly adjusts its position according to its own experience and that of its companions The flight speed changes its own position; the position closest to the food experienced by each bird during the flight is called the individual optimal position, and the optimal position where the entire population can find food at present is called the global optimal position.

In the standard particle swarm optimization algorithm, the position and velocity of the ith particle in the d-dimensional search space are denoted by $X_i(x_{i,1}, x_{i,2}\ldots x_{i,d})$ and $V_i = (v_{i,1}, v_{i,2}\ldots v_{i,d})$ respectively. In each iteration, the particle updates its velocity and position through the optimal solution $P_i = (p_{i,1}, p_{i,2}\ldots p_{i,d})$ found by itself and the optimal solution $P_g = (p_{g,1}, p_{g,2}\ldots p_{g,d})$ currently found by the entire population. At the same time, a certain inertial velocity is retained, to achieve the purpose of generating new populations. Particles update their velocity according to the Eq. 1 and update their positions according to Eq. 2. Position update is realized by speed update (Zhong et al., 2022).

$$v_{i,j}(t+1) = wv_{i,j}(t) + c_1 r_1\left[p_{i,j} - x_{i,j}(t)\right] + c_2 r_2\left[p_{g,t} - x_{i,j}(t)\right] \quad (1)$$

$$x_{i,j}(t+1) = x_{i,j}(t) + v_{i,j}(t+1), j = 1, 2, \ldots .d \quad (2)$$

where w is the inertia weight, which generally takes the value range between 0.4 and 0.9; c_1 and c_2 are the learning factors, which generally take c_1 and c_2 as 2; r_1 and r_2 take the random numbers uniformly distributed between 0 and 1; t is the number of iterations (Marini and Walczak, 2015).

2.1 Self-adaptive particle swarm optimization

The Self-Adaptive Particle Swarm Optimization (SAPSO) improves the convergence speed and optimization effect of the algorithm by introducing an adaptive mechanism. The SAPSO algorithm solves the imbalance problem between the ability to search the local optimal solution and the global optimal solution of the PSO algorithm, and changes the constant inertia weight coefficient to a nonlinear inertia weight coefficient that dynamically changes according to the fitness value (Chun and Zhenglin, 2012). The equation is as follows:

$$w = \begin{cases} w_{\min} - \dfrac{(w_{\max} - w_{\min}) \times (f - f_{\min})}{(f_{avg} - f_{\min})} & f \le f_{avg} \\ w_{\max} & f > f_{avg} \end{cases} \quad (3)$$

where f is the current fitness value of the particle; f_{avg} is the average fitness value of all the current particles of the particle; $f_{\min}$ is the minimum fitness value of all the current particles of the particle; $w_{\min}$, $w_{\max}$ are the minimum and maximum values of inertia coefficient, generally take $w_{\min} = 0.4$, $w_{\max} = 0.9$.

In Eq. 3, the inertia coefficient changes with the change of particle fitness. When the fitness of each particle tends to be the same or tends to be the optimal solution, the inertia coefficient will increase, otherwise the inertia coefficient will decrease. The inertia coefficient is smaller for particles with better-than-average fitness values, and conversely, it is larger for particles with worse-than-average fitness values.

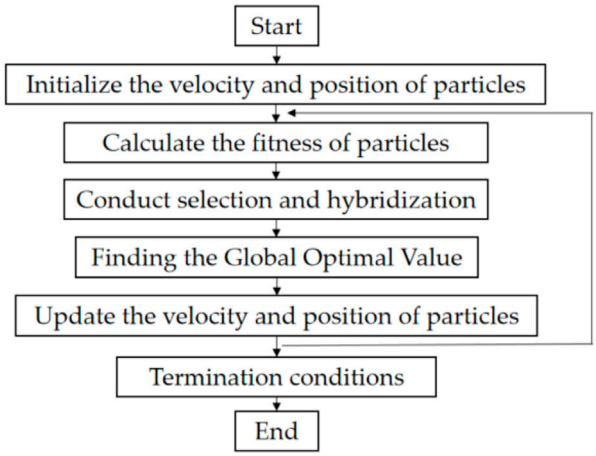

FIGURE 1
Flow chart of IPSO.

2.2 Breed particle swarm optimization

Breed Particle Swarm Optimization (BPSO) is an algorithm obtained by referring to hybridization in genetic algorithm based on the standard particle swarm algorithm (Chun and Zhenglin, 2012). After each iteration of the algorithm is completed, a certain number of particles are randomly selected for hybridization according to a certain hybridization probability, and the same number of offspring particles (*child*) are generated by hybridization, and the offspring particles are used to replace the parent particles (*parent*). Through the hybridization operation, the diversity of the particle population is increased, which is conducive to the optimization results jumping out of the local optimal solution. The calculation equation of offspring position is as follows.

$$child(x) = p \cdot parent_1(x) + (1-p) \cdot parent_2(x) \quad (4)$$

$$child(x) = (1-p) \cdot parent_1(x) + p \cdot parent_2(x) \quad (5)$$

where p is a random number between 0 and 1; $parent_1(x)$ is the position of the first parent particle; $parent_2(x)$ is the position of the second parent particle.

The velocity equations of the offspring particles are as follows.

$$child(v) = \frac{parent_1(v) + parent_2(v)}{|\, parent_1(v) + parent_2(v) \,|} \,|\, parent_1(v) \,| \quad (6)$$

$$child(v) = \frac{parent_1(v) + parent_2(v)}{|\, parent_1(v) + parent_2(v) \,|} \,|\, parent_2(v) \,| \quad (7)$$

where $parent_1(v)$ is the velocity of the first parent particle; $parent_2(v)$ is the velocity of the second parent particle.

2.3 Improved particle swarm optimization

The improved particle swarm optimization (IPSO) is based on the BPSO, adding an algorithm for selecting a hybrid operation, that is, after each iteration is completed, the fitness values are sorted, and the target fitness value is selected from it. After each iteration is completed, the fitness values are sorted, and some particles with good target fitness are selected from them to directly enter the next-generation, instead of simply randomly selecting a certain proportion of particles for hybridization; the remaining particles are randomly hybridized, Then compare with the particles of the parent generation, and select the better particles to enter the next-generation. At the same time, the adaptive inertia weight is used to improve the learning strategy of the particles, making full use of the excellent performance of the population, which is more conducive to jumping out of the local optimal results and speeding up the convergence speed. The search ability of the area between particles is improved, and it is easy to get rid of the local optimal solution, to obtain better search results. The flow chart of the IPSO is shown in Figure 1, and the specific steps are as follows.

Step 1. Determining the population size;

Step 2. Initialize the velocity and position of the population particles;

Step 3. Calculate the fitness value of each particle, then sort the fitness value, and select the particles with better fitness value to directly enter the next-generation

Step 4. Perform hybrid selection on the particles with poor fitness, and select the same number of particles from the results to enter the next-generation

Step 5. The speed and position are updated by Eqs 1, 2, and the inertia weight is updated by Eq. 3

Step 6. Check whether the iteration termination condition is satisfied, if not, go to Step 3, until the convergence condition is met or the maximum number of iterations is reached, and the corresponding optimal fitness value is obtained.

2.4 Comparison of algorithm convergence

The fitness of PSO is the value of the objective function. This section compares the convergence performance of each optimization algorithm by solving the minimal value of the Ackley function, which has the characteristics of a large space of feasible solutions and the existence of a large number of local minima, so it is more difficult to solve the global optimal solution, which has the following functional form.

$$f(x) = -20\exp\left(-0.2\sqrt{\frac{1}{n}\sum_{i=1}^{n}x_i^2}\right) - \exp\left(\frac{1}{n}\sum_{i=1}^{n}\cos(2\pi x_i)\right) + 20 + e \quad (8)$$

The PSO, SAPSO, BPSO, and IPSO are used to calculate the Ackley function, respectively. The iterative process of calculating the Ackley function by four different algorithms is shown in Figure 2. From Figure 2, it can be seen that the smallest fitness is obtained by using the IPSO calculation. Therefore, it can be proved that the IPSO proposed in this article is less likely to fall into the local optimum and the optimal solution obtained is more accurate compared with the other three algorithms.

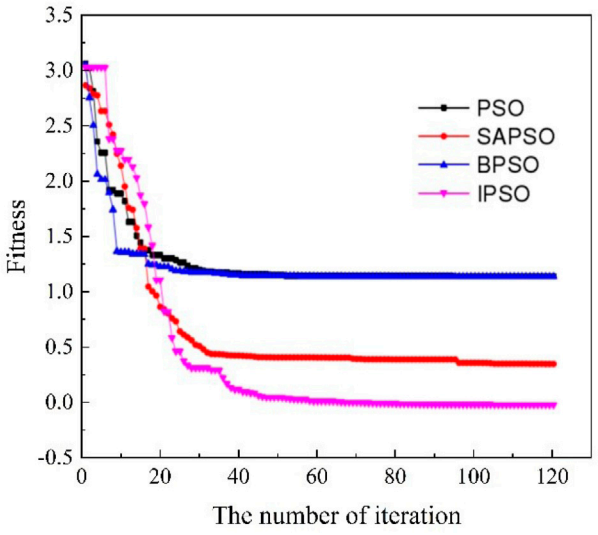

FIGURE 2
Iterative process of calculating Ackley function by different algorithms.

3 Optimal design

Many factors affect the cost of the main beam in bridge design. The main parameters include the concrete strength grade, the type of prestressed steel bars and ordinary steel bars, the size of the main beam section, the formwork cost, and the construction cost. It is very complicated and unnecessary. To simplify the calculation, in the optimal design, the parameters that control the project cost are directly selected as design variables, while other factors do not change much and can be regarded as constants.

3.1 Design load

3.1.1 Permanent load

(1) Self-weight: calculated based on the actual UHPC and reinforcement dosage. The self-weight of UHPC is 26 kN/m^3, and the self-weight of reinforcement is 78.5 kN/m^3.
(2) Auxiliary facilities and secondary dead loads: Consider bridge paving and guardrails, calculated according to the actual situation.

3.1.2 Live load

The moving load is in accordance with the "General Code for Design of Highway Bridges and Culverts" (JTGD60-2015), the road is grade I, the lateral distribution coefficient is calculated according to the hinged beam method, and the impact coefficient is calculated using the fundamental frequency of the structure.

3.2 Section parameters

The elastic modulus of UHPC used in this paper is 48.5 GPa, and the compressive strength is 150 MPa. The ordinary reinforced UHPC and prestressed UHPC T-beam bridges are shown in Figure 3.

3.3 Structural parameters and design variables

In this article, the width of the bridge deck is 12 m. When the bridge span is less than 20 m, the flange width is 1.5 m and eight beams are used in the transverse direction; when the bridge span is greater than or equal to 20 m, the flange width is 2 m, and six beams are used in the transverse direction.

(1) The equivalent thickness of the upper flange plate is taken as $h_f \geq$ 13 cm, the thickness of the root of the stalk axle is taken as $h_{fl} \geq$ 13 cm + b, and the angle of the stalk axle is set at the intersection of the upper flange and the web, with a slope of tanα = 1:1;
(2) The arrangement of reinforcement for the lower flange plate is taken into consideration, with ordinary reinforcement section $h_d \geq$ 13 cm, and prestressed section $h_d \geq$ 18 cm, the lower flange and web intersection to set the stem axle, stem axle slope to take tanβ = 1:1;
(3) The width of the web is taken as $b \geq$ 10 cm, and the thickness of the end web is taken as $b_{end} \geq b$ + 8 cm;
(4) Ordinary reinforcement uses HRB400 steel bar with a diameter of 28 mm. Prestressing reinforcement employs Φs 15.2 1860 steel strand, with the number N of steel bars used as the design variable during calculation.

3.4 Calculation method

3.4.1 Calculation model for flexural capacity

For ordinary concrete members, due to the small tensile strength of ordinary concrete, the contribution of its tensile strength to the structural bearing capacity has not been considered. Compared with ordinary concrete, UHPC materials have higher tensile strength, so their contribution to bearing capacity cannot be ignored, and the contribution of material tensile strength is considered in existing foreign codes or guidelines. According to the literature (Li, 2010), the contribution of the tensile strength of UHPC to the section bearing capacity varies with the reinforcement ratio, and the variation range is 10%–40%.

Theoretically, the strain value at each position on the section can be calculated according to the assumption of a plane section, the stress value can be obtained according to the constitutive relationship, and finally the bearing capacity of the section can be obtained through integral calculation. But such a calculation process is too complicated. In this paper, the compressive stress distribution and tensile stress distribution of UHPC are both equivalent to a rectangle, as shown in Figure 4. According to the principle that the resultant force and acting position of the UHPC compressive stress remain unchanged and the resultant force and acting position of the UHPC tensile stress remain unchanged, the equivalent coefficient of the compression zone can be determined as α = 0.87, β = 0.68, and the equivalent coefficient of the tension zone can be determined as k = 0.25.

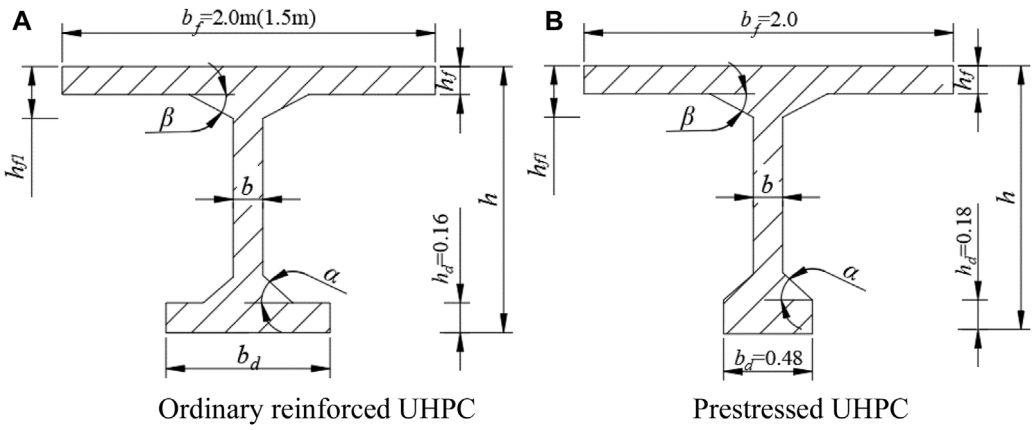

FIGURE 3
Basic section of T-beam. **(A)** Ordinary reinforced UHPC, **(B)** Prestressed UHPC.

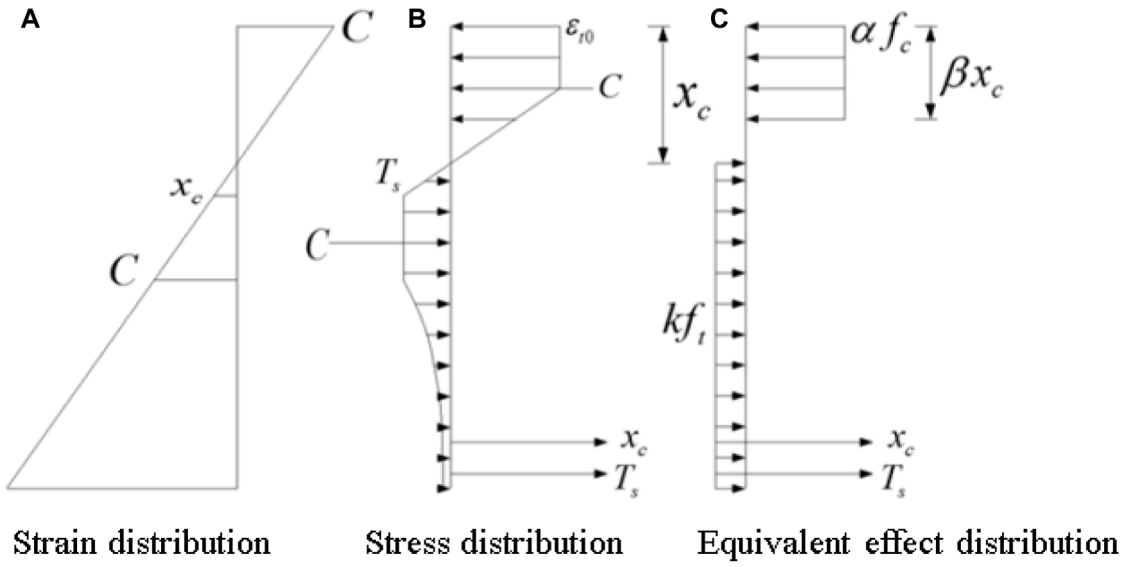

FIGURE 4
Stress-strain distribution diagram. **(A)** Strain distribution, **(B)** stress distribution, **(C)** equivalent effect of distribution.

The T-shaped section can be divided into two types according to the height of the compression zone of the section. The first category is that the height of the compression zone is smaller than the thickness of the flange plate; the second category is that the height of the compression zone is greater than the thickness of the flange plate. The formulas for calculating the flexural capacity of these two sections are introduced below.

When the following formula is satisfied, it is the first type of section:

$$kf_t(b_d - b)h_d + kf_t b\left(h - h_f/\beta\right) + f_y A_s + f_p A_p \leqslant \alpha f_c b_f h_f \quad (9)$$

The height of the compression zone is calculated according to the following formula:

$$\alpha f_c b_f x = kf_t(b_d - b)h_d + kf_t b(h - x/\beta) + f_y A_s + f_p A_p \quad (10)$$

The formula for calculating the flexural capacity of the first type of section is as follows:

$$M = \alpha f_c b_f x(h_0 - x/2) - kf_t b(h - x/\beta)\left(\frac{h_0 - x/\beta}{2} - c_0\right) \quad (11)$$

When Eq. 9 is not satisfied, the section belongs to the second type of section. The height of the compression zone is calculated according to the following formula:

$$\alpha f_c\left[bx + \left(b_f - b\right)h_f\right] = kf_t(b_d - b)h_d + kf_t b(h - x/\beta) + f_y A_s + f_p A_p \quad (12)$$

TABLE 1 Stress constraints of prestressed members.

Calculation project	Load combination	Stress limit(MPa)
Construction stage stress test calculation	Standard combination	58.8
Positive cross-section cracking in the use stage	Frequent combination	4.8
	Quasi-permanent combination	0
Positive cross-sectional pressure stress testing during the use stage	Standard combination	52.5
The main pressure stress test of the use stage	Standard combination	63.0

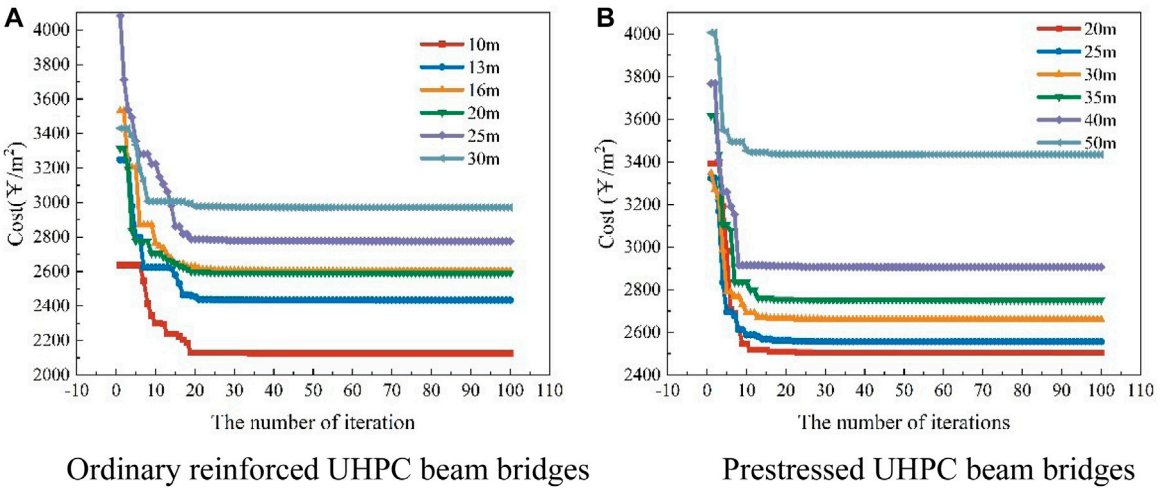

FIGURE 5
Iteration curve. **(A)** Ordinary reinforced UHPC beam bridges, **(B)** Prestressed UHPC beam bridges

The formula for calculating the flexural capacity of the second type of section is as follows:

$$M = \alpha f_c\left[bx\left(h_0 - x/2\right) + \left(b_f - b\right)h_f\left(h_0 - h_f/2\right)\right] - kf_t b\left(h - x/\beta\right)\left(\frac{h_0 - x/\beta}{2} - c_0\right) \quad (13)$$

where M is the design value of flexural capacity; f_c is the compressive strength of UHPC; f_t is the tensile strength of UHPC; f_y and f_p are the tensile strength of steel bar and steel strand respectively; A_s, A_p are the cross-section areas of steel bars and steel strands, respectively; h_0 is the distance from the steel bar to the edge of the compression zone of the section; and c_0 is the distance from the steel bar to the edge of the tension zone of the section.

3.4.2 Calculation model for shear capacity

According to the French guidelines for the design of UHPC structures (AFGC/SETRA, 2013), the shear capacity of ordinary reinforced UHPC and prestressed UHPC members is calculated according to the following equation:

$$V_{Rd} = V_{Rd,c} + V_{Rd,s} + V_{Rd,f} \quad (14)$$

$$V_{Rd,s} = A_{sw} z f_{ywd} \cot\theta / s \quad (15)$$

$$V_{Rd,f} = A_{fv}\sigma_{Rd,f} / \tan\theta \quad (16)$$

For ordinary reinforced UHPC members:

$$V_{Rd,c} = 0.21k'\sqrt{f_{ck}}b_w d / \gamma_{cf}\gamma_E \quad (17)$$

For prestressed UHPC members:

$$V_{Rd,c} = 0.24k'\sqrt{f_{ck}}b_w d / \gamma_{cf}\gamma_E \quad (18)$$

where $V_{Rd,c}$, $V_{Rd,s}$, $V_{Rd,f}$ are the contributions of UHPC, reinforcement, and fibers to the shear carrying capacity, respectively; γ_{cf}, γ_E are material sub-factors taken as γ_{cf} γ_E=1.5; f_{ck} is the standard value of the compressive strength of UHPC; b_w is the minimum width of the section in tension; d is the distance from the tensile reinforcement to the compression zone of the section; A_{sw} is the area of the vertical shear reinforcement; s is the spacing of the shear reinforcement; f_{ywd} is the yield strength of shear resistant reinforcement; θ is the angle between the principal compressive stress and the beam axis; A_{fv} is the area of the fiber affected zone, $A_{fv} = b_w d$; $\sigma_{Rd,f}$ is the participating tensile strength.

Maximum shear capacity:

$$V_{Rd,\max} = 2 \times 1.14\frac{\alpha_{cc}}{\gamma_c}b_w z f_{ck}^{2/3} / \left(\cot\theta + \tan\theta\right) \quad (19)$$

The following equation determines the final shear capacity:

$$V = \min\left(V_{Rd}, V_{Rd,\max}\right) \quad (20)$$

TABLE 2 Optimization results of ordinary reinforced UHPC beams.

L/m	*h*/mm	b_d/mm	*N*	Height-span ratio	Weight(kg/m^2)	Reinforcement(kg/m^2)	Cost(¥/m^2)
10	750	280	7	1/13.3	548.0	21.9	2125.9
13	850	330	9	1/15.3	624.6	27.4	2433.8
16	980	380	10	1/16.3	664.2	31.5	2602.9
20	1,320	460	13	1/15.2	650.0	29.2	2590.5
25	1,450	580	15	1/17.2	706.8	36.0	2776.5
30	1,600	720	20	1/18.8	746.0	46.8	2971.5

TABLE 3 Optimization results of prestressed UHPC beams.

L/m	*h*/mm	*N*	Height-span ratio	Weight (kg/m^2)	Reinforcement (kg/m^2)	Cost (¥/m^2)
20	740	27	1/27.0	641.5	16.2	2524.9
25	910	31	1/27.5	651.6	18.4	2575.8
30	1,110	34	1/27.0	677.0	20.1	2680.8
35	1,300	37	1/26.9	698.6	21.9	2771.7
40	1,500	40	1/26.7	737.8	23.4	2926.6
50	1920	47	1/26.0	813.4	27.4	3442.1

3.4.3 Crack width calculation formula

According to the French Design Guide for UHPC structures, the crack width at the location of the reinforcement is calculated according to the following formula:

$$w_s = s_{r,\max,f}\left(\varepsilon_{sm,f} - \varepsilon_{cm,f}\right) \tag{21}$$

where $s_{r,max,f}$ is the maximum crack spacing; $\varepsilon_{sm,f}$ is the average strain of the reinforcement; $\varepsilon_{cm,f}$ is the average strain of the UHPC.

The width of surface cracks in UHPC structures can be calculated based on the width of cracks at the location of reinforcement:

$$w_t = w_s \cdot (h - x - x') / (d - x - x') \tag{22}$$

where h is the height of the section; d is the effective height of the section; x is the height of the compression zone; x' is the height of the elastic tension zone.

3.5 Constraint condition

For the design of bridge structures, there are many constraints to be considered, such as strength constraints, cracking constraints, and deflection constraints. For ordinary reinforced UHPC structures, the following constraints are defined:

(1) Flexural capacity constraints

$$g_1 = M_d - M_u \le 0 \tag{23}$$

where M_d is the design value of the bending moment; M_u is the flexural capacity.

(2) Deformation constraints

$$g_2 = k \cdot 5M_s L^2 / 48BI - L/600 \le 0 \tag{24}$$

where k is the long-term growth coefficient of deflection, taken as 1.35; Ms is the frequency value of the moving load; BI is the converted stiffness of the mid-span section.

(3) Crack width constraint

Due to the excellent crack self-healing ability of UHPC, the durability of the structure will not be affected when the cracks in UHPC structures do not exceed 0.05 mm (Makita and Brühwiler, 2014).

$$g_3 = w_{\max} - 0.05 \le 0 \tag{25}$$

where w_{max} is the maximum crack width.

(4) Stress condition constraints

According to the literature (Ministry of Transport of the People's Republic of China, 2004), the stress constraint conditions of prestressed members are shown in Table 1.

3.6 Objective functions

The determination of the objective function is the most important step in the optimization design. In the optimal design of bridge section, the most applicable price standard is the lowest bridge section cost. The minimum cost of the main

TABLE 4 Optimization results of the fixed beam height of ordinary reinforced UHPC beams.

Span (m)	h (mm)	b_d (mm)	N	Height-span ratio	Cost (¥/m²)
10	500	540	13	1/20.0	2582.8
	600	390	11	1/16.7	2271.4
	750	280	7	1/13.3	2125.9
	850	270	7	1/11.8	2215.9
13	650	510	14	1/20.0	2660.8
	750	430	12	1/17.3	2569.5
	850	330	9	1/15.3	2433.8
	1,000	320	8	1/13.0	2524.3
16	800	510	15	1/20.0	2770.2
	900	480	13	1/17.8	2727.8
	980	380	11	1/16.3	2602.9
	1,100	380	10	1/14.5	2628.1
20	1,000	620	17	1/20.0	2683.3
	1,150	540	15	1/17.4	2627.9
	1,320	460	13	1/15.2	2590.6
	1,500	410	11	1/13.3	2657.0
25	1,250	710	19	1/20.0	2916.8
	1,400	620	17	1/17.9	2809.4
	1,450	580	16	1/17.2	2776.2
	1,600	540	15	1/15.6	2815.9
30	1,250	960	27	1/24.0	3245.2
	1,500	790	22	1/20.0	3125.7
	1,600	720	20	1/18.8	2971.5
	1700	700	19	1/17.6	3096.7

beam of the upper structure is the objective function, as shown in Eq. 26.

$$\min\ P = A_c \cdot P_{cu}/B + G_s \cdot P_{su} \tag{26}$$

where P is the cost per unit area; B is the bridge deck width; A_c is the cross-sectional area of the main beam; G_s is the amount of reinforcement per unit area; P_{cu} is the unit price of UHPC; P_{su} is the unit price of reinforcement.

4 Optimization results and analysis

4.1 Optimization results

In this paper, the commonly used particle swarm optimization algorithm is improved, and the optimization program of particle swarm optimization algorithm is compiled. Using the compiled MATLAB optimization program, the design and optimization of ordinary reinforced UHPC beams with spans of 10, 13, 16, 20, 25, and 30 m and prestressed UHPC beams with spans of 20, 25, 30, 35, 40, and 50 m were carried out. For ordinary reinforced UHPC beams, only three variables changed during the optimization design process, namely, beam height: h, base plate width: b_d, and number of steel bars: N. For prestressed UHPC beams, only two variables changed during the optimization design process, namely, the beam height h and the number of prestressed steel bars N. The cost iteration curves of simply supported beam bridges are shown in Figure 5, where (a) is the cost of ordinary reinforced UHPC beams with spans of 10–30 m under different iterations; (b) is the cost of prestressed UHPC beams with spans of 20–50 m under different iterations.

It can be seen from Figure 5 that when the IPSO is used to optimize the design of ordinary reinforced UHPC beams and prestressed UHPC beams with different spans, the number of iterations is stable and the convergence process is rapid. The optimization results of ordinary reinforced UHPC beams are shown in Table 2, and the optimization results of prestressed UHPC beams are shown in Table 3.

TABLE 5 Optimization results of the fixed beam height of prestressed UHPC beams.

Span (m)	h (mm)	b_d (mm)	N	Height-span ratio	Cost (¥/m²)
20	700	610	29	1/28.6	2658.0
	740	480	27	1/27.0	2504.9
	800	480	24	1/25.0	2529.7
25	800	840	38	1/31.3	3076.3
	910	480	31	1/27.5	2555.8
	1,000	480	27	1/25.0	2600.7
30	1,000	740	38	1/30.0	3013.6
	1,110	480	34	1/27.0	2660.8
	1,200	480	30	1/25.0	2694.7
35	1,200	690	42	1/29.2	3118.8
	1,300	480	37	1/26.9	2751.7
	1,400	480	34	1/25.0	2856.3
40	1,400	670	45	1/28.6	3172.4
	1,500	480	40	1/26.7	2906.6
	1,600	480	37	1/25.0	2950.3
50	1,800	660	53	1/27.8	3618.7
	1,920	480	48	1/26.0	3434.3
	2,000	480	46	1/25.0	3471.5

It can be seen from Table 2 and Table 3 that with the increase of the span, the optimal beam height of ordinary reinforced UHPC beams increases, the optimal height-span ratio decreases, and the width of the bottom plate, the number of steel bars, and the cost all increase; With the increase of the span, the optimal beam height of the prestressed UHPC beam increases, the height-span ratio first decreases and then increases, and the number of steel bars and the cost increase.

4.2 Optimization results for fixed beam heights

In the bridge design process, there are often requirements for the clearance height under the bridge, and the height of the main beam needs to be controlled. Based on the improved particle swarm optimization algorithm, the optimization results can be obtained when the beam height is limited to different values. Among them, Table 4 shows the optimization results of the fixed beam height of ordinary reinforced UHPC beams, and Table 5 shows the optimization results of the fixed beam height of prestressed UHPC beams.

From Table 4 and Table 5, it can be seen that when the beam height is increased on the basis of the optimal beam height, the base plate width and the number of steel bars of the ordinary reinforced UHPC beam are reduced; the base plate width of the prestressed UHPC beam is unchanged, and the amount of steel bars is reduced. When the beam height is reduced on the basis of the optimal beam height, the base plate width and the number of steel bars of the ordinary reinforced UHPC beam and the prestressed UHPC beam both increase. When the span of the bridge increases, the cost per square meter of the ordinary reinforced UHPC beam and the prestressed UHPC beam both increase; under the condition of the same span of the bridge, with the increase of beam height, the cost per square meter decreases at first and then increases.

According to the optimization results, the following conclusions are obtained: 1) The thickness of the upper flange does not change, the main reason is that the upper flange is wide, and increasing the thickness has a greater impact on the cost; The thickness of the web does not change, the main reason is that compared with increasing the bottom plate width, increasing the web width contributes less to the stiffness of the beam. 2) When the beam height is increased on the basis of the optimal beam height, in order to meet the layout of the prestressed pipe, the width of the beam floor remains unchanged; when the beam height is reduced on the basis of the optimal beam height, it is necessary to greatly increase the width of the bottom plate to meet the requirements of structural stiffness. 3) Under the same span, the number of steel bars increases with the decrease of beam height, because with the decrease of beam height, the internal force arm of steel bar also decreases. In order to meet the requirements of flexural capacity, it is necessary to increase the number of steel bars. 4) As the UHPC cost is the main factor affecting the construction cost, the price of steel bar and steel strand is only a small part, so the change of beam section size will directly affect the construction cost. For the beam with higher beam height, the increase of beam height is the main reason for the increase of cost; for the beam with lower beam height, in order to meet the needs of stiffness, the horseshoe section increases greatly, which leads to the increase of cost.

TABLE 6 Statistical parameters of random variables.

Random variables	Average/standard value	Mutant coefficient	Distributed type	References
M_{D1}	1.0212	0.0462	Normality	Literature Ministry of Transport of the People's Republic of China (1999)
M_{D2}	0.9891	0.1114	Normality	Literature Ministry of Transport of the People's Republic of China (1999)
V_{D1}	1.0212	0.0462	Normality	Literature Ministry of Transport of the People's Republic of China (1999)
V_{D2}	0.9891	0.1114	Normality	Literature Ministry of Transport of the People's Republic of China (1999)
M_{Q1}	0.7995	0.0862	Extreme value I-type	Literature Ministry of Transport of the People's Republic of China (1999)
M_{Q2}	0.7995	0.0862	Extreme value I-type	Literature Ministry of Transport of the People's Republic of China (1999)
V_{Q1}	0.7187	0.0769	Extreme value I-type	Literature Ministry of Transport of the People's Republic of China (1999)
V_{Q2}	0.7187	0.0769	Extreme value I-type	Literature Ministry of Transport of the People's Republic of China (1999)
f_{pk}	1.0000	0.1000	Normality	Literature Ministry of Transport of the People's Republic of China (1999)
f_y	1.0873	0.0645	Normality	Literature Ministry of Transport of the People's Republic of China (1999)
A_s	1.0000	0.0125	Normality	Literature Ministry of Transport of the People's Republic of China (1999)
f_c	1.0146	0.2500	Normality	Literature Steinberg (2010)
f_t	1.0330	0.0600	Extreme value I-type	Literature Steinberg (2010)
h_f	1.0320	0.1019	Normality	Literature Ministry of Transport of the People's Republic of China (1999)
b_f	1.0013	0.0081	Normality	Literature Ministry of Transport of the People's Republic of China (1999)
b	1.0013	0.0081	Normality	Literature Ministry of Transport of the People's Republic of China (1999)
b_d	1.0013	0.0081	Normality	Literature Ministry of Transport of the People's Republic of China (1999)
h_0	1.0124	0.0229	Normality	Literature Ministry of Transport of the People's Republic of China (1999)
An	1.0000	0.0800	Normality	Literature Li and Bao (1997)
f_{pe}	1.0000	0.0400	Normality	Literature Li and Bao (1997)
W_n	1.0000	0.0640	Normality	Literature Li and Bao (1997)
W_0	1.0000	0.0064	Normality	Literature Li and Bao (1997)
e_{pn}	1.0000	0.0060	Normality	Literature Li and Bao (1997)
I_0	1.0000	0.0300	Normality	Literature Li and Bao (1997)
E_C	1.0000	0.0200	Normality	Literature Steinberg (2010)

5 Reliability analysis

The reliability analysis of the bridge section optimized results was conducted under the current bridge design codes in China. Based on these codes, limit state equations were defined for the bridge structure's load-carrying capacity and normal use states. The Monte Carlo (MC) important sampling method was used to analyze the reliability of the optimized structure in these limit states. The reliability levels of beams with different span and height-span ratios were compared.

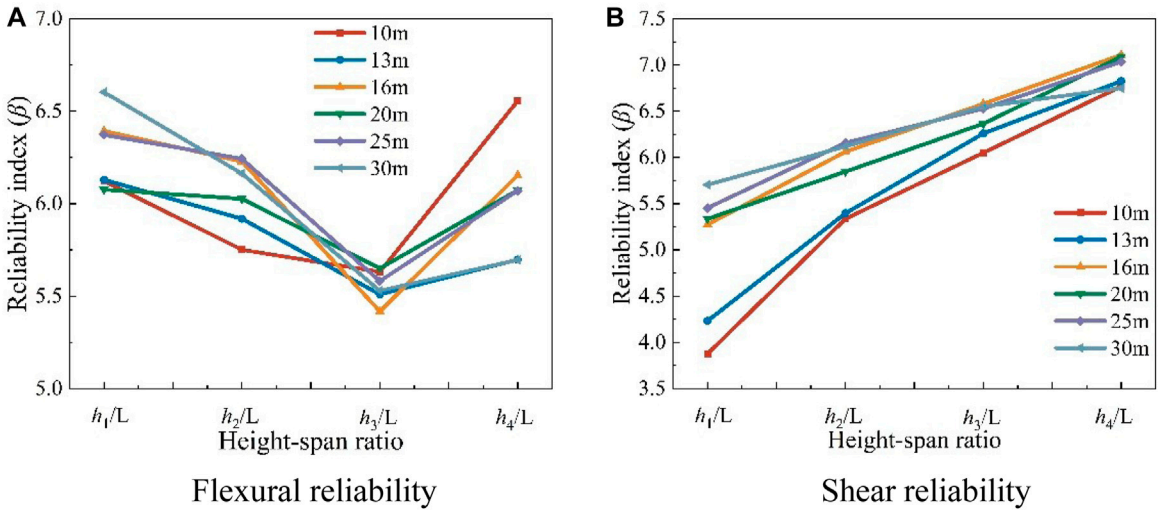

FIGURE 6
Reliability index of ordinary reinforced UHPC beam. **(A)** Flexural reliability, **(B)** Shear reliability.

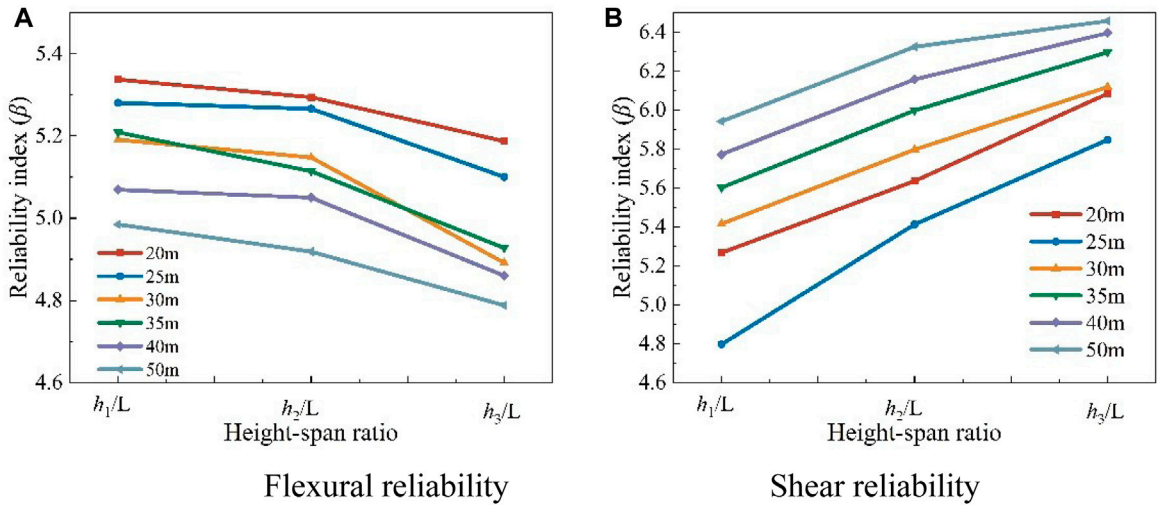

FIGURE 7
Reliability index of prestressed UHPC beam. **(A)** Flexural reliability, **(B)** Shear reliability.

5.1 Load effects and random variable parameters

5.1.1 Load effects

For simply supported beams, the effects of constant load and live load (vehicle load) are mainly considered, and the values of the mid-span moment and support shear force generated by both are calculated. M_{D1} is the value of the mid-span moment for the self-weight of the precast beam, M_{D2} is the value of the mid-span moment for the secondary dead load (including paving and guardrail), V_{D1} is the value of support point shear for the self-weight of the precast beam, V_{D2} is the value of support point shear for the secondary dead load (including paving and guardrail); M_{Q1} is the bending moment value of vehicle load for the mid-span section, M_{Q2} is the bending moment value of the impact load; V_{Q1} is the value of vehicle load shear at the support point section, V_{Q2} is the value of impact load shear. The load value is calculated based on the optimization results.

5.1.2 Random variable parameters

Take each parameter in the reliability calculation function as a random variable, and refer to the relevant domestic and foreign literature to list the statistical parameters of each random variable in Table 6. There is no relevant literature on the statistical parameters of the tensile strength f_{pk} of prestressed steel bars in actual engineering statistics parameters in China. Here, reference is made to the data of ordinary steel bars, and its coefficient of variation is taken as 0.1.

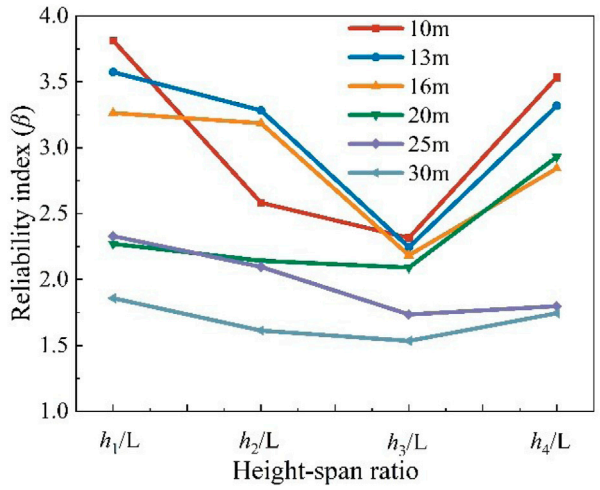

FIGURE 8
Reliability index of maximum crack width.

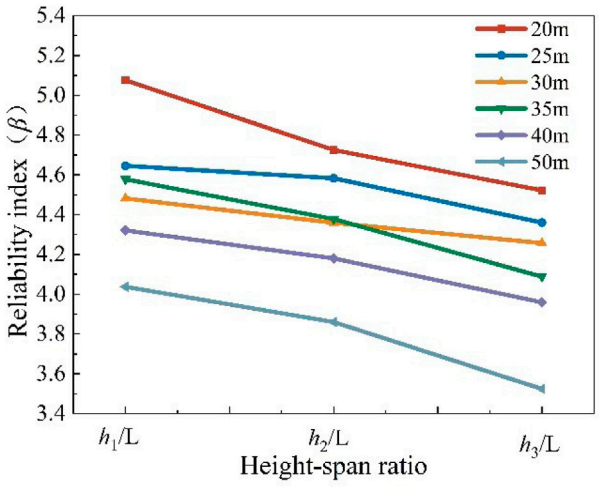

FIGURE 9
Reliability index of normal section crack resistance.

5.2 Reliability of ultimate limit state

For the T-section, the flexural capacity function in the ultimate limit state is as follows:

The first type of cross-section can be expressed as:

$$g_1 = \alpha f_c b_f x (h_0 - x/2) - k f_t b (h - x/\beta)\left(\frac{h - x/\beta}{2} - c_0\right) - 1.1 \times (M_{D1} + M_{D2} + M_{Q2} + M_{Q2}) \quad (27)$$

where α is the equivalent rectangular stress distribution conversion factor in the compressive zone; f_c is the design value of concrete axial compressive strength; b_f is the calculated width of the flange in the compressive zone of the T-shaped section; x is the height of the compressive zone; h_0 is the effective height of the section; f_t is the design value of concrete axial tensile strength; β is the equivalent rectangular stress coefficient in the tensile zone UHPC.

The second type of cross-section can be expressed as:

$$g_2 = \alpha f_c \left[bx\left(h_0 - \frac{x}{2}\right) + (b_f - b) h_f \left(h_0 - \frac{h_f}{2}\right)\right] - k f_t b \left(h - \frac{x}{\beta}\right) \cdot \left(\frac{h - x/\beta}{2} - c_0\right) - 1.1 \times (M_{D1} + M_{D2} + M_{Q2} + M_{Q2}) \quad (28)$$

The shear capacity function of the prestressed UHPC beam is as follows:

$$g = \frac{0.24}{\gamma_{cf}\gamma_E} k' \sqrt{f_{ck}} b_w d + \frac{A_{fv}\sigma_{Rd,f}}{\tan\theta} - 1.1 \times (V_{D1} + V_{D2} + V_{Q1} + V_{Q2}) \quad (29)$$

where γ_{cf}, γ_E are the material sub-factor, taken as: $\gamma_{cf}\,\gamma_E = 1.5$; f_{ck} is the standard value of UHPC compressive strength; b_w is the minimum width of the section in tension; d is the distance from the tensile reinforcement to the compressive flange of the section; A_{fv} is the area of the fiber affected zone; $\sigma_{Rd,f}$ is the participating tensile strength; θ is the angle between the principal compressive stress and the beam axis; $\sigma_{Rd,f}$ is the participating tensile strength.

According to the structural requirements of ordinary reinforced UHPC beams, double-leg stirrups with a diameter of 8 mm are used, and the distance between the stirrups is 15 cm; the function of the shear reliability of ordinary reinforced UHPC beams is as follows:

$$g = \frac{0.21}{\gamma_{cf}\gamma_E} k' \sqrt{f_{ck}} b_w d + \frac{A_{sw}}{s} z f_{ywd} \cot\theta + \frac{A_{fv}\sigma_{Rd,f}}{\tan\theta} - 1.1 \times (V_{D1} + V_{D2} + V_{Q1} + V_{Q2}) \quad (30)$$

where A_{sw} is the area of the vertical shear reinforcement; s is the spacing of the shear reinforcement; f_{ywd} is the yield strength of shear-resistant reinforcement.

As shown in Figure 6, the reliability index of the flexural capacity of ordinary reinforced UHPC beams decreases and then increases as the beam height increases. This is mainly because, at lower beam heights, the stiffness of the beam and the crack width are the primary constraints, while the flexural capacity is a secondary constraint. In order to meet the crack width constraint, additional reinforcement must be added, which causes an increase in the reliability index.

As the beam height increases, the reliability index of the shear capacity of ordinary reinforced UHPC beams also gradually increases. This is because the web mainly provides the shear capacity of the beam, and as the height of the beam increases, so does the height of the web. Although the increase in height is accompanied by an increase in the self-weight of the beam, the increase in self-weight is slower than the increase in shear capacity.

In the "Unified standard for reliability design of highway engineering structures (JTG 2120-2020)," the target reliability index of the bearing capacity limit state of highway bridge structures with a safety level of one and ductile failure is 4.7, while the target reliability index corresponding to brittle failure is 5.2. The flexural failure of concrete beams belongs to ductile failure, while the shear failure belongs to brittle failure, so 4.7 and 5.2 can be taken as the target reliability indexes of flexural and shear capacities respectively. It can be seen from Figure 6 that the minimum reliability indexes of the flexural and shear capacities of ordinary reinforced UHPC beams at the optimum beam height are 5.42 and 5.39, respectively. It can be seen from Figure 7 that

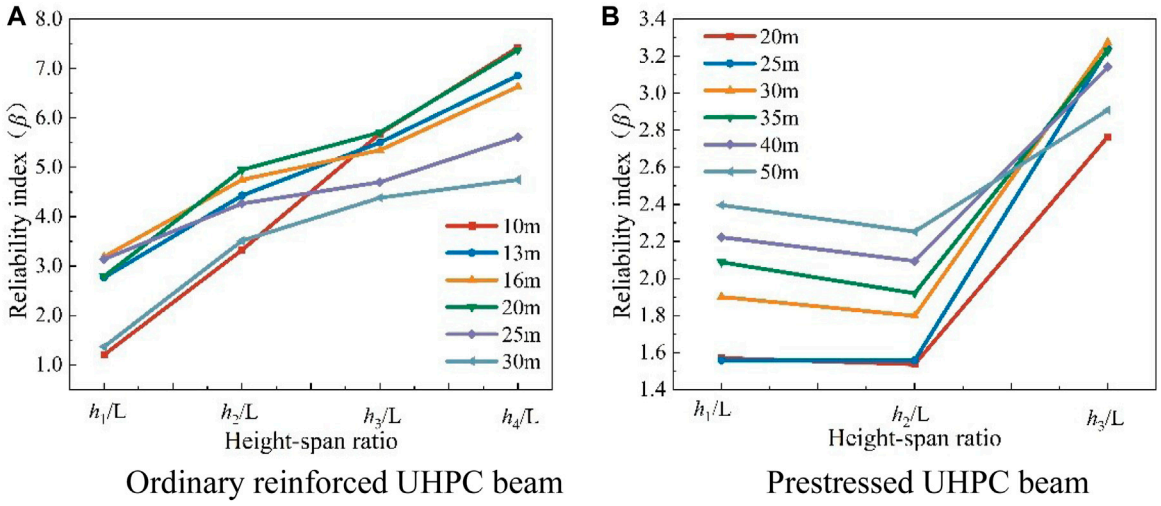

FIGURE 10
Deflection reliability index. **(A)** Ordinary reinforced UHPC beam, **(B)** Prestressed UHPC beam.

the minimum reliability indexes of the flexural and shear capacity of the prestressed UHPC beam at the optimal beam height are 4.92 and 5.35, respectively. The calculated reliability indexes all meet the requirements of "Unified standard for reliability design of highway engineering structures."

As shown in Figure 7, the reliability index of the flexural capacity of the prestressed UHPC beam gradually decreases as the beam height increases. This is because as the beam height increases, the stiffness constraint condition weakens, and the constraint effect of the load-carrying capacity increases. In order to find the minimum solution that meets the requirements of the code, the reliability index of the flexural capacity is reduced.

5.3 Reliability of serviceability limit states

The reliability standard for highway projects does not clearly specify the requirements for the reliability of serviceability limit states. The literature (Li and Bao, 1997) suggests that the acceptable probability of failure for serviceability limit states is approximately between 5% and 25%, and the corresponding target reliability index ranges from 0.675 to 1.645.

5.3.1 Reliability index of maximum crack width

For the serviceability limit state, the specified crack width limit is taken as the resistance that the structural member should have. The maximum crack width generated by the beam under the actual load is considered the load effect. The limit state equation is established as follows:

$$g = [w_{max}] - w_t \quad (31)$$

where $[w_{max}]$ is the allowable value of the maximum crack width.

As shown in Figure 8, the change law of the maximum crack width reliability index of ordinary reinforced UHPC beams increases first and then decreases. The reliability index is the smallest at the optimal result.

5.3.2 Reliability index of normal section crack resistance of prestressed concrete

The crack resistance of prestressed concrete includes two parts: the normal section crack resistance and the inclining crack resistance. This article focuses on the normal section crack resistance. The normal section crack resistance is primarily governed by the normal tensile stress of the concrete. The normal section crack resistance test involves selecting many sections, such as a simply supported beam's mid-span section or a continuous beam's mid-span section and support point section. The normal tensile stress of the concrete at the edge of the crack resistance test is calculated under the combined effect of load frequency.

For fully prestressed concrete structures, the limit state equation for the reliability of normal section crack resistance can be expressed as:

$$g = \left(\frac{\sigma_{pe}A_p}{A_n} + \frac{\sigma_{pe}A_p e_{pn}}{W_n}\right) - \frac{M_{D1} + M_{D2} + 0.7M_{Q1}}{W_0} + 0.7f_{tk} \quad (32)$$

Calculate the reliability index of the normal section crack resistance of prestressed UHPC simply supported beams under different height-span ratios, as shown in Figure 9.

It can be seen from Figure 9 that the reliability index of normal section crack resistance of prestressed UHPC beam increases gradually with the decrease of the height-span ratio. The main reason is that as the beam height decreases, it is necessary to increase the steel strands to meet the requirements of the flexural capacity. Adding steel strands will increase the prestress of the entire section, the restraint effect of the normal section crack resistance will be weakened, and the reliability index will be improved.

5.3.3 Reliability index of deflection

In order to ensure that the structure does not produce excessive deformation during use, the deflection of the beam in the service phase is limited. The formula for calculating the deflection of a simply supported beam is as follows:

$$f_s = \frac{5}{48} \cdot \frac{M_s L^2}{B} \tag{33}$$

For class A components, take $B_0 = 0.95E_cI_0$; for concrete components, the section conversion stiffness B is calculated according to the following equation:

$$B = \frac{B_0}{\left(\frac{M_{cr}}{M_s}\right) + \left[1 - \left(\frac{M_{cr}}{M_s}\right)^2\right] \frac{B_0}{B_{cr}}} \tag{34}$$

The function of deflection reliability is as follows:

$$Z = \frac{L}{600} - \eta_\theta f_s \tag{35}$$

where L is the calculated span; η_θ is the long-term growth coefficient of deflection, which is 1.35; f_s is the deflection value generated by deducting the self-weight under the combination of short-term effects. The results of the deflection reliability calculation are shown in Figure 10.

The results show that the deflection reliability index of ordinary reinforced UHPC beams decreases gradually with the decrease of beam height; The reliability index of prestressed UHPC beams is the smallest at the optimal beam height. The main reason is that the deflection constraints of ordinary reinforced UHPC beams are not the main constraints, while the deflection constraints of prestressed UHPC beams are the main constraints. In the optimization process, the deflection value is close to the limit value, reducing the beam height of the prestressed UHPC beam requires increasing the transverse dimension of the section to meet the deflection constraints, which has little effect on the reliability index of the deflection. However, increasing the beam height greatly improves the deflection reliability index.

6 Conclusion

Based on the improved particle swarm optimization algorithm, the optimal design of ordinary reinforced UHPC and prestressed UHPC simply supported beam bridges with commonly used highway spans is carried out.

1) The IPSO is based on the strategy of genetic algorithm to select hybridization. Non-linear adaptive weights are used to update the weight coefficients, which solves the deficiency that the traditional particle swarm algorithm is easy to fall into local optimal solutions and improves the convergence speed and convergence accuracy of the algorithm.
2) The optimal height-span ratio of ordinary reinforced UHPC beams decreases with the increase of the span, and the construction cost gradually increases; the optimal height-span ratio of the prestressed beam decreases first and then increases with the increase of the span, and the construction cost gradually increases.
3) For ordinary reinforced UHPC beams, the main factors affecting the optimization results are the flexural capacity and the crack width constraint.
4) For prestressed UHPC beams, the main factors affecting the optimization results are the flexural capacity and deflection constraints. As the high-span ratio approaches 1/27, deflection becomes the primary factor affecting optimization results while meeting flexural capacity.
5) The calculation results of load capacity reliability indexes of optimization results are all higher than the target reliability indexes of similar components stipulated in China's "Uniform Standard for Structural Reliability Design of Highway Engineering".

Data availability statement

The original contributions presented in the study are included in the article/Supplementary Material, further inquiries can be directed to the corresponding author.

Author contributions

BL: Conceptualization, Data curation, Methodology, Writing–original draft. YL: Conceptualization, Methodology, Writing–review and editing. XGL: Formal Analysis, Investigation, Writing–original draft. XLL: Formal Analysis, Investigation, Writing–original draft. SZ: Supervision, Validation, Writing–review and editing. LK: Supervision, Validation, Writing–review and editing.

Funding

The authors declare financial support was received for the research, authorship, and/or publication of this article. This research was supported by the Department of Science and Technology of Guangxi Zhuang Autonomous Region (Nos: 2022AB23056).

Acknowledgments

The authors acknowledge the support extended to the work by postgraduate students working under the guidance of the authors.

Conflict of interest

Authors BL, XGL, and XLL were employed by Guangxi Xinxiang Expressway Co., Ltd.

The remaining authors declare that the research was conducted in the absence of any commercial or financial relationships that could be construed as a potential conflict of interest.

Publisher's note

References

AFGC/SETRA (2013). *Ultra high performance fiber reinforced concrete recommendation*. Paris.

Aje, O. F., and Josephat, A. A. (2020). The particle swarm optimization (PSO) algorithm application–A review. *Glob. J. Eng. Technol. Adv.* 3 (3), 1–6. doi:10.30574/gjeta.2020.3.3.0033

Akintunde, O. P. (2021). Optimal design prediction of a singly reinforced concrete beam steel using artificial neural network. *J. Civ. Eng. Res. Technol.* 110, 3. SRC/JCERT-110. doi:10.47363/JCERT/2021(3)110

Aydın, Z., and Ayvaz, Y. (2013). Overall cost optimization of prestressed concrete bridge using genetic algorithm. *KSCE J. Civ. Eng.* 17, 769–776. doi:10.1007/s12205-013-0355-4

Chun, G., and Zhenglin, W. (2012). *Proficient in MATLAB optimization calculations*. 2nd ed. Beijing: Electronic Industry Press.

Guo, K., and Zhang, L. (2022). Multi-objective optimization for improved project management: current status and future directions. *Automation Constr.* 139, 104256. doi:10.1016/j.autcon.2022.104256

Jain, N. K., Nangia, U., and Jain, J. (2018). A review of particle swarm optimization. *J. Institution Eng. (India) Ser. B* 99, 407–411. doi:10.1007/s40031-018-0323-y

Ke, L., Liang, L., Feng, Z., Zhou, J., and Li, Y. (2023a). Bond performance of CFRP bars embedded in UHPFRC incorporating orientation and content of steel fibers. *J. Build. Eng.* 73, 106827. doi:10.1016/j.jobe.2023.106827

Ke, L., Ai, Z., Feng, Z., Chen, Z., and Yoo, D. Y. (2023b). Interfacial bond behavior between ribbed CFRP bars and UHPFRC: effects of anchorage length and cover thickness. *Eng. Struct.* 286, 116140. doi:10.1016/j.engstruct.2023.116140

Ke, L., Zhu, F., Chen, Z., Feng, Z., Zhou, J., and Li, Y. (2023c). Fatigue failure mechanisms and probabilistic S-N curves for CFRP–steel adhesively bonded joints. *Int. J. Fatigue* 168, 107470. doi:10.1016/j.ijfatigue.2022.107470

Khajehzadeh, M., Taha, M. R., El-Shafie, A., and Eslami, M. (2011). Modified particle swarm optimization for optimum design of spread footing and retaining wall. *J. zhejiang university-science A* 12, 415–427. doi:10.1631/jzus.a1000252

Li, Y. H., and Bao, W. G. (1997). *Structural reliability and probability limit state design of highway bridge structure*. Beijing: China Communications Press. In Chinese.

Li, L. (2010). *Research on the force performance and design method of activated powder concrete beams*. Harbin: Harbin Institute of Technology.

Luh, G., and Lin, C. (2011). Optimal design of truss-structures using particle swarm optimization. *Comput. Struct.* 89 (23-24), 2221–2232. doi:10.1016/j.compstruc.2011.08.013

Makita, T., and Brühwiler, E. (2014). Tensile fatigue behaviour of ultra-high performance fibre reinforced concrete (UHPFRC). *Mater. Struct.* 47 (3), 475–491. doi:10.1617/s11527-013-0073-x

Marini, F., and Walczak, B. (2015). Particle swarm optimization (PSO). A tutorial. *Chemom. Intelligent Laboratory Syst.* 149, 153–165. doi:10.1016/j.chemolab.2015.08.020

Ministry of Transport of the People's Republic of China (1999). *Uniform standard for structural reliability design of highway engineering: GB/T50283-1999*. Beijing.

Ministry of Transport of the People's Republic of China (2004). *Code for design of highway reinforced concrete and prestressed concrete bridges and Culverts: Jtg D62-2004*. Beijing.

Quaranta, G., Fiore, A., and Marano, G. C. (2014). Optimum design of prestressed concrete beams using constrained differential evolution algorithm. *Struct. Multidiscip. Optim.* 49, 441–453. doi:10.1007/s00158-013-0979-5

Steinberg, E. (2010). Structural reliability of prestressed UHPC flexure models for bridge girders. *J. Bridge Eng.* 15 (1), 65–72. doi:10.1061/(asce)be.1943-5592.0000039

Wang, Z., Li, D., Wang, Z., Liu, A., and Tao, R. (2021). Research on dynamic balance of spindle rotor system based on particle swarm optimization. *Adv. Mater. Sci. Eng.* 2021, 1–12. doi:10.1155/2021/9728248

Wei, Z., Shen, M., Song, X., Wang, J., Lv, M., Jia, S., et al. (2022). Study on the main cable curve of suspension bridge based on the improved particle swarm optimization (IPSO) method. *Appl. Sci.* 12 (11), 5445. doi:10.3390/app12115445

Xue, J., Briseghella, B., Huang, F., Nuti, C., Tabatabai, H., and Chen, B. (2020). Review of ultra-high performance concrete and its application in bridge engineering. *Constr. Build. Mater.* 260, 119844. doi:10.1016/j.conbuildmat.2020.119844

Zhong, X., Tao, W., Zou, L., Yang, H., and Yao, S. (2022). Servo system control of turntable lipstick-filling machine based on particle swarm optimization. *Adv. Mater. Sci. Eng.* 2022, 1–11. doi:10.1155/2022/8968510

Zhou, M., Lu, W., Song, J., and Lee, G. C. (2018). Application of ultra-high performance concrete in bridge engineering. *Constr. Build. Mater.* 186, 1256–1267. doi:10.1016/j.conbuildmat.2018.08.036

Zhou, C., Wang, J., Jia, W., and Fang, Z. (2022). Torsional behavior of ultra-high performance concrete (UHPC) rectangular beams without steel reinforcement: experimental investigation and theoretical analysis. *Compos. Struct.* 299, 116022. doi:10.1016/j.compstruct.2022.116022

Zhou, C., Wang, J., Shao, X., Li, L., Sun, J., and Wang, X. (2023). The feasibility of using ultra-high performance concrete (UHPC) to strengthen RC beams in torsion. *J. Mater. Res. Technol.* 24, 9961–9983. doi:10.1016/j.jmrt.2023.05.185

frontiers | Frontiers in Materials

TYPE Original Research
PUBLISHED 20 October 2023
DOI 10.3389/fmats.2023.1289225

OPEN ACCESS

EDITED BY
Anbang Li,
Xi'an University of Architecture and Technology, China

REVIEWED BY
Jianan Qi,
Southeast University, China
Lu Ke,
Guangxi University, China

*CORRESPONDENCE
Jun Yang,
yangjun@cqjtu.edu.cn

RECEIVED 05 September 2023
ACCEPTED 06 October 2023
PUBLISHED 20 October 2023

CITATION
Jiang Z, Yang J and Su H (2023), Mechanical response of masonry structure strengthened with ultra-high performance concrete (UHPC): a comparative analysis for different strengthening tactics.
Front. Mater. 10:1289225.
doi: 10.3389/fmats.2023.1289225

Mechanical response of masonry structure strengthened with ultra-high performance concrete (UHPC): a comparative analysis for different strengthening tactics

Zhimei Jiang[1,2], Jun Yang[1,2,3]* and Hao Su[1,2]

[1]State Key Laboratory of Mountain Bridge and Tunnel Engineering, Chongqing Jiaotong University, Chongqing, China, [2]School of Civil Engineering, Chongqing Jiaotong University, Chongqing, China, [3]Guangxi Communications Investment Group Co., Ltd., Nanning, China

Rehabilitation and strengthening of existing masonry structures can improve their safety, prolong life and save economic costs. In this study, a total of eighteen masonry column specimens strengthened by ultra-high performance concrete (UHPC) were fabricated and tested in compression. The effects of strengthening method, strengthening thickness and loading eccentricity were investigated. The failure mode, bearing capacity, strain, ductility, and energy dissipation were discussed in before and after strengthening to evaluate the UHPC strengthening effectiveness. A three-dimensional numerical model established using finite element analysis (FEA) was validated with the experimental results. Results indicated that the brittle failure of masonry columns in compression could be significantly avoided using UHPC strengthening. Among three methods of strengthening, hoop strengthening was the most effective in increasing the ultimate load, ductility, and dissipated energy of masonry columns by 185.81%, 49.09%, and 297.12%, respectively. With the strengthening thickness increased from 0 to 20 and 30 mm, the ultimate bearing capacity of masonry columns was respectively increased by 29.17% and 117.26%, while the corresponding lateral displacement was decreased by 32.44% and 37.24%, respectively. The horizontal buckling of masonry columns can be relieved by UHPC, and the increase in eccentricity did not weaken the contribution of UHPC in strengthened masonry columns. The numerical results were in good agreement with the test results, with errors below 7.6%.

KEYWORDS

ultra-high performance concrete (UHPC), performance improvement, masonry structure, compressive performance, building structure

1 Introduction

Brick and stone are the most commonly used building materials (Babaeidarabad et al., 2014). Statistically, more than 70% of buildings worldwide are masonry structures built of brick and stone (Marthys and Noland, 1989). Masonry structures are typical anisotropic materials. In the direction of horizontal and vertical mortar joints, its mechanical properties are clearly distinguished, with high compressive strength and poor tensile and shear strengths. Consequently, the extremely weak integrity and seismic performance of masonry structures were presented. Owing to functional changes of use, deterioration of

materials, lack of maintenance and exceptional events such as earthquakes, masonry structures accounted for a relatively substantial proportion of the existing building stock that needed strengthening or rehabilitation (Krevaikas and Triantafillou, 2005). The research on the strengthening performance of masonry arches can be carried out using segmental modeling tests because of the uncertainties in the constitutive relationships and mechanical parameters of masonry structures (Zhang, 2014). The ability of both strengthening layer and original masonry in coordinated deflections and bearing loads is validated by segmental model tests of masonry arches, i.e., experimental study of compression of composite masonry column strengthened (Qiao, 2014). Different strengthening techniques have been developed in the past to improve the load-bearing and deformation capacity of masonry structures. In particular, the strengthening of masonry compression elements through the use of external confinement has become a common practice.

The available literature indicated that the commonly used external confinement for masonry structures were fiber reinforced polymer (FRP) jackets (Witzany et al., 2014; Youssf et al., 2017; Alotaibi and Galal, 2018; El-Sokkary and Galal, 2019; Zou et al., 2023a), textile reinforced concrete (TRC) jackets (Wang et al., 2020; Li et al., 2021a; Jing et al., 2021), high ductile concrete (HDC) jackets (Deng and Li, 2020; Li et al., 2021b; Li et al., 2022), fabric reinforced cementitious matrix (FRCM) jackets (Fossetti and Minafò, 2017; Murgo and Mazzotti, 2019; Angiolilli et al., 2020). These strengthening techniques have been demonstrated to be effective in the field of retrofitting or strengthening masonry structures. The FPR has become a hot study material for masonry structures due to its advantages, including high strength to weight ratio, corrosion resistance, easy construction and so on (Vincent and Ozbakkaloglu, 2013; Witzany et al., 2014; Fossetti and Minafò, 2016; Fossetti and Minafò, 2017; Youssf et al., 2017). The most typical external confinement used in masonry structures is also the FRP jacket (Witzany et al., 2014; Youssf et al., 2017; Alotaibi and Galal, 2018; El-Sokkary and Galal, 2019). However, some drawbacks and limitations have been exposed in the application of FRP-strengthened masonry structures. The strict external environment was demanded by epoxy adhesives in order to avoid or mitigate their being subjected to oxidation and ageing (Fossetti and Minafò, 2016; Murgo and Mazzotti, 2019; Li et al., 2021a). Otherwise, there was negatively influence on the effectiveness of the strengthening, i.e., the durability of masonry structures is weakened (Kouris and Triantafillou, 2018; Wang et al., 2020). Meanwhile, brittle failure behavior was exhibited by the structure strengthened using FRP jacket, due to the low compatibility of FRP with masonry substrate (Khan et al., 2018). Replacing FRP by ultra-high performance concrete (UHPC) in FRP jacket may compensate these problems.

An advanced cement-based composite material, UHPC had been designed based on the principle of densified particle packing (Shi et al., 2015; Zhang et al., 2023; Zou et al., 2023b). The raw material of UHPC was composed of cement, silica fume, quartz sand, quartz powder, superplasticizer and steel fibers. The high compressive and tensile strengths of UHPC were exhibited (up to 150 and 8 MPa, respectively) (Yoo and Banthia, 2016; Zou et al., 2023c). Over the past few decades, the mechanical properties and engineering applications of UHPC have gained numerous studies by civil engineering scholars (Ragalwar et al., 2020; Zhu et al., 2020; Bajaber and Hakeem, 2021; Bahmani and Mostofinejad, 2022; Wang et al., 2022; Yang et al., 2023). Shao et al. (2021); Dadvar et al. (2020); Hung and Yen (2021); Zhang et al. (2022) used UHPC jacket for strengthening reinforced concrete (RC) columns to enhance the mechanical properties. Farzad et al. (2020) proposed a simplified calculation method for predicting the structural performance and durability of RC columns strengthened with UHPC. The calculations showed that using UHPC as the repair material of RC columns will extend the service life up to 5 to 10 times. Zhang et al. (2020) applied UHPC strengthening to the damaged RC beams and experimentally investigated the flexural performance of the UHPC-RC combination beams. It was found that the cracking of the RC beams was successfully restricted after the utilization of UHPC layer. Prem and Murthy (2016) experimentally investigated the influence of UHPC on the flexural performance of damaged RC beams. The results showed that the utilization of UHPC was able to restore the initial flexural load capacity of the damaged beam, meanwhile, no debonding was observed at the UHPC-RC interface under bending action. Yuan et al. (2022) tested 3 circular RC piers strengthened with UHPC jackets under quasi-static cyclic loading. The experimental results revealed that the strength and stiffness of the RC piers were enhanced after strengthening with UHPC. The authors pointed out that the post-earthquake serviceability of the strengthened RC piers could be significantly improved through the use of a 50 mm-thick UHPC jacket. Zhang et al. (2019) investigated the effectiveness of UHPC to strengthening damaged RC bridge deck slabs subjected to positive and negative bending moments. Their experimental results indicated that the crack propagation of RC slabs could be restrained and delayed with ultra-high ductility and strain hardening properties of UHPC.

To sum, the validity of UHPC in the strengthening of various structures has been demonstrated by extensive research. However, most of these studies have focused on RC columns, beams, piers and slabs. The research work on masonry structures strengthened with UHPC is relatively unavailable. To investigate the compression performance of masonry arches strengthened with UHPC, the compression performance tests under vertical static loads were carried out on 18 segmental models of masonry columns strengthened with UHPC in this paper. The effects of strengthening method, strengthening thickness and loading eccentricity were investigated to comprehend the compression performance of masonry columns. The failure mode, load-displacement response and load-strain of the specimens were further analyzed and discussed. Based on ABAQUS, a three-dimensional nonlinear numerical model was developed in order to simulate and calculate the segmental model bearing capacity of masonry arch bridges strengthened with UHPC, which was validated with experimental results. The numerical model was further used to evaluate the mechanical property of masonry columns strengthened with UHPC under vertical static loading conditions.

2 Experimental program

2.1 Description of test specimens

A total of eighteen masonry column specimens were fabricated in the compression test. Identical dimension of the specimens, i.e., a height of 870 mm and cross-sectional dimensions of 200 mm × 200 mm, was adopted. Each specimen was assembled from two

TABLE 1 Details of test specimens.

Specimen notation	Methods of strengthening	Thickness of strengthening/mm	Load eccentricity/mm	No. of specimens
US-F0-T0-E0	-	-	0	2
S-F1-T30-E0	One-sided UHPC jacket	30	0	2
S-F3-T30-E0	Three-sided UHPC jacket	30	0	2
S-F4-T20-E0	hoop	20	0	2
S-F4-T30-E0	hoop	30	0	2
S-F4-T20-E30	hoop	20	30	2
US-F0-T0-E60	-	0	60	2
S-F4-T20-E60	hoop	20	60	2
S-F4-T30-E60	hoop	30	60	2

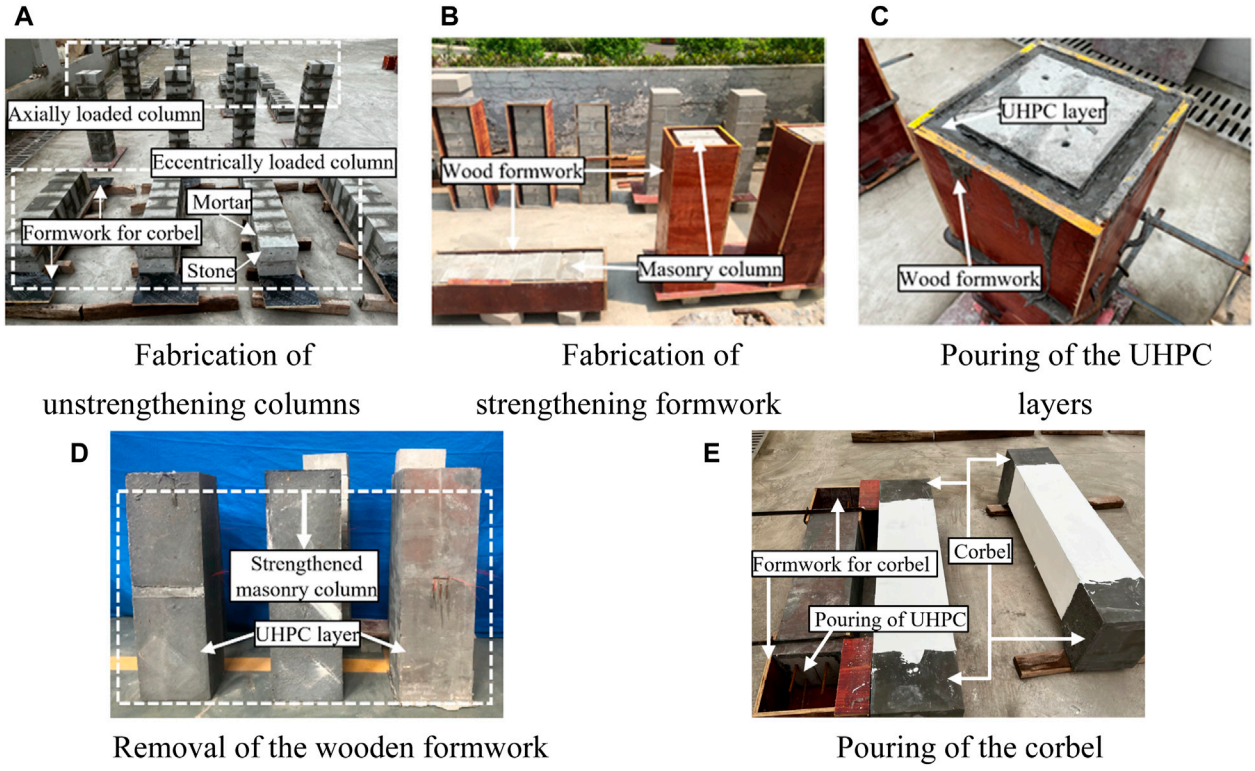

FIGURE 1
Process of making specimens.

stones per course, i.e., a total of sixteen stones were used. Cement-based mortar with an average thickness of 10 mm was used to connect the stones. The experimental parameters were strengthening method (one-sided, three-sided, hoop), strengthening thickness (0, 20, and 30 mm) and loading eccentricity (0, 30, and 60 mm). A number of 18 specimens and the associated parameter variables were designed as listed in Table 1. The experimental parameters were included in the specimen notation. Each column was provided with the notation B-FX-TY-EZ-G. The letter B indicated strengthening technique (US for unstrengthened, S for strengthened with UHPC). The symbol FX stood for strengthening method type (1 for one-sided strengthening, 3 for three-sided strengthening, 4 for hoop strengthening). The symbols TY and EZ stood for strengthening thickness and loading eccentricity, respectively. The letter G indicated the number of identical columns in one group. As an example, column S-F4-T20-E30-b was the second masonry column strengthened with a 20 mm UHPC layer on the hoop and tested a loading eccentricity of 30 mm.

After the 18 masonry columns were completely fabricated, they were placed at room temperature for 14 days. Then, four unstrengthened columns were retained and strengthening

TABLE 2 Results of the stone compressive test.

Group	Block number	Specimen dimensions/mm	Damage load/kN	Compressive strength/MPa	Average and COV
1	1	70 × 70 × 70	625.2	127.6	122.8 (8.96%)
	2	70 × 70 × 70	524.8	107.1	
	3	70 × 70 × 70	671.3	137.0	
	4	70 × 70 × 70	647.3	132.1	
	5	70 × 70 × 70	603.7	123.2	
	6	70 × 70 × 70	538.0	109.8	
2	7	70 × 70 × 70	699.2	142.7	134.4 (14.78%)
	8	70 × 70 × 70	727.6	148.5	
	9	70 × 70 × 70	564.9	115.3	
	10	70 × 70 × 70	500.7	102.2	
	11	70 × 70 × 70	787.4	160.7	
	12	70 × 70 × 70	671.3	137.0	

Note: COV, is the coefficient of variation.

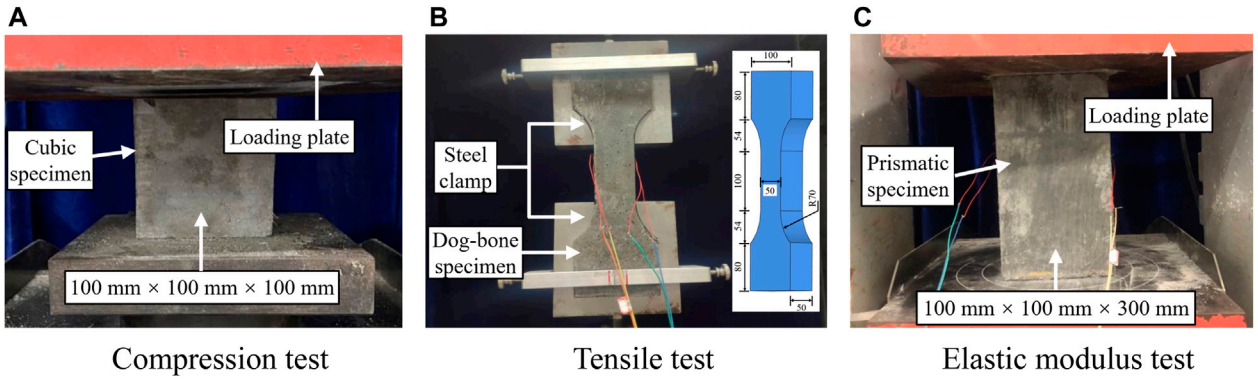

FIGURE 2
Mechanical properties testing of UHPC (unit: mm).

formworks were fabricated for the remaining 14 columns that required to be strengthened. For masonry columns that were subjected to eccentric loading, in order to achieve the eccentric compression effect, both ends of the specimens were designed with corbels and poured with UHPC. The masonry columns were cured for 7 days after the UHPC had been completely poured. The process of making the test column is given in Figure 1.

2.2 Material properties

2.2.1 Stone

The material properties test was carried out on 12 specimens [tested by 70 mm × 70 mm × 70 mm cubes as per the JTG E41-2005 Standard (JTG E41-2005, 2005)]. The compressive strength of stones was tested in two groups of six each. All stones used in this test were prepared from the same batch of quarried stone as the material properties test. Meanwhile, they were cut and processed in the same factory. The results of the two test groups are listed in Table 2. The average value of both test groups, 128.6 MPa, was used as the compressive strength of the stone to minimize the effect of errors.

2.2.2 Mortar

The mortar was prepared as per the standard strength grade of M7.5. Six cubic specimens of 70.7 mm × 70.7 mm × 70.7 mm were prepared and tested according to JTG D61-2005 code (JTG D61-2005, 2005) to evaluate the compressive strength of mortar. The test results are summarized in Table 3.

2.2.3 UHPC

The UHPC used in the experiment was independently researched and developed. The specific proportions of the raw materials are given in Table 4. Compared to conventional UHPC,

TABLE 3 Results of compressive strength of mortar specimen blocks.

Strength grade	Damage load/kN						Average and COV	Average strength/MPa
	1	2	3	4	5	6		
M7.5	34.2	37.2	36.2	35.8	36.6	35.0	35.8 (2.7%)	7.1

TABLE 4 Mix proportions of UHPC (unit: kg/m^3).

Component	Amount
Cement	1,000
Silica fume	100
Fly ash	300
Basalt sand	1,100
Water	240
Steel fiber	170

this material has faster early growth in strength. It has excellent flowability which is convenient for pouring, and does not demand steam curing. The slump flow of UHPC can reach 850 mm, and the setting time of initial and final is 6 and 14 h, respectively.

The compressive strength of UHPC was determined through standard compression tests of 100 mm × 100 mm × 100 mm cubes with a testing procedure conforming to GB/T 31387-2015 (GB/T 31387-2015, 2015). For determining the tensile strength of UHPC, a direct tension test was performed on 3 dog-bone specimens as per T/CBMF 37-2018 (T/CBMF37-2018, 2018). According to GB/T 31387-2015 Standard (GB/T 31387-2015, 2015), the elastic modulus was obtained by three prismatic specimens with dimensions of 100 mm × 100 mm × 300 mm for UHPC. The tests set-up for the mechanical properties of UHPC are shown in Figure 2, and the test results are listed in Table 5.

2.3 Test set-up and instrumentation

In this study, the positive face of the load was used as the A face, followed by the B to the D face in a clockwise direction. In addition, the D face of specimens subjected to eccentric compression was the near eccentric face.

For axial compression columns, three vertical and one lateral strain gauges were assigned in the middle of the A and D faces. To measure the lateral displacement of the masonry column, one dial gauge was placed at 3/8H and another at 6/8H from the bottom of the B face. To measure the vertical displacement of the masonry columns, one of the dial gauges was placed in the middle of the C face. For eccentric compression columns, three vertical and one lateral strain gauges were arranged on the A face, meanwhile, three vertical strain gauges were arranged on the B and D faces. The dial gauge layout was the same as the axial compression column. Details of the layout are shown in Figure 3A.

During the experiments, the columns were loaded by hydraulic jacks with a range of 2000 kN and the data was obtained from the pressure sensor below the jack, as shown in Figure 3B. The center line of the specimen was marked out in advance to establish the loading point, following which the loading point was aimed at the test set-up (before loading). The masonry columns were tested under displacement control at a rate of 0.1 mm/min. Before formal loading, the specimen was pre-loaded with 20 kN to determine the accuracy of the test set-up.

3 Results and discussion

3.1 Experimental phenomena and failure modes

3.1.1 Unstrengthened

Brittle failure behavior was observed on unstrengthened columns in the compression test. The failure modes of unstrengthened columns are presented in Figure 4A. For the axial compression columns, no visible phenomena were observed in the early stage of loading. When the load was increased to 56% P_{max} (P_{max} is the peak load of masonry column), the initial crack was observed in the stones of the middle of specimen. After thet, different degrees of peeling appeared in the masonry joints, and the cracks gradually extended from the middle to the ends of the specimen. Finally, with the increase in loading, the cracks propagated through the mortar joints and local continuous cracks were formed, which resulted in the crushing of the specimen. For eccentric compression columns, the primary crack was discovered in the upper middle of the D face of the specimen (D is the near eccentric face). Then, the cracks rapidly extended in a downward direction along the masonry joints. As the load increased, the masonry joints were found to be detached on the D face. Masonry joints cracking and vertical tension cracks were observed on the B face, meanwhile, the primary crack extended towards the A and C faces. With the cracks being penetrated in the stone, the specimen lost its load-bearing capacity due to the crushing failure.

3.1.2 One-sided strengthening

The failure of UHPC-masonry composite columns was masonry crush damage when one-sided strengthening was used. The masonry columns played a major role in the overall loading process. The UHPC layer completely detached from the masonry column substrate after the peak load. Under the axial compression, the detached UHPC layer was observed to be only slightly cracked on the surface. This was attributed that the surface of the masonry column was not fully wetted when the UHPC layer was poured. This resulted in the weak bonding performance that was exhibited between the UHPC layer and masonry columns. In this case, the compressive strength of the UHPC cannot be adequately utilized. These are illustrated in Figure 4B.

TABLE 5 Material properties of UHPC at various ages.

Age	1 d	3 d	7 d	14 d	28 d
Compressive strength/MPa	48.2	76.9	115.1	131.4	142.5
Tensile strength/MPa	3.25	5.26	8.02	8.82	9.30
Modulus of elasticity/GPa	25.8	41.1	46.7	50.6	51.5

3.1.3 Three-sided strengthening

For masonry columns with three-sided strengthening, it was observed during loading that the cracks rapidly propagated from the upper to the lower end of the specimen as the load increased. When the load was increased to 42%P_{max}, the sound of the steel fibers being pulled off could be heard. This indicated that the UHPC was participating in the common forces for the masonry columns during this time. With the load increased to 51%P_{max}, the cracks appeared in the middle of the C face of the masonry column (C is the unstrengthened face). Subsequently, cracks were discovered in the UHPC at the bottom of the D face. In this area, the debonding was exhibited between the UHPC and masonry columns as loading increased, as given in Figure 4C. This demonstrated that the effectiveness of the UHPC layer on the end restraint of the masonry columns was not obvious with three-sided strengthening. Compared to one-sided strengthening, the UHPC was better bonded to the masonry column using three-sided strengthening. To a certain extent, this can prevent the early damage of specimens caused by poor construction techniques.

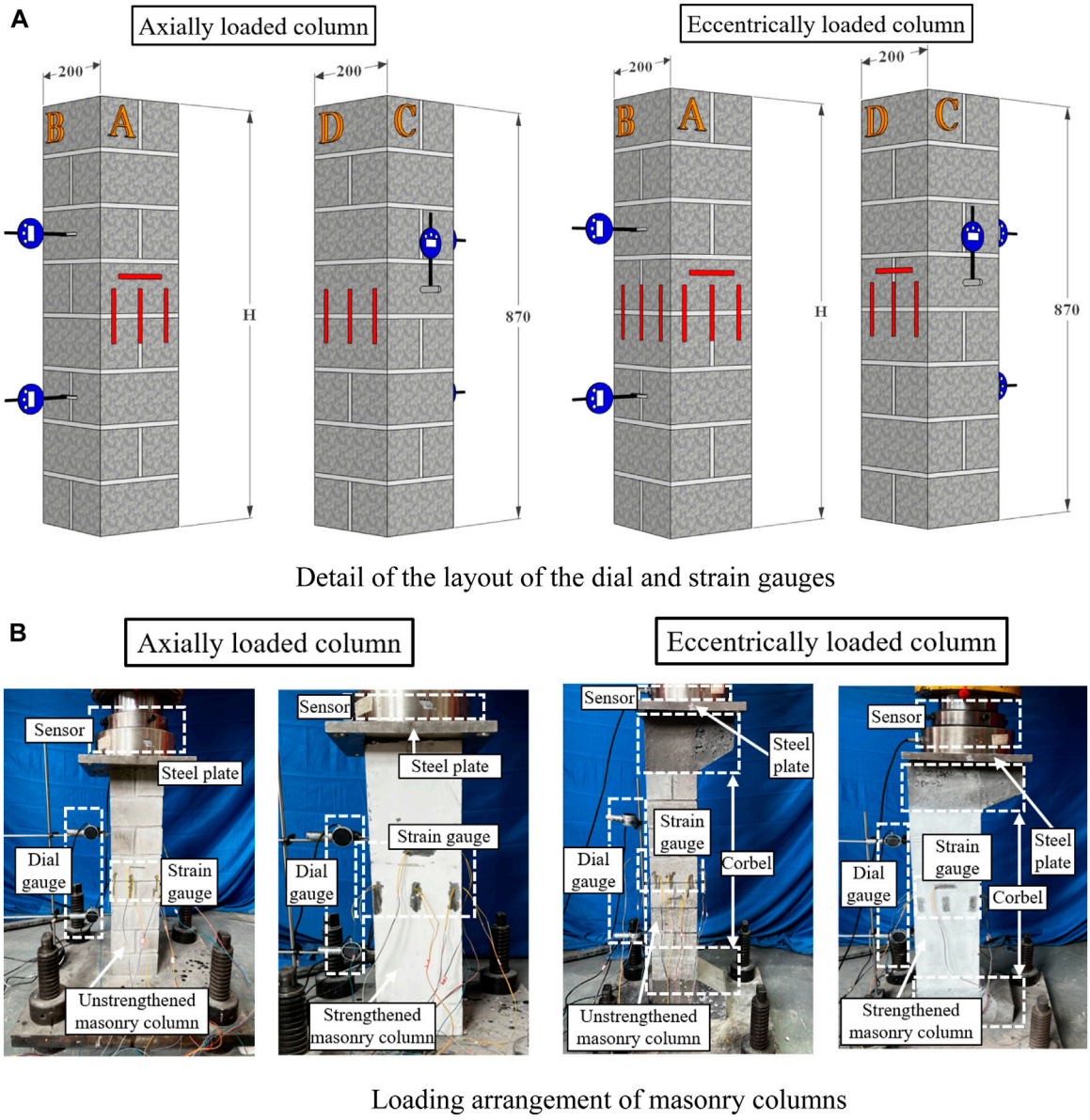

FIGURE 3
Measuring point arrangement and test setup (unit: mm).

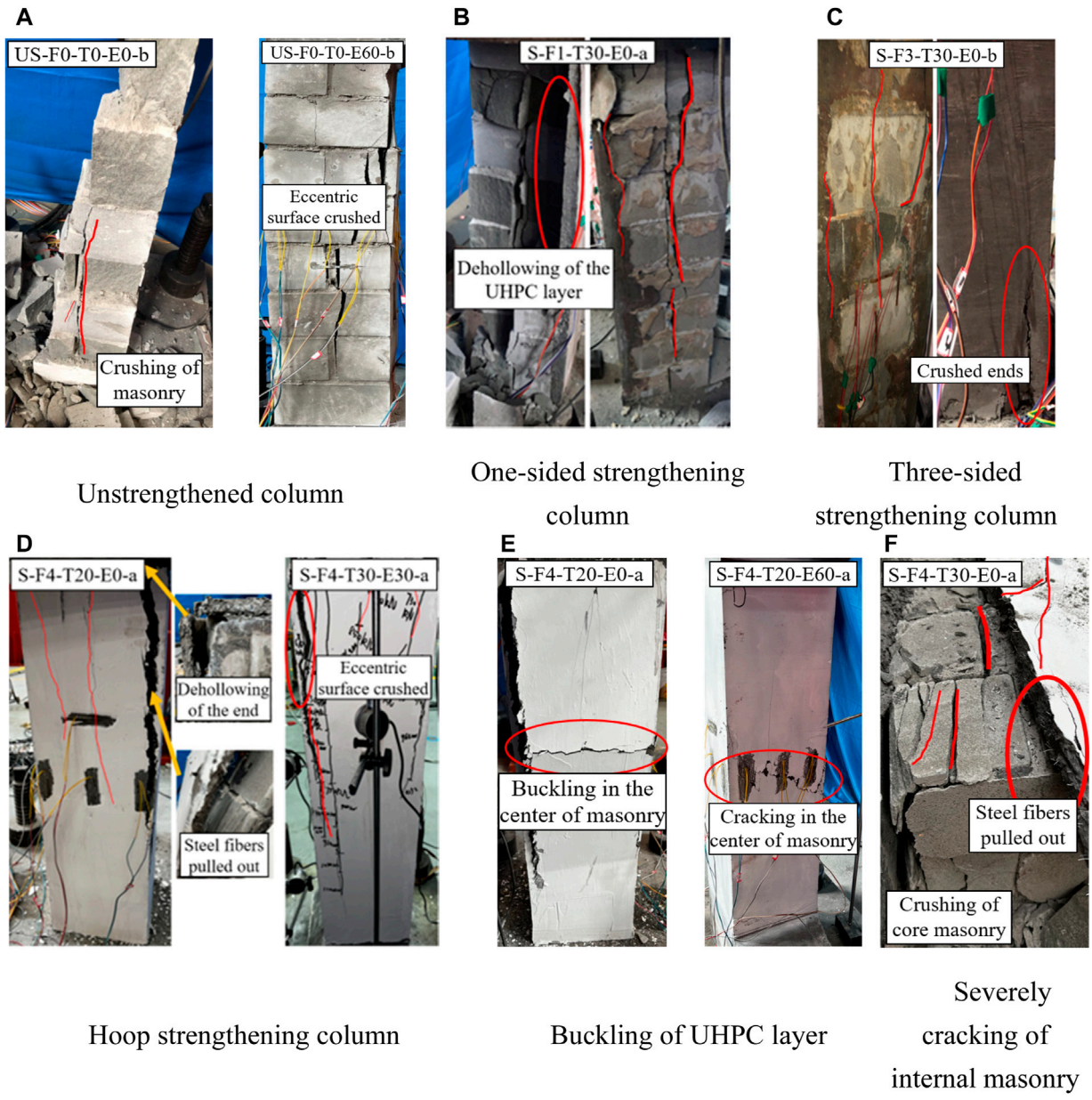

FIGURE 4
Failure modes **(A)** unstrengthened column; **(B)** one-sided strengthening column; **(C)** three-sided strengthening column; **(D)** hoop strengthening column; **(E)** buckling of UHPC layer; **(F)** severely cracking of internal masonry.

3.1.4 Hoop strengthening

In comparison to the previous two strengthening methods, the strengthening efficiency of masonry columns was significantly enhanced through hoop strengthening. For the axial compression columns, the initial crack was discovered at the upper end of the specimen. The cracks extended towards the middle when the load was being further increased. In this case, the specimen had different degrees of damage at the ends and the UHPC appeared slightly debonded at the upper end. When loaded to peak load, a resounding sound occurred, this indicated that the strengthened columns were crushed. For the eccentric compression columns, the majority of cracks were initiated in the near eccentric face. Then, it extended to the adjacent face and formed the primary crack. With a further increase in the load, the cracks continually propagated towards the downside of the specimen. At later stage of loading, the upper end joints of the specimens were opened up. As the strengthened column was loaded to the peak load, the strengthened column was destroyed, as shown in Figure 4D.

For the strengthened columns, the final failure was caused by masonry crushing and the UHPC debonding at the mid-height of specimen. In other words, after cracks were formed in the stone and mortar, horizontal cracks appeared in the UHPC. As the load was increased, the swelling and slight buckling of the UHPC were observed in near the horizontal cracks, resulting in the UHPC layer being dehollowed, as illustrated in Figure 4E. This can be attributed to that the masonry columns did not provide lateral

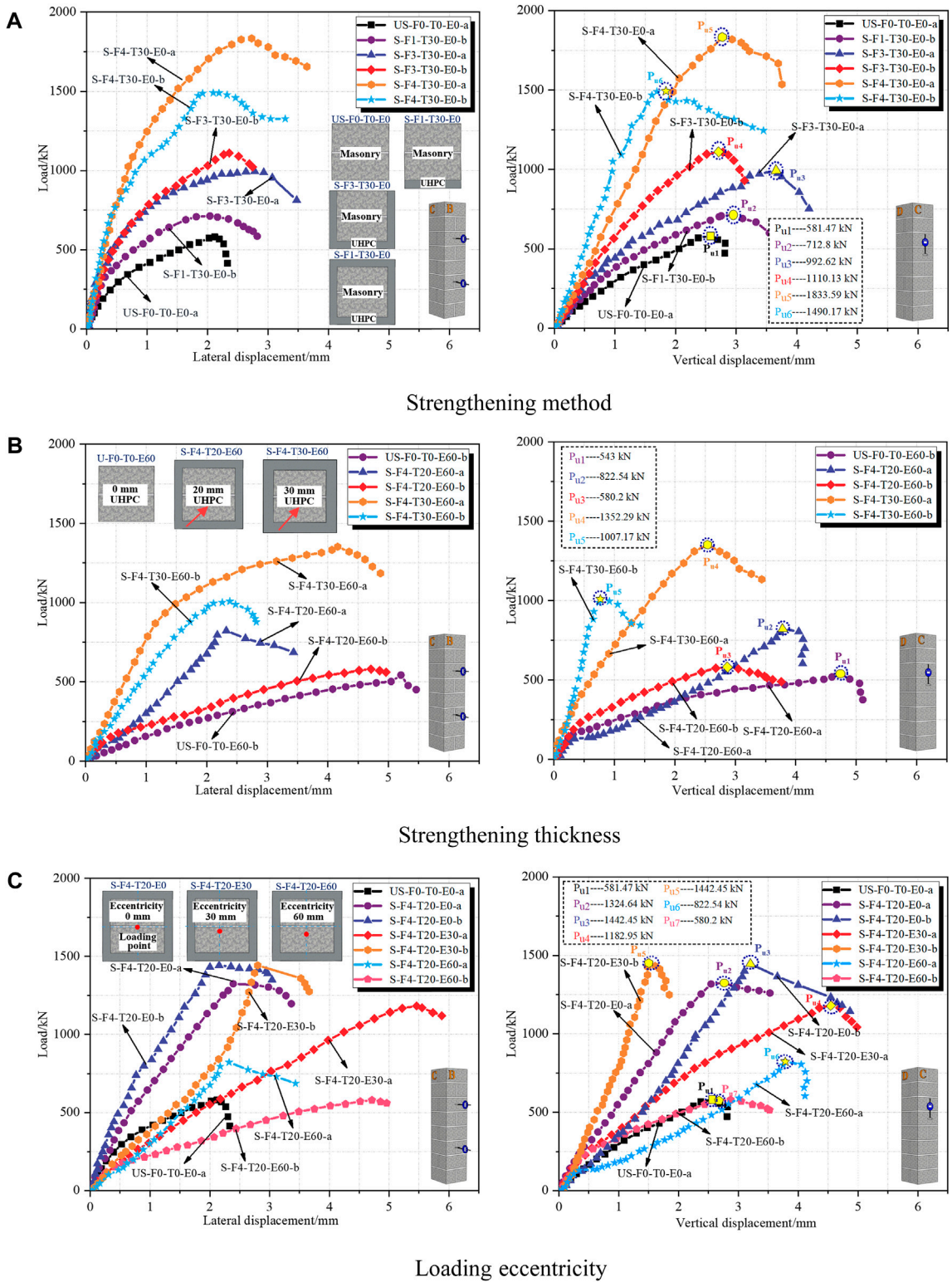

FIGURE 5
Load-displacement curves.

support to resist buckling and were allowed to swell, thus aggravating the buckling of the UHPC layer.

Additionally, the UHPC layer was chiselled away along the primary cracks of the masonry columns that were strengthened by the hoop, when the loadings were completely finished. It was noticed that the UHPC layer was tightly bonded to the masonry columns, meanwhile, the interior masonry was seriously damaged, as depicted in Figure 4F. This demonstrated that the bearing

capacity of both the UHPC layer and the masonry column was maximized. Hence, the high-strength properties of UHPC can be fully exploited through hoop strengthening when masonry columns were strengthened with UHPC.

3.2 Load-displacement curves

The load-displacement curves obtained from compression tests are shown in Figure 5. The force was obtained by the load cell on the steel plate. The lateral deformation was an average reading of two LVDTs (Linear Variable Displacement Transducer) on the B face and the vertical deformation was obtained from LVDT readings on the C face. It can be seen that the peak load and the stiffness of masonry columns strengthened with UHPC were improved. Overall, the loading process of the masonry columns can be divided into three stages: elastic stage, strengthening stage and descending stage.

The elastic stage had high structural stiffness and the displacement varied relatively little with increasing load. This stage of the load-displacement curves exhibited a linear growth trend. The strengthening stage was characterized by displacements significantly greater with increasing load. Compared to the unstrengthened column, the masonry columns strengthened with UHPC exhibited a slower increase in displacement during this stage. Thus, this stage was a relatively high proportion of the whole loading process. This also clearly indicated the effectiveness of UHPC in improving the strength and ductility of masonry columns. The descending stage occurred following the peak load. In contrast to unstrengthened columns, the load on columns strengthened with UHPC did not immediately drop when the peak load was reached, instead fluctuating for a period of time. This was probably attributed to the "bridging" influence of the steel fibers in the UHPC.

3.3 Performance indices

The strengthening effectiveness of UHPC on masonry columns was further researched in terms of various performance parameters, such as the peak load (P_{max}), displacement at peak [i.e., the displacement corresponding to the peak load, including the lateral displacement (D_L) and vertical displacement (Dv)], ultimate displacement (Du), ductility (μ) and energy dissipation (E). The ductility of each group of specimens can be defined, with reference to (Wang et al., 2020), as the ratio of ultimate axial displacement (Du) to its peak axial displacement (Dv). Based on the American ACI 440.2R guideline (ACI Committee 440, 2008), the ultimate displacement was defined as the displacement corresponding to $0.85P_{max}$ in the descending stage of axial load-displacement curves. The energy dissipation of each specimen was quantified as the area under the axial load-displacement curve to the ultimate state, i.e., the area of the shaded region in Figure 6.

Table 6 and Table 7 list the performance indices for the masonry columns with different parameters that were obtained from the tests. It is worth noting that the peak loads of the same groups of specimens exhibited a high degree of scatter. Based on the overall results, it was attributable to the construction quality differences and damage caused during handling.

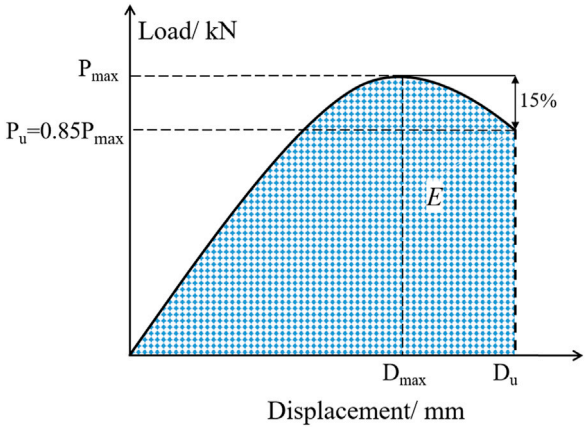

FIGURE 6
Analytical diagram of load-displacement curves.

The statistical results of peak load of masonry columns are presented in the form of a histogram in Figure 7A. It is obviously noticeable that the considerable gain in peak load of the masonry columns was provided by the UHPC. Compared to unstrengthened columns, the three strengthening methods, namely, one-sided strengthening, three-sided strengthening and hoop strengthening, improved the ultimate load capacity by approximately 33.59%, 80.81%, and 185.81% respectively. Those enhancements in peak loads could be attributed to UHPC, which sustained some of the axial loads from direct contact with the masonry columns. When one-sided strengthening was utilized, the masonry columns were not adequately bonded to the UHPC, resulting in an earlier debonding of the UHPC layer from the masonry columns. Therefore, the improved bearing capacity of the masonry columns was not significant. It demonstrated that the more effective and beneficial strengthening method for masonry columns was hoop strengthening. Also, a similar rule of change could be observed between strengthening layer thickness and strengthening method. The peak load was increased by 29.17% and 117.26% with the thickness of strengthening layer from 0 to 20–30 mm. Compared to the unstrengthened columns, the peak loads were enhanced by 137.94%, 125.79% and 20.62%, respectively, with loading eccentricity from 0 to 30–60 mm. Observably, the growth rate of peak load of specimens decreased with the increase in eccentricity. The average peak load drops of groups S-F4-T20-E30 and S-F4-T20-E60 were 12.15% and 117.32%, respectively, in comparison to S-F4-T20-E0. An explanation for the fact that masonry columns failed with lower load carrying capacity under eccentric loading can be given as follows: 1) the loading eccentricity reduced the area of compression region of specimen cross-section, which directly caused the reduction of bearing capacity; 2) the lateral deformation was increased as a result of the eccentric compression. The lateral deformation would increase eccentricity of load, which further reduced the bearing capacity of specimen. It is interesting to mention that UHPC strengthening could significantly improve the peak loads of masonry columns under all eccentric loads. This improvement was especially apparent for specimens with eccentricity distances up to 30 mm (125.79%). With other eccentricity distances, the enhancement of peak loads was relatively weak.

TABLE 6 Comparison of peak load and displacement.

Specimens	P_{max}/kN	Average and COV	D_L/mm	Average and COV	Dv/mm	Average and COV
US-F0-T0-E0-a	581.47	581.47 (–)	2.12	2.12 (–)	2.57	2.57 (–)
US-F0-T0-E0-b	-		-		-	
S-F1-T30-E0-a	-	712.8 (–)	-	2.04 (–)	-	2.95 (–)
S-F1-T30-E0-b	712.8		2.04		2.95	
S-F3-T30-E0-a	992.62	1051.38 (5.59%)	2.63	2.5 (5.41%)	3.65	3.18 (14.96%)
S-F3-T30-E0-b	1110.13		2.36		2.7	
S-F4-T30-E0-a	1833.59	1661.88 (10.33%)	2.73	2.41 (13.28%)	2.77	2.23 (24.22%)
S-F4-T30-E0-b	1490.17		2.09		1.69	
US-F0-T0-E60-a	-	543 (–)	-	5.21 (–)	-	4.73 (–)
US-F0-T0-E60-b	543		5.21		4.73	
S-F4-T20-E60-a	822.54	701.37 (17.28%)	2.32	3.52 (34%)	3.78	3.33 (13.68%)
S-F4-T20-E60-b	580.2		4.71		2.87	
S-F4-T30-E60-a	1352.29	1179.73 (14.63%)	4.16	3.27 (27.21%)	2.54	1.65 (54.51%)
S-F4-T30-E60-b	1007.17		2.38		0.75	
US-F0-T0-E0-a	581.47	581.47 (–)	2.12	2.12 (–)	2.57	2.57 (–)
US-F0-T0-E0-b	-		-		-	
S-F4-T20-E0-a	1324.64	1383.55 (4.26%)	2.39	2.27 (5.27%)	2.76	2.94 (6.12%)
S-F4-T20-E0-b	1442.45		2.15		3.12	
S-F4-T20-E30-a	1182.95	1312.7 (9.88%)	5.46	4.13 (32.2%)	4.55	2.97 (53.46%)
S-F4-T20-E30-b	1442.45		2.80		1.38	
S-F4-T20-E60-a	822.54	701.37 (17.28%)	2.32	3.52 (34%)	3.78	3.33 (13.68%)
S-F4-T20-E60-b	580.2		4.71		2.87	

Note: Specimen of US-F0-T0-E0-b and S-F1-T30-E0-a damaged during handling, test invalid.
Data loss of US-F0-T0-E60-a due to equipment damage during the test.
P_{max} is the peak load of masonry column. D_L, is the lateral displacement of masonry column at peak load. Dv is the vertical displacement of masonry column at peak load.

The average peak displacements (including lateral and vertical displacements) of the masonry columns are shown in Figures 7B, C, respectively. It is noticeable that the deformation capacity at peak load of specimens decreased with increasing thickness of strengthening layer. This was probably caused that the UHPC layer confined the horizontal buckling deformation of masonry columns. On the other hand, the high elastic modulus of UHPC improved the bending stiffness for masonry columns. The bending stiffness was beneficial in restricting deformations. In particular, the average increases in peak lateral displacement were 7.08%, 94.81% and 66.04%, and the average increases in peak vertical displacement were 14.4%, 15.56%, and 29.57% for masonry columns strengthened with UHPC under loading eccentricities of 0mm, 30mm and 60 mm. It is worth noting that monotonic and consistent relationships were presented between deformation and loading eccentricity for control and strengthened specimens. However, the groups S-F4-T20-E30 exhibited relatively larger lateral and vertical displacements compared to the groups S-F4-T20-E60. This could be explained by the fact that, with little eccentricity, the ductility of the UHPC can provide a certain deformation capacity for masonry columns. However, masonry column substrates played a dominant role in the loading process as the eccentricity was further increased. The specimens had failed before the high ductility properties of UHPC were fully exploited, due to crushing of the masonry column substrate.

The ductility data of masonry columns with and without UHPC strengthening are shown in Figure 7D. It can be observed that the average increases in ductility were 13.08% and 44.86% when the strengthening layer thicknesses were varied from 0 to 20 and 30 mm. This can be explained in two aspects: 1) the lateral dilation of masonry core was inhibited by UHPC layer, which resulted in a significantly high axial deformation capacity. In particular, for the post-peak load, the confinement capacity could be greater owing to the rapid lateral dilation; 2) the high toughness characteristics were provided by the presence of steel fibers in the UHPC under compression. Hence, UHPC can consistently carry loads and absorb energy during the decline stage after peak loading. For masonry columns whose eccentricity was increased from 0mm to 30 mm and 60mm, the average increases in ductility were 30.91%, 13.64%, and 10%. However, the increasing trend of drop was exhibited in the average ductility. This could be influenced by the tensile effect of UHPC layers. In this case, the masonry columns

TABLE 7 Test results on characteristic parameters.

Specimens	Pu/kN	Average and COV	Du/mm	Average and COV	μ(Du/D_L)	E(J)	Average and COV
US-F0-T0-E0-a	494.25	494.25 (–)	2.82	2.82 (–)	1.1	1007	1007 (–)
US-F0-T0-E0-b	-		-			-	
S-F1-T30-E0-a	-	605.88 (–)	-	3.53 (–)	1.2	-	1724 (–)
S-F1-T30-E0-b	605.88		3.53			1724	
S-F3-T30-E0-a	843.73	893.73 (5.59%)	4.06	3.59 (13.09%)	1.13	2614	2422 (7.93%)
S-F3-T30-E0-b	943.61		3.12			2230	
S-F4-T30-E0-a	1558.55	1412.6 (10.33%)	3.74	3.5 (6.86%)	1.64	3566	3999 (10.83%)
S-F4-T30-E0-b	1266.64		3.26			4432	
US-F0-T0-E60-a	-	461.55 (–)	-	5.08 (–)	1.07	-	1884 (–)
US-F0-T0-E60-b	461.55		5.08			1884	
S-F4-T20-E60-a	699.16	596.17 (17.28%)	4.17	3.97 (5.04%)	1.21	1705	1649 (3.4%)
S-F4-T20-E60-b	493.17		3.77			1593	
S-F4-T30-E60-a	1149.45	1002.77 (14.63%)	3.55	2.42 (47%)	1.55	2983	1928 (54.76%)
S-F4-T30-E60-b	856.1		1.28			872	
US-F0-T0-E0-a	494.25	494.25 (–)	2.82	2.82 (–)	1.1	1007	1007 (–)
US-F0-T0-E0-b	-		-			-	
S-F4-T20-E0-a	1125.94	1176.01 (4.26%)	3.87	4.22 (8.29%)	1.44	3440	3662 (6.06%)
S-F4-T20-E0-b	1226.08		4.57			3884	
S-F4-T20-E30-a	1005.51	1115.8 (9.88%)	5.06	3.49 (45%)	1.25	3777	2588 (45.94%)
S-F4-T20-E30-b	1226.08		1.92			1399	
S-F4-T20-E60-a	699.16	596.16 (17.28%)	4.17	3.97 (5.04%)	1.21	1705	1649 (3.4%)
S-F4-T20-E60-b	493.17		3.77			1593	

Note: Pu is the ultimate load of masonry column. Du is the ultimate displacement of masonry column at ultimate load. μ is the ductility of masonry column. E is the energy dissipation.

were similar to concrete elements under compression subjected to a combination of axial and bending loads, presenting a weak ductility.

The energy of destruction is a crucial parameter to estimate the compressive performance of UHPC-confined masonry columns (Jing et al., 2021). The destructive energy data of each group of masonry columns are shown in Figure 7E. It can be observed that the energy absorption capacity of masonry columns strengthened with UHPC was significantly enhanced. In comparison to unstrengthened columns, when the strengthening method was changed from one-sided to three-sided and hoop, the average increases in energy of destruction were 71.2%, 140.52%, and 297.12%. The increase in energy was the lowest for group S-F2-T30-E0 (71.2%) due to the earlier dehollowing between masonry part and UHPC. The best energy dissipation was observed in group S-F4-T30-E0 (297.12%). This improvement of energy dissipation capacity was attributable to the considerable increase in masonry strength and ductility, which highlighted the superior confinement capacity of UHPC. In addition, the destruction energy of specimens increased with the increase of loading eccentricity. Compared to the control group, the average increases in destruction energy were 263.65%, 157%, and 63.75% for loading eccentricity of 0, 30, and 60 mm. Interestingly, the trend of monotonically decreasing average destruction energy was revealed, with increasing eccentricity. This indicated that the energy required to destroy masonry columns could be truly decreased by eccentricity, in spite of the additional confinement. In general, all the characteristic indices, i.e., peak load, peak displacement, ductility and energy of destruction, as well as the load-displacement curves, demonstrated that the mechanical properties of masonry columns could be significantly enhanced by UHPC.

3.4 Load-strain curves

The effect of the strengthening method, strengthening thickness and loading eccentricity on the load-strain relationship of the masonry column is depicted in Figure 8. The positive value indicated tensile strain while the negative value meant compressive strain. As shown in Figure 8, the UHPC was subject to compression in the vertical direction and tension in the lateral direction. Furthermore, the UHPC exhibited high compressive strains, of which the yield strains in the peak state were exceeded in most specimens (e.g., S-F1-T30-E0-b, S-F4-T30-E0-a, S-F4-T20-E30-b, and S-F4-T20-E60-a). This indicated that the UHPC could be well utilized in masonry column strengthening.

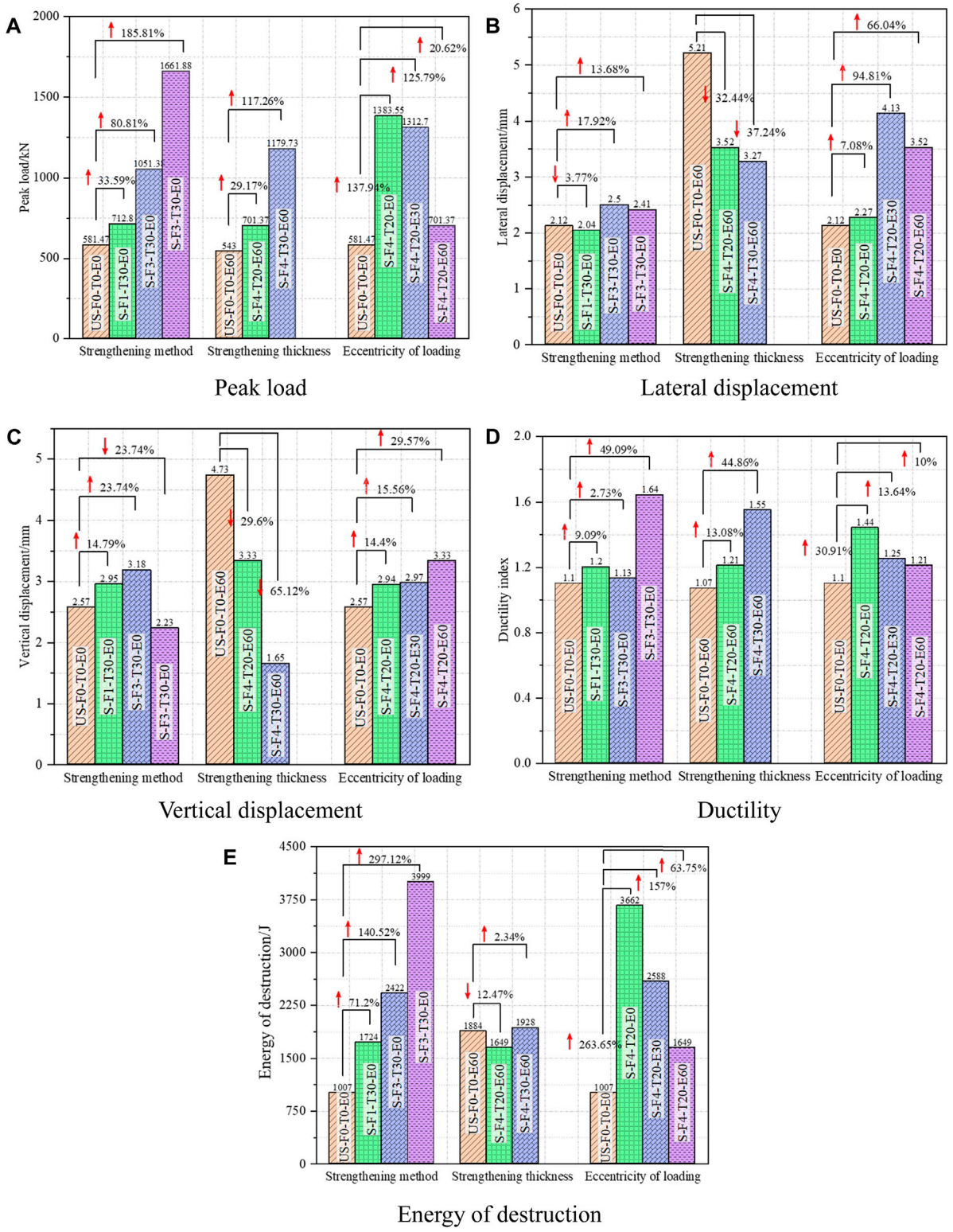

FIGURE 7
Effect of strengthening method, strengthening thickness and eccentricity on peak load **(A)**, lateral displacement **(B)**, vertical displacement **(C)**, ductility **(D)** and energy of destruction **(E)** of specimens.

It can be observed that the load-strain curves of the masonry column were approximately linear during the initial stage of the loading. The significant elastic behavior of the specimen was observed. With the increase in load, mortar joints spalling and stone internal cracking were observed under compression. The load-strain curves of the masonry column were displayed as the non-

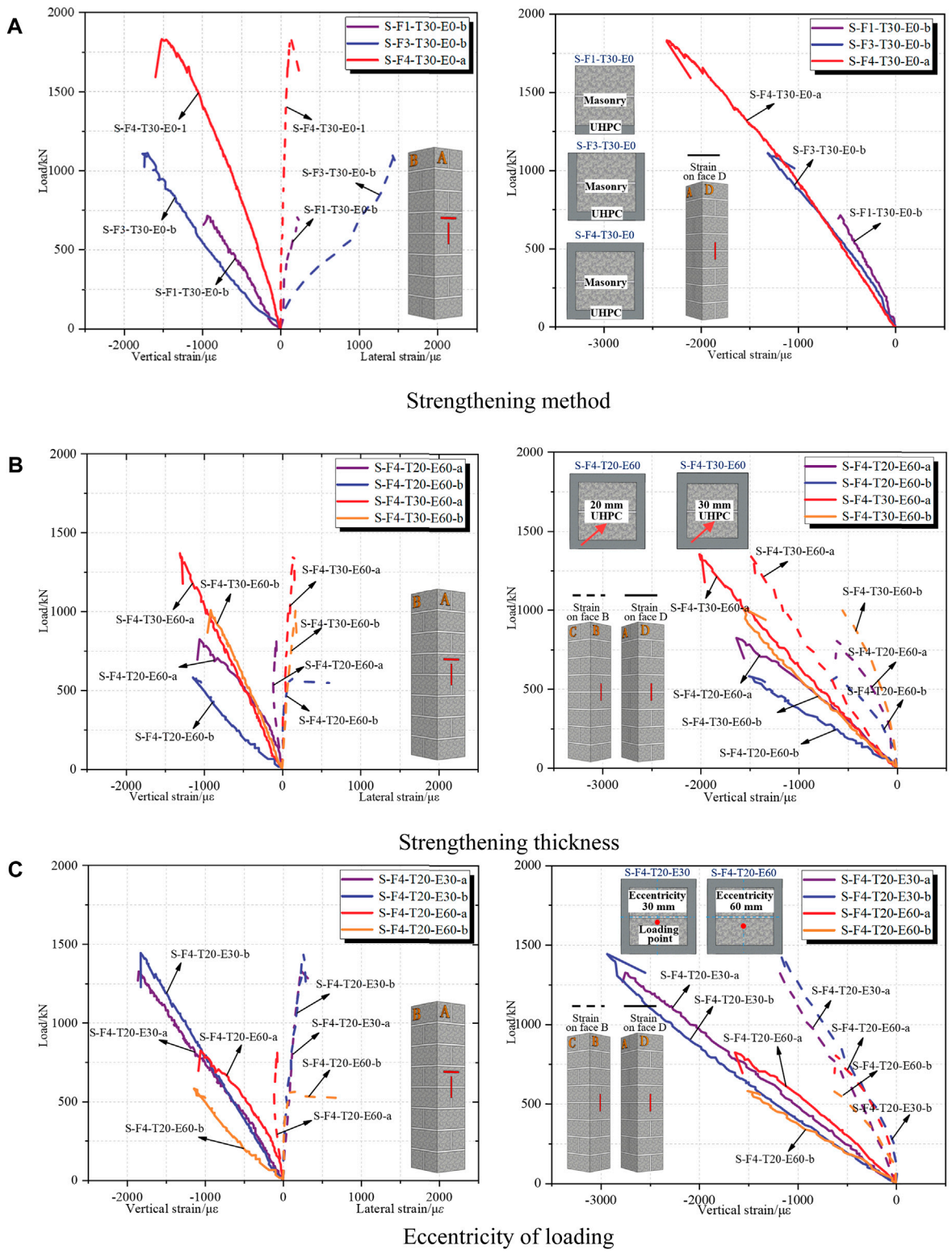

FIGURE 8
Load-strain curves.

linear growth and the specimens entered the crack progression stage. With the further increase in load, the internal cracks of masonry columns continually progressed and formed local continuous cracks. This can be expressed by the load-strain curve which reached the peak and appeared to soften, i.e., the presence of a descending stage.

The load-strain relationship of the three strengthening methods is presented in Figure 8A. As expected, the strength of the masonry

columns strengthened with UHPC exhibited different degrees of growth as the strengthening method was improved. For one-sided, three-sided and hoop strengthening, i.e., S-F1-T30-E0-b, S-F3-T30-E0-b. and S-F4-T30-E0-a, the strengths of the specimens were 712.8, 1110.13, and 1833.59 kN, and the ultimate tensile strains were 225.19, 1434.7, and 137.26 με, respectively in the A face, and the ultimate compressive strains were 932.27, 1694.33, and 1511.25 με, respectively in the A face, and the ultimate compressive strains were 563.02, 1309.19, and 2348.17 με, respectively in the D face. It is worth noting that the tensile strain growth of S-F4-T30-E0-a specimen (strengthened by the hoop) was relatively slow in the initial stage of loading. This can be explained that the lateral deformation of the masonry column substrate was not obvious. With the further increase in load, the lateral displacement of the masonry columns was increased, causing the tensile strain to increase rapidly. Additionally, the lower ultimate strain can be observed on the A face of the one-sided strengthened specimen, i.e., S-F1-T30-E0-b. This is mainly attributed to the earlier debonding of the UHPC-masonry interface, resulting that the strength of UHPC was not fully utilized under one-sided strengthening.

The essence of UHPC strengthened masonry columns is to work by confining the lateral deformation of the column. Hence, the lateral confining pressure exerted by UHPC on the masonry column was directly related to the strengthening effectiveness. Figure 8B shows the effect of strengthening thickness on the load-strain relationship. It can be seen that the ultimate strain of the masonry column was improved as the strengthening thickness increased. This is due to the increase in strengthening thickness, which enhanced the confinement effect of UHPC on the masonry columns. Correspondingly, the ultimate load capacity and strain of the masonry columns were raised. The results of these tests indicated that the confining effect created by the UHPC layer provided additional horizontal support to the masonry columns. In addition, it should be noted that the strain of specimens under the same load decreased with increasing strengthening thickness. Comparing specimens S-F4-T30-E60-a and S-F4-T20-E60-b, the compressive strains on the A face were 298.34 and 698.89 με respectively when the load was 300 kN. This is because, with increasing strengthening thickness, the stiffness of the masonry columns was enhanced. The confinement effect of the UHPC on masonry column increased, and the lateral deformation of masonry column strengthened with UHPC was decreased, resulting in the reduction of strains.

The effect of eccentricity on the load-strain relationship of masonry columns is shown in Figure 8C. It can be observed that the initial stiffness of the masonry columns showed great differences even in the same group of specimens. This may be caused by the complicated deformation of columns strengthened with UHPC. During the whole loading process, the ultimate strain of masonry columns decreased with the increase in eccentricity. This can be explained that the increase in eccentricity decreased the load-carrying capacity of the masonry column. Consequently, the ultimate strain of the masonry column was reduced. Besides, it can be seen that the strain growth rate of the specimen near the eccentric face (i.e., D face) was faster than that far from the eccentric face (i.e., B face). Taking specimen S-F4-T20-E30-b as an example, the strain on the B face was 221.75 με and the strain on the D face was 1,242.96 με under the same load of 500 kN. This is attributed that eccentric loading causing a strain gradient in the axial deformation of the masonry column. It exhibited a non-uniform distribution in strain and the strain growth was faster on the near eccentric face.

4 Finite element modeling

4.1 Establishment of finite element model

4.1.1 Introduction to numerical simulation of masonry

Presently, there are two main categories for masonry modeling, separated and monolithic (Pérez and Ortiz-Lozano, 2020). For the monolithic model, mortar and block, which are originally discrete medium aggregates, are treated as a unity of homogeneous and continuous materials. Then, the blocks and mortar are assigned the integral material properties of the masonry in ABAQUS. In this modeling approach, the bond slip and corresponding elastic compression of the block and mortar are ignored. This resulted that the mechanical mechanisms of the masonry cannot be adequately displayed after cracking. Cerrolaza et al. (1999) had shown that the monolithic model was more effective for the macro component size five times larger than the block. Separate modeling, in which the block and mortar are distinguished and given separate material properties. The difference in the constitutive relationship between block and mortar can be reflected by this model. In this paper, the separated modeling was used to model the masonry specimens. The stone and mortar units were modeled separately and were assigned separate material properties. Additionally, the analysis of the strengthening effect of UHPC on masonry columns was concentrated in the present paper, while the mechanical properties between stone and mortar were not investigated. Therefore, the contact properties of the stone and mortar can be referred to in literature (Guo, 2020), using the "Tie" function as simple bonding.

4.1.2 Element type and meshing

The extensive unit library is available in ABAQUS. In this numerical simulation, the eight-noded hexahedral linear reduction integration element (C3D8R) was utilized to simulate the UHPC, stone, mortar, and loaded end. The C3D8 element has the advantages of accurate displacement solution, excellent stability of element twist, suitable for contact analysis and no "shear self-locking" (Shi, 2006). In this study, the finite element (FE) model was a symmetrical structure and half of the structure was modeled to save computational resources. Taking specimen S-F4-T20-E60 as an example, the FE model and meshing of the UHPC-masonry column specimen are shown in Figure 9.

4.1.3 Modelling of traction separation at the UHPC-masonry interface

Hussein et al. (2017); Jang et al. (2018) applied a traction-separation model to simulate the behavior of the UHPC-HPC interface and the UHPC joint push-out tests, respectively. This approach was similarly applied in this paper to simulate the bonding behavior of the UHPC-masonry interface. The traction-

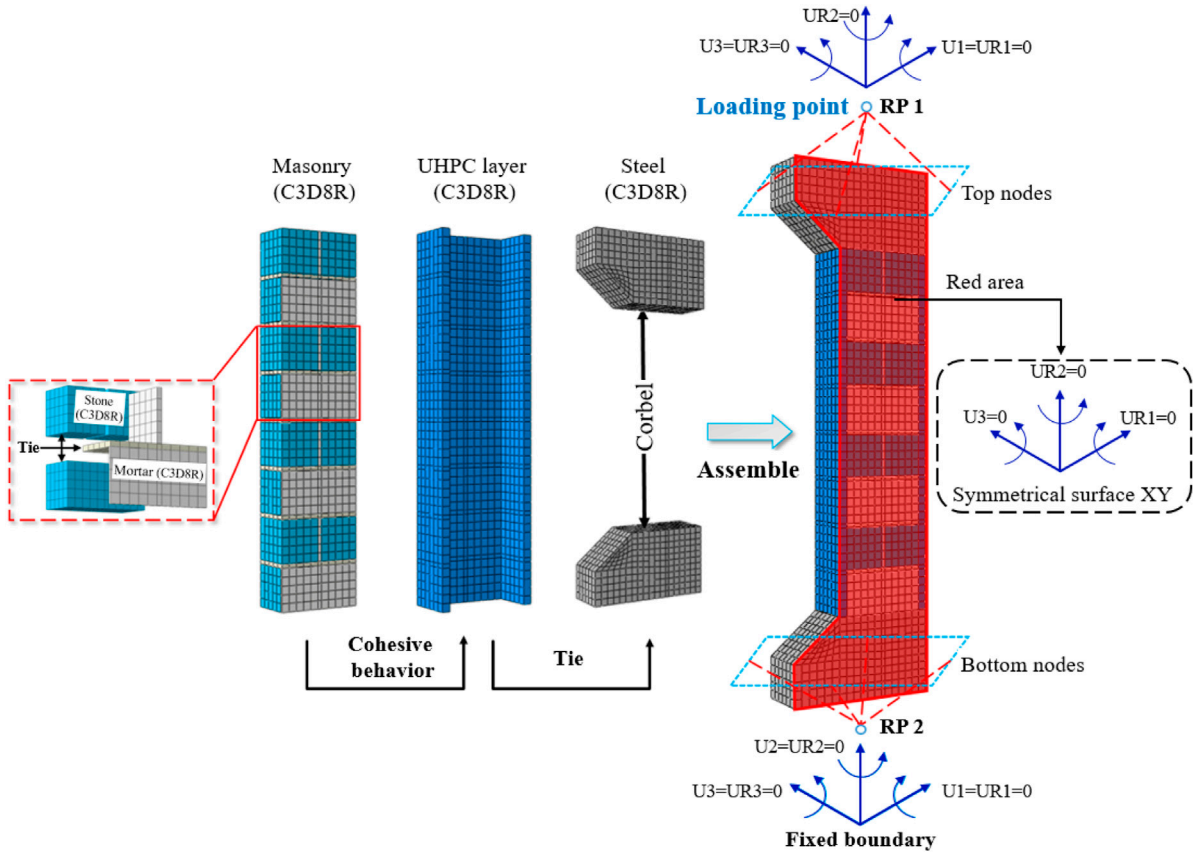

FIGURE 9
The FE model and meshing of UHPC-masonry column.

separation model, which establishes the constitutive relationship between the interfacial stress and the separation. It consists of the linear elastic traction-separation, the damage initial criterion (DIC) and the damage evolution. The traction-separation response described in the ABAQUS analysis manual is given in Figure 10.

Where t_n^0 (t_s^0, t_t^0) is the peak values of traction, $(t_n^0, t_s^0, t_t^0) = (1.75, 1.2, 1.2)$. δ_n^0 (δ_s^0, δ_t^0) is the separation of the t_n^0 (t_s^0, t_t^0), $\delta_n^{\max}$ $(\delta_s^{\max}, \delta_t^{\max})$ is an effective separation at complete failure. K_n (K_s, K_t) is the contact stiffness at the elastic stage, $(K_n, K_s, K_t) = (3.5, 2.4, 2.4)$. The plastic displacement is 4.5 mm. The stabilization is 0.0001. The area surrounded by the curve and the horizontal axis of the coordinate is the fracture energy (G_{IC}) (ABAQUS, 2012). Damage evolution is divided into linear and non-linear evolution. In order to simplify the calculations, the linear damage evolution was chosen for the simulations in this paper.

There are four primary damage criteria in ABAQUS, namely, Maxs Damage, Maxe Damage, Quads Damage and Quade Damage. However, the failure strain is extremely difficult to measure, and Maxs Damage would lead to a conservative result. Therefore, Quads Damage was used in this paper, as shown in Eq. 1.

$$\left(\frac{t_n}{t_n^0}\right)^2 + \left(\frac{t_s}{t_s^0}\right)^2 + \left(\frac{t_t}{t_t^0}\right)^2 = 1 \tag{1}$$

Where t_n, t_n^0 are the contact stress values and the maximum stress values in the normal directions of the bonded interface, respectively. t_s, t_s^0 are the contact stress value and the maximum stress value in the first shear direction at the bond interface, respectively. t_t, t_t^0 are the contact stress value and the maximum stress value in the second shear direction at the bond interface, respectively.

4.1.4 Constitutive model

4.1.4.1 UHPC

The concrete damage plasticity (CDP) model is based on the uniaxial compressive and tensile stress-strain relationship of concrete materials. Its theory of tensile and compressive damage was used to characterize the inelastic behavior of concrete. In this paper, the CDP model was utilized to simulate the UHPC material. The UHPC constitutive model used for the numerical simulations was obtained from the literature (Yang, 2007; Zhang et al., 2015) and is shown in Figure 11. The calculated procedures for UHPC compressive and tensile stress-strain relationship are given in Eq. 2, 3. Where, f_c is 142.5MPa, n is 1.19, ε_{cp} is 0.0035 $\xi = \varepsilon/\varepsilon_{cp}$, f_{ct} is 9.3MPa, ε_{ca} is 0.002, ε_{pc} is 0.01, ω_p is 1 mm, and p is 0.95.

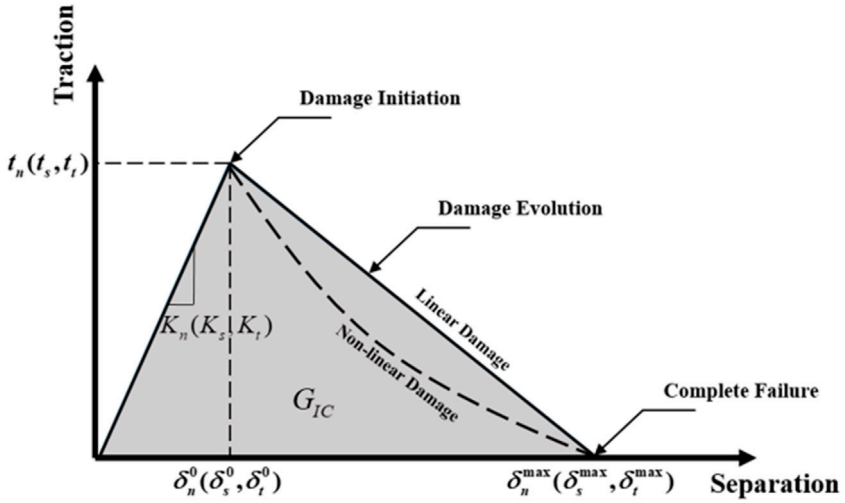

FIGURE 10
Typical traction-separation response with exponential damage evolution.

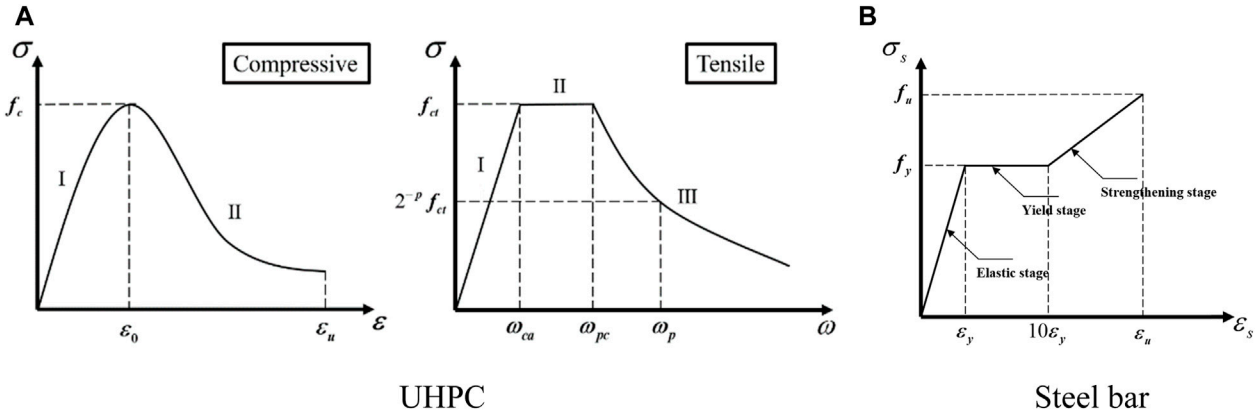

FIGURE 11
Constitutive law of UHPC and steel bar 4.1.4.3 Stone and mortar.

$$\sigma\begin{cases}\text{I} & f_c\dfrac{n\xi-\xi^2}{1+(n-2)\xi} \quad 0<\varepsilon<\varepsilon_{cp}\\ \text{II} & f_c\dfrac{\xi}{2(\xi-1)^2+\xi} \quad \varepsilon>\varepsilon_{cp}\end{cases} \tag{2}$$

$$\sigma\begin{cases}\text{I} & \dfrac{f_{ct}}{\varepsilon_{ca}}\varepsilon \quad 0<\varepsilon\le\varepsilon_{ca}\\ \text{II} & f_{ct} \quad \varepsilon_{ca}<\varepsilon\le\varepsilon_{pc}\\ \text{III} & \dfrac{f_{ct}}{\left(1+w/w_p\right)^p} \quad 0<w\end{cases} \tag{3}$$

In order to accomplish the definition of the CDP model. Five main parameters [i.e., the dilation angle (ψ), the eccentricity (e), the stress ratio (σ_{b0}/σ_{c0}), the yield surface shape (K) and the viscosity regularization (μ)] of the UHPC in the CDP were obtained by Li (2009), as shown in Table 8.

The damage factor d_k for UHPC in the plastic stage was determined from Eq. 4, by Liu (2021).

$$d_k=\frac{(1-\eta_k)\tilde{\varepsilon}_k^{in}E_0}{\sigma_k+(1-\eta_k)\tilde{\varepsilon}_k^{in}E_0} \tag{4}$$

where the subscripts $k = c$ and t indicate axial compression and tension, respectively. $\tilde{\varepsilon}_k^{in}$ indicates the plastic strain. E_0 is the initial elastic modulus of the UHPC. η_k is 0.6 in compression and 0.9 in tension.

4.1.4.2 Steel

The trilinear constitutive model proposed by the code (GB 50010-2010, 2010) was used for the reinforcement, as shown in Figure 11.

Where f_y and ε_y are the yield strength and yield strain of the reinforcement, f_y is 335MPa, ε_y is 0.0017. f_u and ε_u are the ultimate stress and ultimate strain, f_u is 455MPa, ε_u is 0.075.

TABLE 8 Values of CDP model parameters of UHPC, stone and mortar.

Materials	ψ	e	σ_{b0}/σ_{c0}	K	μ
UHPC	38°	0.1	1.14	0.6667	0.0005
Stone	30°	0.1	1.16	0.667	0.00015
Mortar	26°	0.1	1.16	0.667	0.00001

According to the relevant literature, the compressed constitution of stone and mortar in this study are shown in Eq. 5, 6, respectively.

$$\begin{cases} \dfrac{\sigma}{f_c} = 1.96\left(\dfrac{\varepsilon}{\varepsilon_0}\right) - 0.96\left(\dfrac{\varepsilon}{\varepsilon_0}\right)^2 & \left(0.0 \le \dfrac{\varepsilon}{\varepsilon_0} \le 1.0\right) \\ \dfrac{\sigma}{f_c} = 1.2 - 0.2\left(\dfrac{\varepsilon}{\varepsilon_0}\right)^2 & \left(1.0 \le \dfrac{\varepsilon}{\varepsilon_0} \le 1.6\right) \end{cases} \tag{5}$$

$$\begin{cases} \dfrac{\sigma}{f_m} = \dfrac{\varepsilon/\varepsilon_m}{0.3\left(\dfrac{\varepsilon}{\varepsilon_m}\right)^2 + 0.4\left(\dfrac{\varepsilon}{\varepsilon_m}\right) + 0.3} & \dfrac{\varepsilon}{\varepsilon_m} \le 1 \\ \dfrac{\sigma}{f_m} = \left(1.1 - 0.1\dfrac{\varepsilon}{\varepsilon_m}\right) & \dfrac{\varepsilon}{\varepsilon_m} > 1 \end{cases} \tag{6}$$

Where f_c and f_m are the peak compressive stresses of the stone and mortar. ε_0 and ε_m are the corresponding peak compressive strains, where f_c is 128.6MPa, f_m is 7.2MPa, ε_0 is 0.002 and ε_m is 0.0016.

Considering the plastic damage of stone and mortar, the formula for calculating the damage factor (Eq. 7) and the values of CDP model parameters (Table 8) were given.

$$d = 1 - \sqrt{\frac{\sigma}{E_0 \varepsilon}} \tag{7}$$

4.2 Verification of finite element model

In this section, the damage evolution and failure modes of FE model of masonry columns were summarized. The extent of damage to the model is quantified depending on the compression damage variable (DAMAGEC), where 0 indicates no damage and 1 indicates that the model is total loss of strength (El Ezz and Galal, 2017). Meanwhile, the peak loads of the FE model were compared with the test results, as showed in Figure 12. In particular, the errors were between 0.7% and 7.6%, indicating a good agreement on the simulation and test results. The validity of the ABAQUS simulation results was confirmed. It is notable that the bearing capacities predicted by the numerical simulations were slightly higher than the results of the experimental investigation. This can be attributed to shortcomings during fabrication and testing of the specimen in the experiment.

4.2.1 Effect of strengthening method and loading eccentricity

The damage progression and failure modes predicted by the numerical model were compared with experimental results. Comparison of failure modes for masonry columns under strengthening methods is illustrated in Figure 13A, i.e., the specimens of US-F0-T0-E0, S-F1-T30-E0, S-F3-T30-E0, and S-F4-T30-E0. As the peak load was reached, it can be seen that all the mortar joints were slightly damaged and the upper stones were seriously damaged. With improved methods of strengthening, the damage factor of the UHPC was increased, meanwhile the damage to the masonry columns was effectively relieved. This confirmed the usability of UHPC in masonry strengthening applications. Comparing the compressive damage progression under the failure load, the failure mode was observed to be consistent with the test. For the one-sided strengthening model, the failure was caused by the masonry columns being completely crushed and no extensive damage was observed by the UHPC. The similar phenomenon was observed during the experiments due to the earlier debonding of the UHPC from the masonry columns. In contrast, the effectiveness of the masonry column strengthening with three-sided and hoop strengthening was significantly enhanced. This is attributed to the bond between the UHPC and masonry columns was significantly improved, which resulted in the UHPC being adequately utilized and the synergy between the UHPC and the masonry columns was achieved. The satisfactory agreement was found in the test and FE model, except for the S-F1-T30-E0 group. The main reason is that the specimens were damaged during the tests due to fabrication and handling, which resulted in the lower load capacity of the masonry columns. However, the error of ultimate load carrying capacity between the tested and simulated was 7.6%, which was within the acceptable range. It was observed that the ultimate load capacity of the masonry columns was most significantly increased by the hoop strengthening. Compared to S-F3-T30-E0, the UHPC was subject to heavier damage in S-F4-T30-E0. This means that the masonry columns were protected by the UHPC, which caused in less damage to the masonry columns.

Figure 13A, i.e., the specimens of S-F4-T20-E0, S-F4-T20-E30, and S-F4-T20-E60, shows the progression of compression damage of FE models under different eccentric distances. It can be seen that the trend was approximately the same for the compressive damage in the models as the crack propagation in the tests. The masonry interior of the axial model was crushed at the peak load, where the UHPC damage was also substantial. At an eccentricity of 30 and 60 mm, the models exhibited the similar form of damage. The damage initially appeared on the near eccentric face of the masonry column, and progressed along the adjacent face. Meanwhile, the damage of the UHPC layer was extended from this area towards the adjacent face. The damage of masonry columns and UHPC was drastically reduced with increasing eccentricity when the failure load was reached. Simultaneously, the compression damage to the dorsal eccentric face showed a decreasing trend. When the eccentricity was increased to 60 mm, the compression damage factor of the dorsal eccentric face became 0, and it probably presented tensile damage state.

The experimental load-displacement curves and FEM numerical curves of masonry columns under different strengthening methods and loading eccentricities are presented in Figure 13B. The predicted curves obtained by FEM specimens were in excellent agreement in terms of initial stiffness and peak load in comparison with the test results. However, the overestimates of FEM were observed in the post-peak behavior. This could be attributed to the fact that, in the FEM, a perfect bond between stone units and mortar was assumed. In conclusion, the overall trends of load-displacement curves obtained from FEM were satisfactory with test results. In

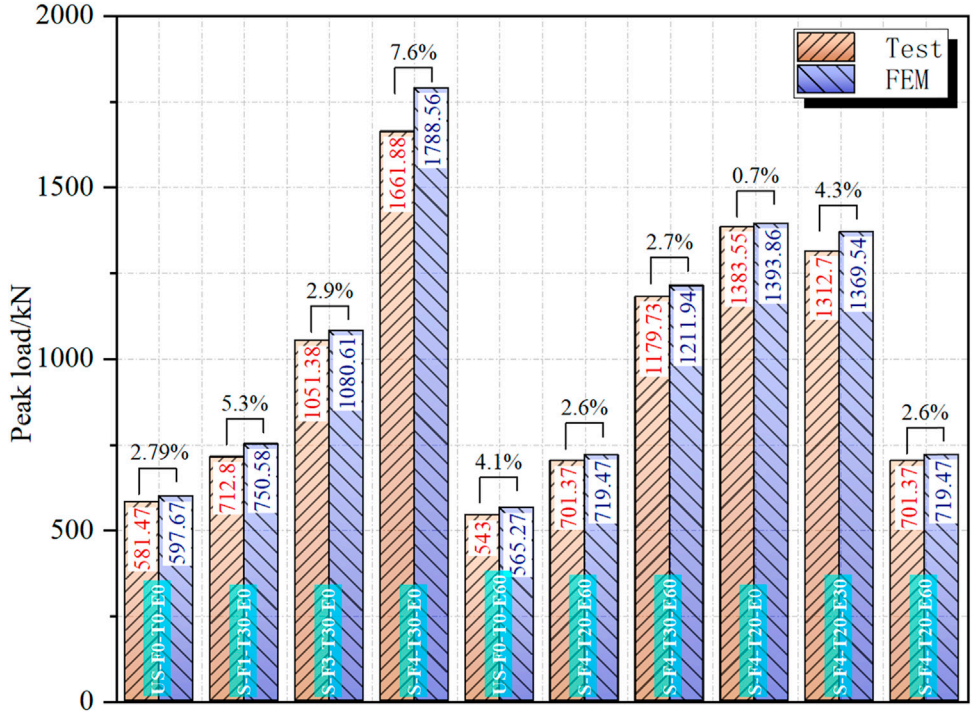

FIGURE 12
The comparison of peak loads from teats and FE models.

comparison with test results, the peak load discrepancy of specimens was within 7.6%, and the overall behavior was adequately captured by the FEM.

4.2.2 Effect of UHPC layer thickness

Figure 14 presents the progression of compression damage to the model under different strengthening thicknesses. As can be seen from Figure 14A, the damages of the masonry columns decreased as the strengthening thickness increased, in the meantime the damage of UHPC increased. This means that the UHPC was involved in the masonry column synergy, and shared partial loads of the masonry column. This phenomenon was particularly noticeable in the compressive damage progression of the failure load. With increasing strengthening thickness, the damage to the masonry columns did not differ significantly, while the damage to the UHPC was considerably increased. This confirmed the effectiveness of UHPC in strengthening masonry columns.

The experimental load-displacement curves and FEM numerical curves of masonry columns under strengthening thickness are presented in Figure 14B. For specimens with thickness of strengthening layer increased, the strength in failure was overestimated by the models owing to the changes in stiffness and confinement stresses of UHPC. The results of numerical modelling and experimental results showed that numerical models were in close agreement with the experimental results with regard to the overall response of masonry columns strengthened with UHPC. In addition, the peak loads and corresponding lateral displacements for the FE models were extracted, which were compared with the test, as shown in Figure 14B. It is observed that the lateral displacement was reduced at the peak load due to the UHPC layer being sufficient to restrict the horizontal buckling of the masonry columns. In addition, it is worth noting that the FE models were in good agreement with the peak loads of the test results, but the lateral displacements were considerably different. However, the overall trend in lateral displacement was consistent, both presenting a decrease with the strengthening thickness. The main reason for this was that the lateral displacements could not be accurately modelled by ABAQUS after the masonry columns had cracked. The cracking of masonry columns was only represented by the damage factor reaching a discount to the stiffness. In contrast, the software was relatively accurate for the simulation of the ultimate bearing capacity of masonry columns.

In practical strengthening engineering, the thickness of the strengthening plays an important role in the bearing capacity and durability of the structure. In order to investigate the optimum strengthening thickness for enhancing the ultimate bearing capacity of the masonry columns under axial compression. On the basis of the hoop strengthening, the FE models of 6 groups were designed. These models had a strengthening thickness of 35, 40, 45, 50, 55 and 60 mm, respectively. Figure 15 shows the relationships between strengthening thickness and the peak load raising rate of the FE models together with the corresponding lateral displacement.

Figure 16 presents the compressive damage progression of the FEM under different strengthening thicknesses. No significant distinctions in UHPC damage were observed when the strengthening thickness was less than 50mm, and the majority of damage concentrated in the upper part of the column, as shown in Figure 16A. Eventually, the masonry columns were excessively damaged leading to the overall failure of the structure. At this

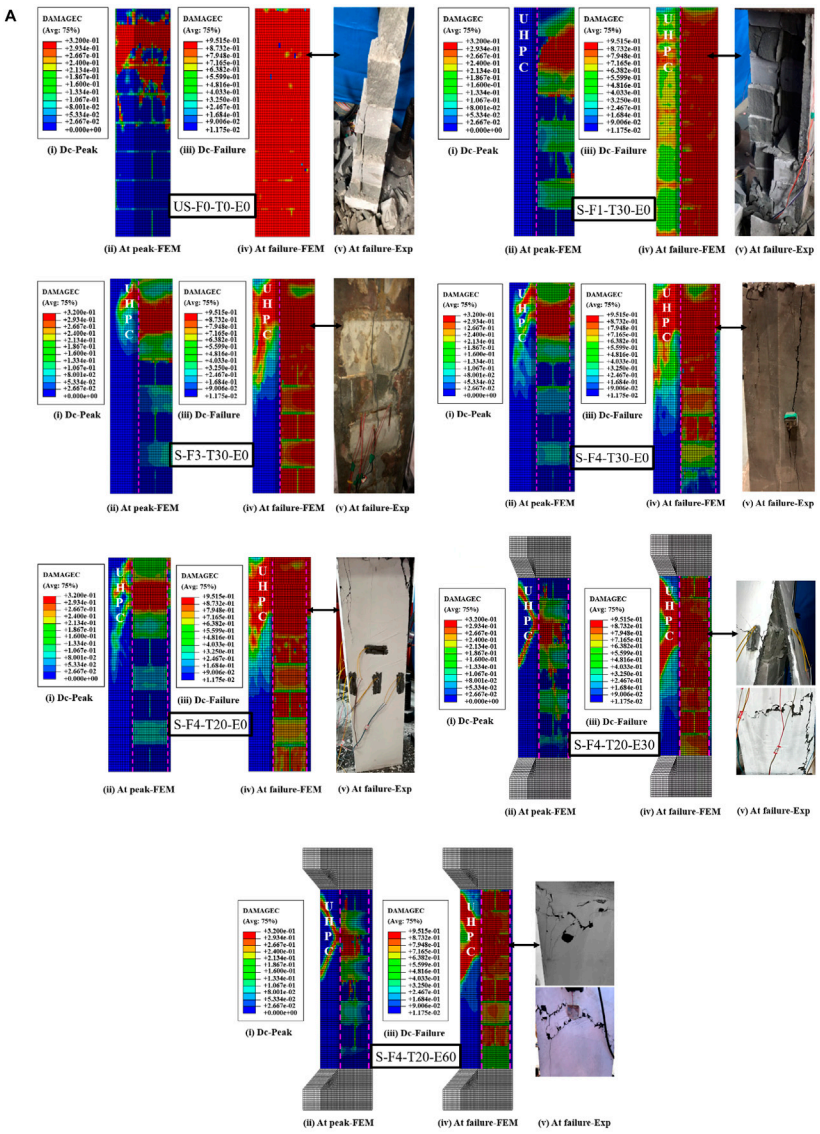

FIGURE 13
Comparison of finite element analysis and experimental results under strengthening methods and eccentric distances.

thickness, the damage of UHPC and masonry column in the lower region was poor, and neither the UHPC nor the masonry column were fully utilized, as can be seen from Figure 16B. It was observed that the damage of UHPC extended towards the lower end of the masonry column when the strengthening thickness reached 50 mm or more. It indicates that the utilization of UHPC had been enhanced, resulting in the whole bearing capacity of the masonry columns was increased.

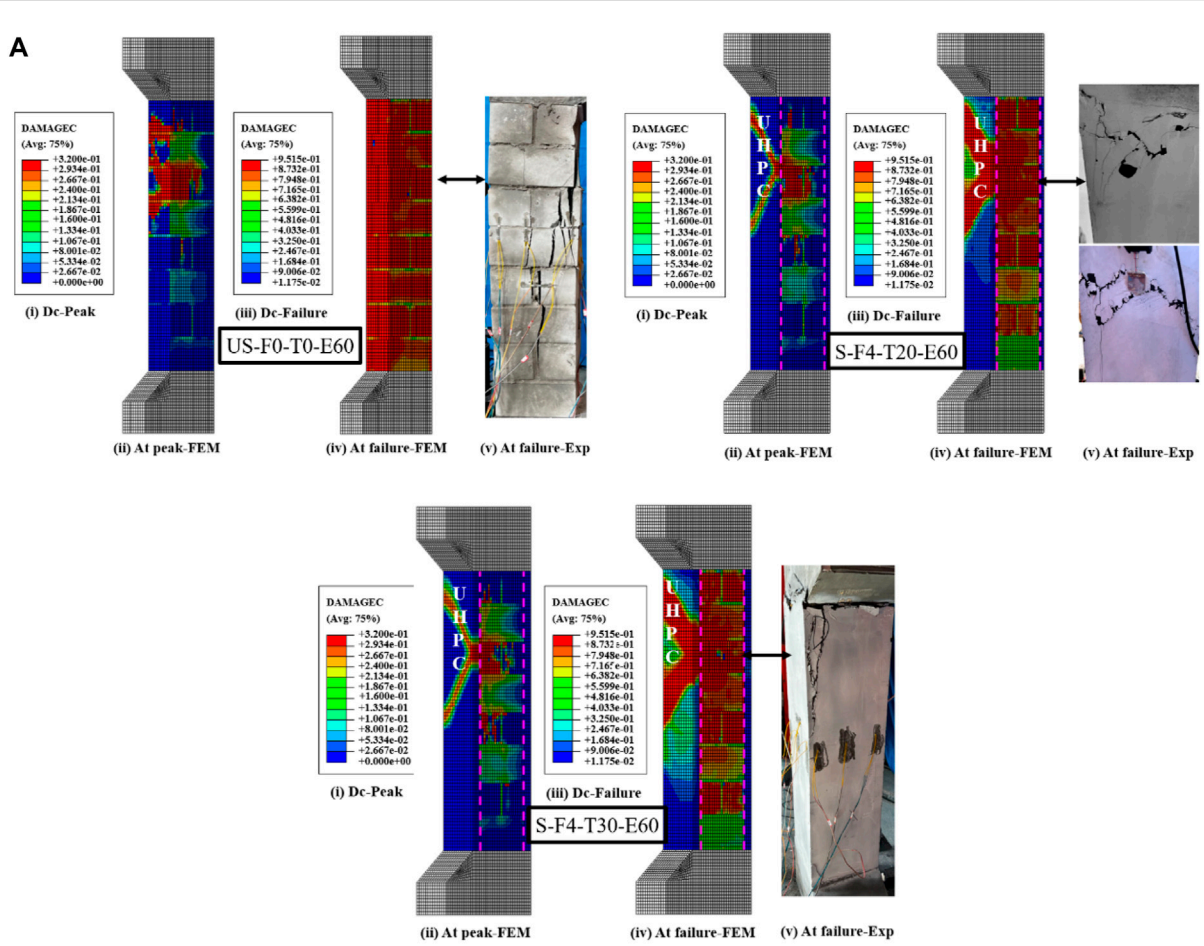

FIGURE 14
Comparison of finite element analysis and experimental results under strengthening thicknesses.

Obviously, as the thickness of the strengthening was increased, the bearing capacity of the masonry columns and the utilization of UHPC were improved. However, in practical engineering, the thickness cannot be increased indefinitely. On the one hand, the phenomenon is easily seen that the original structure had been damaged while the strengthening layer had not yet reached its own

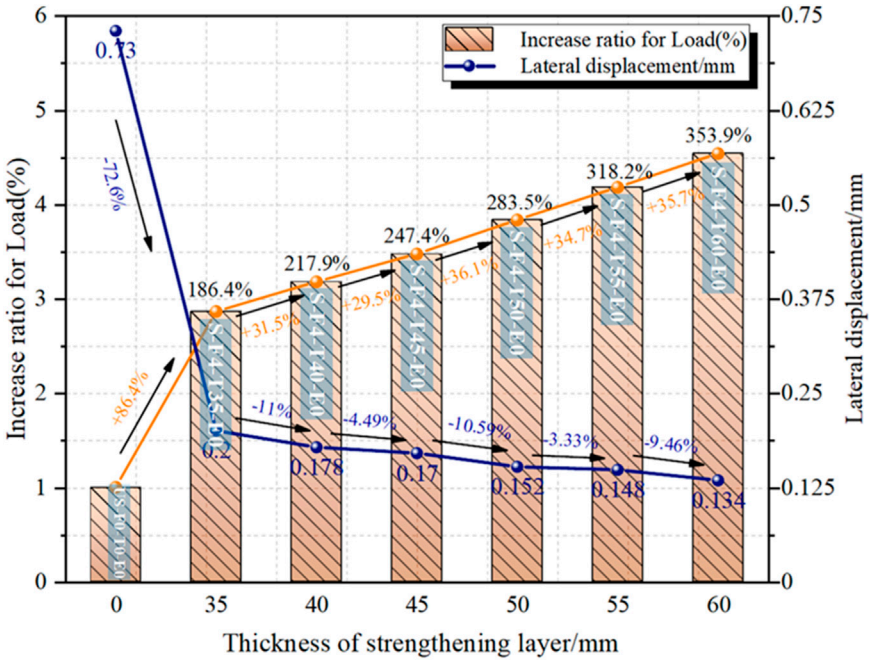

FIGURE 15
Effect of strengthening thickness on peak load raising rate and lateral displacement of masonry columns.

ultimate state. This can result in material properties not being adequately utilized, and economic waste. On the other hand, the weak areas for the overall structure (except for the strengthening layer) are easily formed and result in serious damage, which is a safety risk. Hence, considering economic and safety factors, it was recommended that the thickness of the strengthening should be 50 mm.

Besides, the strengthening layer was extremely susceptible to debonding from the masonry columns, which was observed in the tests. Resulting in that UHPC cannot adequately participate in the synergistic forces of the masonry columns. This was reflected in the FE model by a slight or no damage factor of the strengthening layer. Therefore, based on the optimal strengthening thickness model, the strengthening efficiency of UHPC was analyzed by keyway and planting bars at the bond interface. Figure 17 shows the progression of compression damage for the two types of interface treatment.

The peak loads of the keyway and planting bars calculated using the FE model were 3050 kN and 3377.02kN, respectively. As can be seen in Figures 17B, C, the UHPC damage factor was significantly increased for the model after the interface treatment compared to S-F4-T50-E0 (i.e., Figure 17A). In addition, the masonry columns were more adequately damaged. This was probably caused that the bonding of the UHPC to the masonry column was enhanced by the interface treatment, which increased the effective area to be subjected to the load. Consequently, the whole of the model was subjected to a more homogeneous force, while the bearing capacity of the masonry columns was dramatically increased. Overall, the combination of a keyway or a planting bars with UHPC was recommended when the UHPC was applied to strengthening engineering. Its aims to maximize the superior performance of UHPC, and thus improved the load bearing capacity and durability of the structure.

5 Conclusion

The primary conclusions were the following:

(1) Compared to unstrengthened column, the compressive behavior of masonry columns strengthened with UHPC was considerably improved. The masonry column failure mode was changed by UHPC confinement. Numerous small cracks were observed in the strengthened masonry columns only on the UHPC surfaces, instead of a few large vertical cracks in the unstrengthened columns. Ductile failure behavior was exhibited in masonry columns strengthened using UHPC, owing to the crack bridging capacity of the steel fibers in the interface. Moreover, the high elastic modulus of UHPC provided a guarantee for the initial compressive stiffness of the masonry columns.

(2) In terms of strengthening methods, the hoop strengthening provided a greater gain in maximum load and deformation capacity of masonry columns as compared to one-sided and three-sided strengthening. The increase in peak load, ductility and dissipated energy of masonry columns under hoop strengthening were 185.81%, 49.09% and 185.81%, respectively, against unstrengthened columns. Meanwhile, crushing failure of masonry columns can be retarded by hoop reinforcement, and good integrity of masonry columns

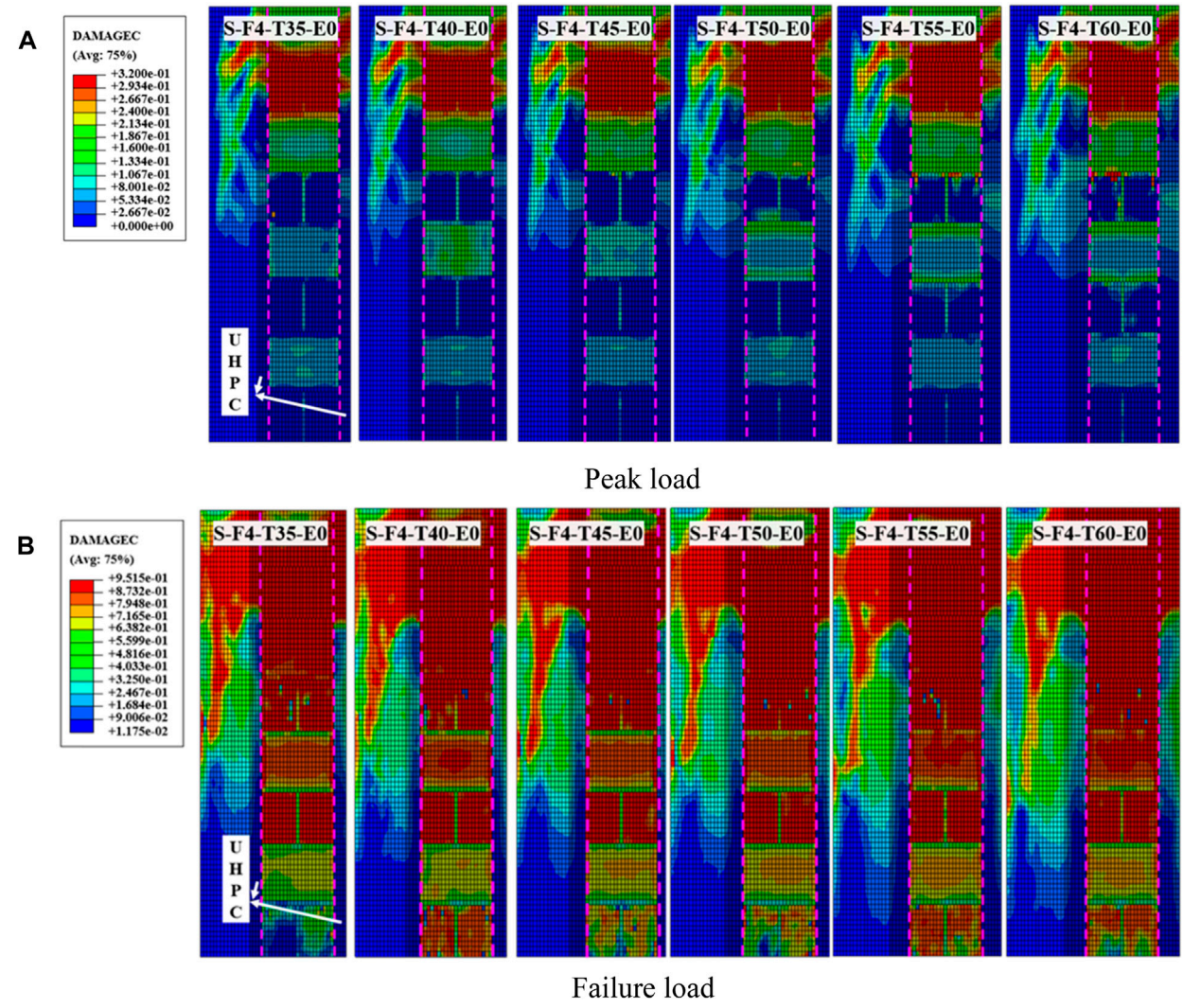

FIGURE 16
Compression damage progression of models with different strengthening thicknesses.

strengthened using hoop was observed at failure. In practical engineering, we recommend that hoop strengthening should be privileged over other strengthening methods in the selection of UHPC strengthening techniques.

(3) For masonry columns strengthened with UHPC, the compressive strength, ductility and energy consumption capacity can be significantly increased by increasing thickness of strengthening layer. As the thickness of strengthening layer was increased from 0mm to 20 mm and 30mm, the increase range of strength was from 29.17% to 117.26%, the increase range of ductility was from 13.08% to 44.86%, and the increase range of energy dissipation capacity was from −12.47% to 2.34%. In addition, the lateral displacement corresponding to the peak load was decreased by 32.44% and 37.24%. It was demonstrated that the strength of masonry columns was raised by UHPC, and crushing damage of the structure could be mitigated.

(4) Whether UHPC was used or not, the bearing capacity of masonry columns was decreased with the increase of eccentricity. However, compared with the unstrengthened masonry columns (US-F0-T0-E60), the peak load of the S-F4-T20-E60 column strengthened with UHPC increased by 29.17%. This phenomenon demonstrated the effectiveness of UHPC in strengthening masonry columns under eccentric loading.

(5) The FE model of UHPC strengthened masonry columns was established by ABAQUS. The simulation results were verified against the experimental results and the error value was within 7.6%. The model was successful in simulating the strength and failure mode of masonry columns.

In general, the capacity, ductility and stiffness of masonry columns can be enhanced significantly by using UHPC strengthening. However, a weak interface existed in the UHPC-masonry columns, which was vulnerable to damage caused by interfacial peeling. Therefore, the shear capacity of these interfaces should be concerned in the design in order to avoid structural damage owing to interfacial peeling.

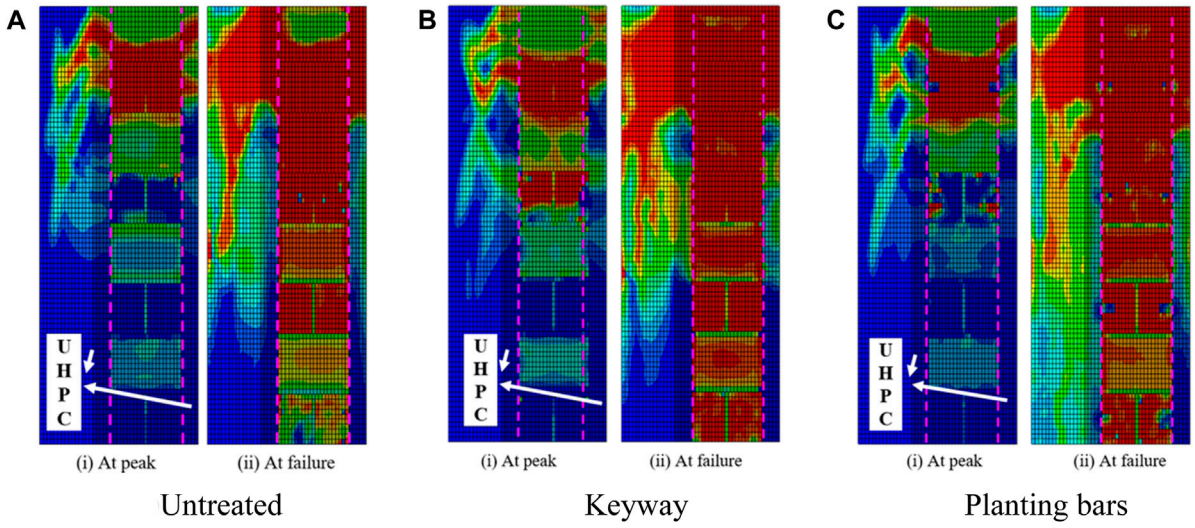

FIGURE 17
Compression damage progression of the models.

Data availability statement

The original contributions presented in the study are included in the article/Supplementary Material, further inquiries can be directed to the corresponding author.

Author contributions

ZJ: Writing–original draft, Investigation. JY: Conceptualization, Data curation, Writing–review and editing. HS: Software, Writing–review and editing.

Funding

The author(s) declare financial support was received for the research, authorship, and/or publication of this article. The authors highly appreciate the financial support from the National Natural Science Foundation of China (Grant Nos 52278293, U20A20314), and Project of Science and Technology Program of Department of Transport, Hubei Province (2020-186-1-6), the Science and Technology Research Program of Chongqing Municipal Education Commission (KJZD-M202300706), Chongqing Science and Technology Project (CSTB2022TIAD-KPX0205), and Guangxi key research and development plan project (Grant No. GuikeAB22036007).

Conflict of interest

Author JY was employed by the company Guangxi Communications Investment Group Co., Ltd.

The remaining authors declare that the research was conducted in the absence of any commercial or financial relationships that could be construed as a potential conflict of interest.

Publisher's note

References

ABAQUS (2012). *ABAQUS, standard user's manual, version 6.12 Providence*. RI (USA): Dassault Systemes Corp.

ACI Committee 440 (2008). *Guide for the design and construction of externally bonded FRP systems for strengthening concrete structures ACI 440.2R-08*. Farmington Hills: MI.

Alotaibi, K. S., and Galal, K. (2018). Experimental study of CFRP-confined reinforced concrete masonry columns tested under concentric and eccentric loading. *Compos. Part B Eng.* 155, 257–271. doi:10.1016/j.compositesb.2018.08.024

Angiolilli, M., Gregori, A., Pathirage, M., and Cusatis, G. (2020). Fiber Reinforced Cementitious Matrix (FRCM) for strengthening historical stone masonry structures: experiments and computations. *Eng. Struct.* 224, 111102. doi:10.1016/j.engstruct.2020.111102

Babaeidarabad, S., Arboleda, D., Loreto, G., and Nanni, A. (2014). Shear strengthening of un-reinforced concrete masonry walls with fabric-reinforced-cementitious-matrix. *Constr. Build. Mater.* 65, 243–253. doi:10.1016/j.conbuildmat.2014.04.116

Bahmani, H., and Mostofinejad, D. (2022). Microstructure of ultra-high-performance concrete (UHPC)–A review study. *J. Build. Eng.* 50, 104118. doi:10.1016/j.jobe.2022.104118

Bajaber, M. A., and Hakeem, I. Y. (2021). UHPC evolution, development, and utilization in construction: a review. *J. Mater. Res. Technol.* 10, 1058–1074. doi:10.1016/j.jmrt.2020.12.051

Cerrolaza, M., Sulem, J., and Elbied, A. (1999). A Cosserat non-linear finite element analysis software for blocky structures. *Adv. Eng. Softw.* 30 (1), 69–83. doi:10.1016/s0965-9978(98)00059-3

Dadvar, S. A., Mostofinejad, D., and Bahmani, H. (2020). Strengthening of RC columns by ultra-high performance fiber reinforced concrete (UHPFRC) jacketing. *Constr. Build. Mater.* 235, 117485. doi:10.1016/j.conbuildmat.2019.117485

Deng, M., and Li, T. (2020). Masonry columns strengthened with bar mesh highly ductile fiber reinforced concrete (BMHDC) jacket under concentric and eccentric loads. *Constr. Build. Mater.* 237, 117606. doi:10.1016/j.conbuildmat.2019.117606

El Ezz, A. A., and Galal, K. (2017). Compression behavior of confined concrete masonry boundary elements. *Eng. Struct.* 132, 562–575. doi:10.1016/j.engstruct.2016.11.043

El-Sokkary, H., and Galal, K. (2019). Performance of eccentrically loaded reinforced-concrete masonry columns strengthened using FRP wraps. *J. Compos. Constr.* 23 (5), 04019032. doi:10.1061/(asce)cc.1943-5614.0000958

Farzad, M., Sadeghnejad, A., Rastkar, S., Moshkforoush, A., and Azizinamini, A. (2020). A theoretical analysis of mechanical and durability enhancement of circular reinforced concrete columns repaired with UHPC. *Eng. Struct.* 209, 109928. doi:10.1016/j.engstruct.2019.109928

Fossetti, M., and Minafò, G. (2017). Comparative experimental analysis on the compressive behaviour of masonry columns strengthened by FRP, BFRCM or steel wires. *Compos. Part B Eng.* 112, 112–124. doi:10.1016/j.compositesb.2016.12.048

Fossetti, M., and Minafò, G. (2016). Strengthening of masonry columns with BFRCM or with steel wires: an experimental study. *Fibers* 4 (4), 15. doi:10.3390/fib4020015

GB 50010-2010 (2010). *Code for design of concrete structures*. Beijing: CN.

GB/T 31387-2015 (2015). *Reactive powder concrete*. Beijing: CN.

Guo, H. B. (2020). *Numerical simulation study on bond behavior of FRP-masonry interface under single shear action*. Yunnan, China: Yunnan University.

H. Marthys and L. Noland (Editors) (1989). *Proceedings of an international seminar on evaluation, strengthening, and retrofitting masonry buildings* (Colorado: TMS).

Hung, C. C., and Yen, C. H. (2021). Compressive behavior and strength model of reinforced UHPC short columns. *J. Build. Eng.* 35, 102103. doi:10.1016/j.jobe.2020.102103

Hussein, H. H., Walsh, K. K., Sargand, S. M., Ai Rikabi, F. T., and Steinberg, E. P. (2017). Modeling the shear connection in adjacent box-beam bridges with ultrahigh-Performance concrete joints. I: model calibration and validation. *J. Bridge Eng.* 22 (8), 4017043. doi:10.1061/(asce)be.1943-5592.0001070

Jang, H. O., Lee, H. S., Cho, K., and Kim, J. (2018). Numerical and experimental analysis of the shear behavior of ultrahigh-performance concrete construction joints, *Adv. Mater. Sci. Eng.* 2018 1–17. doi:10.1155/2018/6429767

Jing, L., Yin, S., and Aslani, F. (2021). Experimental investigation on compressive performance of masonry columns confined with textile-reinforced concrete. *Constr. Build. Mater.* 269, 121270. doi:10.1016/j.conbuildmat.2020.121270

JTG D61-2005 (2005). *Code for design of highway masonry bridges and culverts*. Beijing: CN.

JTG E41-2005 (2005). *Test methods of rock for highway engineering*. Beijing: CN.

Khan, M. I., Al-Osta, M. A., Ahmad, S., and Rahman, M. K. (2018). Seismic behavior of beam-column joints strengthened with ultra-high performance fiber reinforced concrete. *Compos. Struct.* 200, 103–119. doi:10.1016/j.compstruct.2018.05.080

Kouris, L. A. S., and Triantafillou, T. C. (2018). State-of-the-art on strengthening of masonry structures with textile reinforced mortar (TRM). *Constr. Build. Mater.* 188, 1221–1233. doi:10.1016/j.conbuildmat.2018.08.039

Krevaikas, T. D., and Triantafillou, T. C. (2005). Masonry confinement with fiber-reinforced polymers. *J. Compos. Constr.* 9 (2), 128–135. doi:10.1061/(asce)1090-0268(2005)9:2(128)

Li, H. Y. (2009). *Parametric identification for reactive powder concrete damage plasticity constitutive model and FEM verification*. Beijing, China: Beijing Jiaotong University.

Li, T., Deng, M., Jin, M., Dong, Z., and Zhang, Y. (2021a). Performance of axially loaded masonry columns confined using textile reinforced concrete (TRC) added with short fibers. *Constr. Build. Mater.* 279, 122413. doi:10.1016/j.conbuildmat.2021.122413

Li, T., Deng, M., Jin, M., and Zhang, Y. (2022). Experimental study on axial compressive behavior of full-scale masonry columns strengthened with reinforced high ductile concrete (RHDC). *Eng. Struct.* 252, 113650. doi:10.1016/j.engstruct.2021.113650

Li, T., Deng, M., and Zhang, Y. (2021b). Effect of eccentricity on strengthening efficiency of bar mesh high ductile concrete (BMHDC) on slender masonry columns. *Eng. Struct.* 230, 111732. doi:10.1016/j.engstruct.2020.111732

Liu, K. (2021). *Study on interfacial bonding mechanical properties of NSC-UHPC wet joint*. Beijing, China: Beijing University of Civil Engineering and Architecture.

Murgo, F. S., and Mazzotti, C. (2019). Masonry columns strengthened with FRCM system: numerical and experimental evaluation. *Constr. Build. Mater.* 202, 208–222. doi:10.1016/j.conbuildmat.2018.12.211

Pérez, Y. C., and Ortiz-Lozano, J. A. (2020). Fragility curves based on the numerical analysis of masonry walls against subsidence, using the Abaqus/CAE software and relying on the pulldown technique. *Rev. Int. métodos Numér. Cálc. diseño Ing.* 36 (1). doi:10.23967/j.rimni.2019.11.002

Prem, P. R., and Murthy, A. R. (2016). Acoustic emission and flexural behaviour of RC beams strengthened with UHPC overlay. *Constr. Build. Mater.* 123, 481–492. doi:10.1016/j.conbuildmat.2016.07.033

Qiao, W. J. (2014). *Study on model test and engineering application of masonry arch-bridge reinforced with composite arch circle*. Xi'an, China: Chang'an University.

Ragalwar, K., Heard, W. F., Williams, B. A., Kumar, D., and Ranade, R. (2020). On enhancing the mechanical behavior of ultra-high performance concrete through multi-scale fiber reinforcement. *Cem. Concr. Compos.* 105, 103422. doi:10.1016/j.cemconcomp.2019.103422

Shao, Y., Kuo, C. W., and Hung, C. C. (2021). Seismic performance of full-scale UHPC-jacket-strengthened RC columns under high axial loads. *Eng. Struct.* 243, 112657. doi:10.1016/j.engstruct.2021.112657

Shi, C., Wu, Z., Xiao, J., Wang, D., Huang, Z., and Fang, Z. (2015). A review on ultra high performance concrete: part I. Raw materials and mixture design. *Constr. Build. Mater.* 101, 741–751. doi:10.1016/j.conbuildmat.2015.10.088

Shi, Y. P. (2006). *Detailed examples of ABAQUS finite element analysis*. China: Machinery Industry Press.

T/CBMF37-2018 (2018). *Fundamental characteristics and test methods of ultra-high performance concrete*. Beijing: CN.

Vincent, T., and Ozbakkaloglu, T. (2013). Influence of fiber orientation and specimen end condition on axial compressive behavior of FRP-confined concrete. *Constr. Build. Mater.* 47, 814–826. doi:10.1016/j.conbuildmat.2013.05.085

Wang, J., Wan, C., Zeng, Q., Shen, L., Malik, M. A., and Yan, D. (2020). Effect of eccentricity on retrofitting efficiency of basalt textile reinforced concrete on partially damaged masonry columns. *Compos. Struct.* 232, 111585. doi:10.1016/j.compstruct.2019.111585

Wang, Z., Yang, J., Zhou, J., Yan, K., Zhang, Z., and Zou, Y. (2022). Strengthening of existing stone arch bridges using UHPC: theoretical analysis and case study. *Struct* 43, 805–821. doi:10.1016/j.istruc.2022.06.055

Witzany, J., Čejka, T., and Zigler, R. (2014). Failure mechanism of compressed short brick masonry columns confined with FRP strips. *Constr. Build. Mater.* 63, 180–188. doi:10.1016/j.conbuildmat.2014.04.041

Yang, J. (2007). *Flexural behavior of ultra-high performance concrete beams prestressed with CFRP tendons*. Changsha, China: Hunan University.

Yang, J., Chen, R., Zhang, Z., Zou, Y., Zhou, J., and Xia, J. (2023). Experimental study on the ultimate bearing capacity of damaged RC arches strengthened with ultra-high performance concrete. *Eng. Struct.* 279, 115611.

Yoo, D. Y., and Banthia, N. (2016). Mechanical properties of ultra-high-performance fiber-reinforced concrete: a review. *Cem. Concr. Compos.* 73, 267–280. doi:10.1016/j.cemconcomp.2016.08.001

Youssf, O., Hassanli, R., and Mills, J. E. (2017). Retrofitting square columns using FRP-confined crumb rubber concrete to improve confinement efficiency. *Constr. Build. Mater.* 153, 146–156. doi:10.1016/j.conbuildmat.2017.07.108

Yuan, W., Wang, X., Guo, A., Li, C., Dong, Z., and Wu, X. (2022). Cyclic performance of RC bridge piers retrofitted with UHPC jackets: experimental investigation. *Eng. Struct.* 259, 114139. doi:10.1016/j.engstruct.2022.114139

Zhang, J. (2014). *Experimental research on mechanical performance of stone arch bridge strengthened by the enclosed reinforced concrete*. Chengdu, China: Southwest Jiaotong University.

Zhang, Y., Li, X., Zhu, Y., and Shan, X. (2020). Experimental study on flexural behavior of damaged reinforced concrete (RC) beam strengthened by toughness-improved ultra-high performance concrete (UHPC) layer. *Compos. Part B Eng.* 186, 107834. doi:10.1016/j.compositesb.2020.107834

Zhang, Y., Yang, J., Li, T., and Deng, M. (2022). Mechanical behavior of RC columns strengthened with thin UHPC jacket under cyclic loads. *J. Build. Eng.* 49, 104065. doi:10.1016/j.jobe.2022.104065

Zhang, Y., Zhu, Y., Yeseta, M., Meng, D., Shao, X., Dang, Q., et al. (2019). Flexural behaviors and capacity prediction on damaged reinforcement concrete (RC) bridge deck strengthened by ultra-high performance concrete (UHPC) layer. *Constr. Build. Mater.* 215, 347–359. doi:10.1016/j.conbuildmat.2019.04.229

Zhang, Z., Shao, X. D., Li, W. G., Zhu, P., Chen, H., Zhang, D. W., et al. (2015). Prediction of the next highly pathogenic avian influenza pandemic that can cause illness in humans. *China J. Highw. Transp.* 28 (8), 50. doi:10.1186/s40249-015-0083-8

Zhang, Z., Pang, Z., Xu, L., Zou, Y., Yang, J., and Wang, C. (2023). The bond properties between UHPC and stone under different interface treatment methods. *Constr. Build. Mater.* 365, 130092.

Zhu, Y., Zhang, Y., Hussein, H. H., and Chen, G. (2020). Flexural strengthening of reinforced concrete beams or slabs using ultra-high performance concrete (UHPC): a state of the art review. *Eng. Struct.* 205, 110035. doi:10.1016/j.engstruct.2019.110035

Zou, Y., Yu, K., Heng, J., Zhang, Z., Peng, H., and Wu, C. (2023a). Feasibility study of new GFRP grid web - Concrete composite beam. *Compos. Struct.* 305, 116527.

Zou, Y., Zheng, K., Zhou, Z., Zhang, Z., Guo, J., and Jiang, J. (2023b). Experimental study on flexural behavior of hollow steel-UHPC composite bridge deck. *Eng. Struct.* 274, 115087.

Zou, Y., Jiang, J., Yang, J., Zhang, Z., and Guo, J. (2023c). Enhancing the toughness of bonding interface in steel-UHPC composite structure through fiber bridging. *Cem. Concr. Compos.* 137, 104947.

frontiers | Frontiers in Materials

TYPE Original Research
PUBLISHED 13 November 2023
DOI 10.3389/fmats.2023.1286197

OPEN ACCESS

EDITED BY
Zhongya Zhang,
Chongqing Jiaotong University, China

REVIEWED BY
Lei Zhao,
Guizhou Communications Polytechnic, China
Shaoyun Pu,
Shaoxing University, China
Jinyu Jiang,
Ningbo University, China

*CORRESPONDENCE
Bin Du,
bindu1982@163.com

RECEIVED 31 August 2023
ACCEPTED 13 October 2023
PUBLISHED 13 November 2023

CITATION
Li Y, Shen M, Du B and Yuan S (2023), An elastic-viscoplastic creep model for describing creep behavior of layered rock.
Front. Mater. 10:1286197.
doi: 10.3389/fmats.2023.1286197

An elastic-viscoplastic creep model for describing creep behavior of layered rock

Yukun Li, Mingxuan Shen, Bin Du* and Shisong Yuan

College of Civil Engineering, Guizhou University, Guiyang, Guizhou, China

To describe the full-stage creep behavior of layered rock accurately, a new elastic-viscoplastic creep model is proposed based on fractional order theory in this manuscript, which consists of a Hooke elastomer, a fractional Abel dashpot, a Kelvin body, and a new non-linear visco-plastic component. The non-linear creep model can not only describe the changes in three creep stages (primary creep, steady-state creep and accelerating creep) but also reflect the influence of different bedding angles of rock. The constitutive equations of the non-linear creep model are deduced by the empirical model method and plastic theory method, respectively. The parameters of the non-linear creep model are identified using the Levenberg-Marquardt algorithm from Origin. It shows that the creep model in this paper are highly consistent with the experimental data under different load levels, creep stages and bedding angles, and the accuracy and rationality of the model are verified. Moreover, the creep constitutive equations for layered rock derived by the two methods have the same fitting effect on the same set of experimental data.

KEYWORDS

layered rock, elastic-viscoplastic creep, constitutive model, fractional calculus, non-linear analysis

1 Introduction

Rock rheology refers to the continuous adjustment and recombination of rock and mineral fabric (skeleton) with the growth of time, resulting in the continuous increase and change of its stress and strain state with time (Sun, 2007a). The rheology of rock includes creep, stress relaxation and elastic aftereffects. Especially, the creep characteristics of rock are of great significance to the stability of rock engineering, and the research on this aspect is also of great significance and engineering application value. The study of creep characteristics of rock began in the 1930s, Griggs (Griggs, 1939) carried out a series of creep tests on rocks such as limestone, shale and sandstone in 1939, and concluded that rock creep occurs when the load reaches 12.5%–80.0% of its compressive strength. Several elasto-viscoplastic creep models have been proposed that can well describe the time-dependent behavior of rock under certain conditions (Wu et al., 2018; Brantut et al., 2013; Sone et al., 2014; Xia et al., 2009). In general, the classical rock rheological model theory is mainly limited to linear rheological problems, and there are two main methods to describe non-linear rheological problems of rock. The first method is to replace the linear model theory with a new non-linear rheological theory completely, such as internal time theory, fracture and damage mechanics theory, etc. The other method is to improve the classical model theory by using non-linear components (non-linear spring or non-linear dashpot) instead of linear elements.

The component model is widely used because of its intuitive concept and clear meaning. Classical component combination models include the Maxwell model, Kelvin model, Poyting-Thomson model, Burgers model and Nishihara model. However, the basic element of the classical model is linear, it is still linear whether connection in series or parallel, and can not describe the non-linear creep characteristics of the rock in the accelerating stage. Therefore, establishing a creep model which can describe the non-linear characteristics of the rock creep process has always been a hot and difficult point in the theoretical research of rock mechanics. In the present research, scholars (Cheng et al., 2020; Shan et al., 2020; Wang and Wan, 2016; Yang and Jiang, 2022) having been established different non-linear creep models by introducing creep damage theory (Shen et al., 2023a; Zhang et al., 2022a) and fractional calculus theory. The constitutive model based on fractional calculus theory with fewer parameters and better fitting effect has been widely applied in rock rheological mechanics. A classical example is Koeller (Koeller, 1984) used Riemann–Liouville (R-L) fractional dashpot to replace the traditional Newtonian dashpot in the component model in 1978. The R-L type (Zhou et al., 2018) or Caputo type (Liu et al., 2020) fractional order calculus theory is used to construct fractional dashpot to replace the traditional Newtonian dashpot in the element model, and to establish a creep model that can describe the three stages (primary creep, steady-state creep and accelerating creep) of rock creep. However, it lacks physical significance in the accelerating creep, and it can not well characterize the internal mechanism of accelerating creep of rock. Therefore, damage factors were introduced to describe the accelerating creep of rock, and establish an elasto-viscoplastic creep model reflecting the complete creep process of rock by combining fractional calculus theory and damage theory (Deng et al., 2022; Shen et al., 2022; Wu et al., 2018) becoming a relatively popular study method. In addition, scholars have study the mechanical characteristics about the concrete-rock combination (Shen et al., 2022; Zhang et al., 2019) and other interface (Shen et al., 2023b; Zhang et al., 2023). By comparing the creep model established by fractional calculus theory, it is based on the assumption that there are two stages (hardening and damage) in the creep of rock, and with clear physical significance for describing the accelerating creep stage. However, due to various ways of defining damage factors and increasing model parameters, the calculation is inconvenient.

There are abundant of achievements on creep characteristics for common rock, but few studies on creep characteristics for layered rock. In the basic mechanics study area, Ramamurthy (Ramamurthy, 1993) carried out a study on the physical and mechanical properties of rock with different bedding angles, explored the anisotropy law of strength and deformation. Yong (Yong Tsao, 2000; Yong, 2001) studied the effect of the bedding angle on the strength and elastic modulus for layered rock, proposed corresponding damage guidelines. Fortsakis (Fortsakis et al., 2012) modeled the bedding as separate units and the rock masses as anisotropic materials to investigate the differences in the analysis of isotropic, anisotropic and transverse isotropic analysis methods. Studies has also shown the influence of bedding angles in the basic mechanical properties for layered rock (Celleri et al., 2018; Chang et al., 2020; Hb et al., 2003; Saeidi et al., 2014; Wu et al., 2015; Yang et al., 2021). In the experimental creep study, Dubey (Dubey and Gairola, 2008) investigated the creep properties of salt rocks containing horizontal, vertical and diagonal laminations at different stress levels by uniaxial compression creep tests, and noted that the higher the stress level, the less the laminations affected the anisotropy of the creep properties of salt rocks. In recent years, some scholars (Hu et al., 2019; Liu et al., 2015; Xu et al., 2019; Zhang et al., 2021) have also studied the anisotropic creep law of layered rock by uniaxial compression creep tests and triaxial compression creep tests. In addition, the creep properties of layered rock under the coupling of multiple factors have been studied (Tang et al., 2018). In the study of creep constitutive model for layered rock, an approach is to inductively derive an empirical model from experimental phenomena (Park et al., 2016; Zhang et al., 2022b). It is based on the assumption of constant volume modulus, then to establish a creep constitutive model by identifying the creep parameters in different directions as different mutually independent values. Another approach is the plasticity theory model by assumption of Poisson's ratio constant (Aravas et al., 1995; Kou et al., 2023; Wang et al., 2018), which to establish the three-dimensional creep constitutive model for transverse isotropic rock by using the transverse isotropic flexibility matrix replace the isotropic flexibility matrix.

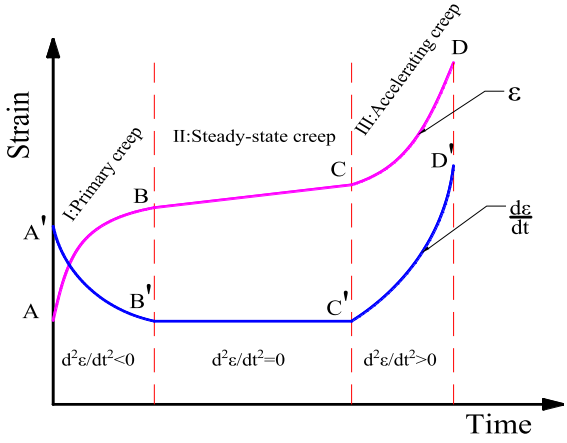

FIGURE 1
Three stages of the typical creep curve.

Based on the above analysis, the creep mechanics properties of rock has been widely studied, but less for layered rock. Therefore, a non-linear fractional creep model for layered rock was established in this manuscript by introducing a non-linear Abel dashpot. The model connected the Hooke body, non-linear Abel dashpot body, linear Kelvin body and non-linear viscoplastic body in series. Further more, the non-linear elastic-viscoplastic creep constitutive equations for layered rock were derived. A practical method for model parameters identification is proposed, and finally the accuracy and applicability of the model is verified by using different rock compression creep test data from relevant literature.

2 Rock creep processes and basic mechanical models

The typical creep curve of rock is shown in Figure 1. The *ABCD* is strain curve, and the $A'B'C'D'$ is strain rate curve, stage I, II, III is

TABLE 1 The basic mechanical components.

Name	Diagram	Constitutive equation
Hooke elastomer		$\varepsilon = \frac{\sigma}{E}$
Plastic body		$\left.\begin{array}{l}\varepsilon = 0, \sigma < \overset{s}{\sigma} \\ \varepsilon \to \infty, \sigma \geq \overset{s}{\sigma}\end{array}\right\}$
Newtonian dashpot	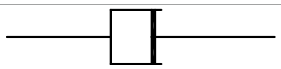	$\sigma = \eta \frac{d\varepsilon}{dt}$

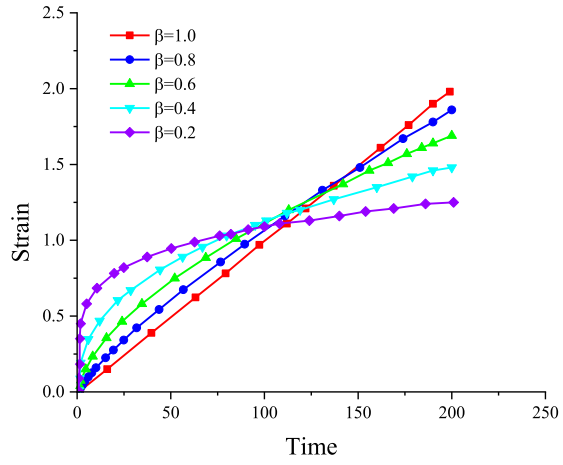

FIGURE 2
$0 < \beta \leq 1$.

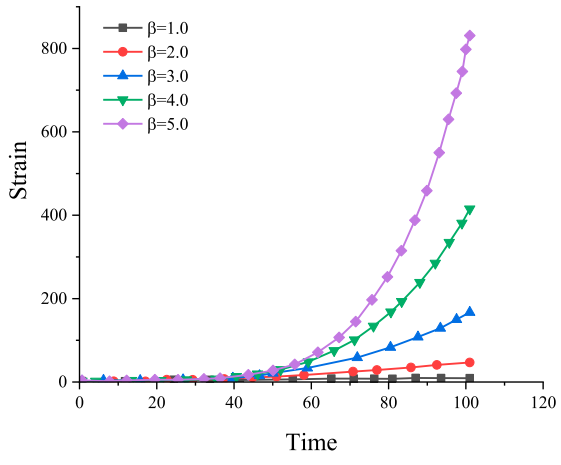

FIGURE 3
$\beta > 1$.

the primary creep, steady-state creep and accelerating creep, respectively.

When a load is applied, the rock then undergoes a transient elastic creep in section *OA*. Continuing to loading, the rock enters primary creep in the *AB* section, which exhibits a non-linear viscoelastic character. With increasing loading stress, the rock then undergoes steady-state creep in the *BC* section, which exhibits an approximately linear viscoelastic-viscoplastic character. When the loading stress level exceeds the long-term strength of the rock, the rock undergoes primary creep, steady-state creep and then enters the accelerating creep phase in the *CD* section until creep damage. Thus, the basic equation for the variation of rock creep strain with time can be expressed as

$$\varepsilon(t) = \varepsilon_e(t) + \varepsilon_{ve}(t) + \varepsilon_{vp}(t) \tag{1}$$

Where $\varepsilon_e(t), \varepsilon_{ve}(t), \varepsilon_{vp}(t)$ are elastic strain, viscoelastic strain and viscoplastic strain, respectively.

In rheological theory, a rock creep model should be able to characterise the processes of decay creep, steady-state creep and accelerating creep, and reflect the creep characteristics of the rock at different stress levels. The basic units of the rheological model are generally divided into elastic, plastic and viscous elements, and the mechanical model of the three basic units is shown in Table 1.

As the intrinsic relationships of the basic components are linear, the various classical rheological models, such as the Maxwell, Kelvin, Burgers and Nishihara models (Behbahani et al., 2016; Feng, 2021), which consist of basic components connected in series or parallel, are also linear in nature.

3 Establishment of elastic-viscoplastic creep model

3.1 Plastic body elements based on fractional order derivatives

3.1.1 Definition of fractional calculus

Fractional order calculus is an extension of integer order calculus. Since the 1990s, the theory and methods of fractional order calculus have been widely applied to various fields of the natural and social sciences. In the area of viscous fluid mechanics, the introduction of fractional order calculus theory allows for more realistic theoretical models to be developed in the study of mechanical physical problems associated with real fluids, leading to accurate conclusions. The Riemann–Liouville (R-L) type fractional order calculus is commonly used in the theory of rock rheology studies (Zhou

10.3389/fmats.2023.1286197

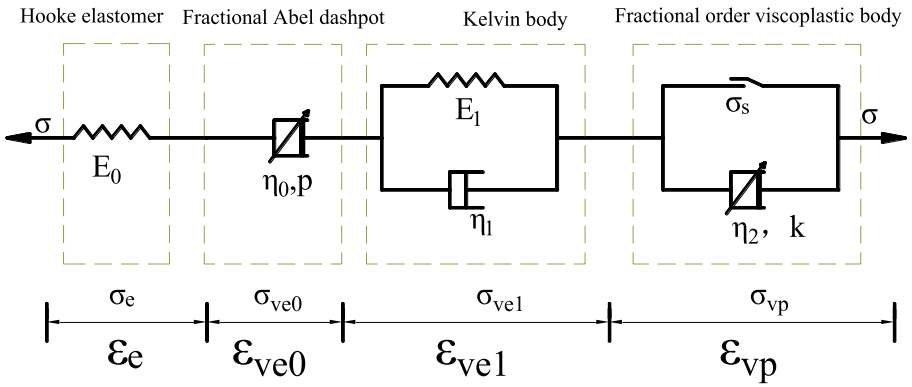

FIGURE 4
The six-element non-linear elastic-viscoplastic creep model.

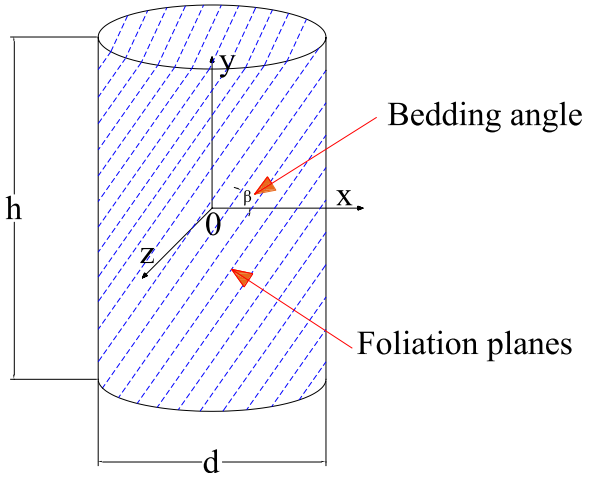

FIGURE 5
Diagram of bedding angle.

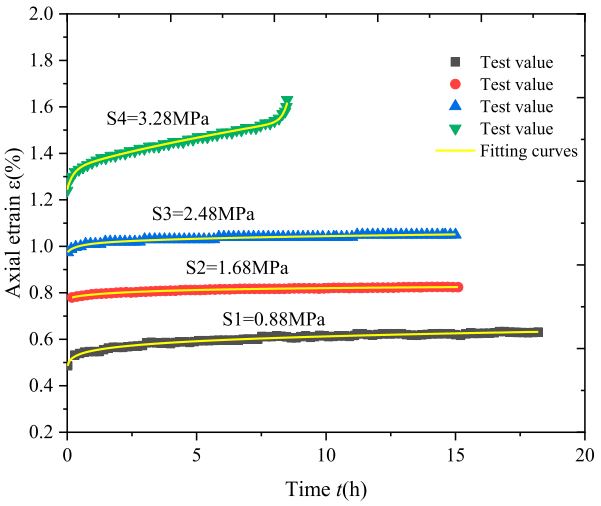

FIGURE 7
Creep equation fitting curves (ω= 4.56%).

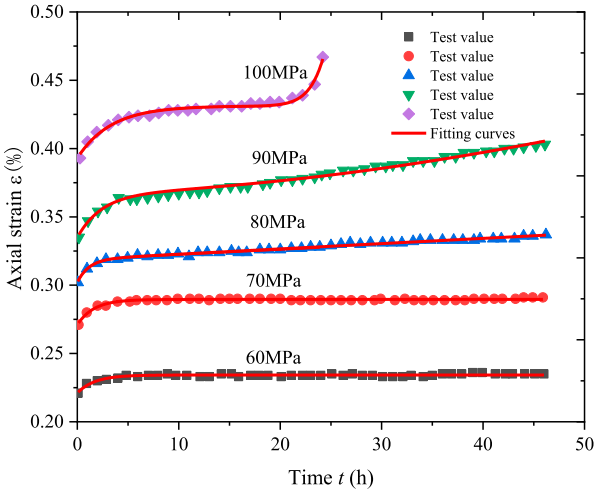

FIGURE 6
Creep equation fitting curves (ω= 0%).

et al., 2018), but its fractional order derivatives are hyper-singular and limited in applications in engineering and technology and in physical modeling. In this paper, we use a theory of fractional order derivatives with weak singular properties proposed by the Italian geophysicist Caputo. The Caputo fractional order derivative solves the fractional order initial value problem in the definition of R-L type fractional order calculus and has been widely used in the modeling process of many practical application problems (Liu et al., 2021). The definition of Caputo fractional order derivative is

$$ {}_{0}^{C}D_{t}^{\beta} f(t) = {}_{0}D_{t}^{\beta-n} D^{n} f(t) = \frac{1}{\Gamma(n-\beta)} \int_{0}^{t} (t-\xi)^{n-\beta-1} f^{(n)}(\xi) d\xi, \ (\beta > 0) \tag{2} $$

where n is the smallest integer greater than or equal to β; ξ is an integral variable of $[0, t]$; $f^{(n)}(\xi)$ is the n th order derivative of function $f(\xi)$; Γ is Gamma function, defined as

TABLE 2 Parameters of the one-dimensional creep model.

ω%	Loading stress	E_0 (MPa)	η_0 (MPa)	p	E_1 (MPa)	η_1 (MPa)	η_2 (MPa)	k	R^2
0	60	271.49	3.5×10^{19}	1	4533.69	7792.56			0.872
	70	258.30	2.6×10^{19}	1	3769.68	6155.71			0.955
	80	264.90	2.21×10^{5}	1	4783.74	5480.30	200892.84	0.805	0.989
	90	268.66	1.37×10^{19}	1	2767.25	6797.60	257095.94	1.737	0.988
	100	254.45	1.25×10^{21}	1	2619.23	8715.35	9.43×10^{11}	17.45	0.983

TABLE 3 Graded loading scheme.

ω/%	Confining pressure (MPa)	S1/MPa	S2/MPa	S3/MPa	S4/MPa
4.56	1	0.88	1.68	2.48	3.26
8.47	1	0.88	1.28	1.68	
12.38	1	0.88	1.28		

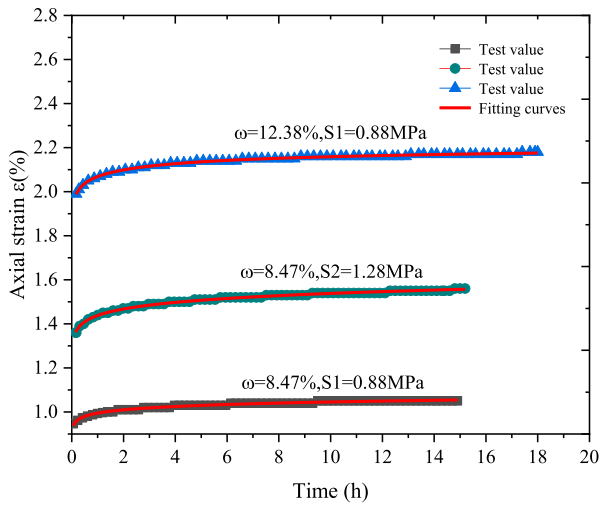

FIGURE 8
Creep equation fitting curves (ω= 8.47%,ω= 12.38%).

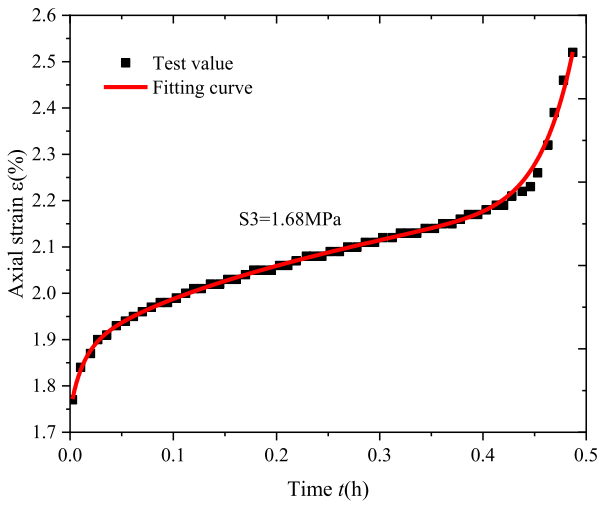

FIGURE 9
Creep equation fitting curve (ω= 8.47%).

$$\Gamma(z) = \int_0^{\infty} t^{z-1}e^{-t}dt = 2\int_0^{\infty} t^{2z-1}e^{-t^2}dt \tag{3}$$

$$\Gamma(1+z) = z\Gamma(z)(z \in N^*), \mathrm{Re}(z) > 0. \tag{4}$$

The Caputo fractional operator is shown in Eq. 5:

$${}_0^C D_t^{-\beta} f(t) = {}_0 D_t^{-\beta} f(t) = \frac{1}{\Gamma(\beta)}\int_0^t (t-\xi)^{\beta-1} f(\xi)d\xi, (\beta > 0) \tag{5}$$

The Laplace transform formula for the Caputo fractional order derivative is

$$L\left({}_0^C D_t^{\beta} f(t)\right) = s^{\beta}U(s) - \sum_{j=0}^{n-1} u^{(j)}(0)s^{\beta-j-1}, (n-1 < u \le n) \tag{6}$$

where $U(s)$ is the Laplace transform operator of the function $f(t)$.

3.1.2 Establishment of fractional order viscoelastic and viscoplastic bodies

The theory of fractional order calculus is applied to the traditional Newtonian dashpot to construct a fractional dashpot, called the Abel dashpot. As shown in Figure 4:

Define the stress-strain equation for the Abel dashpot as

$$\sigma(t) = \eta_0 \frac{d^{\beta}\varepsilon(t)}{dt^{\beta}} \tag{7}$$

Where η is the viscosity coefficient; $\sigma(t)$ is the axial stress and $\varepsilon(t)$ is the axial strain.

When β= 0,$\eta_0 = E, \sigma = E\varepsilon$, representing linear elastomer, namely, Hooke elastomer; When β= 1, $\sigma = \eta_0 d\varepsilon/dt$, corresponding to Newtonian dashpot and satisfying the ideal

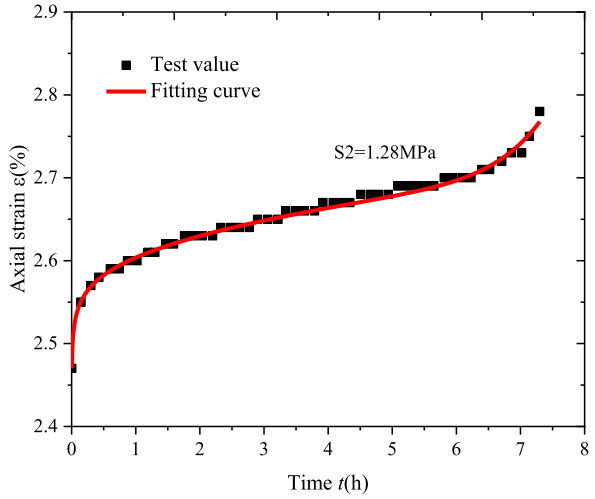

FIGURE 10
Creep equation fitting curve (ω= 12.38%).

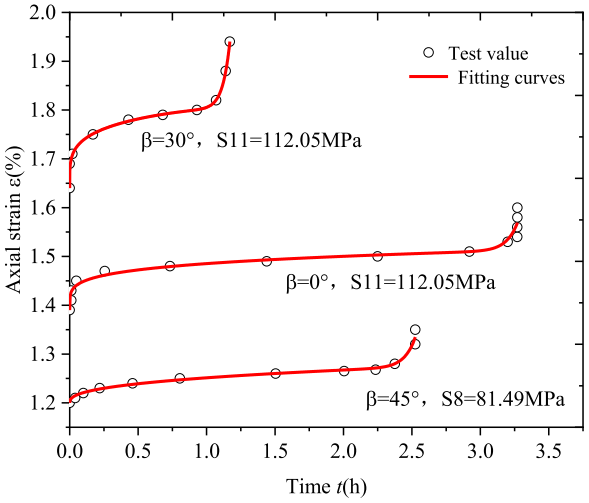

FIGURE 12
Creep equation fitting curves of different bedding angles (β = 0°, 30°, 45°).

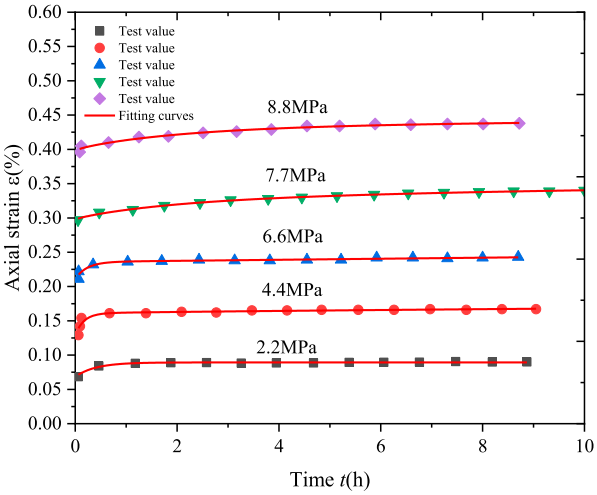

FIGURE 11
Creep equation fitting curves (ω= 0%).

fluid. So, the physical meaning of Abel dashpot can be defined as a fluid element between Hooke elastomer and Newtonian body.

In the study of rock creep mechanics, $\sigma(t) = \sigma = const$, Eq. 7 is integrated with Caputo fractional operator, and the creep equation of fractional Abel dashpot can be expressed as

$$\varepsilon(t) = \frac{\sigma}{\eta_0} \cdot \frac{t^{\beta}}{\Gamma(1+\beta)}, m \le \beta \le m+1 \tag{8}$$

For Eq. 8, if σ/η_0 is a constant, select $0 < \beta \le 1$ and $\beta > 1$ to draw the figure of strain time as follows:

As shown in Figures 2, 3, the growth rate of ε is variate non-linear follow β. Combining with Figure 1, the constitutive relationship curves of Abel dashpot can be used to describe the typical creep properties of the rock. When the stress level is below the long-term strength of the rock, the decay creep stage can be characterized by Abel daspot with $0 < \beta < 1$. When the stress level exceed the long-term strength of the rock, the accelerating creep stage can be characterized by Abel despot with $\beta > 1$. Therefore, the Abel dashpot body is introduced by paralleling with the friction plate to construct a fractional order viscoplastic body, as shown in Figure 4. The stress relationship of fractional order plastic body as:

$$\sigma = \sigma_s + \sigma_{Abel} \tag{9}$$

Substituting Eq. 7 into Eq. 9, the fractional order viscoplastic body creep constitutive relationship as:

$$\varepsilon_{vp}(t) = \frac{\sigma - \sigma_s}{\eta_2} \cdot \frac{t^k}{\Gamma(1+k)}, (k > 1) \tag{10}$$

where η_2 is the viscosity coefficient of the viscoplastic body, and σ_s is the long-term strength of the rock.

3.2 Elastic-viscoplastic creep model

3.2.1 The elastic-viscoplastic creep model and one-dimensional creep equation

Based on fractional order calculus theory and Boltzmann superposition principle, a six-element non-linear elastic-viscoplastic creep model is proposed as shown in Figure 4 in this paper. The model consists of a Hooke elastomer, an Abel dashpot body, a Kelvin body, and a fractional order viscoplastic body in series. In this case, the instantaneous creep of the rock is characterized by Hooke elastomer. The non-linear decay creep is characterized by the Abel dashpot body. The steady-state creep is approximated by a constant strain with time, as $t \to \infty$, the slope of the strain-time curve $k = d\varepsilon(t)/dt = const$, and the constitutive relationship for this stage is described by the conventional linear

TABLE 4 Parameters of the three-dimensional creep model.

ω%	Confining stress	G_0 (MPa)	K_0 (MPa)	η_0 (MPa)	p	G_1 (MPa)	η_1 (MPa)	η_2 (MPa)	k	R^2
4.56	0.88	2.12	1.65	2.11	0.15	110.75	0.08			0.983
	1.68	1.41	1.44	20.22	0.21	41.54	102.22			0.995
	2.48	1.44	1.60	20.74	0.23	61.06	26.46			0.968
	3.28	1.36	1.59	26.63	0.74	14.32	3.30	1.37×10^{-11}	40.94	0.997
8.47	0.88	1.27	1.19	0.77	0.04	9.70	25.92			0.987
	1.28	1.13	1.14	0.70	0.06	17.61	15.29			0.995
	1.68	0.63	0.61	1.16	0.52	6.12	0.07	1.63×10^{-18}	15.40	0.996
12.38	0.88	0.96	1.02	0.28	0.04	1.06	0.001			0.994
	1.28	0.50	0.53	0.51	0.03	3.26	39.65	214.95	10.25	0.992

TABLE 5 Parameters of the creep model.

Stress/MPa	Model parameters					R^2
	E_0/MPa	η_0/MPa	p	E_1/MPa	η_1/MPa	
2.2	32.16	5.41×10^{17}	1	105.24	42.04	0.963
4.4	34.11	3775.19	0.77	138.57	23.34	0.893
6.6	31.28	8261.98	1	264.86	60.38	0.933
7.7	25.93	1306.20	0.50	341.93	767.04	0.995
8.8	22.22	1198.97	0.34	338.98	779.09	0.978

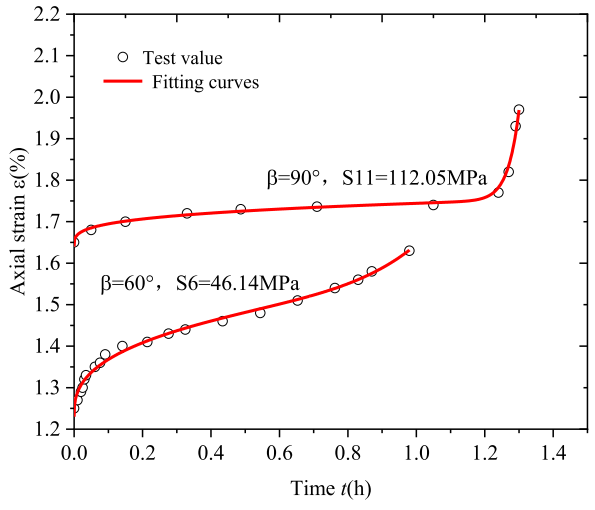

FIGURE 13
Creep equation fitting curves of different bedding angles (β = 60°, 90°).

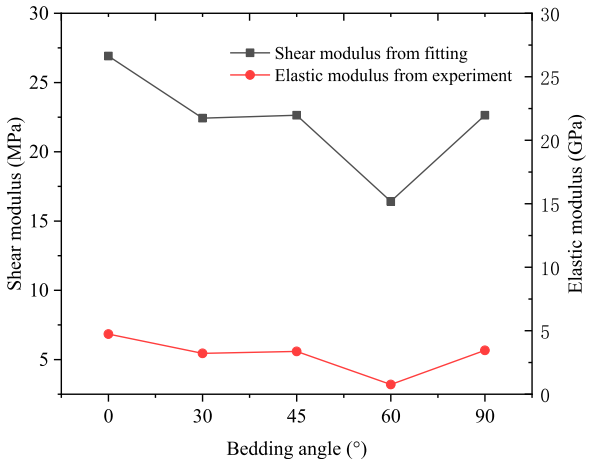

FIGURE 14
Shear modulus vs. elastic modulus.

Kelvin body. Finally, the accelerating creep stage is described by the fractional order viscoplastic body.

According to the series-parallel law for the combined element model, when the stress is a constant, the stress-strain relationship for the six-element non-linear elastic-viscoplastic creep model as the following equation shows:

$$\left.\begin{aligned} \sigma &= \sigma_e = \sigma_{ve0} = \sigma_{vel} = \sigma_{vp} \\ \varepsilon(t) &= \varepsilon_e(t) + \varepsilon_{ve0}(t) + \varepsilon_{vel}(t) + \varepsilon_{vp}(t) \end{aligned}\right\} \tag{11}$$

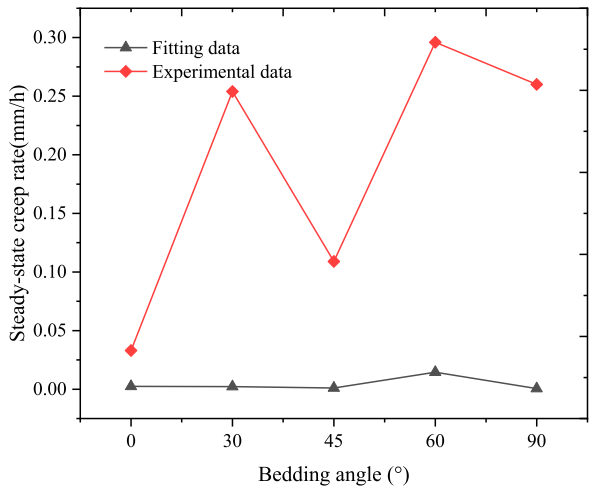

FIGURE 15
Steady-state creep rate.

where $\sigma_e, \sigma_{ve0}, \sigma_{vel}, \sigma_{vp}$ is the stress of Hooke elastomer, Abel dashpot body, Kelvin body and fractional order viscoplastic body, respectively. $\varepsilon(t)_e, \varepsilon(t)_{ve0}, \varepsilon(t)_{vel}, \varepsilon(t)_{vp}$ is the strain of Hooke elastomer, Abel dashpot body, Kelvin body and fractional order viscoplastic body, respectively.

(i) When $\sigma < \sigma_s$, there is only transient elastic creep, decay creep and steady-state creep in the rock, no accelerating creep has occurred, and only Hooke elastomer, Abel dashpot, kelvin body at work, the stress-strain relationship of the model equation is

$$\left.\begin{aligned} \sigma &= \sigma_e = \sigma_{ve0} = \sigma_{vel} \\ \varepsilon(t) &= \varepsilon_e(t) + \varepsilon_{ve0}(t) + \varepsilon_{vel}(t) \end{aligned}\right\} \tag{12}$$

The creep equation of the Hooke elastomer and Abel dashpot body is

$$\left.\begin{aligned} \varepsilon_e(t) &= \frac{\sigma}{E_0} \\ \varepsilon_{ve0}(t) &= \frac{\sigma}{\eta_0}\frac{t^p}{\Gamma(1+p)} \end{aligned}\right\} \tag{13}$$

For kelvin body, according to the parallel law, there is

$$\left.\begin{aligned} \sigma &= \sigma_{E_1} + \sigma_{\eta_1} \\ \varepsilon &= \varepsilon_{E_1} + \varepsilon_{\eta_1} \\ \sigma_{E_1} &= E_1\varepsilon \\ \sigma_{\eta_1} &= \eta_1\dot{\varepsilon} \end{aligned}\right\} \tag{14}$$

So, the creep constitutive equation of kelvin body is

$$\sigma = E_1\varepsilon + \eta_1\frac{d\varepsilon}{dt} \tag{15}$$

Solve Eq. 15, obtain the creep equation of the linear kelvin body is

$$\varepsilon_{vel}(t) = \frac{\sigma}{E_1}\left[1 - \exp\left(-\frac{E_1}{\eta_1}t\right)\right] \tag{16}$$

where σ is strain, E_1, η_1 is elastic modulus and viscosity coefficient, respectively.

Substituting Eqs 13, 16 into Eq. 12, access the equation of $\varepsilon(t)$ as

$$\varepsilon(t) = \frac{\sigma}{E_0} + \frac{\sigma}{\eta_0}\frac{t^p}{\Gamma(1+p)} + \frac{\sigma}{E_1}\left[1 - \exp\left(-\frac{E_1}{\eta_1}t\right)\right], (\sigma < \sigma_s, 0 < p < 1) \tag{17}$$

(ii) When $\sigma \geq \sigma_s$, the rock undergoes accelerating creep and the fractional order viscoplastic body is added to the work, the stress-strain relationship of the model is given by

$$\left.\begin{aligned} \sigma &= \sigma_e = \sigma_{ve0} = \sigma_{vel} = \sigma_{vp} \\ \varepsilon(t) &= \varepsilon_e(t) + \varepsilon_{ve0}(t) + \varepsilon_{vel}(t) + \varepsilon_{vp}(t) \end{aligned}\right\} \tag{18}$$

Combining Eq. 10, Eq. 13 and Eq.16 and substituting them into Eq. 18, access the equation of $\varepsilon(t)$ as

TABLE 6 Parameters of creep model.

Bedding angles	Confining stress	G_0 (MPa)	K_0 (MPa)	η_0 (MPa)	p	G_1 (MPa)	η_1 (MPa)	η_2 (MPa)	k	R^2
0°	112.05	26.91	1.09×10^{18}	418.07	0.20	2.33×10^{26}	3.12×10^{26}	3.12×10^{-10}	24.14	0.947
30°	112.05	22.43	9.69×10^{17}	448.66	0.20	807.03	214.28	2.43×10^{-14}	18.67	0.981
45°	81.49	22.64	8.77×10^{16}	968.18	0.48	1284.48	234.23	6.69×10^{-13}	24.06	0.998
60°	61.12	16.42	2.24×10^{14}	68.91	0.42	8.06×10^{16}	8.05×10^{14}	5.40×10^{-5}	9.54	0.989
90°	112.05	22.64	1.00×10^{18}	1708.78	0.08	547.43	139.69	2.59×10^{-15}	20.02	0.998

TABLE 7 Creep parameters of plasticity theory model and empirical model.

θ	Model	η_0/MPa	p	E_1/MPa	η_1/MPa	η_2/MPa	k	R^2
0	Theoritical model	2393.96	0.15	3.33×10^{16}	2.54×10^{18}	1.17×10^{19}	61.28	0.918
	Empirical model	851.83	0.15	3.53×10^{16}	2.78×10^{18}	4.38×10^{7}	61.18	0.918
90	Theoritical model	13338.32	0.81	1752.24	825.82	100469.59	20.53	0.999
	Empirical model	4246.85	0.81	557.90	262.94	111.87	20.53	0.999

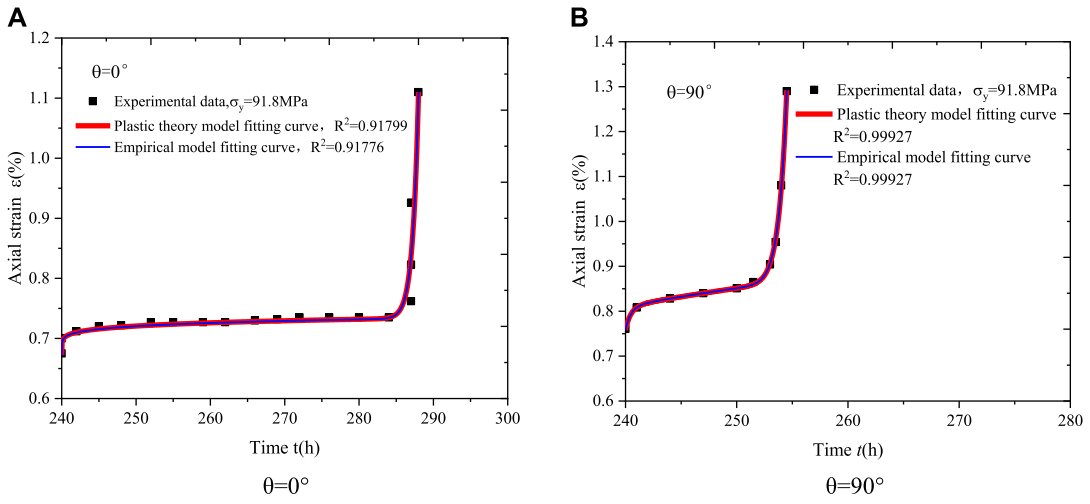

FIGURE 16
Fitting curves of creep equation by empirical model and plastic theory model [**(A,B)** is the bedding angle of 0°,90° respectively].

$$\varepsilon(t)=\frac{\sigma}{E_0}+\frac{\sigma}{\eta_0}\frac{t^p}{\Gamma(1+p)}+\frac{\sigma}{E_1}\left[1-\exp\left(-\frac{E_1}{\eta_1}t\right)\right]+\frac{\sigma-\sigma_s}{\eta_2}\frac{t^k}{\Gamma(1+k)},\ (\sigma\geq\sigma_s,k>1) \tag{19}$$

In summary, the non-linear creep equation for rock in a one-dimensional stress state is as follows:

$$\varepsilon(t)=\begin{cases}\dfrac{\sigma}{E_0}+\dfrac{\sigma}{\eta_0}\dfrac{t^p}{\Gamma(1+p)}+\dfrac{\sigma}{E_1}\left[1-\exp\left(-\dfrac{E_1}{\eta_1}t\right)\right],\ (\sigma<\sigma_s,0<p<1)\\ \dfrac{\sigma}{E_0}+\dfrac{\sigma}{\eta_0}\dfrac{t^p}{\Gamma(1+p)}+\dfrac{\sigma}{E_1}\left[1-\exp\left(-\dfrac{E_1}{\eta_1}t\right)\right]+\dfrac{\sigma-\sigma_s}{\eta_2}\dfrac{t^k}{\Gamma(1+k)},\ (\sigma\geq\sigma_s,k>1)\end{cases} \tag{20}$$

3.2.2 Three-dimensional creep equation

In geotechnical engineering, rocks are often in a complex three-dimensional stress state. Therefore, in order to reflect the creep properties of rocks in geotechnical engineering more accurately, the three-dimensional creep constitutive equation should be adopted. According to the theory of elasticity, the internal stress tensor σ_{ij} of rock can be decomposed into a spherical stress tensor σ_m and deviatoric stress tensor s_{ij} under the condition of the three-dimensional stress. Similarly, the total strain tensor ε_{ij} of rock can be decomposed into a spherical strain tensor ε_m and a deviatoric strain tensor e_{ij}, and their constitutive relationship can be expressed, respectively, as follow:

$$\begin{cases}\sigma_{ij}=s_{ij}+\sigma_{ij}\delta_{ij}\\ \varepsilon_{ij}=e_{ij}+\varepsilon_m\delta_{ij}\end{cases} \tag{21}$$

where σ_{ij} is the Kronecker delta. The relationship between different stress tensors and strain tensors is as follows:

$$\left.\begin{aligned}\sigma_m&=\frac{1}{3}(\sigma_1+\sigma_2+\sigma_3)=\frac{1}{3}\sigma_{kk}\\ \varepsilon_m&=\frac{1}{3}(\varepsilon_1+\varepsilon_2+\varepsilon_3)=\frac{1}{3}\varepsilon_{kk}\end{aligned}\right\} \tag{22}$$

Under the condition of the three dimensional stress, assuming the total strain of the non-linear creep model is $\varepsilon_{ij}(t)$. $\varepsilon_{ij}^{0}(t)$, $\varepsilon_{ij}^{ve0}(t)$, $\varepsilon_{ij}^{vel}(t)$, $\varepsilon_{ij}^{vp}(t)$ is the strain of Hooke elastomer, Abel dashpot body, Kelvin body and fractional order viscoplastic body, respectively. Based on the theoretical superposition principle of the component combination model, the relationship of strain is

$$\varepsilon_{ij}(t)=\varepsilon_{ij}^{e}(t)+\varepsilon_{ij}^{ve0}(t)+\varepsilon_{ij}^{vel}(t)+\varepsilon_{ij}^{vp}(t) \tag{23}$$

In rock creep tests, when the first order stress level applied is less than the long-term strength of the rock, the rock develops transient strain rapidly, and the constitutive relationship at this stage can be described by a Hooke elastomer.

For the Hooke elastomer, the elastic constitutive relation can be expressed by Hooke's Law as

$$\left.\begin{aligned}s_{ij}&=2Ge_{ij}\\ \sigma_{ij}&=3K\varepsilon_{ij}\end{aligned}\right\} \tag{24}$$

where G, K is the shear modulus and bulk modulus, respectively. The relationship between the shear modulus G, bulk modulus K, elastic modulus E, and Poisson`s ratio μ of soil is

$$\left.\begin{aligned}G&=\frac{E}{2(1+\mu)}\\ K&=\frac{E}{3(1-2\mu)}\end{aligned}\right\} \tag{25}$$

Hence, the strain of the Hooke elastomer can be written as

$$\varepsilon_{ij}^{e}(t)=\frac{1}{2G_0}S_{ij}+\frac{1}{3K_0}\sigma_m\delta_{ij} \tag{26}$$

When the stress keep loading, the rock enters a non-linear decay creep phase, which is described by the Abel dashpot in this paper, and the three-dimensional creep constitutive equation as:

$$\varepsilon_{ij}^{ve0}=\frac{1}{2\eta_0}S_{ij}\frac{t^p}{\Gamma(1+p)} \tag{27}$$

Then, the rock will undergo steady-state creep, use the conventional linear Kelvin body to describe this phase of the rock creep process in this paper. Assuming that the volume change is elastic and the rheological properties are mainly in terms of shear deformation (Sun, 2007b), the three-dimensional creep constitutive equation is

$$\varepsilon_{ij}^{ve1} = \frac{1}{2G_1} S_{ij}\left[1 - \exp\left(-\frac{G_1}{\eta_1}t\right)\right] \tag{28}$$

where G_1 and η_1 are the shear modulus and viscosity coefficient of the Kelvin body, respectively.

When the stress deviator tensor $s \geq \sigma_s$, significant plastic deformation occurs, and the rock enters a phase of accelerating creep until it breaks down.

In a three-dimensional stress state, when stress exceeds the viscoplastic yield surface, a viscoplastic strain will be generated. Based on Perzyna's limit stress flow law (Perzyna, 1966; Aydan, 2016), the three-dimensional creep equation for fractional order viscoplastic body in the accelerating creep phase can be obtained as

$$\varepsilon_{ij}^{vp}(t) = \frac{1}{\eta_2}\left\langle \Phi\left(\frac{F}{F_0}\right)\right\rangle \frac{\partial Q}{\partial \sigma_{ij}} \frac{t^k}{\Gamma(1+k)}, (k>1) \tag{29}$$

where $\Phi\left(\frac{F}{F_0}\right)$ is the power function, $\Phi\left(\frac{F}{F_0}\right) = \left(\frac{F}{F_0}\right)^m$. Q is the plastic potential function. $\langle \bullet \rangle$ is switch function, expressed as:

$$\left\langle \Phi\left(\frac{F}{F_0}\right)\right\rangle = \begin{cases} 0, F<0 \\ \left(\frac{F}{F_0}\right), F \geq 0 \end{cases} \tag{30}$$

F is the rock yield function. F_0 is the initial value of the rock yield function, generally taken as $F_0 = 1$ (Al-Rub et al., 2013). The exponent m is a constant and generally taken as $m = 1$.

Combining Eqs 26–30 into Eq. 23, obtain the three-dimensional creep equation as follow

$$\varepsilon_{ij}(t) = \begin{cases} \frac{1}{2G_0}S_{ij} + \frac{1}{3K_0}\sigma_m\delta_{ij} + \frac{1}{2\eta_0}S_{ij}\frac{t^p}{\Gamma(1+p)} + \frac{1}{2G_1}S_{ij}\left[1-\exp\left(-\frac{G_1}{\eta_1}t\right)\right] \\ (F<0) \\ \frac{1}{2G_0}S_{ij} + \frac{1}{3K_0}\sigma_m\delta_{ij} + \frac{1}{2\eta_0}S_{ij}\frac{t^p}{\Gamma(1+p)} + \frac{1}{2G_1}S_{ij}\left[1-\exp\left(-\frac{G_1}{\eta_1}t\right)\right] \\ +\frac{1}{\eta_2}\left(\frac{F}{F_0}\right)^m\frac{\partial Q}{\partial\sigma_{ij}}\frac{t^k}{\Gamma(1+k)} \\ (F\geq 0) \end{cases} \tag{31}$$

The classical rock strength criterion includes Mohr-coulomb criterion, Tresca criterion, Von-Mises criterion and Drucker-Prager criterion, et al. However, the Mohr-coulomb and Tresca criterion considers only the maximum and minimum principal stress of the three principal stresses and does not consider the effect of intermediate principal stresses in the material. The Von-Mises criterion does not consider the effect of hydrostatic pressure on yielding and damage. The Drucker-Prager yield criterion improves the corner singularity problem of the Mohr-Coulomb criterion, and is also suitable for describing the yield behavior of rock materials. Therefore, the Drucker-Prager criterion is chosen as the yield criterion for rock creep analysis in this paper. In creep deformation, the creep yield deformation of rock materials mainly results from the deviator stress tensor, and the spherical stress tensor has little effect on yield deformation (Zheng and Kong, 2006), which is defined by

$$F = \sqrt{J_2} - \sigma_s/\sqrt{3} \tag{32}$$

where J_2 is the second deviatoric stress tensor invariant. The tested material is suitable for the associated flow rule when $F = Q$ (Moghadam et al., 2013).

In the true triaxial stress environment, the rock is stressed from three directions, and there is

$$\left.\begin{aligned} &\sigma_1 > \sigma_2 > \sigma_3 \\ &\sigma_m = \frac{\sigma_1+\sigma_2+\sigma_3}{3} \\ &S_{11} = \sigma_1 - \sigma_m = \frac{2\sigma_1-\sigma_2-\sigma_3}{3} \end{aligned}\right\} \tag{33}$$

Considering the triaxial creep experiment in the normal triaxial stress status, i.e., σ1 >σ2 = σ3, we can obtain

$$\left.\begin{aligned} &\sigma_m = \frac{\sigma_1+2\sigma_3}{3} \\ &S_{11} = \frac{2(\sigma_1-\sigma_3)}{3} \\ &\sqrt{J_2} = \frac{1}{\sqrt{3}}(\sigma_1-\sigma_3) \\ &F\frac{\partial F}{\partial\sigma_{11}} = \frac{\sigma_1-\sigma_3-\sigma_s}{3} \end{aligned}\right\} \tag{34}$$

Substituting Eqs 32–34 into Eq. 31, the full-stage creep strain under the three-dimensional stress state is obtained as follows:

$$\varepsilon_{11}(t) = \begin{cases} \frac{\sigma_1-\sigma_3}{3G_0} + \frac{\sigma_1+2\sigma_3}{9K_0} + \frac{1}{\eta_0}\frac{(\sigma_1-\sigma_3)}{3}\frac{t^p}{\Gamma(1+p)} + \frac{\sigma_1-\sigma_3}{3G_1}\left[1-\exp\left(-\frac{G_1}{\eta_1}t\right)\right] \\ (\sigma_1-\sigma_3<\sigma_s) \\ \frac{\sigma_1-\sigma_3}{3G_0} + \frac{\sigma_1+2\sigma_3}{9K_0} + \frac{1}{\eta_0}\frac{(\sigma_1-\sigma_3)}{3}\frac{t^p}{\Gamma(1+p)} \\ +\frac{\sigma_1-\sigma_3}{3G_1}\left[1-\exp\left(-\frac{G_1}{\eta_1}t\right)\right] + \frac{1}{\eta_2}\frac{\sigma_1-\sigma_3-\sigma_s}{3}\frac{t^k}{\Gamma(1+k)} \\ (\sigma_1-\sigma_3\geq\sigma_s) \end{cases} \tag{35}$$

Where $\varepsilon_{11}(t)$ represents the vertical strain of the sample under constant stress.

3.3 Non-linear creep model for layered rock

Due to the existence of weak bedding planes, layered rock often shows obvious anisotropy characteristic, specifically transverse isotropic characteristics. According to the results of tests in the available literature (Hu et al., 2019; Liu et al., 2015; Xu et al., 2019; Zhang et al., 2021), the angle of the laminae has a large influence on the creep properties of the rock. For transverse isotropic material creep models, the research literature (Wang et al., 2018) is divided into two main types, namely, empirical models generalized by experiment and theoretical models resolved by plasticity theory. Based on the viscoelastic-plastic creep model

established in this paper, the empirical model method and the plasticity theory analytical method are used to derive the intrinsic constitutive equations of the creep model for layered rock, and the relevant experimental data are used for comparative analysis and verification.

3.3.1 Creep equation of empirical model

The establishment method of the empirical model for layered rock creep is based on the model of isotropic materials. The creep equation of layered rock is derived by introducing the influence of laminae on the mechanical properties of rock creep. For example, Tang (Tang et al., 2018) gave the relationship between the elastic modulus, creep rate and bedding angle at the same moisture content by uniaxial compression creep test as

$$\left.\begin{aligned} E &= A\, e_{B\beta} \\ \frac{1}{\eta} &= D\, e_{m\beta} \end{aligned}\right\} \tag{36}$$

where A, B, C, D, m is a fitting coefficient, β is the bedding angle.

The paper introduces functional expressions of elastic modulus and creep rate, and proposes a one-dimensional creep constitutive equation for layered shale based on the Burgers model. However, the creep model for the accelerating creep stage was not given in that paper. Wang (Wang, 2020) obtained the anisotropic characteristics of long-term strength, peak strength and elastic modulus of sandstones with different bedding angles by triaxial creep tests.

In this paper, based on the research, the non-linear elastic-viscoplastic whole process creep equation for layered rock is derived analogously from the isotropic rock material creep model constitutive equation. The one-dimensional creep equation of the elastic-viscoplastic creep of layered rock is

$$\varepsilon(t) = \begin{cases} \dfrac{\sigma}{E_0(\beta)} + \dfrac{\sigma}{\eta_0(\beta)}\dfrac{t^p}{\Gamma(1+p)} + \dfrac{\sigma}{E_1}\left[1-\exp\left(-\dfrac{E_1}{\eta_1}t\right)\right], (\sigma<\sigma_s, 0<p<1) \\ \dfrac{\sigma}{E_0(\beta)} + \dfrac{\sigma}{\eta_0(\beta)}\dfrac{t^p}{\Gamma(1+p)} + \dfrac{\sigma}{E_1}\left[1-\exp\left(-\dfrac{E_1}{\eta_1}t\right)\right] + \dfrac{\sigma-\sigma_s(\beta)}{\eta_2}\dfrac{t^k}{\Gamma(1+k)}, (\sigma\geq\sigma_s, k>1) \end{cases} \tag{37}$$

where β is bedding angle, and the diagram of bedding angle is shown in Figure 5. $E_0(\beta), \eta_0(\beta), \sigma_s(\beta)$ is the functions of the effect of changes in bedding angle on the elastic modulus, viscosity coefficient and long-term strength of rock, respectively.

Accordingly, with reference to the derivation of the three-dimensional creep equation for isotropic rock materials, the three-dimensional creep equation of the elastic-viscoplastic creep of layered rock is

$$\varepsilon_{11}(t) = \begin{cases} \dfrac{\sigma_1-\sigma_3}{3G_0(\beta)} + \dfrac{\sigma_1+2\sigma_3}{9K_0(\beta)} + \dfrac{1}{\eta_0(\beta)}\dfrac{(\sigma_1-\sigma_3)}{3}\dfrac{t^p}{\Gamma(1+p)} + \dfrac{\sigma_1-\sigma_3}{3G_1}\left[1-\exp\left(-\dfrac{G_1}{\eta_1}t\right)\right] \\ (\sigma_1-\sigma_3<\sigma_s(\beta)) \\ \dfrac{\sigma_1-\sigma_3}{3G_0(\beta)} + \dfrac{\sigma_1+2\sigma_3}{9K_0(\beta)} + \dfrac{1}{\eta_0(\beta)}\dfrac{(\sigma_1-\sigma_3)}{3}\dfrac{t^p}{\Gamma(1+p)} \\ +\dfrac{\sigma_1-\sigma_3}{3G_1}\left[1-\exp\left(-\dfrac{G_1}{\eta_1}t\right)\right] + \dfrac{1}{\eta_2}\dfrac{\sigma_1-\sigma_3-\sigma_s(\beta)}{3}\dfrac{t^k}{\Gamma(1+k)} \\ (\sigma_1-\sigma_3\geq\sigma_s(\beta)) \end{cases} \tag{38}$$

3.3.2 Creep equation based on plastic theory

The plasticity theory analytical method based on the assumption of constant Poisson's ratio (Dathe et al., 2001). It is assumed that Poisson's ratio does not change with time and stress, and is equivalent to the value of elastic stage, $\mu(\sigma,t)=\mu$. Based on the creep constitutive equation established under one-dimensional condition, the equation can be extended from one-dimensional stress state to three-dimensional. Let the creep compliance $J(t)$ in Eq. 20 is given as:

$$J(t) = \begin{cases} \dfrac{1}{E_0} + \dfrac{1}{\eta_0}\dfrac{t^p}{\Gamma(1+p)} + \dfrac{1}{E_1}\left[1-\exp\left(-\dfrac{E_1}{\eta_1}t\right)\right], (\sigma<\sigma_s) \\ \dfrac{1}{E_0} + \dfrac{1}{\eta_0}\dfrac{t^p}{\Gamma(1+p)} + \dfrac{1}{E_1}\left[1-\exp\left(-\dfrac{E_1}{\eta_1}t\right)\right] + \dfrac{1-\sigma_s/\sigma}{\eta_2}\dfrac{t^k}{\Gamma(1+k)}, (\sigma\geq\sigma_s) \end{cases} \tag{39}$$

Then, Eq. 20 can be described as

$$\varepsilon = J(t)\sigma \tag{40}$$

For isotropic rock, the creep compliance substitution method can be used to obtain the basic form of the three-dimensional creep equation of rock as follows (Li et al., 2021):

$$\{\varepsilon\} = J(t)[A]\{\sigma\} \tag{41}$$

where $[A]$ is Poisson's ratio matrix for isotropic material; $\{\varepsilon\}$ and $\{\sigma\}$ are strain tensor and stress tensor, respectively.

For Eq. 41, scholars (Aravas et al., 1995; Kou et al., 2023) have carried out a detailed solution, which is not repeated in this paper. Based on the creep constitutive model established in this paper, the three-dimensional creep constitutive equation for layered rock is derived as

$$\begin{aligned} \varepsilon_{11}(t) =& \left\{\frac{1}{E_0} + \frac{1}{\eta_0}\frac{t^p}{\Gamma(1+p)} + \frac{1}{E_1}\left[1-\exp\left(-\frac{E_1}{\eta_1}t\right)\right] + \frac{1-\sigma_s/\sigma}{\eta_2}\frac{t^k}{\Gamma(1+k)}\right\} \\ &\times\left\{-\frac{\mu'}{n}\left(\sin^4\theta+\cos^4\theta+\frac{\sin^2 2\theta}{2}\right)\sigma_x + \left[\sin^4\theta + \frac{\cos^4\theta}{n} + \frac{\sin^2 2\theta}{4}\left(1+\frac{1}{n}\right)\right]\sigma_y - \left(\mu\sin^2\theta\frac{\mu'}{n}\cos^2\theta\right)\sigma_z\right\} \end{aligned} \tag{42}$$

where μ, μ' is Poisson's ratio parallel to and perpendicular to foliation plane, respectively. θ is the bedding angle, defined as the angle with the horizontal plane. Defining $n = E^{\theta=90^\circ}/E^{\theta=0^\circ}$, $E_{\theta=90^\circ}$、$E_{\theta=0^\circ}$ is elastic modulus perpendicular to and parallel to foliation plane, individually. $\sigma_x, \sigma_y, \sigma_z$ are the three axes of positive pressure in the direction of the overall orthogonal coordinate axes, respectively.

4 Parameter identification and model validation

4.1 Parameter identification of non-layered rock creep model

4.1.1 The one-dimensional non-linear creep model

The uniaxial compression non-linear creep model is shown in Eq. 20, and parameters of the model to be determined are $E_0, \eta_0, p, E_1, \sigma_s, \eta_2, k$.

(i) The parameters of E_0, σ_s

In the transient elastic creep stage, E_0 could be calculated from $E = \sigma/\varepsilon$. σ_s could be obtained from experimental data.

(ii) The parameters of η_0, p, E_1, η_1

σ, E_0 already known. Selecting the corresponding creep test data of $\sigma\,(\sigma < \sigma_s)$ to establish the non-linear function of Eq. 17, fitted by Origin using the Levenberg-Marquardt iterative method, then η_0, p, E, η_1 were obtained.

(iii) The parameters of η_2, k

Selecting the corresponding creep test data of $\sigma\,(\sigma \geq \sigma_s)$ to perform step-by-step fitting, the operation process as follows: the first step is to take the test data from the decay creep and steady creep stages and follow the operation of (i) and (ii) in turn to obtain $E_0, \eta_0, p, E_1, \eta_1, \sigma_s$, the second step is to take the test data of $\sigma\,(\sigma \geq \sigma_s)$ to perform the non-linear fitting, then η_2, k obtained.

4.1.2 Three-dimensional non-linear creep model

The triaxial compression non-linear creep model is shown in Eq. 35, and the model parameters to be determined are $G_0, K_0, \eta_0, G_1, \eta_1, p, \sigma_s, \eta_2, k$. Let the constant as

$$\left.\begin{aligned} M &= \frac{\sigma_1 - \sigma_3}{3G_0} + \frac{\sigma_1 + 2\sigma_3}{9K_0} \\ N &= \frac{\sigma_1 - \sigma_3}{3} \\ R &= \frac{\sigma_1 - \sigma_3 - \sigma_s}{3} \end{aligned}\right\} \tag{43}$$

then Eq. 35 can be described as

$$\varepsilon_{11}(t) = \begin{cases} M + \dfrac{1}{\eta_0} N \dfrac{t^p}{\Gamma(1+p)} + \dfrac{N}{G_1}\left[1 - \exp\left(-\dfrac{G_1}{\eta_1} t\right)\right] \\ (\sigma_1 - \sigma_3 < \sigma_s) \\ M + \dfrac{1}{\eta_0} N \dfrac{t^p}{\Gamma(1+p)} + \dfrac{N}{G_1}\left[1 - \exp\left(-\dfrac{G_1}{\eta_1} t\right)\right] + \dfrac{1}{\eta_2} R \dfrac{t^k}{\Gamma(1+k)} \\ (\sigma_1 - \sigma_3 \geq \sigma_s) \end{cases} \tag{44}$$

The process of parameter identification is:

(i) The parameters of $G_0, K_0, \eta_0, G_1, \eta_1, p$

Based on the elastic modulus E and Poisson's ratio μ from conventional triaxial compression tests on rocks under the same circumferential pressure, G_0 and K_0 are obtained through Eq. 25. Then, combining G_0, K_0 into Eq. 35 to perform the non-linear fitting with the creep experimental data from the stress of $\sigma\,(\sigma < \sigma_s)$.

(ii) The parameters of σ_s, η_2, k

The parameter of σ_s could be calculated from triaxial creep experimental data. Selecting the full process of high-stress creep experimental data and fitting it to obtain $G_0, K_0, \eta_0, G_1, \eta_1, p$ firstly, then referring to the step-wise fitting method in Section 4.1.1, we could obtain η_2, k.

4.2 Parameter identification of layered rock creep model

The non-linear creep model for layered rock is shown in Eqs 37, 38 and Eq. 42, and the parameters identification method is similar to the non-layered rock creep model. In view of space, do not repeat.

4.3 Parameter identification and model validation

4.3.1 One-dimensional non-linear creep model

The experimental data used for parameter identification in the one-dimensional creep equation is chosen from Wang (Wang et al., 2020). The test was carried out using the MTS815.02 Multifunctional Servo Test System for uniaxial compression creep testing of sandstone with graded loading, and the long-term strength given in the paper is 70 MPa. In this paper, data from the water content test set ω= 0% is taken for parameter identification of the creep model. The graded loading scheme of the uniaxial compression creep test is $60MPa, 70MPa, 80MPa, 90MPa, 100MPa$, respectively. The contrastive analysis of the creep calculation curve and experimental data are illustrated in Figure 6.

Showing in Figure 7, the proposed creep model can accurately describe the characteristics of three phases of rock creep, the rationality is verified. The parameters of the creep model listed in Table 2.

4.3.2 The three-dimensional non-linear creep model

The experimental data used for parameter identification in the three-dimensional creep equation is chosen from Ye (Ye et al., 2022). This test was carried out for triaxial compression creep tests at different water contents ω at an confining pressure of 1 MPa. The graded loading scheme of the triaxial compression creep test is shown in Table 3 and the long-term strength of rock is $2.48MPa, 1.28MPa, 0.88MPa$, respectively.

Using the method of the previous Section 4.1.2 for model parameters identification. When the loading stress level is less than the yield strength, the first equation of Eq. 35 is used for nonlinear fitting. The fit of the experimental data to the creep equation was obtained as shown in Figures 8–10.

When the loading stress level is greater than the yield strength, a step-wise non-linear fitting is made by the second equation of Eq. 35. The fitting curve of the moisture content under low-stress level is shown in Figure 8, and the fitting curve of the moisture content of ω= 8.47%,ω= 12.38% under high-stress level is shown in Figures 11, 12. The parameters of the creep model listed in Table 4.

Analyzing Figures 7, 10, the creep model not only describes the viscoelastic behavior in the decay creep and steady-state creep phases of the rock in uniaxial creep experiment and triaxial creep experiment well under low stress, but also has a good representation of the non-linear mechanical behavior in the accelerating creep phase of the rock under high-stress

conditions. Furthermore, as seen in Tables 2, 4, the correlation between experimental data and fitting curves is high. The reasonableness and applicability of the fractional order creep model proposed in this paper are verified.

4.3.3 Creep model for layered rock

(i) Creep Equation of Empirical Model

The experimental data used for parameter identification in the one-dimensional creep equation is chosen from Tang (Tang et al., 2018). Selecting the data of 60^0 (ω= 0%), and fitting by Eq. 37. The fitting curves are shown in Figure 11.

The parameters of the creep model listed in Table 5.

The experimental data used for parameter identification in the three-dimensional creep equation is chosen from Wang (J. Wang et al., 2020). The author took the triaxial compression creep tests on five sets of specimens with bedding angles of $0^0, 30^0, 45^0, 60^0$ and 90^0 under the confining pressure condition of 5 MPa. In this paper, selecting five sets of experimental data from the accelerating creep phase with different bedding angles to be fitted to identify the model parameters. The fitting curve is shown in Figures 12, 13.

The parameters of the creep model are listed in Table 6.

Based on the parameters from Table 6, giving the plotting of G_0 and $1/\eta_0$ with different bedding angles separately, and comparing with the experimental data in the original paper. We find that the parameters have a similar trend to the parameters from the experiment, verifying the influence of the bedding angle on the creep properties of the rock. As shown in Figures 14, 15.

(ii) Creep Equation of Plasticity Theory

Experimental data were used from the literature (Kou et al., 2023). In the literature, step-wise loading triaxial creep tests of phyllite specimens with three kinds of bedding angles (0°, 45° and 90°) are carried out with the confining pressure of 10 MPa. In this paper, the last stage accelerating creep test data of 0° and 90° layered rock is taken to validate the plasticity theory creep equation and compared with the empirical model creep equation simultaneously. The elastic mechanical parameters of the rock are shown in Table 7. For the bedding angle of 0°, the elastic modulus, poission ratio and long-term strength of rock is $26.25GPa, 0.29, 91MPa$, respectively. For the bedding angle of 90°, the elastic modulus, poission ratio and long-term strength of rock is $29.31GPa, 0.36, 91MPa$, respectively.

For Eq. 42, let

$$F(\theta)= -\frac{\mu'}{n}\left(\sin^4\theta+\cos^4\theta+\frac{\sin^2 2\theta}{2}\right)\sigma_x+\left[\sin^4\theta+\frac{\cos^4\theta}{n}+\frac{\sin^2 2\theta}{4}\left(1+\frac{1}{n}\right)\right]\sigma_y-\left(\mu\sin^2\theta\frac{\mu'}{n}\cos^2\theta\right)\sigma_z \tag{45}$$

Then Eq. 42 is expressed as

$$\varepsilon_{11}(t)=F(\theta)\left\{\frac{1}{E_0}+\frac{1}{\eta_0}\frac{t^p}{\Gamma(1+p)}+\frac{1}{E_1}\left[1-\exp\left(-\frac{E_1}{\eta_1}t\right)\right]+\frac{1-\sigma_s/\sigma}{\eta_2}\frac{t^k}{\Gamma(1+k)}\right\} \tag{46}$$

Substituting the elastic parameters from Table 9 into Eq. 45, then

$$F(\theta)=\begin{cases}76.6305, \theta=0^\circ\\ 85.6391, \theta=90^\circ\end{cases} \tag{47}$$

Substituting Eq. 47 into Eq. 46, fitting the experimental data as shown in Figure 16. For the creep equation of the empirical model, the same set of experimental data was fitted by Eq. 38 using the method described in Section 4.1.2.

The creep constitutive equations for layered rock derived by the above two methods were fitting by the same set of experimental data, and a curve fit of the experimental data to the creep equation was obtained as shown in Figure 16.

The parameters of the two models are shown in Table 7.

As seen in Figure 16 and Table 7, the fitting curves of the creep constitutive equation for layered rock derived by the two methods are almost identical and have the same fitting correlation coefficients.

In summary, the non-linear creep model derived in this paper can not only better characterize the creep properties of layered rock under low and high-stress conditions, but also better reflect the influence of different bedding angles on the creep mechanical properties of rocks. In addition, the empirical creep constitutive equation derived in this paper and the plastic theory creep constitutive equation has almost the same fitting results for the same set of experimental data, which further verifies the accuracy and applicability of the creep constitutive model for layered rock established in this paper.

5 Conclusion

Based on fractional-order calculus theory and rheological element combination model theory, a six-element nonlinear elastic-viscoplastic creep model is given. The model is used as the basis for deriving the non-linear elastic-viscoplastic creep constitutive equation for layered rock, and the accuracy and applicability of the creep constitutive equation are verified by selecting creep experimental data for rocks of different lithologies. The main conclusions are as follows:

(1) Based on fractional calculus theory to introduce the Abel dashpot body, combined with the classical creep strain-time curve of rock for analysis, the Hooke elastomer, Abel dashpot body, Kelvin body and non-linear viscoplastic body are connected in series, and a six-element non-linear elastic-viscoplastic creep model is established. Then, the creep constitutive equation for one-dimensional and three-dimensional are derived respectively.

(2) Analysing the creep experimental data of layered rock, and concluding that the effects of different bedding angles on the creep properties of the rock are mainly the elastic modulus, creep rate and long-term strength, and deriving the full process creep constitutive equation for layered rock by empirical model method and the plastic theory method, respectively.

(3) Based on the Levenberg-Marquardt iterative method of Origin software, a practical identification method of creep model parameters is proposed, and parameters are identified by

using rocks of different lithologies under different stress conditions from experimental data.

(4) By fitting the creep experimental data of layered rock with different lithologies to the theoretical curves of the model, it is shown that the model proposed in this paper can not only accurately describe the full-stage creep (primary creep, steady-state creep and accelerating creep) of layered rock, but also better reflect the influence of different bedding angles on the creep properties of rocks. As shown in the tables, the average value of R^2 is beyond 0.97, with the meaning of highly accuracy and applicability for the creep constitutive equation proposed in this paper. In addition, the empirical model creep constitutive equation and plastic theory constitutive equation have almost the same fitting results for the same set of experimental data.

Data availability statement

The original contributions presented in the study are included in the article/Supplementary Material, further inquiries can be directed to the corresponding author.

Author contributions

YL: Data curation, Investigation, Writing–original draft, Writing–review and editing. MS: Investigation, Methodology, Writing–review and editing, Writing–original draft. BD: Funding acquisition, Investigation, Methodology, Resources, Supervision, Writing–review and editing. SY: Investigation, Writing–original draft.

Funding

The author(s) declare financial support was received for the research, authorship, and/or publication of this article. This research was supported by the National Natural Science Foundation of China (No. 52268022). The author BD is the leader of this project.

Conflict of interest

The authors declare that the research was conducted in the absence of any commercial or financial relationships that could be construed as a potential conflict of interest.

The reviewer JJ declared a shared affiliation with the authors to the handling editor at the time of review.

Publisher's note

References

Al-Rub, R., Darabi, M. K., Kim, S. M., Little, D. N., and Glover, C. J. (2013). Mechanistic-based constitutive modeling of oxidative aging in aging-susceptible materials and its effect on the damage potential of asphalt concrete. *Constr. Build. Mater.* 41 (apr), 439–454. doi:10.1016/j.conbuildmat.2012.12.044

Aravas, N., Cheng, C., and Casta Eda, P. P. (1995). Steady-state creep of fiber-reinforced composites: constitutive equations and computational issues. *Int. J. Solids Struct.* 32 (15), 2219–2244. doi:10.1016/0020-7683(94)00251-Q

Aydan, Ö. (2016). *Time-dependency in rock mechanics and rock engineering*.

Behbahani, H., Ziari, H., and Kamboozia, N. (2016). Evaluation of the visco-elasto-plastic behavior of glasphalt mixtures through generalized and classic burger's models modification. *Constr. Build. Mater.* 118, 36–42. doi:10.1016/j.conbuildmat.2016.04.157

Celleri, H. M., Martín, S., and Otegui, J. L. (2018). Fracture behavior of transversely isotropic rocks with discrete weak interfaces: fracture behavior of ti rocks with discrete weak interfaces. *Int. J. Numer. Anal. Methods Geomech.* 42, 2161–2176. doi:10.1002/nag.2849

Chang, X., Zhao, H., and Cheng, L. (2020). Fracture propagation and coalescence at bedding plane in layered rocks. *J. Struct. Geol.* 141 (2), 104213. doi:10.1016/j.jsg.2020.104213

Cheng, H., Zhou, X., Pan, X., and Berto, F. (2020). Damage analysis of sandstone during the creep stage under the different levels of uniaxial stress using nmr measurements. *Fatigue Fract. Eng. Mater. Struct.* 44, 719–732. doi:10.1111/ffe.13389

Dathe, A., Eins, S., Niemeyer, J., and Gerold, G. (2001). The surface fractal dimension of the soil-pore interface as measured by image analysis. *Geoderma Int. J. Soil Sci.* 103 (1/2), 203–229. doi:10.1016/S0016-7061(01)00077-5

Deng, H., Zhou, H., Jia, W., Li, L., and Su, T. (2022). A nonlinear triaxial damage creep model for granite based on atangana–baleanu fractional derivative. *Int. J. Appl. Mech.* 14. doi:10.1142/S1758825122500685

Dubey, R. K., and Gairola, V. K. (2008). Influence of structural anisotropy on creep of rocksalt from simla himalaya, India: an experimental approach. *J. Struct. Geol.* 30 (6), 710–718. doi:10.1016/j.jsg.2008.01.007

Feng, Z. Q., Yang, X. J., Liu, J. G., and Chen, Z. Q. (2021). A new fractional nishihara-type model with creep damage considering thermal effect. *Eng. Fract. Mech.* 242 (1), 107451. doi:10.1016/j.engfracmech.2020.107451

Fortsakis, P., Nikas, K., Marinos, V., and Marinos, P. (2012). Anisotropic behaviour of stratified rock masses in tunnelling. *Eng. Geol.* 141-142 (none), 74–83. doi:10.1016/j.enggeo.2012.05.001

Griggs, D. (1939). Creep of rocks. *J. Geol.* 47 (3), 225–251. doi:10.1086/624775

Hb, M., Nasseri, H., S, K., Rao, et al. (2003). Anisotropic strength and deformational behavior of himalayan schists. *Int. J. Rock Mech. Min. Sci.* 40, 3, 23. doi:10.1016/S1365-1609(02)00103-X

Hu, B., Yang, S. Q., Xu, P., and Cheng, J. L. (2019). Cyclic loading–unloading creep behavior of composite layered specimens. *Acta geophys.* 67, 449–464. doi:10.1007/s11600-019-00261-x

Koeller, R. C. (1984). Applications of fractional calculus to the theory of viscoelasticity. *Trans. Asme J. Appl. Mech.* 51 (2), 299–307. doi:10.1115/1.3167616

Kou, H., He, C., Yang, W., Wu, F., Zhou, Z., Fu, J., et al. (2023). A fractional nonlinear creep damage model for transversely isotropic rock. *Rock Mech. Rock Eng.* 56 (56), 831–846. doi:10.1007/s00603-022-03108-y

Li, L., Guan, J., Xiao, M., and Zhuo, L. (2021). Three-dimensional creep constitutive model of transversely isotropic rock. *Int. J. Geomech.* 21 (8), 21. doi:10.1061/(asce)gm.1943-5622.0002111

Liu, X., Li, D., and Han, C. (2020). A nonlinear damage creep model for sandstone based on fractional theory. *Arab. J. Geosci.* 13 (6), 246. doi:10.1007/s12517-020-5215-1

Liu, X., Li, D., and Han, C. (2021). A caputo fractional damage creep modeland its experimental validation. *Mech. Time-Depend. Mater.* 26 (26), 909–922. doi:10.1007/s11043-021-09519-8

Liu, Z. B., Xie, S. Y., Shao, J. F., and Conil, N. (2015). Effects of deviatoric stress and structural anisotropy on compressivecreep behavior of a clayey rock. *Appl. Clay Sci.* 114, 491–496. doi:10.1016/j.clay.2015.06.039

Moghadam, S. N., Mirzabozorg, H., and Noorzad, A. (2013). Modeling time-dependent behavior of gas caverns in rock salt considering creep, dilatancy and failure. *Tunn. Undergr. Space Technol.* 33 (Jan.), 171–185. doi:10.1016/j.tust.2012.10.001

Park, K. H., Jung, Y. H., and Chung, C. K. (2016). Evolution of stiffness anisotropy during creep of engineered silty sand in South Korea. *KSCE J. Civ. Eng.* 21, 2168–2176. doi:10.1007/s12205-016-1105-1

Perzyna, P. (1966). Fundamental problems in viscoplasticity. *Adv. Appl. Mech.* 9 (2), 243–377. doi:10.1016/S0065-2156(08)70009-7

Ramamurthy, T. (1993). *Strength and modulus responses of anisotropic rocks*.

Saeidi, O., Rasouli, V., Vaneghi, R. G., Gholami, R., and Torabi, S. R. (2014). A modified failure criterion for transversely isotropic rocks. *Geosci. Front.* 5 (2), 215–225. doi:10.1016/j.gsf.2013.05.005

Shan, R. L., Bai, Y., Ju, Y., Han, T. Y., and Li, Z. L. (2020). Study on the triaxial unloading creep mechanical properties and damage constitutive model of red sandstone containing a single ice-filled flaw. *Rock Mech. Rock Eng.* 54 (6), 833–855. doi:10.1007/s00603-020-02274-1

Shen, M., Bi, J., Zhao, Y., Wang, C., Wei, T., and Du, B. (2022). Study on the mechanical characteristics and damage evaluation of concrete-rock combination after high temperatures exposure. *Constr. Build. Mater.* 330, 127278. doi:10.1016/j.conbuildmat.2022.127278

Shen, M., Zhao, Y., Bi, J., Wang, C., Du, B., and Zhang, K. (2023b). *In situ* experimental study on mechanical properties of interlayer in roller compacted concrete (rcc) dam. *Constr. Build. Mater.* 379, 131268. doi:10.1016/j.conbuildmat.2023.131268

Shen, M., Zhao, Y., Bi, J., Wang, C., Ning, L., Deng, X., et al. (2023a). Micro-damage evolution and macro-mechanical property of preloaded sandstone subjected to high-temperature treatment based on nmr technique. *Constr. Build. Mater.* 369, 130638. doi:10.1016/j.conbuildmat.2023.130638

Sun, J. (2007a). Rock rhelogical mechanicals and its advance in engineering applications. *Chin. J. Rock Mech. Eng.* 26 (6), 1081–1106. doi:10.1097/00000542-199411000-00017

Sun, J. (2007b). Rock rhelogical mechanicals and its advance in engineering applications. *Chin. J. Rock Mech. Eng.* 26 (6), 1081–1106.

Tang, J., Teng, J., and Zhang, C. (2018). Experimental study of creep characteristics of layered water bearing shale. *Rock Soil Mech.* 39 (S1), 33–41. doi:10.16285/j.rsm.2017.1709

Wang, J., Meng, L., Liu, T., and Chen, H. (2020). Analysis of the influence of sandstone bedding structure on its mechanical properties. *Railw. Stand. Des.* 64 (04), 130–135. doi:10.13238/j.issn.1004-2954.201904040003

Wang, X., and Wan, L. (2016). Nonlinear creep model of rock in consideration of damage. *Sci. Technol. Eng.*

Wang, Y. (2020). Study on uniaxial compression creep test of sandstone and improvement of nishihara model. *J. Lanzhou Inst. Technol.* 27 (05), 10–14.

Wang, Z., Zong, Z., Qiao, L., and Li, W. (2018). Elastoplastic model for transversely isotropic rocks. *Int. J. Geomech.* 18 (2), 4017141–4017149. doi:10.1061/(ASCE)GM.1943-5622.0001070

Wu, B., Jia, S. P., and Luo, J. Z. (2015). Anisotropic composite model for layered rock mass based on characteristics of soft interfaces. *Material Res. Innovations* 19 (1)–S1-245. doi:10.1179/1432891715Z.0000000001478

Wu, F., Jie, C., and Zou, Q. (2018). A nonlinear creep damage model for salt rock. *Int. J. Damage Mech.* 28, 1281561184. doi:10.1177/1056789518792649

Xu, G., He, C., Yan, J., and Ma, G. (2019). A new transversely isotropic nonlinear creep model for layered phyllite and its application. *Bull. Eng. Geol. Environ.* 78, 5387–5408. doi:10.1007/s10064-019-01462-w

Yang, X., and Jiang, A. (2022). An improved nonlinear creep damage model of slates considering freeze–thaw damage and bedding damage. *Bull. Eng. Geol. Environ.* 81, 240–246. doi:10.1007/s10064-022-02740-w

Yang, X. W., Zhang, X. P., Zhang, Q., Li, C. D., and Wang, D. J. (2021). Study on the mechanisms of crack turning in bedded rock. *Eng. Fract. Mech.* 247, 107630. doi:10.1016/j.engfracmech.2021.107630

Ye, W., Qili, W., Wenjing, L., Xiongyao, X., and Biao, Z. (2022). Compressive creep property and model for unsaturated argillaceous siltstone. *J. TONGJI Univ. Sci.* 50 (08), 1154–1162. doi:10.11908/j.issn.0253-374x.21326

Yong, M. T., and Tsao, P. F. (2000). Preparation and mechanical properties of artificial transversely isotropic rock. *Int. J. Rock Mech. Min. Sci.* 37 (6), 1001–1012. doi:10.1016/S1365-1609(00)00024-1

Yong, T., and Kuo, M. C. (2001). A failure criterion for transversely isotropic rocks. *Int. J. Rock Mech. Min. Sci.* 38, 399–412. doi:10.1016/S1365-1609(01)00007-7

Zhang, J., Zhang, X., Huang, Z., and Fu, H. (2022a). Transversely isotropic creep characteristics and damage mechanism of layered phyllite under uniaxial compression creep test and its application. *Environ. Earth Sci.* 81 (20), 499–518. doi:10.1007/s12665-022-10585-5

Zhang, J., Zhang, X., Huang, Z., Yi, Y., and Zhao, X. (2021). Energy evolution mechanism of the mechanical and creep properties of layered phyllite under uniaxial compression and creep tests. *Arab. J. Geosci.* 14 (22), 2437–2513. doi:10.1007/s12517-021-08757-x

Zhang, Z., Jin, X., and Luo, W. (2019). Long-term behaviors of concrete under low-concentration sulfate attack subjected to natural variation of environmental climate conditions. *Cem. Concr. Res.* 116, 217–230. doi:10.1016/j.cemconres.2018.11.017

Zhang, Z., Pang, K., Xu, L., Zou, Y., Yang, J., and Wang, C. (2023). The bond properties between uhpc and stone under different interface treatment methods. *Constr. Build. Mater.* 365, 130092. doi:10.1016/j.conbuildmat.2022.130092

Zhang, Z., Zou, Y., Yang, J., and Zhou, J. (2022b). Capillary rise height of sulfate in portland-limestone cement concrete under physical attack: experimental and modelling investigation. *Cem. Concr. Compos.* 125 (125-), 104299. doi:10.1016/j.cemconcomp.2021.104299

Zheng, Y., and Kong, L. (2006). Generalized plastic mechanics and its application. *Eng. Sci.* 4 (1), 21–36. doi:10.1007/s11769-005-0030-x

Zhou, H., Di, L., Lei, G., Xue, D., and Yang, Z. (2018). The creep-damage model of salt rock based on fractional derivative. *Energies* 11 (9), 2349. doi:10.20944/preprints201807.0584.v1

frontiers | Frontiers in Materials

TYPE Original Research
PUBLISHED 21 November 2023
DOI 10.3389/fmats.2023.1291434

OPEN ACCESS

EDITED BY
Zhongya Zhang,
Chongqing Jiaotong University, China

REVIEWED BY
Junwei Chen,
Wuhan University, China
Zhang Xiaoqiang,
Kunming University, China
Sonia Mariel Vrech,
Universidad Nacional de Tucumán, Argentina

*CORRESPONDENCE
Xin-Bao Gu,
15823405952@163.com

RECEIVED 09 September 2023
ACCEPTED 06 November 2023
PUBLISHED 21 November 2023

CITATION
Zhao B, Xue E-W and Gu X-B (2023), Evaluation of coarse aggregate quality grade of recycled concrete based on the principal component analysis-cloud model.
Front. Mater. 10:1291434.
doi: 10.3389/fmats.2023.1291434

Evaluation of coarse aggregate quality grade of recycled concrete based on the principal component analysis-cloud model

Bing Zhao[1], Er-Wei Xue[2] and Xin-Bao Gu[1,3]*

[1]School of Civil Engineering, Nanyang Institute of Technology, Nanyang, Henan, China, [2]China MCC Group Co., Ltd., Chengdu, Sichuan, China, [3]Henan International Joint Laboratory of Dynamics of Impact and Disaster of Engineering Structures, Nanyang Institute of Technology, Nanyang, China

The quality grade assessment of coarse aggregate in recycled concrete has great significance for engineering quality, so the accurate estimation of its quality grade is vital. However, many factors affect its quality level, and its assessment procedure has a certain fuzziness and randomness. To overcome the abovementioned problems, the principal component analysis-cloud model was introduced. It is a combination of the principal component analytical method (PCA) and the normal cloud model and has the advantages of the two methods, as well as being widely applied to assess the quality level of different construction materials. To evaluate the coarse aggregate quality grade of recycled concrete in the present paper, the principal component analytical method (PCA) was applied to reduce the dimension of data and calculate the weight of each index, then a model of coarse aggregate quality based on cloud theory was constructed. According to the characteristic parameters of the cloud model, the coarse aggregate quality grade was determined. The conclusions indicate that the method is feasible for the accurate assessment of quality grade assessment of coarse aggregate, and its accuracy is very high. So, a new approach can be provided for the quality grade assessment of coarse aggregate in the future.

KEYWORDS

cloud model, recycled concrete, quality grade, evaluation, coarse aggregate

1 Introduction

The quality grade evaluation of recycled concrete is of great significance in engineering construction. It can provide a powerful reference for construction units to achieve a rational use of recycled coarse aggregate and to comprehensively and accurately reflect the physical and mechanical properties of recycled concrete aggregate (Gu et al., 2021).

Because recycled concrete aggregate is defined as the recycling and application of the waste concrete block, it not only saves many construction costs but can also play a good role in energy conservation and environmental protection (Gu et al., 2021). As such, recycled concrete aggregates have gained increasingly more attention in many developed countries, which have carried out an abundance of experimental research (Gu et al., 2022), especially in determining the quality grade of recycled concrete aggregates. At present, there is a "Quality trial regulation of recycled concrete", which was published in Japan in 1994, that selects water absorption and crushing index as the main measurement parameters to evaluate the quality grade of aggregates. However, the British Standards (1992) and the ASTM standards (USA) (2003), as well as other foreign scholars in this area of evaluation research, take the minimum

apparent density, the maximum water absorption, the maximum content of needle-like particles, the maximum impact value, the maximum content of chlorine, and the maximum content of sulfate as the criteria for judging the quality grade of recycled coarse aggregate (Gu et al., 2021). Of course, domestic research on quality grade evaluation of recycled concrete coarse aggregate has never been interrupted. Based on a large number of experimental studies, the Ministry of Construction in China promulgated the standard of recycled aggregate for concrete in 2010 (GB/T 25,177-2010). It was put forward that the recycled coarse aggregate of concrete can be divided into three grades by 10 indexes, such as particle gradation, micro-powder content, mud content, water absorption rate, and needle-like particle content (Gu and Wu, 2016). Based on the uncertainty of the influence degree of each evaluation parameter on the quality grade of recycled concrete coarse aggregate, a fuzzy comprehensive evaluation method was put forward (Li and Wu, 2019). According to the knowledge of gray clustering evaluation theory, Bao and Wang. (2014) proposed a gray clustering evaluation model to evaluate the quality grade of recycled concrete coarse aggregates. Chai and Liu (2018) performed the quality grade evaluation of recycled concrete coarse aggregates based on the entropy weight extension theory.

The abovementioned research and evaluation methods play an essential role in guiding the rational selection of coarse aggregate in the concrete construction process (Gu et al., 2019; Gu et al., 2019). However, the methods mentioned above are limited in their ability due to the complexity and variability of influential factors that affect the coarse aggregate quality of concrete, for example, some factors are certain, some are uncertain, and some are random variables. Therefore, a comprehensive evaluation method that can better solve this kind of uncertainty and the multi-attribute problem should be sought.

The principal component analysis cloud was used in the present study to solve the problems mentioned above. For the method, the inner relationship between fuzziness and randomness was described, and the conversion between qualitative concepts and quantitative features was considered (Zhou et al., 2008; Zhou et al., 2021). Compared to the abovementioned methods, its assessment process has higher reliability and efficiency, so the suggested model has enormous application prospects.

The present research paper has been organized as follows: in Section 1, the methodology is introduced; in Section 2, a new quality assessment model of coarse aggregate is established based on the principal component analysis-cloud model; in Section 3, the results are analyzed and discussed; and in Section 4, conclusions are drawn.

2 Methodology

The principal component analysis-cloud model is a combination of the principal component analytical method (PCA) and the normal cloud model and possesses the advantages of the two methods. The principal component analytical method (PCA) was applied to reduce the dimension of data and calculate the weight of each index, whereas the normal cloud model was used to estimate the quality level.

2.1 The principal component analysis

The principal component analysis was provided by Pirsson (Sheng, 1991) in 1901. It is a statistical analysis method that converts many variables into a few principal components by dimensional reduction. The respective principal component is usually composed of the original variables by using the linear combination. They are independent of each other, and most of the information of the original variable is reflected. This method is mainly applied for dimensional reduction and weight calculation. The calculative model is listed as follows: it is assumed that there are n samples and m variables in one instance. Then, the original assessment index of $n \times m$ relative matrix X can be constructed as follows:

$$X = \begin{bmatrix} x_{11} & \cdots & x_{1m} \\ \cdots & \cdots & \cdots \\ x_{1n} & \cdots & x_{nm} \end{bmatrix} \tag{1}$$

Where x_{nm} denotes the mth variable in the nth sample. Assuming that new variables $z_1\ z_2\ z_3\ ,\ \ldots\ ,\ z_t\ \ (t \le m)$ are the synthetic index of dimensional reduction, then it can be met with:

$$\begin{cases} z_1 = l_{11}x_1 + l_{12}x_2 + \ldots + l_{1m}x_m \\ z_2 = l_{21}x_2 + l_{22}x_2 + \ldots + l_{2m}x_m \\ \ldots \\ z_m = l_{m1}x_1 + l_{m2}x_2 + \ldots + l_{mm}x_m \end{cases} \tag{2}$$

Where the defining principle of coefficients l is the square sum of coefficients in the different equations in the formula and is equal to 1, the principle components are independent of each other, and z_1 is the maximum variance of all the linear combination about the variables $x_1, x_2, \ldots, x_m$; z_2 is irrelevant of z_1 and the maximum variance of all the linear combination about the variables $x_1, x_2, \ldots, x_m$; likewise, z_i is irrelevant of $z_1, z_2, \ldots z_{i-1}$ and the maximum variance of all the linear combination about the variables $x_1, x_2, \ldots, x_m$.

Based on the relevant matrix, the weight coefficients of different indices can be obtained as follows (Alison et al., 2020):

1) the normalization of the sample matrix:

$$X_{\mathrm{ij}} = \frac{x_{ij} - \overline{x_j}}{s_i}\ (i = 1, 2, \ldots, n;\ j = 1, 2, \ldots, m) \tag{3}$$

$$\overline{x_j} = \frac{\sum_{i=1}^{n} x_{ij}}{n},\ s_j^2 = \frac{\sum_{i=1}^{n} \left(x_{ij} - \overline{x_j}\right)}{n-1} \tag{4}$$

Where x_{ij} represents the normalized jth index of the ith sample; $\overline{x_j}$ and s_j^2 represent the mean and variance of the jth index, respectively.

2) The calculation of the Pearson relative coefficient matrix R among the different indices, namely:

$$R = \left(r_{ij}\right)_{m \times m}\ (i = 1, 2, \ldots, m) \tag{5}$$

Where r_{ij} is the relative coefficient between the ith and jth indexes; r_{ij} can be depicted as:

$$r_{ij} = \frac{\sum_{k=1}^{m}\left(x_{ki} - \overline{x_i}\right)\left(x_{ki} - \overline{x_j}\right)}{\sqrt{\sum_{k=1}^{m}\left(x_{ki} - \overline{x_i}\right)^2\left(x_{ki} - \overline{x_j}\right)^2}} \quad (6)$$

3) The calculation of eigenvalues and eigenvectors of the relevant coefficient matrix R; the eigenvalue is marked as λ and the normalized unit eigenvector corresponding to the eigenvalue is marked as p.
4) Calculating the number of principal components. The cumulative contribution rate of principle components was calculated. Its eigenvalue was greater than 1. The accumulative contribution rate of 85%–95% corresponding to the former k principal component is depicted as:

$$\nu_s = \lambda_s \Big/ \sum_{s=1}^{m}\lambda_s \ (s = 1, 2, ..., m) \quad (7)$$

$$\nu_{\text{sumk}} = \sum_{s=1}^{k}\lambda_s \Big/ \sum_{s=1}^{m}\lambda_s \ (k = 1, 2, ..., m) \quad (8)$$

Where ν_s is the contribution rate of variance at the *sth* principal component. ν_{sumk} is the contribution rate of accumulative variance at the former k principal components.

5) the coefficient matrix of the principal component to meet the cumulative contribution rate of 80% can be extracted as:

$$U_k = (p_1, p_2, ..., p_k) \quad (9)$$

6) The calculation of different index weights ω:

$$\omega = \left|U_k \times \nu_k / \nu_{sumk}\right| \Big/ \sum_{i=1}^{k}\left|U_k \times \nu_i / \nu_{sumk}\right| \quad (10)$$

2.2 The normal cloud model

The cloud model was provided by Li et al. (1995) in the 1990s; it is a cognitive model applied to deal with the two-way conversion between qualitative concepts and quantitative data. According to vague mathematics and random mathematics, the theory is performed as a unified portrayal between the uncertainty of vague problems and the randomness of membership degree. It can deal with vague and random events; the cloud model has been successfully applied to wide-field (Xu et al., 2011).

The cloud model is defined as follows: x, Y, C is assumed as a common quantitative set, Y is called the domain; where $x \in Y$, C is the qualitative conception in the domain Y. For the random research object x in the domain Y, there still exists a random number with a stable tendency $u(x) \in [0, 1]$, then is called the membership degree of x corresponding to C, or it is called the definitive degree. The distribution of the definitive degree in the domain Y is called the membership cloud. If x meets with $x \sim N(Ex, En^2)$, and $En \sim N(En, He^2)$, and then can be expressed as:

$$u(x) = \exp\left[-\frac{(x - Ex)^2}{2En^2}\right] \quad (11)$$

Where the distribution definitive degree in the domain Y is also called a normal cloud or Gauss cloud. For the quality grade of coarse aggregate, the Expectation Ex, Entropy En, and hyperentropy $\frac{dx^{(1)}}{dt} + ax^{(1)} = u$ are applied to represent the digital features of stable definition at certain coarse aggregates to demonstrate the uncertainty of the stable state. Ex can represent the point of certain conception in the domain of quality grade of coarse aggregates, namely, it is the center value of conception in the domain space; En is determined by the vagueness and randomness of the conception of quality grade of coarse aggregates and it reflects the accepting range of conception; $\frac{dx^{(1)}}{dt} + ax^{(1)} = u$ demonstrates the uncertainty of Entropy and its magnitude reflects the thickness of cloud drop. Expectation Ex, Entropy En, and hyperentropy $\frac{dx^{(1)}}{dt} + ax^{(1)} = u$ of different grades in the cloud model can be calculated as follows (Chen et al., 2022; Gu et al., 2022):

$$Ex = \frac{c^+ + c^-}{2} \quad (12)$$

$$En = \frac{c^+ - c^-}{6} \quad (13)$$

$$H_e = k_1 \quad (14)$$

Where c^+ and c^- are, respectively, the upper and lower bounds corresponding to the grade standard of a specific index; for the case of a single boundary, the default bound can be determined by using the upper and lower bounds of actual data at the same grade. The hyperentropy $\frac{dx^{(1)}}{dt} + ax^{(1)} = u$ can be selected as a proper constant k according to the maximum range of different indices, commonly in the cloud model, $H_e \leq 0.5$. If $H_e \geq 0.5$, it demonstrates the distance of adjacent cloud drops is too great, so the discreteness of cloud drops is bad. k is set as 0.01 in the investigation.

If a variable has only a single boundary, such as $[-\infty, x_u]$ or $[x_l, +\infty]$, the corresponding characteristic parameters are depicted as follows (Zhou et al., 2016; Klauer et al., 2016):

$$E_x = 1.5x_l \quad (15)$$

$$E_n = \frac{E_x}{6} \quad (16)$$

3 The establishment of the assessment model

To assess the quality grade assessment of coarse aggregates, the assessment model should be established. The procedure is listed as follows:

3.1 The construction of an index system

Many factors result in the quality grade of coarse aggregate; according to the relevant research (Wang and Park, 2001), the quality grade of coarse aggregate is affected by seven assessment indicators: apparent density(X_1), the porosity (X_2), the sturdiness(X_3), the crushing index(X_4), the micronutrient content(X_5), the soil content(X_6), and the water absorption(X_7).

TABLE 1 The classification standard of the assessment index.

Assessment index	The stability level of seismic slopes				
	I	II	III	IV	V
X_1	>2,450	(2,350, 2,450)	(2,300, 2,350)	(2,250, 2,300)	≤2,250
X_2	<47	(47, 49)	(49, 51)	(51, 53)	≥53
X_3	<5.0	(5.0, 9.0)	(9.0, 12.0)	(12.0, 15.0)	>15.0
X_4	<12	(12, 18)	(18, 24)	(24, 30)	≥30
X_5	<1	(1, 2)	(2, 2.5)	(2.5, 3)	≥3
X_6	<0.5	(0.5, 0.7)	(0.7, 0.85)	(0.85, 1)	≥1
X_7	<3	(3, 5)	(5, 6)	(6, 7)	≥7

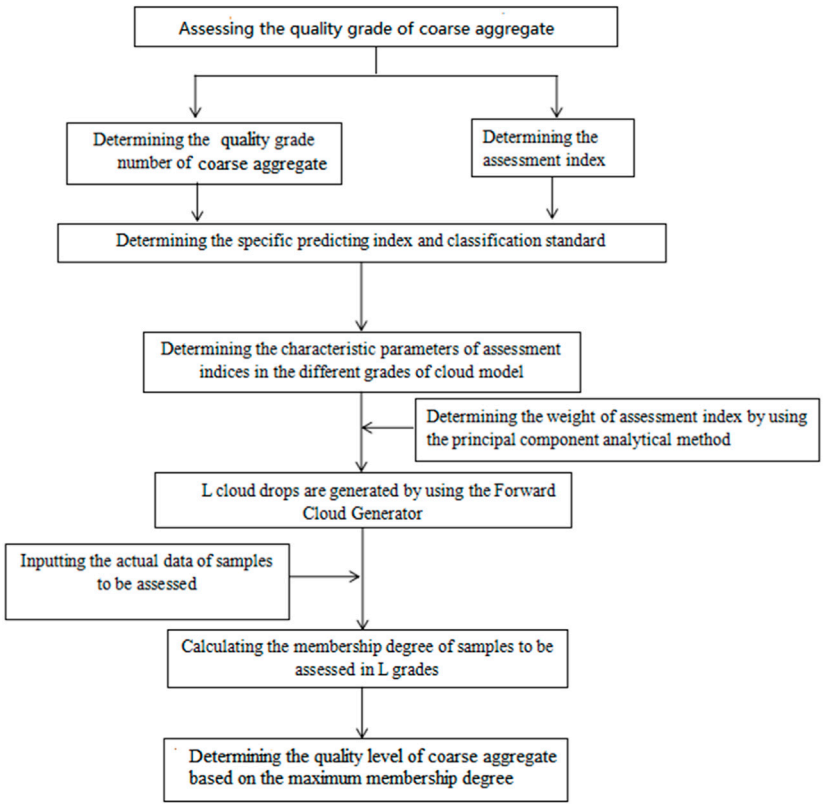

FIGURE 1
The flowchart of the assessment frame.

These indicators are quantitative ones and the seven risk assessment indicators are classified into five levels: excellent (I), good (II), medium (III), qualified (IV), and bad (V), as shown in Table 1.

3.2 The construction of the assessment frame

The quality grade of coarse aggregates not only affects the construction of concrete engineering but can also endanger human life. Consequently, evaluating the coarse aggregate quality grade of recycled concrete is essential (Chen and Li, 2008).

The flowchart of the assessment frame is plotted in Figure 1. At first, the predicting index and corresponding quality level intervals were determined and then, the weight calculation of a sample datum was performed using the principal component analytical method. Based on the classification interval of the assessment index, characteristic parameters Ex, En, and $\frac{dx^{(1)}}{dt} + ax^{(1)} = u$ were calculated in the cloud model. Finally, the synthetic membership degree

TABLE 2 Measured index values of waiting for the estimated sample.

Number of the pending judgment sample	X_1	X_2(%)	X_3(%)	X_4(%)	X_5(%)	X_6(%)	X_7(%)
1# sample	2,300	53	12	17.5	1.4	0.7	9
2# sample	2,500	50	9.2	9.8	2.4	0.5	10.2
3# sample	2,435	44	1.4	23.1	0.18	1	4.9
4# sample	2,360	46	3.1	31.6	0.43	0.4	5.8
5# sample	2,620	53	1	16	3.4	0.9	2.5

TABLE 3 The correlation coefficient matrix.

Correlation	X_1	X_2(%)	X_3(%)	X_4(%)	X_5(%)	X_6(%)	X_7(%)
X_1	1	0.237	−0.519	−0.47	0.745	0.366	−0.504
X_2	0.237	1	0.487	−0.642	0.808	0.000	0.153
X_3	−0.519	0.487	1	−0.471	0.08	−0.425	0.906
X_4	−0.47	−0.642	−0.471	1	−0.742	−0.156	−0.401
X_5	0.745	0.808	0.08	−0.742	1	0.091	−0.098
X_6	0.366	0.000	−0.425	−0.156	0.091	1	−0.568
X_7	−0.504	0.153	0.906	−0.401	−0.098	−0.568	1

TABLE 4 The accumulative contribution rate.

Component	Initial eigenvalues			Extraction sums of squared loadings		
	Total	% Of variable	Cumulative %	Total	% Of variable	Cumulative %
1	2.956	42.236	42.236	2.956	42.236	42.236
2	2.769	39.561	81.797	2.769	39.561	81.797
3	0.734	10.572	92.369			
4	0.534	7.631	100			
5	5.601×10^{-16}	8.002×10^{-15}	100			
6	1.931×10^{-16}	2.758×10^{-15}	100			
7	-9.462×10^{-18}	-1.352×10^{-16}	100			

M (shown in Eq. 17) of different samples could be obtained by using the datum to be assessed, and in combination with the weight of the assessment index. The quality grade of coarse aggregate could be determined according to the maximum certainty degree criterion.

$$M = \sum_{i=1}^{n} u_i \omega_i \tag{17}$$

3.3 The determination of index weight coefficients

The abnormal cloud model was constructed because of the randomness and fuzziness of quality assessment. To evaluate the weight coefficients of each assessment index, the original data of six assessment indexes are shown in Table 2.

Based on Eqs 1–6, and in combination with Table 2, the correlation coefficient matrix is shown in Table 3.

According to Eqs 7–9, the accumulative contribution rate of the principal component is shown in Table 4.

It can be seen in Table 4 that the accumulative contribution rate of the former two principal components arrived at 81.797%. Its magnitude was greater than 80%, so the former two principal components were selected to calculate the weight of the predicting index. According to Eq. 10, the corresponding index weight was calculated as follows.

$$\omega = \left[0.0011 \quad 0.003 \quad 0.3894 \quad 0.0768 \quad 0.3619 \quad 0.0598 \quad 0.1079 \right] \tag{18}$$

TABLE 5 The digital feature of the cloud model.

Quality grade	The digital feature	X_1	X_2	X_3	X_4	X_5	X_6	X_7
I	*Ex*	2,500	23.5	2.5	6	0.5	0.25	1.5
	En	16.667	7.833	0.833	2	0.167	0.0833	0.5
	$\frac{dx^{(1)}}{dt} + ax^{(1)} = u$	0.01	0.01	0.01	0.01	0.01	0.01	0.01
II	*Ex*	2,400	48	7	15	1.5	0.6	4
	En	16.667	0.333	0.667	1	0.167	0.033	0.333
	$\frac{dx^{(1)}}{dt} + ax^{(1)} = u$	0.01	0.01	0.01	0.01	0.01	0.01	0.01
III	*Ex*	2,325	50	10.5	21	2.25	0.775	5.5
	En	8.333	0.333	0.5	1	0.0833	0.025	0.167
	$\frac{dx^{(1)}}{dt} + ax^{(1)} = u$	0.01	0.01	0.01	0.01	0.01	0.01	0.01
IV	*Ex*	2,275	52	13.5	27	2.75	0.925	6.5
	En	8.33	0.333	0.5	1	0.0833	0.025	0.167
	$\frac{dx^{(1)}}{dt} + ax^{(1)} = u$	0.01	0.01	0.01	0.01	0.01	0.01	0.01
V	*Ex*	2,225	79.5	22.5	45	4.5	1.5	10.5
	En	8.33	13.25	3.75	7.5	0.75	0.25	1.75
	$\frac{dx^{(1)}}{dt} + ax^{(1)} = u$	0.01	0.01	0.01	0.01	0.01	0.01	0.01

It was found that indexes X_3, X_5, and X_7 had a great influence on the quality grade of coarse aggregate, and the effects of the other four indices were small in comparison.

3.4 The determination of digital features in the normal cloud model

Based on Table 1, and in combination with Eqs 11–14, the classification standard of normal cloud about the coarse aggregate is depicted in Table 5.

According to Table 1, the characters of the cloud model corresponding to different indices were calculated using the forward cloud generator and are plotted in Figure 2. The horizontal coordinates represent the magnitude of other variables, whereas the vertical coordinates denote the magnitude of certainty degree. A sub-figure in Figure 2 includes five clouds, namely, I, II, III, IV, and V. When a particular variable was fixed, the certainty degree of a certain point at the state grade could be obtained.

According to Tables 2, 4, and in combination with Eqs 11, 17 18, finally, a comprehensive certainty degree was obtained, and it was compared with the actual investigation results. This is listed in Table 6.

The principal component analysis-cloud model was applied to assess the quality grade of coarse aggregate. The outcomes are shown in Table 6. As shown in Table 5, the quality grades of coarse aggregate from samples 1 to 5 were different. The stable level from samples 2 to 5 was I, which means that the quality grade of coarse aggregate in these samples was excellent, so no measurement needed to be done. The quality grade of coarse aggregate in sample 1 was V, meaning that its grade of coarse aggregate was bad and that the necessary consolidation measurement should be performed for the sample.

According to the comparative results of the different evaluation models in Table 5, it could be concluded that the outcomes assessed by the principal component analysis-cloud method were consistent with the actual investigations for five different samples; its accuracy reached 100%, which is higher than the results from the Extension Theory (80%) (Chen and Li, 2008). The conclusion was drawn that it is feasible to evaluate the quality grade of the coarse aggregate of recycled concrete using the text model.

The model not only achieved accurate results but also provided more details for the quality grade of coarse aggregate. For example, the quality grade of sample 4 more likely belonged to level I than that of samples 2 and 3 because the certainty degree of sample 4 for grade I (0.644) was higher than that of samples 2 (0.123) and 3 (0.221).

In total, the results based on the principal component analysis-cloud model could reflect the quality grade of coarse aggregate. It provides a new method and knowledge for the quality grade of coarse aggregate in the future.

3.5 Engineering example II

The regenerated fine aggregate produced by the Resource Company Limited was taken as the evaluation object. Its monitoring magnitude is listed as follows: X_1 is 2351 kg/m^3, X_2 is 4.7%, X_3 is 3.6%, X_4 is 1.33, X_5 is 0.71%, X_6 is 0.95%, and X_7 is 8.2%. The quality grade of recycled fine aggregate produced by the company was evaluated by the model in this paper; its procedure was similar to the abovementioned example and its results are shown in Table 7.

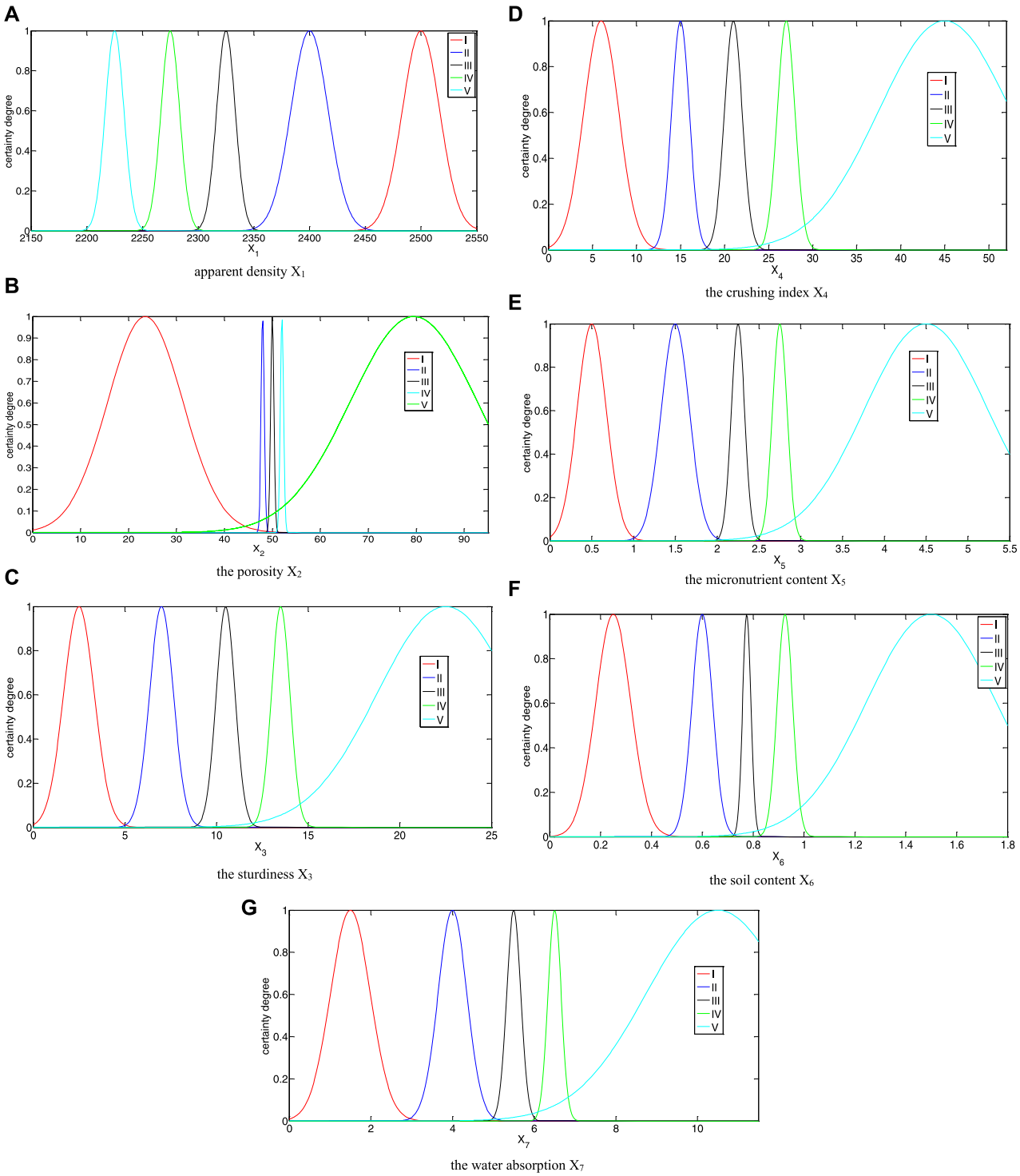

FIGURE 2
Cloud model of each assessment index.

The results obtained from Table 7 demonstrate that the suggested method is consistent with the current specification, and unascertained theory (Wan et al., 2019). The principal component analysis-cloud model is feasible for the accurate assessment of coarse aggregate quality grade of recycled concrete.

4 Conclusion

Taking into consideration the value of apparent density (X_1), porosity (X_2), sturdiness (X_3), crushing index (X_4), micronutrient content (X_5), soil content (X_6), and water absorption (X_7), a new multi-index evaluation method was introduced in this research

TABLE 6 Comprehensive certainty degree.

Sample No	The quality grade of coarse aggregate					Comprehensive assessment	Extension theory	Actual investigation
	I	II	III	IV	V			
1#sample	0	0.307	0.005	0.004	0.383	V	V	V
2#sample	0.123	0.011	0.088	0.001	0.114	I	I	I
3#sample	0.221	0.003	0.009	0.001	0.009	I	II	I
4#sample	0.644	0	0.022	0	0.019	I	I	I
5#sample	0.192	0.047	0	0.037	0.127	I	I	I

TABLE 7 Assessment results.

Evaluation method	The quality grade of coarse aggregate					Suggested model	Current specification	Unascertained theory
	I	II	III	IV	V			
results	0.25	0.4026	0.321	0.11	0.03	II	II	II

paper to evaluate the quality grade of the coarse aggregate of recycled concrete using the principal component analysis-cloud model. The different indexes' weighting coefficients were calculated using the principal component analysis method. The seismic stable level of slopes was judged using the normal-cloud model.

The present model was used for the quality grade of the coarse aggregate of recycled concrete. Finally, its outcomes were compared with the actual investigation and the calculated results obtained by using the Extension method; its accuracy reached 100%, which is higher than the results from the Extension method (80%), leading to the conclusion that it is feasible to evaluate the quality grade of the coarse aggregate of recycled concrete using the text model. It provides a new method and knowledge for the future quality grade evaluation of coarse aggregate.

Data availability statement

The original contributions presented in the study are included in the article/Supplementary Material, further inquiries can be directed to the corresponding author.

Author contributions

BZ: Conceptualization, Investigation, Writing–review and editing. E-WX: Funding acquisition, Validation, Writing–review and editing. X-BG: Formal Analysis, Methodology, Writing–original draft.

Funding

The author(s) declare financial support was received for the research, authorship, and/or publication of this article. This work is supported by the Opening Project of Sichuan Province University Key Laboratory of Bridge Non-destruction Detecting and Engineering Computing (2022QYJ02 and 2022QYY02), Key scientific research projects of colleges and universities in Henan province (23B560019).

Conflict of interest

Author E-WX was employed by China MCC Group Co., Ltd.

The remaining authors declare that the research was conducted in the absence of any commercial or financial relationships that could be construed as a potential conflict of interest.

Publisher's note

References

Alison, M. Q., Canbulat, I., and Oh, J. (2020). Methods applied in Australian industry to evaluate coal mine slope stability. *Int. J. Min. Sci. Technol.* 30 (2), 151–155. doi:10.1016/j.ijmst.2019.11.001

Astm, D. (2003). *2940 03 Standard specification for graded aggregate material for bases or sub bases for high ways or airports*. USA: American Society for Testing and Materials.

Bao, X. Y., and Wang, Q. C. (2014). Application of grey clustring method for quality grade estimate of recycled concrete coarse aggregate. *J. Civ. Archit. Environ. Eng.* 36 (3), 112–117.

British Standards (1992). *BS 882 Specification for aggregates from natural sources for concrete*. London: British Standards Institution.

Chai, N. J., and Liu, X. M. (2018). Evaluation of coarse aggregate quality grade of recycled concrete in China based on entropy weight extension theory. *Bull. Chin. Ceram. Soc.* 37 (1), 1–9. (in Chinese).

Chen, J., Shou, Y., and Zhou, X. (2022). Implementation of the novel perfectly matched layer element for elastodynamic problems in time-domain finite element method. *Soil Dyn. Earthq. Eng.* 152, 107054. doi:10.1016/j.soildyn.2021.107054

Chen, X. T., and Li, L. (2008). Prediction of tunnel rockburst based on AHP-FUZZY method. *J. China Coal Soc.* 33 (11), 1230–1234.

Gu, X. B., Ma, Y., Wu, Q. H., Ji, X. J., and Bai, H. (2021). The risk assessment of landslide hazards in Shiwangmiao based on intuitionistic fuzzy sets-Topsis model. *Nat. Hazards* 20.

Gu, X. B., Shao, J. L., Wu, S. T., Wu, Q. H., and Bai, H. (2021). The risk assessment of debris flow hazards in zhouqu based on the projection pursuit classification model. *Geotechnical Geol. Eng.* 8, 4–17.

Gu, X. B., Wang, L., and Wu, Q. H. (2022). The risk assessment of debris flow in the duba river watershed using intuitionistic fuzzy sets: TOPSIS model. *Math. Problems Eng.* 2022, 2022. Article ID 2031907, 12 pages. doi:10.1155/2022/2031907

Gu, X. B., and Wu, Q. H. (2016). The application of nonordinary, state-based peridynamic theory on the damage process of the Advances in Materials Science and Engineering rock-like materials. *Math. Problems Eng.* 3 (8), 1–9.

Gu, X. B., and Wu, Q. H. (2019). Seismic stability analysis of waterfront rock slopes using the modified pseudodynamic method. *Geotech. Geol. Eng.* 37 (3), 1743–1753. doi:10.1007/s10706-018-0718-1

Gu, X. B., Wu, Q. H., and Ma, Y. (2022). Risk assessment of the rockburst intensity in a hydraulic tunnel using an intuitionistic fuzzy sets-TOPSIS model. *Adv. Mater. Sci. Eng.* 2022, 1–14. Article ID 4774978. doi:10.1155/2022/4774978

Gu, X. B., Wu, Q. H., and Zhu, Y. H. (2019). The experimental investigation on the propagation process of crack for brittle rock similar material. *Geotechnical Geol. Eng.* 37 (6), 4731–4740. doi:10.1007/s10706-019-00934-w

Gu, X. B., Wu, S. T., Ji, X. J., and Zhu, Y. H. (2021). The risk assessment of debris flow hazards in Banshanmen gully based on the entropy weight normal cloud method. *Adv. Civ. Eng.* 2021, 1–11. doi:10.1155/2021/8841310

Klauer, S. G., Dingus, T. A., and Neale, V. L. (2016). *The impact of driver inattention on near-crash/crash risk: analysis using the 100-car naturalistic driving study data [R]*. Washington: National Highway Traffic Safety.

Li, D., Meng, H. J., and Shi, X. M.(1995). Affiliate cloud and affiliate cloud generator [J]. *J. Comput. Res. Dev.* 32(6): 15–26.

Li, S. C., and Wu, J. (2019). A multi-factor comprehensive risk assessment method of karst tunnels and its engineering application. *Bull. Eng. Geol. Environ.* 78 (6), 1761–1776. doi:10.1007/s10064-017-1214-1

Sheng, P. I. (1991). Application of grid steel frame to primary support for loess tunnel on Haolebaoji-Ji an railway. *Tunn. Constr.* 41 (4), 604–615.

Wan, B. T., Bao, X. Y., and Li, A. C. (2019). Evaluation on quality grade of recycled concrete fine aggregate. *Bull. Chin. Ceram. Soc.* 38 (9), 2758–2764. (in Chinese).

Wang, J. A., and Park, H. D. (2001). Comprehensive prediction of rock burst based on analysis of strain energy in rocks. *Tunneling Undergr. Space Technol.* 41, 49–57. doi:10.1016/s0886-7798(01)00030-x

Xu, Z. H., Li, S. C., and Li, L. P. (2011). Risk assessment of water or mud inrush of karst tunnels based on analytic hierarchy process. *Rock Soil Mech.* 32 (5), 1757–1766.

Zhou, X. P., Gu, X. B., and Qian, Q. H. (2016). Seismic bearing capacity of shallow foundations resting on rock masses subjected to seismic loads. *KSCE J. Civ. Eng.* 20 (1), 216–228. doi:10.1007/s12205-015-0283-6

Zhou, X. P., Pan, X. K., and Cheng, H. (2021). The nonlinear creep behaviors of sandstone under the different confining pressures based on NMR Technology. *Rock Mech. Rock Eng.* 54 (9), 4889–4904. doi:10.1007/s00603-021-02557-1

Zhou, X. P., Zhang, Y. X., Ha, Q. L., and Zhu, K. S. (2008). Micromechanical modelling of the complete stress–strain relationship for crack weakened rock subjected to compressive loading. *Rock Mech. Rock Eng.* 41 (5), 747–769. doi:10.1007/s00603-007-0130-2

frontiers | Frontiers in Materials

TYPE Original Research
PUBLISHED 15 December 2023
DOI 10.3389/fmats.2023.1318366

OPEN ACCESS

EDITED BY
Anbang Li,
Xi'an University of Architecture and Technology, China

REVIEWED BY
Kun Xu,
Beijing University of Technology, China
Yefei Ren,
China Earthquake Administration, China

*CORRESPONDENCE
Lang Liu,
janice_liu@cqjtu.edu.cn

RECEIVED 11 October 2023
ACCEPTED 27 November 2023
PUBLISHED 15 December 2023

CITATION
Wang X, Zhang G, Liu L, Li Y, Kong H and Zhang C (2023), Mechanical and fatigue properties of graphene oxide concrete subjected to sulfate corrosion.
Front. Mater. 10:1318366.
doi: 10.3389/fmats.2023.1318366

Mechanical and fatigue properties of graphene oxide concrete subjected to sulfate corrosion

Xu Wang[1,2], Guoliang Zhang[1,2], Lang Liu[1,2]*, Yongguang Li[1,2], Hu Kong[3] and Cheng Zhang[4]

[1]State Key Laboratory of Mountain Bridge and Tunnel Engineering, Chongqing Jiaotong University, Chongqing, China, [2]School of Civil Engineering, Chongqing Jiaotong University, Chongqing, China, [3]Department of Civil and Transportation Engineering, Hohai University, Nanjing, China, [4]Shenzhen Y. S. Mao Bridge Design Group Co Ltd., Shenzhen, China

Concrete structures usually have to experience some unfavorable environmental actions during their service life, leading to the mechanical properties degradation, moreover, cyclic loadings such as traffic loads, wind loads may further accelerate structural damage, therefore, improving durability of concrete is of vital for structures servicing in severe environment. Graphene oxide (GO), as a new nano-reinforced material, has ultra-high mechanical properties and large specific surface area as a concrete reinforcing material. This study entailed an examination of the properties of Graphene Oxide Concrete (GOC) with varying levels of GO incorporation (0, 0.02, 0.05, 0.08 wt%). It also encompassed an analysis of the fatigue properties of GOC under different stress levels and varying sulfate wetting and drying cycles. Additionally, the investigation delved into the degradation mechanisms affecting Graphene Oxide Concrete (GOC) when subjected to sulfate erosion conditions. Furthermore, the study assessed the mass loss of specimens and their fatigue life under diverse environmental conditions. The results showed that appropriate GO incorporations could enhance concrete's mechanical and fatigue properties after sulfate attack. In addition, scanning electron microscope (SEM) analysis showed that GO could adjust the aggregation state of cement hydration products and its own reaction with some cement hydration crystals to form strong covalent bonds, to improve and enhance microstructural denseness.

KEYWORDS

graphene oxide, mechanical property, sulfate corrosion, fatigue life, concrete, SEM

1 Introduction

In recent years, with the rapid development of nanomaterials, scholars have been researching ways to improve structural performance (mechanical properties, durability, and long-term performance, etc.) by incorporating nanomaterials (Zhang and Li, 2011; Ali et al., 2013; Zhu et al., 2022; Gul et al., 2023). However, the application of nanotechnology in construction engineering is complex (Pacheco-Torgal and Jalali, 2011). The main nanomaterials currently incorporated into concrete are carbonaceous nanomaterials, nano metals and metal oxides and inorganic nanomaterials. Among them, GO is one of hot spots in nanomaterial researches (Chen et al., 2018; Li et al., 2018; Lu et al., 2018). The oxygen-containing functional groups make the GO-dispersion hydrophilic and dispersive (Dreyer et al., 2014), which can help forming hydration products. These make hydration products interweave and penetrate into a uniform and dense microstructure (Raki et al.,

2010; Amin and Abu el-Hassan, 2015; Nirmala and Dhanalakshmi, 2015), resulting in microcosmic defect reductions (Zhao et al., 2020), and thus significantly improve the strength, toughness, and durability of cement composites (Peng et al., 2019).

Lv et al. (2013) investigated the effect of GO nanosheets on the microstructure and mechanical properties of cement composites. They showed that GO nanosheets could modulate the formation of flower-like crystals and significantly enhance the tensile and flexural strength of the materials. Jiang et al. (2018) studied the effects of GO and polyvinyl alcohol (PVA) fibers on the mechanical properties, durability, and microstructure of cement materials, and the results showed that the addition of polyvinyl alcohol fibers and GO significantly enhanced the mechanical strength and durability of cement-based materials. Gong et al. (2015) also demonstrated that the usage of GO in cement composites and mortar could enhance their mechanical properties.

On the other hand, sulfate attack is one of main reasons that may reduce durability of concrete (Zhang et al., 2021), developing high-performance concrete has critical engineering applications (Han and Tian, 2018). Yang et al. (2017) used long-term immersion to simulate structures immersed in seawater or groundwater to study the corrosion resistance, and the test results showed that incorporating GO could significantly improve the corrosion resistance coefficient of concrete. Cheng et al. (2021) investigated the durability performance of concrete specimens exposed to sulfate attack, the results showed that the integral area of sulfate ion distribution was a suitable index to describe the nonhomogeneous deterioration behavior of sulfate-attacked concrete. Mohammed et al. investigated the effect of GO on concrete properties by experiment, which showed that GO enhanced resistance to chloride attack and water permeability (Mohammed et al., 2015), demonstrating that GO could refine the pore structure of cementitious materials (Mohammed et al., 2016).

For GOC, a new high-performance concrete material, there are few studies on its durability and fatigue performance under sulfate attack. Since the applications of GO nanomaterials in constructions will significantly impact properties and durability of structures in long term, it is necessary to investigate the degradation mechanism of GOC under corrosive environments, to comprehensively understand the performance of this new material and its application in concrete structures. This study concerns GO nanomaterials' effects on mechanical properties of concrete, and mainly focus on the degradation of mechanical properties of GOC in sulfate erosion environments as well as its fatigue performance after sulfate attack, by conducting static loading test and fatigue loading test. In which, different stress levels and number of cycles are taken into account, to understand if these variable factors will impact on the fatigue performance of GO concrete.

2 Experimental investigation

2.1 GOC material

The specimens were prepared in accordance with Chinese code GB/T 50081 (Ministry of Housing and Urban-Rural Construction of China, 2019), having standard dimensions of 100 mm × 100 mm × 100 mm and consisting of complex Portland cement, multilayer GO-dispersion, aggregates (crushed stone as coarse aggregates and manufactured sand as fine aggregates) and water.

TABLE 1 The components of the P.C. 42.5.

Components of P.C. 42.5	Percentage (%)
CaO	65.32
SiO_2	21.48
Al_2O_3	4.12
Fe_2O_3	3.22
MgO	2.82
K_2O	0.93
SO_3	0.68
Na_2O	0.47
TiO_2	0.19
P_2O_5	0.10
MnO	0.06
Loss on ignition	0.56

TABLE 2 The physical parameters and chemical components of GO.

	Specification	Contents
Physical parameters	Purity	>95 wt%
	Thickness	3.42–7.82 nm
	Layers	0.79 nm
	Specific surface area	130–260 m^2/g
	Lamellar diameter	12–40 μm
Chemical components (from XRD test)	C	69.26 %
	O	30.16 %
	S	0.28 %
	Si	0.16 %
	Cl	0.11 %

2.1.1 Complex portland cement

All indexes (fineness, stability, mechanical properties, etc.) of P.C. 42.5 complex Portland cement meet the requirements of Chinese code GB175 (Chinese Standards Institute, 2020). 3 and 28 days flexural strengths are no less than 3.5 and 6.5 MPa, respectively, while compressive strengths are no less than 15 and 42.5 MPa, respectively. Its chemical composition is shown in Table 1.

2.1.2 Multilayer GO-dispersion

The multilayer GO was frozen, dried and dispersed by the modified *Hummers* method (Hummers and Offeman, 1958), and the finished product had no precipitation but good dispersion. Its dispersion is black oily liquid with a concentration of 10 mg/mL. The parameters and components of GO are shown in Table 2.

TABLE 3 The particle gradation of fine aggregates.

Nominal diameter (mm)	0	0.15	0.3	0.6	1.18	2.38	4.72
Accumulated sieve residue (%)	100	89.34	74.98	52.96	37.45	18.76	0.96

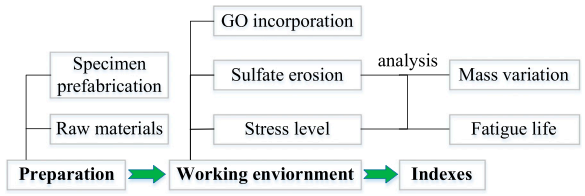

FIGURE 1
Test Procedure.

2.1.3 Concrete aggregates

The coarse aggregate of GOC specimens is 5–20 mm grade crushed stone, and the fine aggregate is manufactured sand, whose details are shown in Table 3.

2.2 Specimen testing

The test procedure in this study is shown in Figure 1.

2.2.1 Preparation for specimens

The tested GOC specimens were all with a water-cement ratio of 0.50 and a sand rate of 35%, and the GO-dispersions of 0, 0.02, 0.05, 0.08wt% (the mass ratio of GO to cement) were thoroughly mixed with water before the test. The concrete was configured according to the mixture proportion (Table 4) and injected into the cube mold of 100 mm × 100 mm × 100 mm, finally, the marked specimens were put into the curing room and cured in standard conditions. All the above procedures were completed according to the requirements of Chinese code GB/T50082 (Ministry of Housing and Urban-Rural Construction of China, 2009).

2.2.2 Test situation

1) Load test after sulfate attack

Na_2SO_4 solution with a mass fraction of 10 wt% was added into the test chamber, and specimens were subjected to 0, 30, 60, 90, and 120 dry-wet cycles according to the cyclic system. The fabricated samples were named according to the test environment and GO incorporation; for example, SA_{30}-$GOC_{0.02\%}$ indicated sulfate erosion GOC with 30 wetting and drying cycles and 0.02 wt% GO.

2) Fatigue test after sulfate attack

Another 18 prisms GO concrete specimens (marked as S45-FGOC-*a*-1~3 and S90-FGOC-*a*-1~3, respectively) were fabricated for fatigue testing, where S45 and S90 represented the specimens underwent 45 times and 90 times sulfate wetting and drying cycles, respectively; *a* represented the stress level, which was individually set as 0.75, 0.80 and 0.85 in the fatigue test. To be comparable, the counterpart specimens without sulfate erosion were also accordingly prepared to carry out the same fatigue test. The axial compression fatigue test was carried out by an electrohydraulic servo fatigue testing machine. The test parameters were set according to the load test results. Fatigue loading was carried out in a load-controlled manner, and the fatigue loading was carried out in the form of a sin-constant amplitude load spectrum. The cyclic loading started, ranging from the minimum fatigue stress to the maximum fatigue stress at the specific frequency of 10 Hz. Herein, the stress ratio was the ratio of the minimum fatigue stress to the maximum fatigue stress and was set at 0.1 in this study.

3) Measurement indexes

This test was referenced to Chinese code GB/T 50081 (Ministry of Housing and Urban-Rural Construction of China, 2019), and the measurements included mass and fatigue life. The detailed steps were as follows:

a. When the cycle number reached to the test design values, specimens were firstly dried to observe surface damages.
b. Then the mass of each specimen was measured and recorded in detail.
c. The prism specimens were taken fatigue load, the stress level and fatigue life were measured during the test.
d. Fractures of the specimens were observed using the Quattro setup, to investigate the effect of GO incorporation on concrete microstructure at different cycle counts.

TABLE 4 Test design and mixture proportion (unit: kg/m³).

Specimen No.	Cement	Manufactured sand	Crushed stone		Water	GO
			5–10 mm	10–20 mm		
$GOC_{0\%}$	398	623	450	734	195	0
$GOC_{0.02\%}$	398	623	450	734	195	0.080
$GOC_{0.05\%}$	398	623	450	734	195	0.199
$GOC_{0.08\%}$	398	623	450	734	195	0.318

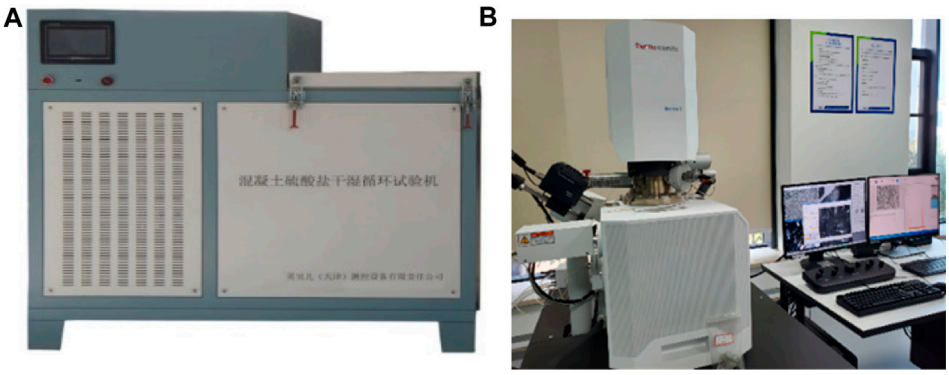

FIGURE 2
Test setup **(A)** IMGS-54 setup for sulfate attack; **(B)** Quattro setup for SEM.

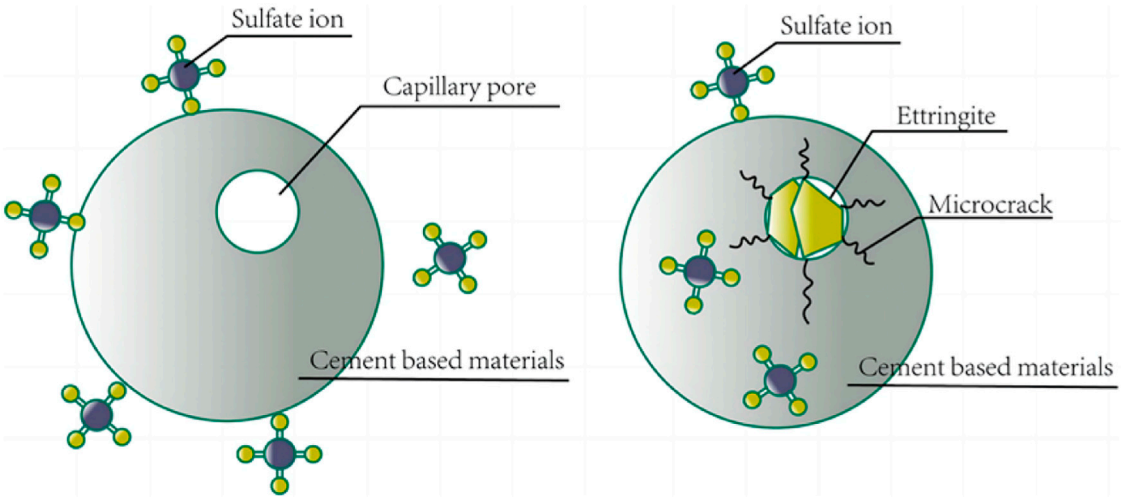

FIGURE 3
Schematic diagram of damage to concrete under sulfate attack.

The environmental and mechanical test setup described in this section was shown in Figure 2.

3 Results and discussion

In this study, properties of GOC with different GO incorporations (0, 0.02, 0.05, 0.08 wt%, respectively) and fatigue properties of GOC with different stress level and sulfate wetting and drying cycles were tested. Generally speaking, GO incorporation was in the range of 0–0.08 wt%, GO can disperse nicely, participate in and regulate the cement hydration process, making the formation and aggregation of cement hydration products more regular and effective, reducing the cracks and pores inside the concrete. There were physical and chemical reactions. Graphene oxide had excellent mechanical strength and stiffness, and its plate structure could prevent sulfate from invading the interior of concrete, thereby improving the ability to resist sulfate corrosion. At the same time, the high surface area and functional groups of GO may also adsorb and hydrate with sulfate ions, thereby forming protection inside the concrete.

3.1 Appearance phenomena

The sulfate attack of concrete can be divided into two main categories: physical and chemical erosion (Liu et al., 2011). During the physical attack, the cracking damage of concrete is caused by the swelling stress generated around the concrete's pore walls, which is greater than the tensile strength of concrete, and the swelling stress originates from the pressure generated by the crystals on the pore walls. During the chemical attack, sulfate ions react with cement hydration products to produce swelling products, which are about 2.5 times larger than the initial reaction phase, thus causing swelling cracking of concrete (Neville, 1995; Leng et al., 2012), as shown in Figure 3.

This damage usually causes peeling, and many micro-cracks appear on the surface of concrete specimens. The specimens show spalling at the edges and corners when the attack is aggravated. As shown in Figure 4, the GO-doped specimens maintained good integrity, and the surface condition remained intact in the less severe case (60 cycles). In the case of severe erosion (120 cycles), both GO-doped and non-GO-doped specimens were severely

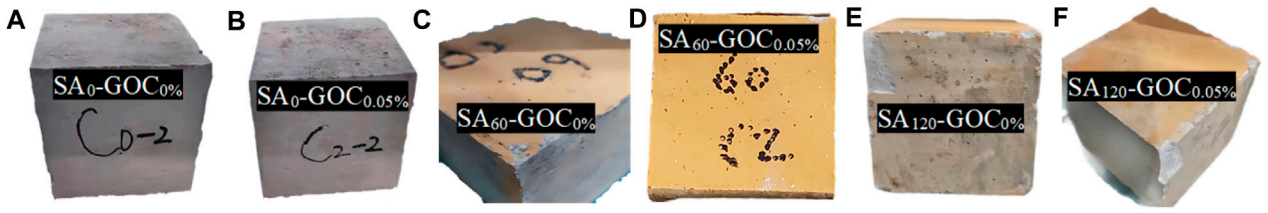

FIGURE 4
The appearance of specimens under the sulfate attack test.

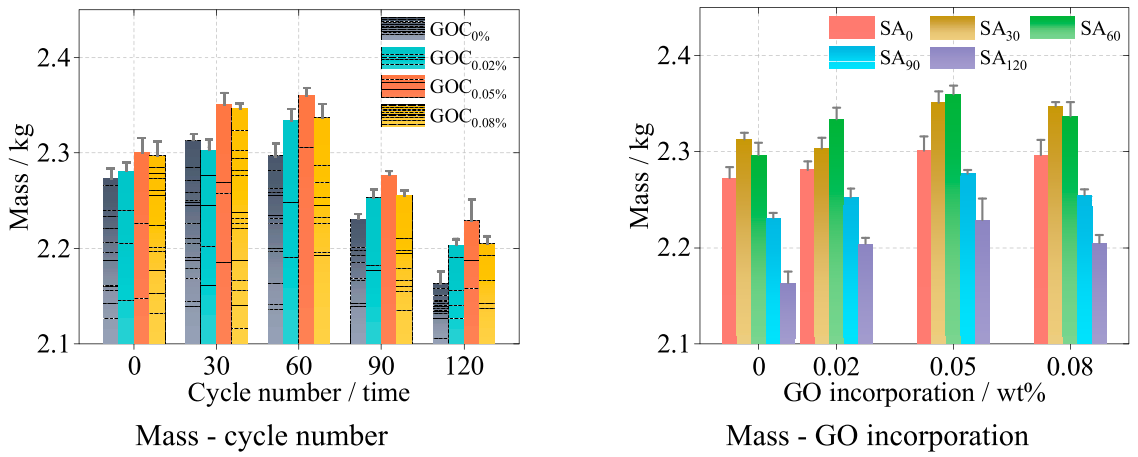

FIGURE 5
The mass of specimens under the sulfate attack test.

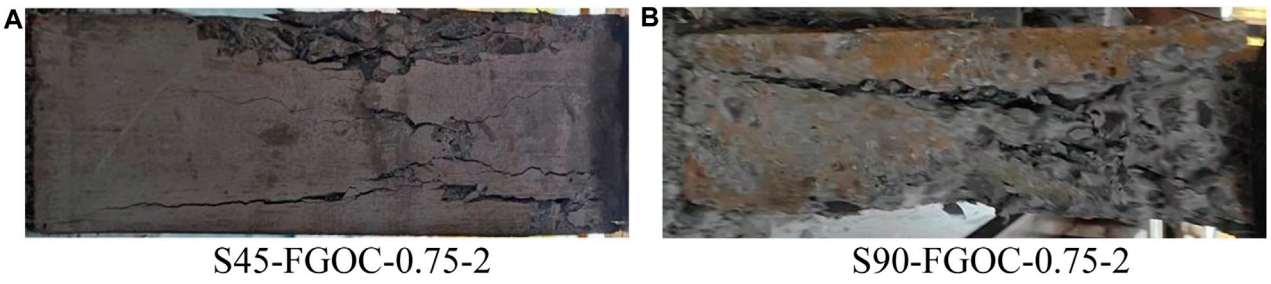

FIGURE 6
Failure mode of sulfate erosive specimens under fatigue testing.

damaged, compared to the GO-doped specimens, which had relatively good integrity and fewer internal traces of sulfate attack.

3.2 Mass variation

Figure 5 shows the mass variation of the specimens under the sulfate attack test. The results show that the masses of all specimens showed a trend of "first increase and then decrease" with the increase of cycle time and GO incorporation, respectively, and the masses of GOC specimens with 60 cycles and 0.05 wt% GO increased most significantly. The mass of all specimens was higher than the initial mass for 30–60 cycles and lower than the initial mass for 90–120 cycles. After the specimens started to show a mass loss, the mass loss rate of GO-doped specimens was significantly lower than that of the non-GO-doped specimens. For example, the mass loss rate of GO-doped specimens ranged from 3.073% to 3.991% after 120 cycles, compared with 4.839% for non-GO-doped specimens. The test results indicate that GO enhances the performance of concrete in resisting mass loss under the action of a sulfate attack environment.

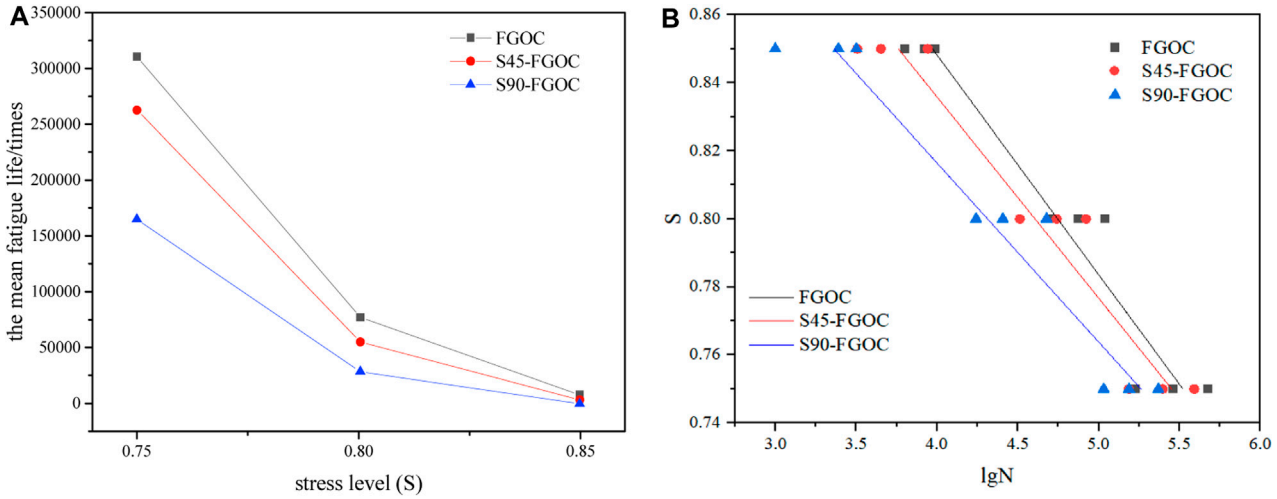

FIGURE 7
Relationship between fatigue life and stress level: **(A)** Mean fatigue life vs stress level, and **(B)** S-N curves.

TABLE 5 Linear regression results for general environmental condition.

Specimen number	Fatigue life *Ni*	ln*Ni*	Survival Rate *P*	ln[ln(1/*P*)]	*b*	*a*
FOC-0.75-1	135537	11.817	0.75	−1.2459	1.568	−19.747
FOC-0.75-2	226534	12.331	0.50	−0.3665		
FOC-0.75-3	369827	12.821	0.25	0.3266		
FOC-0.80-1	36558	10.507	0.75	−1.2459	1.677	−18.777
FOC-0.80-2	53344	10.885	0.50	−0.3665		
FOC-0.80-3	91831	11.428	0.25	0.3266		
FOC-0.85-1	2496	7.822	0.75	−1.2459	1.361	−11.941
FOC-0.85-2	5652	8.640	0.50	−0.3665		
FOC-0.85-3	7383	8.907	0.25	0.3266		
FGOC-0.75-1	168641	12.036	0.75	−1.2459	1.519	−19.506
FGOC-0.75-2	288475	12.572	0.50	−0.3665		
FGOC-0.75-3	475368	13.072	0.25	0.3266		
FGOC-0.80-1	51917	10.857	0.75	−1.2459	1.717	−19.609
FGOC-0.80-2	74583	11.220	0.50	−0.3665		
FGOC-0.80-3	109532	11.604	0.25	0.3266		
FGOC-0.85-1	6338	8.7543	0.75	−1.2459	1.897	−17.172
FGOC-0.85-2	8449	9.042	0.50	−0.3665		
FGOC-0.85-3	9746	9.185	0.25	0.3266		

3.3 Fatigue properties

The maximum fatigue load was determined by the mean value of ultimate load for the static load test, multiplying the stress level, while the minimum fatigue load was then calculated by the stress ratio of 0.1. The failure mode of specimens was shown in Figure 6.

As seen, specimens seriously damaged with wide cracks and local concrete collapse. A large amount of concrete debris fell off in Figure 6B, indicating specimens under 90 times sulfate wetting and drying cycles suffering severer damages. The relationship between fatigue life of specimens and stress level was plotted in Figure 7. In which, (a) compared the mean fatigue life of normal GO concrete

TABLE 6 Linear regression results for sulfate erosion condition.

Specimen number	Fatigue life *Ni*	ln*Ni*	Survival Rate *P*	ln[ln(1/*P*)]	*b*	*a*
S45-FGOC-0.75-1	153523	11.942	0.75	−1.2459	1.691	−21.415
S45-FGOC-0.75-2	248765	12.424	0.50	−0.3665		
S45-FGOC-0.75-3	389501	12.873	0.25	0.3266		
S45-FGOC-0.80-1	32488	10.389	0.75	−1.2459	1.666	−18.553
S45-FGOC-0.80-2	54981	10.915	0.50	−0.3665		
S45-FGOC-0.80-3	83541	11.333	0.25	0.3266		
S45-FGOC-0.85-1	3204	8.072	0.75	−1.2459	1.494	−13.154
S45-FGOC-0.85-2	4497	8.411	0.50	−0.3665		
S45-FGOC-0.85-3	8742	9.076	0.25	0.3266		
S90-FGOC-0.75-1	107455	11.585	0.75	−1.2459	2.014	−24.531
S90-FGOC-0.75-2	154331	11.947	0.50	−0.3665		
S90-FGOC-0.75-3	233764	12.362	0.25	0.3266		
S90-FGOC-0.80-1	17407	9.765	0.75	−1.2459	1.521	−15.984
S90-FGOC-0.80-2	25518	10.147	0.50	−0.3665		
S90-FGOC-0.80-3	47554	10.770	0.25	0.3266		
S90-FGOC-0.85-1	998	6.906	0.75	−1.2459	1.262	−10.006
S90-FGOC-0.85-2	2451	7.804	0.50	−0.3665		
S90-FGOC-0.85-3	3166	8.060	0.25	0.3266		

TABLE 7 Linear regression results for freeze-thaw condition.

Specimen number	Fatigue life *Ni*	ln*Ni*	Survival Rate *P*	ln[ln(1/*P*)]	*b*	*a*
D75-FGOC-0.75-1	130547	11.779	0.75	−1.2459	1.683	−21.110
D75-FGOC-0.75-2	243433	12.403	0.50	−0.3665		
D75-FGOC-0.75-3	322520	12.684	0.25	0.3266		
D75-FGOC-0.80-1	31464	10.357	0.75	−1.2459	1.944	−21.427
D75-FGOC-0.80-2	54522	10.906	0.50	−0.3665		
D75-FGOC-0.80-3	68534	11.135	0.25	0.3266		
D75-FGOC-0.85-1	3185	8.066	0.75	−1.2459	1.750	−15.230
D75-FGOC-0.85-2	4327	8.373	0.50	−0.3665		
D75-FGOC-0.85-3	7552	8.930	0.25	0.3266		
D150-FGOC-0.75-1	76553	11.246	0.75	−1.2459	1.837	−21.762
D150-FGOC-0.75-2	101568	11.528	0.50	−0.3665		
D150-FGOC-0.75-3	173764	12.065	0.25	0.3266		
D150-FGOC-0.80-1	13407	9.504	0.75	−1.2459	2.018	−20.467
D150-FGOC-0.80-2	22518	10.022	0.50	−0.3665		
D150-FGOC-0.80-3	28554	10.260	0.25	0.3266		
D150-FGOC-0.85-1	868	6.766	0.75	−1.2459	1.915	−14.011
D150-FGOC-0.85-2	1351	7.209	0.50	−0.3665		
D150-FGOC-0.85-3	1684	7.429	0.25	0.3266		

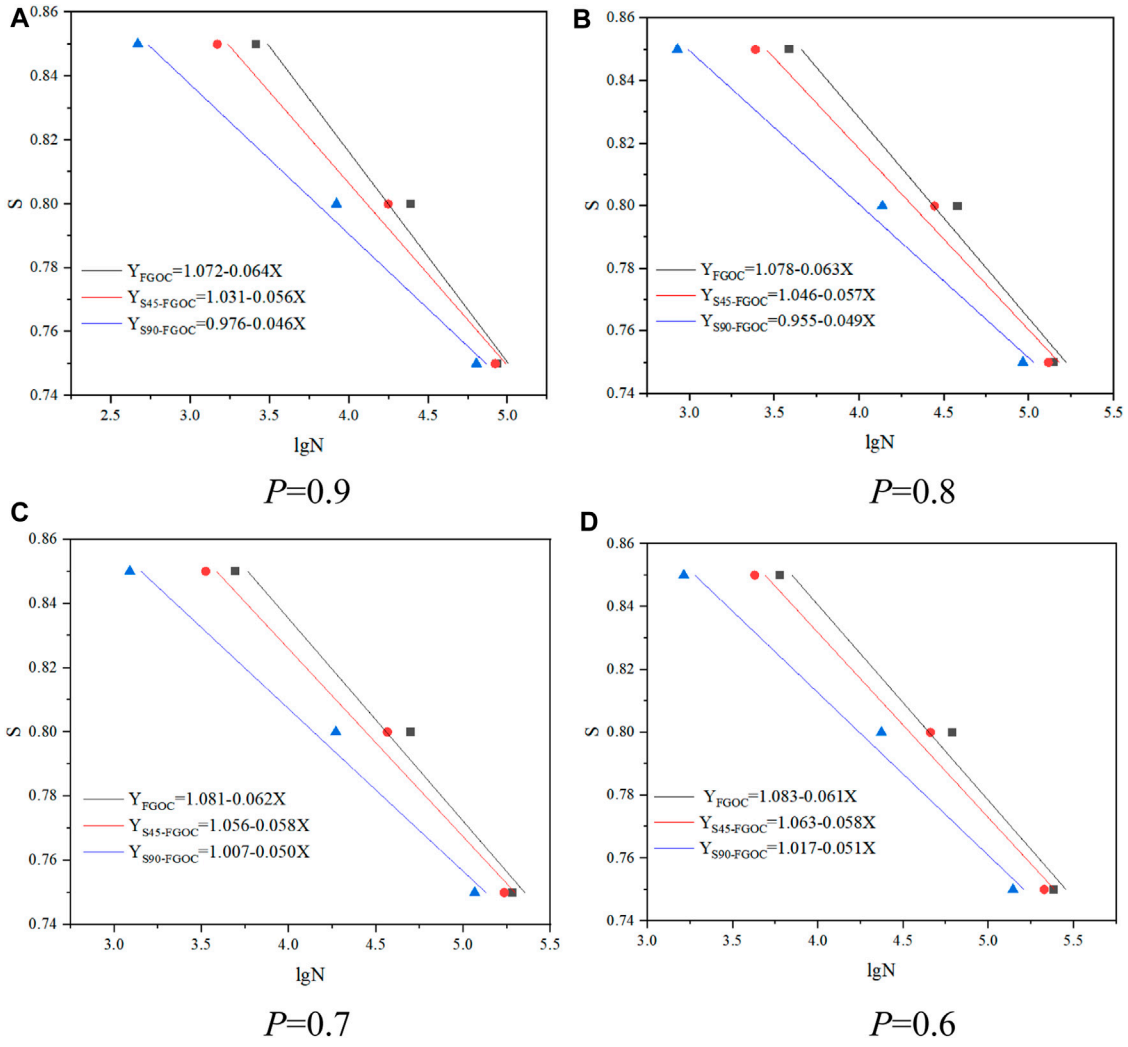

FIGURE 8
Linear regression equations for sulfate condition.

with that of GO concrete with sulfate erosion, and (b) showed the corresponding *S-N* curves. It can be seen in both two figures, high stress level and sulfate erosion would remarkably reduce fatigue life.

3.3.1 Weibull distribution

The Weibull distribution is a widely used probability distribution that is used to depict the correlation between an object's life and various factors such as stress, strain, or durability (Zhang et al., 2019; Zhang et al., 2020a; Zhang et al., 2020b; Zhang et al., 2022). Previous studies show that a Weibull distribution is proper for fatigue estimation of concrete materials (Hong et al., 2020). Therefore, a Weibull distribution is used to assess fatigue life of concrete specimens in this study, which can be expressed as

$$\boldsymbol{ln[ln(1/P)] = blnN_P - blnN_a} \quad (1)$$

in which, P is the survival rate; N_p is the fatigue life, N_a is the characteristic life parameter; and b is the slope of the linear equation.

The empirical formula of survival rate P is

$$\boldsymbol{P = 1 - \frac{i}{1+k}} \quad (2)$$

where i is the serial number of the test specimen according to the fatigue life from low to high; and n is the number of test specimen per group.

Letting the Weibull parameters $Y = ln[ln(1/P)]$, $X = lnN_P$ and, $a = -blnN_a$, then using $Y = bX+a$ to conduct Weibull distribution tests on the fatigue life of specimens at different stress levels. The results by linear regression analysis for general environmental condition, sulfate erosion condition and freeze-thaw condition were listed in Tables 5–7 as below.

3.3.2 Fatigue equation and S-N curve

Fatigue equation is usually used to present the relationship between fatigue life N and stress level S, by which, the stress level and cycle number can be obtained when structure fails. The fatigue equation can also be expressed by curves in logarithmic coordinates, namely, the so-

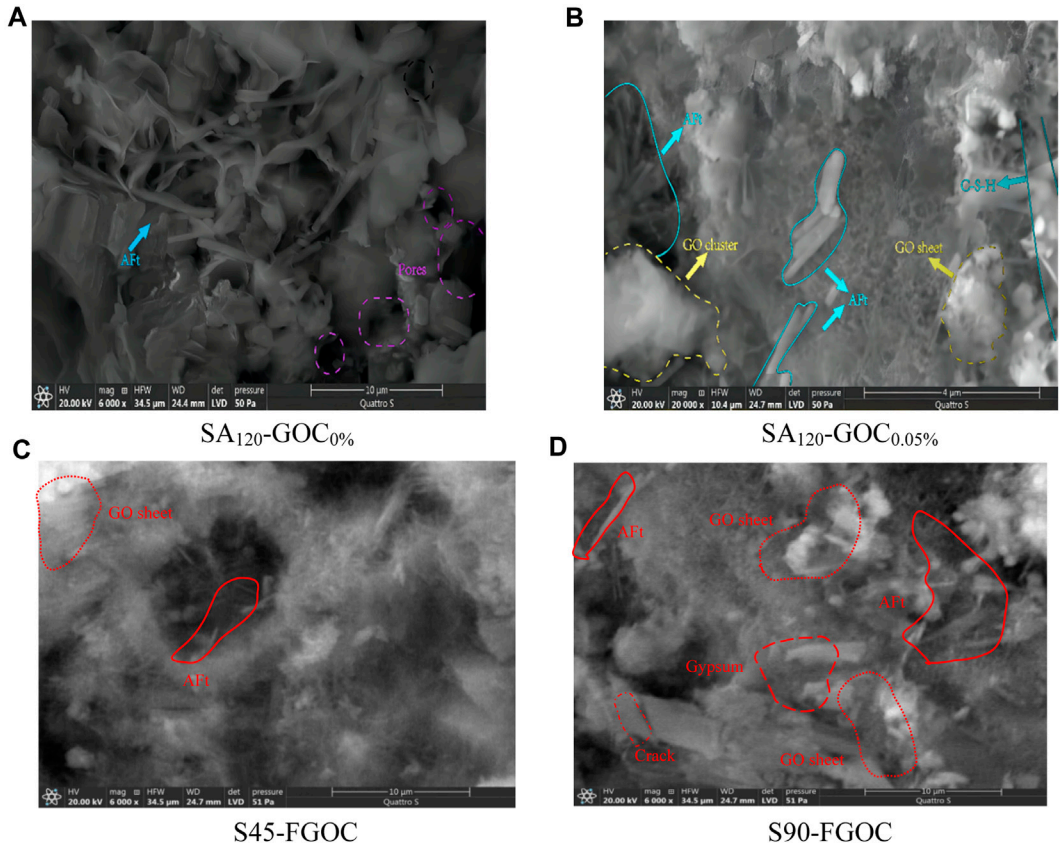

FIGURE 9
The SEM images of specimens under the sulfate attack test.

called *S-N* curve, to demonstrate fatigue characteristics of materials. The fatigue equation can be expressed as

$$S = AlgN + B \tag{3}$$

in which, S donates the stress level; N is the fatigue life; A and B are coefficients.

Note that a survival rate of 0.5 is taken in default and failure probability is not covered in Equation 3, for structure safety, fatigue equation with higher survival rate needs to establish. Taking the regression results of Weibull distribution, the fatigue life with survival rate P could be calculated by Equation 4, where the parameters are the same as before. Let N_p replace N, then fatigue life considering different survival rates could be obtained. In this study, four survival rates of 0.6, 0.7, 0.8 and 0.9 were taken.

$$N_P = exp\frac{ln(ln(1/P)) - a}{b} \tag{4}$$

Figure 8 depicts the linear regression equation that represents the relationship between sulfate corrosion and various survival rates. The observation depicted in Figure 8A reveals a steady decrease in the fatigue properties of GOC specimens as the number of sulfate dry and wet cycles increases, while maintaining a constant stress level, when the survival rate P is 0.9. The sensitivity of the sample to stress increases in proportion to the extent to which it is influenced by the frequency of sulfate exposure during dry and wet cycles. Furthermore, it is evident from Figures 8A–D that as the survival rate P lowers from 0.9 to 0.6, there is a rise in the horizontal coordinate values for each set of curves. The findings indicate that the fatigue life of GOC specimens exhibits an upward trend when the survival rate P decreases following various durations of sulfate dry and wet cycling.

3.4 SEM

To explain the results obtained in the previous section, the microstructure of specimens with different GO incorporations under 120 sulfate dry-wet cycles was compared and analyzed. The SEM images are shown in Figure 9. Figure 9A shows a large number of AFt produced by sulfate attack in non-GO-doped specimens. These AFt crystals are arranged disorderly, and there are many cracks and pores around them, further aggravating the attack of sulfate ions on concrete. When some amount of GO is incorporated, GO sheets and clusters appear in large-scale agglomeration or clustering (Figure 9B). Many cement hydration crystals are distributed around them in a disorganized manner, the number of pores increases, the denseness of microstructure decreases, and the load transfer efficiency between cement matrix and GO is affected and starts to decrease, which instead affects the concrete resistance to sulfate attack. As seen in Figures 9C, D, GO

sheets prevented interior concrete from sulfate eroding at some extent, but with the occurrence of cracks on GO sheets, the structural fatigue performance declined and finally failed.

The results show that, on the one hand, GO can reduce the number of products produced by sulfate attack so that the microstructure of concrete remains relatively dense when subjected to sulfate attack. On the other hand, it improves the erosion resistance of concrete by promoting the generation of regular cement hydration products and optimizing the crystal arrangement to reduce the size and number of micro-cracks and pores.

4 Conclusion

This paper tested the mechanical and fatigue properties of GOC under sulfate erosion. The test results were given and explained concerning the mechanical behavior of GO cement paste and the microstructures of GO cement paste observed by SEM. The following conclusions can be obtained in this study:

1) For the sulfate erosion environment, the degradation of the mechanical properties of concrete-resistant sulfate attack was significantly improved by incorporating GO, and this enhancement was most significant at 0.05 wt% GO incorporation.
2) Sulfate erosion would accelerate fatigue damage accumulation in concrete, then remarkably reduce fatigue life and strength. But comparatively, stress level would affect the fatigue life more seriously. While Weibull distribution can be used to assess the fatigue life of GO concrete under any environmental conditions.
3) It can be seen from SEM microstructure that GO sheets generally improved the compactness of concrete and restrained crack development and spread further, even under severe environmental condition, GO sheets could also relieve sulfate erosion damage.

Data availability statement

The raw data supporting the conclusion of this article will be made available by the authors, without undue reservation.

Author contributions

XW: Conceptualization, Methodology, Resources, Writing–original draft. GZ: Data curation, Formal Analysis, Software, Writing–original draft. LL: Methodology, Writing–original draft, Writing–review and editing. YL: Validation, Visualization, Writing–original draft. HK: Data curation, Writing–original draft. CZ: Software, Writing–original draft.

Funding

The authors declare financial support was received for the research, authorship, and/or publication of this article. This research was funded by the Natural Science Foundation of Chongqing (Grant No. CSTB2022NSCQ-MSX1655) and the State Key Laboratory of Structural Dynamics of Bridge Engineering and Key Laboratory of Bridge Structure Seismic Technology for Transportation Industry Open Fund (Grant No. 202205).

Conflict of interest

Author CZ was employed by Shenzhen Y. S. Mao Bridge Design Group Co Ltd.

The remaining authors declare that the research was conducted in the absence of any commercial or financial relationships that could be construed as a potential conflict of interest.

Publisher's note

References

Ali, M., Li, X., and Chouw, N. (2013). Experimental investigations on bond strength between coconut fibre and concrete. *Mater. Des.* 44, 596–605. doi:10.1016/j.matdes.2012.08.038

Amin, M., and Abu el-Hassan, K. (2015). Effect of using different types of nano materials on mechanical properties of high strength concrete. *Constr. Build. Mater* 80, 116–124. doi:10.1016/j.conbuildmat.2014.12.075

Chen, Z., Zhou, X., Wang, X., and Guo, P. (2018). Mechanical behavior of multilayer GO carbon-fiber cement composites. *Constr. Build. Mater* 159, 205–212. doi:10.1016/j.conbuildmat.2017.10.094

Cheng, H., Liu, T., Zou, D., and Zhou, A. (2021). Compressive strength assessment of sulfate-attacked concrete by using sulfate ions distributions. *Constr. Build. Mater* 293, 123550. doi:10.1016/j.conbuildmat.2021.123550

Chinese Standards Institute (2020). *Common Portland cement (GB175-2020)*. Beijing, China: Chinese Standards Institute.

Dreyer, D. R., Todd, A. D., and Bielawski, C. W. (2014). Harnessing the chemistry of graphene oxide. *Chem. Soc. Rev.* 43, 5288–5301. doi:10.1039/C4CS00060A

Gong, K., Pan, Z., Korayem, A. H., Qiu, L., Li, D., Collins, F., et al. (2015). Reinforcing effects of graphene oxide on Portland cement paste. *J. Mater Civ. Eng.* 27, A4014010. doi:10.1061/(ASCE)MT.1943-5533.0001125

Gul, W., Akbar Shah, S. R., Khan, A., Ahmad, N., Ahmed, S., Ain, N., et al. (2023). Synthesis of graphene oxide (GO) and reduced graphene oxide (rGO) and their application as nano-fillers to improve the physical and mechanical properties of medium density fiberboard. *Front. Mater* 10, 1206918. doi:10.3389/fmats.2023.1206918

Han, N., and Tian, W. (2018). Experimental study on the dynamic mechanical properties of concrete under freeze–thaw cycles. *Struct. Concr.* 19, 1353–1362. doi:10.1002/suco.201700170

Hong, F., Oiao, H., and Wang, P. (2020). Predicting the life of BNC-coated reinforced concrete using the Weibull distribution. *Emerg. Mater Res.* 9, 1–10. doi:10.1680/jemmr.19.00087

Hummers, W. S., and Offeman, R. E. (1958). Preparation of graphitic oxide. *J. Am. Chem. Soc.* 80, 1339. doi:10.1021/ja01539a017

Jiang, W., Li, X., Lv, Y., Zhou, M., Liu, Z., Ren, Z., et al. (2018). Cement-based materials containing graphene oxide and polyvinyl alcohol fiber: mechanical properties, durability, and microstructure. *Nanomaterials* 8, 638. doi:10.3390/nano8090638

Leng, F. G., Zhou, Y. X., and Wang, J. (2012). *Inspection and assessment of concrete durability*. Beijing, China: China Building Materials Press.

Li, G., Yuan, J. B., Zhang, Y. H., Zhang, N., and Liew, K. M. (2018). Microstructure and mechanical performance of graphene reinforced cementitious composites. *Compos Part A-Appl S* 114, 188–195. doi:10.1016/j.compositesa.2018.08.026

Liu, Z., Deng, D., De Schutter, G., and Yu, Z. (2011). Micro-analysis of "salt weathering" on cement paste. *Cem. Concr. Comp.* 33, 179–191. doi:10.1016/j.cemconcomp.2010.10.010

Lu, L., Zhao, P., and Lu, Z. (2018). A short discussion on how to effectively use graphene oxide to reinforce cementitious composites. *Constr. Build. Mater* 189, 33–41. doi:10.1016/j.conbuildmat.2018.08.170

Lv, S., Ma, Y., Qiu, C., Sun, T., Liu, J., and Zhou, Q. (2013). Effect of graphene oxide nanosheets of microstructure and mechanical properties of cement composites. *Constr. Build. Mater* 49, 121–127. doi:10.1016/j.conbuildmat.2013.08.022

Ministry of Housing and Urban-Rural Construction of China (2009). *Standard for test methods of long-term performance and durability of ordinary concrete (GB/T 50082-2009)*. Beijing, China: China Architecture & Building Press.

Ministry of Housing and Urban-Rural Construction of China (2019). *Standard for test methods of concrete physical and mechanical properties (GB/T50081-2019)*. Beijing, China: China Architecture & Building Press.

Mohammed, A., Sanjayan, J. G., Duan, W. H., and Nazari, A. (2015). Incorporating graphene oxide in cement composites: a study of transport properties. *Constr. Build. Mater* 84, 341–347. doi:10.1016/j.conbuildmat.2015.01.083

Mohammed, A., Sanjayan, J. G., Duan, W. H., and Nazari, A. (2016). Graphene oxide impact on hardened cement expressed in enhanced freeze–thaw resistance. *J. Mater Civ. Eng.* 28, 04016072. doi:10.1061/(ASCE)MT.1943-5533.0001586

Neville, A. M. (1995). *Properties of concrete*. Longman London: National Academies.

Nirmala, J., and Dhanalakshmi, G. (2015). Influence of nano materials in the distressed retaining structure for crack filling. *Constr. Build. Mater* 88, 225–231. doi:10.1016/j.conbuildmat.2015.04.022

Pacheco-Torgal, F., and Jalali, S. (2011). Nanotechnology: advantages and drawbacks in the field of construction and building materials. *Constr. Build. Mater s* 25, 582–590. doi:10.1016/j.conbuildmat.2010.07.009

Peng, H., Ge, Y., Cai, C. S., Zhang, Y., and Liu, Z. (2019). Mechanical properties and microstructure of graphene oxide cement-based composites. *Constr. Build. Mater* 194, 102–109. doi:10.1016/j.conbuildmat.2018.10.234

Raki, L., Beaudoin, J., Alizadeh, R., Makar, J., and Sato, T. (2010). Cement and concrete nanoscience and nanotechnology. *Materials* 3, 918–942. doi:10.3390/ma3020918

Yang, Y. L., Yuan, X. Y., Shen, X., and Yin, L. (2017). Research on the corrosion resistance of graphene oxide on cement mortar. *J. Funct. Mater* 48, 5144–5148. doi:10.3969/j.issn.1001-9731.2017.05.026

Zhang, C., Chen, W., Mu, S., Šavija, B., and Liu, Q. (2021). Numerical investigation of external sulfate attack and its effect on chloride binding and diffusion in concrete. *Constr. Build. Mater* 285, 122806. doi:10.1016/j.conbuildmat.2021.122806

Zhang, M., and Li, H. (2011). Pore structure and chloride permeability of concrete containing nano-particles for pavement. *Constr. Build. Mater* 25, 608–616. doi:10.1016/j.conbuildmat.2010.07.032

Zhang, Z. Y., Jin, X., Lin, S., and Bi, J. (2019). Direct shear behavior of sulfate-exposed shotcrete: experimental and modelling research. *Constr. Build. Mater* 210, 607–619. doi:10.1016/j.conbuildmat.2019.03.229

Zhang, Z. Y., Zhou, J. T., Yang, J., Zou, Y., and Wang, Z. (2020b). Cracking characteristics and pore development in concrete due to physical attack. *Mater Struct.* 53, 104–113. doi:10.1617/s11527-020-01541-5

Zhang, Z. Y., Zhou, J. T., Zou, Y., Yang, J., and Bi, J. (2020a). Change on shear strength of concrete fully immersed in sulfate solutions. *Constr. Build. Mater* 235, 117463. doi:10.1016/j.conbuildmat.2019.117463

Zhang, Z. Y., Zou, Y., Yang, J., and Zhou, J. T. (2022). Capillary rise height of sulfate in Portland-limestone cement concrete under physical attack: experimental and modelling investigation. *Cem. Concr. Comp.* 125, 104299. doi:10.1016/j.cemconcomp.2021.104299

Zhao, L., Guo, X., Song, L., Song, Y., Dai, G., and Liu, J. (2020). An intensive review on the role of graphene oxide in cement-based materials. *Constr. Build. Mater* 241, 117939. doi:10.1016/j.conbuildmat.2019.117939

Zhu, J., Jia, B., Di, Y., Liu, B., Wan, X., Wang, W., et al. (2022). Effects of graphene content on the microstructure and mechanical properties of alumina-based composites. *Front. Mater* 9, 965674. doi:10.3389/fmats.2022.965674

frontiers | Frontiers in Materials

TYPE Original Research
PUBLISHED 04 January 2024
DOI 10.3389/fmats.2023.1323274

OPEN ACCESS

EDITED BY
Zhongya Zhang,
Chongqing Jiaotong University, China

REVIEWED BY
Tao Yan,
Southwest Jiaotong University, China
Luo Gang,
Chang'an University, China

*CORRESPONDENCE
Xiaohan Zhou,
cqzhouxhan@126.com
Ninghui Liang,
lnh83249@cqu.edu.cn

RECEIVED 17 October 2023
ACCEPTED 11 December 2023
PUBLISHED 04 January 2024

CITATION
Liu X, Zhuang Y, Zhou X, Liang N, Mao J and Chen H (2024), Study of the damage characteristics and corrosion mechanism of tunnel lining in a sulfate environment.
Front. Mater. 10:1323274.
doi: 10.3389/fmats.2023.1323274

Study of the damage characteristics and corrosion mechanism of tunnel lining in a sulfate environment

Xinrong Liu, Yang Zhuang, Xiaohan Zhou*, Ninghui Liang*, Jinwang Mao and Hai Chen

School of Civil Engineering, Chongqing University, Chongqing, China

Sulfate corrosion is one of the main causes of tunnel lining deterioration. An accurate understanding of the damage characteristics and corrosion mechanism of sulfate-corroded tunnels is the basis for the anti-corrosion design and damage control of the tunnel lining. Based on a project concerning a sulfate-corroded tunnel in the mountainous area of Southwest China, this study conducted a field investigation and laboratory tests and, combined with existing research data, summarized the damage characteristics and corrosion mechanism of this type of tunnel and proposed the characteristic corrosion state of tunnel lining in a sulfate environment. The results show that 1) sulfate corrosion led to leakage, surface spalling crystallization, and strength loss, and the corrosion typically occurred at the arch waist and arch foot. 2) Physical and chemical corrosion occurred in the tunnel lining, and the corrosion products included sodium sulfate, calcium carbonate, gypsum, ettringite, and thaumasite. 3) In China, this type of tunnel is mainly located in the Southwest and Northwest, and its lining is in a special state of "one-sided accelerated corrosion."

KEYWORDS

sulfate corrosion, lining corrosion, water leakage, strength degradation, one-sided accelerated corrosion

1 Introduction

Concrete corrosion will result in the loss of the bearing capacity of a structure. The lining of a tunnel is an important part of the underground structure. Most of the lining is made from reinforced concrete; therefore, it also faces the problem of concrete corrosion. Up until now, tunnel construction in many countries has passed the period of rapid development and begun to transition to a period of maintenance (Zhang et al., 2019). Thus, lining corrosion problems are a growing concern for scholars all over the world. Among various corrosion factors, sulfate is one of the most important causes of tunnel lining corrosion (Zhuang et al., 2022; Zhang et al., 2023).

At present, there are many reports of tunnels corroded by sulfate. For example, Long et al. (2011) investigated the Fala Tunnel and found that a large number of white crystals were distributed on the lining surface, accompanied by surface spalling and even paste substances. Qi et al. (2005) introduced the phenomenon of salt crystallization and cracking on the lining surface of the Jinjiguan Tunnel. Liu et al. (2023) conducted a damage survey on a highway tunnel in Chongqing that was severely corroded by sulfate and found that the strength of the corroded lining was lower than the designed value. However, the relevant reports were

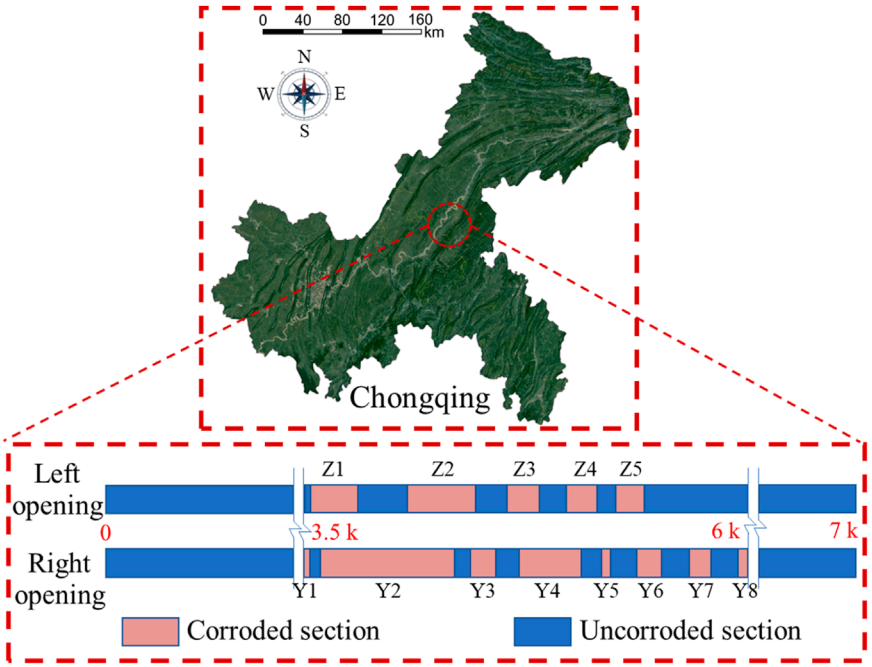

FIGURE 1
Schematic diagram of the location of the damaged tunnel.

mainly focused on a simple description of the service environment of a tunnel and its damage phenomenon, but there is a lack of systematic and comprehensive analysis and summary of the corrosion environment and typical damage characteristics of this type of sulfate-corroded tunnel.

The full-immersion corrosion test is widely used to study the mechanism of sulfate attack on tunnel lining. Results have shown that sulfate chemically reacts with the cement hydration products of concrete, such as calcium hydroxide, calcium silicate hydrate, and calcium aluminate hydrate, and generates insoluble and expansive corrosion products, such as ettringite and gypsum (Hobbs and Taylor, 2000; Crammond, 2002; Lee et al., 2008). These corrosion products will continuously accumulate in the pores of the concrete and generate crystallization pressure on the pore wall. When the expansion stress is greater than the tensile strength of the concrete, serious material cracking and mortar spalling will occur, resulting in a reduction in the concrete bearing capacity (Chen et al., 2008; Ma et al., 2012). However, the actual corrosion condition of the tunnel lining cannot be reproduced in a laboratory environment, and full immersion is not the real corrosion condition of the tunnel lining; therefore, the experimental results cannot capture the real phenomena of tunnel lining corrosion.

Therefore, based on the field investigation and testing of a tunnel severely corroded by sulfate in the mountainous area of Southwest China, this study summarizes the typical damage characteristics of this type of tunnel. Furthermore, a combination with existing tunnel reports corroded by sulfate and the typical working environment of "one-sided accelerated corrosion" of tunnel lining in a sulfate environment was revealed. Finally, the corrosion mechanism was discussed. This study could provide a reference for the corrosion protection design of tunnel lining in a sulfate environment.

2 Damage characteristics of tunnel lining

2.1 Tunnel profile

The project tunnel is an extended tunnel in the mountainous area of Southwest China, with the length of both the left and right openings exceeding 7 km. The distance between the left and right openings of the entrance is approximately 18–10 m, and the distance between the left and right openings of the central section is 30 m. The maximum depth of the tunnel is approximately 650 m. The corrosive ions in the tunnel groundwater are mainly sulfate ions, and the highest concentration reaches 2,775.56 mg/L. The average annual temperature at the location of the tunnel is 16°C–18°C, and the average temperature in the coldest month is 4°C–8°C.

A previous investigation showed that there were a lot of circumferential oblique longitudinal cracks and some network cracks in the secondary lining of the tunnel, and some areas with dense cracks were also the corrosion areas of the lining. Additionally, the rest of the sections were found to be corroded to different degrees in the follow-up investigation. Five years after the grouting treatment of the cracks of a larger width, it was observed that the number of cracks increased again, and the area of corrosion in the secondary lining increased. The corroded sections of the tunnel lining were mainly concentrated in the middle and back sections of the tunnel.

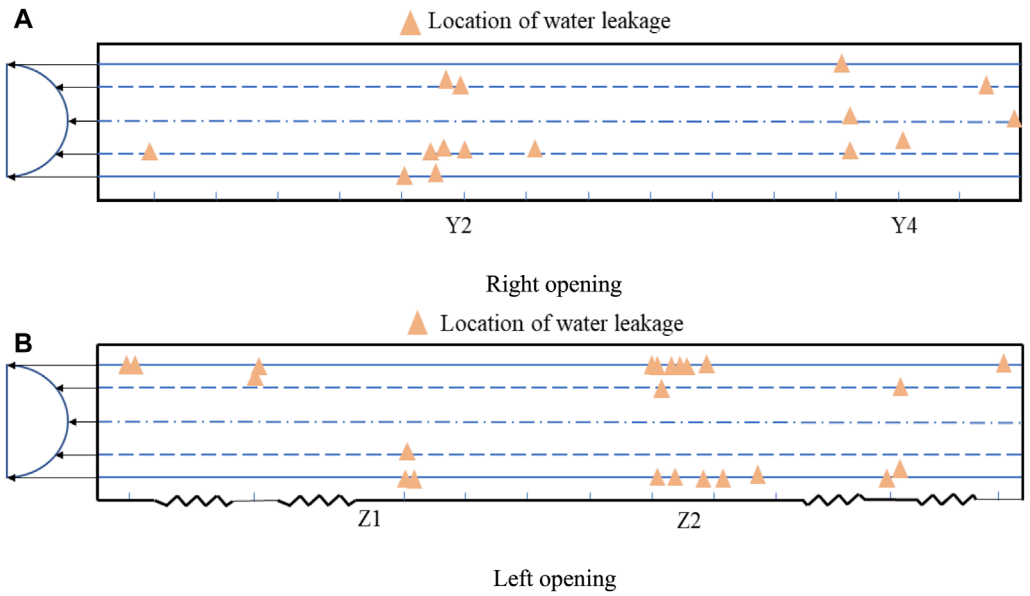

FIGURE 2
Leakage locations in the right opening **(A)** and left opening **(B)**.

As shown in Figure 1, there were five main corrosion sections on the left opening and eight on the right opening.

2.2 Leakage analysis

Water leakage is a common problem in mountain tunnels, with corrosive ions corroding the lining structure. Therefore, first of all, the leakage situation of the left and right openings of the tunnel was comprehensively investigated, the position of the lining leakage section was determined, and the leakage status was observed and recorded. At the same time, a typical leakage section was selected for water quality sampling to detect the concentration of corrosive ions in the water.

As shown in Figure 2, there were 15 leakage points on the right opening and 23 leakage points on the left opening of the tunnel. The leakage mainly occurred at the arch foot of the tunnel, as shown in Figure 3A, then at the arch waist, and occasionally occurred at the vault. Additionally, the leakage was not isolated but usually occurred with cracks and corrosion in the lining, as shown in Figure 3B. Furthermore, no freezing phenomena were observed during the coldest months.

A certain amount of water leakage was collected and analyzed in the left and right openings where the leakage was serious and could be easily sampled. The results showed that the leakage water mainly contained sulfate ions; the concentration of sulfate ions in most of the leakage water was greater than 200 mg/L and the highest was 1,410 mg/L. According to the Code for Durability Design of Concrete Structures in Highway Engineering (JTG T3310-2019), the environmental levels of water in the chemical corrosion environment were divided, and the results are shown in Figure 4. Most of the leakage points in this tunnel were moderately corroded, but in certain places, the degree of corrosion even reached a serious level.

2.3 Lining corrosion

Based on the investigation of the corrosion section of the tunnel, it was found that the corrosion areas were mainly concentrated at the arch foot and waist of the Z1 and Z2 sections of the left opening. This may be because the drainage system of these sections of the tunnel was blocked and corrosive groundwater accumulated in the site, converting the site to a long-term contact site, resulting in lining corrosion.

The corrosion phenomenon is shown in Figure 5. The lining surface, which had a certain strength, was dry and peeled off in large areas, as shown in Figure 5A. Soft white crystals that could be easily removed were present on some parts of the corroded lining surfaces, as shown in Figure 5B. Additionally, the corrosion was deeper in the area of the cracks as shown in Figure 5C. Travertine that was hard and difficult to remove was present in some parts of the cracks, as shown in Figure 5D. Some areas of the arch foot lining were immersed in leakage water, appearing muddy and completely losing their strength, and could be easily observed, as shown in Figure 5E. Cracks and lining corrosion reappeared in some grouting repair sites, as shown in Figure 5F.

3 Testing and results

Owing to the construction period and other factors, we only tested the lining corrosion of the left opening in detail. The strength of the corroded lining was measured using the rebound

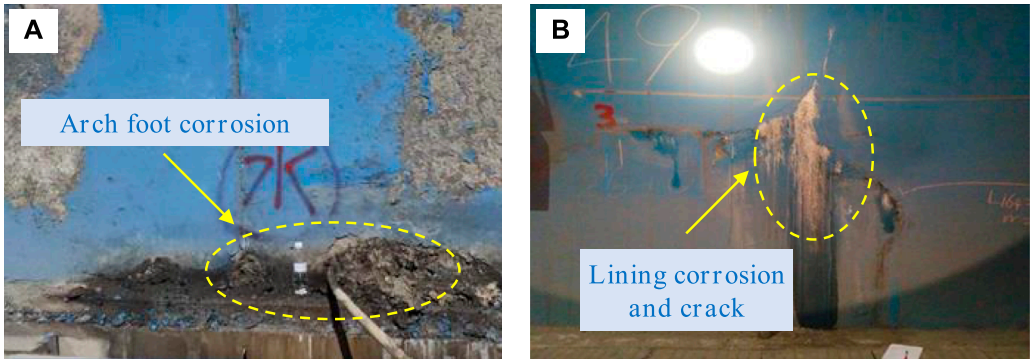

FIGURE 3
Typical tunnel leakage phenomena at the arch foot **(A)** and lining cracks **(B)**.

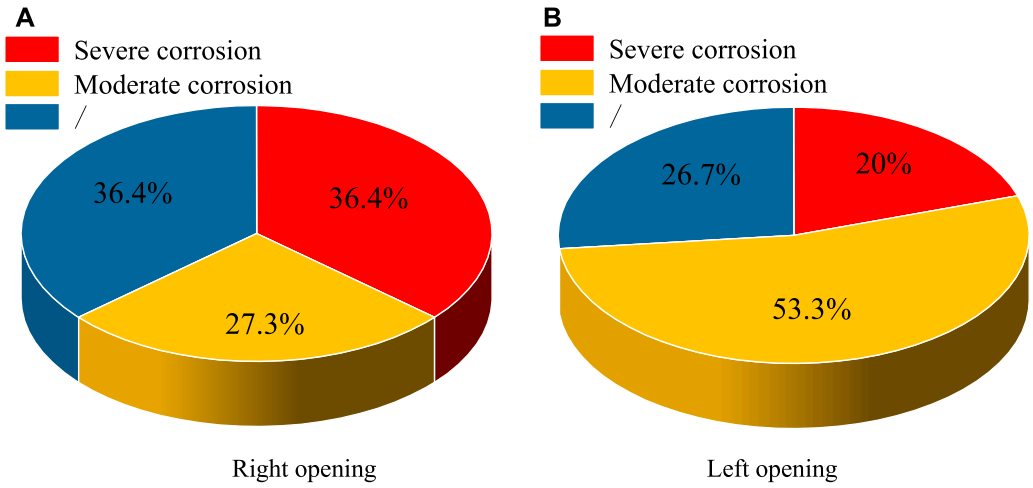

FIGURE 4
Corrosion degree of water leakage in the right opening **(A)** and left opening **(B)**.

method on the areas with a smooth surface and easy to test, and drill holes were used for strength testing in the areas where corrosion was too severe for testing with the rebound method. At the same time, the corrosion products of the tunnel lining were analyzed microscopically to obtain the corrosion mechanism of the tunnel lining.

3.1 Rebound strength test

To facilitate the operation process, 40 test samples in the Z1 section and 63 test samples in the Z2 section were tested to determine the rebound strength. The test methods referred to the Technical Specifications for Testing Concrete Compressive Strength by Rebound Method (JGJ/T23-2011). The whole process is shown in Figure 6, and the test results are shown in Figure 7, with the yellow line indicating design strength of the lining. Only 12.6% of the measured samples from the two sections reached or exceeded the design value in terms of strength. The maximum value was 29.4 MPa; this may be due to the initial stage of sulfate corrosion and carbonation, which made the reaction products fill the pores of the concrete, thereby reducing the porosity, and increasing the density and strength. The lowest strength was only 10.9 MPa, which was lower than the design value.

3.2 Core strength test

In the zones of Z1 and Z2 where the lining was seriously corroded or the surface could not be easily measured using the rebound method, a core drilling machine was used to test the strength of core, as shown in Figure 8; 60 test samples in Z1 and 88 in Z2 were tested. The test results after removing the data with a large degree of discretization are shown in

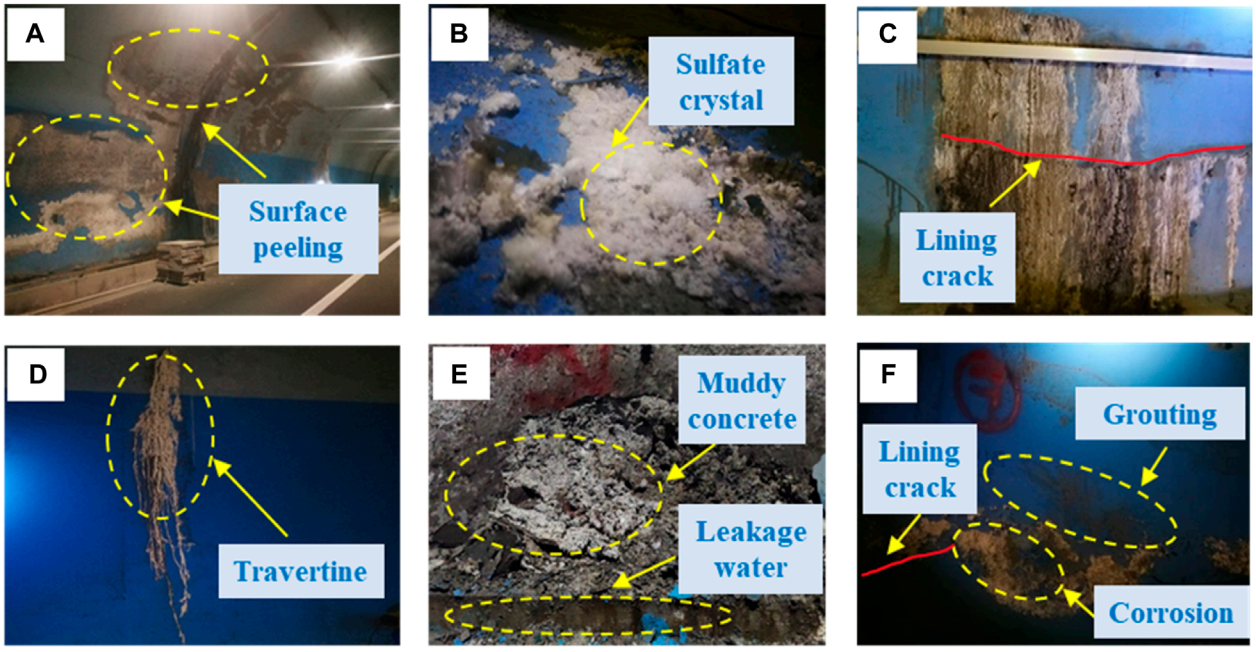

FIGURE 5
Corrosion of the tunnel lining: **(A)** surface peeling; **(B)** sulfate crystal; **(C)** lining crack corrosion; **(D)** travertine; **(E)** muddy concrete; **(F)** grouting repair site corrosion.

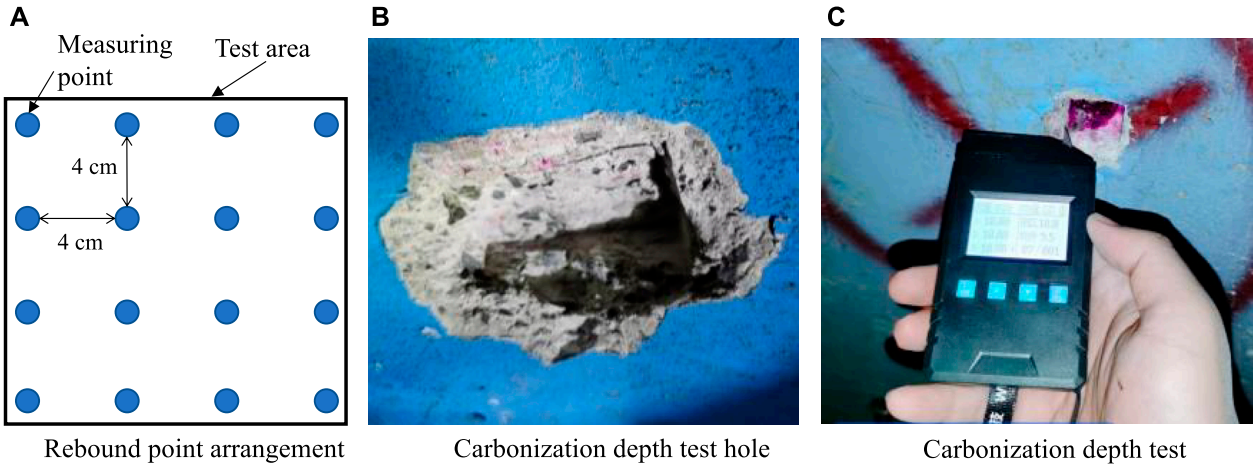

FIGURE 6
Measurement of the tunnel lining strength using the rebound method: **(A)** rebound point arrangement; **(B)** carbonization depth test hole; **(C)** carbonization depth test.

Figure 9, with the yellow line indicating the design strength of the lining.

The average strength of Z1 was 25.12 MPa, 50% of which met or exceed the design standard, and the maximum strength was 31.2 MPa. The reason for this phenomenon may be that part of the core sample came from the lining surface, which had not been corroded, and due to carbonization, the compressive strength increased. However, the lowest strength was only 14.9 MPa, which only reached 59.6% of the designed strength, indicating that the deterioration of the lining was not uniform, and this would lead to stress concentration.

The average strength of Z2 was 22.1 MPa, and only 21.6% reached the design strength, with a maximum value of 30.5 MPa and a minimum value of 13.0 MPa. This indicated that the lining corrosion of Z2 was more serious than that of Z1. After the lining was corroded, the lining material deteriorated seriously, and the lowest strength was only 52% of the designed strength. The safety factor of the structure was greatly reduced, and there were hidden risks that compromised operation safety.

The average value of the core strength of the two corrosion sections was larger than the average value of the strength measured by the rebound method. The reason for this phenomenon was not

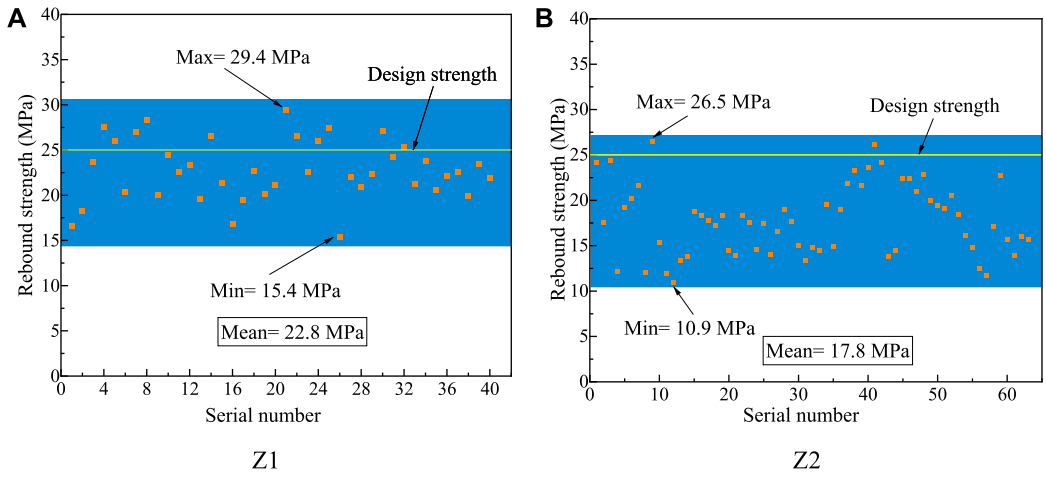

FIGURE 7
Rebound strength of the corroded lining at Z1 **(A)** and Z2 **(B)**.

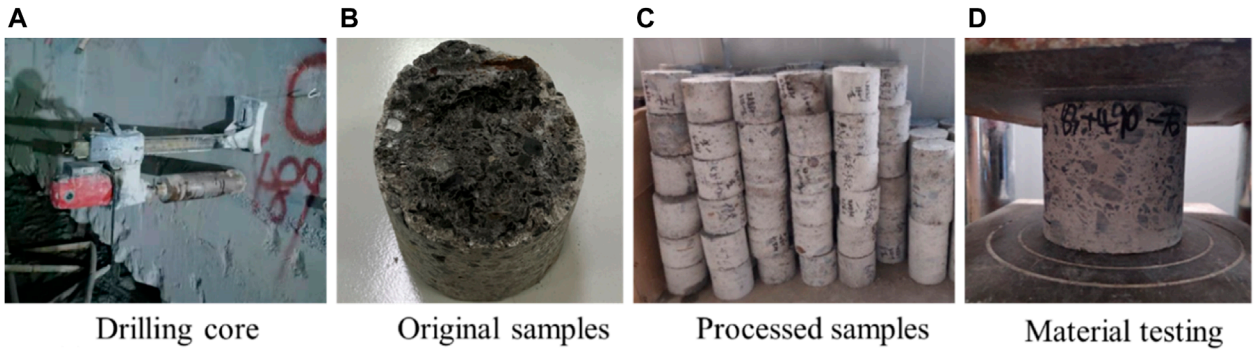

FIGURE 8
Drill core test of the corroded lining: **(A)** drilling core; **(B)** original samples; **(C)** processed samples; **(D)** material testing.

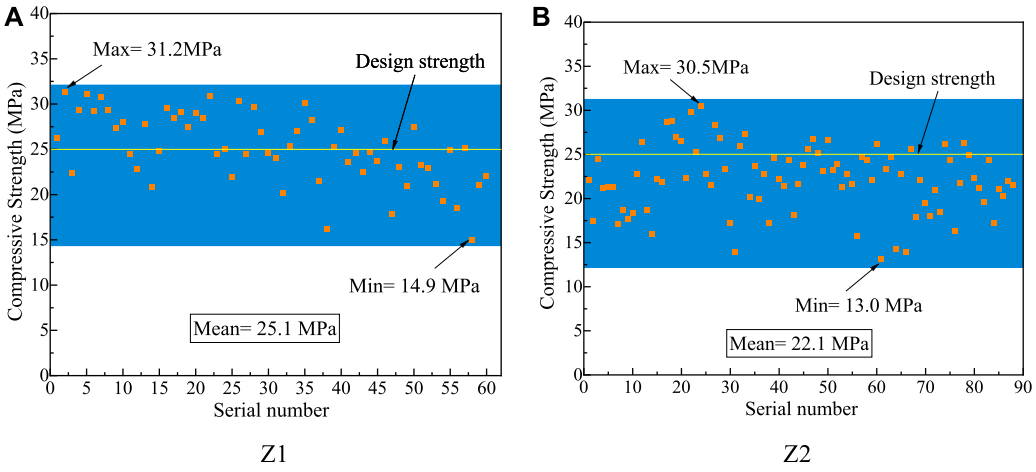

FIGURE 9
Core strength of the corroded lining at Z1 **(A)** and Z2 **(B)**.

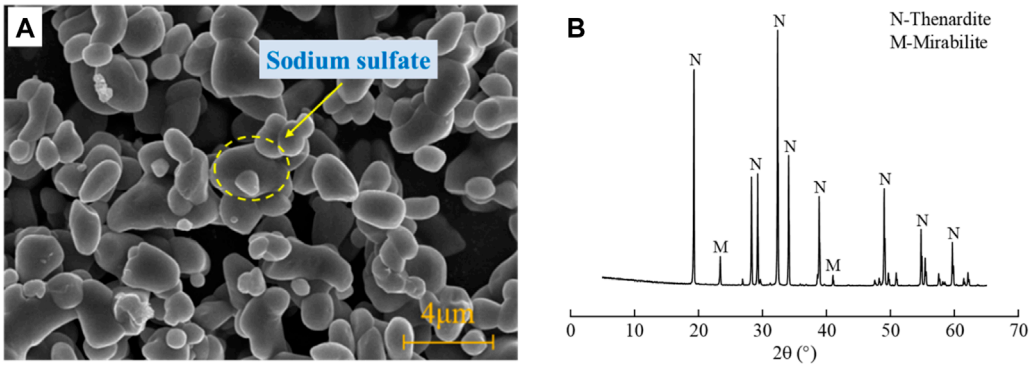

FIGURE 10
Microstructure **(A)** and XRD pattern **(B)** of the soft white crystals.

only related to the measurement error and the fact that part of the core sample analyzed above was from the carbonized surface, but also because some of the core samples were from the corrosion crack, which had been repaired by grouting, and thus the strength of the secondary lining concrete there was improved. However, in general, different degrees of material deterioration occurred in the secondary lining of the two corroded sections, which affected the safety of the structure.

3.3 Analysis of the corrosion products

To further explore the corrosion mechanism of the tunnel lining, samples were taken from the soft white crystallites on the surface (Figure 5B), hard travertine products at the cracks (Figure 5D), corroded lining concrete with strength (Figure 5A), and muddy corroded lining without strength at the arch foot (Figure 5E). Scanning electron microscopy (SEM), energy-dispersive X-ray spectroscopy (EDS), Fourier transform infrared spectrometry (FTIR), and powder X-ray powder diffraction (XRD) were used to investigate the micromorphology and chemical products of the tunnel lining after sulfate corrosion.

3.3.1 White crystals on the surface

Figure 10 shows the results of SEM and XRD analysis of the white crystals. It can be observed that the white crystals were mainly sodium sulfate crystals, and their microscopic morphology is shown in Figure 10A, with a diameter of 0.2–2 μm. According to the XRD pattern (Figure 10B), the white crystals were mainly a mixture of thenardite (Na2SO4) and mirabilite (Na2SO4·10H2O), and the thenardite content was higher.

3.3.2 Travertine

The SEM, EDS, and XRD images of travertine are shown in Figure 11. SEM images showed that the crystal shape was scaly in shape. EDS analysis showed that the main components of travertine were Ca, Si, O, and C, with a small amount of Mg, Al, and Na. The XRD results showed that the main phase of travertine was calcium carbonate, with a small amount of gypsum and quartz, which was consistent with the EDS results.

3.3.3 Corroded lining concrete

The results of SEM, EDS, and XRD of corroded lining concrete of strength are shown in Figure 12. As can be observed in Figures 12A, B, needle-rod and massive crystals were produced in the lining concrete corroded by sulfate. EDS analysis revealed that the elements Ca, Al, S, O, C, and Si were present in the needle-rod crystals, while the elements Ca, S, O, and Na were present in the massive crystals. XRD revealed that the needle-rod crystals were ettringite, whereas the massive crystals were gypsum. After sulfate had corroded the concrete, common corrosion products such as ettringite and gypsum were produced, demonstrating that conventional chemical corrosion occurred in the tunnel lining.

The shape of the muddy corroded lining without strength at the arch foot was completely different from that of ordinary sulfate-corroded concrete. Thus, it can be initially assumed that the corrosion products were not conventional ettringite or gypsum. Figure 13A shows the SEM and EDS images of the muddy corroded lining, and Figure 13B shows the XRD images. The XRD patterns show that thaumasite, ettringite, calcite, gypsum, and a small amount of quartz were present in the samples. As the characteristic peaks of thaumasite (0.956 nm, 0.551 nm, 0.467 nm, 0.387 nm, etc.) were basically consistent with those of ettringite (0.972 nm, 0.561 nm, 0.486 nm, 0.387 nm, etc.) (Barnett et al., 2002), the diffraction peaks of the two have high overlap in the XRD pattern; therefore, it is difficult to distinguish them with XRD (Ma et al., 2012). The SEM image shows that there were many needle-rod crystals with a diameter of 0.5 μm and a length of 3–4 μm in the muddy products, but it was still impossible to identify thaumasite or ettringite. The EDS image showed the presence of O, S, Si, and Ca but not Al, indicating that there was almost no ettringite. Therefore, it can be initially determined that the corrosion product appeared to be thaumasite. However, amorphous phases associated with thaumasite and ettringite crystals can lead to erroneous EDS analysis results (Barnett et al., 2002).

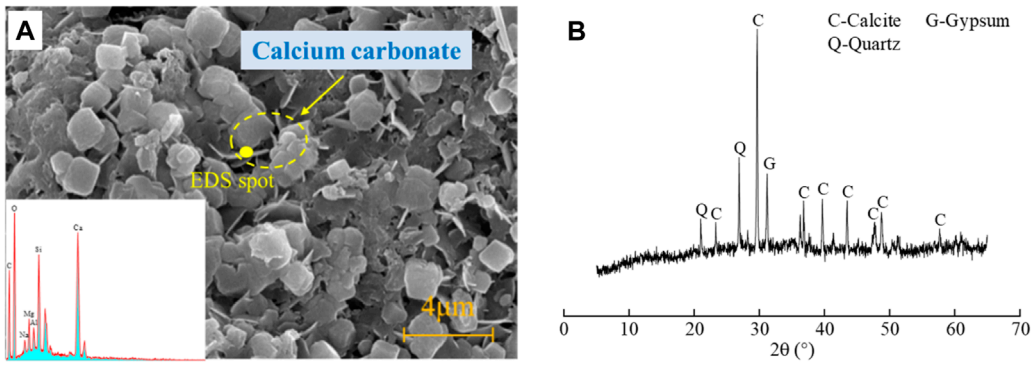

FIGURE 11
Microstructure, EDS analysis **(A)**, and XRD pattern **(B)** of travertine.

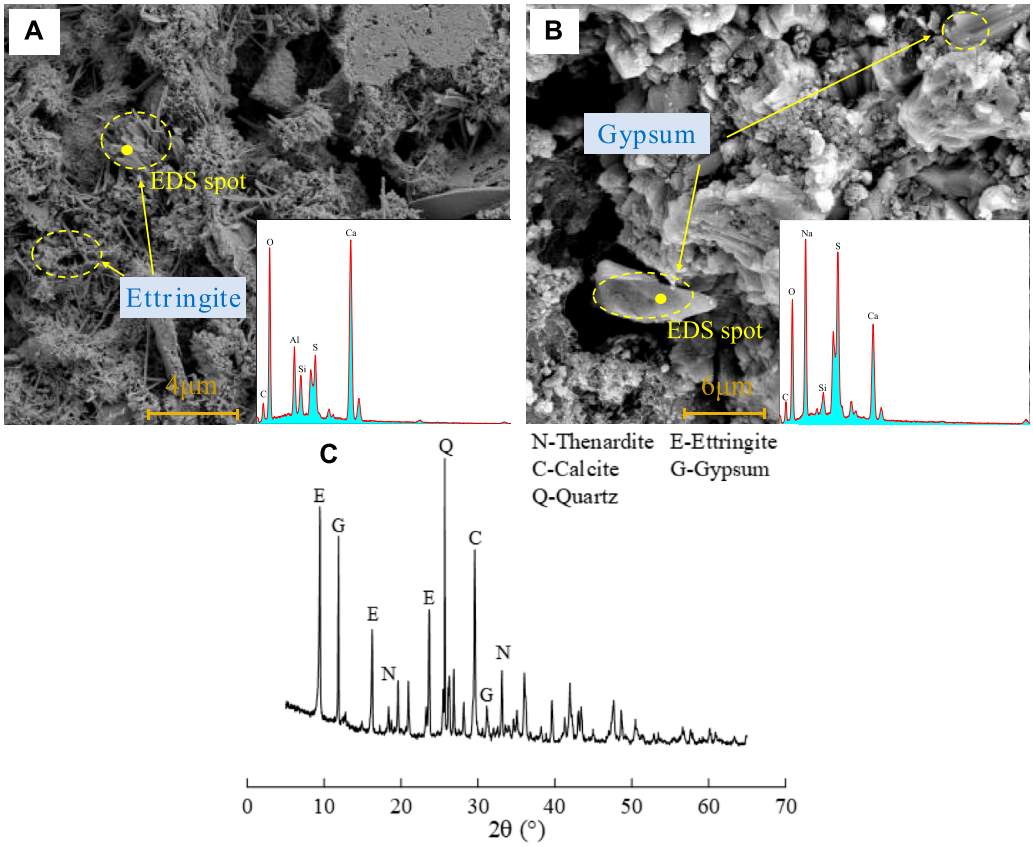

FIGURE 12
Microstructure, EDS analysis **(A,B)**, and XRD pattern **(C)** of the corroded lining concrete of strength.

To further determine the muddy corrosion products, the residual powder samples were analyzed by FTIR. The FTIR spectra are shown in Figure 13C, and the wavenumber of important infrared absorption bands refers to the available data (Ma et al., 2019). The results showed that there was a C-O stretching vibration at approximately 1,400 cm^{-1}, indicating the presence of CO32-. In addition, there was a S-O stretching vibration at approximately 1,100 cm^{-1}, indicating the presence of SO42-. Moreover, a peak was detected at 497 cm^{-1}; this peak was related to the existence of an SiO6 bond. Octahedral silicon is a rare coordination state for mineral silicates. Therefore, the existence of this peak indicated the presence of thaumasite or solid solution containing thaumasite. Second, no peak was found at approximately 850 cm^{-1}, indicating the absence of AlO6. The results of FTIR showed that the composition of the muddy lining concrete was mainly

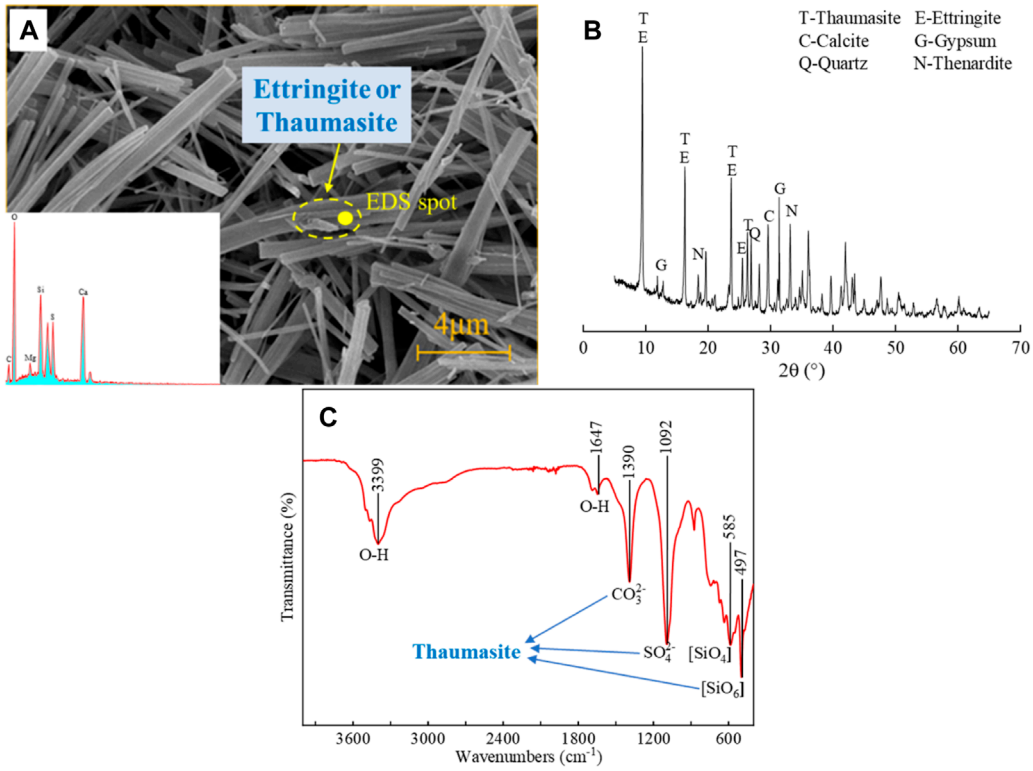

FIGURE 13
Microstructure, EDS analysis **(A)**, XRD pattern **(B)**, and FITR analysis **(C)** of muddy corroded lining without strength.

thaumasite. Therefore, a relatively rare sulfate corrosion occurred in the tunnel.

4 Discussion

4.1 The typical corrosion environment of tunnel lining

In the last century, there were relevant reports on sulfate-corroded tunnels. The main corrosion causes of some sulfate-corroded tunnels are shown in Table 1. Based on the above research results and Table 1, it can be found that the current reports on tunnel damage in a sulfate environment were mainly concentrated in China. Figure 14 shows the regional statistics of the sulfate-corroded tunnels in China featured in Table 1. It can be observed that sulfate-corroded tunnels were mainly distributed in Southwest China and Northwest China. This was because, in Southwest China, the geological conditions are complex, the topography is large, and the salt-bearing strata are widely distributed. Some mountain tunnels are located in areas with a lot of groundwater and gypsum rock. Under the influence of groundwater, corrosive minerals such as gypsum rock will dissolve and produce sulfate, which makes the water environment of tunnel lining contain a large number of sulfate ions, resulting in lining corrosion. At the same time, Southwest China is a tropical monsoon climate area, with a temporal and spatial precipitation distribution that is not uniform, which exposes the lining to dry and wet cycles over a long period, and this will contribute to increasing the sulfate concentration in the environment of the lining, accelerating sulfate corrosion. Moreover, there are many salt lakes and saline soils in Northwest China, and these areas are full of corrosive ions such as sulfate and chloride ions, which will cause compatible corrosion. At the same time, the low winter temperature in this region subjects the lining structure to a freeze-thaw cycle, which damages the concrete lining and accelerates sulfate corrosion.

At the same time, Table 1 shows that the groundwater in the sulfate-corroded tunnel is generally rich, and the sulfate content in the groundwater is high. The main source of sulfate may be sulfur-containing minerals (such as gypsum and mirabilite) and organic matter (such as petroleum and coal) in the surrounding rock, which will be dissolved in the groundwater or even react with the groundwater, or it may be an external pollution resource. In some tunnel linings, the concrete mix contains sulfates, causing the lining to corrode from the inside. In addition, some coupling effects (such as the wet-dry cycle, freeze-thaw cycle, and high geothermal temperature) also accelerate the corrosion of tunnel lining by sulfate.

At present, most scholars have adopted the full-immersion corrosion mode for sulfate erosion of concrete (Liang et al., 2022; Lu et al., 2022; Zhang et al., 2022), and the corrosion mechanism in this corrosion mode has been relatively clear: chemical corrosion

TABLE 1 Sulfate-corroded tunnels and the main cause of their corrosion.

Tunnels	The main cause of corrosion
Luodai Tunnel	The leachate of landfill near the upstream of the tunnel contains sulfate ions (Zhang, 2019)
Fenjieliang Tunnel and Tanjiazhai Tunnel	The corroded section of the tunnel is located in the Badong Formation of the Triassic system, in which gypsum mineral is rich. Groundwater is developed in the section with severe local erosion, and the sulfate content was high in a water quality test (Peng, 2018)
Zagros Tunnel	The tunnel passes through organic-containing strata (oil and coal) with abundant H_2S and water (Salmi et al., 2019)
Fala Tunnel	The groundwater is rich in sulfate, and pulverized coal adheres to the lining surface when trains carrying coal pass through (Long et al., 2011)
Liupanshan Tunnel	The contents of sulfate, chloride ion, and bicarbonate in the tunnel leakage are high (Jiang et al., 2007), and the water quality at the same point is deteriorating constantly. The freeze-thaw cycle accelerates the lining damage (Zhang and Huang, 2012)
Shiziya Tunnel	Gypsum dolomite aggregate causes sulfate erosion in the concrete (Xing et al., 2014). Acid sulfate is produced after karst erosion of anhydrite in the strata where the tunnel is located (Liu et al., 2011)
Jinjiguan Tunnel	Gypsum dissolves in water to produce sulfate in the formation (Qi et al., 2005)
Gaoligong Mountain Tunnel	Highland heat and sulfate coupling (He, 2016)
Pandaoling Tunnel	The groundwater contains higher sulfate, and the freeze-thaw cycle accelerates the corrosion (Yin, 2016)
Ninadu Tunnel	The area where the tunnel is located has a large number of coal seams and abundant surface water and groundwater containing high levels of sulfate (Liu and Sun, 2009)
Jiaozi Mountain Tunnel	Rock salts such as gypsum, Glauber, and chloride are developed in the rock strata surrounding the tunnel. In the water environment, sulfate and chloride ions are ionized by rock salts (Liu, 2018)
Baijialing Tunnel	The stratum where the tunnel is located is rich in gypsum, and the dry-wet cycle accelerates the corrosion (Han, 1999)
Koblenz Tunnel	Sulfate in surrounding rock and groundwater (Romer, 2003)
Jiaozhou Bay Subsea Tunnel	The seawater in the area where the tunnel is located has high levels of sulfate, chloride, and magnesium ions, and the lining is in an alternating wet and dry environment, which accelerates the corrosion (Liu, 2008)
Podixia Tunnel	Sulfate ion concentration in the groundwater exceeds the corrosion resistance index of sulfate-resistant cement (Cai, 1986)
Qinling Tunnel	Abnormal groundwater, in which the levels of sulfate ions, salinity, and calcium ions increased significantly (Wang et al., 2002)
Dajiangkou Tunnel and XinXuefeng Mountain Tunnel	Sulfate content in the leakage water is at a level that is moderately corrosive, and the construction quality is problematic (Sun et al., 2004)

mainly occurs, and its corrosion products are gypsum and ettringite, which is the conventional sulfate corrosion. However, some scholars have found that the corrosion mechanism of concrete will change when concrete is in semi-immersion mode (Zhang et al., 2020a; Zhang et al., 2022).

Therefore, combined with the field investigation results, it can be concluded that compared with conventional sulfate corrosion, tunnel lining is in a special state of "one-sided accelerated corrosion" as shown in Figure 15: the inner side of the tunnel lining is in contact with groundwater containing sulfate, resulting in unilateral corrosion under a wet-dry cycle. Furthermore, the outside part of the lining is in contact with the air, which leads to water evaporation on the lining surface; this will accelerate the transfer of sulfate from the inside to the outside and consequently subject the tunnel lining to both physical and chemical sulfate corrosion, and the whole process will be accompanied by carbonization.

4.2 The mechanisms of one-sided accelerated corrosion on tunnel lining

4.2.1 Physical corrosion

With the appearance of sodium sulfate crystals on the surface of the lining, it can be inferred that the tunnel lining had been subjected to physical corrosion. The reason for this phenomenon was because the tunnel lining was in a "one-sided accelerated corrosion" state: the inside part was in contact with corrosive groundwater, while the outside part was in contact with air. In this case, the inner side of the area in contact with the groundwater permitted the sulfate to enter the lining, while the outer side, which was in contact with the air, constituted an evaporation area. The sulfate solution migrated from the inside to the outside due to capillary suction and diffusion, while the outside part was supersaturated due to water evaporation, and the sulfate solution precipitated out. When the sulfate precipitated out, the resulting

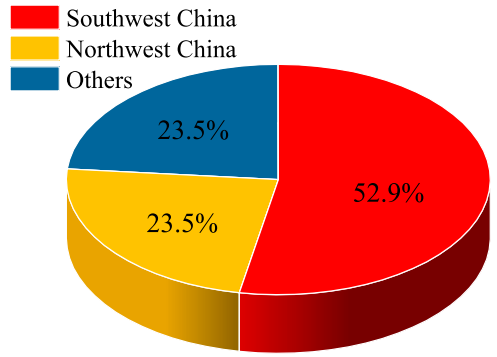

FIGURE 14
Distribution of some sulfate-corroded tunnels in China.

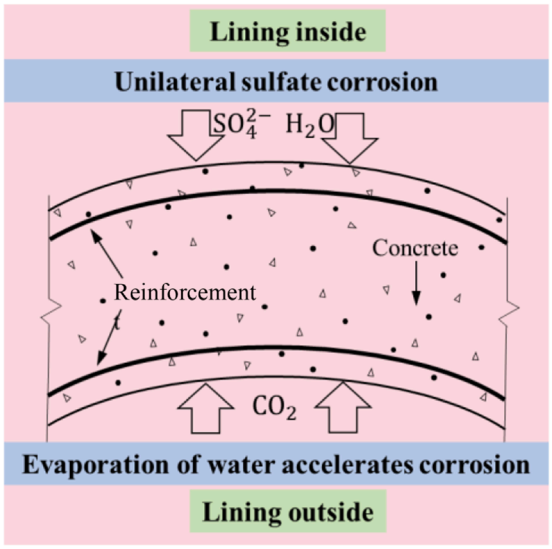

FIGURE 15
One-sided accelerated corrosion of tunnel lining.

concentration difference pushed the inner sulfate solution to migrate outward. When the pressure of sulfate crystallization exceeds the tensile strength of the concrete, it will damage the concrete. This type of corrosion is called physical corrosion. On the other hand, the tunnel is located in an area of seasonal precipitation, which means that in the rainy season, the groundwater containing sulfate would come into contact with the lining inside. In the dry season, the lining was relatively dry. Thus, the tunnel lining was also in a wet-dry cycle, and this would accelerate the physical corrosion.

4.2.2 Chemical corrosion

4.2.2.1 Soluble chemical corrosion

The generation of travertine indicated that the tunnel lining had undergone soluble chemical corrosion, and this was due to the following reasons: first, under the influence of underground water, the $Ca(OH)_2$ in the cement constantly dissolved from inside to outside, and the outside of the tunnel was in contact with the air, where CO_2 reacted with $Ca(OH)_2$ to form $CaCO_3$, which was almost insoluble in water (Liu et al., 2015). Then CO2 reacted with $CaCO_3$ in the surface layer and dissolved it to form Ca2+ and HCO_3^-. When Ca^{2+} and HCO_3^- were carried by leakage water from cracks to the lining surface, travertine was formed again due to a sudden drop in pressure (Li and Zhou, 1996). When the crystallization pressure was greater than the tensile strength of the concrete, the lining surface would crack or flake off.

4.2.2.2 Ettringite- and gypsum-type chemical corrosion

The presence of ettringite and gypsum, which were found in the lining concrete, proved that the tunnel lining had been subjected to ettringite- and gypsum-type chemical corrosion, which are the most common corrosion mechanisms in sulfate-corroded concrete.

4.2.2.3 Thaumasite-type chemical corrosion

The muddy concrete was thaumasite, which proved that rare thaumasite-type chemical corrosion occurred in the tunnel. Currently, it is generally believed that the five conditions of carbonite, silicate, carbonate, sufficient water, and low temperature need to be met for thaumasite sulfate corrosion to occur (Crammond, 2003). The content of sulfate ions in the groundwater was sufficient. The design data showed that Portland cement was used as the secondary lining concrete of the tunnel, and C-S-H gel, which was produced after hydration, was the main source of silicate. The aggregate in concrete was mostly limestone, and the carbonized concrete was the main source of carbonate. Water leakage provided ample water for corrosion. Although existing studies had shown that thaumasite is easily generated when the temperature is lower than 15°C, especially at 0°C–5°C, and the average annual temperature of the tunnel site was approximately 16.4°C, some scholars found that thaumasite can also be generated when the temperature is higher than 15°C (Diamond, 2003). When all of this is considered, it can be concluded that the tunnel environment created the conditions for the formation of thaumasite.

4.2.3 Damage mechanism

Different from the full-immersion test in the laboratory, physical and chemical corrosion occurred in the tunnel lining in the actual environment because of one-sided accelerated corrosion. The chemical corrosion consumed the cementing matrix of cement slurry, damaged the cementing structure of the concrete, reduced the bond between the aggregate, and then greatly reduced the concrete compactness and bearing capacity. The corrosion products generated by chemical and physical corrosion accumulated continuously in the pores of concrete and squeezed the pores, resulting in pore tip or pore wall cracking. As the corrosion continued, a large number of cracks were generated, and then new defects such as through-cracks were formed, which increased the lining damage, as shown in Figure 16.

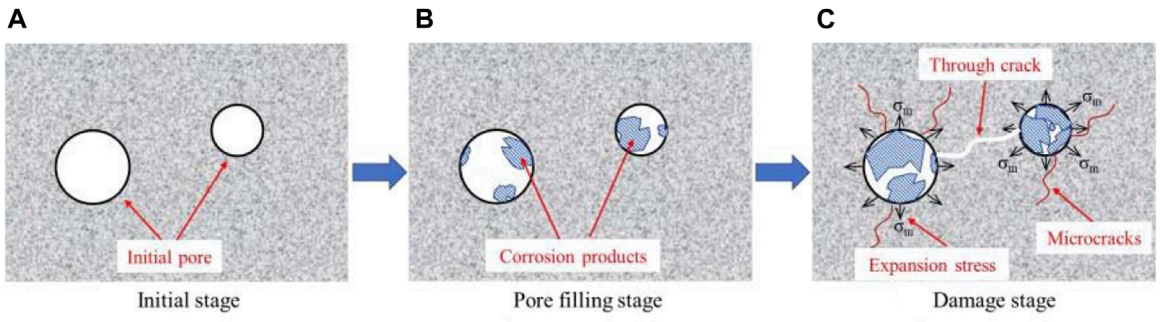

FIGURE 16
Diagram of the whole process of sulfate corrosion in concrete: **(A)** initial stage; **(B)** pore filling stage; **(C)** damage stage.

5 Conclusion

Based on a sulfate-corroded highway tunnel in Southwest China, this study analyzed the damage characteristics of tunnel lining in a sulfate environment through field investigation and laboratory tests. Moreover, this study summarized the typical working environment and corrosion mechanism of a tunnel under sulfate attack by combining the results with an analysis of existing reports related to sulfate-corroded tunnels. The main conclusions are as follows.

(1) The leakage position of the tunnel was concentrated mainly in the arch foot and arch waist and mostly in the lining cracks or corrosion area. It was found that sulfate ions were the main corrosive ions in the tunnel leakage water, which was at a moderate-to-serious corrosion level.
(2) The lining of the tunnel had been subjected to serious corrosion, which manifested as a large area of surface shedding, surface crystallization, and travertine. The concrete in some areas of the arch foot was muddy, and the corrosion degree was higher at cracks. The areas repaired with grouting had become corroded again.
(3) The strength of most of the tested areas was lower than the designed value. The strength of a small part of the tested area was higher than the design value, which may be due to the decrease in the porosity of the concrete lining and increase in strength at the early stage of carbonization or sulfate corrosion.
(4) The white crystals on the surface were mainly thenardite. The travertine was mainly calcium carbonate. Ettringite and gypsum were detected in the corroded lining concrete, and the muddy concrete in the arch foot was thaumasite.
(5) The sulfate-corroded tunnels in China are mainly distributed in the Southwest and Northwest. The common feature of the tunnels is that the soil and rock strata are rich in groundwater and contain a large number of sulfur-containing substances, such as gypsum salt and coal, which dissolve in groundwater or react with it to form sulfate ions, and this is the direct cause of lining structure corrosion.
(6) The special environment of the tunnel lining rendered it in a state of "one-sided accelerated corrosion," which causes physical and chemical corrosion and accelerates the damage to the lining concrete.

Data availability statement

The original contributions presented in the study are included in the article/Supplementary Material, further inquiries can be directed to the corresponding authors.

Author contributions

XL: Conceptualization, Investigation, Methodology, Project administration, Validation, Writing–review and editing. YZ: Data curation, Formal Analysis, Investigation, Methodology, Writing–original draft, Writing–review and editing. XZ: Data curation, Methodology, Project administration, Supervision, Writing–review and editing. NL: Data curation, Investigation, Project administration, Supervision, Validation, Writing–original draft. JM: Data curation, Investigation, Writing–original draft. HC: Investigation, Writing–original draft.

Funding

The author(s) declare financial support was received for the research, authorship, and/or publication of this article. This study is supported by the National Natural Science Foundation for Young Scientists of China (Grant No. 52104076), the Science and Technology Foundation of the Department of Transportation of Zhejiang Province, China (Grant No. 2020028).

Acknowledgments

Additionally, editors and reviewers proposed helpful and pertinent comments. The authors gratefully acknowledge this support.

Conflict of interest

The authors declare that the research was conducted in the absence of any commercial or financial relationships that could be construed as a potential conflict of interest.

Publisher's note

References

Barnett, S. J., Macphee, D. E., Lachowski, E. E., and Crammond, N. J. (2002). XRD, EDX and IR analysis of solid solutions between thaumasite and ettringite. *Cem. Concr. Res.* 32 (5), 719–730. doi:10.1016/s0008-8846(01)00750-5

Cai, X. Z. (1986). Discussion on anti-corrosion of railway tunnel invert. *Railw. Eng.* (01), 12–16.

Chen, J. K., Jiang, M. Q., and Zhu, J. (2008). Damage evolution in cement mortar due to erosion of sulphate. *Corros. Sci.* 50 (9), 2478–2483. doi:10.1016/j.corsci.2008.05.021

Crammond, N. (2002). The occurrence of thaumasite in modern construction - a review. *Cem. Concr. Comp.* 24 (3-4), 393–402. doi:10.1016/s0958-9465(01)00092-0

Crammond, N. J. (2003). The thaumasite form of sulfate attack in the UK. *Cem. Concr. Comp.* 25 (8), 809–818. doi:10.1016/s0958-9465(03)00106-9

Diamond, S. (2003). Thaumasite in Orange County, Southern California: an inquiry into the effect of low temperature. *Cem. Concr. Comp.* 25 (8), 1161–1164. doi:10.1016/s0958-9465(03)00138-0

Han, T. C. (1999). Evaluation for concrete corrosion of baijialing tunnel. *Chin. Railw.* 1999 (8), 29–31+25.

He, M. M. (2016). *The influence of heat sulfate solution to mechanics performance of concrete*. Chengdu, China: Southwest Jiaotong University.

Hobbs, D. W., and Taylor, M. G. (2000). Nature of the thaumasite sulfate attack mechanism in field concrete. *Cem. Concr. Res.* 30 (4), 529–533. doi:10.1016/s0008-8846(99)00255-0

Jiang, W. D., Chen, X., and Liu, B. (2007). Analysis and treatment of lining concrete corrosion failure in Liupanshan Tunnel. *J. Highw. Transp. Res. Dev.* 24 (10), 108–112.

Lee, S. T., Hooton, R. D., Jung, H. S., Park, D. H., and Choi, C. S. (2008). Effect of limestone filler on the deterioration of mortars and pastes exposed to sulfate solutions at ambient temperature. *Cem. Concr. Res.* 38 (1), 68–76. doi:10.1016/j.cemconres.2007.08.003

Li, D. L., and Zhou, Z. A. (1996). Possibility of corrosion failure of comcrete shaftwall due to water infiltration. *J. China Coal Soc.* 21 (2), 158–163.

Liang, N. H., Mao, J. W., Yan, R., Liu, X., and Zhou, X. (2022). Corrosion resistance of multiscale polypropylene fiber-reinforced concrete under sulfate attack. *Case Stud. Constr. Mater.* 16, e01065. doi:10.1016/j.cscm.2022.e01065

Liu, J. H., Bian, L. B., He, W., and Ji, H. G. (2015). Investigation and destruction mechanism on corrosion of concrete shaft in coal mine. *J. China Coal Soc.* 40 (03), 528–533.

Liu, W. (2008). *Research on durability of lining concrete of qingdao jiaozhou bay submarine tunnel*. Qingdao, China: Qingdao Technological University.

Liu, X. R., Zhuang, Y., Zhou, X. H., Li, C., Lin, B. B., Liang, N. H., et al. (2023). Numerical study of the mechanical process of long-distance replacement of the definitive lining in severely damaged highway tunnels. *Undergr. Space* 9, 200–217. doi:10.1016/j.undsp.2022.07.007

Liu, Y. M. (2018). Anti-corrosion construction technique research for tunnel with complex formation at halite area. *Constr. Technol.* 47 (16), 56–60+139.

Liu, Y. M., Yu, H. M., Wang, C., and Wang, C. L. (2011). Research on mechanism of damage of anhydrock in dolomite layer to tunnel structure. *Rock Soil Mech.* 32 (9), 2704–2708+2752.

Liu, Z. Q., and Sun, S. Q. (2009). "Analysis of sulfate corrosion of concrete in Ninadu Tunnel and its prevention measures," in Proceedings of the 3rd Conference of Geo-Engineering, Chengdu, Sichuan, China, October, 2009.

Long, G. C., Xie, Y. J., Deng, D. H., and Li, X. K. (2011). Deterioration of concrete in railway tunnel suffering from sulfate attack. *J. Central South Univ. Technol.* 18 (3), 881–888. doi:10.1007/s11771-011-0777-4

Lu, F., Wang, H., Wang, L., Zhao, K., and Zhang, J. (2022). Degradation law and service life prediction model of tunnel lining concrete suffered combined effects of sulfate attack and drying-wetting cycles. *Materials* 15 (13), 4435. doi:10.3390/ma15134435

Ma, B. G., Gao, X. J., Byars, E. A., and Zhou, Q. Z. (2019). Thaumasite formation in a tunnel of bapanxia dam in Western China. *Cem. Concr. Res.* 36 (4), 716–722. doi:10.1016/j.cemconres.2005.10.011

Ma, K. L., Long, G. C., and Xie, Y. J. (2012). Railway tunnel concrete lining damaged by formation of gypsum, thaumasite and sulfate crystallization products in southwest of China. *J. Cent. South Univ.* 19 (8), 2340–2347. doi:10.1007/s11771-012-1280-2

Peng, Z. L. (2018). *Study on the coupling effect of hydrological-chemical-mechanical in deep buried tunnel with gypsum salt and its prevention and control countermeasures*. Chongqing, China: Chongqing Jiaotong University.

Qi, J. H., Hou, Z. L., Jia, S. Y., and Wang, N. F. (2005). The research on the characteristics of Jinjiguan Tunnel's water penetration and deformation with defects control measures. *J. Disaster Prev. Mitig. Eng.* 25 (2), 222–226.

Romer, M. (2003). Steam locomotive soot and the formation of thaumasite in shotcrete. *Cem. Concr. Comp.* 25 (8), 1173–1176. doi:10.1016/s0958-9465(03)00155-0

Salmi, E. F., AsadiBayati, Z. S. M., and Sharifzadeh, M. (2019). Assessing the hydrogeological conditions leading to the corrosion and deterioration of pre-cast segmental concrete linings (case of zagros tunnel). *Geotechnical Geol. Eng.* 37 (5), 3961–3983. doi:10.1007/s10706-019-00886-1

Sun, Y. B., Yu, G. X., and Wang, H. (2004). The sulfate attack on the lining concrete in tunnel and it's renovation engineering. *J. Railw. Eng. Soc.* (04), 89–92+88.

Wang, J. X., Liu, D., and Yang, L. Z. (2002). Evaluation and prevention of concrete erosion caused by chemical abnormity of groundwater in Qinling tunnel. *Mod. Tunn. Technol.* 39 (4), 33–36.

Xing, Z. S., Deng, M., Wang, A. G., and Liu, K. C. (2014). Internal sulfate attack on concrete caused by gypsum-bearing aggregates. *J. Build. Mater.* 17 (1), 30–34+41.

Yin, T. J. (2014). *Study on causes and treatment technologies of diseases in Pandaoling Tunnel in Datonghe-Qingwangchuan diversion project*. Lanzhou, China: Lanzhou Jiaotong University.

Zhang, J., and Huang, H. (2012). Comprehensive improvement of the liupanshan tunnel disease. *Energy Energy Conservation* (10), 89–91.

Zhang, Z. Y. (2019). *Mesoscopic erosion mechanism and shear properties of shotcrete materials under sulfate-containing environments*. Chongqing, China: Chongqing University.

Zhang, Z. Y., Jin, X. G., and Luo, W. (2019). Numerical study on the collapse behaviors of shallow tunnel faces under open-face excavation condition using mesh-free method. *J. Eng. Mech.* 145 (11), 04019085. doi:10.1061/(asce)em.1943-7889.0001661

Zhang, Z. Y., Pang, K., Xu, L. H., Zou, Y., Yang, J., and Wang, C. B. (2023). The bond properties between UHPC and stone under different interface treatment methods. *Constr. Build. Mater* 365, 130092. doi:10.1016/j.conbuildmat.2022.130092

Zhang, Z. Y., Zhou, J. T., Yang, J., Zou, Y., and Wang, Z. S. (2020b). Cracking characteristics and pore development in concrete due to physical attack. *Mater Struct.* 53 (4), 104. doi:10.1617/s11527-020-01541-5

Zhang, Z. Y., Zhou, J. T., Zou, Y., Yang, J., and Bi, J. (2020a). Change on shear strength of concrete fully immersed in sulfate solutions. *Constr. Build. Mater* 235, 117463. doi:10.1016/j.conbuildmat.2019.117463

Zhang, Z. Y., Zou, Y., Yang, J., and Zhou, J. T. (2022). Capillary rise height of sulfate in Portland-limestone cement concrete under physical attack: experimental and modelling investigation. *Cem. Concr. Comp.* 125, 104299. doi:10.1016/j.cemconcomp.2021.104299

Zhuang, Y., Liu, X. R., Zhou, X. H., and Du, L. B. (2022). Diffusion model of sulfate ions in concrete based on pore change of cement mortar and its application in mesoscopic numerical simulation. *Struct. Concr.* 23 (6), 3786–3803. doi:10.1002/suco.202100760

frontiers | Frontiers in Materials

TYPE Original Research
PUBLISHED 10 January 2024
DOI 10.3389/fmats.2023.1342249

OPEN ACCESS

EDITED BY
Zhongya Zhang,
Chongqing Jiaotong University, China

REVIEWED BY
Wanli Guo,
Nanjing Hydraulic Research Institute, China
Kai Kang,
Jiangnan University, China
Yang Lu,
Hohai University, China

*CORRESPONDENCE
Tiantian Du,
18845792497@163.com

RECEIVED 21 November 2023
ACCEPTED 26 December 2023
PUBLISHED 10 January 2024

CITATION
Liu T, Du T, Lu H, Hu B, Yang X and Liu G (2024), The influence of cement proportion and curing age on the mixed mode I-II fracture characteristics of cement soil. *Front. Mater.* 10:1342249. doi: 10.3389/fmats.2023.1342249

The influence of cement proportion and curing age on the mixed mode I-II fracture characteristics of cement soil

Tao Liu[1], Tiantian Du[2]*, Huaming Lu[1], Baichun Hu[1], Xun Yang[1] and Gang Liu[3]

[1]Power China Guiyang engineering corporation limited, Guiyang, China, [2]Sichuan Xuanhan Vocational Secondary School, Dazhou, China, [3]China Construction Sixth Engineering Bureau Corp Ltd., Tianjing, China

To study the fracture failure mechanism of cement soil under tensile-shear stress, mixed mode I-II fracture tests were conducted on cement soil semi-circular bending specimens with different cement proportions (p = 5%, 10%, 15%, 20%, and 25%) and curing ages (T = 1, 3, 5, and 7 days). The test results showed that the cracks were jagged as they propagated, and mode I stress intensity factor (K_I) and mode II stress intensity factor (K_{II})gradually increased with the increase of cement proportion and curing age. In addition, the K_{II}/K_{IC} values were between 0.39 and 0.45 under different cement proportions and between 0.40 and 0.44 under different curing ages. Subsequently, the limitations of using traditional fracture criteria (MTS, S, G, and circular criteria) to describe cement soil fracture damage were identified. In contrast, the generalized maximum tangential stress (GMTS) criterion fitted the test results well, with the K_{II}/K_{IC} value and the crack initiation angle near the critical size r_c = 1 mm curve. Based on the generalized maximum tangential stress (GMTS) criterion, the r_c of the cement soil crack tip micro-fracture zone was calculated as 0.3 mm–1.9 mm.

KEYWORDS

mixed mode I-II fracture, GMTS criteria, cement soil, cement proportion, curing age

1 Introduction

Adding cement to clay with poor engineering properties can greatly improve its strength and reduce its permeability and plasticity (Sukontasukkul and Jamsawang, 2012; Voottipruex and Jamsawang, 2014). This method has the advantages of low cost, fast construction speed, and remarkable effect. Cement soil has been widely used in engineering, such as foundation reinforcement, retaining walls, and seepage prevention of Earth dams. However, defects in the form of impurities, voids, and cracks are inevitable in such structures (Zhang et al., 2019; Yang et al., 2023; Zhang et al., 2023; Zou et al., 2023). Under the actions of environmental conditions or external loads, crack propagation may be triggered in cement soil, which may even cause structural instability, causing major economic, environmental, and human life losses (Rizvi et al., 2022; Xu et al., 2022). To provide reference for safety evaluation and parameter optimization of such projects, it is necessary to study the crack resistance of soil-cement.

In practical applications, cement soils are subjected to different loads, resulting in different modes of fracture, such as openings (I) and mixed mode (I-II) fractures. The

TABLE 1 Test schemes.

Schemes	Crack inclination angle α (°)	Relative crack length (*a/R*)	Length-span ratio (*S/2R*)	Cement proportion (%)	Curing age (*d*)
1	0, 10, 20, 30, 40, 50	0.4	0.51	15	1, 3, 5, 7
2	0, 10, 20, 30, 40, 50	0.4	0.51	5, 10, 15, 20, 25	3

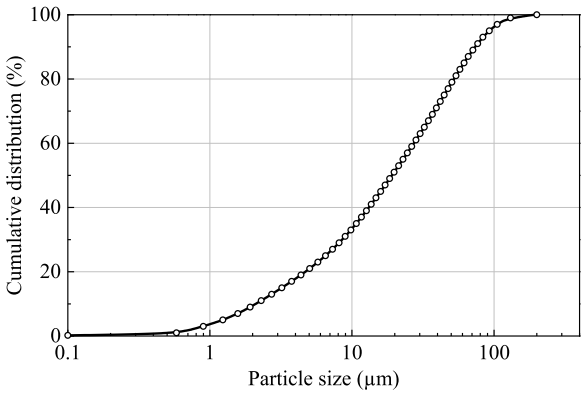

FIGURE 1
The curve for the clay particle size distribution.

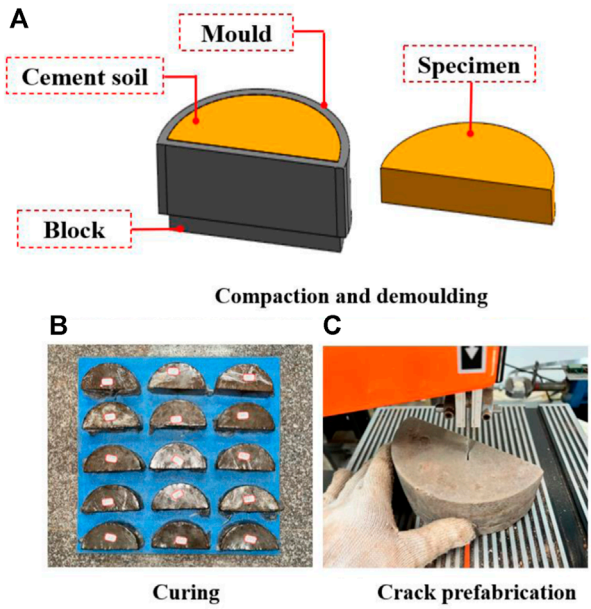

FIGURE 2
Schematic diagram of specimen preparation. (A) Mold diagram. (B) Sample curing.

failure mechanism of the latter is more complex. Therefore, studying the mixed mode I-II fracture behavior of cement soil is of great significance to engineering applications. In this regard, researchers have proposed different types of test methods and specimen structures, e.g., single-edge notched beam (SENB) specimens (Wagoner et al., 2005; Kim et al., 2008), double-edged notched beam (DENB) specimens (Campbell et al., 2018; Sun et al., 2020), incline notched semi-circular bending (SCB) specimens (Chong, 2012; Ajdani et al., 2021), edge cracked semi-cylinder disc (ECSD) specimens (Zhou et al., 2021), and asymmetric SCB (ASCB) specimens (Aliha and Ayatollahi, 2010; Aliha et al., 2014).

At present, fracture criteria are yet to be established specifically for cement soil, and their fracture failures are described with the fracture criteria of rock materials. Scholars worldwide have established three typical failure criteria for mixed mode I-II fractures: the maximum energy release rate criterion (G criterion) (Hussain et al., 1973), the minimum strain energy density criterion (S criterion) (Liu et al., 2015), and the maximum tangential stress criterion (MTS criterion) (Erdoga and Sih, 1963). Most of the existing research has adopted the three fracture criteria above to describe fracture failures. Subsequently, scholars found large errors in the test results when using the classic criteria for fracture failure description and made corresponding improvements. Based on the MTS criterion, Smith et al. (Smith et al., 2010) considered the effect of the non-singular term T-stress and proposed the generalized MTS criterion (GMTS criterion). Aliha et al. (Aliha et al., 2012) conducted mixed mode I-II fracture tests on SCB specimens of marble, concluding that the traditional fracture criteria could not predict the test results, while the GMTS criterion could accurately predict the fracture results. Yin et al. (Yin et al., 2020) conducted Mixed mode I-II fracture tests on the Brazilian disc specimens of heated granite and found that the GMTS criterion could predict the fracture failure curve. Based on the ratio of the stress intensity factor to the fracture toughness of any plane, Sun et al. (Sun et al., 2021) established a rock mixed mode fracture criterion considering the effect of anisotropy.

In summary, there are few researches on the cracking resistance of soil-cement, and its cracking initiation mechanism has not been investigated clearly. Therefore, this study conducted mixed mode I-II fracture tests on the SCB specimens of cement soil, and investigated the effects of cement proportion and curing age on the fracture failure mechanism. Finally, the classical fracture criteria and GMTS criterion were comparatively analyzed.

2 Test methods

2.1 Test materials

The test soil was collected from a construction site in Chongqing. The maximum soil particle diameter was 0.075 mm, and Figure 1

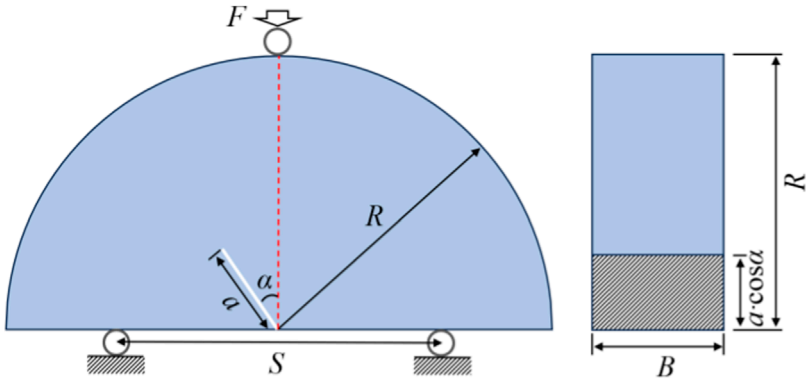

FIGURE 3
Loading method for the CNSCB cement soil specimen.

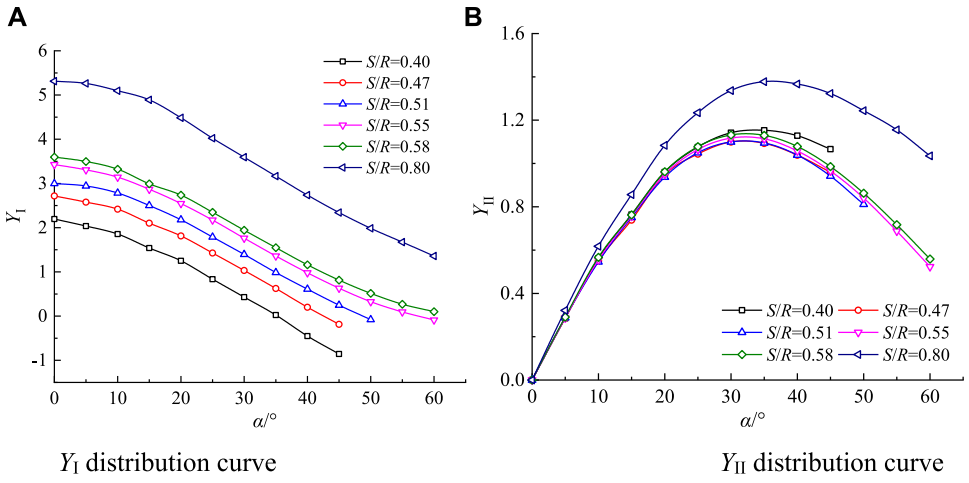

FIGURE 4
Y_I and Y_{II} distributions (Aliha et al., 2012).

showed the grading curve of soil. The soil particle specific gravity *Gs* was 2.72, the plasticity index was 20, the liquid limit was 50%, and the plasticity limit was 30%. Through compaction tests, the optimum moisture content of the clay was determined to be 17.58%, and the maximum dry density was 1.72 g cm^{-3}. The cement used was the P.O 42.5 ordinary Portland cement. Its insoluble content is 1.30%, the firing loss is 4.2%, the magnesium oxide content is 3.1%, the sulfur trioxide content is 1.8%, the specific surface area is greater than 300 square meters/kg, and the fineness of 80 μm square hole sieve is 8.7%.

2.2 Specimen preparation

The "dry specimen preparation' method was adopted, as shown in Figure 2 with the following specific preparation steps: 1) The qualities of soil, cement and water were calculated based on the sample size, moisture content and dry density. 2) After adding water to the clay powder and stirring, the mixed clay was sealed in a bag and allowed 24 h for full moisture diffusion before mixing with the cement powder to obtain cement soil. 3) The steel mould was installed, with a layer of petrolatum and a layer of cling film applied on its inner wall, and the cement soil was compacted layer by layer (Figure 2A). 4) The specimen was slowly pushed out of the mould using an ingot. 5) The demoulded specimen was wrapped in cling film and placed in a shade for curing (Figure 2B). 6) The inclination angle and length of the precast crack were marked on the cured specimen, and a crack with a width of 1 mm was formed with a cutting machine (Figure 2C).

2.3 Test scheme

To study the fracture failure mechanism of cement soil, different cement proportions and curing ages were considered in this experimental research. Specifically, the cement proportions were 5%, 10%, 15%, 20%, and 25%, and the curing ages were 1, 3, 5, and 7 days.

Table 1 shows the specific test schemes. Using the control variable method, Scheme 1 was designed to consider the effect of curing age, and Scheme 2 was designed to consider the effect of

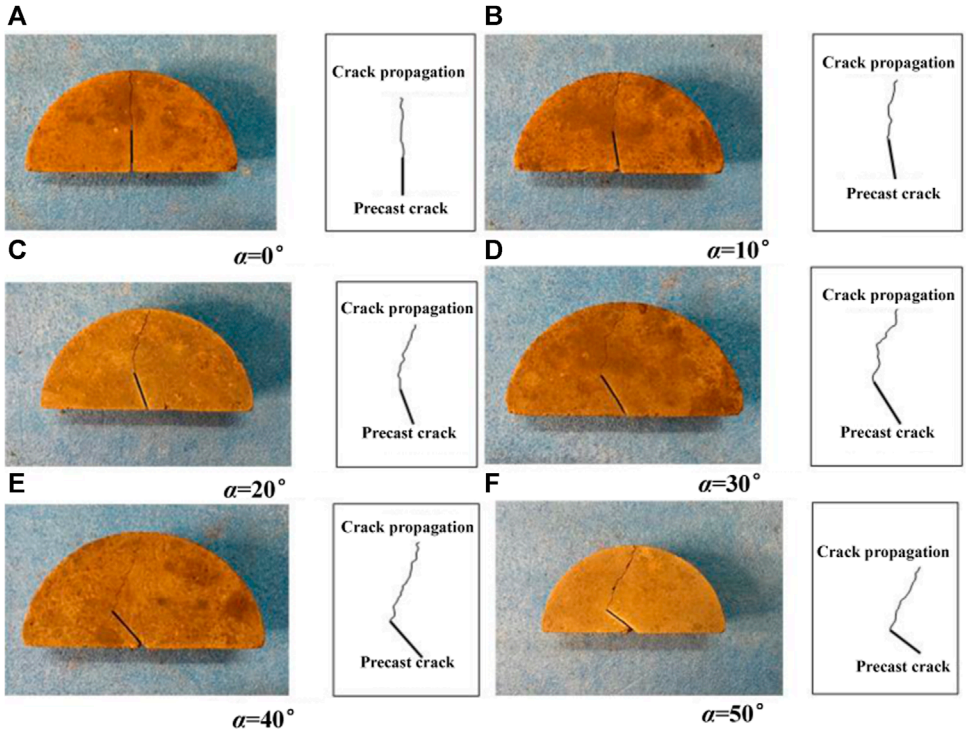

FIGURE 5
Crack propagation patterns.

cement proportion. The crack angles of 0°, 10°, 20°, 30°, 40°, and 50° were selected, and the calculations were conducted based on the average peak load of 3 specimens. A total of 132 specimens were used.

The tests were performed using chevron-notched SCB (CNSCB) specimens, and the loads were applied through three-point bending (Figure 3). According to the ISRM recommendation (Kuruppu et al., 2014), the length-span ratio $S/2R$ was 0.51, and the relative length of the crack a/R was 0.4. The specimens in this study had a radius R of 75 mm and a thickness B of 50 mm. The loading rate was 0.6 mm/min.

3 Test results and analysis

The K_I and K_{II} values of the CNSCB specimens can be calculated with Eqs. 1, 2 (Ayatollahi and Aliha, 2007).

$$K_I = \frac{F\sqrt{\pi a}}{2BR} Y_I\left(\alpha, \frac{a}{R}, \frac{S}{2R}\right) \tag{1}$$

$$K_{II} = \frac{F\sqrt{\pi a}}{2BR} Y_{II}\left(\alpha, \frac{a}{R}, \frac{S}{2R}\right) \tag{2}$$

where K_I is the mode I stress intensity factor, K_{II} is the mode II stress intensity factor, F is the load, B is the specimen thickness, R is the specimen radius, a is the initial crack length, α is the initial crack angle, and Y_I and Y_{II} are dimensionless mode I and mode II stress intensity factors, respectively, which are related to the crack length-radius ratio, the initial crack inclination angle, and the span-radius ratio. The Y_I and Y_{II} values are shown in Figure 4.

Regarding the mixed mode I-II fractures in this study, $K_I > 0$ and $K_{II} > 0$ indicate the tensile shear stress state, and the combination relationship between K_I and K_{II} is generally expressed as M_e.

$$M^e = \frac{2}{\pi} \arctan\left(\frac{K_I}{K_{II}}\right) \tag{3}$$

3.1 Crack propagation analysis

Using specimens with a cement proportion of 15% and a curing age of 3 days as an example, the typical cement soil failure modes in the mixed mode I-II fracture tests are shown in Figure 5. As can be observed, the propagations begin at the tips of the initial cracks. The specimen with the initial crack inclination angle α of 0° shows a mode I fracture, and the propagation is along the initial crack direction. Specimens with α = 10°–40° show mixed mode I-II fractures. The specimen with α = 50° shows a mode II fracture. The crack propagation deviates from the direction of the initial crack. The greater the inclination angle of the initial crack, the more significant the deviation of the propagation direction. According to the sketch, the crack growth is not along a uniform, straight line but a jagged-like line. This is due to the inhomogeneity of the manually prepared specimens, manifested as many particle granules of varying strength that are bypassed by the propagating cracks. Meanwhile, the original propagation path is restored under the action of stress, and this back-and-forth process leads to jagged cracks.

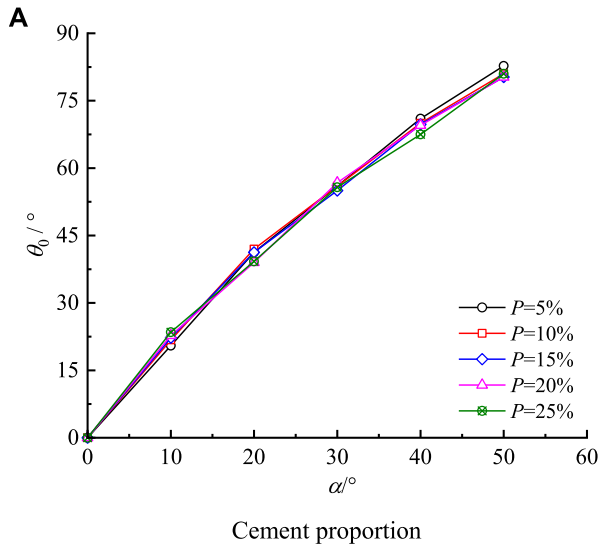

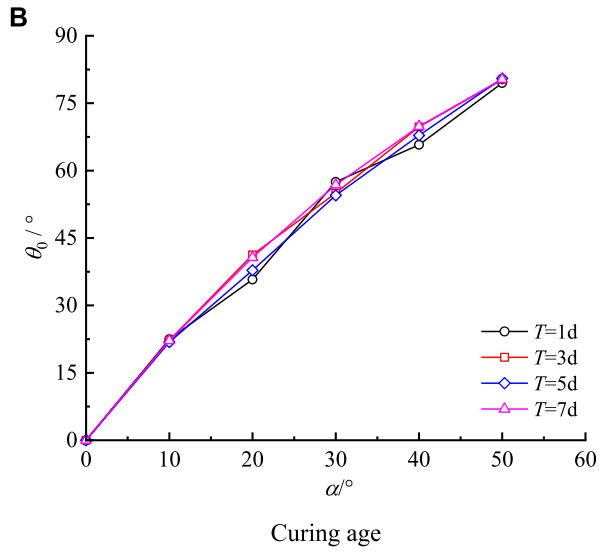

FIGURE 6
Crack initiation angle variation patterns.

3.2 Crack initiation angle (θ_0) analysis

Figure 6A shows the variation patterns of the crack initiation angle, i.e., the angle between the initial crack and the extended crack, under different cement proportions. With the cement proportion being 5%–25%, the value of θ_0 varies between 23.5° and 20.5° at the α of 10°. The value of θ_0 varies between 42° and 39° at the α of 20°. The value of θ_0 varies between 56.75° and 55° at the α of 30°. The value of θ_0 varies between 71° and 67° at the α of 40°; the value of θ_0 varies between 82.75° and 80.25° at the α of 50°. Overall, the variations of θ_0 are within 4°, not exceeding the margin of error. Thus, it can be considered that the cement proportion has basically no effect on θ_0. Therefore, the average values of θ_0 were selected for the subsequent analysis, namely, 0°, 22.15°, 40.55°, 55.90°, 69.55°, and 81.05°, respectively.

Figure 6B shows the variation patterns of crack initiation angle under different curing ages. With the curing age being 1 day–7 days,

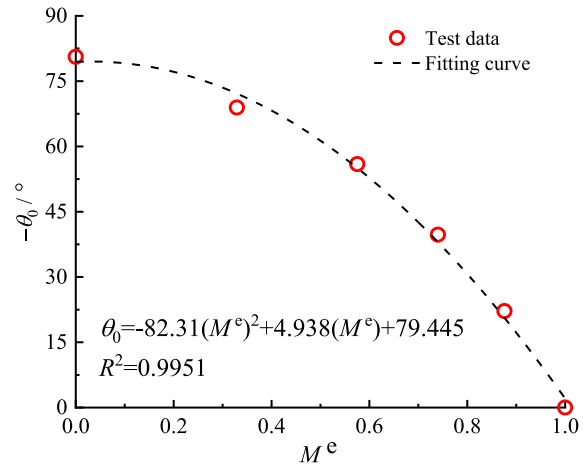

FIGURE 7
Curve of the relationship between θ_0 and M_e.

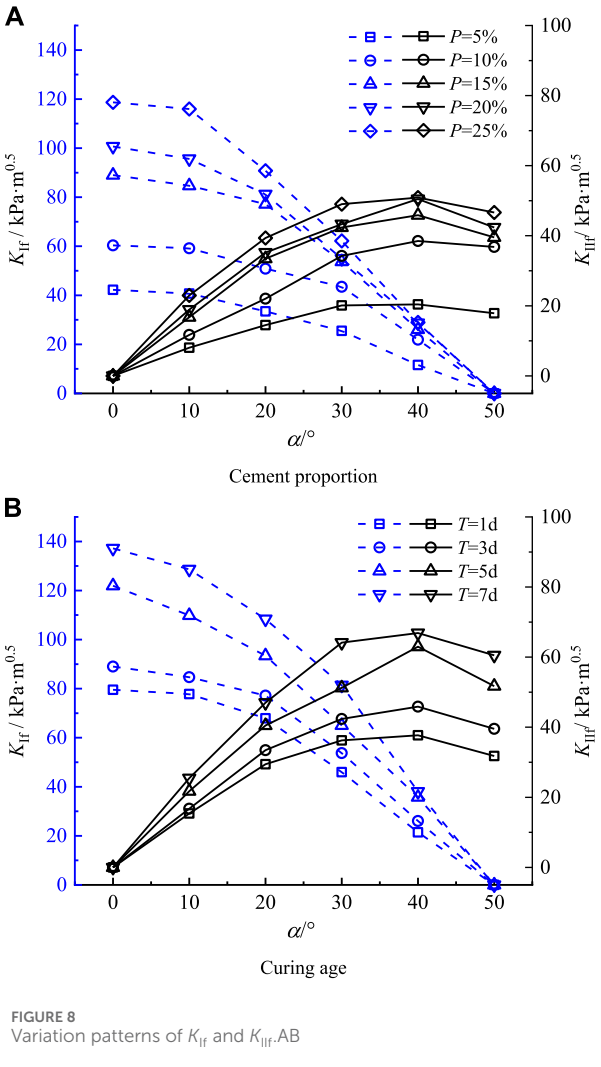

FIGURE 8
Variation patterns of K_{If} and K_{IIf}.AB

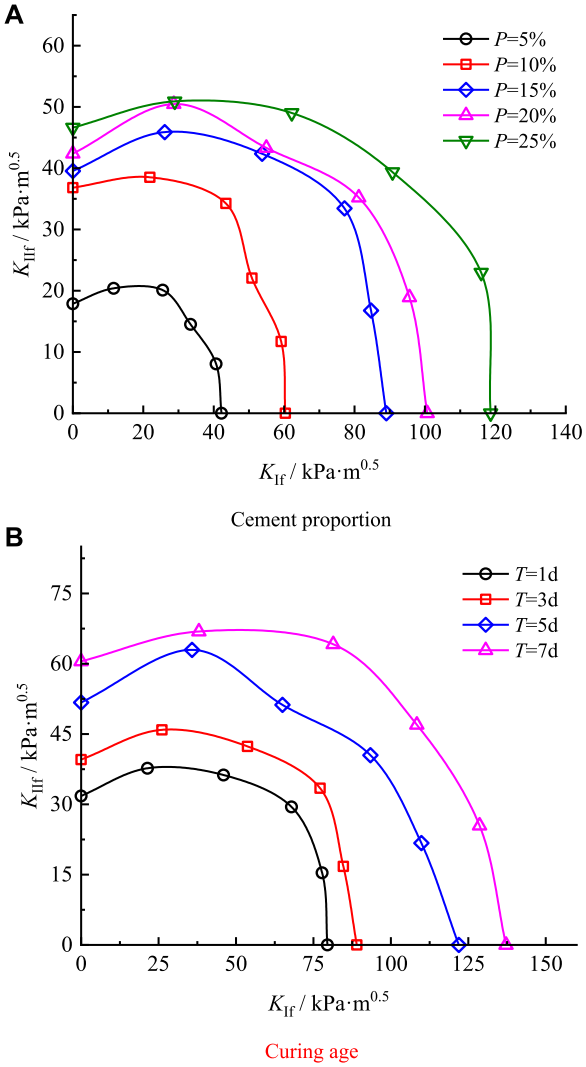

FIGURE 9
K_{IIf} and K_{If} test value envelopes.

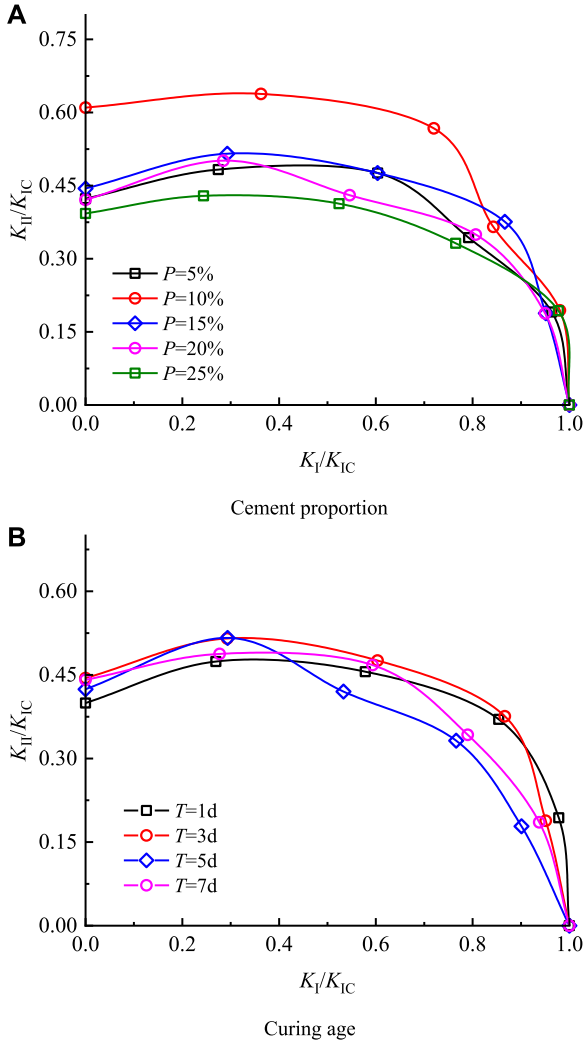

FIGURE 10
K_{II}/K_{IC} and K_I/K_{IC} test value envelopes.

the value of θ_0 varies between 22.5° and 21.83° at the α of 10°; the value of θ_0 varies between 41.25° and 35.75° at the α of 20°; the value of θ_0 varies between 57.5° and 54.5° at the α of 30°; the value of θ_0 varies between 69.83° and 65.75° at the α of 40°; the value of θ_0 varies between 80.5° and 79.5° at the α of 50°. Overall, the variations of θ_0 are within 5.5°, not exceeding the margin of error. Therefore, the curing age has basically no effect on θ_0. Under different curing ages, the average values of θ_0 are 0°, 22.19°, 38.88°, 55.96°, 69.83°, and 80.33°.

In summary, the effects of cement proportion and curing age. The mathematical relationship between its average values and M_e is modeled as Eq. 4, and the curve is plotted as shown in Figure 7.

$$\theta_0 = -82.31(M^e)^2 + 4.9383(M^e) + 79.445 \quad (4)$$

3.3 Stress intensity factor analysis

Figure 8 shows the relationship between the critical stress intensity factors K_{If} and K_{IIf} with the initial crack inclination angle α. With the gradual increase of the initial crack inclination angle, the critical stress intensity factor K_{If} gradually decreases while K_{IIf} gradually increases, and K_{If} and K_{IIf} also increase with the increase of cement proportion (Figure 8A) and curing age (Figure 8B). It can be observed that $K_{IIf} = 0$ corresponds to mode I fracture, at which time K_{If} is the fracture toughness K_{IC} of mode I fracture; $K_{If} = 0$ corresponds to pure mode II fracture, at which time K_{IIf} is the fracture toughness K_{IIC} of pure mode II fracture.

Figure 9 shows the K_{IIf} and K_{If} test value envelopes. Under different cement proportions, K_{If} and K_{IIf} gradually increase with the increase of cement proportion, and the envelopes are more inward at lower cement proportions (Figure 9A). Under different curing ages, K_{If} and K_{IIf} exhibit the same variation patterns as described above (Figure 9B).

Figure 10 shows the K_{II}/K_{IC} and K_I/K_{IC} test value envelopes. It can be observed that the envelopes under different cement proportions intersect, and the K_I/K_{IC} and K_{II}/K_{IC} envelopes are close to basically stable within certain intervals. With $K_I/K_{IC} = 0$, the K_{II}/K_{IC} value varies between 0.61 and 0.39. Other than the obvious deviated points in the figure, the rest are between 0.39

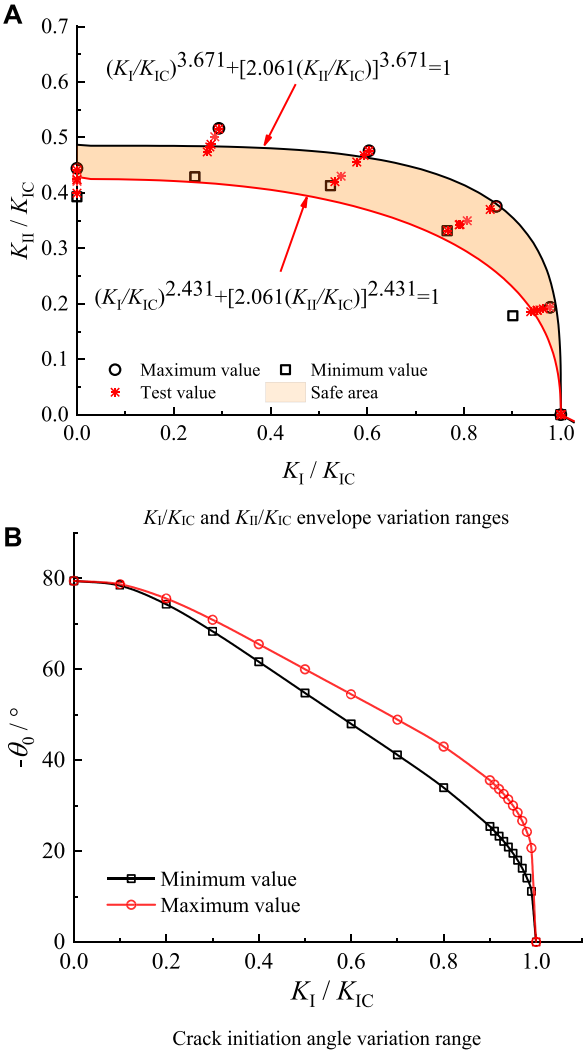

FIGURE 11
Parameter variation intervals upon cement soil failure.

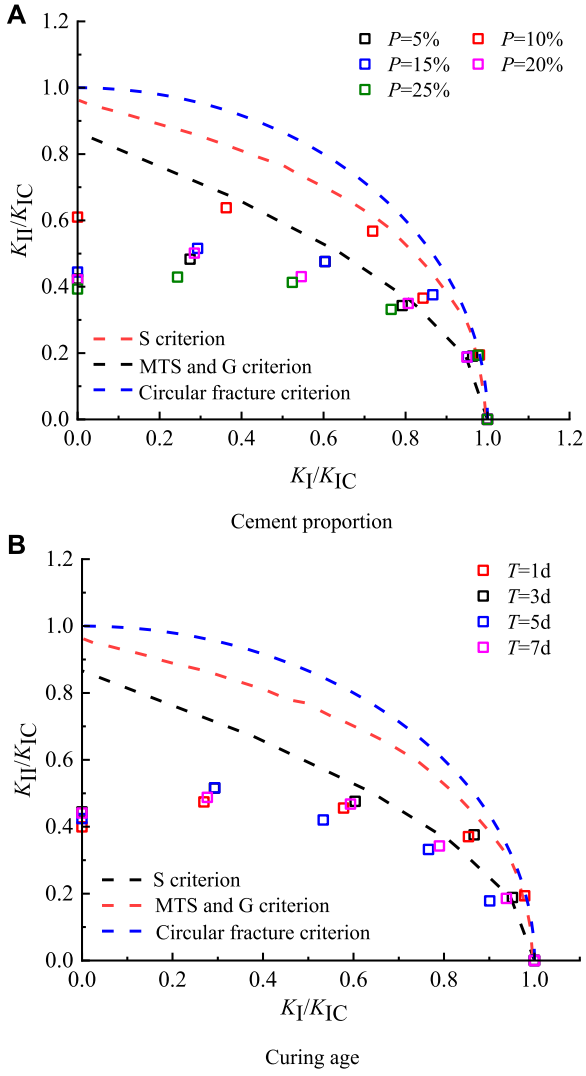

FIGURE 12
Comparison between the test results and classical fracture criteria.

and 0.45 (Figure 10A). The envelopes under different curing ages also intersect, and the K_I/K_{IC} and K_{II}/K_{IC} envelopes are close to basically stable within certain intervals. With $K_I/K_{IC} = 0$, the K_{II}/K_{IC} value varies between 0.44 and 0.40, which is within the 0.40 to 0.44 range (Figure 10B). The reason for the above phenomenon is that the soil-cement heterogeneity is more significant under the influence of factors such as material mixing degree, curing temperature and test conditions.

4 Cement soil fracture failure mechanism analysis

4.1 Cement soil fracture failure analysis with empirical equations

Figure 11 shows the variation ranges of K_{II}/K_{IC}, K_I/K_{IC}, and crack initiation angle upon cement soil fracture failure obtained based on the test data. Based on the envelope variation intervals in Figure 11A, the upper and lower boundary functions of the K_{II}/K_{IC} value are fitted, i.e., the K_{II}/K_{IC} variation range of the cement soil with the cement proportion of 5%–25% and the curing age of 1 day–7 days. The variation range of θ_0 under the K_{II}/K_{IC} and K_I/K_{IC} mixed stress states can be obtained based on Eq. 4, as shown in Figure 11B.

4.2 Comparative analysis of the results of the classical fracture criteria

Soil fracture analyses are often based on rock fracture criteria, such as the MTS criterion, G criterion, and S criterion mentioned above. Additionally, Wang et al. (Suits et al., 2006) adopted a circular fracture criterion in their analysis of Nuozhadu clay. Their equation is as follows:

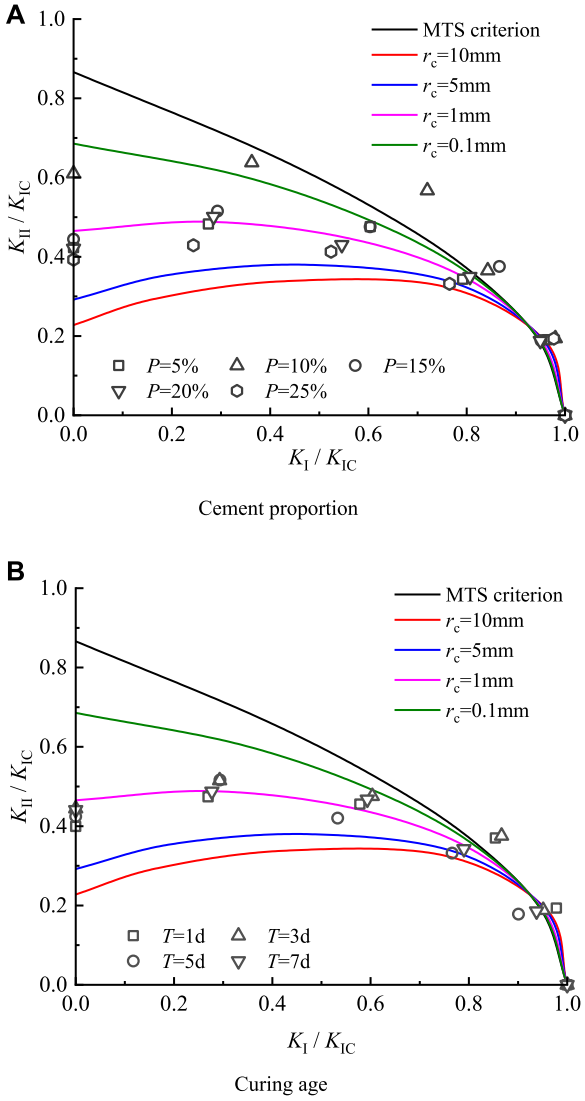

FIGURE 13
GMTS criterion and test values (K_{II}/K_{IC} and K_I/K_{IC}).

$$\left(\frac{K_I}{K_{IC}}\right)^2+\left(\frac{K_{II}}{K_{IC}}\right)^2=1 \tag{5}$$

As shown in Figure 12, the crack initiation angle upon pure mode II fracture is 70.53° according to the MTS criterion, which is significantly different from the θ_0 in this study. In contrast, the K_{II}/K_{IC} obtained in this study is between 0.39 and 0.45, and those according to the MTS criterion are between 0 and 0.87, which is significantly not consistent. With the S criterion, both the crack initiation angle and the envelope are related to μ, which is set to 0.3 in this study. At this time, the crack initiation angle is 82.34°, and the K_{II}/K_{IC} value is between 0 and 0.96. According to Figure 12, the envelope is still above that of the MTS criterion. Compared with the two criteria above, the K_{II}/K_{IC} value based on the circular fracture criterion is above that of the S criterion, and the theoretical and test results are significantly different. Therefore, describing the cement soil fracture failure mechanism with classical fracture criteria has certain limitations.

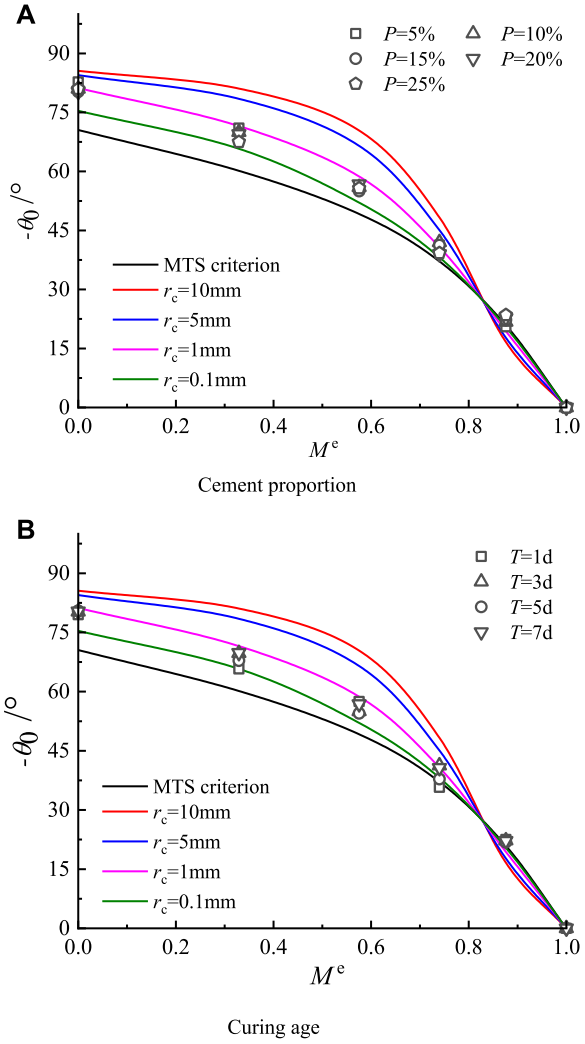

FIGURE 14
GMTS criterion and test values (θ_0).

4.3 Comparative analysis of cement soil fractures under the GMTS criterion

Considering the unsatisfactory results of the above classical fracture criteria, further analysis is conducted with the GMTS criterion. The stress field at the crack tip is as follows:

$$\left.\begin{aligned}\sigma_r&=\frac{1}{2\sqrt{2\pi r}}\left[K_I\cos\frac{\theta}{2}(3-\cos\theta)+K_{II}\sin\frac{\theta}{2}(3\cos\theta-1)\right]+T\cos^2\theta+O(r^{0.5})\\ \sigma_\theta&=\frac{1}{2\sqrt{2\pi r}}\cos\frac{\theta}{2}[K_I(1+\cos\theta)-3K_{II}\sin\theta]+T\sin^2\theta+O(r^{0.5})\\ \tau_{r\theta}&=\frac{1}{2\sqrt{2\pi r}}\cos\frac{\theta}{2}[K_I\sin\theta+K_{II}(3\cos\theta-1)]-T\sin\theta\cos\theta+O(r^{0.5})\end{aligned}\right\} \tag{6}$$

Compared to the MTS criterion, the T-stress is included, and the critical size r_c of the crack tip micro-fracture zone is also taken into account. According to the GMTS criterion, the crack is initiated when the maximum tangential stress is reached. Then, we have:

$$\frac{\partial\sigma(\theta)}{\partial\theta}=0\rightarrow K_I\sin\theta_0+K_{II}(3\cos\theta_0-1)-\frac{16}{3}T\sqrt{2\pi r_c}\sin\frac{\theta_0}{2}\cos\theta_0=0 \tag{7}$$

$$K_{IC} = \frac{1}{2}\cos\frac{\theta_0}{2}\left[K_I(1+\cos\theta_0) - 3K_{II}\sin\theta_0\right] + T\sqrt{2\pi r_c}\sin^2\theta_0 \quad (8)$$

Equation 8 can be normalized as:

$$\frac{K_{IC}}{K_I} = \frac{1}{2}\cos\frac{\theta_0}{2}\left[(1+\cos\theta_0) - \frac{3Y_{II}}{Y_I}\sin\theta_0\right] + \frac{T^*}{Y_I}\sqrt{\frac{2r_c}{a}}\sin^2\theta_0 \quad (9)$$

$$\frac{K_{IC}}{K_{II}} = \frac{1}{2}\cos\frac{\theta_0}{2}\left[\frac{Y_I}{Y_{II}}(1+\cos\theta_0) - 3\sin\theta_0\right] + \frac{T^*}{Y_{II}}\sqrt{\frac{2r_c}{a}}\sin^2\theta_0 \quad (10)$$

As shown in Figure 13, the envelope of the MTS criterion is the outermost, while the envelope with a larger r_c is more inward under the GMTS criterion. Under different cement proportions and curing ages, the test data envelopes are all far smaller than those under the MTS criterion, indicating the insufficiency of the MTS criterion in explaining the cement soil fracture mechanism. In contrast, the GMTS criterion is basically consistent with the test results. Other than the discrete points with large deviations, the test points are basically near the r_c = 1 mm envelope.

As shown in Figure 14, the test values of θ_0 under different cement proportions and curing ages are in the ranges of theoretical curves r_c = 1 mm to r_c = 0.1 mm, indicating that the r_c of the cement soil at this time is 0.1–1 mm. Considering the theoretical curves of K_{II}/K_{IC} and K_I/K_{IC} in Figure 13, the test values also fall near the r_c = 1 mm curve. In summary, the K_{II}/K_{IC} and K_I/K_{IC} values and θ_0 values of cement soil under the GMTS criterion are near the r_c = 1 mm theoretical curve, indicating that the GMTS criterion can better describe the cement soil fracture failure mechanism.

Through inversion based on the θ_0 test values, the theoretical value of r_c is 0.3 mm–1.9 mm. In essence, adding cement and changing the curing age alter the brittleness of the material, and the r_c corresponding to different cement proportions and curing ages should be different. Therefore, the r_c value of cement soil should not be a fixed value but within a recommended range.

5 Conclusion

The following conclusions are reached through the mixed mode fracture tests on cement soil CNSCB specimens under different cement proportions (p = 5%, 10%, 15%, 20%, and 25%) and curing ages (T = 1, 3, 5, and 7 days):

1) Under different cement proportions and curing ages, the crack propagation in the CNSCB specimens is not a uniform, straight line but a jagged line.
2) K_I and K_{II} increase with the increase of cement proportion and curing age, and the area between the envelope and the axes also increases. The K_{II}/K_{IC} value is between 0.39 and 0.45 under different cement proportions and between 0.40 and 0.44 under different curing ages.
3) According to the test results, the traditional MTS criterion, S criterion, and G criterion have limitations in describing cement soil fracture failures, while the GMTS criterion can better describe cement soil fracture failures, with the test data consistent with the r_c = 1 mm theoretical curve. The recommended range of r_c for cement soil is 0.3 mm–1.9 mm.

Data availability statement

The original contributions presented in the study are included in the article/Supplementary material, further inquiries can be directed to the corresponding author.

Author contributions

TL: Writing–review and editing. TD: Writing–original draft. HL: Investigation, Supervision, Writing–review and editing. BH: Conceptualization, Writing–review and editing. XY: Investigation, Visualization, Writing–review and editing. GL: Writing–review and editing.

Funding

The author(s) declare that no financial support was received for the research, authorship, and/or publication of this article.

Conflict of interest

Authors TL, HL, BH, and XY were employed by Guiyang Engineering Corporation Limited. Author GL was employed by China Construction Sixth Engineering Bureau Corp Ltd.

The remaining author declares that the research was conducted in the absence of any commercial or financial relationships that could be construed as a potential conflict of interest.

Publisher's note

All claims expressed in this article are solely those of the authors and do not necessarily represent those of their affiliated organizations, or those of the publisher, the editors and the reviewers. Any product that may be evaluated in this article, or claim that may be made by its manufacturer, is not guaranteed or endorsed by the publisher.

References

Ajdani, A., Ayatollahi, M. R., and Silva, L. F. M. D. (2021). Mixed mode fracture analysis in a ductile adhesive using semi-circular bend (SCB) specimen. *Theor. Appl. Fract. Mech.* 112 (8), 102927. doi:10.1016/j.tafmec.2021.102927

Aliha, M. R. M., and Ayatollahi, M. R. (2010). Brittle fracture evaluation of a fine grain cement mortar in combined tensile-shear deformation. *Fatigue and Fract. Eng. Mater. Struct.* 32 (12), 987–994. doi:10.1111/j.1460-2695.2009.01402.x

Aliha, M. R. M., Ayatollahi, M. R., and Akbardoost, J. (2012). Typical upper bound-lower bound mixed mode fracture resistance envelopes for rock material. *Rock Mech. Rock Eng.* 45, 65–74. doi:10.1007/s00603-011-0167-0

Aliha, M. R. M., Behbahani, H., Fazaeli, H., and Rezaifar, M. (2014). Study of characteristic specification on mixed mode fracture toughness of asphalt mixtures. *Constr. Build. Mater.* 54, 623–635. doi:10.1016/j.conbuildmat.2013.12.097

Ayatollahi, M. R., and Aliha, M. R. M. (2007). Wide range data for crack tip parameters in two disc-type specimens under mixed mode loading. *Comput. Mater. Sci.* 38 (4), 660–670. doi:10.1016/j.commatsci.2006.04.008

Campbell, S., Ding, H., and Hesp, S. A. M. (2018). Double-edge-notched tension testing of asphalt mastics. *Constr. Build. Mater.* 166, 87–95. doi:10.1016/j.conbuildmat.2018.01.094

Chong, K. K. P. (2012). Fracture toughness testing of brittle materials using semi-circular bend (SCB) specimen. *Eng. Fract. Mech.* 91, 133–150. doi:10.1016/j.engfracmech.2012.01.013

Erdoga, F., and Sih, G. C. (1963). On the crack extension in plates under plane loading and transverse shear. *J. Basic Eng.* 85 (4), 519–525. doi:10.1115/1.3656897

Hussain, M. A., Pu, S. L., and Underwood, J. H. (1973). Strain energy release rate for a crack under combined mode I and mode II. *Strain Energy Release Rate A Crack Under Comb. Mode I Mode II*.

Kim, H., Wagoner, M. P., and Buttlar, W. G. (2008). Micromechanical fracture modeling of asphalt concrete using a single-edge notched beam test. *Mater. Struct.* 42 (5), 677–689. doi:10.1617/s11527-008-9412-8

Kuruppu, M. D., Obara, Y., Ayatollahi, M. R., Chong, K. P., and Funatsu, T. (2014). ISRM-suggested method for determining the mode I static fracture toughness using semi-circular bend specimen. *Rock Mech. Rock Eng.* 47 (1), 267–274. doi:10.1007/s00603-013-0422-7

Liu, X. M., Bian, Y. M., and Liang, Y. C. (2015). The volume strain energy density factor criterion for sharp V-notches under mixed-mode I and II. *Appl. Mech. Mater.* 782, 170–176. doi:10.4028/www.scientific.net/AMM.782.170

Rizvi, Z., Amin, A., Arp, J. C. C., and Wuttke, F. (2022). Fracture toughness mode I of glass fibers improved soil. *Mater. Today Proc.* 62, 3276–3281. doi:10.1016/j.matpr.2022.04.230

Smith, D. J., Ayatollahi, M. R., and Pavier, M. J. (2010). The role of T-stress in brittle fracture for linear elastic materials under mixed-mode loading. *Fatigue and Fract. Eng. Mater. Struct.* 24 (2), 137–150. doi:10.1046/j.1460-2695.2001.00377.x

Suits, L. D., Sheahan, T. C., Wang, J. J., Zhu, J. G., Chiu, C. F., and Chai, H. J. (2006). Experimental study on fracture behavior of a silty clay. *Geotechnical Test. J.* 30 (4), 100715–100719. doi:10.1520/GTJ100715

Sukontasukkul, P., and Jamsawang, P. (2012). Use of steel and polypropylene fibers to improve flexural performance of deep soil–cement column. *Constr. Build. Mater.* 29, 201–205. doi:10.1016/j.conbuildmat.2011.10.040

Sun, B., Zheng, Y., and Li, Z. (2020). Random beam lattice modeling method for catastrophic crack growth simulation of brittle-like materials. *Constr. Build. Mater.* 244, 118396. doi:10.1016/j.conbuildmat.2020.118396

Sun, D. L., Rao, Q. H., Wang, S. Y., Yi, W., and Shen, Q. q. (2021). A new mixed-mode fracture criterion of anisotropic rock. *Eng. Fract. Mech.* 2021 (4), 107730. doi:10.1016/j.engfracmech.2021.107730

Voottipruex, P., and Jamsawang, P. (2014). Characteristics of expansive soils improved with cement and fly ash in Northern Thailand. *Geomechanics Eng.* 6 (5), 437–453. doi:10.12989/gae.2014.6.5.437

Wagoner, M. P., Buttlar, W. G., and Paulino, G. H. (2005). Development of a single-edge notched beam test for asphalt concrete mixtures. *J. Test. Eval.* 33 (6), 1–13.

Xu, J. J., Zhang, H., Tang, C. S., Cheng, Q., Tian, B. g., Liu, B., et al. (2022). Automatic soil crack recognition under uneven illumination condition with the application of artificial intelligence. *Eng. Geol.* 296, 106495. doi:10.1016/j.enggeo.2021.106495

Yang, J., Chen, R., Zhang, Z., Zou, Y., Zhou, J., and Xia, J. (2023). Experimental study on the ultimate bearing capacity of damaged RC arches strengthened with ultra-high performance concrete. *Eng. Struct.* 279, 115611. doi:10.1016/j.engstruct.2023.115611

Yin, T., Wu, Y., Wang, C., Zhuang, D., and Wu, B. (2020). Mixed-mode I+II tensile fracture analysis of thermally treated granite using straight-through notch Brazilian disc specimens. *Eng. Fract. Mech.* 234, 107111. doi:10.1016/j.engfracmech.2020.107111

Zhang, Z., Jin, X., and Luo, W. (2019). Long-term behaviors of concrete under low-concentration sulfate attack subjected to natural variation of environmental climate conditions. *Cem. Concr. Res.* 116, 217–230. doi:10.1016/j.cemconres.2018.11.017

Zhang, Z., Pang, K., Xu, L., Zou, Y., Yang, J., and Wang, C. (2023). The bond properties between UHPC and stone under different interface treatment methods. *Constr. Build. Mater.* 365, 130092. doi:10.1016/j.conbuildmat.2022.130092

Zhou, L., Sarfarazi, V., Haeri, H., Ebneabbasi, P., Fatehi Marji, M., and Hassannezhad Vayani, M. (2021). A new approach for measurement of the fracture toughness using the edge cracked semi-cylinder disk (ECSD) concrete specimens. *Mech. Based Des. Struct. Mach.* 51 (5), 2896–2917. doi:10.1080/15397734.2021.1911667

Zou, Y., Jiang, J., Yang, J., Zhang, Z., and Guo, J. (2023). Enhancing the toughness of bonding interface in steel-UHPC composite structure through fiber bridging. *Cem. Concr. Compos.* 137, 104947. doi:10.1016/j.cemconcomp.2023.104947

frontiers | Frontiers in Materials

TYPE Original Research
PUBLISHED 11 January 2024
DOI 10.3389/fmats.2023.1352243

OPEN ACCESS

EDITED BY
Zhongya Zhang,
Chongqing Jiaotong University, China

REVIEWED BY
Longhao Ma,
Luoyang Institute of Science and Technology, China
Xiaodong Liu,
Tohoku University, Japan

*CORRESPONDENCE
Ke Xu,
xk06260626@163.com

RECEIVED 07 December 2023
ACCEPTED 27 December 2023
PUBLISHED 11 January 2024

CITATION
Xiao T, Xu K, Lu Y and She H (2024), Failure modes and mechanical properties of double-layer rock-like composite specimens with a single fissure under triaxial compression.
Front. Mater. 10:1352243.
doi: 10.3389/fmats.2023.1352243

Failure modes and mechanical properties of double-layer rock-like composite specimens with a single fissure under triaxial compression

Taoli Xiao[1], Ke Xu[1]*, Yifan Lu[2] and Haicheng She[1,3,4]

[1]School of Urban Construction, Yangtze University, Jingzhou, China, [2]Jingzhou Chengfa Construction Engineering Group Co., Ltd., Jingzhou, China, [3]Hubei Key Laboratory of Oil and Gas Drilling and Production Engineering, Yangtze University, Wuhan, China, [4]Key Laboratory of Reservoir and Dam Safety Ministry of Water Resources, Nanjing, China

Introduction: Geotechnical engineering disasters often result from instability failures in layered and heterogeneous fissured rock masses. However, the key mechanisms governing mechanical properties and crack propagation in these rock masses remain unclear.

Methods: This study presents triaxial compression tests on double-layer rock-like specimens composed of limestone and sandstone materials, containing a single fissure, to investigate the effects of fissure angles and positions on the strength and failure modes of these double-layer specimens under varying confining pressure.

Results and Discussion: The experimental results reveal that the intact composite rock approaches the strength of sandstone but is deformation-limited by limestone. Under constant confining pressure (σ_3 = 5 MPa), the fissure angle affects initial crack initiation, and fissure position dictates the failure mode and extent, while increased confining pressure induces overall shear failure in the composite rock, with the failure mode being predominantly influenced by confining pressure. Concerning mechanical deformation, augmenting the fissure angle and confining pressure substantially enhances the elasticity and ductility of the composite rock. Regarding volumetric deformation, the extent of volume shrinkage in the composite rock is influenced by both fissure angle and confining pressure, while volume expansion is influenced by fissure position. Under uniaxial compression, fissured composite rock exhibits the most unstable crack propagation, resulting in early failure. Triaxial compression shows that a higher fissure angle stabilizes crack propagation while confining pressure variation affects stability only when the fissure is in limestone. When the fissure is in sandstone, crack propagation stability remains at its highest. Furthermore, an increase in fissure angle, higher confining pressure, and changes in fissure position from sandstone through the contact interface to limestone contribute to an increasing trend in the peak strength and elastic modulus of the composite rock. Fissure-induced rock degradation is primarily influenced by the fissure angle. These findings are significant for guiding engineering construction and

design, providing valuable insights to geotechnical engineers, and enhancing safety in rock engineering projects.

KEYWORDS

layered rock mass, composite rock-like specimens, pre-existing fissures, triaxial compression, mechanical properties, failure modes

1 Introduction

Following the diagenetic theory, geological formations often exhibit prominent stratification. Layered composite rock masses exhibit an alternation of soft and hard layers in the perpendicular direction to the bedding planes, resulting in distinct lithological differences compared to homogeneous rock mass (Brady and Brown, 2006). In underground geotechnical engineering, composite rocks experience varying stress conditions due to excavation and rock fragmentation. These changing *in-situ* stress conditions contribute to the complex deformation and failure characteristics exhibited by composite rocks (Vogel and Rast, 2000; Fairhurst, 2017; Ranjith et al., 2017). Furthermore, a rock mass is a natural geological material comprised of intact rock and discontinuities (Wittke, 2014). The discontinuities primarily include bedding planes, joints, faults, and fissures (Ivars et al., 2011). These pre-existing defects exert significant influence as release surfaces and nucleation sites for failure in the rock mass. Among the 162 roof collapse accidents in coal mines supported by anchor rods across 18 large mining areas, 107 cases were attributed to joint rock composite deterioration type roof fall. This accounts for 66.04% of the investigated accidents and is identified as the primary cause of roof collapse incidents (Jia, 2007). It is crucial to understand the coupled effects of different confining pressures and fissure characteristics on the mechanical properties and failure mechanisms of composite rocks. This benefits long-term stability analysis and disaster prevention in underground engineering projects.

In the existing research on the mechanical properties and failure mechanisms of layered composite rocks, the initial focus has been on their combination form (Guo et al., 2018; Wang et al., 2020; Yu et al., 2021a; Yu et al., 2021b; Yu et al., 2022) and contact interface parameters (Zhao et al., 2013; Zhao et al., 2015; Yin et al., 2018). In some previous studies, layered composite rocks were commonly formed by bonding rocks with different strengths together using adhesive materials (such as shale-coal, sandstone-coal, *etc.*). Through uniaxial compression tests, it was found that the stronger/stiffer rocks in the composite rocks restricted the lateral deformation of the weaker/softer rocks along the contact interface, ensuring consistent lateral deformation. This phenomenon is commonly known as the "interface effect" (Chen et al., 2019). Furthermore, the bond strength of the contact interface is a crucial factor that influences the failure mode of composite rocks. Strengthening the bonding strength results in an enhancement of the overall integrity and failure strength of the composite rock (Xiao et al., 1988). However, artificially simulated bond strength cannot precisely replicate the authentic stress state at the interfaces of layered composite rocks. To minimize errors arising from human factors and the limitations of unnatural conditions on rock morphology, numerous scholars have extensively conducted experiments using rock-like materials, these studies have provided more convincing conclusions (Tien et al., 2006; Yang et al., 2019; Li et al., 2021; Wang et al., 2022; Yang et al., 2023; Zhang et al., 2023; Zou et al., 2023). For instance, by formulating specific rock-like materials consisting of two different hardness materials, the effects of rock layer inclination and interlayer thickness on the deformation characteristics of composite rocks have been revealed through uniaxial compression tests. The research findings indicated that increasing the strength difference between the materials enhanced the tendency for overall relative sliding of the composite rock. On the other hand, an increase in the inclination angle weakened the deformation of the composite rock, and its compressive strength demonstrated a "U"-shaped variation with the increase in the inclination angle (Yang et al., 2019); thicker interlayers in composite rocks are more susceptible to failure compared to thinner interlayers (Li et al., 2021). Moreover, the deformation of composite rocks under stress is a crucial indicator for evaluating underground construction safety. Through various types of tests, including different loading rates (Huang and Liu, 2013; Ma et al., 2021), cyclic loading and unloading tests (Song et al., 2012; Zuo et al., 2013), static-dynamic loading tests (Liu, 2014; Liu et al., 2014), as well as triaxial compression tests (Lu et al., 2019; Lu et al., 2020; Yu et al., 2021a; Yu et al., 2021b; Yu et al., 2022), researchers further revealed the influence of different stress loading paths on composite rocks, basically in terms of the compressive strength, the deformation modulus, the crack propagation, and the failure behavior. Considering the distinct dynamic properties of rocks compared to their static responses (Du et al., 2020a; Jiang et al., 2021), dynamic impact loading tests have also been conducted on composite rocks with the split Hopkinson pressure bar (SHPB) system. It was found that composite rocks exhibit a higher degree of energy accumulation compared to single rocks, requiring less energy in the event of dynamic disasters (Liu et al., 2021). These testing results provide a comprehensive evaluation of the strength, deformation characteristics, and energy dissipation of composite rocks under different stress conditions.

Compared with existing research on composite rocks, the investigation of crack propagation mechanisms in loaded fissured rocks has primarily concentrated on homogeneous rocks. The study of fissures in rocks follows a qualitative-to-quantitative progression. When considering single fissures without taking into account the mutual interactions of multiple fissures, researchers have mainly

TABLE 1 The particle grading distribution of quartz sand.

Sieve size/mm	0–0.16	0.16–0.32	0.32–0.63	0.63–1.25
Percentage/%	5	30	40	25

focused on the geometric characteristics of fissures, including their length (Bi and Zhou, 2017; Chen et al., 2018; Laghaei et al., 2018; Wang et al., 2018; Ismael and Konietzky, 2019), angle (Cheng et al., 2018; Le et al., 2018; Miao et al., 2018; Wang et al., 2018), width (Wang et al., 2018), and the materials filling (Le et al., 2018; Miao et al., 2018). These studies aim to investigate the impact of these fundamental fissure forms on the mechanical and deformation characteristics of rocks. When considering the interactions of multiple fissures, researchers have shifted their focus to rock bridges (length and angle of rock bridges) (Feng et al., 2019; Du et al., 2020b; Yan et al., 2023), the arrangement patterns of fissure clusters (angle, length, and spacing of fissure clusters) (Lee and Jeon, 2011; Cao et al., 2016), and the combination of fissures with voids (Lin et al., 2020; Zhang et al., 2021). Specifically, the research has yielded the following findings: It is generally believed that the length of fissures inevitably degrades the mechanical properties of rocks. However, when considering the combined effects of fissure angle and length, the conclusion is not absolute. It is argued that the peak strength of fissured rocks demonstrates a quadratic relationship with the fissure angle, while the elastic modulus shows a linear increase with the fissure angle (Feng et al., 2019). Besides, the propagation of cracks in rock masses is influenced by both the number of fissures and the fissure angle (Lin et al., 2020; Zhang et al., 2021). Wong et al. (2004a); Wong et al. (2004b); Wong et al. (2006) also gained significant insights, such as the fact that the mode of surface crack propagation in rock masses is influenced by the ratio of crack depth (d) to rock thickness (t), represented by d/t: when $d/t > 1/3$, the crack propagation length is larger, resembling the extension of two-dimensional cracks; when $d/t < 1/3$, the dominant failure mode in the rock involves anti-wing cracks. It is worth noting that all the literature mentioned above is concentrated on homogeneous rocks, the investigation of composite rocks containing fissures is rather limited. Recently, (Hu et al., 2020; Ma et al., 2023), conducted uniaxial loading tests on fissured layered composite rocks to investigate the impact of fissures on the development and evolution of cracks, as well as the final failure mode of the composite rock.

From the foregoing, considerable efforts have been devoted to studying the anisotropic behavior of transversely isotropic rocks and the impact of fractures on the mechanical properties and failure modes of homogeneous rocks. However, the stress environment of the rock mass, such as the confining pressure, should be considered as a significant influencing factor. Therefore, a comprehensive understanding of the different stress environments, mechanical deformation characteristics, and crack propagation paths of fractured layered composite rocks are crucial for improving the efficiency of deep underground resource exploitation, effectively preventing and controlling hazards in engineering construction, and providing a theoretical basis for practical engineering. However, the study of the fissured composite rock under confining pressure conditions has never been investigated. This study has produced composite rock specimens containing a single fissure and conducted triaxial compression tests. Specifically, the influence of fissure angles and positions on stress-strain response, damage stress, peak strength, elastic moduli, and failure modes under different confining pressures of composite rocks was analyzed and summarized.

2 Materials and methods

2.1 Specimen preparation

In the natural environment, rocks are composed of diverse mineral particles and cementing materials that are bonded together. And their mechanical properties are mainly affected by the friction between particles. Considering that sand particles can provide a frictional force, cement mortar was chosen as the rock-like material for this experiment.

Sedimentary rocks, which account for approximately two-thirds of the Earth's land area, are widely distributed on the Earth's surface. To create composite rock-like materials, limestone and sandstone were chosen as the original rocks, which exhibit distinct differences in physical properties and are commonly found in sedimentary rocks. The quartz sand was used as an aggregate of rock-like material. To ensure a smooth specimen surface, the size gradation distribution of the selected quartz sand particles is presented in Table 1. P.O42.5 Portland cement, silica fume, and iron powder were used as limestone-like materials. The purpose of using silica fume was to lower the peak temperature of the material's curing reaction and prevent cracking. The purpose of selecting iron powder was to improve the density of the rock. To differentiate the sandstone in terms of mechanical properties and visual appearance, P.W.32.5 Portland cement was used in its production. Additionally, a small amount of water reducer and defoamer was added to enhance the fluidity of the material and minimize the formation of pores. Table 2 provides the mass ratios of rock-like material. Table 3 presents the physico-mechanical parameters of cement mortar, which are close to that of natural rocks (Nazir et al., 2013; Cai et al., 2022). Therefore, cement mortar is considered an ideal rock-like material for laboratory experiments.

During the solidification process, cement tends to form a thin layer on the surface (Wang et al., 2018), which is prone to cracking under compression. To ensure accurate observation of real cracks in the specimens, this study first, poured cubic specimens (height × width × thickness = 150 × 150 × 150 mm) and then obtained cylindrical specimens by drilling, as illustrated in Figure 1A For cubic specimen casting, custom molds were created

TABLE 2 Material mass ratios of rock-like.

Material	Cement	Silica fume	Quartz sand	Iron powder	Defoaming agent	Water reducer	Water
Limestone-like	1.00	0.13	0.80	0.25	0.003	0.003	0.30
Sandstone-like	1.00	-	0.70	-	0.003	0.003	0.30

10.3389/fmats.2023.1352243

TABLE 3 Physico-mechanical parameters of rock and rock-like.

Material	Density ρ(g/cm^3)	Young's modulus E (GPa)	Poisson's ratio v	Compressive strength σ_c (MPa)	Tensile strength σ_t (MPa)
Limestone	2.48–2.85	10–80	0.20–0.35	30–200	5–25
Limestone-like	2.61	12.52	0.24	70.12	7.16
Sandstone	2.10–2.40	3-35	0.20–0.25	20–170	4–25
Sandstone-like	2.23	7.87	0.22	40.69	6.32

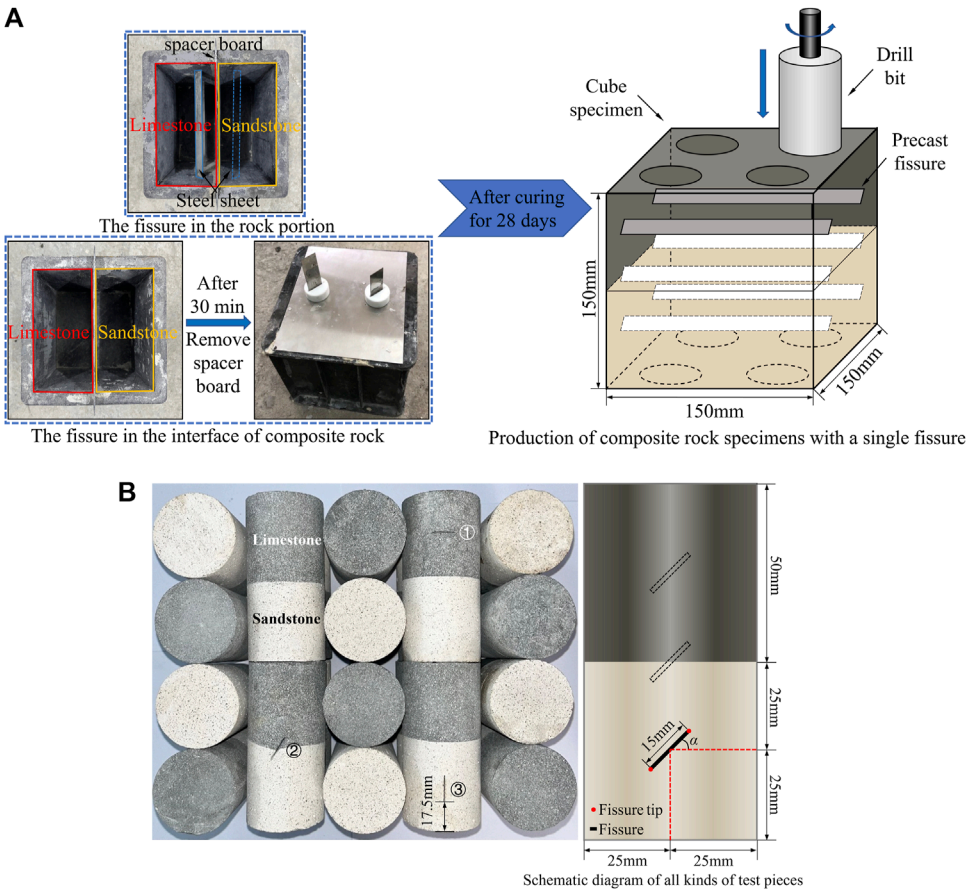

FIGURE 1
Specimens making and processing. **(A)** Schematic drawing of cube specimens making and processing, **(B)** Schematics of fissure geometry configuration in the specimens.

using plastic, steel sheets (15 mm length, 0.5 mm thickness), and spacer boards. Vibrations were applied to the mold during pouring to eliminate trapped air from the slurry. After 30 min, the spacer board was removed to ensure sufficient strength at the contact surface between the two types of rock materials. After 8 h, the steel sheets were removed when the specimens reached the initial setting, resulting in through-opened fissures. After 24 h, the solidified specimens were de-molded and placed in a constant temperature and humidity curing chamber (temperature set to 20°C ± 2°C and humidity set to 85% ± 5%) for 28 days before conducting cylinder specimen drilling.

Following the guidelines of the International Society for Rock Mechanics (ISRM), cylindrical specimens were cut and ground to a height of 100 mm and a diameter of 50 mm. To facilitate the analysis of the effects of fissure angle, position, and confining pressure on the specimens and to prevent the mechanical failure patterns of the specimens from being universally applicable due to excessively long fissure lengths, the fissure length was fixed at

TABLE 4 Specimens' numbers and fissure geometry parameter values used for all specimens.

Number	α(°)	Fissure position	$\sigma_2 = \sigma_3$ (MPa)	Number	α(°)	Fissure position	$\sigma_2 = \sigma_3$ (MPa)
C-0	Intact	Intact	0	CC-45-0	45	Interface	0
C-5	Intact	Intact	5	CC-45-5	45	Interface	5
C-10	Intact	Intact	10	CC-45-10	45	Interface	10
C-15	Intact	Intact	15	CC-45-15	45	Interface	15
CL-0-5	0	Limestone	5	CC-60-5	60	Interface	5
CL-30-5	30	Limestone	5	CC-90-5	90	Interface	5
CL-45-0	45	Limestone	0	CS-0-5	0	Sandstone	5
CL-45-5	45	Limestone	5	CS-30-5	30	Sandstone	5
CL-45-10	45	Limestone	10	CS-45-0	45	Sandstone	0
CL-45-15	45	Limestone	15	CS-45-5	45	Sandstone	5
CL-60-5	60	Limestone	5	CS-45-10	45	Sandstone	10
CL-90-5	90	Limestone	5	CS-45-15	45	Sandstone	15
CC-0-5	0	Interface	5	CS-60-5	60	Sandstone	5
CC-30-5	30	Interface	5	CS-90-5	90	Sandstone	5

15 mm. Five fissure angles (α) were considered: 0°, 30°, 45°, 60°, and 90°. Three different fissure positions were established: ①at the center of the limestone, ②at the center of the contact interface (in this study, the term "*interface*" is used to describe the contact interface parameters of limestone and sandstone), and ③at the center of the sandstone, as shown in Figure 1B Four different confining pressures (σ_3) were applied: 0, 5, 10, and 15 MPa. Considering the uniaxial compressive strength of the simulated sandstone as 40 MPa, and ensuring that the deformation of the specimen remains in the elastic stage during the confining pressure process (typically, the ratio of the threshold stress for sandstone fracturing to the peak stress is approximately 0.5), the maximum value of confining pressure was set to 15 MPa.

For clarity, the specimen numbering is designated as fissure position (FL, FI, FS, C) - fissure angle (α) - confining pressure (σ_3), where FL, FI, FS, and C represent the fissure positions in limestone, interface, sandstone, and the complete composite rock specimen, respectively. For instance, C-5 denotes the complete composite rock specimen under a confining pressure of 5 MPa. FL-45-15 signifies a composite rock specimen with a fissure angle of 45° located in limestone under a confining pressure of 15 MPa. The specific specimen numbering is outlined in Table 4. To obtain more universally applicable experimental data and avoid significant variability in individual specimens, each set of specimens underwent four tests. After removing specimens with noticeable variability, the average of the remaining specimen data was taken as the result for each set of specimens. This approach helps reduce the impact of individual outlier test data on the overall results, enhancing the reliability of the experimental outcomes.

2.2 Experimental equipment and procedure

Triaxial compression strength (TCS) test was processed by HYAS-1000C electrohydraulic servo-controlled testing equipment at the geotechnical mechanics and engineering research center at Yangtze University in China, as shown in Figure 2. In the experiment, the confining pressure was applied using hydraulic oil, while the axial stress was controlled by axial displacement. Before applying the confining pressure, the specimen was placed between the upper and lower platens and encapsulated with heat-shrinkable tubing to prevent hydraulic oil from infiltrating the rock and affecting the test results. The axial and radial strains of the specimen (at the middle section) were simultaneously measured using axial and radial extensometers, with a measurement range of 0–4 mm and a reading accuracy of ±1% at room temperature. Data collection was performed directly by a computer. The test was conducted in two steps as follows: (a) The confining pressure was increased to the target value at a rate of 0.5 MPa/min, then the axial compression was applied to the specimen at a rate of 1 mm/min until reaching an initial axial stress of 2 KN. Additional axial stress (also called deviator stress) was applied to the specimen at a rate of 0.2 mm/min until it experienced unstable failure (Yu et al., 2021b).

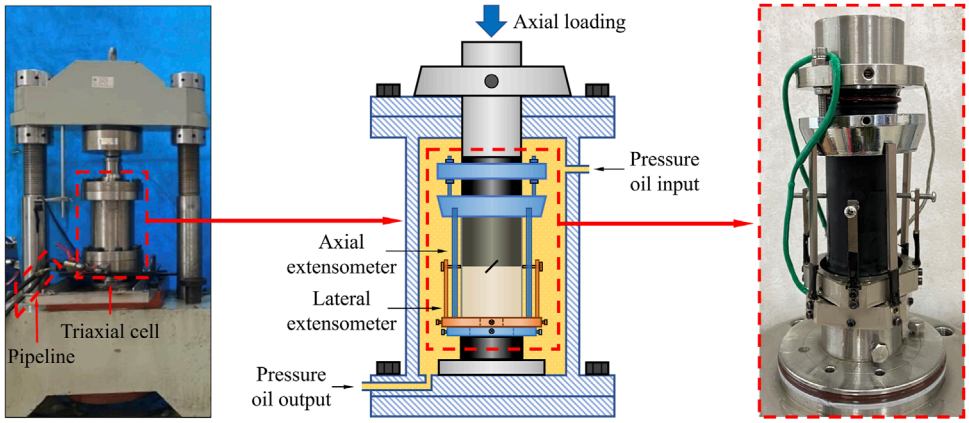

FIGURE 2
Electrohydraulic servo-controlled testing equipment.

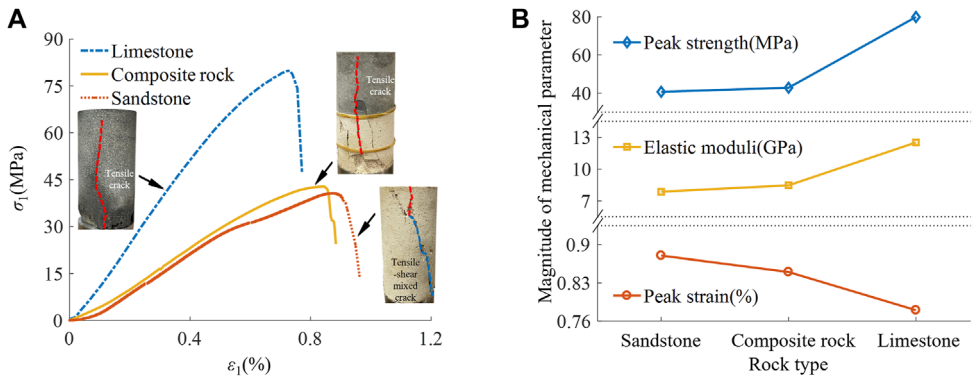

FIGURE 3
Stress-strain curves and change in mechanical of three intact rock specimens. **(A)** Stress-strain curves and failure modes, **(B)** Mechanical parameters.

3 Experimental results and discussion

3.1 Composite and single intact rock specimens under uniaxial compression

To better investigate the mechanical properties of fissured composite rock samples, uniaxial compression tests were initially conducted on individual sandstone, individual limestone, and intact composite rock, and the stress-strain curves and equivalent mechanical parameters are obtained, as shown in Figure 3 and Table 5.

Figure 3A illustrates notable distinctions among the three specimens, particularly in the pre-peak stage. The limestone's compaction phase is relatively inconspicuous, featuring an extended elastic phase. In contrast, composite rock and sandstone show significant compaction stages, with sandstone exhibiting a shorter elastic phase and a slight stress reduction just before the peak. This suggests high compaction in limestone and greater porosity in sandstone, making it more prone to macroscopic cracks before complete failure. Despite these differences, all uniaxial stress-strain curves share similar post-peak characteristics, marked by a rapid stress decline towards residual strength and a swift loss of bearing capacity.

TABLE 5 Mechanical parameters and failure characteristics of the three configurations of rock specimens.

Rock specimens	Peak strength (MPa)	Peak strain (%)	Elastic moduli (GPa)
Limestone	79.92	0.78	12.52
Composite rock	42.78	0.85	8.47
Sandstone	40.69	0.88	7.87

Statistical analysis of experimental data (Figure 3B; Table 5) reveals limestone's superior strength, surpassing composite rock and sandstone by 86.55% and 96.41%, respectively. Additionally, its elastic modulus exceeds that of composite rock by 47.82% and sandstone by 59.09%. Regarding deformation characteristics, limestone has the lowest peak strain, 12.82% less

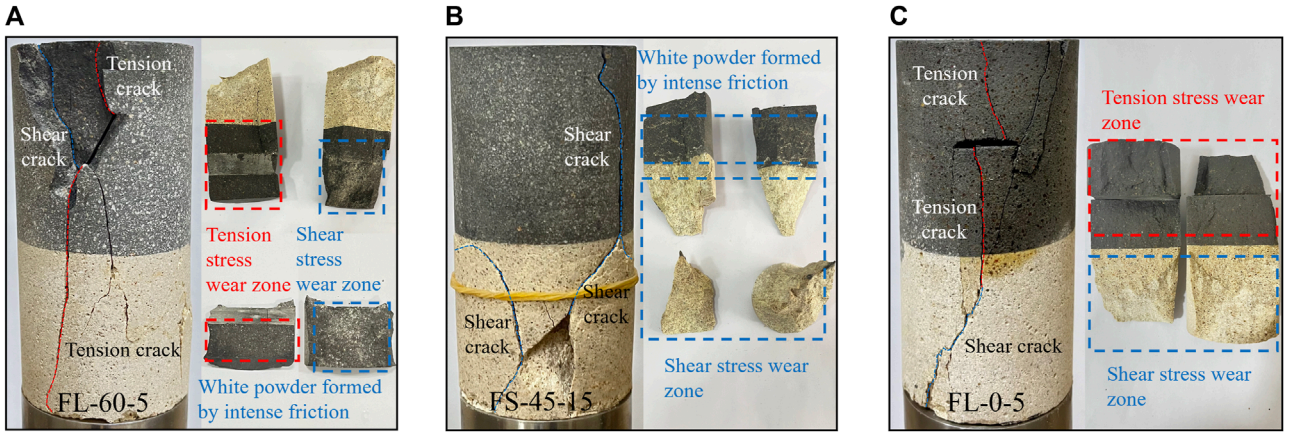

FIGURE 4
Different crack types in composite rock. **(A)** Typical tensile crack, shear crack, and crack fracture surface, **(B)** Typical shear crack and crack fracture surface, **(C)** Typical tensile shear mixed crack and crack fracture surface.

than sandstone, while the peak strain of composite rock falls between the two.

Figure 3A depicts the failure characteristics of three specimen types. Limestone and composite rock experience tensile failure along the axial compression direction, while sandstone undergoes a tensile-shear mixed failure. Deformation upon sandstone failure is notably larger than in limestone, marked by evident surface spalling. Due to lower sandstone strength, composite rock failure initiates in the sandstone portion, forming macroscopic cracks that propagate to the contact interface, penetrating through the limestone, where spalling primarily occurs.

In summary, there exists a significant strength difference between limestone and sandstone. Sandstone, being relatively softer in lithology compared to the harder limestone, exhibits larger deformations under compression. The strength of the composite rock is determined by the weaker sandstone portion, yet its deformation is constrained by the stronger limestone portion.

3.2 Failure mode of composite specimens

In the compression failure modes of rocks, cracks can be classified into three forms based on the angle between the generated cracks and fissures, as well as the scratches on the fractured surface (Lee and Rathnaweera, 2016; Lin et al., 2020; Yu et al., 2021b): (1) Axial splitting, which refers to tensile cracks formed under compression, generally parallel to the direction of maximum principal stress, mostly with an angle greater than 90° to the fissures. The crack fracture edges are neat, and the crack fractured surface is smooth, with only minor undulations in certain areas, as indicated by the red region in Figure 4A; (2) Shear cracks, typically composed of the main shear crack and secondary tensile cracks on the specimen surface. Secondary tensile cracks originate from the main shear crack and extend, with the main shear crack coplanar or less than 90° to the fissures. Most observed shear cracks exhibit evident shear dilation characteristics, with serrated fracture edges and a rough fractured surface. In the limestone portion, there is also a strong frictional effect resulting in white powder. Additionally, at lower confining pressures, shear cracks terminate at the end faces, while at higher confining pressures, shear cracks terminate at the specimen's side, as illustrated by the blue region in Figure 4B; (3) Tensile-shear mixed cracks, observed only in some specimens. These cracks typically start as tensile cracks extending towards the ends and then shift to extend to the specimen's side, forming shear cracks, as shown in Figure 4C.

To visually illustrate the failure characteristics of the specimens more clearly, clear crack trajectories were plotted. The red and blue lines represent the generated main tensile cracks and main shear cracks, respectively. The black fine lines on the specimen surface depict secondary tensile cracks, which do not influence the internal structure of the specimen.

Figure 5 presents the failure modes of composite rock specimens with different fissure angles and positions under a confining pressure of 5 MPa. By comparing various aspects, the characteristics of the cracks and their aggregation forms are summarized.

Under different fissure angles: (1) When α = 0°, regardless of the rock layer in which the fissure is located, tensile cracks always initiate at the middle of the fissure and extend towards the specimen ends. This is because the fissure is perpendicular to the direction of the principal stress, and the inner surface of the fissure is in a bending state. With the increase in axial load, tensile cracks are prone to occur in the middle of the fissure. (2) When α = 30°–60°, as the region with the most concentrated stress, wing cracks or anti-wing cracks are likely to form at the tips of the fissure, resulting in similar failure modes. (3) When α = 90°, large compressive forces leading to tensile cracks are less likely to occur in the fissure. Due to the strength difference between the two types of rocks, shear cracks first initiate and propagate in the sandstone, forming a wedge shape that causes limestone to undergo splitting failure. The failure mode of the specimen mainly depends on the fissure positions.

Under different fissure positions: (1) When the fissure is in limestone, some specimens may develop a small number of shear

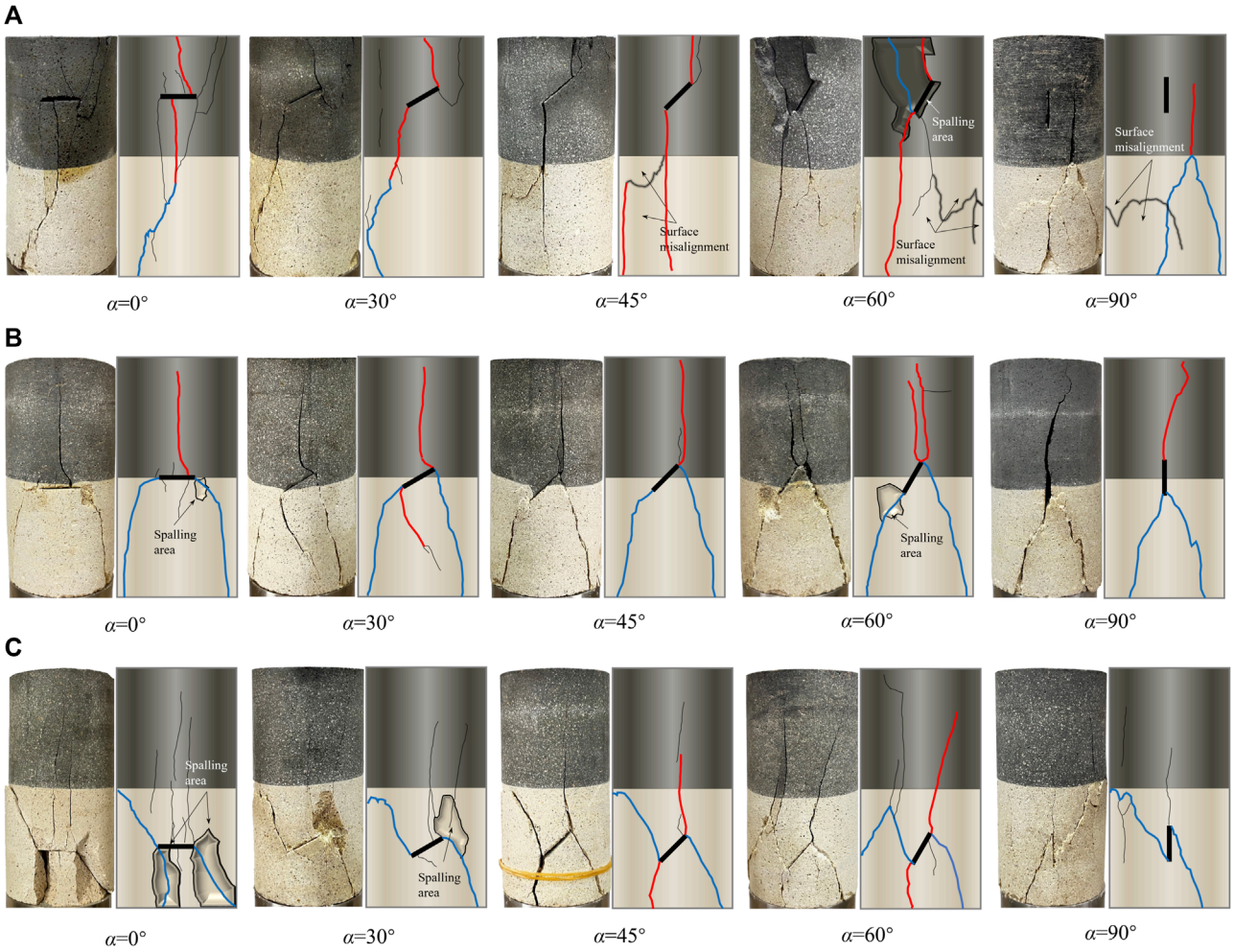

FIGURE 5
The failure mode of composite rock specimens with different fissure angles and positions (σ_3 = 5 MPa). **(A)** Fissure is in limestone, **(B)** Fissure is at the contact interface, **(C)** Fissure is in sandstone.

cracks, but overall, tensile failure predominates. Under α = 0°–60°, tensile cracks generated at the lower part and the lower tip of the fissure easily propagate through the contact interface towards the sandstone end, causing overall failure of the composite rock. However, when α = 0° and 30°, due to the lower strength of the specimen, tensile cracks do not extend to the sandstone end but continue to form shear cracks in the sandstone under the action of axial compression and confining pressure. (2) When the fissure is at the contact interface position, combined with Figure 6, it is observed that in the sandstone part, shear failure leads to the formation of wedge-shaped blocks with distinct signs of sliding friction on the surface. In the limestone part, tensile failure results in a smooth and neat fracture surface, and the failure mode of the specimen is not affected by the fissure angle, exhibiting "λ-shaped failure." This is because the strength of limestone is greater than that of sandstone, and shear cracks generated at both ends of the fissure first extend towards the sandstone end. After forming a wedge-shaped body in the sandstone portion, it continues to be compressed by axial pressure, ultimately leading to tensile failure in limestone. (3) When the fissure is in sandstone, the specimen mainly experiences localized shear failure in the sandstone. This is because the fissure further reduces the strength of the sandstone, and anti-wing shear cracks developed at the ends of the fissure receive sufficient development under lower stress levels. The cracks extend towards the sandstone end and side. Meanwhile, tensile cracks generated by the fissure extend towards the limestone but do not penetrate the limestone portion. (4) Surface sliding and spalling: Surface sliding and spalling mainly occur at the sandstone end and the tip of the fissure. This is primarily due to the sandstone portion and the tip of the fissure being more susceptible to the compressive squeezing effect of confining pressure, resulting in localized substantial shear dilation deformation.

Figure 7 illustrates the failure modes of composite rock specimens under different confining pressures and fissure positions at α = 45°. Under uniaxial compression conditions, the composite rock specimens exhibit conspicuous splitting failure caused by a tensile crack extending along the direction of stress loading (cracks generated can be merged into one). With increasing confining pressure, the following observations are made: (1) The failure modes of all specimens gradually transition from tensile failure to shear

10.3389/fmats.2023.1352243

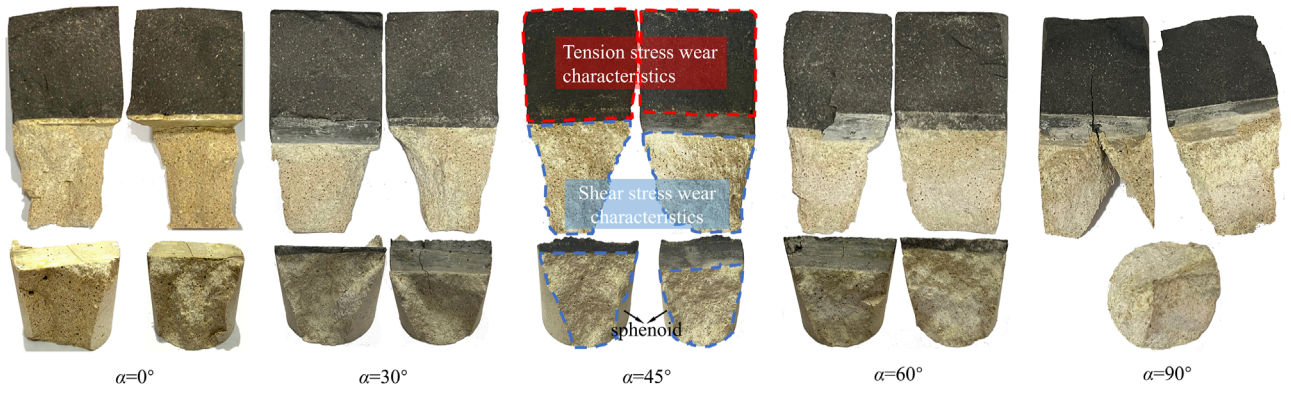

FIGURE 6
Internal wear diagram of composite rock specimens with fissure at the contact interface (σ_3 = 5 MPa).

failure. This is attributed to high confining pressure exerting closure forces on nearly longitudinal cracks, inhibiting the extension of wing-shaped tensile cracks. Additionally, the shear stress acting on the fissure tip becomes more significant, leading to a purer shear failure of the specimen. (2) All specimens experience overall failure. Combined with Figure 8, it is observed that due to the gradual enhancement of shear stress, shear cracks appear at the tips of the fissure in limestone, and the frictional sliding traces on the internal crack fracture surface become more apparent. This ultimately leads to the formation of wedge-shaped bodies in limestone, continuing to be compressed and resulting in overall specimen failure. When the fissure is at the contact interface and in the sandstone, co-planar shear cracks occur at both fissure tips. The specimen slides along the fissure to some extent, and the shear stress developed in the sandstone can extend shear cracks into the limestone, causing shear failure in the limestone portion as well. (3) With the increase in confining pressure, there is an increase in surface spalling. This is attributed to higher confining pressure leading to more effective compaction of the fissure. In this state, the interlocking effect at the fissure tip becomes increasingly pronounced, promoting the extensive development of secondary cracks and resulting in a greater occurrence of local spalling phenomena.

In summary, the geometric distribution of a single fissure has a significant impact on the failure patterns of composite rocks under confining pressure conditions. The analysis of the failure characteristics of each specimen is summarized in Tables 6, 7. From Table 6, it is evident that maintaining a constant confining pressure (σ_3 = 5 MPa), fissure in limestone is prone to generate tensile cracks, leading to the overall failure of the specimen. On the other hand, the fissure tips in sandstone primarily produce shear cracks that are challenging to extend through the contact interface into the limestone, resulting in local failure of the specimen. In this case, the failure mode of the composite rock is dominated by the fissure position, while changes in the fissure angle primarily influence the initiation mode of the specimens. From Table 7, under uniaxial compression conditions, the specimens primarily experience axial splitting failure. With the increase in confining pressure, the failure mode of the specimens gradually transitions from tensile failure to overall shear failure. The influence of the fissure position on the failure of the composite rock becomes less pronounced, indicating a gradual shift in the failure mode of the composite rock to be dominated by the confining pressure.

3.3 Stress-strain behavior of composite specimens

Under 5 MPa confining pressure, the full stress-strain curves of specimens with different fissure angles and positions are depicted in Figure 9. The volumetric strain reflects the overall volume change of the specimen during the loading process and is calculated as follows: $\varepsilon_V = \varepsilon_1 + 2\varepsilon_3$. It can be observed that, with the fissure position held constant, the axial stress-strain trends of all specimens are nearly identical. In the pre-peak stage, as the fissure angle increases, the linear elastic stage of the specimen significantly extends, and the peak stress also rises, gradually approaching that of the intact specimen. However, the plastic yield stage of each specimen is more pronounced compared to the intact specimen. This indicates that an increase in the fissure angle can enhance the strength of the specimen, but the presence of fissure still increases the accumulated damage within the specimen, leading to an elongation of the plastic stage experienced by the specimen before complete failure. In the post-peak stage, due to the constraint of confining pressure, all specimens do not exhibit significant brittle failure characteristics.

The volumetric change trends of all specimens show a pattern of initial contraction followed by expansion. In terms of contraction, the peak volumetric strain of each specimen increases with the rise in fissure angle. This indicates that as the linear elastic stage of the specimen becomes longer with an increasing fissure angle, the ability of the specimen to contract becomes more pronounced. However, the intact rock specimen, without the presence of fissures, does not exhibit significant compression and, therefore, does not possess the strongest contraction ability. In terms of expansion, under the same fissure angle, when the fissure is in the sandstone, the specimen exhibits the weakest expansion ability. This is because

10.3389/fmats.2023.1352243

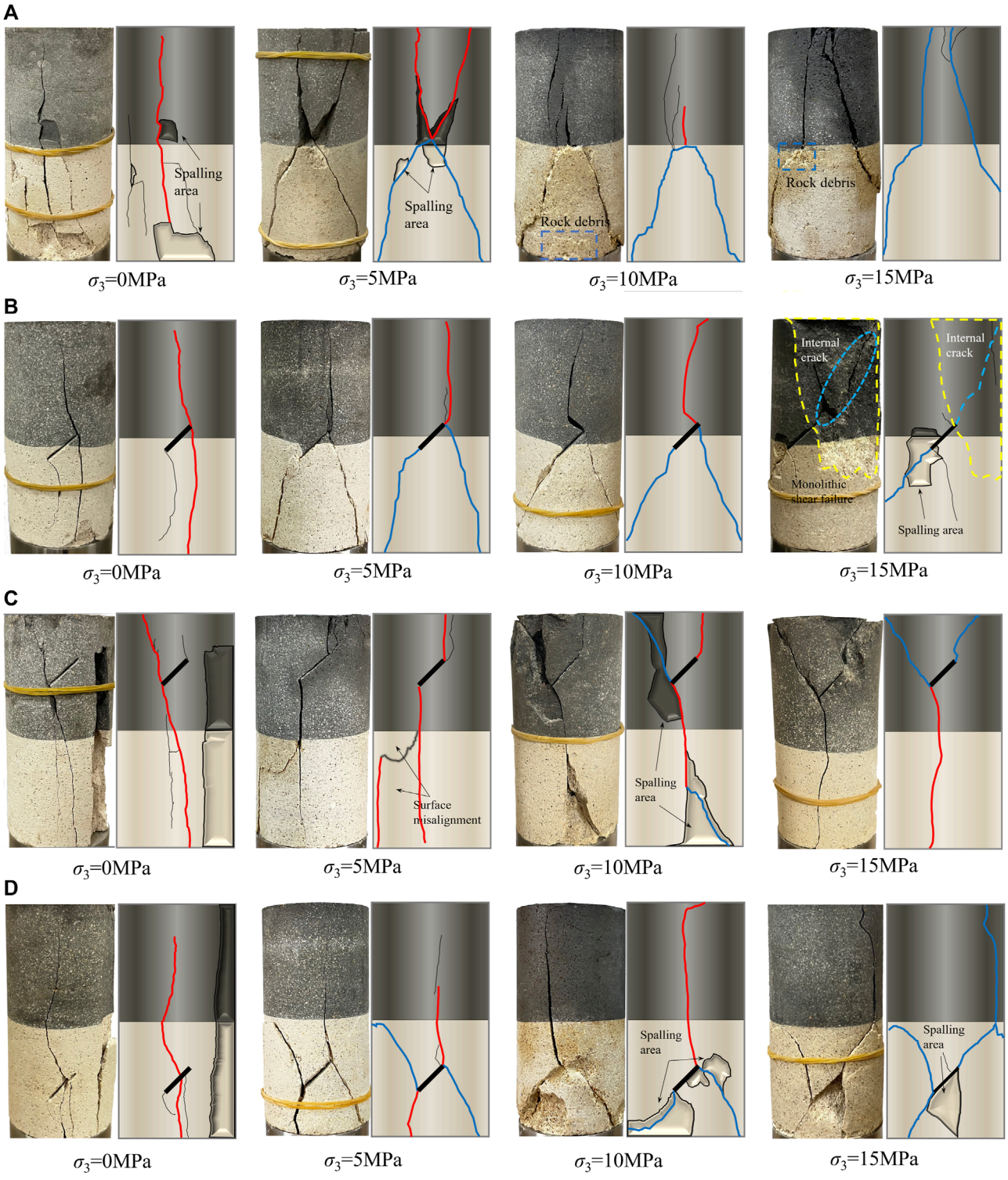

FIGURE 7
The failure mode of rock specimens under different confining pressure and fissure positions (α = 45°). **(A)** Intact specimen, **(B)** Fissure is in limestone, **(C)** Fissure is at the contact interface, **(D)** Fissure is in sandstone.

the FS series specimens experience localized failure in the sandstone during destruction, resulting in a relatively insignificant overall expansion of the specimen. Therefore, at lower confining pressures (σ_3 = 5 MPa), the contraction of the specimen is dominated by the fissure angle, while the expansion is dominated by the fissure position.

10.3389/fmats.2023.1352243

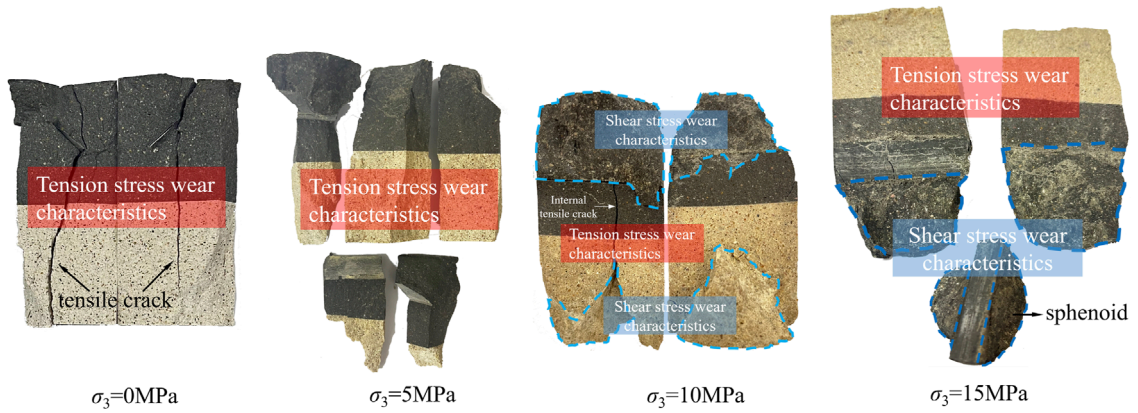

FIGURE 8
Internal wear diagram of composite rock specimens with fissure in the limestone (α = 45°).

TABLE 6 The failure characteristics of composite rock specimens with different fissured angles and positions (σ_3 = 5 MPa).

Fissure position	Fissure angle (°)				
	0	30	45	60	90
Limestone	①More tension and less shear failure	①More tension and less shear failure	①Tensile failure	①More tension and less shear failure	①Tensile-shear mixed failure
	②Overall failure	②Overall failure	②Overall failure	②Overall failure	②Overall failure
Interface	①Tensile-shear mixed failure	①Tensile-shear mixed failure	①Tensile-shear mixed failure	①Tensile-shear mixed failure	①Tensile-shear mixed failure
	②Overall failure	②Overall failure	②Overall failure	②Overall failure	②Overall failure
Sandstone	①Shear failure	①Shear failure	①Less tension and more shear failure	①Less tension and more shear failure	①Shear failure
	②Local failure	②Local failure	②Local failure	②Local failure	②Local failure

TABLE 7 The failure characteristics of composite rock specimens under different confining pressures and fissure positions (α = 45°).

Fissure position	Confining pressure (MPa)			
	0	5	10	15
Intact	①Tensile failure	①Tensile-shear mixed failure	①Less tension and more shear failure	①Shear failure
	②Overall failure	②Overall failure	②Overall failure	②Overall failure
Limestone	①Tensile failure	①Tensile failure	①Less tension and more shear failure	①Less tension and more shear failure
	②Overall failure	②Overall failure	②Overall failure	②Overall failure
Interface	①Tensile failure	①Tensile-shear mixed failure	①Less tension and more shear failure	①Shear failure
	②Overall failure	②Overall failure	②Overall failure	②Overall failure
Sandstone	①Tensile failure	①Less tension and more shear failure	①Less tension and more shear failure	①Shear failure
	②Overall failure	②Local failure	②Overall failure	②Overall failure

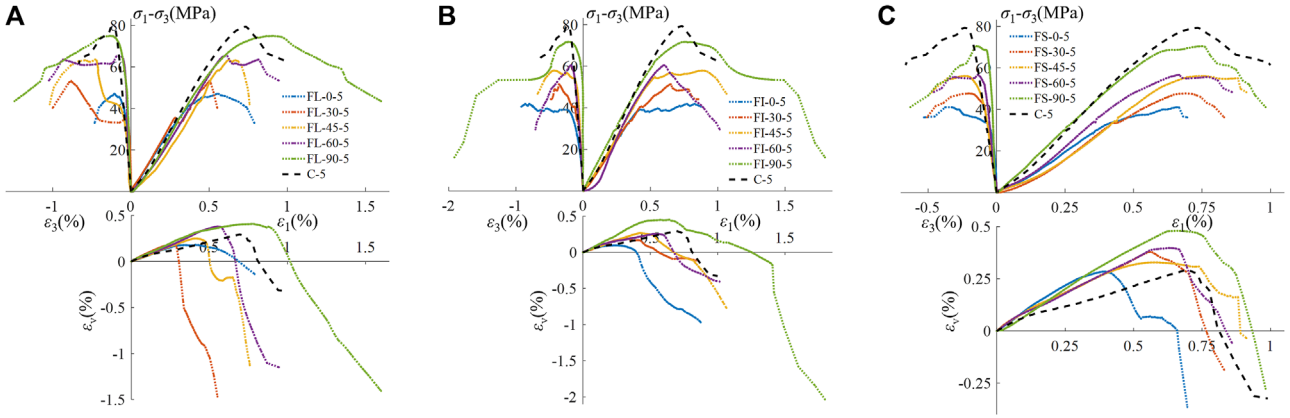

FIGURE 9
Stress-strain curve of rock specimens with different fissured angles and positions. (σ_3 = 5 MPa). **(A)** Fissure is in limestone, **(B)** Fissure is at the contact interface, **(C)** Fissure is in sandstone.

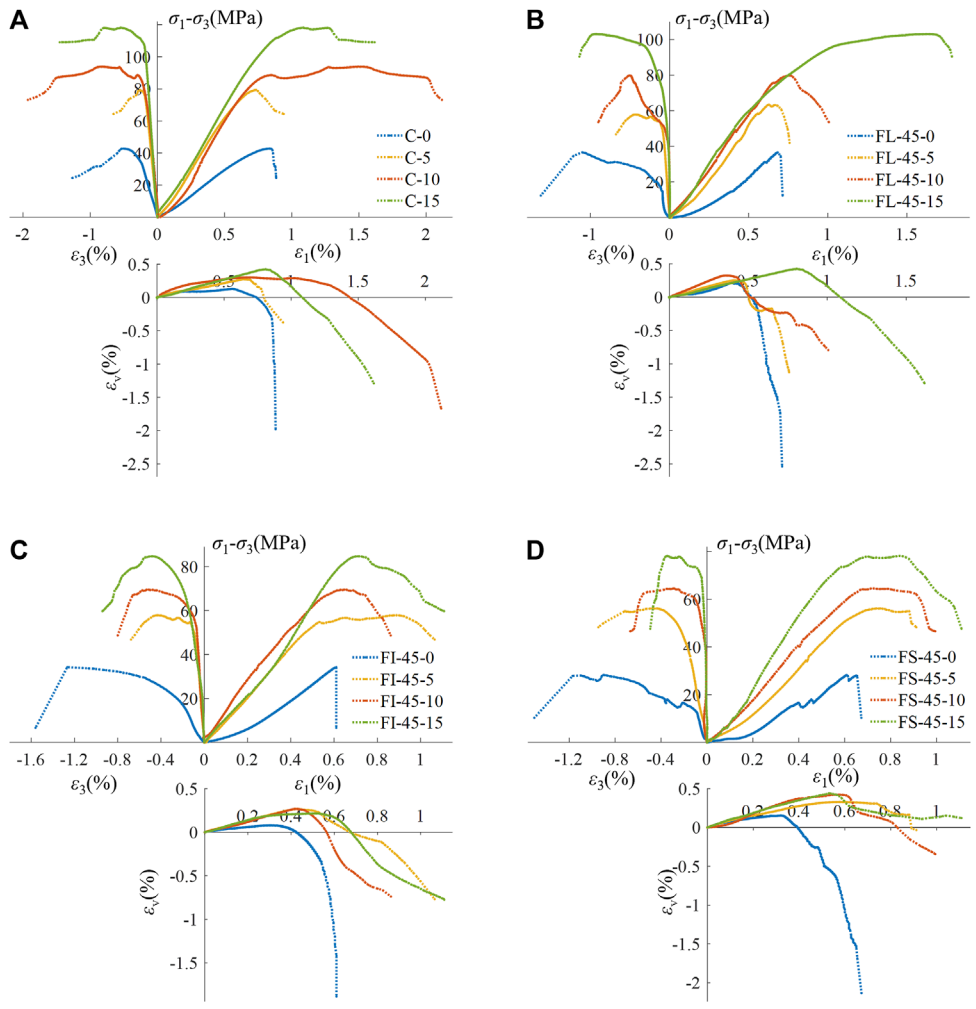

FIGURE 10
Stress-strain curve of rock specimens with different confining pressures and fissure positions (α = 45°). **(A)** Intact specimen, **(B)** Fissure is in limestone, **(C)** Fissure is at the contact interface, **(D)** Fissure is in sandstone.

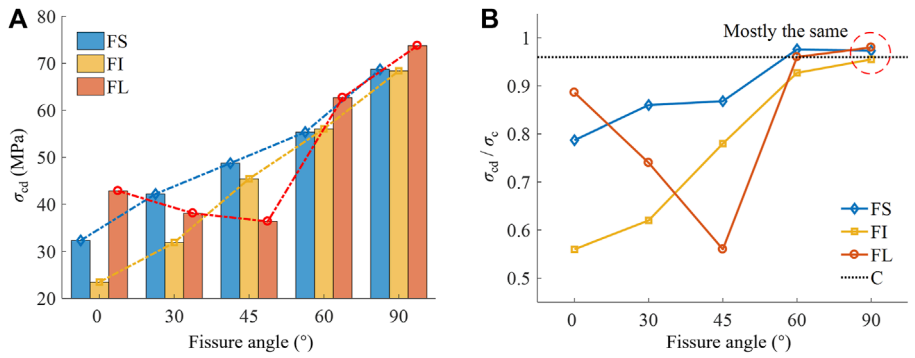

FIGURE 11
Crack damage threshold behavior of rock specimens under different fissure angles and positions (σ_3 = 5 MPa). **(A)** Crack damage threshold, **(B)** Ratios of σcd to peak strength σc.

The full stress-strain curves of various specimens under different confining pressure levels and fissure positions are illustrated in Figure 10. Under uniaxial compression conditions, each specimen exhibits a prolonged compaction stage, sharp peaks appear at the peak stress, followed by a rapid decline after the peak. When the confining pressure is 5 and 10 MPa, the composite rock specimen with a fissure in the limestone part exhibits a stress drop during the loading process, accompanied by a sudden increase in lateral strain, indicating the initiation of macroscopic cracks. The stress-strain curves of the other two types of fissure specimens show similar behavior at this point, with the deformation characteristics of the specimen dominated by the fissure position. As the confining pressure increases to 15 MPa, the compaction stage disappears gradually. The elastic stage and yield stage before the peak becomes significantly extended, and both peak stress and peak strain increase accordingly. This is because, before axial compression, the micro-pores and micro-cracks inside the specimen have been compacted and closed by the confining pressure. After the elastic stage, the macroscopic cracks generated are constrained by the confining pressure and their crack fractured surface interlock and friction with each other. This results in a slow increase in axial bearing capacity, leading to the formation of a plastic flow state characterized by strain hardening during the yield stage. This significantly enhances the strength and ductility of the specimen. At this point, the influence of the fissure position on the mechanical deformation characteristics of the rock specimen diminishes, gradually being dominated by the confining pressure.

Under uniaxial compression conditions, the maximum values of volumetric contraction for all specimens are relatively small and similar. With the increase in confining pressure, the maximum values of volumetric contraction for most specimens become closer, showing an overall trend of slow growth at high confining pressures. In terms of volumetric expansion, regardless of the magnitude of the confining pressure, the degree of volumetric expansion in the composite rock specimens with a fissure in the sandstone portion is the smallest. Even after complete failure under high confining pressure, the overall volume remains contracted. The reason is that when the fissure is in the sandstone, the damage to the limestone part is minimal, resulting in the smallest overall expansion of the specimen. Therefore, the volumetric contraction of the specimen is dominated by confining pressure, while volumetric expansion is dominated by the fissure position.

3.4 Variations in the mechanical properties of composite specimens

3.4.1 Crack damage threshold behavior

The crack damage threshold (σ_{cd}) is crucial in the rock failure process, representing the axial stress corresponding to the volumetric strain peak (Lee and Rathnaweera, 2016). Before reaching σ_{cd}, the volumetric strain caries in the same direction as the axial stress, therefore the specimen is characterized as in a compaction stage, indicating that the specimen is in the compression stage, and the cracks are steadily expanding. Once the axial stress exceeds σ_{cd}, the volumetric strain decreases continuously, indicating that the specimen enters the dilation stage. At this point, cracks begin to connect, intersect, and penetrate, evolving into a macroscopic fracture surface. The crack extension enters an unstable stage, and irreversible damage occurs in the specimen (Huang et al., 2016). The relative damage threshold (σ_{cd}/σ_c) serves as a reliable indicator for predicting specimen failure (Wu et al., 2018). A smaller value implies earlier dilation and more unstable crack propagation.

Figure 11 illustrates the variations of crack damage threshold (σ_{cd}) and relative damage threshold (σ_{cd}/σ_c) of rock specimens with different fissure angles and positions. As shown in Figure 11A, the damage stress (σ_{cd}) of the composite rock specimens with fissure at the contact interface and in the sandstone increases significantly with the fissure angle, by 187.11% and 112.62%, respectively. However, when the fissure angle $\alpha < 45°$ and the crack is in the limestone, the damage stress (σ_{cd}) of the composite rock samples shows a negative correlation with the crack angle. Combining the analysis of the failure modes of the specimens in Figure 5A, it can be explained that when $\alpha = 0°–45°$, the proportion of tensile cracks in the FL series specimens gradually increases and becomes purer. The generation of tensile cracks not only significantly reduces the strength of the specimens but also increases lateral deformation, causing an overall increase in specimen volume. In Figure 11B, it

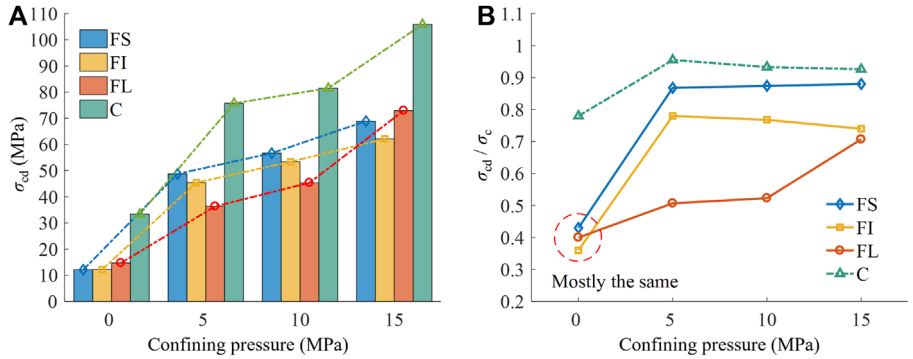

FIGURE 12
Crack damage threshold behavior of rock specimens under different confining pressures and fissure positions (α = 45°). **(A)** Crack damage threshold, **(B)** Ratios of σcd to peak strength σc.

can be observed that the relative damage threshold of the FS series specimens remains consistently the highest and exhibits the most gradual trend, indicating that the crack propagation is most stable when the fissure is in the sandstone. When α = 90°, the relative damage threshold of all specimens is almost the same, indicating the lowest level of damage caused by the fissure at this angle.

Figure 12 displays the crack damage threshold (σ_{cd}) and the relative damage threshold (σ_{cd}/σ_c) of rock specimens under different fissure positions and confining pressures. In Figure 12A, it is evident that σ_{cd} for each specimen increases with the rise in confining pressure. As the confining pressure increases from 5 to 15 MPa, the growth rates of σ_{cd} for the FS, FI, FL, and C series specimens are 41.35%, 12.09%, 141.28%, and 39.79%, respectively, with FL series showing the highest increment. When σ_3 is 5 and 10 MPa, the FL series specimens exhibit the lowest damage stress σ_{cd}. This is attributed to the fissure in the limestone that is prone to the early formation of macroscopic tensile cracks. However, under the constraint of confining pressure, the crack surfaces fractured interlock with each other, allowing the specimen to continue gaining higher bearing capacity. This also explains why some FL specimens exhibit stress drops during the loading process. Figure 12B, under uniaxial compression, the relative damage thresholds of fissured specimens show minimal variation, remaining between 0.36 and 0.43, significantly lower than that of intact specimens. Under triaxial compression, with constant confining pressure, the relative damage thresholds of the FS, FI, and FL series specimens decrease sequentially. When the fissure position remains unchanged, the relative damage threshold of the FL series increases with the rise in confining pressure, while those of the FI and FS series specimens remain stable. It is observed that during uniaxial compression, the fissure has a severe weakening effect on the expansion strength of specimens, and the unstable expansion of cracks occurs earliest, with minimal influence from changes in fissure position. When the fissure is in the sandstone, the expansion of cracks in the composite rock specimens remains stable.

3.4.2 Peak stress behavior

The peak stress (σ_c) and relative peak stress (σ_c/σ_i) of each specimen under different fissure angles and positions are shown in Figure 13. The relative peak stress indicates the ratio of peak strength between specimens with fissures and intact specimens, reflecting the degree of deterioration in rock with fissures, a smaller numerical value corresponds to a greater degree of deterioration.

As depicted in Figure 13A, the peak stress of each specimen increases with the rise in fissure angle and position, but the growth trends vary. In the same rock layer, as the fissure angle transitions from α = 0° to α = 90°, the stress increments for the FS, FI, and FL series are 71.83%, 71.36%, and 55.09%, respectively. Under the same fissure angle, the stress increments from the FS series to the FL series are 17.10%, 9.44%, 6.02%, 15.17%, and 6.23%. It is evident that, under lower confining pressure (σ_3 = 5 MPa), the strength of specimens is notably influenced by changes in fissure angle. Figure 13B reveals that the degree of strength deterioration in specimens is minimal when a fissure is present in limestone; larger fissure angles correspond to less deterioration in specimen strength.

The peak stress (σ_c) and relative peak stress (σ_c/σ_i) of each specimen under different confining pressures and fissure positions are illustrated in Figure 14. As depicted in Figure 14A, with a constant fissure position, the strengths of FS, FI, FL, and C series specimens all significantly increase with the rise in confining pressure (σ_3 = 5–15 MPa), with increments of 39.28%, 46.32%, 62.31%, and 48.88%, respectively. With constant confining pressure, specimens with a fissure in limestone exhibit the highest strength, while those in sandstone show the lowest, with the maximum difference at σ_3 = 15 MPa being 31.83%. This implies that when a fissure is in limestone, specimens can attain higher bearing capacity under the restriction of confining pressure. Consequently, it is evident that the influence of fissure position on the strength of composite rock specimens gradually increases with the augmentation of confining pressure. As indicated in Figure 14B, compared to changes in confining pressure, the degradation of rock is primarily affected by fissure position, with the least deterioration observed when a fissure is in limestone.

3.4.3 Elastic modulus

Figure 15A presents the relationship between the elastic modulus and the fissure angle for the three series of specimens.

10.3389/fmats.2023.1352243

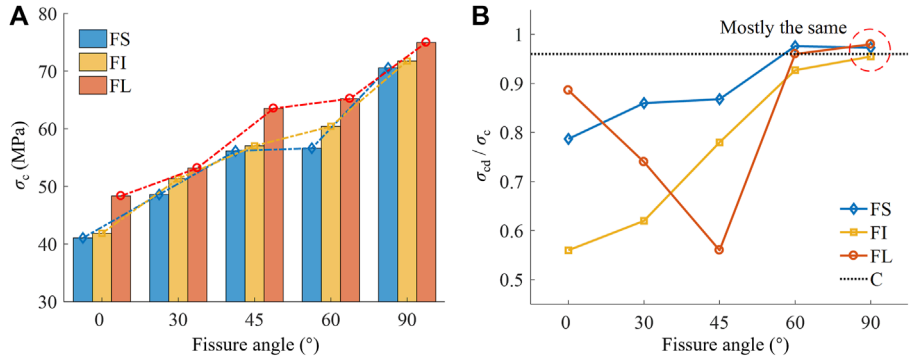

FIGURE 13
Peak stress behavior of rock specimens under different fissure angles and positions (σ_3 = 5 MPa). **(A)** peak stress, **(B)** ratios of σc to σl.

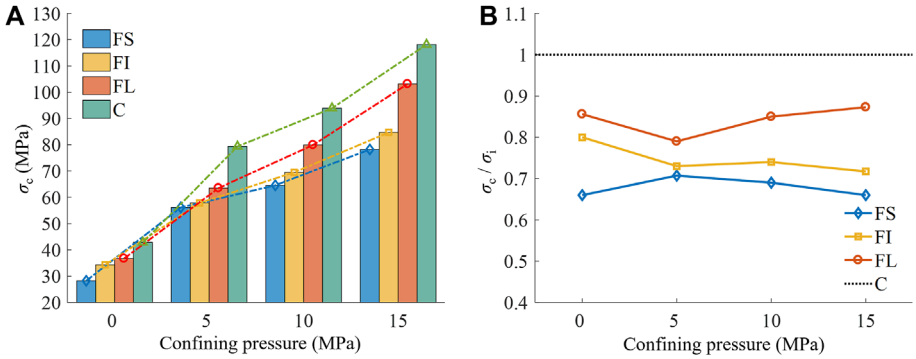

FIGURE 14
Peak stress behavior of rock specimens under different confining pressures and fissure positions (α = 45°). **(A)** peak stress, **(B)** ratios of σc to σl.

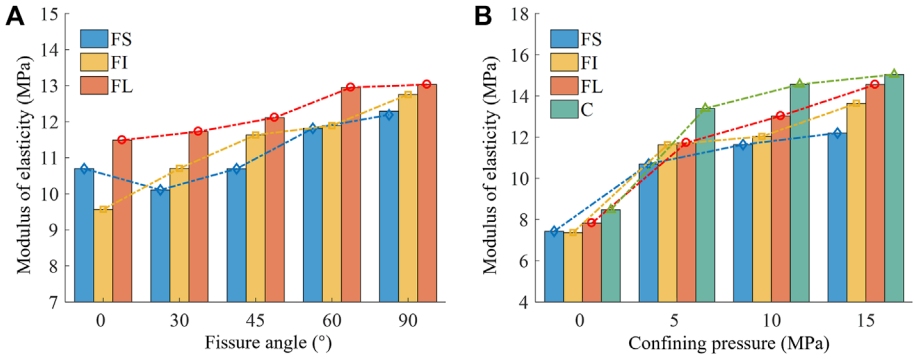

FIGURE 15
Peak stress behavior of rock specimens under different confining pressures and fissure positions (α = 45°). **(A)** Under different fissure angles and positions, **(B)** Under different confining pressures and fissure positions.

The elastic modulus increases with an increasing fissure angle, but the growth trends differ. Within the fissure angle range of 0°–90°, the FL specimens exhibit the smallest increase in elastic modulus (13.43%), while the FI specimens show the largest increase (33.31%).

Keeping the fissure angle constant, except for α = 0°, the variation in elastic modulus with fissure position follows a similar pattern to the changes in peak stress. It is worth noting that the FI-0-5 specimen deviated from the expected results due to difficulties

in precisely positioning the fissure in the interface, caused by mold errors.

Figure 15B illustrates the variations in elastic modulus for four series specimens under different confining pressures. The experimental results indicate that, with a constant fissure position, the elastic modulus of the rock specimens significantly increases with the application of confining pressure, exhibiting an average increment of 52.43%. However, as the confining pressure increases from 5 to 15 MPa, the rate of elastic modulus growth slows down, with an average increment of 16.92%. Under fixed confining pressure, the elastic modulus of the rock specimens increases sequentially from limestone, through the contact zone, to sandstone as the crack position changes. This increasing trend becomes more pronounced with higher confining pressures.

4 Conclusion

Unlike previous studies, a series of triaxial compression tests on limestone-sandstone composite rock-like material containing a single fissure in this paper. The experimental results comprehensively evaluate the influence of the positions and inclination angles (relative to the horizontal) of a pre-existing fissure on the mechanical properties, crack evolution behavior, and failure mode under different confining pressures. The main conclusions in this study can be drawn as follows.

(1) Limestone exhibits the highest strength, while sandstone experiences the most deformation and is susceptible to early macroscopic cracking. The intact composite rock falls between sandstone and limestone in terms of mechanical deformation, with its strength controlled by the sandstone portion and overall deformation constrained by the limestone portion.

(2) At α = 0°, tension cracks develop in the middle of the fissure; at α = 90°, tension cracks are less likely. Other angles result in crack initiation at the fissure tip, with the fissure angle determining the initiation mode of initial cracks. Under low confining pressure, the fissure in limestone leads to tension cracks, causing overall failure. Conversely, the fissure in sandstone primarily produces shear cracks, causing localized failure. With increased confining pressure, the failure mode shifts from tension to shear, and the extent of damage transitions to overall failure, the factor influencing the failure mode becomes the confining pressure.

(3) Increasing the fissure angle and confining pressure prolong the linear elastic stage and enhance ductility in the composite rock. In terms of volumetric strain, Volume shrinkage is influenced by both fissure angle and confining pressure, while volume expansion is affected by fissure position. Higher fissure angle and confining pressure increase volume shrinkage, and when the fissure is in the sandstone, volume expansion is consistently minimal.

(4) Crack damage threshold serves as a crucial indicator for preventing rock mass failure. Under uniaxial compression, the crack propagation in the composite rock is the most unstable, leading to the earliest occurrence of failure. In triaxial compression with constant confining pressure, higher fissure angles lead to more stable crack propagation. With a constant fissure position, increasing confining pressure stabilizes crack propagation when the fissure is in the limestone. When the fissure is in the sandstone, crack propagation in the composite rock remains most stable. Additionally, peak strength and elastic modulus increase with higher fissure angles, greater confining pressure, and changes in fissure position from sandstone to the contact interface and limestone. As opposed to the fissure position and confining pressure, the crack degradation in composite rock is primarily influenced by the fissure angle.

Data availability statement

The original contributions presented in the study are included in the article/Supplementary Material, further inquiries can be directed to the corresponding author.

Author contributions

TX: Data curation, Formal Analysis, Investigation, Software, Writing–original draft. KX: Funding acquisition, Methodology, Project administration, Resources, Supervision, Writing–review and editing. YL: Methodology, Writing–review and editing. HS: Methodology, Writing–review and editing.

Funding

The author(s) declare financial support was received for the research, authorship, and/or publication of this article. National Natural Science Foundation of China [No. 52274007], Open Fund of Hubei Key Laboratory of Oil and Gas Drilling and Production Engineering (Yangtze University) [NO: YQZC202204], Open Fund Project of Key Laboratory of Well Stability and Fluid and Rock Mechanics in Oil and Gas Reservoir of Shanxi Province [WSFRM20210101001], Open Research Fund of Key Laboratory of Reservoir and Dam Safety Ministry of Water Resources [NO: YK323003].

Conflict of interest

Author YL was employed by Jingzhou Chengfa Construction Engineering Group Co., Ltd.

The remaining authors declare that the research was conducted in the absence of any commercial or financial relationships that could be construed as a potential conflict of interest.

Publisher's note

References

Bi, J., and Zhou, X. (2017). A novel numerical algorithm for simulation of initiation, propagation and coalescence of flaws subject to internal fluid pressure and vertical stress in the framework of general particle dynamics. *Rock Mech. Rock Eng.* 50, 1833–1849. doi:10.1007/s00603-017-1204-4

Brady, B. H., and Brown, E. T. (2006). *Rock mechanics: for underground mining*. Berlin, Germany: Springer science and business media.

Cai, W. B., Li, Y., Gao, K., and Wang, K. (2022). Crack propagation mechanism in rock-like specimens containing intermittent flaws under shear loading. *Theor. Appl. Fract. Mech.* 117, 103187. doi:10.1016/j.tafmec.2021.103187

Cao, R. H., Cao, P., Fan, X., Xiong, X. G., and Lin, H. (2016). An experimental and numerical study on mechanical behavior of ubiquitous-joint brittle rock-like specimens under uniaxial compression. *Rock Mech. Rock Eng.* 49, 4319–4338. doi:10.1007/s00603-016-1029-6

Chen, S. J., Yin, D. W., Jiang, N., Wang, F., and Zhao, Z. H. (2019). Mechanical properties of oil shale-coal composite samples. *Int. J. Rock Mech. Min. Sci.* 123, 104120. doi:10.1016/j.ijrmms.2019.104120

Cheng, F. Q., Li, Z. H., Li, G. A., Wei, Y., Yin, S., Liu, S. J., et al. (2018). Influence of prefabricated fissure angle on sandstone damage and infrared radiation temperature characteristics. *J. Geophys. Eng.* 15, 1187–1196. doi:10.1088/1742-2140/aaacaf

Chen, X., Zhang, S. F., and Cheng, C. (2018). Numerical study on effect of joint strength mobilization on behavior of rock masses with large nonpersistent joints under uniaxial compression. *Int. J. Geomechanics* 18, 04018140. doi:10.1061/(ASCE)GM.1943-5622.0001260

Du, H. B., Dai, F., Xu, Y., Yan, Z. L., and Wei, M. D. (2020a). Mechanical responses and failure mechanism of hydrostatically pressurized rocks under combined compression-shear impacting. *Int. J. Mech. Sci.* 165, 105219. doi:10.1016/j.ijmecsci.2019.105219

Du, Y. T., Li, T. C., Li, W. T., Ren, Y. D., Wang, G., and He, P. (2020b). Experimental study of mechanical and permeability behaviors during the failure of sandstone containing two preexisting fissures under triaxial compression. *Rock Mech. Rock Eng.* 53, 3673–3697. doi:10.1007/s00603-020-02119-x

Fairhurst, C. (2017). Some challenges of deep mining. *Engineering* 3, 527–537. doi:10.1016/J.ENG.2017.04.017

Feng, P., Dai, F., Liu, Y., Xu, N. W., and Du, H. B. (2019). Coupled effects of static-dynamic strain rates on the mechanical and fracturing behaviors of rock-like specimens containing two unparallel fissures. *Eng. Fract. Mech.* 207, 237–253. doi:10.1016/j.engfracmech.2018.12.033

Guo, W. Y., Tan, Y. L., Yu, F. H., Zhao, T. B., Hu, S. C., Huang, D. M., et al. (2018). Mechanical behavior of rock-coal-rock specimens with different coal thicknesses. *Geomechanics Eng.* 15, 1017–1027. doi:10.12989/gae.2018.15.4.1017

Huang, B. X., and Liu, J. W. (2013). The effect of loading rate on the behavior of samples composed of coal and rock. *Int. J. Rock Mech. Min. Sci.* 61, 23–30. doi:10.1016/j.ijrmms.2013.02.002

Huang, D., Gu, D., Yang, C., Huang, R., and Fu, G. (2016). Investigation on mechanical behaviors of sandstone with two preexisting flaws under triaxial compression. *Rock Mech. Rock Eng.* 49, 375–399. doi:10.1007/s00603-015-0757-3

Hu, J., Wen, G., Lin, Q., Cao, P., and Li, S. (2020). Mechanical properties and crack evolution of double-layer composite rock-like specimens with two parallel fissures under uniaxial compression. *Theor. Appl. Fract. Mech.* 108, 102610. doi:10.1016/j.tafmec.2020.102610

Ismael, M., and Konietzky, H. (2019). Constitutive model for inherent anisotropic rocks: ubiquitous joint model based on the Hoek-Brown failure criterion. *Comput. Geotechnics* 105, 99–109. doi:10.1016/j.compgeo.2018.09.016

Ivars, D. M., Pierce, M. E., Darcel, C., Reyes-Montes, J., Potyondy, D. O., Young, R. P., et al. (2011). The synthetic rock mass approach for jointed rock mass modelling. *Int. J. Rock Mech. Min. Sci.* 48, 219–244. doi:10.1016/j.ijrmms.2010.11.014

Jia, M. K. (2007). Research on roof falling mechanism of deteriorative strata combination supported by bolts. *Rock Soil Mech.* 28, 1343. doi:10.1016/S1872-5813(07)60008-5

Jiang, R. C., Dai, F., Liu, Y., and Li, A. (2021). Fast marching method for microseismic source location in cavern-containing rockmass: performance analysis and engineering application. *Engineering* 7, 1023–1034. doi:10.1016/j.eng.2020.10.019

Laghaei, M., Baghbanan, A., Hashemolhosseini, H., and Dehghanipoodeh, M. (2018). Numerical determination of deformability and strength of 3D fractured rock mass. *Int. J. rock Mech. Min. Sci.* 110, 246–256. doi:10.1016/j.ijrmms.2018.07.015

Le, H. L., Sun, S. R., Kulatilake, P. H., and Wei, J. H. (2018). Effect of grout on mechanical properties and cracking behavior of rock-like specimens containing a single flaw under uniaxial compression. *Int. J. Geomechanics* 18, 04018129. doi:10.1061/(ASCE)GM.1943-5622.0001225

Lee, B., and Rathnaweera, T. (2016). Stress threshold identification of progressive fracturing in Bukit Timah granite under uniaxial and triaxial stress conditions. *Geomechanics Geophys. Geo-Energy Geo-Resources* 2, 301–330. doi:10.1007/s40948-016-0037-z

Lee, H., and Jeon, S. (2011). An experimental and numerical study of fracture coalescence in pre-cracked specimens under uniaxial compression. *Int. J. Solids Struct.* 48, 979–999. doi:10.1016/j.ijsolstr.2010.12.001

Li, J. G., Yu, Z. Q., Zhou, Z. Y., Wang, Y. C., and Li, J. W. (2021). Mechanical analysis and failure modes prediction of composite rock under uniaxial compression. *Sci. Rep.* 11, 22826. doi:10.1038/s41598-021-02331-x

Lin, Q. B., Cao, P., Cao, R. H., Lin, H., and Meng, J. J. (2020). Mechanical behavior around double circular openings in a jointed rock mass under uniaxial compression. *Archives Civ. Mech. Eng.* 20, 19–18. doi:10.1007/s43452-020-00027-z

Liu, S. H. (2014). Nonlinear catastrophy model and chaotic dynamic mechanism of compound coal-rock unstable failure under coupled static-dynamic loading. *J. China Coal Soc.* 39, 292–300. doi:10.13225/j.cnki.jccs.2013.2007

Liu, S. H., Mao, D. B., Ji, Q. X., and Li, F. M. (2014). Under static loading stress wave propagation mechanism and energy dissipation in compound coalrock. *J. China Coal Soc.* 39, 15–22. doi:10.13225/j.cnki.jccs.2013.0411

Liu, W. J., Yang, K., Zhen, W., Chi, X. L., Xu, R. J., and Lv, X. (2021). Energy dissipation and failure characteristics of layered composite rocks under impact load. *Shock Vib.* 2021, 1–14. doi:10.1155/2021/8775338

Lu, J., Huang, G., Gao, H., Li, X., Zhang, D. M., and Yin, G. Z. (2020). Mechanical properties of layered composite coal–rock subjected to true triaxial stress. *Rock Mech. Rock Eng.* 53, 4117–4138. doi:10.1007/s00603-020-02148-6

Lu, J., Yin, G. Z., Deng, B. Z., Zhang, W. Z., Li, M. H., Chai, X. W., et al. (2019). Permeability characteristics of layered composite coal-rock under true triaxial stress conditions. *J. Nat. Gas Sci. Eng.* 66, 60–76. doi:10.1016/j.jngse.2019.03.023

Ma, Q., Liu, X. L., Tan, Y. L., Elsworth, D., Shang, J. L., Song, D. Q., et al. (2023). Numerical study of mechanical properties and microcrack evolution of double-layer composite rock specimens with fissures under uniaxial compression. *Eng. Fract. Mech.* 289, 109403. doi:10.1016/j.engfracmech.2023.109403

Ma, Q., Tan, Y., Liu, X., Zhao, Z., Fan, D., and Purev, L. (2021). Experimental and numerical simulation of loading rate effects on failure and strain energy characteristics of coal-rock composite samples. *J. Central South Univ.* 28, 3207–3222. doi:10.1007/s11771-021-4831-6

Miao, S. T., Pan, P. Z., Wu, Z. H., Li, S. J., and Zhao, S. K. (2018). Fracture analysis of sandstone with a single filled flaw under uniaxial compression. *Eng. Fract. Mech.* 204, 319–343. doi:10.1016/j.engfracmech.2018.10.009

Nazir, R., Momeni, E., Armaghani, D. J., and Amin, M. M. (2013). Correlation between unconfined compressive strength and indirect tensile strength of limestone rock samples. *Electron J. Geotech. Eng.* 18, 1737–1746.

Ranjith, P. G., Zhao, J., Ju, M. H., De Silva, R. V., Rathnaweera, T. D., and Bandara, A. K. (2017). Opportunities and challenges in deep mining: a brief review. *Engineering* 3, 546–551. doi:10.1016/J.ENG.2017.04.024

Song, D. Z., Wang, E. Y., and Liu, J. (2012). Relationship between EMR and dissipated energy of coal rock mass during cyclic loading process. *Saf. Sci.* 50, 751–760. doi:10.1016/j.ssci.2011.08.039

Tien, Y. M., Kuo, M. C., and Juang, C. H. (2006). An experimental investigation of the failure mechanism of simulated transversely isotropic rocks. *Int. J. rock Mech. Min. Sci.* 43, 1163–1181. doi:10.1016/j.ijrmms.2006.03.011

Vogel, M., and Rast, H. (2000). AlpTransit—safety in construction as a challenge: health and safety aspects in very deep tunnel construction. *Tunn. Undergr. Space Technol.* 15, 481–484. doi:10.1016/S0886-7798(01)00018-9

Wang, Q. H., Wang, J., Ye, Y. C., Jiang, W., and Yao, N. (2020). Failure characteristics and strength model of composite rock samples in contact zone under compression. *Archives Min. Sci.* 65. doi:10.24425/ams.2020.133197

Wang, W. Q., Ye, Y. C., Wang, Q. H., and Hu, N. Y. (2022). Experimental study on anisotropy of strength, deformation and damage evolution of contact zone composite rock with DIC and AE techniques. *Rock Mech. Rock Eng.* 55, 837–853. doi:10.1007/s00603-021-02682-x

Wang, Y. L., Tang, J. X., Dai, Z. Y., and Yi, T. (2018). Experimental study on mechanical properties and failure modes of low-strength rock samples containing different fissures under uniaxial compression. *Eng. Fract. Mech.* 197, 1–20. doi:10.1016/j.engfracmech.2018.04.044

Wittke, W. (2014). *Rock mechanics based on an anisotropic jointed rock model (AJRM)*. Hoboken, New Jersey, United States: John Wiley and Sons.

Wong, R. H., Guo, Y., Li, L., Chau, K. T., Zhu, W., and Li, S. (2006). "Anti-wing crack growth from surface flaw in real rock under uniaxial compression," in Fracture of Nano and Engineering Materials and Structures: Proceedings of the 16th European Conference of Fracture, Alexandroupolis, Greece, July, 2006, 825–826.

Wong, R., Huang, M. L., Jiao, M. R., Tang, C. A., and Zhu, W. S. (2004a). The mechanisms of crack propagation from surface 3-D fracture under uniaxial compression. *Key Eng. Mater.* 261, 219–224. doi:10.4028/www.scientific.net/kem.261-263.219

Wong, R., Law, C., Chau, K. T., and Shen Zhu, W. (2004b). Crack propagation from 3-D surface fractures in PMMA and marble specimens under uniaxial compression. *Int. J. Rock Mech. Min. Sci.* 41, 37–42. doi:10.1016/j.ijrmms.2004.03.016

Wu, J. Y., Feng, M. M., Chen, Z. Q., Mao, X. B., Han, G. S., and Wang, Y. M. (2018). Particle size distribution effects on the strength characteristic of cemented paste backfill. *Minerals* 8, 322. doi:10.3390/min8080322

Xiao, C. F., Lin, X., Wu, G., and Qiu, X. D. (1988). Effect of interlayer bond strength on compressive mechanical properties of composite rock. *J. Chongqing Univ. Nat. Sci.*, 125–131.

Yan, Z. L., Wu, W., Dai, F., and Liu, Y. (2023). Dynamic mechanical response and damage constitutive model of multi-flawed rocks under high strain rates. *Rock Mech. Rock Eng.* 56, 4405–4425. doi:10.1007/s00603-023-03289-0

Yang, S. Q., Yin, P. F., Huang, Y. H., and Cheng, J. L. (2019). Strength, deformability and X-ray micro-CT observations of transversely isotropic composite rock under different confining pressures. *Eng. Fract. Mech.* 214, 1–20. doi:10.1016/j.engfracmech.2019.04.030

Yang, J., Chen, R., Zhang, Z., Zou, Y., Zhou, J., and Xia, J. (2023). Experimental study on the ultimate bearing capacity of damaged RC arches strengthened with ultra-high performance concrete. *Eng. Struct.* 279, 115611. doi:10.1016/j.engstruct.2023.115611

Yin, D. W., Chen, S. J., Chen, B., Liu, X. Q., and Ma, H. F. (2018). Strength and failure characteristics of the rock-coal combined body with single joint in coal. *Geomechanics Eng.* 15, 1113–1124. doi:10.12989/gae.2018.15.5.1113

Yu, X., Kemeny, J., Li, J. L., Song, W. D., and Tan, Y. Y. (2021a). 3D observations of fracturing in rock-backfill composite specimens under triaxial loading. *Rock Mech. Rock Eng.* 54, 6009–6022. doi:10.1007/s00603-021-02498-9

Yu, X., Kemeny, J., Tan, Y. Y., Song, W. D., and Huang, K. (2021b). Mechanical properties and fracturing of rock-backfill composite specimens under triaxial compression. *Constr. Build. Mater.* 304, 124577. doi:10.1016/j.conbuildmat.2021.124577

Yu, X., Song, W. D., Tan, Y. Y., Kemeny, J., and Wang, J. (2022). Energy dissipation and 3d fracturing of Backfill-encased-rock under triaxial compression. *Constr. Build. Mater.* 341, 127877. doi:10.1016/j.conbuildmat.2022.127877

Zhang, K., Liu, X. H., Liu, W. L., and Zhang, S. (2021). Influence of weak inclusions on the fracturing and fractal behavior of a jointed rock mass containing an opening: experimental and numerical studies. *Comput. Geotechnics* 132, 104011. doi:10.1016/j.compgeo.2021.104011

Zhang, Z., Pang, K., Xu, L., Zou, Y., Yang, J., and Wang, C. (2023). The bond properties between UHPC and stone under different interface treatment methods. *Constr. Build. Mater.* 365, 130092. doi:10.1016/j.conbuildmat.2022.130092

Zhao, Z. H., Wang, W. M., Wang, L. H., and Dai, C. Q. (2015). Compression–shear strength criterion of coal–rock combination model considering interface effect. *Tunn. Undergr. Space Technol.* 47, 193–199. doi:10.1016/j.tust.2015.01.007

Zhao, Z. H., Wang, W. M., and Yan, J. X. (2013). Strain localization and failure evolution analysis of soft rock-coal-soft rock combination model. *J. Appl. Sci.* 13, 1094–1099. doi:10.3923/jas.2013.1094.1099

Zou, Y., Jiang, J., Yang, J., Zhang, Z., and Guo, J. (2023). Enhancing the toughness of bonding interface in steel-UHPC composite structure through fiber bridging. *Cem. Concr. Compos.* 137, 104947. doi:10.1016/j.cemconcomp.2023.104947

Zuo, J. P., Wang, Z. F., Zhou, H. W., Pei, J. L., and Liu, J. F. (2013). Failure behavior of a rock-coal-rock combined body with a weak coal interlayer. *Int. J. Min. Sci. Technol.* 23, 907–912. doi:10.1016/j.ijmst.2013.11.005

frontiers | Frontiers in Materials

TYPE Original Research
PUBLISHED 02 February 2024
DOI 10.3389/fmats.2023.1309617

OPEN ACCESS

EDITED BY
Zhongya Zhang,
Chongqing Jiaotong University, China

REVIEWED BY
Viorel Paleu,
Gheorghe Asachi Technical University of Iași, Romania
Femiana Gapsari,
University of Brawijaya, Indonesia

*CORRESPONDENCE
Zhantao Li,
xjtelzt@163.com

RECEIVED 08 October 2023
ACCEPTED 20 November 2023
PUBLISHED 02 February 2024

CITATION
Wang Y, Li Z, Gu Y, Zhang H, Zhao P, Wang Y and Yang J (2024), Experimental study on wear failure of spindle hook teeth of cotton picker.
Front. Mater. 10:1309617.
doi: 10.3389/fmats.2023.1309617

Experimental study on wear failure of spindle hook teeth of cotton picker

Yugang Wang[1], Zhantao Li[2]*, Yanqing Gu[3], Hongwen Zhang[3], Pengda Zhao[2], Yongzheng Wang[2] and Jianning Yang[2]

[1]Shandong Swan Cotton Industrial Machinery Stock Co., Ltd., Jinan, China, [2]Xinjiang Swan Modernization Agricultural Machinery Equipment Co., Ltd., Wujiaqu, China, [3]College of Mechanical and Electrical Engineering, Shihezi University, Shihezi, China

Introduction: The wear failure of spindle will lead to a decrease in cotton harvesting rate of the cotton picker during field operation and serious wastage.

Method: Three types of spindle samples at different installation positions and working areas were obtained through field experiments to explore the wear failure law of spindle hook teeth of cotton picker during field operation. Hardness of hook tooth coating and substrate of spindles were tested, surface and cross-section microstructure of the spindle hook teeth were characterized, and wear area and width of the spindle hook teeth were extracted.

Results: Results showed that the hardness of the hook tooth coating is evidently higher than that of the substrate; the average coating hardness of the No. 3 spindle hook teeth reaches the maximum at 1033.6 HV0.1; defects, such as microcracks and micropores, exist in the coating of the three types of spindle hook teeth; and the thickness of the coating is between 70 and 130 μm. The wear area of spindle hook tooth changes exponentially and the wear width changes linearly with the increase of field operation area at the same installation position. The wear area and width of the spindle hook teeth gradually increase with the decrease of the installation height and the wear change of the hook teeth is negatively correlated with the installation height in the same field operation area.

Discussion: The wear failure of spindle hook tooth is mainly caused by abrasive, fatigue, and oxidation wear. The results of this study can provide a reference for improving the wear resistance of spindle hook teeth.

KEYWORDS

cotton picker spindle, hook tooth, wear failure, wear area, wear width

1 Introduction

Cotton is the second largest crop after food and an important strategic material for the country's livelihood (Wang et al., 2021; Li et al., 2022a). The cotton picker is a large type of equipment for mechanized harvesting of cotton and commonly used in the cotton harvesting process. The spindle is a key core component of the cotton picker, and its performance directly determines the picking efficiency and effect of the cotton picker field operation (Chen et al., 2020b; Bi, 2007; Li et al., 2022b). At the same time, the spindle is also the most consumed among wear parts on the cotton picker, and spindle hook teeth are very prone to wear failure problems (Wu et al., 2013; Zhang et al., 2017;

Li et al., 2018; Gu et al., 2021; Li et al., 2022a). The wear failure of spindle will lead to a decrease in cotton harvesting rate of the cotton picker during field operation and serious wastage.

Improving the wear resistance and prolonging the service life of the spindle in the field are important. At present, the method of electroplating chromium coating is often used to strengthen the spindle, the failure of chromium coating has been extensively investigated (Pina et al., 1997; Wang et al., 2007; Weiss et al., 2015; Lunarska et al., 2001; Zhang et al., 2012; Zhang et al., 2021; Zhang et al., 2018) randomly obtained the spindle samples from the picking head, characterized the wear failure change and morphology of the spindle hook teeth, analyzed the wear change process and failure form of the spindle hook teeth, and applied electromagnetic treatment to different brands of spindles to reduce the residual stress of the matrix and improve wear resistance. Amanov (Amanov et al., 2019) proposed an ultrasonic nanocrystal surface modification technology that uses ultrasonic energy to induce severe plastic deformation, improve the surface integrity of the material, increase the mechanical properties of the spindle surface, and improve wear resistance. Meng (Meng et al., 2016a; Meng et al., 2016b) investigated the friction performance modification of the spindle sleeve and the sleeve and applied nickel coating on the surface of the spindle via chemical method. Sun (Sun et al., 2021) used plasma spraying technology to treat the surface of cotton picker spindles to improve surface hardness and wear resistance. Luo(Luo et al., 2018) characterized the micro-morphology of the spindle hook teeth in different operation periods using scanning electron microscopy, established the friction mechanics model of the de-cotton process, and indicated that the wear failure of the spindle hook teeth is mainly caused by abrasive wear. Gu (Gu et al., 2021; Gu et al., 2022) extracted the area and the width of wear region and used them as evaluation indexes, the results revealed that the wear area of spindle hook teeth increases exponentially and the wear width increases linearly with the increase of the working area. The above research results have certain reference value for exploring the wear failure mechanism of the spindle hook teeth. And, the wear failure of the spindle hook teeth is mainly caused by the wear between the spindle hook teeth and the cotton. Research on the wear change of the spindle has mainly focused on the main picking parts of cotton, and studies on the wear failure of the spindle at the height of the seat tube needs further refinement. Practical field production demonstrated that some differences exist in the wear failure changes of spindle hook teeth at various installation positions on the spindle seat tube.

Causes of the wear failure of spindle hook teeth were analyzed to explore the wear failure changes during the field operation of spindle picking comprehensively. According to the spatial distribution law of cotton bolls in Xinjiang, three different height positions (upper, middle, and lower) on the spindle pipe were determined and spindle samples of field operation were obtained at these positions. Combined with structural parameters of the spindle, the sample preparation method of the spindle sample was developed. The surface and cross-section microstructure of the hook tooth coating, wear failure change of the hook tooth and wear failure morphology, and the cause of wear failure of the hook tooth were analyzed by characterizing the microhardness of the hook tooth coating and the substrate. The research results can provide a reference for further improving the wear failure mechanism and resistance of spindle hook teeth.

2 Materials and methods

2.1 Test materials

The test samples are three types of spindles currently used in Xinjiang market, namely, No. 1, 2, and 3. The overall structure of spindles is shown in Figure 1.

2.2 Test equipment

Cotton picker (Model: CP690, equipped with Pro-16 picking head), scanning electron microscope (Model: S-4800), electric spark wire cutting machine (Model: DK-7735), microhardness tester (Model: Duramin-40), energy spectrum analyzer (Model: XFlash5030), sample mosaic machine (Model: XQ-1), ultrasonic cleaner (Model: DL-720D), metallographic sample grinding and polishing machine (Model: ZMP-2000), special tools for spindle disassembly, sample bag, sandpaper, polishing agent, and marker pen.

2.3 Field test process

A field experiment was carried out from 25 September 2021 to 18 October 2021 during the cotton harvesting process in northern Xinjiang, China by installing spindle samples on the same cotton picker. Cotton bolls in Xinjiang are mainly distributed in 250–750 mm, with a concentration of more than 95% (Zhang, 2013). The test divided the spindle installation site into three different height ranges, namely, 150–250 (lowest installation position of the seat tube spindle height from the ground during field operation), 250–750, and 750–929 (highest installation position of the seat tube spindle height from the ground during field operation) mm, which correspond to the 1st–3rd, 3rd–15th, and 15th–20th spindle positions on the spindle seat tube range, respectively. The 2nd, 9th, and 16th positions within the corresponding position are selected as the installation position of the spindle, as shown in Figure 2. The three types of spindles were installed on No. 4, 5, and 6 picking heads of the cotton picker, and three repeated tests were performed under the same operating interval at the same position of the same spindle. The field operation process of the cotton picker was tracked and recorded, as shown in Figure 3. The three types of installed spindles were disassembled according to the experimental design when the field operation area of the cotton picker reached 133.33, 266.66, 400, and 533.33 ha. Three spindles were disassembled under the same installation position and the same working area. The sample bag was sealed and marked accordingly after antirust treatment. The field operation parameters of the cotton picker are listed in Table 1, and the field environmental conditions during the operation are presented in Table 2.

2.4 Preparation and characterization methods of test samples

The first hook tooth of the spindle was selected as the research object. The microstructure of the surface section of the hook tooth

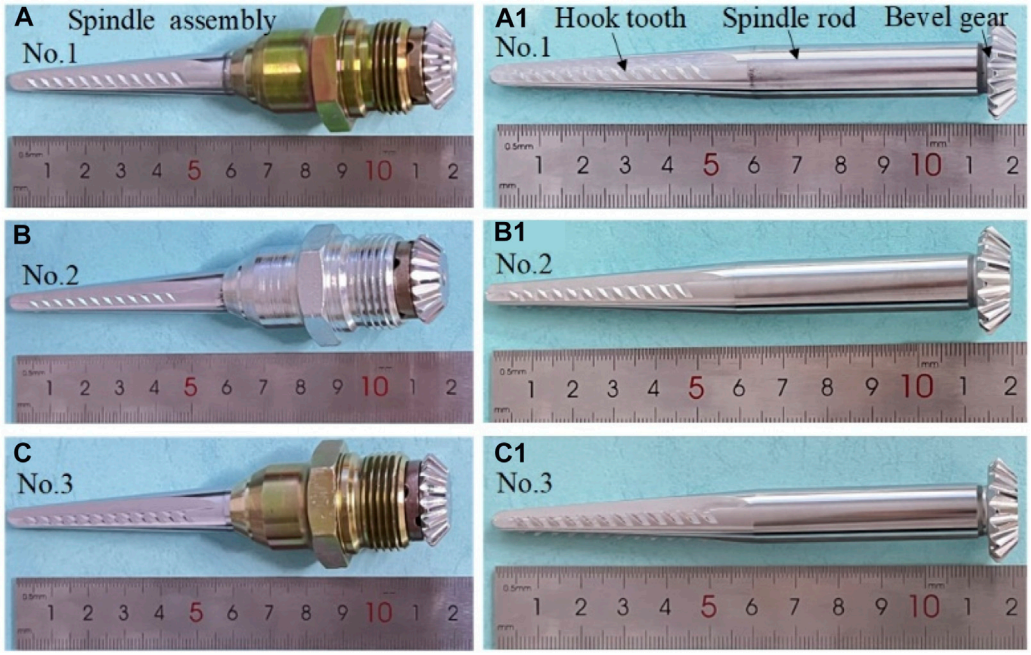

FIGURE 1
Test spindle sample: **(A–C)** spindle assembly and **(a1–c1)** spindle.

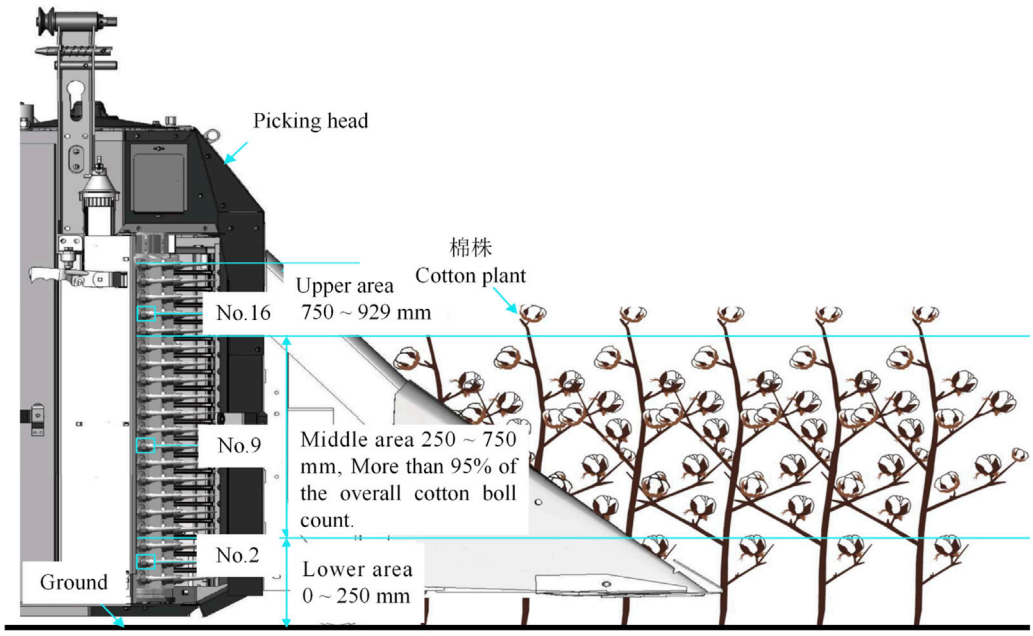

FIGURE 2
Diagram of the installation position of spindle.

coating and the wear failure process of the hook tooth are explored and an electric wire cutting machine is used to cut the spindle sample to facilitate the characterization of the tooth surface structure of the spindle hook tooth. Figure 4A shows the cutting process of the surface sample of the spindle hook. The clamping position, cutting direction, and cutting path of the spindle are presented in Figure 4B. Figure 4C illustrates the observation sample of the tooth surface structure and the micro-morphology of the hook tooth surface of the spindle structure and hook tooth after wire cutting. The first hook tooth of the other row of hook teeth on the spindle was selected for wire cutting to characterize

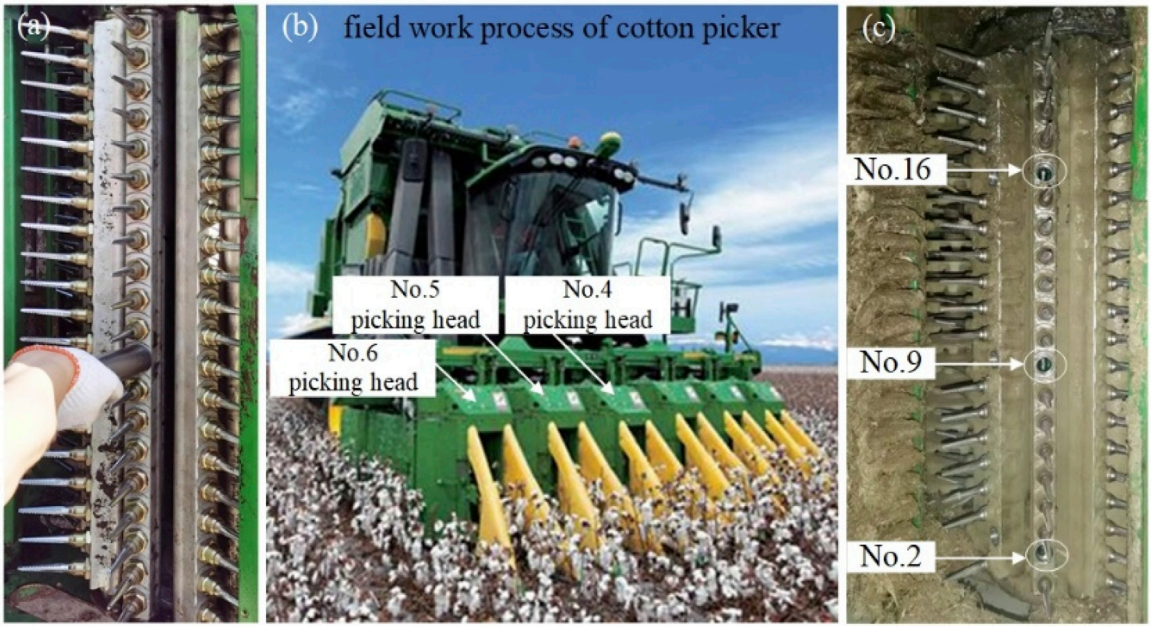

FIGURE 3
Field test process: **(A)** installation process of the spindle, **(B)** field work process of the cotton picker, and **(C)** disassembly process of the spindle.

TABLE 1 Working parameters of the cotton picker field operation.

Cotton picker operating speed (km/h)	Front drum speed (r/min)	Spindle speed (r/min)	Doffer pad speed (r/min)
0 ~ 7.1	0 ~ 152	0 ~ 4652	0 ~ 1960

TABLE 2 Field test environmental factors.

Test place	Field work time	Temperature (°C)	Humidity (%)
Kuitun, Xinjiang	8:00 a.m. ~ 12:00 p.m	−2.00 ~ 18.50	22.62 ~ 67.92

the cross-section microstructure of the hook tooth coating. The wire cutting process is depicted in Figure 4D. At this time, the clamping position, cutting direction, and cutting path of the spindle are shown in Figure 4E. The overall structure and sample of the spindle after cutting are presented in Figure 4F. The characterization samples of the cross section of the spindle hook tooth coating are obtained by inlaying, polishing, and preparing the samples under cutting.

The samples were cleaned ultrasonically for 5 min and then dried with hot air. The hardness of the coating and substrate was tested with a microhardness tester. The test load was 100 g, and the holding time was 15 s. Each test was repeated three times, and the average value of these tests was taken as the hardness value of the coating and substrate. A scanning electron microscope was used to characterize the tooth surface structure of the spindle hook teeth, the microstructure of the surface section of the hook tooth coating, and the wear failure process of the hook teeth. The acceleration voltage was 15 kV, and the scanning time was 30 μs. A spectrometer was utilized to characterize the elemental composition and content of the wear surface of the spindle hook teeth. The acceleration voltage was 16 kV, the maximum scanning area was 1 mm^2, and the maximum scanning distance was 11 mm.

3 Results and discussion

3.1 Coating and substrate hardness test of spindle hook tooth

Figure 5 shows the hardness test diagram of the hook tooth coating and the substrate of the three types of spindles. The average hardness of the hook tooth coating of No. 1, 2, and 3 spindles used in this test is 963.2 ± 36.25, 973.2 ± 20.57, and 1033.6 ± 13.91 $HV_{0.1}$, respectively. The average hardness of No. 1, 2, and 3 spindle hook tooth matrixes is 438.3 ± 8.61, 463.7 ± 9.39, and 482.0 ± 7.92 $HV_{0.1}$, respectively. Hence, the hardness of the hook tooth coating and the substrate of the No. 3 spindle sample is the maximum.

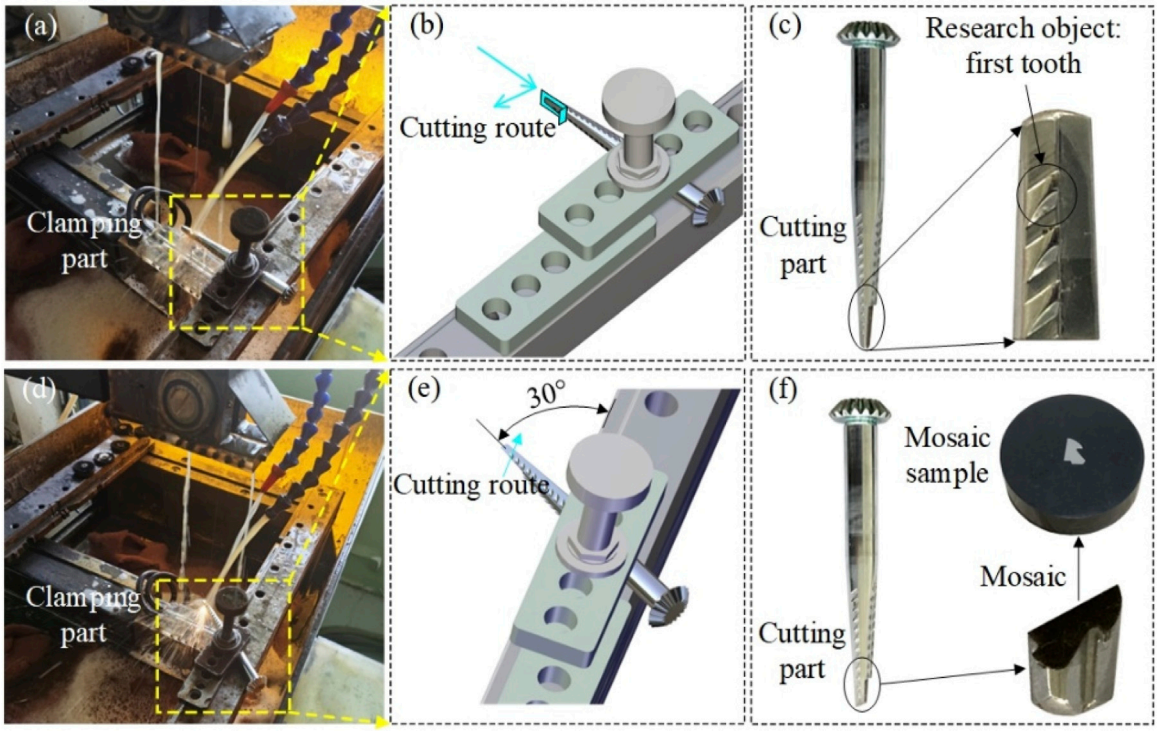

FIGURE 4
Sample preparation process: **(A)** surface sample cutting process, **(B)** clamping method of spindle, **(C)** surface sample, **(D)** section sample cutting process, **(E)** clamping method of spindle, and **(F)** section sample.

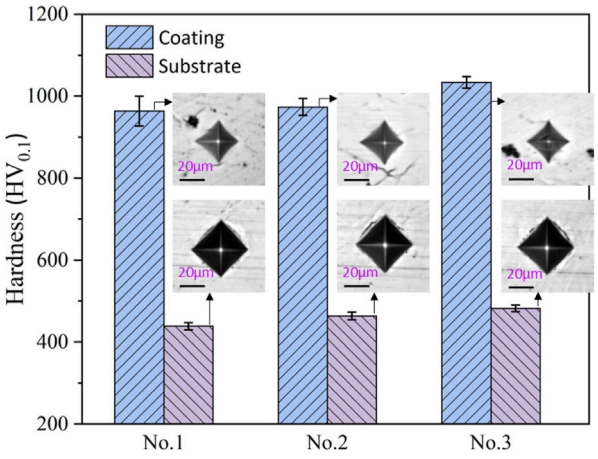

FIGURE 5
Hardness test of hook tooth coating and substrate.3.2. Figures, Tables and Schemes.

3.2 Characterization and analysis of surface and cross-section microstructure of spindle hook tooth coating

Figure 6 presents the tooth surface structure and the cross-section microstructure of the coating surface of the three types of spindle hook teeth. Figures 6A–C illustrate the tooth surface structure of No. 1, 2, and 3 spindle hook teeth, respectively. Among the three types of spindles used in the experiment, No. 2 spindle hook teeth are the sharpest and a certain passivation phenomenon occurs in No. 1 and 3 spindle hook teeth. The evident coating damage of the No. 2 spindle hook tooth tip is related to the accidental collision in the spindle transportation. The surface of the spindle hook tooth presented that the surface of No. 1 and 3 spindle hook tooth coatings is disorderly distributed with many dot-like protrusions of different sizes and the surface of the No. 2 spindle hook tooth coating is relatively smooth. The local enlarged observation of the surface of the three types of spindle hook tooth coating is shown in Figure 6(a1), 6 (b1), and 6 (c1).

Dot-like protrusions in the overall morphology of No. 1 and 3 spindle hook teeth correspond to the convex hull structure on the surface of No. 1 and 3 spindle hook tooth coatings at this time. The convex hull is caused by the partially cleaned surface of the spindle hook teeth before electroplating or impurity-polluted plating solution (Yu et al., 1990; Mahdavi et al., 2020). The surface of the No. 2 spindle hook tooth coating presents a typical electroplating layer surface morphology with cellular structure. The surface quality of the No. 2 spindle hook tooth coating is satisfactory. The microscopic morphology photos of the cross-section micro-morphology of the coating of the three types of spindle hook teeth are shown in Figure 6(a2), 6 (b2), and 6 (c2). Evident microcracks and holes can be observed in the cross section of the coating of the three types of spindle hook teeth. The appearance of microcracks is attributed to the release of residual stress during the electroplating process, while the presence of holes is related to the

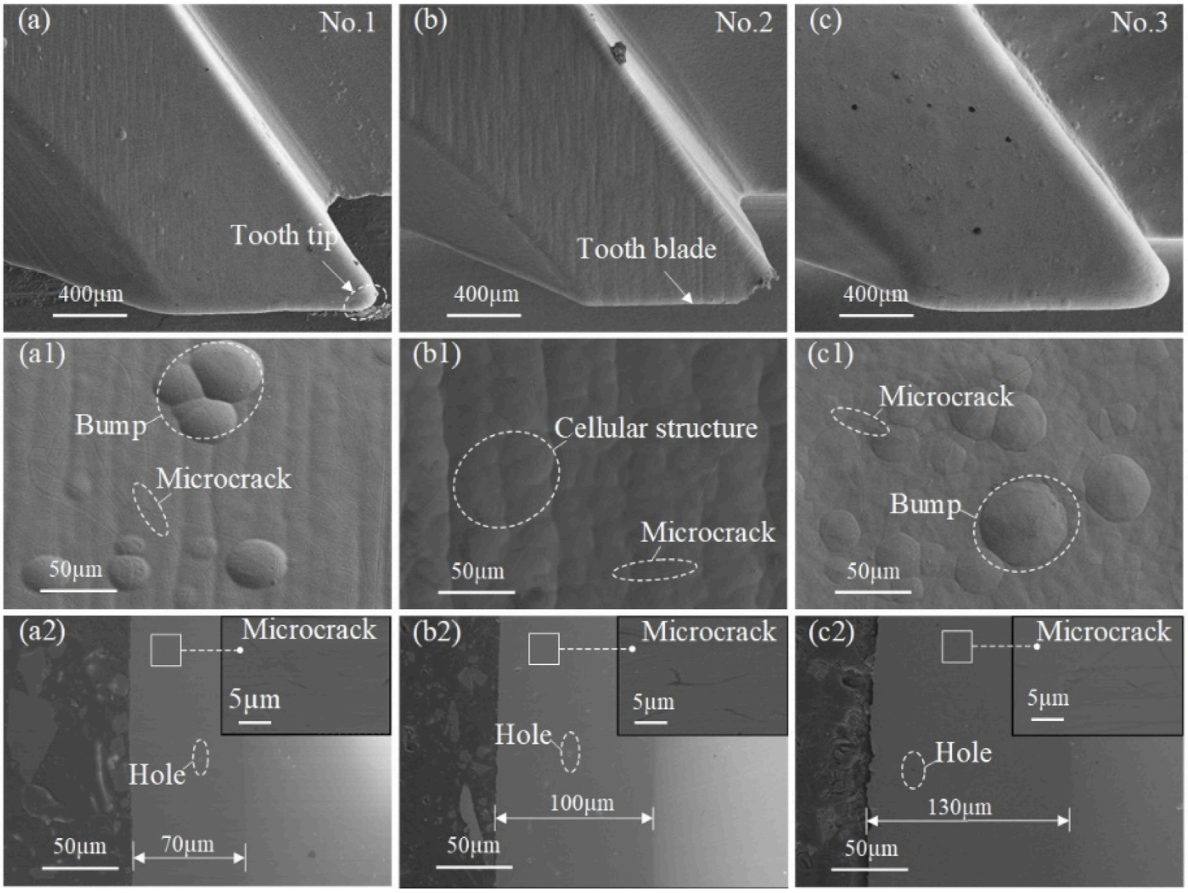

FIGURE 6
Structure of the spindle hook teeth and the microscopic morphology of the hook tooth coating surface and section: **(A–C)** No.1–3 spindle hook teeth, **(a1–c1)** surface morphology of No.1–3 spindle hook teeth, and **(a2–c2)** cross-section morphology of No.1–3 spindle hook teeth.

hydrogen produced by the side reaction (hydrogen evolution reaction) during the electroplating process (Yu et al., 1990). The coating thickness of No. 1, 2, and 3 spindle hook teeth is about 70, 100, and 130 μm, respectively.

3.3 Wear failure changes of spindle hook teeth at different installation positions

Scanning electron microscopy was used to characterize the wear changes of hook teeth in the field test (Figure 7). The three types of spindle hook teeth all show a "trapezoid" wear morphology at different installation positions. The area of the "trapezoid" on the surface of hook teeth gradually increases with the increase of field working area. Evident wear on the surface of the hook teeth of three types of spindles installed in the upper part is absent and slight wear is observed on the surface of the hook teeth of No. 1 and 2 spindles installed in the middle part when the spindle picking area reaches 133.33 ha. The hook teeth of No. 1 and 2 spindles installed on the upper part show slight wear and the wear on the hook teeth of the No. 3 spindle was unclear when the spindle picking area reaches 266.66 ha. Evident wear phenomena were observed on the surface of the hook teeth of the three types of spindles installed in the middle and lower parts. The surface of the three types of spindle hook teeth at different installation positions demonstrated wear when the spindle picking area reached 400 ha. The surface of the three types of spindle hook teeth at different installation positions showed serious wear when the spindle picking area reached 533.33 ha. The wear of the hook teeth of the three kinds of spindle samples first occurred at the tip and edge of the hook teeth. The wear area of the No. 3 spindle hook teeth at different installation positions is smaller than that of No. 1 and 2 spindles under different working areas. The high hardness and thickness of the hook tooth coating of the No. 3 sample can protect the hook tooth of the spindle from wear for a long time.

Curves of the wear area and width of the hook teeth with the installation position are shown in Figures 8A–C and 8(a1)–8(c1) to explore the influence of the field operation area of the spindle on the wear area and width of the hook teeth of the three kinds of spindles. The wear area of the three types of spindle hook teeth at different installation positions exhibited an approximate exponential change, and the wear width presented an approximate linear change. The increase of wear area and width of the three types of spindle hook teeth at different installation positions showed a trend of slow to fast with the increase of the field operation area. The hardness test results demonstrated that the hardness of the coating on the surface of the spindle hook tooth is about two times that of the substrate. The spindle hook tooth matrix is exposed during the field operation when the

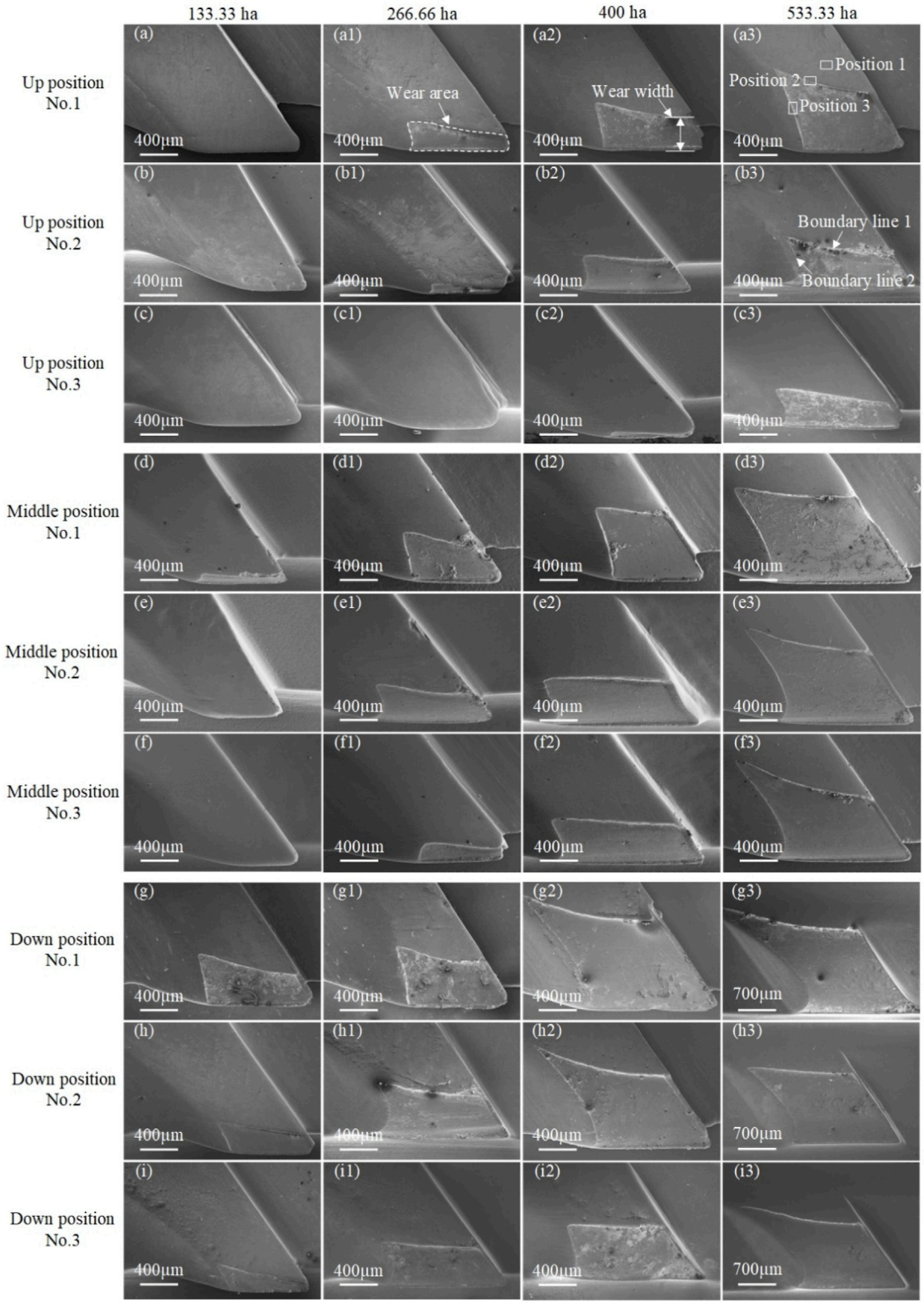

FIGURE 7
Wear variation of No. 1–3 spindle hook teeth under different height locations and working area conditions: wear variation of No. 1–3 spindle hook teeth under different height locations and different working area conditions when the working area is **(A–I)** 133.33 ha, **(a1–i1)** 266.66 ha, **(a2–i2)** 400 ha, and **(a3–i3)** 533.3 ha.

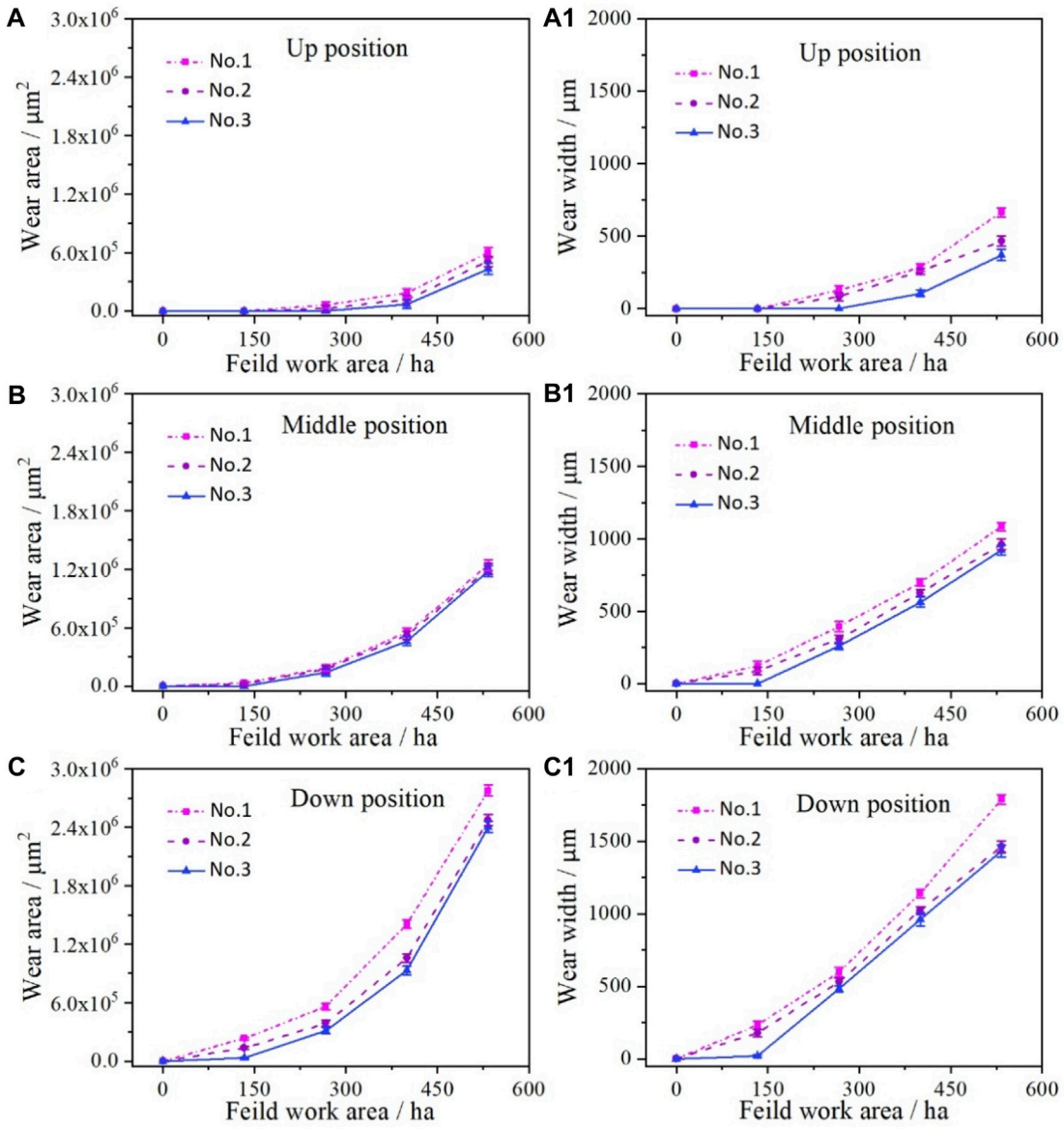

FIGURE 8
Variation curve of wear area and width of No. 1–3 spindle hook teeth under different working area conditions and height locations: variation curve of **(A–C)** wear area and **(a1–c2)** wear width of No. 1–3 spindle hook teeth at different height locations.

coating on the surface of the spindle hook tooth wears out. Rapid wear will occur during the continuous field operation because of the low hardness of the matrix that loses coating protection. At the same time, the microstructure analysis of the wear failure of the spindle hook teeth showed that evident fatigue spalling exists at the wear failure boundary of the coating. According to the literature, fatigue spalling of the coating will further accelerate the wear failure of the coating (Korzynski et al., 2009a; Imaz et al., 2014; Zhang et al., 2014; Chen et al., 2020a). Therefore, the wear area and width of the spindle hook teeth gradually accelerate. The comparison of changes in the three kinds of spindles at different installation positions exhibited that the wear area and width of the No. 3 spindle are always smaller than those of No. 1 and 2 spindle hook teeth during field operation. However, the difference between the wear area and width between No. 2 and 3 spindles gradually decreases with the increase of the field operation area. The coating can improve the wear resistance of the spindle hook teeth and prolong the service life of the spindle in the field. The thick coating of the No. 3 spindle can protect the hook teeth from wear for a long time in the early stage of wear; hence, the wear area and width between the No. 3 and 2 spindles are very different in the early stage of wear. However, the wear rate of the hook teeth of the No. 3 spindle gradually accelerated and the wear area and width gap between the No.3 and No.2 spindles gradually decreased with the increase of the field working area of the spindle because of the poorer coating quality of the No. 3 spindle compared with that of the No. 2 spindle. The coating quality of the spindle hook teeth exerts a certain influence on the wear resistance of the hook teeth during field operation.

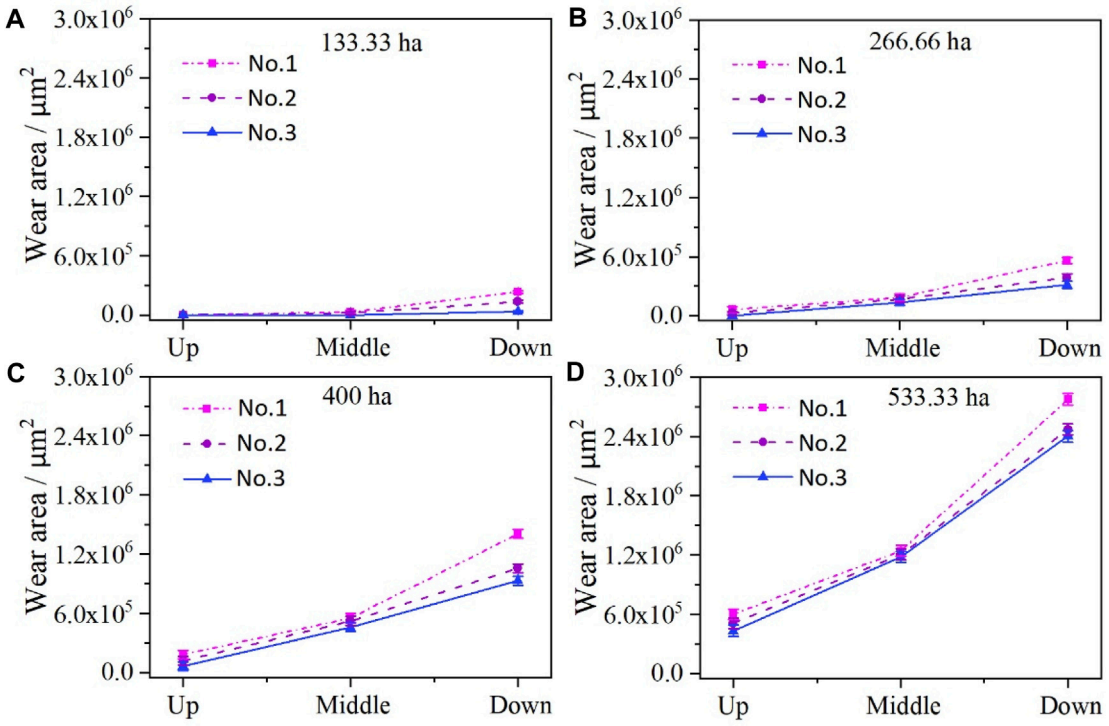

FIGURE 9
Variation curve of wear area of No. 1–3 spindle hook teeth under different height locations when the working area is **(A)** 133.33 ha, **(B)** 266.66 ha, **(C)** 400 ha, and **(D)** 533.33 ha.

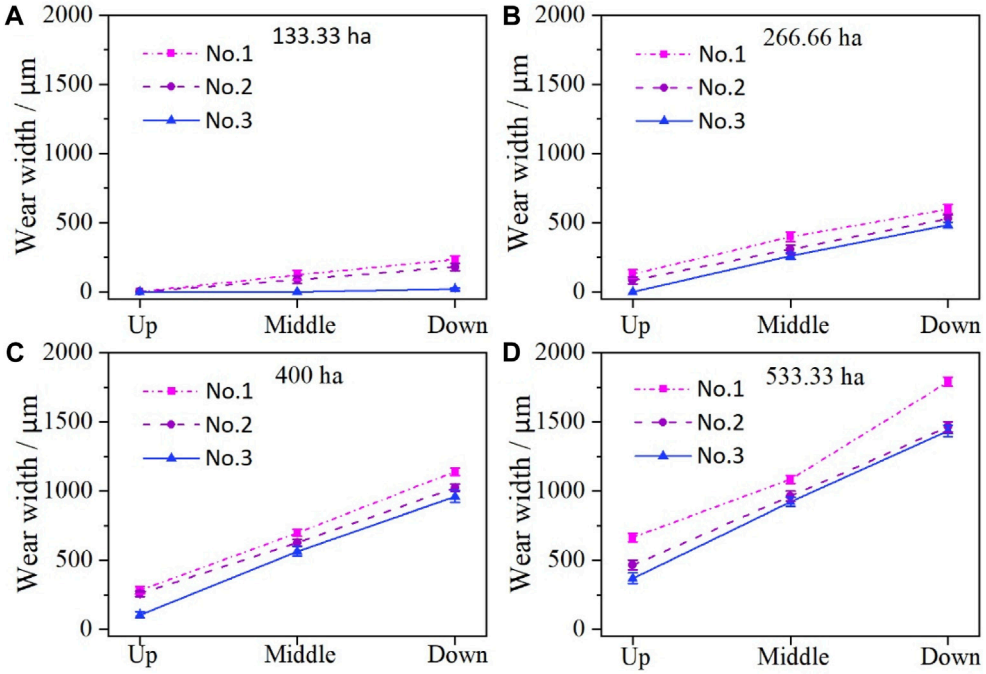

FIGURE 10
Variation curve of wear width of spindle hook teeth under different installation locations when the working area is **(A)** 133.33 ha, **(B)** 266.66 ha, **(C)** 400 ha, and **(D)** 533.33 ha.

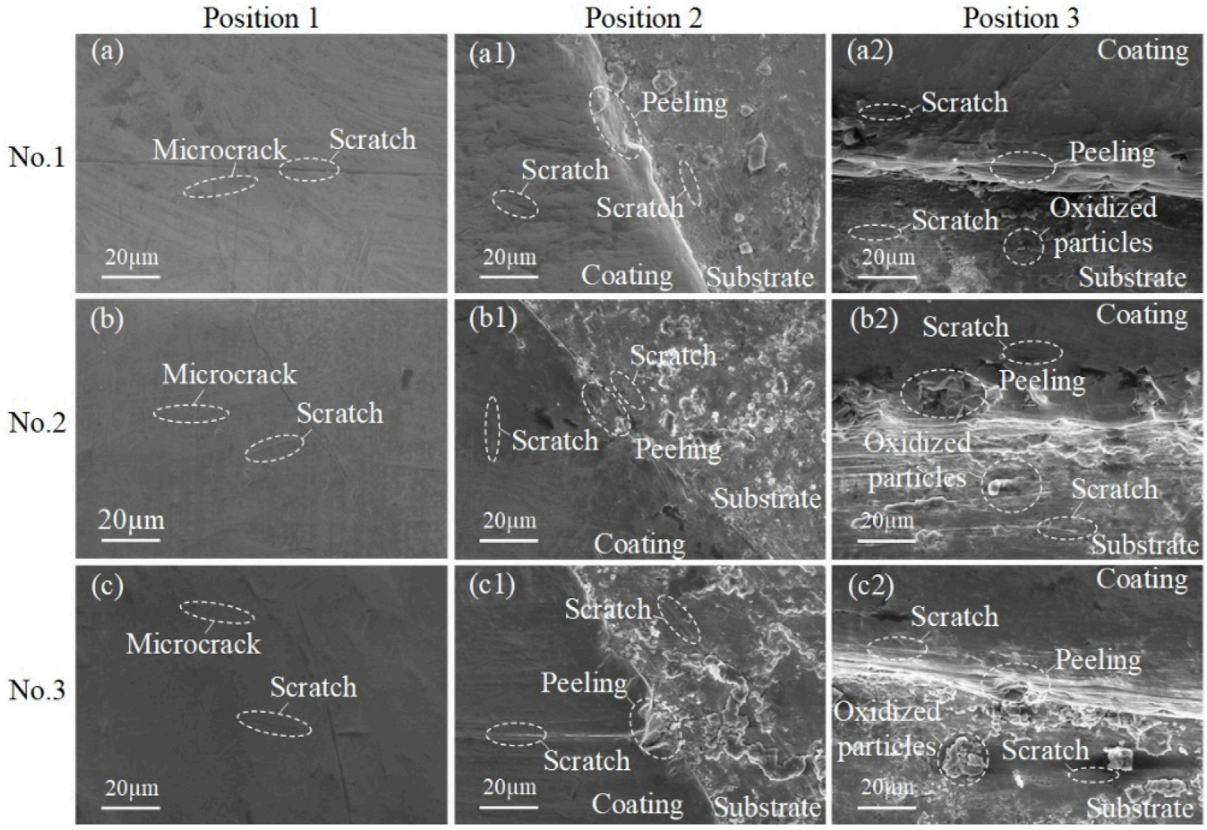

FIGURE 11
Wear morphology of No. 1–3 spindle hook teeth on the upper positions **(A–C)** 1, **(a1–c1)** 2, and **(a2–c2)** 3.

Figures 9, 10 illustrate the influence of the installation position on the wear area and width of the hook teeth of the three kinds of spindles. The wear area and width of the hook teeth of the three kinds of spindles gradually increase from top to bottom under the same working area. The wear area and width of No. 1 spindle hook teeth are the largest while those of No. 3 spindle hook teeth are the smallest in different working areas and installation positions. This wear change is also related to the thickness of the hook tooth coating. The wear area of the hook teeth of the No. 1 spindle at different installation positions showed a trend of slow to fast in the top–down direction, that is, the wear area of the hook teeth between the upper and middle parts changes slowly and that between the middle and lower parts changes rapidly under the condition of the same field working area. The wear area of hook teeth of No. 2 and 3 spindles in the field operation of in 133.33 and 533.33 ha in the direction of top–down installation position also shows a trend of slow to fast. Meanwhile, the wear area of hook teeth of No. 2 and 3 spindles in the field operation of 266.66 and 400 ha gradually increases with the decrease of installation position, thereby indicating that a negative correlation exists between the installation position of the spindle and the wear area. The comparison of changes of the wear width of the cast teeth at different installation positions in the same working area of the three kinds of spindles demonstrated that the linear change of the wear width of the hook teeth of the No. 1 spindle from the top–down installation position is negatively correlated with the installation position when the field operation is 133.33, 266.66, and 400 ha. Meanwhile, the change of the wear width of the hook teeth of the No. 1 spindle from top to bottom is slow and then fast when the field operation is 533.33 ha. The linear change of the wear width of the No. 2 spindle hook teeth is negatively correlated with the installation position under different working areas. The upper and middle spindle pick hook teeth are worn due to the No. 3 spindle pick hook teeth in the field operation of 133.33 ha (as shown in Figure 7). At this time, the wear width of the spindle hook teeth from the middle to lower direction shows a negative linear change. The linear change of the wear width of the hook teeth of the No. 3 spindle is also negatively correlated with the installation position when the field operation is 266.66, 400, and 533.33 ha. However, the difference between the wear widths of No. 1 and 2 spindle hook teeth gradually increases and that between the wear widths of No. 3 and 2 spindle hook teeth gradually decreases under the conditions of different installation positions and the same working area. Note that the most evident change in the lower installation spindle indicated that the change rate of the hook tooth wear width of the No. 3 spindle gradually accelerates with the increase of the working area. This change phenomenon is also related to the quality of the hook tooth coating.

3.4 Wear failure analysis of spindle hook teeth at different installation positions

The wear failure morphology of the spindle hook teeth at different installation positions was characterized using scanning electron microscopy. Three different positions on the hook teeth of three

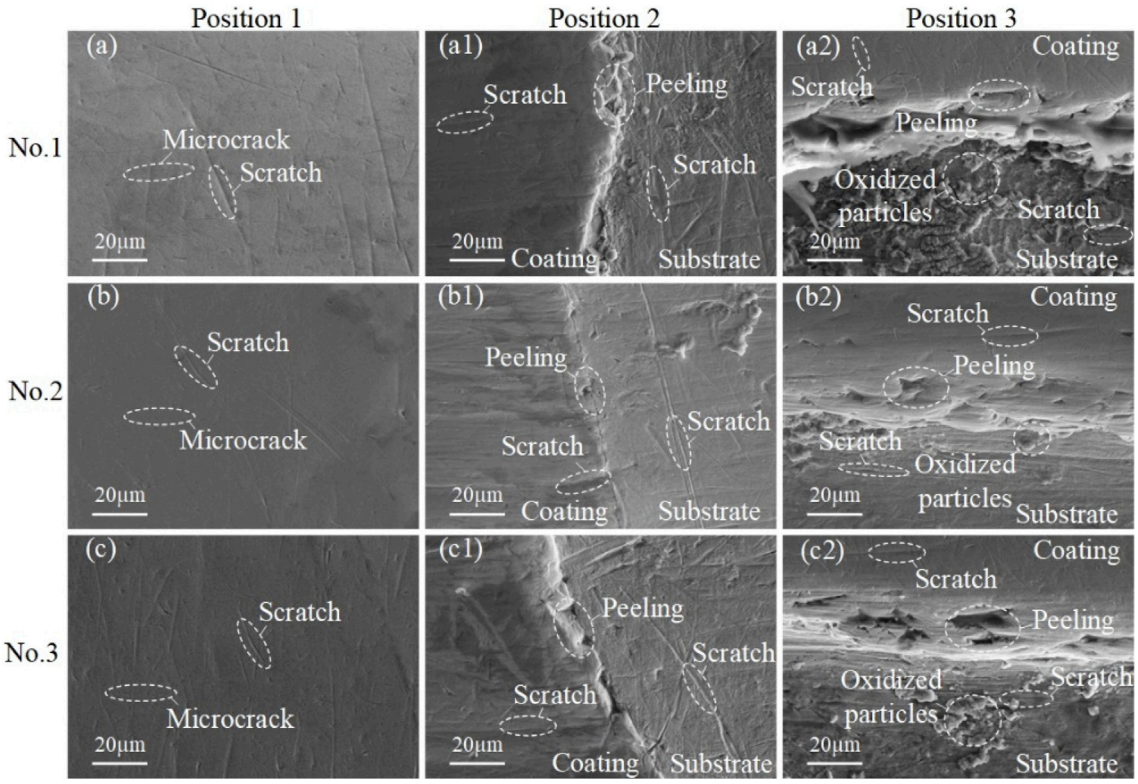

FIGURE 12
Wear morphology of the spindle hook teeth on the middle positions **(A–C)** 1, **(a1–c1)** 2, and **(a2–c2)** 3.

kinds of spindles with different installation positions (as shown in Figure 7[a3]) were selected for analysis when the field operation area reached 533.33 ha. The three selected positions corresponded to the coating surface, wear boundary line 1, and wear boundary line 2 (as shown in Figure 7[b3]). The results are presented in Figures 11–13. Evident micro-cracks and scratches can be observed on the surface of the coating of the three types of spindle hook teeth at three installation positions. The existence of micro-cracks is related to the inevitable residual stress in the electroplating process of the spindle, and scratches are a typical abrasive wear phenomenon. Combined with the field conditions, this phenomenon is mainly due to the plastic deformation and furrows caused by small hard particles in field sliding on the surface of the spindle coating. The comparison of the three installation parts demonstrated that the coating surface of the middle and lower installation spindles exhibits more scratches and the surface condition is more complicated than the upper installation spindle surface. Therefore, the worse working conditions of the middle and lower spindles are consistent with the larger wear failure area and width of the hook teeth of the middle and lower spindles than those of the upper spindles during field operation. The observation of the microstructure of wear boundary lines 1 and 2 of the three types of spindle hook teeth at the three installation sites indicated that evident coating peeling exists at the wear failure boundary line. According to the working condition of the spindle, periodic high-frequency collision will occur between the spindle and cotton stalk in the process of field operation (Dzierwa et al., 2008; Korzynski et al., 2009b). The coating of the spindle will be fatigued and result in fatigue spalling of the coating in the periodic high-frequency collision because many defects, such as microcracks and holes, exist in the coating of the spindle (Korzynski et al., 2009a; Imaz et al., 2014; Zhang et al., 2014; Chen et al., 2020b). The microstructure of the substrate surface after the failure of the three types of spindle coating at three positions demonstrated that additional evident scratches exist on the substrate surface likely due to the abrasive wear phenomenon caused by the sliding of hard particles on the substrate surface. At the same time, many small particles on the surface of the substrate after the coating failed were observed microscopically. The results are shown in Figure 14A. These particles are irregularly distributed on the surface of the substrate, and the composition of particle elements of was examined with an energy spectrum analyzer. The results are shown in Figure 14B. The composition of these particle elements is mainly iron and oxygen. These particles are produced by the oxidation wear of the matrix exposed to the air after the failure of the hook tooth coating (Bensalah et al., 2009; Cellard et al., 2009; Purkayastha and Dwivedi, 2014; Junior et al., 2019). In summary, the damage on the spindle hook teeth is caused by abrasive, fatigue and oxidation wear.

4 Conclusion

(1) The hardness test results showed that the average hardness of the hook tooth coating of No. 1, 2, and 3 spindle samples was 963.2, 973.2, and 1033.6 $HV_{0.1}$ and the average hardness of the substrate was 438.3, 463.7, and 482.0 $HV_{0.1}$, respectively. The surface structure of the hook tooth and the microstructure of

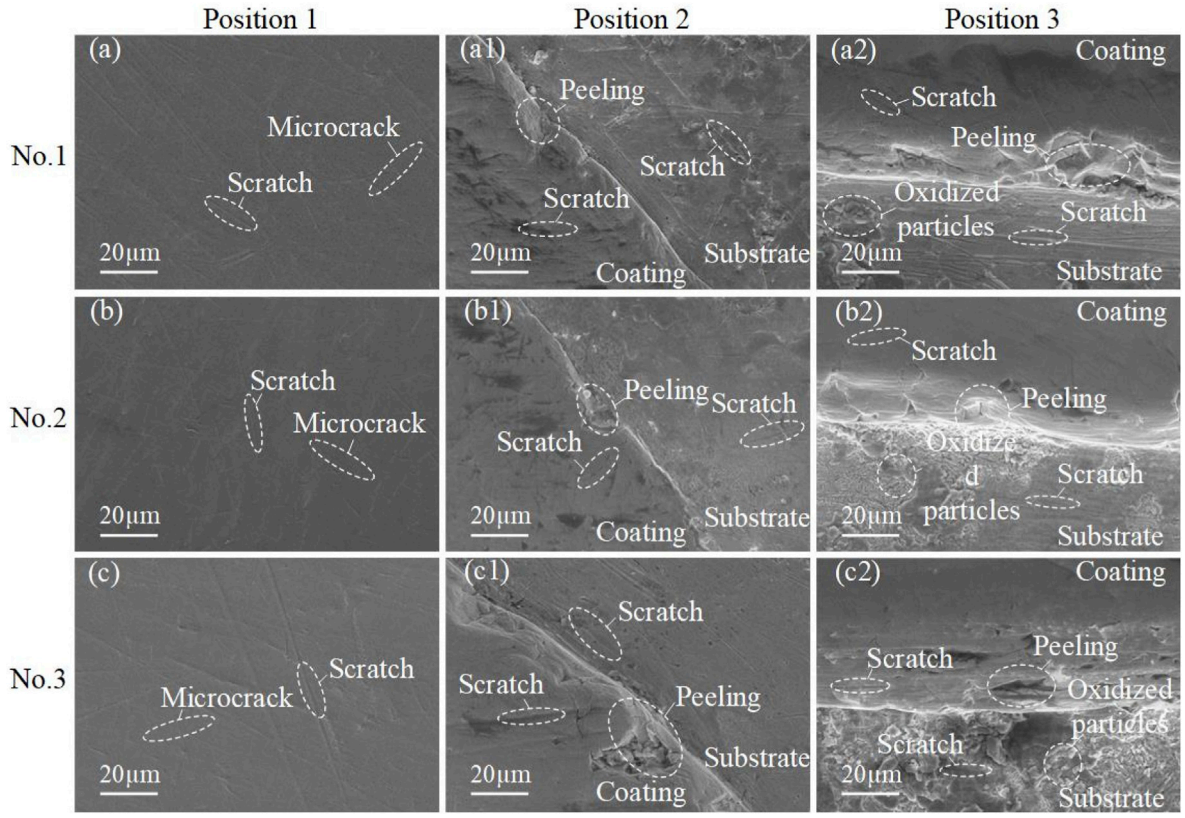

FIGURE 13
Wear morphology of the spindle hook teeth on the lower positions **(A–C)** 1, **(a1–c1)** 2, and **(a2–c2)** 3.

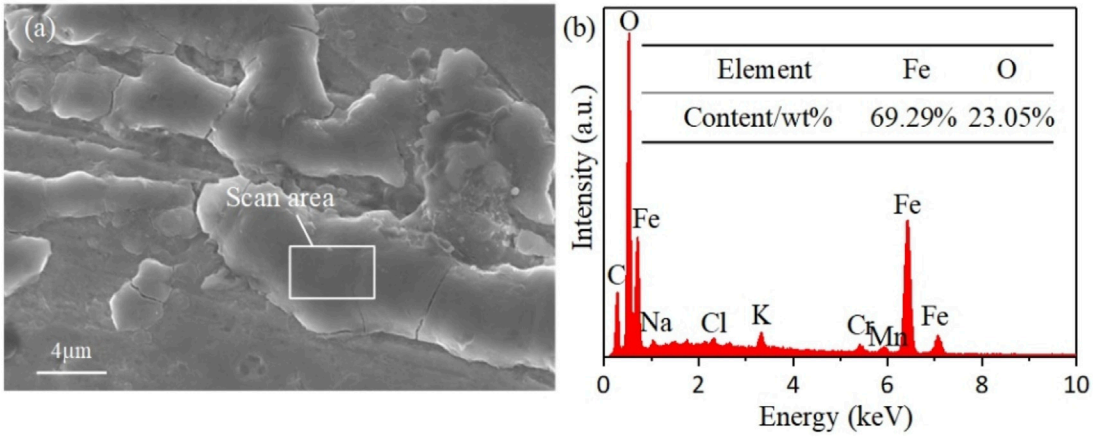

FIGURE 14
(A) Microscopic morphology and **(B)** EDS analysis of oxidized particles on the substrate surface.

the coating surface were characterized via scanning electron microscopy. The results showed that microcrack defects exist on the surface of the hook tooth coating. A convex hull structure was observed on the surface of the hook tooth coating of No. 1 and 3 spindle samples. The surface of the hook tooth coating of the No. 2 spindle sample was a cellular structure, and its surface quality was satisfactory. Defects, such as microcracks and micropores, exist in the cross section of the spindle hook tooth coating. The thickness of the hook tooth coating of 3 types of spindles is between 70 and 130 μm, and the thickness of the hook tooth coating of the No. 3 sample is about 130 μm.

(2) The comparison of hook teeth during field operation at different installation positions of the spindle showed that the wear failure first occurs at the tip and edge of the hook teeth. The wear area and width of the hook teeth of spindle samples installed at different positions gradually increase with the increase of the field operation area. The wear area changes exponentially, and the wear width changes linearly. The wear failure rate of the hook teeth is fast when the installation position is close to the lower part of the spindle. The wear area and width of the hook teeth gradually increase with the decrease of the installation position of the spindle under the same field working area. The negative correlation of the wear area and width of the hook teeth with the installation height of the spindle indicated that the wear between the spindle and the cotton is not the main cause of the wear failure of the hook teeth.

(3) Scanning electron microscopy was adopted to characterize the wear failure morphology at three different positions on the surface of the hook teeth of the spindle sample at different installation positions. The results demonstrated that many irregular scratches exist on the coating and substrate surface of the hook teeth of the spindle sample and evident coating peeling occurs on the wear boundary. Additional oxide particles caused by oxidation wear appeared on the surface of the hook teeth substrate after the coating was worn. The results showed that the wear failure of the hook teeth of the spindle sample is mainly caused by abrasive, fatigue, and oxidation wear.

Data availability statement

The raw data supporting the conclusion of this article will be made available by the authors, without undue reservation.

Author contributions

YuW: Writing–original draft, Writing–review and editing, Conceptualization, Formal Analysis, Methodology, Project administration, Resources, Software. ZL: Writing–original draft, Writing–review and editing, Data curation, Funding acquisition, Investigation, Supervision, Validation, Visualization. YG: Project administration, Writing–review and editing. HZ: Project administration, Writing–review and editing. PZ: Validation, Writing–review and editing. YoW: Conceptualization, Writing–review and editing. JY: Data curation, Writing–review and editing.

Funding

The author(s) declare financial support was received for the research, authorship, and/or publication of this article. This work was financially supported by the Corps Major Scientific and Technological Projects (Grant Number: 2018AA008), and the Corps Key Field Innovative Team Building Project (Grant Number: 2019CB006).

Conflict of interest

Authors PZ, YoW, JY, YuW, and ZL were employed by ShanDong Swan Cotton Industrial Machinery Stock Co., China and Xinjiang Swan Modernization Agricultural Machinery Equipment Co, China.

The remaining authors declare that the research was conducted in the absence of any commercial or financial relationships that could be construed as a potential conflict of interest.

Publisher's note

References

Amanov, A., Sembiring, J. P. B. A., and Amanov, T. (2019). Experimental investigation on friction and wear behavior of the vertical spindle and V-belt of a cotton picker. *Materials* 12 (5), 773. doi:10.3390/ma12050773

Bensalah, W., Elleuch, K., Feki, M., Wery, M., and Ayedi, H. F. (2009). Mechanical and abrasive wear properties of anodic oxide layers formed on aluminium. *J. Mater. Sci. Technol.* 25 (4), 508.

Bi, X. (2007). *Study on work mechanism of cotton picker level spindles* (Shihezi: Shihezi University). [master's thesis]. doi:10.7666/d.y1164989

Cellard, A., Garnier, V., Fantozzi, G., Baret, G., and Fort, P. (2009). Wear resistance of chromium oxide nanostructured coatings. *Ceram. Int.* 35 (2), 913–916. doi:10.1016/j.ceramint.2008.02.022

Chen, T., Zhang, H., and Wang, L. (2020a). Research and experiment on the movement characteristics of the picking mechanism of the horizontal spindle picking cotton picker. *J. Chin. Agric. Mech.* 41 (2), 19–25. doi:10.13733/j.jcam.issn.2095-5553.2020.02.04

Chen, T. G., Zhang, H. W., Wang, L., Zhang, L. C., Wang, J., et al. (2020b). Optimization and experiment of picking head transmission system of horizontal spindle type cotton picker. *Trans. Chin. Soc. Agric. Eng.* 36 (17), 18–26. doi:10.11975/j.issn.1002-6819.2020.17.003

Dzierwa, A., Pawlus, P., and Reizer, R. (2008). Surface topography of chromium coatings after pneumatic ball peening. *Key Eng. Mater.* 381, 113–116. doi:10.4028/www.scientific.net/kem.381-382.113

Gu, Y., Zhang, H., Fu, X., Wang, L., Shen, Z., Wang, J., et al. (2021). Experimental wear behavior analysis of coated spindle hook teeth under real harvesting work conditions. *Materials* 14 (10), 2487. doi:10.3390/ma14102487

Gu, Y., Zhang, H., Fu, X., Wang, L., Wang, J., Cai, Y., et al. (2022). Comparative analysis of the wear performance of spindle hook teeth during fieldwork. *J. Tribol.* 144 (1), 011706. doi:10.1115/1.4052636

Imaz, N., Ostra, M., Vidal, M., Díez, J. A., Sarret, M., and García-Lecina, E. (2014). Corrosion behaviour of chromium coatings obtained by direct and reverse pulse plating electrodeposition in NaCl aqueous solution. *Corros. Sci.* 78, 251–259. doi:10.1016/j.corsci.2013.10.005

Junior, M. D. O., Costa, H. L., Junior, W. S., and De Mello, J. D. B. (2019). Effect of iron oxide debris on the reciprocating sliding wear of tool steels. *Wear* 426, 1065–1075. doi:10.1016/j.wear.2018.12.047

Korzynski, M., Dzierwa, A., Pacana, A., and Cwanek, J. (2009a). Fatigue strength of chromium coated elements and possibility of its improvement with ball peening. *Surf. Coatings Technol.* 204 (5), 615–620. doi:10.1016/j.surfcoat.2009.08.049

Korzynski, M., Pacana, A., and Cwanek, J. (2009b). Fatigue strength of chromium coated elements and possibility of its improvement with slide diamond burnishing. *Surf. Coatings Technol.* 203 (12), 1670–1676. doi:10.1016/j.surfcoat.2008.12.022

Li, H., Fu, X., Wang, H., Zhang, H., Gu, Y., Du, X., et al. (2022a). Research on the wear characteristics of the hook teeth of cotton pickers. *Coatings* 12 (6), 762. doi:10.3390/coatings12060762

Li, H., Fu, X., Zhang, H., Zhang, L., Wang, M., et al. (2022b). Analysis and experiment of dynamic picking process of spindle of cotton picker. *Agriculture* 12 (9), 1346. doi:10.3390/agriculture12091346

Li, W. C., Qiao, Y. Y., Deng, Y. M., Liu, X. M., and Zhang, H. W. (2018). Valuation and analysis of hook tooth wear for cotton picker spindle. *J. Chin. Agric. Mech.* 39 (3), 11–14. doi:10.13733/j.jcam.issn.2095-5553.2018.03.003

Lunarska, E., Nikiforow, K., Wierzchon, T., and Ulbin-Pokorska, I. (2001). Effect of plasma nitriding on hydrogen behavior in electroplated chromium coating. *Surf. Coatings Technol.* 145 (1-3), 139–145. doi:10.1016/S0257-8972(01)01287-7

Luo, S. L., Zhang, Y. Q., and Ma, S. H. (2018). Wear mechanism analysis on spindle of cotton picker. *J. Tarim. Univ.* 30 (7), 132–137. doi:10.3969/j.issn.1009-0568.2018.01.017

Mahdavi, S., Allahkaram, S. R., Heidarzadeh, A., and Tavangar, R. (2020). Characteristics and properties of Co–Cr alloy coatings prepared by electrodeposition. *Surf. Eng.* 36 (9), 966–974. doi:10.1080/02670844.2019.1688012

Meng, F., Chen, N., and Chen, Z. (2016a). Hard chromium coating effects on tribological performances for nonlubricated and lubricated spindle of cotton picker. *Proc. Institution Mech. Eng. Part L J. Mater. Des. Appl.* 230 (2), 446–453. doi:10.1177/1464420715577234

Meng, F., Chen, Y., Yang, Y., and Chen, Z. (2016b). Friction and wear behavior of electroless nick coating used for spindle of cotton picker. *Industrial Lubr. Tribol.* 68 (2), 220–226. doi:10.1108/ILT-06-2015-0070

Pina, J., Dias, A., Francois, M., and Lebrun, J. L. (1997). Residual stresses and crystallographic texture in hard-chromium electroplated coatings. *Surf. coatings Technol.* 96 (2-3), 148–162. doi:10.1016/S0257-8972(97)00075-3

Purkayastha, S., and Dwivedi, D. K. (2014). Abrasive and erosive wear performance of rare earth oxide doped Ni/WC coatings. *J. Tribol.* 136 (1), 011602. doi:10.1115/1.4025099

Sun, Z., Sun, W., and Lu, G. (2021). Study on surface strengthening of cotton pick-up spindle based on plasma spraying. *Hot Work. Technol.* 50 (20), 96–99. doi:10.14158/j.cnki.1001-3814.20190227

Wang, L., Nam, K. S., and Kwon, S. C. (2007). Effect of plasma nitriding of electroplated chromium coatings on the corrosion protection C45 mild steel. *Surf. Coatings Technol.* 202 (2), 203–207. doi:10.1016/j.surfcoat.2007.05.027

Wang, X., Li, Y., Fu, W., et al. (2021). Analysis of meteorological conditions for cotton growth in Xinjiang in 2020. *China Cotton* 48 (3), 42–44. doi:10.11963/1000-632X.wxjlyc.20210302

Weiss, B., Lefebvre, A., Sinot, O., Marquer, M., and Tidu, A. (2015). Effect of grinding on the sub-surface and surface of electrodeposited chromium and steel substrate. *Surf. Coatings Technol.* 272, 165–175. doi:10.1016/j.surfcoat.2015.04.009

Wu, B., Zhang, L. X., Zuo, Y. T., and Wei, M. (2013). Research of material elements distribution in cotton picker's level spindle based on SEM and EDS. *J. Agric. Mech. Res.* 35 (7), 174–178. doi:10.13427/j.cnki.njyi.2013.07.049

Yu, W. P., Zhang, M. J., and He, Y. D. (1990). The effect of hydrogen on the structural transformation of electroplationg chromium coatings. *J. Beijing Univ. Aeronaut. Astronaut.* 2, 129–132. doi:10.13700/j.bh.1001-5965.1990.02.018

Zhang, H. (2013). *The working mechanism and experimental study of the key components of the cotton picking head of the glue stick roller*. Nanjing: Nanjing Agricultural University. doi:10.7666/d.Y2528420

Zhang, Y., Cai, Z., Tian, Y., and Meng, Y. (2018). Improvement of mechanical properties and wear resistance of cotton picker spindle by electromagnetic treatment. *Trans. Chin. Soc. Agric. Eng.* 34 (7), 31–37. doi:10.11975/j.issn.1002-6819.2018.07.004

Zhang, Y., Ma, S., and Ding, W. (2012). Dynamic analysis on picking process of cotton picker spindle. *Trans. Chin. Soc. Agric. Eng.* 28 (13), 54–58. doi:10.3969/j.issn.1002-6819.2012.13.009

Zhang, Y., Tian, Y., and Meng, Y. (2021). Wear behavior of spindles of cotton picker in field work. *J. Tribol.* 143 (2), 021703. doi:10.1115/1.4047790

Zhang, Y., Wang, W., and Liao, J. (2017). Wear failure analysis on spindle of cotton picker. *Trans. Chin. Soc. Agric. Eng.* 33 (18), 45–50. doi:10.11975/j.issn.1002-6819.2017.18.006

Zhang, Z., Zhang, H., and Wang, H. (2014). Virtual design and kinematic simulation for horizontal spindle type cotton picker with picking mechanism. *J. Chin. Agric. Mech.* 35 (3), 31–34. doi:10.13733/j.jcam.issn.2095-5553.2014.03.009

frontiers | Frontiers in Materials

TYPE Original Research
PUBLISHED 06 February 2024
DOI 10.3389/fmats.2024.1361159

OPEN ACCESS

EDITED BY
Zhongya Zhang,
Chongqing Jiaotong University, China

REVIEWED BY
Qiang Pei,
Dalian University, China
Hui Chen,
Wenzhou University of Technology, China

*CORRESPONDENCE
Hu Kong,
kh980407@163.com

RECEIVED 25 December 2023
ACCEPTED 19 January 2024
PUBLISHED 06 February 2024

CITATION
Wang Y, Kong H, Sun Y, Tan M and Chen L (2024), Study on the monitoring method of debonding between concrete beams and reinforced steel plates based on piezoelectric smart materials.
Front. Mater. 11:1361159.
doi: 10.3389/fmats.2024.1361159

Study on the monitoring method of debonding between concrete beams and reinforced steel plates based on piezoelectric smart materials

Yanru Wang[1], Hu Kong[2]*, Yaxi Sun[3], Mingli Tan[4] and Lihua Chen[5]

[1]School of Civil Engineering, Taizhou University, Taizhou, China, [2]Department of Civil and Transportation Engineering, Hohai University, Nanjing, China, [3]School of Digital Economy and Information Management, Chongqing Yitong University, Chongqing, China, [4]Faculty of Architectural Engineering, Huaihua Vocationnal and Technical College, Huaihua, China, [5]Chongqing Vocational Institute of Engineering, Chongqing, China

Concrete reinforcement is essential for ensuring the safety and durability of concrete structures. Bonding steel plates to reinforce concrete is widely used to renovate or strengthen concrete beam structures. Due to construction quality and the influence of factors such as environment and fatigue, debonding often occurs between the steel plate and concrete, making monitoring and early warning after concrete structure reinforcement challenging. This paper proposes a novel approach to monitor the degree of debonding between the steel plate and concrete beam using active sensing technology. The method uses lead zirconate titanate (PZT) as an actuator to generate stress waves. It prepares strip sensors with polyvinylidene fluoride as the sensing element to monitor stress waves passing through the steel plate and concrete beam. The monitoring system detects the degree of debonding between the steel plate and the concrete beam by monitoring the change in surface voltage of the sensor. Experiments show that the degree of debonding significantly correlates with the received voltage signal; the higher the debonding, the larger the received voltage signal. It is also observed that, at the same degree of debonding, the actuator and sensor attachment position have a particular impact on the received voltage signal. Through experiments and numerical simulation analysis, it is found that when the sensor is attached to the left side of the steel plate, that is, the bonded section of the steel plate, the amplitude of the voltage signal collected by the dynamic information acquisition system is the smallest, i.e., V_debonded section > V_middle > V_bonded section. Based on the above research, the active sensing technology proposed in this paper has good sensitivity to the degree of debonding between the steel plate and concrete. It is expected to become an effective monitoring and evaluation method for the degree of debonding between steel plates and concrete.

KEYWORDS

debonding monitoring, active sensing technology, bar sensor, PZT actuator, PVDF

1 Introduction

Concrete beams, as a common transverse component, are widely used in engineering structures. During their long-term use, the components are prone to serious deformation or even cracking due to adverse factors such as external loads (Zhan, et al., 2015), corrosion (Aslani and Dehestani, 2020), fatigue (Zanuy et al., 2007), etc. If the defects in the concrete beams are not detected and repaired in a timely manner, it will seriously threaten the safety of the structure (Kaklauskas, 2017; Fu and Lao, 2023; Yang, et al., 2023).

Common methods for repairing and strengthening concrete beams include increasing section reinforcement (Ye et al., 2010; Li, et al., 2014; Naser, et al., 2019), bonding fiber-reinforced composite material (Dai, et al., 2011; Hawileh, et al., 2018; Zhang, et al., 2023), and bonding steel plate reinforcement (Barnes and Mays, 2006; Arslan, et al., 2008; Qu, et al., 2017; Ma and Liu, 2023). Among them, the method of bonding steel plate reinforcement has been widely used in concrete reinforcement due to its simple and fast construction, and it does not significantly increase the cross-sectional dimensions and weight of the reinforced components. However, the debonding of the steel plate is a common problem in the bonding steel plate reinforcement. The quality of the bonding between the steel plate and the concrete directly affects the safety of the structure (Jones, et al., 1988; Oehlers and Ali, 1998; Ali, et al., 2005; Zou, et al., 2023). Once the steel plate is detached from the concrete bonding layer, it will affect the structural load and may even cause cracks to further develop, leading to structural failure. Due to the invisibility of the bonding between the steel plate and the concrete structure, it is difficult to monitor the quality of the bonding steel plate. Currently, the widely used non-destructive testing methods, such as acoustic emission technology (Zaki, et al., 2023), ultrasonic testing technology (Shah, et al., 2009; Shah and Ribakov, 2009), fiber optic sensing technology (Buda-Ożóg et al., 2022), and digital image processing technology (Galkovski et al., 2023), all involve sophisticated equipment and complex algorithms, requiring high demands on the testing environment and the operator's skill, making them difficult to apply flexibly in some engineering applications. Therefore, there is an urgent need to find a simple and effective non-destructive monitoring method for monitoring the debonding of the steel structure and the concrete beam bonding joint.

Piezoelectric materials are commonly used in active sensing technology for structural health monitoring due to their sensing and actuating functions in recent years (Liao, et al., 2008; Howser, et al., 2011; Huo, et al., 2018). The widely used piezoelectric materials include lead zirconate titanate (PZT) and polyvinylidene fluoride (PVDF). PZT has strong piezoelectric effect (Song, et al., 2002) and a wide bandwidth (Wu, et al., 2019), while PVDF is a piezoelectric polymer that overcomes the shortcomings of piezoelectric ceramics and has the advantages of structural flexibility and stable performance (Audrain, et al., 2004). Both materials have been widely used and have shown good results in the detection of bonding slip (Qin, et al., 2015; Zeng, et al., 2015; Xu, et al., 2018) between concrete and steel, monitoring of structural impact damage (Yu, et al., 2013), and monitoring of asphalt pavement crack damage (Hasni, et al., 2017).

Due to the issue of debonding between reinforced steel plates and concrete beams, and based on the superior performance of lead zirconate titanate (PZT) and polyvinylidene fluoride (PVDF) in the field of structural detection, this paper proposes a new method for real-time monitoring of debonding between steel plates and concrete beams using PVDF as the sensor for debonding monitoring and PZT as the actuator for debonding monitoring. Through active monitoring experiments on the reinforced concrete with attached steel plates, the relationship between the received electrical signal and the degree of debonding was studied. In addition, based on experimental and numerical simulation methods, the correlation between the sensor installation position and the received electrical signal under the same debonding state was analyzed, and the mechanism was explained. Through the above research, the feasibility of the proposed method for monitoring the debonding state between reinforced steel plates and concrete beams was further validated.

2 Preparation and monitoring mechanism of piezoelectric transducer

2.1 The preparation of a bar sensor

The strip sensor is prepared based on polyvinylidene fluoride (PVDF), using a PVDF sensor element with dimensions of 1 cm × 2 cm × 28 μm. The main performance parameters of PVDF are shown in Table 1. A polydimethylsiloxane (PDMS) with an outer ring length of 7cm, inner ring length of 5cm, and a thickness of 500 μm is used as the substrate material to increase the range of the strip sensor. The mechanical performance parameters of PDMS are shown in Table 2. The detailed fabrication process of the strip sensor is as follows: silver is plated on the outer edge of the PVDF with a thickness of 1μm, then copper foil conductive tape is used to attach the shielded wire to one side of the PVDF. The PVDF is then attached to the surface of the PDMS using epoxy resin. The structural fabrication process of the strip sensor is shown in Figures 1A a photo of the actual sensor is shown in Figure 1B.

2.2 Preparation of PZT actuators

The piezoelectric actuator is prepared from lead zirconate titanate (PZT), with the common types being PZT-4, PZT-5, and PZT-8. The performance parameters of the three types of lead zirconate titanate (PZT) materials are shown in Table 3. Among them, PZT-4 piezoelectric ceramics have high dielectric constants and electromechanical coupling coefficients, making them suitable for self-excited sensors that function as both receiving and transmitting ends (Othmani, et al., 2020) PZT-5 piezoelectric ceramics have a small quality factor and high dielectric losses but exhibit high sensitivity, and are therefore commonly used as receiving elements in devices such as accelerometers, piezoelectric sensors, and ultrasonic probes (Bouche, 1975; Benes, et al., 1995; Kumar, et al., 2022). PZT-8 piezoelectric ceramics are a type of high-power piezoelectric material with low dielectric losses, suitable for large amplitude excitation, mainly used in ultrasonic cleaning and ultrasonic surgery (Prabakar, 2007; Zhang, et al., 2017). Through comparison, it is found that PZT-4 is more suitable as a driver

TABLE 1 Main performance parameters of PVDF film.

$\varepsilon/\varepsilon_0$ (KHz)	C (m/s)	Z (Kg/sm^4)	K_{33} (%)	σ_s (N/m^2)	ρ(kg/m^3)	T (°C)
9.5 ± 1.0	2000	2.5–3×10^4	10–14	44–55×10^6	1.78×10^3	−40–80

TABLE 2 PDMS film mechanical properties parameters.

T (°C)	Shore hardness (HA)	Tensile strength (MPa)	Peel strength (KN/m)	Ep (GPa)	Tearing elongation (%)	Dielectric strength (KV/mm)	k_{33}	Volume resistance (Ω·cm)
−40–200	50	4	7	1.6	100	12	2.7	10^{14}

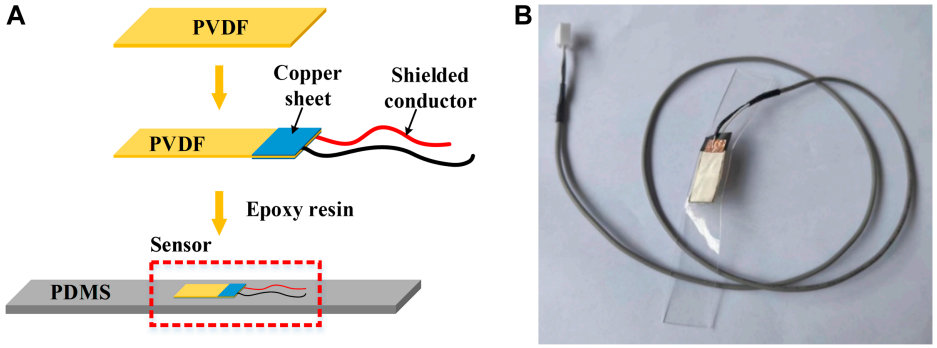

FIGURE 1
Bar Type Piezoelectric Sensor. **(A)** Preparation process diagram **(B)** Physical diagram.

TABLE 3 Mechanical properties parameters of PZT materials.

Material type	S_{11}(N·m^{-2})	d_{33} (pC/N)	$\varepsilon/\varepsilon_0$	E_p (Gpa)	k_{33}	Curie temperature T (°C)
PZT-4	1.35 × 10^{-11}	320	1,350	76.5	0.64	360
PZT-5H	2 × 10^{-11}	650	3,400	60.6	0.8	220
PZT-8	1.1 × 10^{-11}	225	1,300	60	0.63	300

for monitoring tests of bonding seam delamination in reinforced concrete beams. In this study, the selected dimensions of PZT-4 are 1 cm × 2 cm × 28 μm.

2.3 The mechanism of active monitoring for debonding between reinforced steel plate and concrete beam

Piezoelectric materials, after being polarized by an electric field, will generate charges when subjected to force, called the positive piezoelectric effect; under the influence of an electric field, deformation known as the inverse piezoelectric effect will occur. By attaching a strip sensor and PZT actuator to the steel plate, connecting PZT with the piezoelectric ceramic driving power source to generate stress waves, and connecting PVDF with the dynamic information acquisition instrument to convert the received stress waves into electrical signals. The sensing mechanism described above can be represented by the first type of piezoelectric equation as follows:

$$\boldsymbol{x} = \boldsymbol{s}^{E}\boldsymbol{X} + \boldsymbol{d}_{t}\boldsymbol{E} \tag{1}$$

$$\boldsymbol{D} = \boldsymbol{d}\boldsymbol{X} + \boldsymbol{\varepsilon}^{x}\boldsymbol{E} \tag{2}$$

Where Formula (1) represents the ability of piezoelectric materials to convert electrical energy into mechanical energy, which can be used to make PZT actuators; Formula (2) represents the ability of piezoelectric materials to convert mechanical energy into electrical energy, which can be used to make strip sensors. For

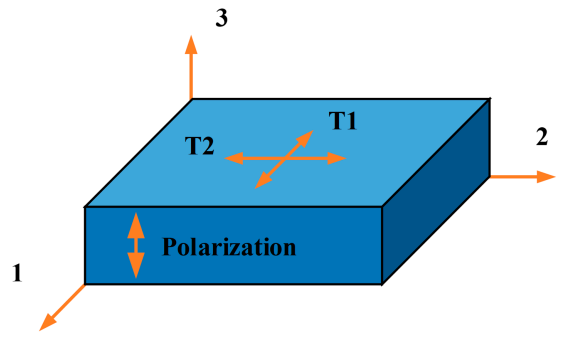

FIGURE 2
Piezoelectric material calculation orientation diagram.

the piezoelectric equations of PZT and PVDF, the piezoelectric coefficients have symmetry with respect to crystal type, so Formula (2) can be simplified to:

$$D_3 = d_{31}X_1 + d_{32}X_2 \tag{3}$$

Where 3 represents the polarization direction. When the strip sensor is subjected to the forces in the 1 and 2 directions, the charge produced in the 3 direction is D3, as shown in Figure 2.

According to the research on the piezoelectric effect of piezoelectric materials after electric field polarization by Zhao and Li (2006) when a bar sensor is subjected to mechanical force, charges will be generated on the upper and lower surfaces, with the amount of charge being:

$$Q = \iint D_3 d_x d_y \tag{4}$$

Moreover, due to the similar structure of piezoelectric materials to that of a capacitor, the voltage, after the capacitance is generated on the upper and lower surfaces, can be determined as follows:

$$U = \frac{Q}{C_q} \tag{5}$$

Where C_q represents the capacitance of piezoelectric material, which only related to the properties of the material, and the capacitance is:

$$C_q = \frac{\varepsilon bl}{t} \tag{6}$$

Where ε represents the relative dielectric constant of the ceramic sheet, and *lbt* represents the length, width, and thickness of the sensor, respectively. Therefore, by applying excitation signals to the PZT, it is possible to monitor the voltage signal output by the strip sensor, which indicates the change in surface voltage of the strip sensor in order to assess the level of debonding between the steel plate and the concrete beam.

3 Monitoring experiment and numerical simulation of debonding between reinforced steel plate and concrete beam

This section includes two sets of experiments and one set of numerical simulations to demonstrate the feasibility of the theoretical model for monitoring the debonding level between steel plates and concrete beam, as well as the effect of different sensor attachment positions on the received stress wave transmission when the debonding level of the steel plate remains the same. The first set of experiments consists of a control experiment with fixed positions of the PZT actuator and strip sensor but different debonding levels of the steel plates. The second set of experiments involves a control experiment with the same debonding level of the steel plates, but different positions of the PZT actuator and strip sensor. Additionally, numerical simulations were conducted for steel plates with different positions of the PZT actuator and sensor attachment but the same debonding level.

TABLE 4 Cracked concrete beam mix proportions.

Concrete	Sand	Aggregate	Water
416.7	624.2	1,159.1	200

3.1 The description of experiment

The apparatus used in the experiment consists of test pieces, steel plates, PZT actuators, strip sensors, DH5922N dynamic information acquisition system, HPV series piezoelectric ceramic drive power supply and signal amplifier. In order to simulate the actual use environment of the steel plate bonding reinforcement method, the test pieces include 4 cracked concrete beams, with crack dimensions of 150 mm × 150 mm × 600 mm and a mix ratio as shown in Table 4. First, when using the steel plate bonding reinforcement method for the cracked concrete beams, it is necessary to repair the cracked cracks, fill the cracks with repair adhesive using an adhesive injector to repair the concrete beams. Secondly, before reinforcing the concrete beams with steel plates, it is necessary to calculate the ultimate load-bearing capacity of the steel plate. Once the calculation meets the requirements, the steel plate is cut into the required shape, and the surface is coated with adhesive. The steel plate is then bonded to the concrete surface. After bonding the steel plate to the concrete beams, the reinforced concrete beams are cured in their natural state for 3 days to ensure a strong bond between the concrete beams and the steel plate, as shown in Figure 3.

After the concrete beams are firmly bonded to the steel plate, the strip sensor and the PZT actuator are bonded to the steel plate using epoxy resin. The strip sensor is connected to an external charge amplifier and then to the dynamic information acquisition system. The charge amplifier connected to the strip sensor is set to an amplification ratio of 100, and the voltage signal acquisition frequency of the dynamic information acquisition system is set to 500Hz. The PZT actuator is connected to the piezoelectric ceramic drive power supply, and the piezoelectric ceramic drive power supply applies a 60Hz–100Hz frequency-sweep sine signal with an amplitude of 5V to the PZT actuator as an excitation signal, with a signal duration of 10s. After the power is turned on, the signal is unstable and needs to wait for the signal to stabilize before starting the timer, then the dynamic information acquisition system is used to collect the signal.

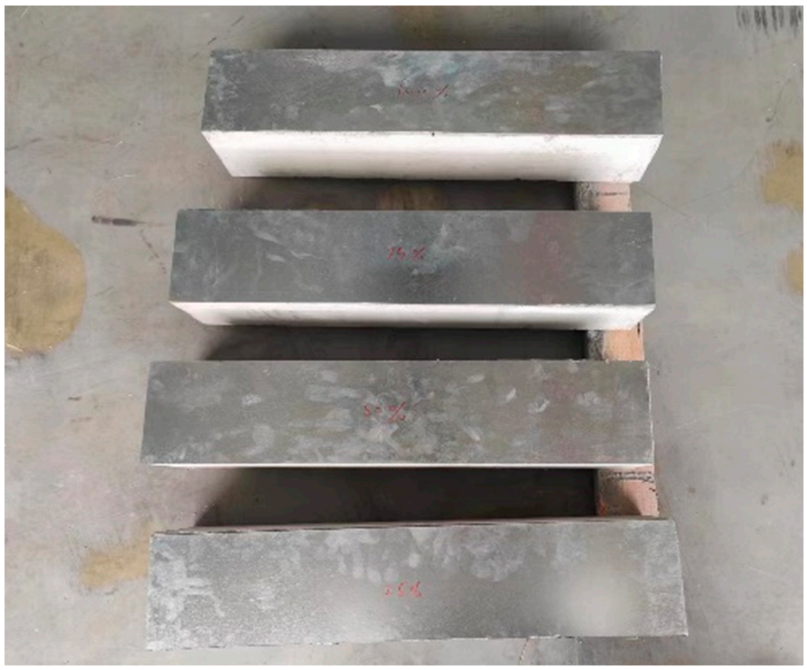

FIGURE 3
Concrete beam with cracks.

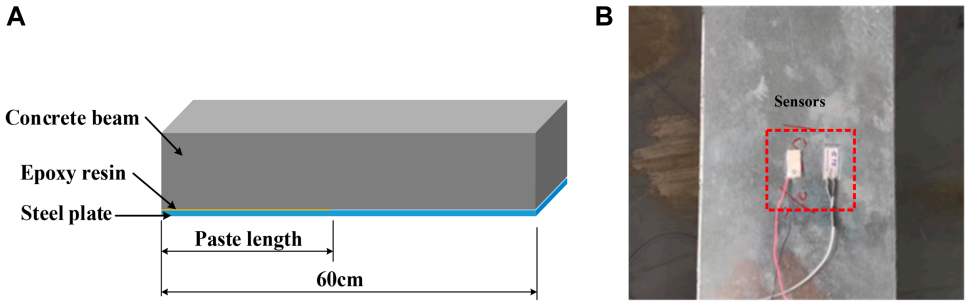

FIGURE 4
Concrete beams with different length of steel plate. **(A)** bonding steel plate reinforcement **(B)** Piezoelectric material paste.

3.2 Debonding monitoring experiment between reinforced steel plates and concrete beams

To study the signal response of piezoelectric materials to the degree of delamination of steel plates, the steel plates were bonded to four concrete beams with adhesive, with bonding lengths of 100%, 75%, 50%, and 25% of the concrete beam length, as shown in Figure 4A. Then, epoxy resin was used to bond the strip sensor and PZT actuator to the middle of the steel plate, as shown in Figure 4B. The electrical signals received by the dynamic information acquisition system are shown in Figure 5.

According to Figure 5, it can be observed that for the same frequency sweep signal, the voltage signal amplitude collected by the dynamic information acquisition instrument varies with different lengths of steel plate bonding. When the bonding length of the steel plate is 100%, the voltage signal amplitude collected by the dynamic information acquisition instrument is 0.017mV; when the bonding length is 75%, the voltage signal amplitude collected is 0.020mV; when the bonding length is 50%, the voltage signal amplitude collected is 0.080mV; and when the bonding length is 25%, the voltage signal amplitude collected is 0.103 mV.

The relationship between the length of steel plate adhesion and the voltage amplitude is shown in Figure 6. As shown in Figure 6, with the decrease in the length of steel plate adhesion, the voltage signal amplitude collected by the dynamic information acquisition instrument gradually increases, especially at a adhesive length of 75%, where a significant turning point in the signal amplitude occurs. Therefore, the characteristics of the voltage signal amplitude collected by the dynamic information acquisition instrument changing with the degree of steel plate detachment can be used to characterize the degree of detachment between the steel

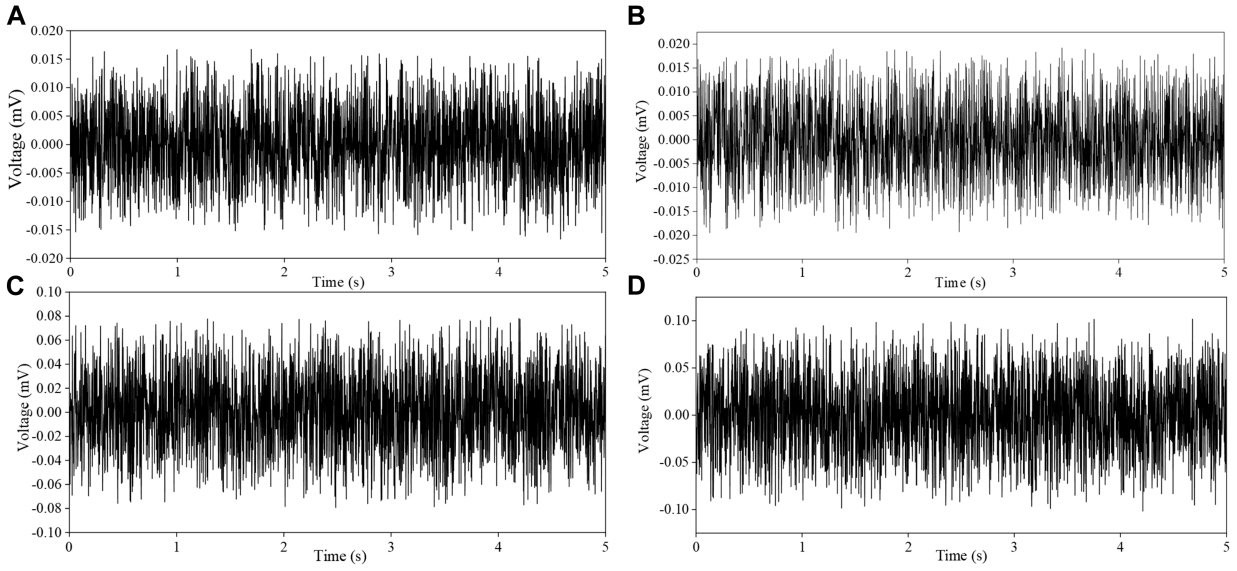

FIGURE 5
Signal response of steel plates with different sticking lengths. **(A)** Paste length 100% **(B)** Paste length 75% **(C)** Paste length 50% **(D)** Paste length 25%.

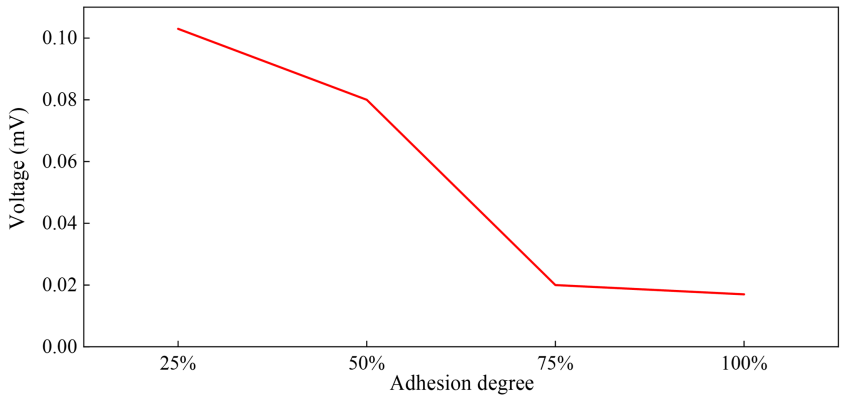

FIGURE 6
Different paste length signal amplitude change diagram.

plate and concrete; that is, the larger the signal amplitude received by the dynamic information acquisition instrument, the shorter the length of steel plate adhesion, the greater the degree of detachment between the steel plate and the concrete beam.

3.3 The experiment on the influence of different monitoring positions on the electrical signal

The monitoring experiment of the debonding degree of steel plates has proved the feasibility of the active sensing technology in monitoring the debonding degree of steel plates. However, the influence of sensor position on signal amplitude cannot be ruled out. In order to study the difference in signal amplitude caused by the different positions of sensors attached to the steel plate, a concrete beam with a steel plate attachment length of 50% was selected. PZT actuators and strip sensors were respectively attached to the left end, middle and right end of the beam, as shown in Figure 7. The dynamic information acquisition system was used to collect the signals generated by the strip sensors attached to different positions of the steel plate, as shown in Figure 8.

As seen in Figure 8, it can be observed that when the PZT actuator and strip sensor are attached to different positions on the steel plate, the voltage signal amplitudes collected by the dynamic information acquisition system are also different. When the sensor is attached to the right side of the steel plate, i.e., the debonding section of the steel plate, the voltage signal amplitude collected by

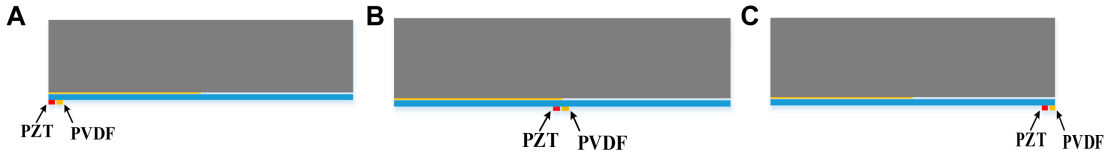

FIGURE 7
Sensors at different positions paste schematics. **(A)** left **(B)** mid **(C)** right.

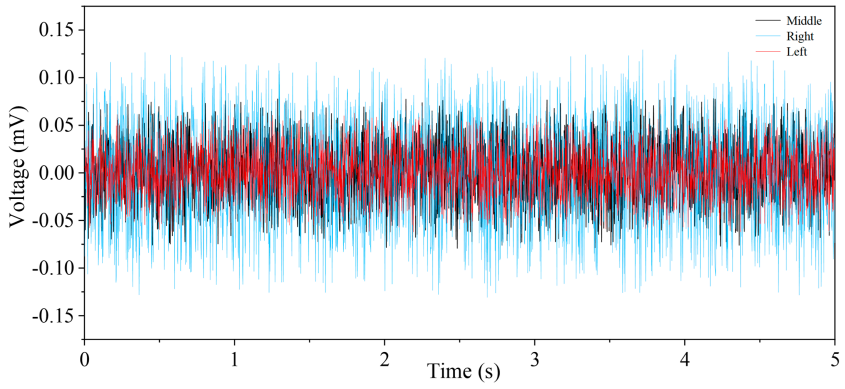

FIGURE 8
Signal response of different position sensors.

the dynamic information acquisition system is the largest. When the sensor is attached to the middle of the steel plate, the voltage signal amplitude collected by the dynamic information acquisition system is significantly smaller than that collected in the debonding section. When the sensor is attached to the left side of the steel plate, i.e., the bonding section of the steel plate, the voltage signal amplitude collected by the dynamic information acquisition system is the smallest, i.e., Vdebonding section > Vmiddle > Vbonding section. Therefore, due to the different bonding conditions between the steel plate and concrete, sensors in different positions perceive external signals differently under the same excitation signal, resulting in different signal amplitudes collected by the dynamic information acquisition system.

3.4 The simulation on the influence of different monitoring positions on the electrical signal

In order to investigate the reasons for the different signal amplitudes collected by the dynamic information acquisition system at different monitoring positions in the experiment of steel plate, this section continues to discuss the impact of PZT actuators and strip sensors at different positions on the received signal amplitudes by establishing a numerical model when the pasting length is fixed.

Using COMSOL software to model the strengthening of steel plates on concrete beams, the three-dimensional elastic wave solid mechanics module was selected for analysis. First, the material properties were set, with concrete, steel plate, and epoxy resin using the materials provided by COMSOL, including Concrete, Structural steel, and Filled epoxy resin (X238). The properties of the materials are shown in Table 5. Then, the pasting length of the steel plate was set to 50%, with the left side being the pasted section and the right side being the debonded section. The constructed three-dimensional model of the steel-reinforced concrete beam is shown in Figure 9. After the model is established, the concrete beam is controlled by the physical field to control the grid, with extremely refined grid divisions. The grid division diagram of the concrete structure is shown in Figure 10.

First, the PZT actuator under the steel-reinforced concrete beam structure is subjected to analysis with a sinusoidal vibration signal source. The amplitude of the sinusoidal signal is 1mm, and the vibration frequency is 500Hz, with specific displacement constraints set. Then, the bottom vibrating block is similarly used as an excitation signal source, utilizing concrete parameters, and the entire structure undergoes transient analysis, with a stop time of 300μs and a step size of 0.1μs. The propagation of stress waves generated by the signal source after its inception is shown in Figure 11.

From Figure 11, it is evident that when the sensor is attached to the left side of the steel plate, i.e., the adhered portion of the steel plate, the stress waves generated by the PZT actuator will rapidly propagate into the concrete due to stress and strain continuity

TABLE 5 Parameters of material performance.

Materials	Density (kg/m3)	Young's modulus (Pa)	Poisson's ratio
Concrete	2,300	2.5×10^{10}	0.2
Steel plate	7,850	2×10^{11}	0.3
Epoxy resin	1730	2.7×10^{5}	0.2

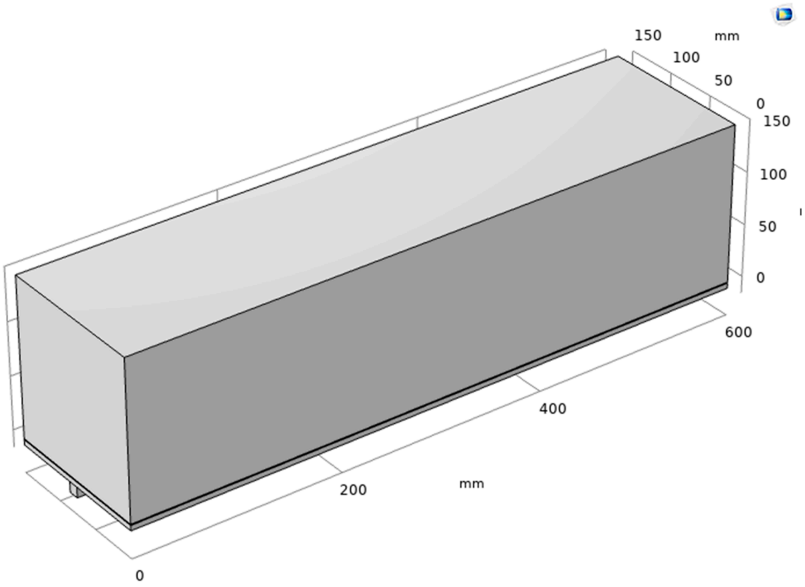

FIGURE 9
Geometric modeling diagram of steel plate reinforced concrete.

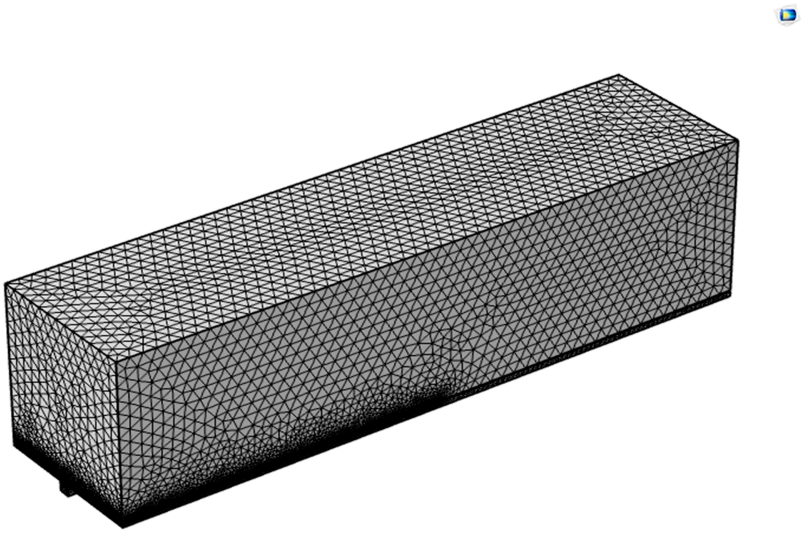

FIGURE 10
Grid division diagram of steel plate reinforced concrete structure.

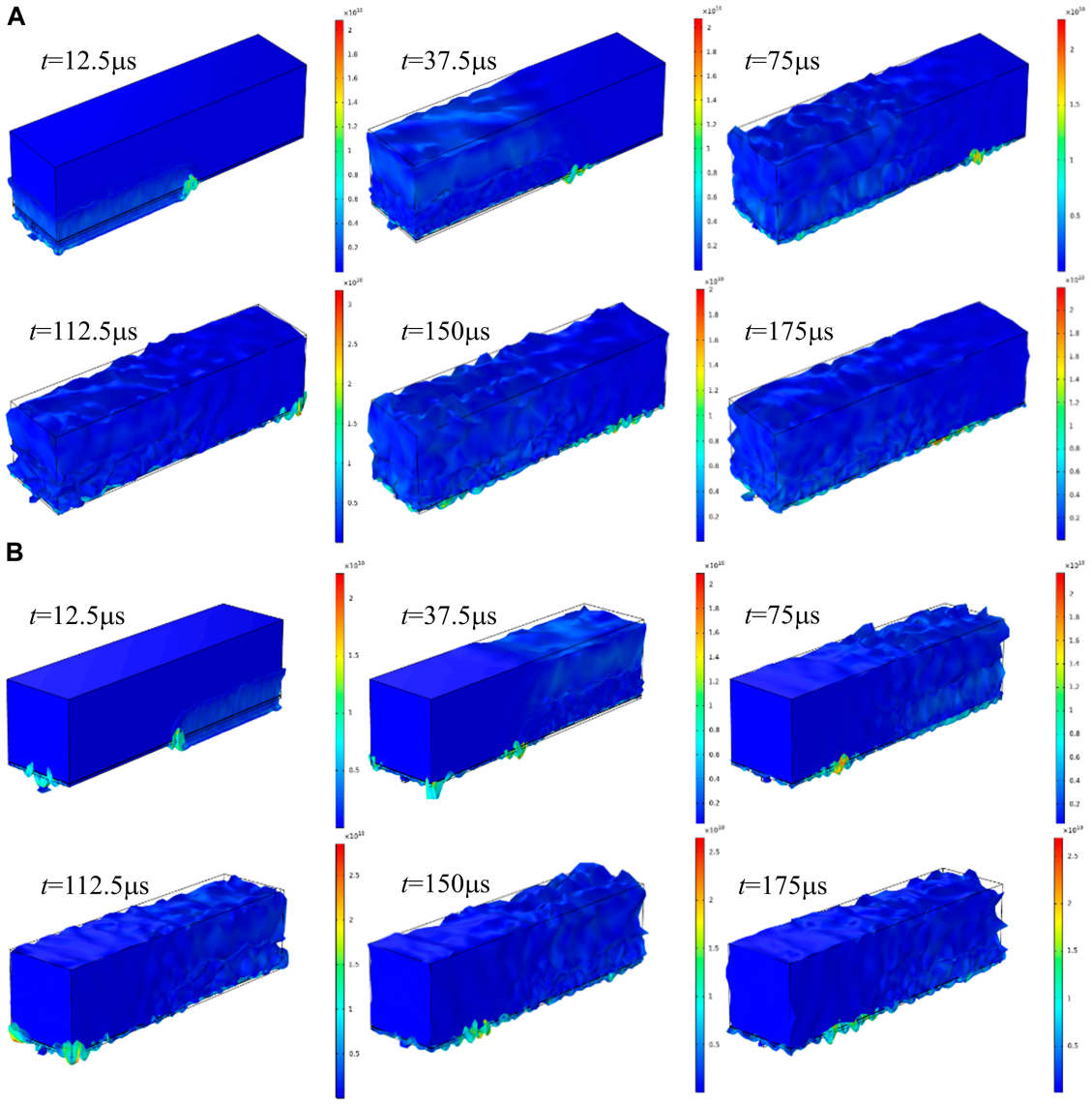

FIGURE 11
The diagram of stress wave propagation. **(A)** Left pasted sensor; **(B)** Right paste sensor.

conditions being met at the adhered region where the steel plate is bonded to the concrete beam with epoxy resin, resulting in stress wave attenuation. When the sensor is attached to the right side of the concrete, i.e., the debonded section of the concrete, the stress waves generated by the PZT actuator first propagate through the steel plate, with a greater range of variation. The majority of the transmitted waves are reflected lback to the strip sensor through the steel plate, and some waves are projected and transmitted into the concrete, causing a rapid reduction in the deformation amplitude of the steel plate. Due to the different forms of energy loss in the adhered and debonded sections of the steel plate, the energy loss in the adhered section is faster, resulting in a smaller signal amplitude in the adhered section. Therefore, the different signal amplitudes captured by the dynamic information acquisition system when the sensor is attached to different positions on the steel plate are due to the different propagation conditions and associated losses during the transmission of stress waves at different positions.

4 Conclusion

In this paper, the active monitoring experiment of steel plate reinforced concrete based on PVDF material is designed. Combined with finite element simulation, the output signal changes of different bond lengths and monitoring positions of steel plates are compared and analyzed, and the debonding law of steel plate-reinforced concrete beams is studied. The main conclusions are as follows:

(1) A piezoelectric theoretical model has been proposed for actively monitoring the degree of concrete debonding of

steel plates. A PZT actuator and a strip sensor using composite materials were prepared to increase the strain range. The voltage signal output by the strip sensor is monitored to evaluate the degree of debonding between the steel plate and the concrete beam by applying an excitation signal to the PZT.

(2) The experiment on active monitoring of bonding between steel plate and reinforced concrete reveals that the signal amplitude received by the strip sensor varies with the degree of debonding of the steel plate when the bonding position of the PZT actuator and strip sensor is fixed. When the length of the paste is 100%, 75%, 50%, and 25%, the output signals of PVDF are 0.017 mV, 0.020 mV, 0.080 mV, and 0.103 mV, respectively. This means that the greater the signal amplitude the strip sensor receives, the greater the degree of debonding between the steel plate and the concrete beam.

(3) Experiments were carried out on concrete beams with different bonding positions of PZT actuators and strip sensors but with the same degree of debonding of steel plates. The results show that under the condition of the same excitation signal, the sensors at different positions have different perceptions of the external signal due to the different external conditions, and the influence of the sensor position change needs to be considered. At this time, the signal received by the sensor installed on the left, middle, and right side, V debonding section > V middle > V pasting section.

(4) The concrete beams with different bonding positions of PZT actuator and strip sensor but the same debonding degree of steel plate were simulated. The simulation results show that the signal amplitude of the strip sensor is different when the sensor is pasted at different positions of the steel plate, which is caused by the different loss of the conduction conditions at different positions in the process of stress wave conduction. The energy loss of the pasting section is fast, so the signal amplitude generated by the pasting section is small.

Data availability statement

The original contributions presented in the study are included in the article/Supplementary Materials, further inquiries can be directed to the corresponding author.

Author contributions

YW: Conceptualization, Methodology, Writing–original draft. HK: Formal Analysis, Software, Writing–original draft. YS: Methodology, Supervision, Writing–original draft. MT: Validation, Writing–original draft. LC: Data curation, Writing–original draft.

Funding

The author(s) declare financial support was received for the research, authorship, and/or publication of this article. This research was funded by the Natural Science Foundation of Chongqing (Grant No. CSTB2022NSCQ-MSX1655) and the State Key Laboratory of Structural Dynamics of Bridge Engineering and Key Laboratory of Bridge Structure Seismic Technology for Transportation Industry Open Fund (Grant No.: 202205).

Conflict of interest

The authors declare that the research was conducted in the absence of any commercial or financial relationships that could be construed as a potential conflict of interest.

Publisher's note

Supplementary material

The Supplementary Material for this article can be found online at: https://www.frontiersin.org/articles/10.3389/fmats.2024.1361159/full#supplementary-material

References

Ali, M. S. M., Oehlers, D. J., and Bradford, M. A. (2005). Debonding of steel plates adhesively bonded to the compression faces of RC beams. *Constr. Build. Mater.* 19 (6), 413–422. doi:10.1016/j.conbuildmat.2004.11.002

Arslan, G., Sevuk, F., and Ekiz, I. (2008). Steel plate contribution to load-carrying capacity of retrofitted RC beams. *Constr. Build. Mater.* 22 (3), 143–153. doi:10.1016/j.conbuildmat.2006.10.009

Aslani, F., and Dehestani, M. (2020). Probabilistic impacts of corrosion on structural failure and performance limits of reinforced concrete beams. *Constr. Build. Mater.* 265, 120316. doi:10.1016/j.conbuildmat.2020.120316

Audrain, P., Masson, P., Berry, A., Pascal, J. C., and Gazengel, B. (2004). The use of PVDF strain sensing in active control of structural intensity in beams. *J. intelligent material Syst. Struct.* 15 (5), 319–327. doi:10.1177/1045389X04039936

Barnes, R. A., and Mays, G. C. (2006). Strengthening of reinforced concrete beams in shear by the use of externally bonded steel plates: Part 2–Design guidelines. *Constr. Build. Mater.* 20 (6), 403–411. doi:10.1016/j.conbuildmat.2005.01.028

Benes, E., Gröschl, M., Burger, W., and Schmid, M. (1995). Sensors based on piezoelectric resonators. *Sensors Actuators A Phys.* 48 (1), 1–21. doi:10.1016/0924-4247(95)00846-2

Bouche, R. R. (1975). "Accelerometers for shock and vibration measurements," in Vibration testing-Instrumentation and data analysis; Proceedings of the Fifth National Vibrations Conference, Washington, D.C. New York, September 17-19 (American Society of Mechanical Engineers), 25–59.

Buda-Ożóg, L., Zięba, J., Sieńkowska, K., Nykiel, D., Zuziak, K., Sieńko, R., et al. (2022). Distributed fibre optic sensing: reinforcement yielding strains and crack

detection in concrete slab during column failure simulation. *Measurement* 195, 111192. doi:10.1016/j.measurement.2022.111192

Dai, J. G., Bai, Y. L., and Teng, J. G. (2011). Behavior and modeling of concrete confined with FRP composites of large deformability. *J. Compos. Constr.* 15 (6), 963–973. doi:10.1061/(ASCE)CC.1943-5614.0000230

Fu, C., and Lao, Y. (2023). Steel–concrete bond deterioration in reinforced concrete tension members due to primary cracks. *Structures* 56, 104895. doi:10.1016/j.istruc.2023.104895

Galkovski, T., Mata-Falcón, J., and Kaufmann, W. (2023). Experimental investigation of bond and crack behaviour of reinforced concrete ties using distributed fibre optical sensing and digital image correlation. *Eng. Struct.* 292, 116467. doi:10.1016/j.engstruct.2023.116467

Hasni, H., Alavi, A. H., Jiao, P., Lajnef, N., Chatti, K., Aono, K., et al. (2017). A new approach for damage detection in asphalt concrete pavements using battery-free wireless sensors with non-constant injection rates. *Measurement* 110, 217–229. doi:10.1016/j.measurement.2017.06.035

Hawileh, R. A., Nawaz, W., and Abdalla, J. A. (2018). Flexural behavior of reinforced concrete beams externally strengthened with Hardwire Steel-Fiber sheets. *Constr. Build. Mater.* 172, 562–573. doi:10.1016/j.conbuildmat.2018.03.225

Howser, R., Moslehy, Y., Gu, H., Dhonde, H., Mo, Y. L., Ayoub, A., et al. (2011). Smart-aggregate-based damage detection of fiber-reinforced-polymer-strengthened columns under reversed cyclic loading. *Smart Mater. Struct.* 20 (7), 075014. doi:10.1088/0964-1726/20/7/075014

Huo, L., Li, C., Jiang, T., and Li, H. N. (2018). Feasibility study of steel bar corrosion monitoring using a piezoceramic transducer enabled time reversal method. *Appl. Sci.* 8 (11), 2304. doi:10.3390/app8112304

Jones, R., Swamy, R. N., and Charif, A. (1988). Plate separation and anchorage of reinforced concrete beams strengthened by epoxy-bonded steel plates. *Struct. Eng.* 66 (5). Available at: http://worldcat.org/issn/14665123.

Kaklauskas, G. (2017). Crack model for RC members based on compatibility of stress-transfer and mean-strain approaches. *J. Struct. Eng.* 143 (9), 04017105. doi:10.1061/(ASCE)ST.1943-541X.0001842

Kumar, A., Varghese, A., Sharma, A., Prasad, M., Janyani, V., Yadav, R., et al. (2022). Recent development and futuristic applications of MEMS based piezoelectric microphones. *Sensors Actuators A Phys.* 2022, 113887. doi:10.1016/j.sna.2022.113887

Li, Y. Y., Guo, B., and Liu, J. (2014). Research on reinforced concrete beam enlarged cross section method experiment and finite element simulation. *Appl. Mech. Mater.* 638, 208–213. doi:10.4028/www.scientific.net/AMM.638-640.208

Liao, W. I., Gu, H., Olmi, C., Song, G., Mo, Y. L., and Loh, C. H. (2008). Structural health monitoring of a concrete column subjected to shake table excitations using smart aggregates. *Earth Space* 2008, 1–8. doi:10.1061/40988(323)169

Ma, X., and Liu, L. (2023). Fatigue properties of RC beams reinforced with ECC layer and steel plate. *Constr. Build. Mater.* 372, 130799. doi:10.1016/j.conbuildmat.2023.130799

Naser, M. Z., Hawileh, R. A., and Abdalla, J. A. (2019). Fiber-reinforced polymer composites in strengthening reinforced concrete structures: a critical review. *Eng. Struct.* 198, 109542. doi:10.1016/j.engstruct.2019.109542

Oehlers, D. J., and Ali, M. S. M. (1998). Debonding of steel plates glued to RC flexural members. *Prog. Struct. Eng. Mater.* 1 (2), 185–192. doi:10.1002/pse.2260010211

Othmani, C., Zhang, H., and Lü, C. (2020). Effects of initial stresses on guided wave propagation in multilayered PZT-4/PZT-5A composites: a polynomial expansion approach. *Appl. Math. Model.* 78, 148–168. doi:10.1016/j.apm.2019.10.017

Prabakar, K. (2007). Acoustic emission from PZT-5A and PZT-8 ceramics during the application of AC field at different frequencies. *Int. J. Mod. Phys. B* 21 (27), 4707–4714. doi:10.1142/S0217979207038095

Qin, F., Kong, Q., Li, M., Mo, Y. L., Song, G., and Fan, F. (2015). Bond slip detection of steel plate and concrete beams using smart aggregates. *Smart Mater. Struct.* 24 (11), 115039. doi:10.1088/0964-1726/24/11/115039

Qu, Y., Liu, W., Gwarzo, M., Zhang, W., Zhai, C., and Kong, X. (2017). Parametric study of anti-explosion performance of reinforced concrete T-shaped beam strengthened with steel plates. *Constr. Build. Mater.* 156, 692–707. doi:10.1016/j.conbuildmat.2017.08.150

Shah, A. A., and Ribakov, Y. (2009). Non-linear ultrasonic evaluation of damaged concrete based on higher order harmonic generation. *Mater. Des.* 30 (10), 4095–4102. doi:10.1016/j.matdes.2009.05.009

Shah, A. A., Ribakov, Y., and Hirose, S. (2009). Nondestructive evaluation of damaged concrete using nonlinear ultrasonics. *Mater. Des.* 30 (3), 775–782. doi:10.1016/j.matdes.2008.05.069

Song, G., Qiao, P. Z., Binienda, W. K., and Zou, G. P. (2002). Active vibration damping of composite beam using smart sensors and actuators. *J. Aerosp. Eng.* 15 (3), 97–103. doi:10.1061/(ASCE)0893-1321(2002)15:3(97)

Wu, A., He, S., Ren, Y., Wang, N., Ho, S., and Song, G. (2019). Design of a new stress wave-based pulse position modulation (PPM) communication system with piezoceramic transducers. *Sensors* 19 (3), 558. doi:10.3390/s19030558

Xu, K., Ren, C., Deng, Q., Jin, Q., and Chen, X. (2018). Real-time monitoring of bond slip between GFRP bar and concrete structure using piezoceramic transducer-enabled active sensing. *Sensors* 18 (8), 2653. doi:10.3390/s18082653

Yang, J., Chen, R., Zhang, Z., Zou, Y., Zhou, J., and Xia, J. (2023). Experimental study on the ultimate bearing capacity of damaged RC arches strengthened with ultra-high performance concrete. *Eng. Struct.* 279, 115611. doi:10.1016/j.engstruct.2023.115611

Ye, Y., Laishun, Z., and Man, Z. (2010). Experimental investigation of axial compression column be strengthened with the method of enlarging sectional areas. *Build. Struct.* 40 (6), 412–414. doi:10.19701/j.jzjg.2010.s2.122

Yu, Y., Zhao, X., Wang, Y., and Ou, J. (2013). A study on PVDF sensor using wireless experimental system for bridge structural local monitoring. *Telecommun. Syst.* 52, 2357–2366. doi:10.1007/s11235-011-9558-5

Zaki, Y. A., Abouhussien, A. A., Hassan, A. A. A., et al. (2023). Crack detection and classification of repaired concrete beams by acoustic emission monitoring. *Ultrasonics* 2023, 107068. doi:10.1016/j.ultras.2023.107068

Zanuy, C., de la Fuente, P., and Albajar, L. (2007). Effect of fatigue degradation of the compression zone of concrete in reinforced concrete sections. *Eng. Struct.* 29 (11), 2908–2920. doi:10.1016/j.engstruct.2007.01.030

Zeng, L., Parvasi, S. M., Kong, Q., Huo, L., Lim, I., Li, M., et al. (2015). Bond slip detection of concrete-encased composite structure using shear wave based active sensing approach. *Smart Mater. Struct.* 24 (12), 125026. doi:10.1088/0964-1726/24/12/125026

Zhan, T., Wang, Z., and Ning, J. (2015). Failure behaviors of reinforced concrete beams subjected to high impact loading. *Eng. Fail. Anal.* 56, 233–243. doi:10.1016/j.engfailanal.2015.02.006

Zhang, Y., Tang, L., Tian, H., Wang, J., Cao, W., and Zhang, Z. (2017). Determination of temperature dependence of full matrix material constants of PZT-8 piezoceramics using only one sample. *J. alloys Compd.* 714, 20–25. doi:10.1016/j.jallcom.2017.04.124

Zhang, Z., Pang, K., Xu, L., Zou, Y., Yang, J., and Wang, C. (2023). The bond properties between UHPC and stone under different interface treatment methods. *Constr. Build. Mater.* 365, 130092. doi:10.1016/j.conbuildmat.2022.130092

Zhao, X., and Li, H. (2006). Health monitoring of reinforced concrete frame-shear wall using piezoceramic transducer. *J. Vib. Shock* 25 (4), 82–84. doi:10.13465/j.cnki.jvs.2006.04.022

Zou, Y., Jiang, J., Yang, J., Zhang, Z., and Guo, J. (2023). Enhancing the toughness of bonding interface in steel-UHPC composite structure through fiber bridging. *Cem. Concr. Compos.* 137, 104947. doi:10.1016/j.cemconcomp.2023.104947

frontiers | Frontiers in Materials

TYPE Original Research
PUBLISHED 06 February 2024
DOI 10.3389/fmats.2023.1321177

OPEN ACCESS

EDITED BY
Anbang Li,
Xi'an University of Architecture and Technology, China

REVIEWED BY
Xiaoqiang Yang,
Fuzhou University, China
Fengjiang Qin,
Chongqing University, China
Jun He,
Changsha University of Science and Technology, China

*CORRESPONDENCE
Ligui Yang,
yangligui@cqjtu.edu.cn

RECEIVED 13 October 2023
ACCEPTED 29 December 2023
PUBLISHED 06 February 2024

CITATION
Wang S, Feng J, Yang L, Cai G and Jiang D (2024), Harnessing the joint effect of approach bridges in arch bridge construction: an analytical study on thrust stiffness and elevation error mitigation.
Front. Mater. 10:1321177.
doi: 10.3389/fmats.2023.1321177

Harnessing the joint effect of approach bridges in arch bridge construction: an analytical study on thrust stiffness and elevation error mitigation

Shaorui Wang[1,2], Ji Feng[1,2], Ligui Yang[1,2]*, Guoqing Cai[1,2] and Daimin Jiang[1,2]

[1]State Key Laboratory of Mountain Bridge and Tunnel Engineering, Chongqing Jiaotong University, Chongqing, China, [2]School of Civil Engineering, Chongqing Jiaotong University, Chongqing, China

Achieving full equilibrium for the horizontal component force of the backstay in cable-stayed arch bridges is challenging, and the stiffness of the buckle tower has a notable influence on the overall shape of the main arch structure. Increased stiffness in the buckle tower leads to reduced construction complexity. Therefore, this study proposed a method of enhancing the longitudinal thrust stiffness of the buckle tower using the joint effect of approach bridges. A sensitivity analysis was conducted on the approach bridge–composite buckle tower structure to determine the optimal combination method, resulting in the formulation of an analytical expression for the thrust stiffness of this structure. In this study, numerical analysis was performed to explore the composition mechanism of the thrust stiffness influenced by the pier–girder connection, and we discussed the applicability of the joint effect of approach bridges during the cantilever assembly process of arch ribs. The following conclusions were obtained: 1) prior to installing the main girder of the approach bridge, when the steel buckle tower and the junction pier have already been secured, the most effective approach is to form a "T" rigid structure by firmly connecting the main girder of the approach bridge with the composite buckle tower. This configuration provides self-weight deflection and pier–girder rotation restriction effects. 2) The study presents analytical formulas for the completely rigid pier–girder connection of the approach bridge–composite buckle tower structure, partially rigid pier–girder connection, and pre-deviation. Combined with the calculation program, this can guide structural design. 3) When a large downward elevation error of the arch ribs occurs in the middle and later stages, the cable force needed to install new arch segments becomes overly large. Therefore, the joint effect of approach bridges can be utilized to substitute for a portion of the cable force, effectively reducing potential elevation errors that might arise in subsequent arch ribs in the absence of this joint effect.

KEYWORDS

bridge engineering, tower deviation control, stay button hanging, pushing stiffness, joint effect

1 Introduction

Cable-stayed suspension is the most common construction method for large-span arch bridges (Liu, 2008; Ding et al., 2023). During the cable-stayed suspension construction of arch bridges, due to installation or manufacturing errors and dynamic changes in the construction process, the horizontal component force of buckle anchor cables faces difficulties in reaching equilibrium, causing the buckle tower to deviate in the longitudinal direction of the bridge (Zhou et al., 2000b; Xu et al., 2016a). Moreover, once the control points of the cable-stayed construction arch rib reach the design elevation, buckle backstay anchoring is no longer tensioned. When there is a deviation in the shape of the arch rib, making subsequent adjustments can become a complicated or even impossible task (Xu et al., 2016b; Chen et al., 2023). Therefore, the buckle tower stiffness significantly impacts the line shape of the main arch ring. Increased stiffness in the buckle tower not only reduces construction complexity but also enhances the construction quality of the main arch. Under the same conditions, the stiffness of the buckle tower should be increased as much as possible to reduce the tower deviation. Currently, owing to the widespread use of the cable-stayed suspension method in building large-span arch bridges, various researchers have undertaken extensive research to manage and optimize the line shape of the cable-stayed construction arch rib.

Zheng et al. (1996) utilized the principle of torque equilibrium to calculate the cable force on the arch rib during the cable-stayed hoisting construction, resulting in promising results when this method was used to compute the hinge joint conditions between arch segments. Subsequently, Zhou et al. (2000a) delved deeper into the torque equilibrium method, introducing the "zero bending moment method." By utilizing integral calculations, they enhanced the accuracy of determining the cable force on the arch rib. Subsequently, Zhou (2002) introduced the fixed-length buckle cable technique. This approach considered both the elastic elongation of the buckle cable and the deflection due to the self-weight of the arch segment during the hoisting process, thereby aligning the arch rib with the design arch axis. However, this method necessitated the tensioning of the buckle cable all at once, posing challenges for subsequent adjustments if discrepancies arose between the calculated and actual results. Qin (2003; 2008) introduced the stress-free state method, revealing that if the structural system, stress-free state quantities, boundaries, and external loads of the bridge being constructed in segmented main arch rings were maintained, the internal forces and displacements of the completed bridge structure had a unique solution. Interestingly, this was irrespective of the construction sequence. Subsequently, Wang (2013) suggested that the stress-free state method could eliminate the impact of temperature effects and tower deviation on the arch rib's line shape during hoisting. Hao and Gu (2015) noted that the practice of inserting gaskets between flanges to compensate for bending angles when controlling the hoisting of steel pipe arch ribs using the pre-elevation method would alter the stress-free state quantity of the arch rib. Consequently, error in the line shape and internal forces after closure was inevitable. Studying the causes of errors and their transfer mechanism during the hoisting of steel pipe arch ribs, Hao et al. (2018) utilized the stress-free state method to analyze the construction process of the arch rib and proposed several adjustable error control intervals. Focusing on the error in the hoisting and splicing of the arch rib, Zhang (2001) was the first to introduce the optimization theory into the calculation of cable forces. Combined with the Kalman filter method, he calculated the optimal cable force matrix and the preliminary arch degree during the bridge construction process. Subsequently, Zhang et al. (2004) integrated ANSYS finite element software with the optimization theory to calculate variations in cable forces, thereby addressing the requirement for an accurate adjustment of cable forces during the line shape adjustment process. Xu (2011) used the Bayesian temperature prediction model to discern the pattern of seasonal temperature changes on the installation line shape of the arch rib. He then used the influence matrix and optimization algorithms to adjust the errors caused by the temperature during the splicing process of the arch rib. Hao and Gu (2016) also studied the line shape adjustment issue during the splicing and hoisting processes of the arch rib. Considering the deviation between the real and design line shapes of the arch rib, they proposed a theoretical calculation method for a "feasible optimal solution" based on the influence matrix. Using the stress equilibrium equation considering only the tensile stress, permissible tensile stress of the arch rib, and the influence matrix method, Liu et al. (2022) put forward an initial buckle cable force calculation method based on the stress equilibrium method. This improvement on the original stress equilibrium method resulted in a significant increase in work efficiency. Finally, using the influence matrix and linear programming to determine the initial value of iterative cable forces, Li et al. (2017) observed that appropriate cable forces, installed forward through the golden selection method and iterations, achieved a one-time tension of the cable force for cable-stayed steel pipe concrete arch bridges tailored to the installation shape.

Long (2012) discovered that the key to the integrated construction of cable towers and buckle towers was to control the displacement at the tower top. This approach guaranteed that the cable tower and buckle tower could withstand smaller bending moments. To control this displacement, it is essential to minimize the horizontal forces caused by hoisting arch ribs and tensioning buckle cables. Deng et al. (2020) used the suspension element method to derive the calculation formula for the tower deviation of the cable-stayed system with a push-down cable set. This achieved effective integration and unification of the computations during the cable-stayed construction stage and tower deviation calculation, which is extremely important for accurate control of tower deviation. Deng (2009) used geometric analysis to derive the calculation formula for the influence of buckle tower deviation on the elevation of arch rib segments. This provides a valuable reference for the design of cable-stayed hoisting and the control of segment installation elevation. Mo (2021) studied the impact of main cable slippage on tower deviation in the cable-stayed hoisting system design. He observed that the main cable slippage significantly affected the cable-stayed hoisting system, leading to noticeable changes in top tower displacement and top tower stress.

Regarding the study of line shape control in the construction of cable-stayed arch ribs, adjustments for various errors affecting the accuracy of the arch rib line shape are mainly based on buckle cable force calculations (Gu et al., 2015). However, there remains a dearth of research dedicated to the control of tower deviations

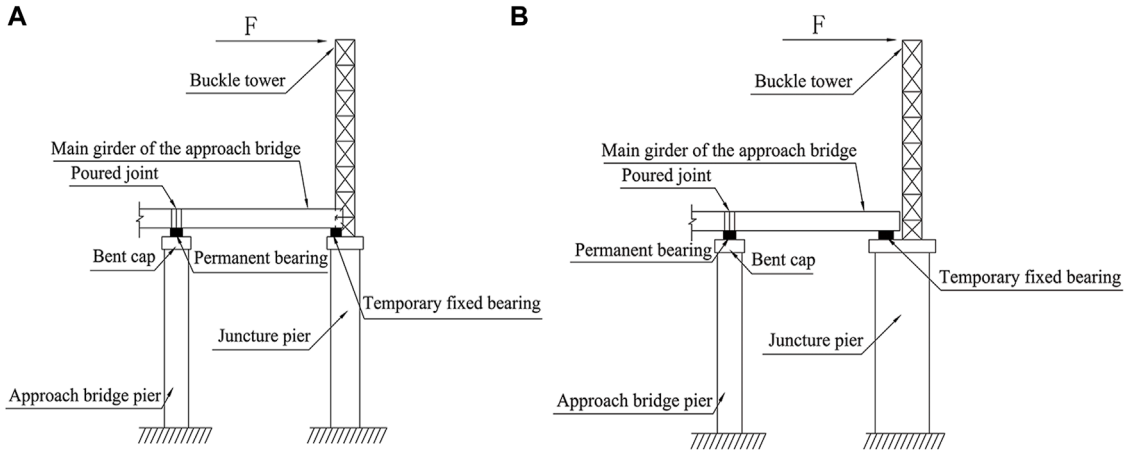

FIGURE 1
Schematic diagram of the synergistic effect of the buckle tower and the approach bridge. **(A)** Passing through the main girder. **(B)** Without passing through the main girder.

by improving the longitudinal thrust stiffness of the buckle tower. Furthermore, there is a notable absence of studies examining the mechanism behind thrust stiffness formation, taking into account factors like self-weight deflection and local deformation effects in approach bridge–composite buckle tower structures. Therefore, this paper uses a large-span deck-type steel pipe concrete arch bridge built through a cable-stayed cantilever assembly as the engineering background. The study then delves into the calculation techniques and investigates the effects of buckle tower stiffness, considering the joint effect of approach bridges.

2 Formation mechanism of the joint effect of approach bridges

The construction of a cable-stayed arch bridge requires the erection of a temporary buckle tower to complete the tensioning of the buckle anchor cable. For the construction of arch bridges with restricted construction sites and larger rise-to-span ratios, a combination of permanent and temporary structures, i.e., a composite cable tower, is generally adopted. This involves erecting a steel buckle tower on juncture piers, allowing both the juncture pier and steel buckle tower to jointly withstand the horizontal thrust caused by the pull cable (Chen et al., 2017). Depending on the dimensions of the juncture pier along the longitudinal direction of the bridge, the steel buckle tower may either pass through the main girder of the approach bridge via a wet joint or not pass through it at all (Figure 1). However, the main paths of force transmission between the components in both cases do not differ.

As shown in Figure 2, the steel buckle tower is consolidated to the juncture pier. The increased overall height results in increased flexibility of the entire structure. During construction, significant deflection deformations occur due to differences in horizontal cable forces, which, in turn, cause significant deviations in the buckle tower in the longitudinal direction of the bridge (Yu, 2018).

This paper aims to enhance the longitudinal thrust stiffness of the composite buckle tower by harnessing the joint effect of approach bridges. The core concept is to facilitate cooperative support among the buckle tower, juncture pier, approach bridge piers, and main girder of the approach bridge, thereby controlling buckle tower deviations.

3 Analysis of factors influencing the buckle tower stiffness considering the joint effect of approach bridges

3.1 Finite-element model establishment

The main bridge and approach bridge juncture piers use a "gate"-type hollow thin-walled pier with a variable box cross section. The center distance of the two lateral limbs of the pier is the same width as the main arch rib, 16.0 m, and the material is C50. It is 89.9 m high (91.9 m including the bent cap). The cross-sectional size of a single-limb pier is 5.5 m in the transverse direction of the bridge and 6.5 m in the longitudinal direction, with the internal wall thickness varying from 60 to 80 cm. The steel buckle tower, 31.19 m high, is made of Q345 material and is a truss structure composed of columns, connecting horizontal bars, and diagonal bars. The columns use φ630 × 20 mm steel pipes, and the horizontal and diagonal bars use φ325 × 10 mm and φ273 × 8 mm steel pipes, respectively. All bar members are connected by welding. There are two truss cross braces between the two limbs of the steel buckle tower, and the steel buckle tower is anchored on the top of the juncture pier. The approach bridge piers are set as thin-walled double-limb piers with a height of 90.1 m. The cross-sectional size is 2.5 m × 2.0 m, the thickness is 40 cm, and the material is C35. The two piers are connected by two inter-column tie beams. The material of the main girder of the approach bridge is C50, with each 42.0 m span divided into 9 T girders. The overall effect of the model is illustrated in Figure 3. The model was created using Midas/Civil finite-element software.

This study examines the effects of external factors on the thrust stiffness of the composite buckle tower. Therefore, the size of the horizontal cable force difference is determined using only the

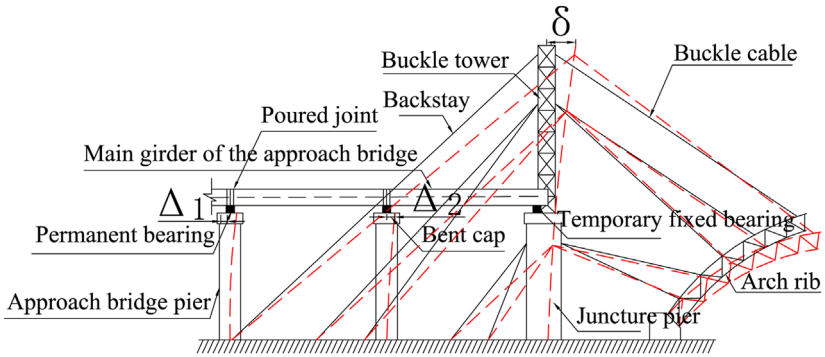

FIGURE 2
Schematic diagram of the buckle tower deflection-induced deviation.

situation with the composite buckle tower. According to the theory of thrust stiffness, the thrust stiffness of the series structure is only related to the flexural stiffness EI and height h and is independent of the external load of the system. Therefore, horizontal loads can be exclusively applied at the top of the composite buckle tower to represent the horizontal cable force difference.

To keep the deformation of the structure within the range of linear elasticity and make the research more reasonable, the size of the horizontal cable force difference should be set based on relevant specifications.

According to the specification JTG/T 3650, 2020, the tower deviation with the fixed foot is H/400–H/600, where H is the height of the steel buckle tower. Considering that the height of the juncture pier increases the structural flexibility, the horizontal load when the tower deviation is H/400 is taken as the maximum difference in horizontal cable forces. When the height of the steel buckle tower is 31.19 m, H/400 is approximately 7.8 cm.

To ensure uniform stress, the load is applied to both limbs of the steel buckle tower (the tower deviation equals the average horizontal displacement at the top of the two limbs). When the tower deviation is approximately 7.8 cm, the load is 2 × 200 kN = 400 kN. Thus, a horizontal load of 400 kN in the longitudinal direction of the bridge is taken as the horizontal cable force difference, as demonstrated in Supplementary Appendix Figure A1.

3.2 Pier–girder connection mode

To control the variables, our study focuses solely on one approach bridge pier. There are four types of pier–girder connections: hinge joints between the two piers and the main girder of the approach bridge (double-hinged), a fixed connection between the juncture pier and the main girder of the approach bridge (right-fixed), a fixed connection between the approach bridge pier and the main girder of the approach bridge (left-fixed), and a fixed connection between the two piers and the main girder of the approach bridge (double-fixed).

There are three types of loads: self-weight, horizontal cable force difference toward the midspan, and horizontal cable force difference away from the midspan. To clarify the impact of these three loads on tower deviations with different pier–girder connection modes, they should be investigated separately. Both tower deviations and horizontal cable force differences are considered positive when directed toward the midspan. If the model only suffers a horizontal load, it is normal for the bearing to be under tension because the horizontal load will reduce the axial pressure on the bearing caused by self-weight. If both types of loads act simultaneously, the axial resultant force on the bearing is always compressive.

3.3 Under self-weight

The self-weight is applied to the structure, and Supplementary Appendix Table A1 and Supplementary Appendix Figure A1 are obtained.

After analyzing Supplementary Appendix Table A1 and Supplementary Appendix Figure A1, we can observe the following:

In the case of only the composite buckle tower, the structure deviated 0.104 mm away from the midspan under self-weight, indicating that the structure is eccentric in the longitudinal direction. The double-hinged connection also caused a 0.135-mm tower deviation away from the midspan, implying that the combined structure also has a longitudinal eccentricity. However, the tower deviation in both cases was far less than 1 mm, suggesting a relatively weak influence on tower deviations.

In the case of double-fixed and right-fixed connections, the negative bending moment caused by the self-weight of the main girder of the approach bridge at the fixed connection between the juncture pier and the main girder caused the composite buckle tower to bend away from the midspan, resulting in tower deviations of 66.785 mm and 69.295 mm, respectively. Disregarding the influence of shear, the bending moment and deformation caused by self-weight in both cases are delineated in Figure 4.

It is evident that $M_y > M_s$ and that their E_jI_j values are the same, and the double-hinged approach bridge pier tends to bend toward the midspan, so $\delta_y > \delta_s$. Therefore, based on the model data and principles of general mechanics, it can be concluded that the influence of the right-fixed connection on tower deviations due to self-weight is more significant than that of the double-fixed connection.

In the case of the left-fixed connection, the negative bending moment at the fixed connection between the approach bridge pier

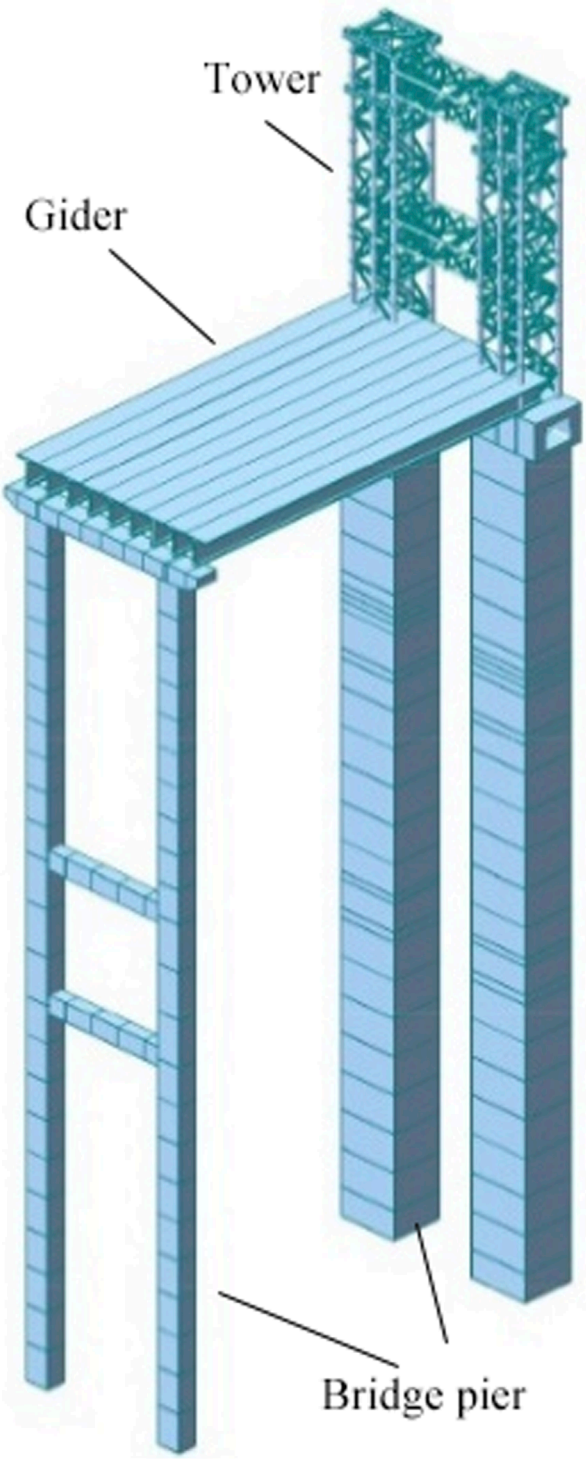

FIGURE 3
Midas/Civil model of the tower and approach bridge.

and the main girder of the approach bridge caused the approach bridge pier to bend toward the midspan, pushing the buckle tower to bend toward the midspan and resulting in a tower deviation of 2.352 mm. The bending moment and deformation are shown in Figure 4:

The mechanical principle analysis is a general trend. Notwithstanding, according to the tower deviation data, the impact of the left-fixed connection on tower deviations under self-weight is weaker compared with the right-fixed connection.

3.4 Under horizontal cable force differences

When the structure is subjected to a horizontal cable force difference, refer to Supplementary Appendix Table A2 and Supplementary Appendix Figure A1.

Note: a) The tower deviation change refers to the absolute value of the difference between the tower deviation without approach bridge piers and other cases. b) The percentage refers to the absolute value of the ratio of the tower deviation change to the tower deviation without approach bridge piers.

Through an examination of the mechanical principles underlying the data in Supplementary Appendix Table A2 and Supplementary Appendix Figure A2, conclusions can be drawn regarding the impact of the horizontal cable force difference at the midspan.

The tower deviation with the double-hinged connection mode decreased by 0.239 mm compared to the case of no approach bridge piers, indicating a weak regulation effect on tower deviations.

The tower deviation with the right-fixed connection mode decreased by 18.407 mm compared to the case of no approach bridge piers, a reduction of 23.781%, indicating a sound regulation effect. This demonstrates that apart from the deflection effect induced by the self-weight in the right-fixed connection, there are other factors that significantly influence tower deviations. The schematic comparison of deflection between the right-fixed connection and the double-hinged connection is plotted in Figure 5.

When the structure is subjected to the horizontal cable force difference toward the midspan, θ_s is an acute angle and θ_y is a right angle (under ideal circumstances in the model); thus, $\theta_y - \theta_s = \Delta\theta > 0$ and $\Delta_s \approx \Delta_y + \Delta\theta \times h_g > \Delta_y$.

The double-hinged connection relies entirely on the approach bridge pier to improve the thrust stiffness, while the right-fixed connection, in addition to the impact of the thrust stiffness of the approach bridge pier itself, also reduces tower deviations by virtue of the geometric relationship between the piers and girders. Therefore, the right-fixed connection has a significant advantage over the double-hinged connection in terms of tower deviation control.

The tower deviation with the left-fixed connection mode decreased by 0.964 mm compared to the case of no approach bridge piers, a reduction of 1.245%, indicating slightly stronger control than the double-hinged connection. Compared to the double-hinged connection, the left-fixed connection reduces tower deviations not only by relying on the thrust stiffness of the approach bridge pier but also by virtue of the geometric relationship between the piers and girders. The schematic comparison of deflection between the double-hinged connection and the left-fixed connection is provided in Figure 5.

When the structure is subjected to the horizontal cable force difference toward the midspan, with the longitudinal girder stiffness being large enough, the elongation of the longitudinal girder is a higher-order trace, and the approach bridge pier is approximately

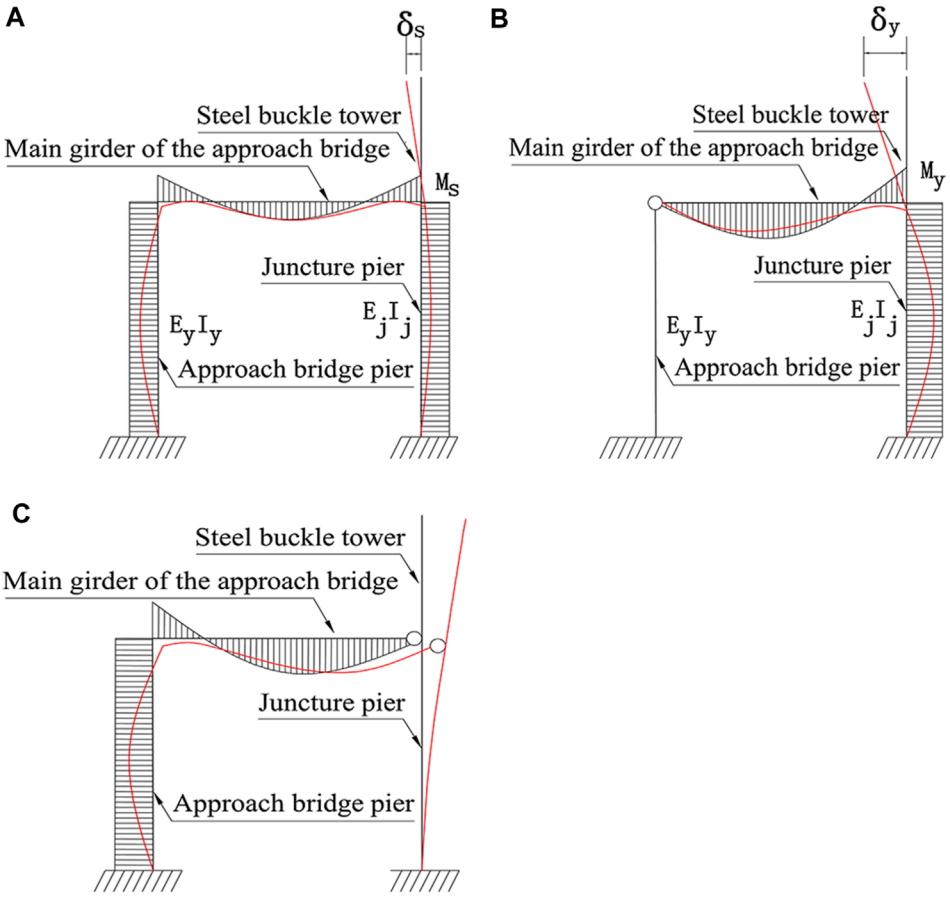

FIGURE 4
Deflection modes under self-weight: **(A)** double-fixed, **(B)** right-fixed, and **(C)** left-fixed.

parallel to the juncture pier. Since θ_s' is an obtuse angle and θ_z' is a right angle, then $\theta_z - \theta_s = \Delta\theta' > 0$ and $\Delta_s \approx \Delta_z + \Delta\theta' \times h_g\Delta_z$.

Compared with the right-fixed connection, since the flexibility of the approach bridge pier is much larger than that of the main girder of the approach bridge, the left-fixed connection has a weaker effect on restricting the composite buckle tower from rotating toward the midspan relative to the main girder, and its effect on controlling tower deviations is also relatively diminished.

The tower deviation with the double-fixed connection mode decreased by 19.18 mm compared to the case of no approach bridge piers, a reduction of 24.781%. The double-fixed connection can be regarded as a combination of left-fixed and right-fixed connections, so its control effect is slightly stronger than the right-fixed connection alone. However, the disparity in the control effects between the two is merely 1%, rendering it statistically insignificant.

The tower deviation data under the influence of the horizontal cable force difference away from the midspan is the opposite number of the tower deviation data under the influence of the horizontal cable force difference toward the midspan. Therefore, without considering the self-weight, the approach bridge–composite buckle tower structure has in-plane isotropic mechanical properties.

So far, we have separately studied the tower deviation and mechanical principles of different pier–girder connection modes under self-weight load and horizontal cable force differences. The former reveals that the right-fixed connection has the greatest impact on tower deviations under self-weight, while the latter unveils that the right-fixed connection has the best regulation effect on tower deviations under horizontal cable force differences.

Since the tower deviation caused by these two loads in the right-fixed connection is in opposite directions, the right-fixed pier–girder connection can effectively control the tower deviation induced by the horizontal cable force difference toward the midspan. The control effect mainly stems from the "T"-type rigid frame formed by the main girder of the approach bridge and the composite buckle tower. The deflection effect caused by the self-weight of the main girder of the approach bridge makes the composite buckle tower bend away from the midspan and also restricts the composite buckle tower from rotating toward the midspan relative to the main girder. However, this approach necessitates the prior consolidation of the steel buckle tower and junction pier before the installation of the main girder of the approach bridge.

Based on the source of the impact of the approach bridge on tower deviations, it can be deduced that the first span of the approach bridge has the greatest impact on tower deviations. Therefore, only the first span of the approach bridge is considered. The effects of the approach bridge pier height and component flexural stiffness

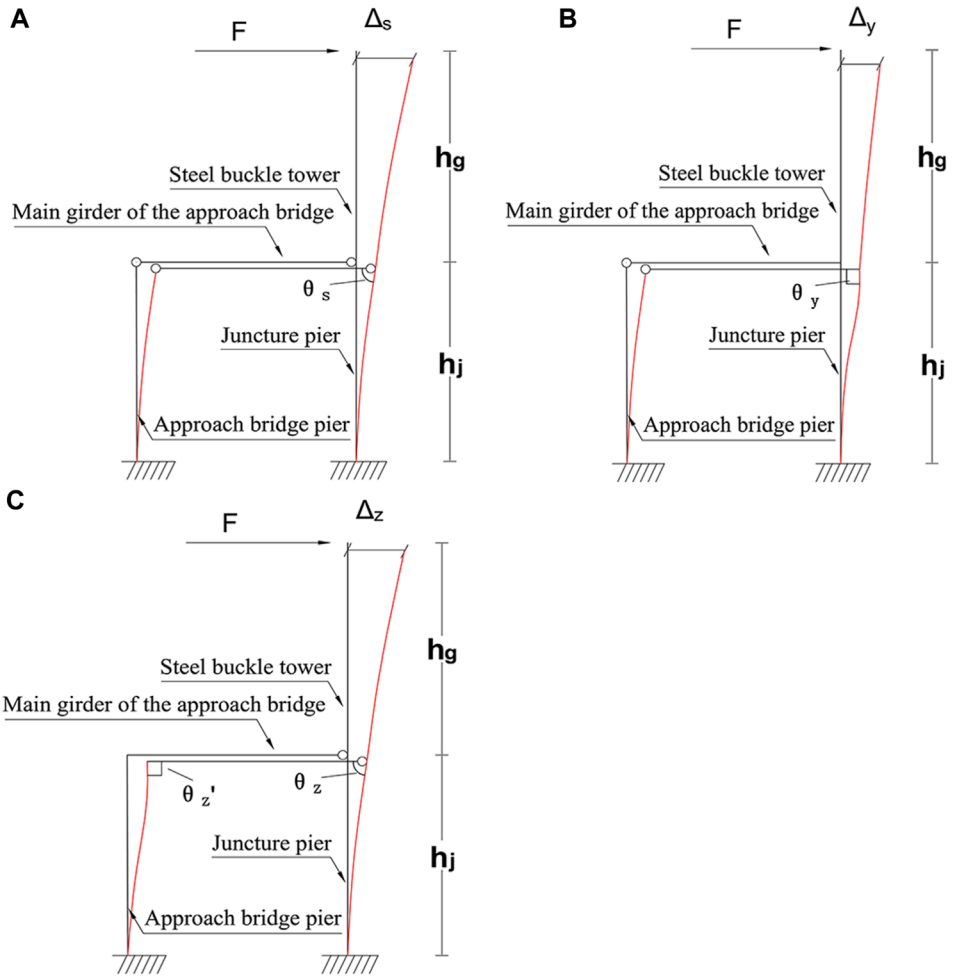

FIGURE 5
Different deflection modes under horizontal cable force toward the midspan: **(A)** double-hinged, **(B)** right-fixed, and **(C)** left-fixed.

on the thrust stiffness of the approach bridge–composite buckle tower structure can be discussed after the theoretical formula. By combining computer programs with analytical formulas, a sensitivity analysis of the impact of component properties on the thrust stiffness can be conducted.

4 Thrust stiffness analytical expression

4.1 Determination of the mechanical calculation model

According to Section 2, the optimal method for connecting the approach bridge to the composite buckle tower is consolidating the juncture pier and the main girder of the approach bridge while hinging the approach bridge pier with the main girder. The mechanical model is shown in Figure 6, with the basic assumptions as follows:

(1) The influence of the longitudinal slope and temperature changes is ignored.

(2) The self-weight of vertical components is ignored.

In Figure 6, h_y denotes the approach bridge pier height, h_j represents the juncture pier height, h_g symbolizes the steel buckle tower height, L_z stands for the span length of the main girder of the approach bridge, q_z signifies the self-weight uniform load of the main girder of the approach bridge, F_c represents the equivalent horizontal cable force difference, E_yI_y denotes the flexural stiffness of the approach bridge pier, E_jI_j signifies the flexural stiffness of the juncture pier, E_gI_g symbolizes the flexural stiffness of the steel buckle tower, and E_zI_z is the flexural stiffness of the main girder of the approach bridge.

4.2 Solution of the thrust stiffness of the completely rigid pier–girder connection

Figure 6 reveals that the structure is a second hyper-static structure. Assuming that the bearing compression between the piers and girders is the positive direction of the vertical basic unknown force, the structure is simplified, and the basic system is shown in Figure 7.

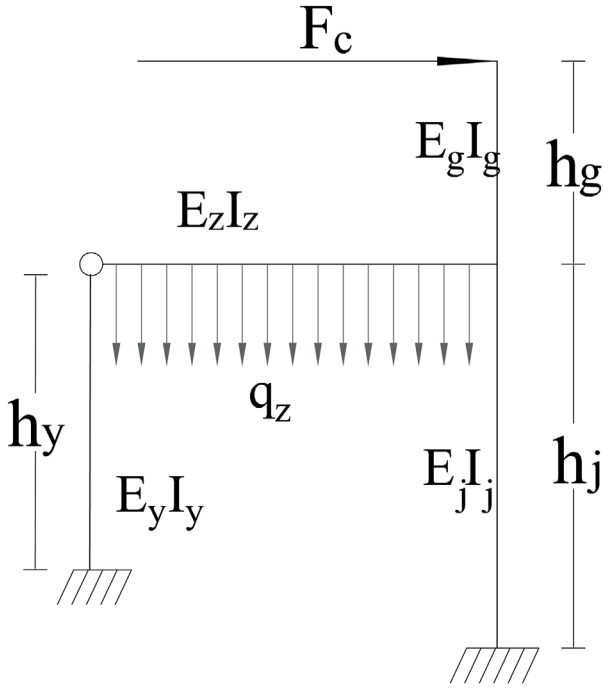

FIGURE 6
Mechanical model.

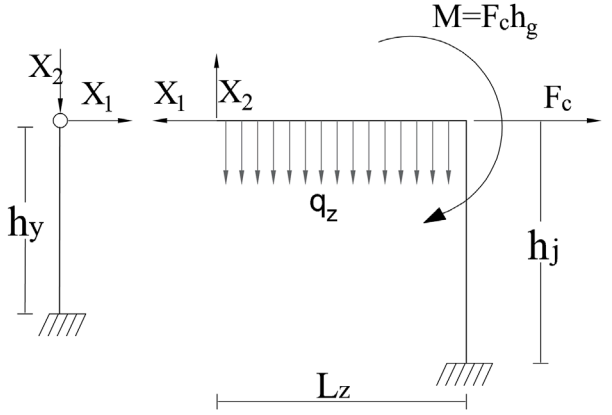

FIGURE 7
Basic system.

The basic equation of the force method is obtained from the displacement coordination conditions:

$$\begin{cases} \Delta_1 = \delta_{11}X_1 + \delta_{12}X_2 + \Delta_{1P} = 0, \\ \Delta_2 = \delta_{21}X_1 + \delta_{22}X_2 + \Delta_{2P} = 0. \end{cases} \tag{1}$$

The expression of the basic unknown quantity is obtained by the elimination method:

$$\begin{cases} X_1 = \dfrac{\Delta_{2P}\delta_{12} - \Delta_{1P}\delta_{22}}{\delta_{11}\delta_{22} - \delta_{21}\delta_{12}}, \\ X_2 = \dfrac{\Delta_{2P}\delta_{11} - \Delta_{1P}\delta_{21}}{\delta_{21}\delta_{12} - \delta_{11}\delta_{22}}. \end{cases} \tag{2}$$

The displacement coefficients and free terms are obtained from the principle of virtual work and the multiplication method:

$$\begin{cases} \delta_{11} = \dfrac{h_y^3}{3E_yI_y} + \dfrac{h_j^3}{3E_jI_j}, \\ \delta_{12} = -\dfrac{L_z h_j^2}{2E_jI_j}, \\ \Delta_{1p} = \dfrac{q_z {L_z}^2 h_j^2}{4E_jI_j} - \dfrac{F_c h_j^3}{3E_jI_j} - \dfrac{F_c h_g h_j^2}{2E_jI_j}. \end{cases} \tag{3}$$

$$\begin{cases} \delta_{21} = -\dfrac{h_j^2 L_z}{2E_jI_j}, \\ \delta_{22} = \dfrac{{L_z}^3}{3E_zI_z} + \dfrac{{L_z}^2 h_j}{E_jI_j}, \\ \Delta_{2P} = \dfrac{F_c h_j^2 L_z}{2E_jI_j} + \dfrac{F_c h_g h_j L_z}{E_jI_j} - \dfrac{q_z {L_z}^4}{8E_zI_z} - \dfrac{q_z {L_z}^3 h_j}{2E_jI_j}. \end{cases} \tag{4}$$

First, the parameters are substituted into Equations 3 and 4 to derive the coefficients and free terms, respectively, and then the coefficients and free terms are substituted into Eq. 2 to obtain the basic unknown quantities X_1 and X_2.

The tower deviation of the completely rigid connection is obtained using the graph multiplication method:

$$\begin{aligned} \Delta_w = {} & \frac{\left(h_j + 2h_g\right)\left(X_2 L_z - q_z {L_z}^2/2 + F_c h_g\right)h_j}{2E_jI_j} \\ & + \frac{\left(2h_j + 3h_g\right)\left(F_c - X_1\right)h_j^2}{6E_jI_j} + \frac{F_c h_g^3}{3E_gI_g}. \end{aligned} \tag{5}$$

4.3 Solution of the thrust stiffness of the partially rigid pier–girder connection

According to Section 2, one of the effects of the right fixed pier–girder connection mode in controlling tower deviations is to restrict the rotation of the composite buckle tower relative to the main girder of the approach bridge. However, it is important to note that the materials and boundary conditions used in the finite-element design represent idealized states, which may differ from the actual situation. As illustrated in Figure 8, when the rigid connection is subjected to the deflection effect caused by the self-weight of the main girder of the approach bridge, one side of the rigid device is compressed and the other side is tensioned, causing a relative rotation angle between the piers and girders. Therefore, it is necessary to consider the local force situation at the pier–girder connection and add a correction term for the partially rigid pier–girder connection in the theoretical calculation.

From an overall perspective, the basic unknown force has been obtained in the last section, i.e., the known force of the approach bridge pier on the main girder of the approach bridge. From a local perspective, the steel buckle tower is fixed on the top of the juncture pier, and the main girder of the approach bridge is fixed with the juncture pier through the anchoring device. Therefore, the deflection effects of the main girder of the approach bridge on the anchoring device and the steel buckle tower on the juncture pier are demonstrated in Figure 9.

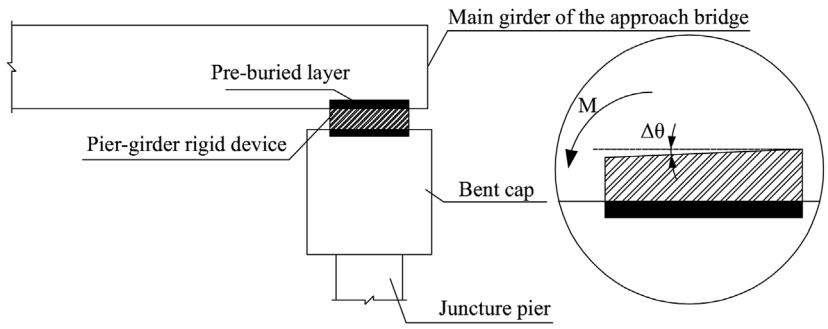

FIGURE 8
Schematic diagram of the deformation of the rigid connection details.

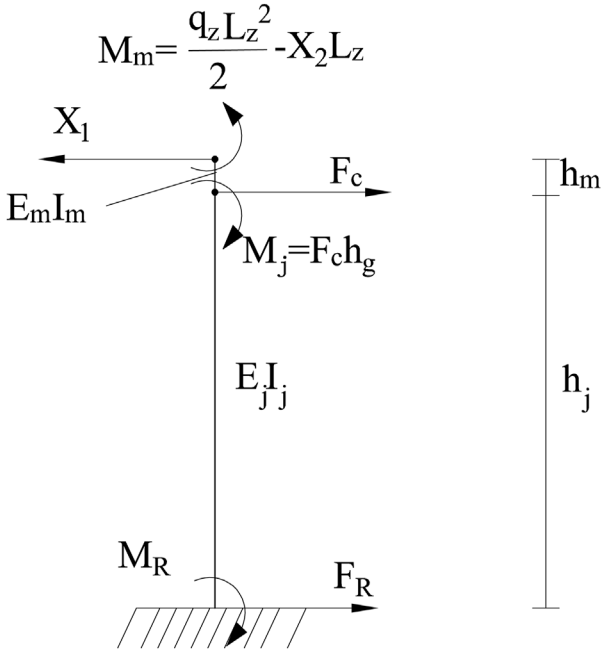

FIGURE 9
Schematic diagram of the local stress on the pier–girder connection.

Figure 9 shows that M_j and M_m represent the bending moment effects at the top of the juncture pier and the top of the anchoring device, respectively; E_mI_m denotes the flexural stiffness of the anchoring device; h_m symbolizes the anchoring device height; and M_R and F_R are constraint reaction forces at the rigid connection between the juncture pier and the ground, respectively. The bearing reaction force is obtained by static equilibrium as follows:

$$\begin{cases} M_R = M_m - M_j - F_c h_j + X_1\left(h_j + h_m\right), \\ F_R = X_1 - F_c. \end{cases} \tag{6}$$

The bearing reaction force is simplified to the top surface of the juncture pier, as presented in Figure 10.

Based on the simplified calculation method of cantilever beam rotation angles, the relative rotation angle between the juncture pier and the main girder of the approach bridge is as follows:

$$\Delta\theta = \frac{X_1 h_m^2 + q_z L_z{}^2 h_m - 2X_2 L_z h_m}{2E_m I_m}. \tag{7}$$

From the completely rigid tower deviation Δ_w, considering the tower deviation correction caused by the relative rotation angle between the composite buckle tower and the main girder of the approach bridge, the tower deviation of the partially rigid pier–girder connection is obtained as follows:

$$\Delta_b = \Delta_w + \Delta\theta \times h_g. \tag{8}$$

The thrust stiffness of the partially rigid pier–girder connection is as follows:

$$K_b = \frac{F_c}{\Delta_b}. \tag{9}$$

5 Thrust stiffness considering the pier–girder connection

The determination of displacement coefficients and free terms serves as the foundation for calculating the thrust stiffness. By observing the free term, it is found that there are two types of load terms in the formula. If $F_c = 1$, it cannot be determined whether the calculated thrust stiffness is consistent, so the relationship between the thrust stiffness and two load terms is verified by numerical analysis, and the formula is further corrected.

5.1 Finite-element calculation results of the thrust stiffness under different load conditions

We apply the self-weight load to the approach bridge–composite buckle tower structure and sequentially apply a 0.4 to 1 times horizontal cable force difference, as plotted in Supplementary Appendix Figure A3.

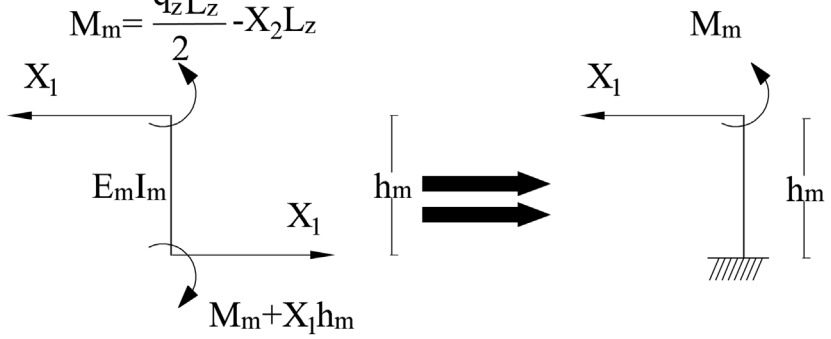

FIGURE 10
Mechanical model of the anchoring device.

It can be seen that when the approach bridge–composite buckle tower structure bears self-weight, the tower deviation is linearly related to the horizontal cable force difference. The thrust stiffness solution at this time is as follows:

$$K = \frac{400-160}{-10.302-(-45.698)} = 6780kN/m,$$
$$K = \frac{-160-(-400)}{-92.893-(-128.288)} = 6780kN/m.$$

A 0.4 to 1 times horizontal cable force difference toward the midspan is applied to the approach bridge–composite buckle tower structure, as shown in Supplementary Appendix Figure A4.

The thrust stiffness solution is $K = \frac{400-160}{58.993-23.597} = 6780kN/m$. As a result, the tower deviations under three situations—the simultaneous action of the self-weight load and horizontal cable force difference away from the midspan, the simultaneous action of the self-weight load and horizontal cable force difference toward the midspan, and only the action of horizontal cable force difference toward the midspan—are all linearly related to the horizontal cable force difference, and the thrust stiffness values of the three situations are equal.

Therefore, within the range of small deformation, the thrust stiffness of the completely rigid pier–girder connection of the approach bridge–composite buckle tower structure is only related to the bending stiffness EI and height h. The effect of self-weight is to move the "horizontal cable force difference–tower deviation" line down as a whole. Meanwhile, according to the mechanics of materials, the size of the relative rotation angle between the piers and girders is related to the external load, so the effect of the self-weight of the main girder of the approach bridge is to provide pre-deviation and an initial relative rotation angle.

5.2 Correction of the thrust stiffness of the completely rigid pier–girder connection

The thrust stiffness of the completely rigid pier–girder connection remains unaffected by external loads and self-weight. Therefore, we can exclude the self-weight load term, and the horizontal cable force difference can be treated as the horizontal unit load, at which point the free term is as follows:

$$\begin{cases} \Delta_{1p}{}' = -\dfrac{h_j^3}{3E_jI_j} - \dfrac{h_g h_j^2}{2E_jI_j}, \\ \Delta_{2p}{}' = \dfrac{h_j^2 L_z}{2E_jI_j} + \dfrac{h_g h_j L_z}{E_jI_j}. \end{cases} \tag{10}$$

The basic unknown forces solved at this time are denoted as $X_1{}'$ and $X_2{}'$, and the tower deviation of the completely rigid connection is as follows:

$$\begin{aligned} \Delta_w{}' = {} & \frac{\left(h_j+2h_g\right)\left(X_2{}'L_z+h_g\right)h_j}{2E_jI_j} \\ & + \frac{\left(2h_j+3h_g\right)\left(1-X_1{}'\right)h_j^2}{6E_jI_j} \\ & + \frac{h_g^3}{3E_gI_g}. \end{aligned} \tag{11}$$

The thrust stiffness of the completely rigid connection is as follows:

$$K_w{}' = \frac{1}{\Delta_w{}'}. \tag{12}$$

5.3 Correction of the thrust stiffness of the partially rigid pier–girder connection

The size of the relative rotation angle is related to the external load, so the relative rotation angle comprises two parts: one part is the initial relative rotation angle caused by q_z, and the other part is the relative rotation angle caused by the horizontal cable force difference F_c.

Within the range of small deformation, the tower deviation caused by the initial relative rotation angle also moves the "horizontal cable force difference–tower deviation" line up and down as a whole and does not affect the slope, so the relative rotation angle caused by the self-weight of the main girder of the approach bridge has no impact on the overall thrust stiffness of the structure,

at which point the free term is as follows:

$$\begin{cases} \Delta_{1p}'' = -\dfrac{F_c h_j^3}{3E_j I_j} - \dfrac{F_c h_g h_j^2}{2E_j I_j}, \\ \Delta_{2P}'' = \dfrac{F_c h_j^2 L_z}{2E_j I_j} + \dfrac{F_c h_g h_j L_z}{E_j I_j}. \end{cases} \tag{13}$$

The basic unknown forces at this time are denoted as X_1'' and X_2'', and the tower deviation and relative rotation angle of the completely rigid connection are as follows:

$$\begin{cases} \Delta_w'' = \dfrac{\left(h_j + 2h_g\right)\left(X_2'' L_z + F_c h_g\right)h_j}{2E_j I_j} \\ \qquad + \dfrac{\left(2h_j + 3h_g\right)\left(F_c - X_1''\right)h_j^2}{6E_j I_j} \\ \qquad + \dfrac{F_c h_g^3}{3E_g I_g} \\ \Delta\theta' = \dfrac{X_1'' h_{\mathrm{m}}^2 - 2X_2'' L_z h_m}{2E_m I_m}. \end{cases} \tag{14}$$

The thrust stiffness of the partially rigid pier–girder connection is as follows:

$$K_b' = \frac{F_c}{\Delta_w'' + \Delta\theta' \cdot h_g}. \tag{15}$$

According to Eq. 15, the thrust stiffness considering local deformation at the rigid connection of the pier and girder is not unique.

5.4 Calculation of pre-deviation

Although the self-weight of the main girder of the approach bridge does not affect the calculation of the thrust stiffness, it has a great impact on tower deviations, so it needs to be solved. The free term at this time is as follows:

$$\begin{cases} \Delta_{1p}''' = \dfrac{q_z {L_z}^2 h_j^2}{4E_j I_j}, \\ \Delta_{2P}''' = -\dfrac{q_z {L_z}^4}{8E_z I_z} - \dfrac{q_z {L_z}^3 h_j}{2E_j I_j}. \end{cases} \tag{16}$$

The basic unknown forces are represented as X_1''' and X_2''', and the pre-deviation is as follows:

$$\begin{aligned} \Delta_0 = & \frac{\left(h_j + 2h_g\right)\left(X_2''' L_z - q_z {L_z}^2/2\right)h_j}{2E_j I_j} \\ & - \frac{\left(2h_j + 3h_g\right)X_1''' h_j^2}{6E_j I_j}. \end{aligned} \tag{17}$$

The initial relative rotation angle is as follows:

$$\Delta\theta_0 = \frac{X_1''' h_{\mathrm{m}}^2 + q_z {L_z}^2 h_m - 2X_2''' L_z h_m}{2E_m I_m}. \tag{18}$$

The total pre-deviation is as follows:

$$\Delta_0' = \Delta_0 - \Delta\theta_0 \times h_g. \tag{19}$$

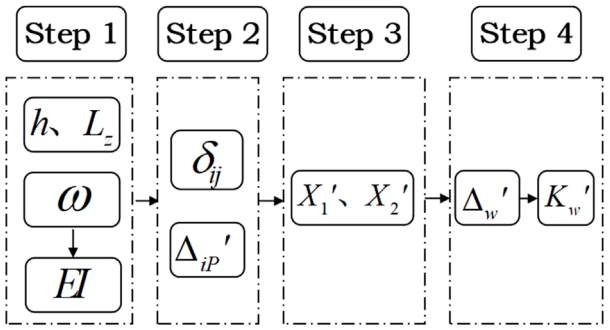

FIGURE 11
Flow chart of calculating the thrust stiffness using programs.

5.5 Program implementation of the calculation method

There are various formulas for the theoretical calculation method of thrust stiffness, and manual calculation is cumbersome and prone to errors, so it is calculated with the help of programs. MATLAB, VB, Python, and other calculation programs can be combined with the theoretical calculation method. The detailed process is as follows:

The heights of the approach bridge pier, juncture pier, and steel buckle tower, and the span length of the main girder of the approach bridge are as follows:

$$\begin{cases} h_y = 90.1m, \\ h_j = 91.9m, \\ h_g = 31.19m, \\ L_z = 42m. \end{cases} \tag{20}$$

Using the deflection formula of the cantilever girder and finite-element software, the corresponding flexural stiffness values are obtained as follows:

$$\begin{cases} E_y I_y = 6.82944 \times 10^7 kN \cdot m^2, \\ E_j I_j = 4.31915 \times 10^9 kN \cdot m^2, \\ E_g I_g = 2.03093 \times 10^8 kN \cdot m^2, \\ E_z I_z = 3.51995 \times 10^8 kN \cdot m^2. \end{cases} \tag{21}$$

After a series of calculations, the tower deviation of the completely rigid pier–girder connection under the action of the unit tower top horizontal cable force difference is obtained as follows:

$$\Delta_w' = 1.477 \times 10^{-4}. \tag{22}$$

The thrust stiffness of the completely rigid connection is obtained as follows:

$$K_w' = 6769kN/m. \tag{23}$$

The detailed calculation process of the thrust stiffness by computer programs is illustrated in Figure 11.

The thrust stiffness value calculated entirely by Midas/Civil is 6,780 kN/m, which differs from the value calculated by the analytic formula by 11 kN/m, with a deviation percentage of 0.16%, which is satisfactorily consistent.

When the calculation program is used to solve the thrust stiffness, the formula needs to be input only for the first time; the subsequent calculations only need to input the data of step 1 to derive the value of thrust stiffness, achieving a rapid calculation of the thrust stiffness of the approach bridge–composite buckle tower structure. Therefore, the analytic formula can be used to validate the model's accuracy and perform sensitivity analysis, providing guidance for the design of structural member dimensions, sections, and materials. The other formulas share the same purpose.

5.6 Sensitivity analysis of the thrust stiffness

Section 5.5 used a computer program to achieve a rapid calculation of the theoretical formula of thrust stiffness, and this section will further study the influence rule of changing component properties on the overall thrust stiffness of the structure.

There are a total of eight component property indexes: h_y, h_j, h_g, L_z, E_yI_y, E_jI_j, E_gI_g, and E_zI_z. When one of these properties changes, the other properties are consistent with those in Section 5.5, as shown in Supplementary Appendix Figure A5, A6.

By comparing Supplementary Appendix Figure A5 with each set of data, taking the first value as a reference to solve the change percentage, the findings can be listed as follows:

(1) The impact of changing the approach bridge pier height h_y on the overall thrust stiffness of the structure is negligible.
(2) For every 2.439% increase in the juncture pier height h_j, the thrust stiffness increases on average by 0.124%; for every 6.250% increase in the span of the main girder of the approach bridge L_z, the thrust stiffness increases, on average, by 1.897%.
(3) For every 9.091% increase in the steel buckle tower height h_g, the thrust stiffness decreases, on average, by 2.719%.

Analyzing Supplementary Appendix Figure A6 and similarly calculating the percentage changes, we can find the following:

(1) For every 3.223% increase in the flexural stiffness of the approach bridge pier E_yI_y, the thrust stiffness decreases, on average, by 7.610×10^{-3}%. Therefore, the impact of the flexural stiffness of the approach bridge pier on the overall thrust stiffness of the structure is negligible.
(2) For every 6.250% increase in the flexural stiffness of the juncture pier E_jI_j, the overall thrust stiffness of the structure increases, on average, by 2.738%. For every 16.667% increase in the flexural stiffness of the steel buckle tower E_gI_g, the overall thrust stiffness of the structure increases, on average, by 5.324%. For every 7.692% increase in the flexural stiffness of the main girder of the approach bridge E_zI_z, the overall thrust stiffness of the structure increases, on average, by 1.204%.

In conclusion, the height and flexural stiffness of the approach bridge pier have minimal impacts on the overall thrust stiffness of the structure; hence, the design of the approach bridge pier height and sectional size can be tailored to match the specific on-site conditions. The higher the steel buckle tower, the less advantageous it is for the overall thrust stiffness of the structure. Enhancements in the span length and flexural stiffness of the main girder of the approach bridge, as well as increases in the height and flexural stiffness of the juncture pier, collectively contribute to the improved overall thrust stiffness of the structure.

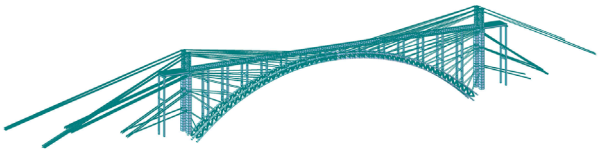

FIGURE 12
Cantilever assembly model for arch ribs using Midas/Civil.

6 Influence of the joint effect of approach bridges on the cantilever assembly of arch ribs

6.1 Establishment of the cantilever assembly model for arch ribs

A particular deck-type steel pipe concrete arch bridge has a calculated span length of 475.0 m and a rise-to-span ratio of 1/5.278, and the arch axis is a catenary line with an arch axis coefficient of m = 2.2. The main arch rib adopts a constant-width and variable-height space truss structure. The radial height of the main chord tube at the arch crown is 7.0 m, and the radial height of the main chord tube at the arch foot is 10.0 m, with the radial height of the arch section varying according to a quadratic parabola. Each single arch rib is composed of two steel pipe concrete chord tubes each at the top and bottom, with an external diameter of 1,400 mm. The transverse center distance of the chord tubes is 2.5 m, and the center distance between the two arch ribs in the transverse bridge direction is uniformly 16.0 m. Lateral braces are set up inside the ribs, and wind braces, flat braces, and "X" braces are set up between the ribs. The main arch rib is divided into 15 sections from the arch foot to the arch crown, plus the joint segment at the arch crown, and there are a total of 62 segments in the entire bridge. The Midas/Civil finite-element analysis model was established, consisting of a total of 3,654 beam elements and 240 tension-only elements, as presented in Figure 12.

6.2 Derivation of the theoretical relationship between buckle tower deviations and thrust stiffness and the line shape of the arch rib

The basic assumptions are as follows:

(1) When the buckle tower is displaced, the buckle cable length remains unchanged.
(2) The arch rib is a rigid body that does not undergo elastic deformation but only rigid displacement.
(3) The change in the buckle tower height is a higher-order trace compared to tower deviations.

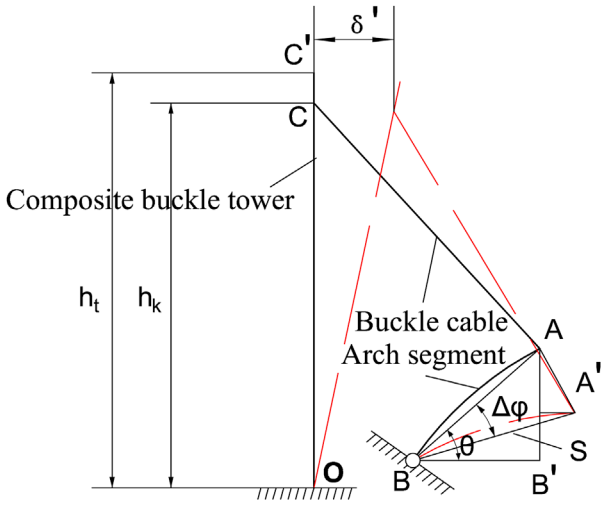

FIGURE 13
Schematic diagram of the influence of tower deflections on the line shape of the arch rib.

Figure 13 shows the calculation diagram, where the red dashed lines indicate the positions of the buckle cable, buckle tower, and arch segment after displacement.

According to the principle of small deformation and basic assumptions, we can obtain

$$\begin{cases} \delta' \approx S\Delta\varphi, \\ \angle BAA' \approx \pi/2, \end{cases} \tag{24}$$

where δ' represents the displacement of the buckle point on the buckle tower, S denotes the chord length of the arch segment, and $\Delta\varphi$ is the rotation angle of the arch segment.

According to Eq. 24 and the complementary angle theorem of right angles, we know that $\angle B'AA' \approx \theta$; hence,

$$\begin{cases} \delta_x' \approx S\Delta\varphi \sin\theta = \delta' \sin\theta, \\ \delta_y' \approx S\Delta\varphi \cos\theta = \delta' \cos\theta, \end{cases} \tag{25}$$

where δ_x' and δ_y' denote the change in mileage and elevation of the buckle point on the arch segment caused by the displacement of the buckle point on the buckle tower, respectively; and θ represents the angle between the original arch segment chord length and the horizontal line.

Knowing the relationship between the displacement of the buckle point C and the line shape of the arch rib, while the study of the thrust stiffness is the displacement at the top of the structure, to determine the relationship between the longitudinal thrust stiffness of the buckle tower and the line shape of the arch rib, the deviation of the tower top C′ needs to be distributed to the buckle point C first.

By using the triangular distribution method, we obtain

$$\delta' = \frac{h_k}{h_t}\delta, \tag{26}$$

where h_k is the buckle point height on the tower and h_t is the buckle tower height.

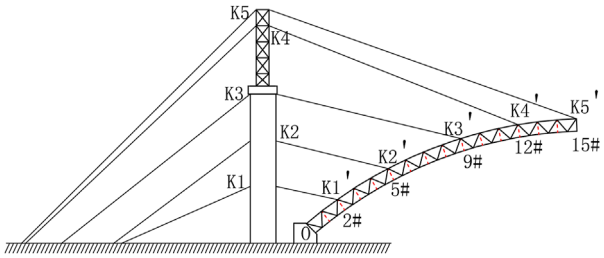

FIGURE 14
Schematic diagram of the distribution of buckle points on the composite buckle tower and arch rib.

According to the thrust stiffness theory, $\delta = F_c/K_z$, and by combining Eq. 25, the relationship between the thrust stiffness of the buckle tower and the line shape of the arch rib is as follows:

$$\begin{cases} \delta_x' = \dfrac{h_k}{h_t}\dfrac{F_c}{K_z}\sin\theta, \\ \delta_y' = \dfrac{h_k}{h_t}\dfrac{F_c}{K_z}\cos\theta. \end{cases} \tag{27}$$

6.3 Influence of the joint effect of approach bridges on the elevation of the arch rib

As demonstrated in Figure 14, the various stages where the buckle point will change are explored. There are a total of five buckle points on the composite buckle tower, K1–K5. The last arch segments lifted by them are #2, #5, #9, #12, and #15. The remaining buckle cables are equivalent to increasing the stiffness of the arch segments, so the elastic deformation of the middle part of the arch segment is not considered. The change in distance between the arch foot point O and the buckle points K1′–K5' is ignored, focusing only on their elevation changes. At the same time, we maintain the initial tension of the buckle cables, taking into account the influence of the approach bridges, at the same level as the initial tension of the buckle cables in the standard tangent assembly. This approach aims to minimize elevation deviations resulting from the elongation of the buckle cables.

During the installation stage of the juncture pier and steel buckle tower, an approach bridge is incorporated, forming a right fixed joint effect of approach bridges, as plotted in Figure 3.

By comparing it with the elevation changes during the normal tangent assembly of the arch rib, the difference is obtained, as provided in Supplementary Appendix Figure A7.

As can be seen from Supplementary Appendix Figure A7, it is evident that the influence of the joint effect of approach bridges on the elevation of the arch rib becomes more pronounced with increasing distance, which is consistent with the rules described in Equations 25 and 26. The node coordinates of Midas/Civil were extracted, and geometric calculations were performed to obtain the related parameters, as tabulated in Supplementary Appendix Table A3.

Note:

(1) According to Eq. 21, the EI of the steel buckle tower and the juncture pier is different by an order of magnitude. At this time, using the triangular distribution method results in a relatively large error in tower deviations, so we calculate separately for #2, #5, and #9 and #12 and #15 according to the distribution of buckle points.
(2) What is extracted is the deviation at the top of the juncture pier and steel buckle tower under the self-weight load of the approach bridge–composite buckle tower structure.

After calculation, the theoretical elevation change deviation value caused by pre-deviation is obtained. It is compared with the elevation change deviation value obtained from the model, as listed in Supplementary Appendix Table A4:

Note: The second-order deviation is the difference between the elevation change deviation values calculated by the model and the theory.

Supplementary Appendix Table A4 reveals that there is a second-order deviation between the elevation change deviation values obtained by theoretical calculation and model calculation, and the second-order deviation of the later stage is greater. According to the research in Section 2, the influence of the right fixed pier–girder connection mode on tower deviations stems from two aspects: 1) the deflection effect caused by the self-weight of the main girder of approach bridges makes the composite buckle tower deflect away from the midspan; and 2) it restricts the rotation of the composite buckle tower relative to the main girder of approach bridges toward the midspan.

Therefore, the second-order deviation is caused by the effect of constrained rotation, and it can be found that the higher the buckle point elevation and the later the construction stage, the greater the impact of constrained rotation on the tower deviation and arch rib elevation.

6.4 Influence of the joint effect of approach bridges on cable forces

Utilizing the relationship between thrust stiffness and arch rib elevation changes, we have extracted the relevant calculation parameters from the preceding text, as displayed in Supplementary Appendix Table A5.

Upon substituting relevant parameters into Eq. 27, the effects of pre-deviation and constrained rotation on the cable force in the joint effect of approach bridges can be observed in Supplementary Appendix Figure A8. The influences of pre-deviation and constrained rotation on the cable force tend to become more significant in the later stages. During these stages, with greater h_k and $\cos\theta$, to generate the same arch rib elevation change, a larger horizontal cable force difference is required. Given that changes in elevation typically occur more rapidly in later stages, the overall impact of the joint effect of approach bridges on the cable force in these stages far surpasses its effect in the earlier stages.

Therefore, the joint effect of approach bridges can function as a remedial measure. When the actual construction line of the arch ribs in the middle and later stages deviates significantly downward from the design line, the cable force that is needed to install new arch segments becomes overly large. In such cases, the joint effect of approach bridges can be utilized to generate pre-deviation in the buckle tower and to constrain pier–girder rotation, effectively substituting for a portion of the cable force. This also reduces the potential elevation errors that may arise in subsequent arch ribs compared with the case without approach bridges. Moreover, the function of constrained rotation serves as a manifestation of enhanced thrust stiffness in buckle towers. Therefore, through the application of the thrust stiffness analytical formula for sensitivity analysis, it becomes possible to guide the design of structural member properties, ultimately identifying the most cost-effective approach to enhance thrust stiffness.

7 Conclusion and outlook

7.1 Conclusion

In summary, this study, centered around the engineering scenario of a large-span, deck-type, steel pipe concrete arch bridge assembled through a cantilever suspension with stay cables, investigates the calculation method and the impact on the buckle tower stiffness, considering the joint effect of approach bridges. The primary conclusions are as follows:

(1) The main girder of the approach bridge and the composite buckle tower are firmly interconnected, creating a robust "T"-type rigid structure. In this configuration, the junction of the pier and girder imposes constraints on the rotation of the composite buckle tower. When subjected to self-weight, the deflection of the main girder causes the composite buckle tower to deflect away from the midspan.
(2) The weight of the approach bridge's main girder imparts a pre-deviation to the buckle tower, resulting in axial compression between the pier and the girder. This, however, does not impact the thrust resistance stiffness of the tower–girder structure.
(3) The height and flexural stiffness of the approach bridge pier have minimal influence on the overall thrust resistance of the structure. Additionally, a greater height for the steel buckle tower is detrimental to the overall thrust resistance of the structure. However, increasing the length and bending stiffness of the main girder of the approach bridge, as well as raising the height and enhancing the bending stiffness of the junction pier, can effectively enhance the overall thrust resistance of the structure.
(4) In situations where a significant downward elevation error occurs in the middle and later stages of arch rib construction, the tension in the back cables can become excessively high for the installation of a new arch segment. In such cases, the joint effect of the approach bridge can be used to decrease the tension in the back cables, resulting in a smaller elevation error in the subsequent arch ribs when compared to the joint effect without an approach bridge.

7.2 Outlook

(1) The derivation of the thrust stiffness analytical formula does not consider the impact of the longitudinal slope and temperature changes of the main girder; thus, the analytical formula needs further refinement.
(2) The buckle-anchored stay cables and the composite buckle tower form a multiple-time hyper-static structure. However, this paper calculates the equivalent horizontal cable force difference at the tower top, i.e., the horizontal cable force difference ratio relative to the actual position distribution and size, which can generate horizontal loads on the tower top equal to the tower deviation. Therefore, further research is needed to facilitate the intelligent calculation of the impact on each cable.

Data availability statement

The original contributions presented in the study are included in the article/Supplementary Material; further inquiries can be directed to the corresponding author.

Author contributions

SW: writing–original draft and writing–review and editing. JF: writing–original draft. LY: writing–review and editing. GC: writing–review and editing. DJ: writing–review and editing.

Funding

The author(s) declare that financial support was received for the research, authorship, and/or publication of this article. This work was supported by the National Natural Science Foundation of China (nos 51608080 and 52108267), the Science and Technology Innovation Project for the Construction of the Chengdu Chongqing Double City Economic Circle (KJCXZD2020032), the Natural Science Foundation of Chongqing (cstc2021jcyj-msxm2491), the Chongqing Science and Technology Innovation and Application Development Special Key Project (CSTB2022TIAD-KPX0205), and the Guangxi Key R&D Plan Project (AB22036007-8), which are all gratefully acknowledged.

Conflict of interest

The authors declare that the research was conducted in the absence of any commercial or financial relationships that could be construed as a potential conflict of interest.

Publisher's note

All claims expressed in this article are solely those of the authors and do not necessarily represent those of their affiliated organizations, or those of the publisher, the editors, and the reviewers. Any product that may be evaluated in this article, or claim that may be made by its manufacturer, is not guaranteed or endorsed by the publisher.

Supplementary material

The Supplementary Material for this article can be found online at: https://www.frontiersin.org/articles/10.3389/fmats.2023.1321177/full#supplementary-material

References

Chen, B. W., Han, L. H., Qin, D. Y., and Li, W. (2023). Life-cycle based structural performance of long-span CFST hybrid arch bridge: a study on arch of Pingnan Third Bridge. *J. Constr. Steel Res.* 207 (1), 107939. doi:10.1016/J.JCSR.2023.107939

Chen, H. D., Wu, X. G., Yao, S. S., and Li, Z. (2017). Longitudinal anti-push rigidity of the non side tower for multi-tower cable-stayed bridge based on the principle of deformation coordination. *J. Beijing Jiaot. Univ.* 41 (4), 40–46. doi:10.11860/j.issn.1673-0291.2017.04.00

Deng, H. C., Lu, W., Li, Q. P., Zhou, Y. K., Tao, L., and Qiang, Y. L. (2020). Research on accurate calculation method of cable tower deviation in cable hoisting system. *Highway* 65 (8), 226–232.

Deng, J. M. (2009). Geom etrical analysis of arch rib elevation change caused by tower deviation during cable hoisting construction. *J. Chongqing Jiaot. Univ. Nat. Sci. Ed.* 28 (3), 505–507. doi:10.3969/j.issn.1674-0696.2009.03.08

Ding, W., Kang, H. J., Zhang, X. Y., Su, X. Y., and Cong, Y. Y. (2023). Dynamic modeling and analysis on planar free vibration of long-span arch bridges during construction. *Appl. Math. Model.* 121 (1), 843–864. doi:10.1016/J.APM.2023.05.028

Gu, Y., Li, Y. D., and Liu, S. Z. (2015). Research on construction control of long-span CFST arch bridge. *Appl. Mech. Mater.* 4075 (777), 88–93. doi:10.4028/www.scientific.net/AMM.777.88

Hao, N. B., and Gu, A. B. (2015). Construction control of 500 m scale concrete-filled steel tubular arch bridge. *J. Southwest Jiaot. Univ.* 50 (4), 635–640. doi:10.3969/j.issn.0258-2724.2015.04.010

Hao, N. B., and Gu, A. B. (2016). Alignment adjustment method of concrete filled steel tubular arch bridge in arch rib hoisting. *J. Chongqing Jiaot. Univ.* 35 (3), 1–5. doi:10.3969/j.issn.1674-0696.2016.03.01

Hao, N. B., and Gu, A. B. (2018). Error control method for super-long span concrete filled steel tubular arch bridge. *Sci. Technol. Eng.* 18 (15), 149–154. doi:10.3969/j.issn.1671-1815.2018.15.022

JTG/T 3650 (2020). *Technical specifications for construction of highway bridges and culverts*. Beijing: People's Communications Publishing House.

Li, Y., Wang, J. L., and Ge, S. S. (2017). Optimum calculation method for cable force of concrete-filled steel tube arch bridge in inclined cable-stayed construction. *J. Highw. Transp. Res. Dev. Engl. Ed.* 11 (1), 42–48. doi:10.1061/JHTRCQ.0000549

Liu, X. C. (2008). *Construction process monitoring of cable suspension for large span box arch bridge*. Chengdu: Master's thesis of Southwest Jiaotong University.

Liu, Z. G., Zhou, S. X., Zou, K. R., and Qu, Y. H. (2022). A numerical analysis of buckle cable force of concrete arch bridge based on stress balance method. *Sci. Rep.* 12 (1), 12451. doi:10.1038/S41598-022-15755-W

Long, X. H. (2012). *Analysis of mechanical performance on cable tower and buckle tower system of A big span steel box arched bridge during construction*. Hunan: Master's Degree Thesis of Central South University.

Mo, Z. Q. (2021). Research on the influence of main cable slippage and tower deflection in the design of cable hoisting system. *Highway* 66 (3), 163–168.

Qin, S. Q. (2003). Control method of stress-free status for erection of cable-stayed bridges. *Bridge Constr.* 33 (2), 31–34. doi:10.3969/j.issn.1003-4722.2003.02.009

Qin, S. Q. (2008). Application of unstressed state control method to calculation for erection of cable-stayed bridge. *Bridge Constr.* 38 (2), 13–16.

Wang, H. P. (2013). *Research on application of unstressed state method in the construction control of long-span cfst arch bridge*. Chengdu, China: Master's Degree Thesis of Southwest Jiaotong University.

Xu, Y., Shen, C. Y., Zhu, Y. B., and Wang, C. S. (2016a). Improved iteration algorithm for determination of tension of fastening stays for cantilever construction of arch bridge. *Bridge Constr.* 46 (2), 65–69. doi:10.3969/j.issn.1002-0268.2016.06.010

Xu, Y., Zhan, B. L., Li, Y., and Shen, C. Y. (2016b). An optimum calculation method of cable force of CFST arch bridge in inclined cable hoisting construction. *J. Highw. Transp. Res. Dev.* 33 (6), 61–67. doi:10.3969/j.issn.1002-0268.2016.06.010

Xu, Z. Q. (2011). *Technology research on timely adjustment of installation linear error about arch rib of large span arch bridge*. Chongqing: Master's Degree Thesis of Chongqing Jiaotong University.

Yu, Y. J. (2018). Integrated stiffness analysis of girder bridge piers. *Highway* 63 (2), 106–110.

Zhang, J. M. (2001). *Bearing capacity and construction control research of long-span concrete filled steel tubular arch bridges*. Guangdong: Doctoral Dissertation of South China University of Technology.

Zhang, Z. C., Ye, G. R., and Wang, Y. F. (2004). Optimization of cable tension in adjustment of arch rib alignment of long-span cantilever bridge. *Appl. Mech.* 21 (6), 187–192.

Zheng, J. L., Xu, F. Y., and Tang, B. S. (1996). *Simulation and calculation method for construction of steel arch trusses erected by jacked diagonal pulling and buckling suspension of yongning yongjiang bridge in Guangxi. Bridge and structural engineering society of China highway society 1996 bridge academic proceedings*. Beijing: People's Transportation Press. 214–228.

Zhou, S. X. (2002). Rib assemble and construction control calculation of Zhejiang Sanmen Jiantiao bridge. *J. Chongqing Jiaot. Inst.* 11 (6), 1–5. doi:10.3969/j.issn.1674-0696.2002.02.001

Zhou, S. X., Jiang, L. Z., Zeng, Z., and Zhou, J. T. (2000a). Simulation and calculation of cable suspension force of diagonal buckling for segmental construction of arch bridges. *J. Chongqing Inst. Transp.* 19 (3), 8–12. doi:10.3969/j.issn.1674-0696.2000.03.003

Zhou, S. X., Jiang, L. Z., Zeng, Z., and Zhou, J. T. (2000b). Simulate calculation study of cable-stayed force for arch bridge segmental constructions. *J. Chongqing Jiaot. Inst.* 19 (3), 8–12. doi:10.3969/j.issn.1674-0696.2000.03.003

frontiers | Frontiers in Materials

TYPE Original Research
PUBLISHED 06 February 2024
DOI 10.3389/fmats.2023.1332269

OPEN ACCESS

EDITED BY
Zhongya Zhang,
Chongqing Jiaotong University, China

REVIEWED BY
Chengdong Xia,
Hong Kong Polytechnic University, Hong Kong SAR, China
Dong Lu,
Hong Kong Polytechnic University, Hong Kong SAR, China
Jie Nie,
UHPC, China
Ali Raza,
University of Engineering and Technology, Taxila, Pakistan
E. Chen,
Chalmers University of Technology, Sweden

*CORRESPONDENCE
Xinzhong Wang,
wangxinzhong811@126.com

RECEIVED 02 November 2023
ACCEPTED 26 December 2023
PUBLISHED 06 February 2024

CITATION
Wang X, Li L, Xiang Y, Wu Y and Wei M (2024), The influence of basalt fiber on the mechanical performance of concrete-filled steel tube short columns under axial compression.
Front. Mater. 10:1332269.
doi: 10.3389/fmats.2023.1332269

The influence of basalt fiber on the mechanical performance of concrete-filled steel tube short columns under axial compression

Xinzhong Wang[1]*, Linshu Li [1], Yi Xiang [1], Yuexing Wu[1] and Mei Wei[2]

[1]School of Civil Engineering, Hunan City University, Yiyang, China, [2]School of Digital Arts, Hunan Arts and Crafts Vocational College, Yiyang, China

With rapid economic and social development, both concrete-filled steel tube (CFST) composite structures and basalt fiber (BF) have been widely applied in the field of civil engineering. To investigate the laws and characteristics of the influence of chopped BF on the mechanical properties of CFST columns and further promote the application of BF in CFST structures, the axial compressive bearing capacity test of 18 CFST short columns was carried out, and the influence of BF of different lengths on their structural mechanical properties was analyzed. The test results were compared with the theoretical calculation results and the finite element analysis results to verify the reasonableness of the test results. The results reveal that the axial compressive bearing capacity of the CFST short column after adding BF is significantly improved compared to the ordinary CFST short column, in which the bearing capacity and the ductility coefficient are increased by approximately 8.1% and 31.6%, respectively, on average. In addition, changing the length of BF has less effect on the bearing capacity of CFST short columns, the rate of increase in bearing capacity decreases with an increase in the steel ratio of CFST, and the coefficient of ductility increases with the increase in the steel ratio.

KEYWORDS

concrete-filled steel tube, basalt fiber, short columns, finite element analysis, bearing capacity, ductility coefficient

1 Introduction

Under the background of the dual requirements of sustainable development strategy and green construction in the civil engineering industry, various new materials and composite structures are continually emerging (Wang et al., 2017; Lu et al., 2023a; Zhang Z. Y. et al., 2023; Lu et al., 2023b; Wang et al., 2023; Yang et al., 2023; Zou et al., 2023). A concrete-filled steel tube (CFST), as a composite structure, has been widely used in high-rise buildings, large-span bridges, and complex structures due to their advantages of high bearing capacity, good ductility, and convenient construction (Zhou et al., 2022; Lai et al., 2023; Zhen et al., 2023). As a composite structure, steel tubes can provide effective constraints on the core concrete to improve its strength and ductility. Conversely, the core concrete can also significantly prevent local buckling of the

TABLE 1 Core concrete mix ratio.

Target strength	Water–binder ratio	Cement/ kg·m^{-3}	Water/ kg·m^{-3}	Sand/kg·m^{-3}	Aggregate/ kg·m^{-3}	Water-reducing agent/kg·m^{-3}	Expansive agent/kg·m^{-3}
C50	0.35	401	156	502	1,201	4.5	44.5

steel tube, which improves the overall bearing capacity of CFST. At present, the continuous growth of building structure height and bridge span and the emergence of specially shaped structures have put forward higher requirements for the mechanical properties of CFST structures. Sharif et al. (2019) and Yu et al. (2023) showed that increasing the steel ratio and enhancing the mechanical properties of core concrete can effectively improve the bearing capacity and ductility of these composite structures. Basalt fiber, as a low-cost, environmentally friendly green material, has good mechanical properties and chemical stability and plays a role in reinforcing the crack-blocking effect on concrete (Dong et al., 2017). It has been shown that the concrete strength can be improved by adding BF, and the maximum increase in compressive strength of basalt fiber-reinforced concrete (BFRC) reaches 47.5% (Lian et al., 2007). However, there are few research studies on the mechanical performance of CFST structures with the addition of BF. If adding BF to CFST structures improves their mechanical performance, both BF and CFST will be more widely used.

For the past few years, scholars in various countries have carried out extensive research studies on the mechanical performance enhancement of CFST structures. Xia et al. (2023) found that the use of stirrup connection mode effectively improved the bearing capacity of CFST. Fang et al. (2019) proposed a new type of composite member of corrugated steel pipe, CFST, that increases the bearing capacity and ductility index by 10.1% and 35.6%, respectively, compared with CFST under the same conditions. He et al. (2017), Güneyisi (2023), and Xiamuxi et al. (2023) showed that the strength, stiffness, and ductility of CFST are related to the shape of the cross section, steel tubes' diameter, or width-to-thickness ratio. Essentially, the above scholars were trying to promote the mechanical properties of CFST by changing the steel ratio. However, other scholars chose to enhance the core concrete properties of CFST. Zong et al. (2023) studied the influence of the volume fraction of steel fiber on the eccentric-compressive behavior of steel fiber-reinforced recycled concrete-filled square steel tube short columns. Hu et al. (2023) noticed that adding steel fiber at a volume fraction of 0.75% essentially did not improve specimens with 130-MPa matrix concrete. Wen et al. (2021) strengthened square concrete-filled square steel tube short columns by the application of the circularization technique. Chen et al. (2023) analyzed the effect of ultra-high-performance concrete (UHPC) on axial load–axial strain curves, axial compressive load capacity, and ductility of members. Bian et al. (2023) investigated the stress–strain relationship of BFRC under uniaxial compression, and concluded that the optimal amount of BF was 0.12%. Zhang Q. et al. (2023) determined that at lower concrete strength, the bearing capacity and displacement ductility of BFRC columns can be improved more significantly. Zhang et al. (2021) concluded that BF can effectively inhibit crack expansion due to its good bridging effect, which helps improve the flexural capacity and crack morphology of composite beams, and Dong et al. (2023) obtained the same conclusion as Zhang. Abushanab et al. (2022) proposed a finite element model to predict the load-carrying capacity of BFRC beams, finding that BF can effectively improve the load-carrying capacity of beams. Zhang et al. (2020) measured the damage patterns and load–displacement/strain curves of the basalt fiber-reinforced recycled concrete-filled square steel tube short columns, proving that BF has an enhancing effect on the load-carrying capacity of CFST columns. Wang and Li (2016), Wang et al. (2019), and Wang et al. (2022) investigated the effect of BF on the mechanical performance of reinforced concrete short columns and long columns and found that the optimal fiber length of the former was 12 mm and the optimal fiber volume fraction was 0.15%, resulting in a maximum increase of 28% in axial compressive ultimate bearing capacity compared to ordinary reinforced concrete columns. For the latter, the maximum increase in bearing capacity under small eccentric compression was 13%, while the maximum increase in bearing capacity under large eccentric compression was 41%.

In summary, most scholars improve the mechanical performance of CFST structures by changing the steel ratio, adding steel fiber to the core concrete, or using ultra-high-performance core concrete. While the application of BF is mostly found in concrete structures, its impact on the mechanical performance of CFST structures is rarely explored. Therefore, experimental research on the influence of BF of different lengths on the mechanical characteristics of CFST short columns under axial compression load was conducted. The bearing capacity, ductility, and axial compression mechanisms of the members were investigated through axial compression testing on 18 short columns. The findings of this work are expected to be useful for the promotion of BF in civil engineering.

2 Test program

2.1 Material properties

The core concrete mix ratio of all test columns in this study is shown in Table 1. The following materials were used: common Portland cement (P.O 42.5); two-gradation aggregate with a diameter of 5–25 mm and a crushing value of 10.5; Dongting Lake yellow sand with a fineness modulus of 2.85; Huiba concrete water-reducing agent produced by Shandong Laiyang Hongxiang Building Admixture Factory; and Jinwang concrete expansive agent produced by Changsha Bada New-type Building Materials Factory. The chopped basalt fiber produced by Zhejiang Hengdian Shijin Basalt Fiber Co., Ltd. was used in this study, and the two types of fiber with different lengths are shown in Figure 1. The key parameters are

TABLE 2 Details of specimens.

Type	Specimen	Outer diameter/mm	Volume fraction/%	Wall thickness/mm	Length/mm
S_I	A1	108	0	4	/
	B1	108	0	4	/
S_{II}	A2	108	0.15	4	12
	B2	108	0.15	4	12
S_{III}	A3	108	0.15	4	24
	B3	108	0.15	4	24
S_{IV}	A4	108	0	5	/
	B4	108	0	5	/
S_V	A5	108	0.15	5	12
	B5	108	0.15	5	12
S_{VI}	A6	108	0.15	5	24
	B6	108	0.15	5	24
S_{VII}	A7	108	0	6	/
	B7	108	0	6	/
S_{VIII}	A8	108	0.15	6	12
	B8	108	0.15	6	12
S_{IX}	A9	108	0.15	6	24
	B9	108	0.15	6	24

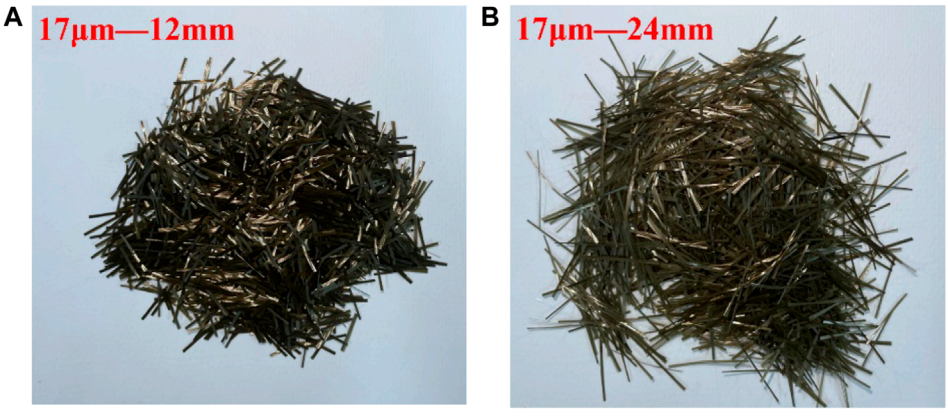

FIGURE 1
Basalt fiber. **(A)** Diameter, 17 μm; length, 12 mm. **(B)** Diameter, 17 μm; length, 24 mm.

as follows: fiber diameter, 17 μm; fiber density, 2,650 kg/m^3; tensile strength, 3,000 MPa; modulus of elasticity, 90 GPa; and fiber length, 12 mm and 24 mm. The seamless steel tube short columns were made of Q345B-grade steel, and their elastic modulus and yield strength were 206 GPa and 345 MPa, respectively.

2.2 Details of specimens

In order to minimize test errors, two separate tests were successively conducted, the specimens of which were numbered A1–A9 and B1–B9, respectively. In this study, 18 short columns

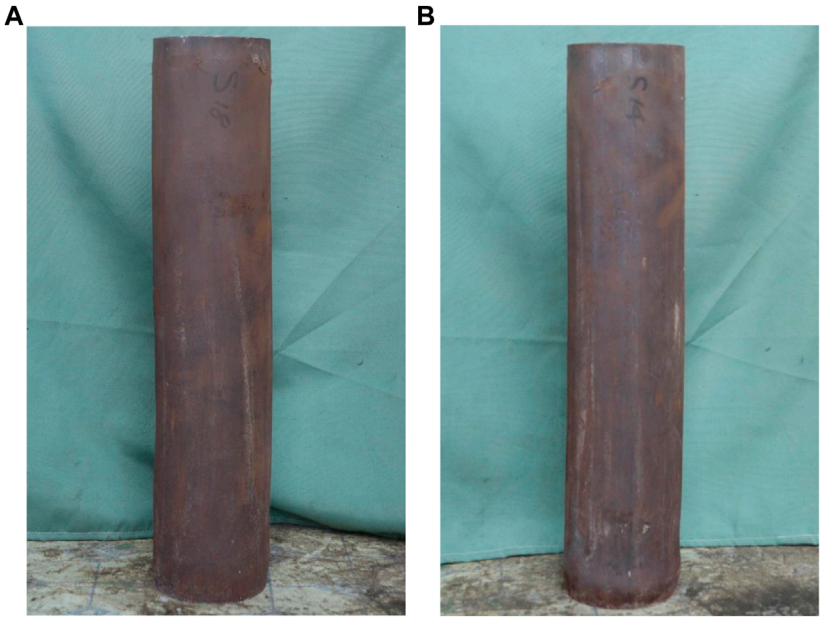

FIGURE 2
Short columns. **(A)** BFRC-filled steel tube. **(B)** Concrete-filled steel tube.

were fabricated using steel tubes with wall thicknesses of 4 mm, 5 mm, and 6 mm, an outer diameter of 108 mm, and a length of 540 mm, of which 12 were BFRC-filled steel tubes (Figure 2A) and 6 were CFSTs (Figure 2B). Particularly, 0.15% is selected for the fiber volume fraction of BFRC-filled steel tubes, according to Wang et al. (2022). The information of all test columns in this study is shown in Table 2.

2.3 Test loading procedure

The test columns S_I– S_{IX} were preloaded with 20 kN for 3 min using a 5,000 kN compression machine to observe the operational reliability of the loading system and measuring points. After pre-loading, unloading and formal loading were performed. The formal loading was conducted under step load at a step of 50 kN for 2 min until failure. The resistance strain gauges were uniformly arranged in the middle section of each test specimen, and a total of eight measuring points were defined, with one strain gauge located circumferential and longitudinal to each measuring point. Three displacement meters were placed to measure the deformation of the test specimens. Displacement meter 1 was used to measure the vertical deformation of the test specimens, and displacement meters 2 and 3 were positioned on the side of the column at a 90-degree angle to measure the lateral deformation of the middle part of the test specimens (Figure 3). The displacement and strain values under each load level were recorded.

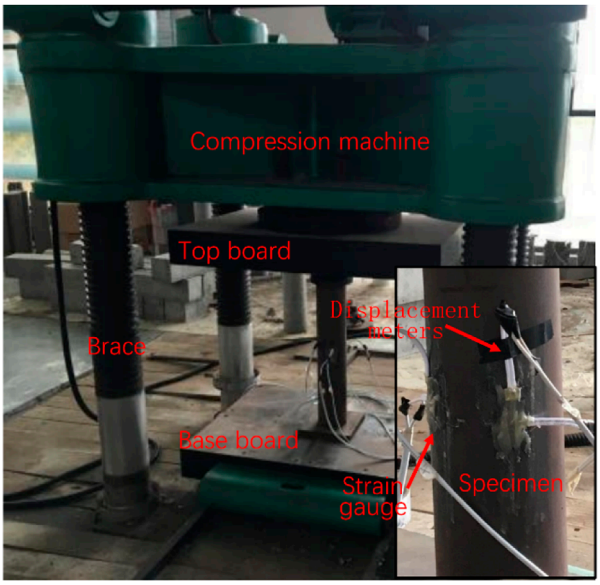

FIGURE 3
Photograph of the strain test on site.

2.4 Test phenomena

The short columns S_I– S_{IX} after failure are shown in Figure 4. For the test column S_I, there was no abnormality in the short columns at the initial stage of loading. When the load reached its peak, the steel tubes bulged followed by a sudden increase in displacement and strain, with no obvious plastic deformation before reaching the peak. The test columns S_{II} and S_{III} showed similar structural responses (strain, displacement, and shape) to S_I at the initial stage of loading, but with larger displacement and strain, along with relatively evident plasticity, before reaching the peak. There was little difference among S_{IV}, S_V, and S_{VII} at the initial stage of loading. However, as the load increases, the steel tubes bulged with greater

FIGURE 4
Shape of the test short columns after failure.

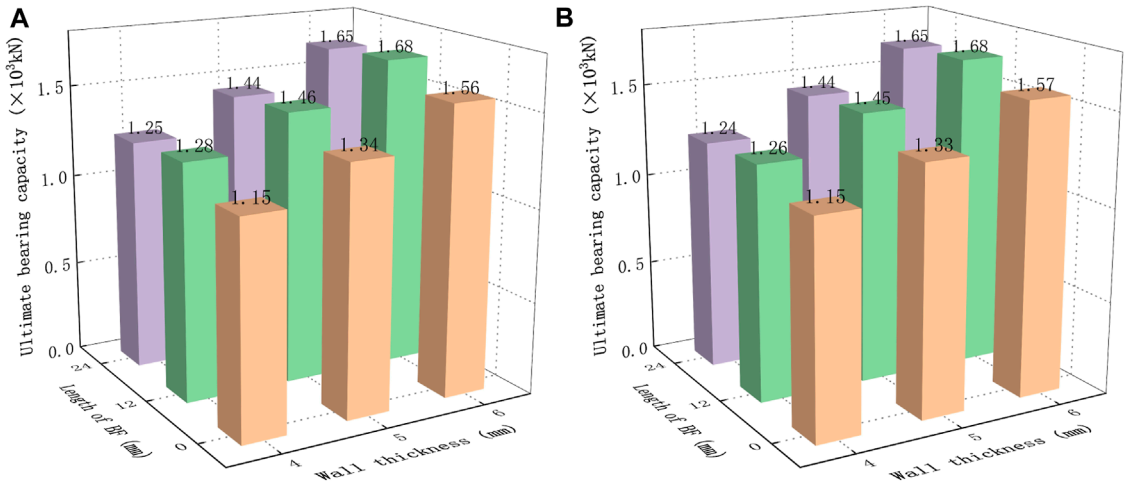

FIGURE 5
Ultimate bearing capacity. **(A)** Specimens A1–A9. **(B)** Specimens B1–B9.

displacement and rapidly increased at a load of 1,200 kN, as well as with obvious plasticity at a peak load of approximately 1,330 kN in test column S_{IV}. A similar pattern was noted in test column S_V, but at a load of 1,340 kN and a peak load of approximately 1,450 kN. For test column S_{VI}, bulged steel tubes, larger displacement, rapidly increased strain, and evident plasticity were found under a load of approximately 1,300 kN. The test columns S_{VII}, S_{VIII}, and S_{IX} exhibited obvious plasticity with a small difference at the initial loading stage or before reaching the peak, and the deformation of S_{VIII} was greater at the peak value of bearing capacity. These results suggested that in the test short columns with the same wall thickness, BFRC-filled steel tube short columns had advantages of late bulging, long elastic stage, obvious plastic characteristics, and large bearing capacity compared with CFST short columns.

2.5 Test results

2.5.1 Ultimate bearing capacity

The test results of ultimate bearing capacity under axial compression are shown in Figure 5 for short columns A1–A9 and B1–B9.

As can be seen from Figure 5, BF has an enhancing effect on the ultimate bearing capacity of CFST short columns under axial compression, and the improvement rate of the ultimate bearing capacity gradually decreases as the wall thickness of the steel tube increases. After adding BF with a length of 12 mm, the ultimate bearing capacity of CFST short columns with wall thicknesses of 4 mm, 5 mm, and 6 mm increased by 10.3%, 9.5%, and 7.2%, respectively. When BF with a length of 24 mm was added, the ultimate bearing capacity of CFST short columns with wall thicknesses of 4 mm, 5 mm, and 6 mm increased by 8.4%, 7.8%, and 5.3%, respectively. Obviously, BF with a length of 12 mm has a greater effect on improving the ultimate bearing capacity of CFST columns than BF with a length of 24 mm. In addition, another conclusion can be reached that BFRC contributed little to the bearing capacity of test columns with a greater steel ratio. This is due to the fact that the presence of BF may constrain the circumferential stress of core concrete, which is limited to slight deformation. When extensive deformation occurs in concrete, BF loses its constraint on core concrete, and the steel ratio will be a dominant factor influencing the bearing capacity of CFST short columns.

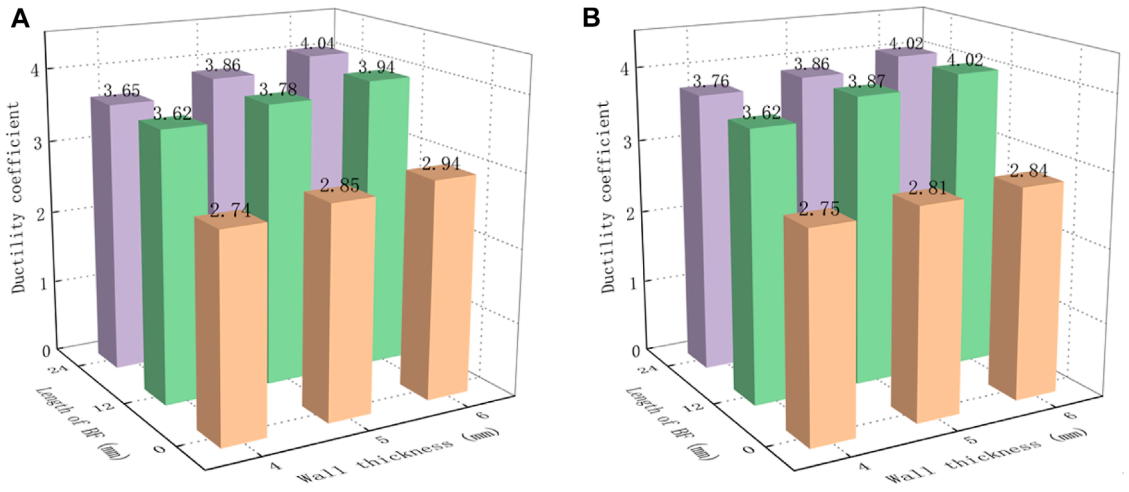

FIGURE 6
Ductility coefficient. **(A)** Specimens A1–A9. **(B)** Specimens B1–B9.

2.5.2 Ductility coefficient

According to Bian et al. (2023), the ductility coefficient of BFRC-filled steel tube short columns can be calculated as

$$DI = \frac{\mu_{0.85}}{\mu_{\Delta}}, \tag{1}$$

where μ_{Δ} is the displacement at peak load and $\mu_{0.85}$ is the corresponding displacement when the load reduces to 85% of peak load.

The test results of the ductility coefficient are shown in Figure 6 for short columns A1–A9 and B1–B9 (Eq. 1).

As can be seen from Figure 6, BF significantly impacts the ductility of CFST short columns. For the test short columns with three different wall thicknesses (4 mm, 5 mm, and 6 mm), the displacement ductility coefficient of BFRC-filled steel tube short columns increased by 33.4%, 35.8%, and 38.6%, respectively, compared to CFST short columns. The ductility coefficient of BFRC-filled steel tube short columns increases with an increase in the steel ratio, and the variation law of the increase rate of the ductility coefficient is similar to the former. The change in fiber length has little effect on the ductility coefficient of the test short columns. When the bearing capacity of short columns reduces to 85% of peak load, the toughening of concrete after adding BF can lead to a larger displacement. Therefore, the blending of BF into CFST is effective in improving the ductility of CFST short columns.

2.5.3 Load–strain curve

The relationship curve between the strain at the midpoint of the short column and axial compressive load is shown in Figure 7.

As can be seen from Figure 7, the influence of BF on the load–strain curve of CFST columns is not significant at the initial loading stage. As the load increases, the slope of the load–strain curve of the CFST short columns after adding BF is greater than that of the CFST short columns. When the ultimate load is reached, the CFST short columns after adding BF have a greater ultimate strain, a clear yield stage, and a plastic stage. In addition, the load–circumferential strain curve and load–axial strain curve of BFRC-filled steel tube short columns have similar characteristics. The test results indicate that BF has an improved effect on the deformation coordination ability of the concrete inside the CFST short columns before crushing.

2.5.4 Load–displacement curve

The relationship curve between the displacement of the CFST short column and axial compressive load is shown in Figure 8.

As can be seen from Figure 8, the CFST short columns and BFRC-filled steel tube short columns with three different wall thicknesses are both at the elastic stage, with a slight difference in load–displacement curves between the two types of short columns. With an increase in load, the plastic stage of BFRC-filled steel tube short columns starts later than that of CFST short columns, and the displacement of BFRC-filled steel tube short columns is larger than that of CFST short columns before reaching the peak load. The results indicate that the effect of BF on bearing capacity and displacement of CFST short columns depends on the steel ratio, and a higher steel ratio of CFST is associated with a lesser effect.

3 Calculation results of bearing capacity of BFRC-filled steel tube columns

When the BFRC-filled steel tube columns are axially compressed, the steel tube and BFRC are jointly stressed. The structural deformation was small, and no cracks were found in the internal concrete at lower loads. As external load increased, numerous micro-cracks and lateral expansion appeared in BFRC. After the steel tube reached its yield strength under axial compression–circumferential tension, the strain of the BFRC-filled steel tube increased rapidly; the external volume also increased due to the lateral expansion of the core concrete, followed by the ultimate load. This demonstrates that the mechanical characteristics

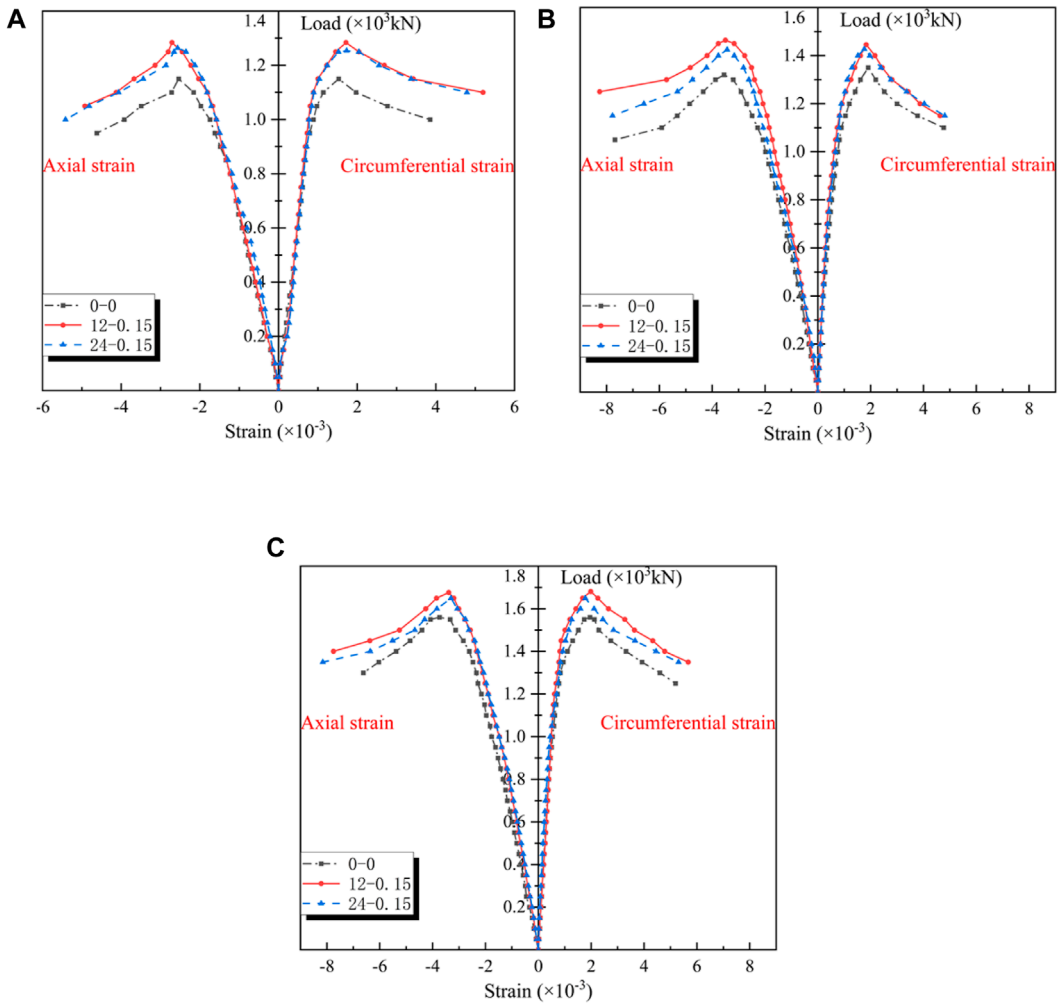

FIGURE 7
Load–strain curve of BFRC-filled steel tube short columns under axial compression. **(A)** Wall thickness 4 mm. **(B)** Wall thickness 5 mm. **(C)** Wall thickness 6 mm.

of BFRC-filled steel tube columns are roughly identical to those of CFST columns. Therefore, in this section, the limit equilibrium and finite element methods were applied for calculating CFST columns. The parameters of core concrete were replaced by those of core BFRC, and the calculations were then compared with the experimental results to verify the correctness and rationality of the test results.

3.1 Calculation methods for bearing capacity

3.1.1 Limit equilibrium method

Many studies have been conducted on the ultimate bearing capacity of CFST short columns, including the limit equilibrium method (Qi et al., 2020) which allows for the direct determination of the ultimate load based on the equilibrium condition of the member in limit states. This method does not require consideration of the challenging elastic–plastic stage and the constitutive relationship of materials, making it relatively simple (Eqs 2–4). According to the limit equilibrium method, the following assumptions are made:

1) The strain field of axially compressed short columns is axisymmetric.
2) In limit states, the radial stress of thin-walled steel tubes with D/T ≥ 20 is much lower than the circumferential stress and thus negligible.
3) The yield conditions of steel tube and core concrete were stable and were not changed or weakened by plastic deformation.

The basic formula is as follows:

$$N_u = \varphi_1 \varphi_2 N_0, \tag{2}$$

$$N_0 = A_c f_c \left(1 + \sqrt{\theta} + \theta\right), \tag{3}$$

$$\theta = \frac{A_s f_s}{A_c f_c}, \tag{4}$$

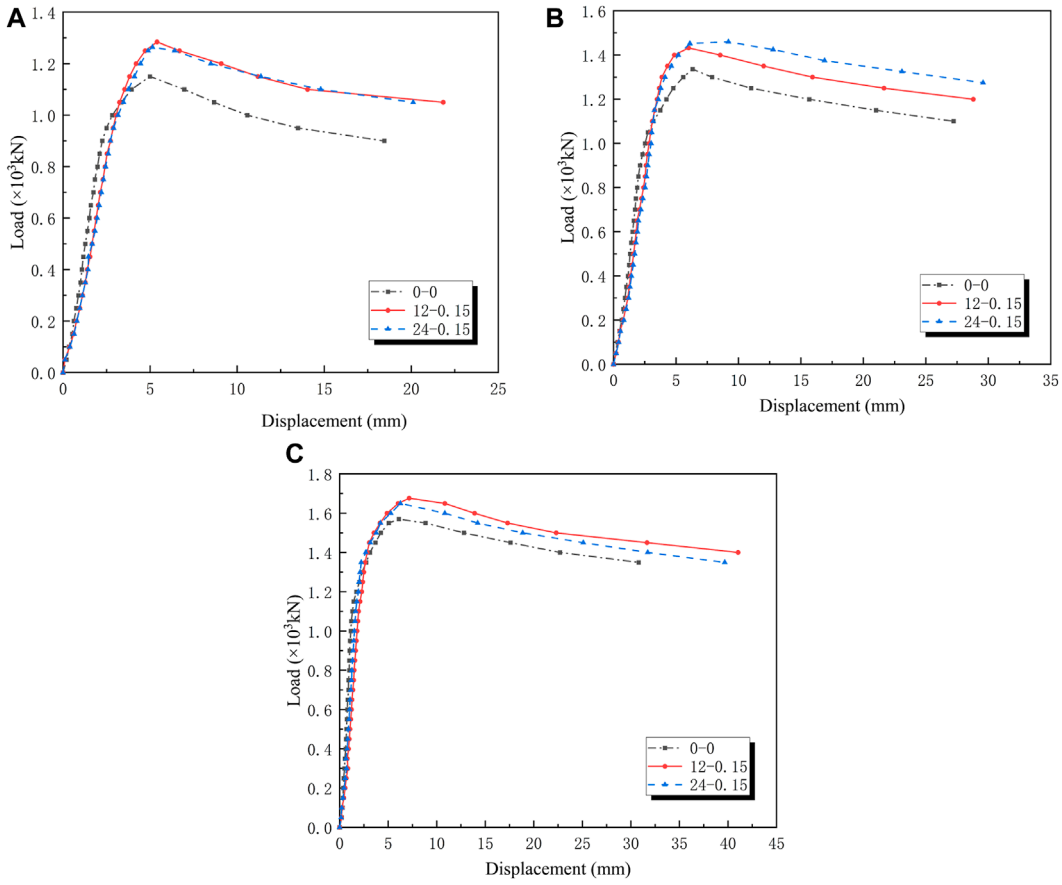

FIGURE 8
Load–displacement curve of BFRC-filled steel tube short columns under axial compression. **(A)** Wall thickness 4 mm. **(B)** Wall thickness 5 mm. **(C)** Wall thickness 6 mm.

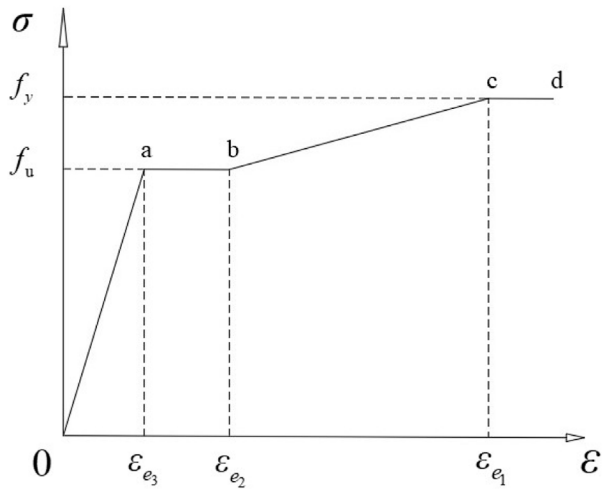

FIGURE 9
Schematic diagram of the simplified stress–strain relationship curve of a steel tube.

where φ_1 is the influence coefficient of bearing capacity accounting for eccentricity; φ_2 is the reduction factor of bearing capacity accounting for the slenderness ratio of compressed members; f_c is the designed compressive strength of BFRC; f_s is the designed tensile strength of the steel tube; A_c is the cross-sectional area of BFRC; and A_s is the cross-sectional area of the steel tube.

3.1.2 Finite element method

The finite element method can better determine the bearing capacity of CFST columns. The key is to define the constitutive relationship between concrete and steel first. Particularly, the stress–strain relationship (constitutive relationship) of concrete is very important to calculate the bearing capacity and deformation characteristics of CFSTs. Numerical results close to real structural stress may be obtained only using a reasonable constitutive model.

3.1.2.1 Stress–strain relationship model of the steel tube

According to Han (2016), given the complex three-dimensional stress of CFST structures, the complex stress of the steel tube is represented by a one-dimensional stress–strain relationship to simplify the calculation (Eq. 5). A nonlinear analysis is performed by introducing the equivalent strain and modifying the elastic matrix to address the three-dimensional stress with a one-dimensional stress–strain relationship. The one-dimensional stress–strain relationship curve composed of four straight lines of the steel tube is shown in Figure 9.

The specific expression is as follows:

$$\begin{array}{ll} \text{Reinforcement section (oa section):} & \sigma = E_y\varepsilon \quad (0 \le \varepsilon \le \varepsilon_{e_1}) \\ \text{Yield section (ab section):} & \sigma = f_y \quad (0 < \varepsilon \le \varepsilon_{e2}) \\ \text{Reinforced section (bc section):} & \sigma = f_y + E_y/150(\varepsilon - \varepsilon_{e2}) \quad (\varepsilon_{e2} < \varepsilon \le \varepsilon_{e3}) \\ \text{Secondary plastic flow section (cd section):} & \sigma = f_u \quad (\varepsilon \ge \varepsilon_{e3}), \end{array} \tag{5}$$

where E_y is the elastic modulus in the elastic stage; ε_{e1} is the ultimate elastic strain; and f_y and f_u are the yield strength and ultimate strength of steel, respectively. The ultimate elastic strain is taken as $\varepsilon_{e2} = 10\varepsilon_{e1}$; the reinforced ultimate strain is taken as $\varepsilon_{e3} = 100\varepsilon_{e1}$; and the ultimate strength of steel is taken as $f_u = 1.6f_y$.

3.1.2.2 Stress–strain relationship model of concrete

Han (2016) proposed a stress–strain relationship model of core concrete using the standard axial compressive strength of concrete (for circular concrete-filled steel tubes) through verification and analysis of the experimental results of various short specimens of CFST under axial compression, as shown below (Eqs 6–9).

$$\sigma_c = \sigma_0\left[A\frac{\varepsilon_c}{\varepsilon_0} - B\left(\frac{\varepsilon_c}{\varepsilon_0}\right)^2\right]\varepsilon_c \le \varepsilon_0, \tag{6}$$

$$\begin{cases} \sigma_c = \sigma_0(1-q) + \sigma_0 \cdot q \cdot (\varepsilon_c/\varepsilon_0)^{0.1\xi} (\xi \ge 1.12) \\ \sigma_c = \sigma_0(\varepsilon_c/\varepsilon_0)/\left[\beta(\varepsilon_c/\varepsilon_0 - 1)^2 + (\varepsilon_c/\varepsilon_0)\right] (\xi < 1.12) \end{cases} \varepsilon_c > \varepsilon_0, \tag{7}$$

where $\sigma_0 = f_{ck}\left[1.194 + (13/f_{ck})^{0.45} \cdot (-0.07485\xi^2 + 0.5789\xi)\right]$;

$\varepsilon_0 = \varepsilon_{cc} + [1400 + 800 \cdot (f_{ck} - 20)/20]\xi^{0.2}(\mu\varepsilon)$;

$\varepsilon_{cc} = 1300 + 14.93 f_{ck}(\mu\varepsilon)$;

$A = 2 - k; B = 1 - k; k = 0.1\xi^{0.745}$;

$q = k/(0.2 + 0.1\xi)$; and

$\beta = (2.36 \times 10^{-5})^{[0.25+(\xi-0.5)^7]} \cdot f_{ck}{}^2 \times 5 \times 10^{-4}$.

For the lateral deformation coefficient of core concrete, the suggested expression is as follows:

$$\mu_c = 0.173 \quad \frac{\sigma_c}{\sigma_0} \le 0.55 + 0.25\left(\frac{f_{ck} - 33.5}{33.5}\right), \tag{8}$$

$$\mu_c = 0.173 + \left[0.7036(\sigma_c/\sigma_0 - 0.4)^{1.5}\left(\frac{20}{f_{ck}}\right)\right] \quad \frac{\sigma_c}{\sigma_0} > 0.55 + 0.25\left(\frac{f_{ck} - 33.5}{33.5}\right). \tag{9}$$

3.2 Results and analysis

A finite element analysis is conducted using ABAQUS software. Both core concrete and steel tubes are simulated using the C3D8R solid element. A reference point is set at the top and bottom, respectively, and is connected to the corresponding surfaces through a "coupling" boundary condition. The top reference point is used for loading, and the bottom reference point is used for applying the "rigid connection" boundary condition. The steel tube is connected to the core concrete under a "tie" boundary condition. According to the cube compression test of concrete specimens, the compressive strength of plain concrete cubes is 51.4 MPa, while the compressive strengths of concrete cubes after adding BF of lengths 12 mm and 24 mm are 61.5 MPa and 58.6 MPa, respectively. When calculating the bearing capacity using the finite element method, the measured compressive strength of the cube is used to calculate its constitutive relationship. The yield strength of steel tubes is specified as 345 MPa. The results of the stress nephogram of specimens at the peak load stage are shown in Figure 10.

The comparison of the test average value, normative calculation value, and finite element results of the bearing capacity of short columns can be seen in Figure 11.

As can be seen from Figure 11, the finite element calculation results of bearing capacity are relatively close to the measured results, verifying the correctness and rationality of the latter.

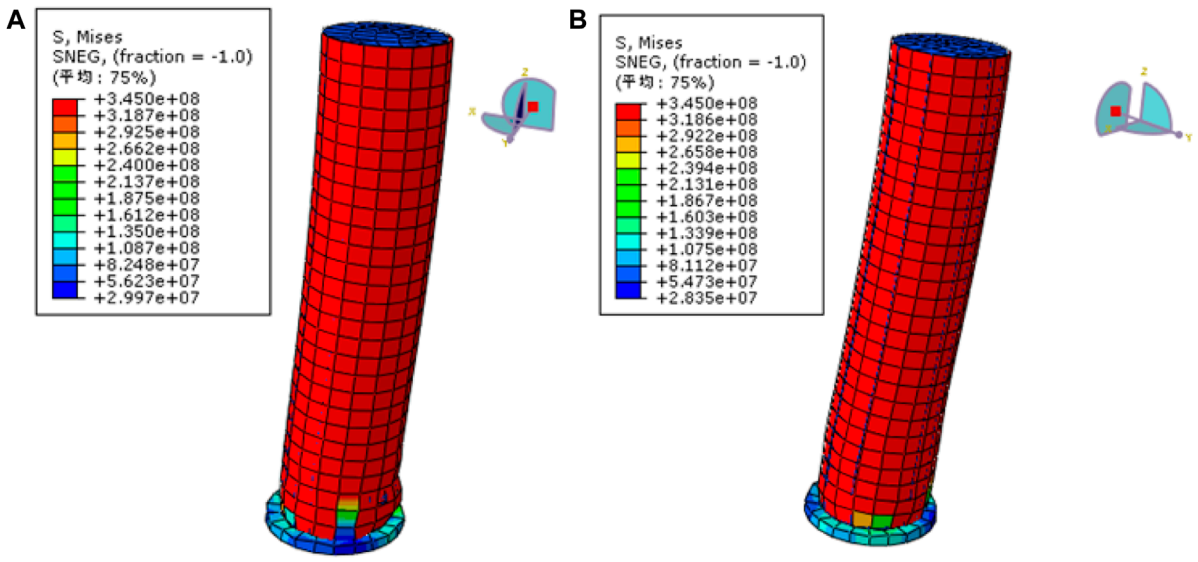

FIGURE 10
Stress nephogram of specimens at the peak load stage (units: MPa). **(A)** CFST short column. **(B)** BFRC-filled steel tube short column.

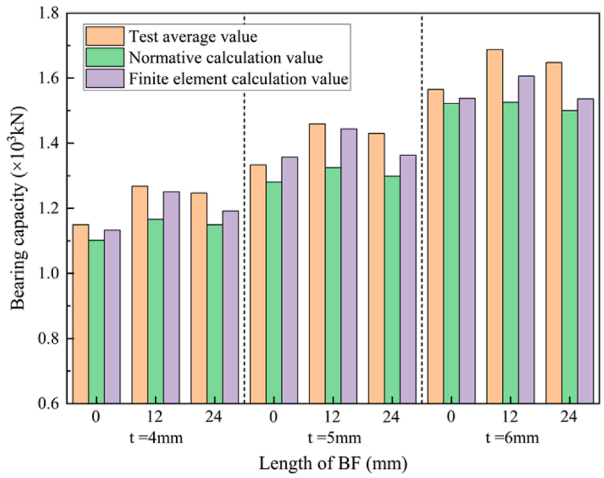

FIGURE 11
Comparison of bearing capacity results of short columns.

However, the normative calculation value of the bearing capacity of BFRC-filled steel tube short columns is less than the test average value by approximately 10%. The reason for the deviation is that when using normative formulas to calculate the bearing capacity of columns, the ultimate bearing capacity is directly determined based on the equilibrium conditions of the component in the ultimate state, without involving the constitutive relationship of the material.

4 Conclusion

The axial compressive bearing capacity test of CFST short columns was conducted, and the effect of BF on the mechanical performance of the CFST short columns under axial compression was investigated. The comparison of test results, normative calculation results, and finite element results was made to prove that the test results are reasonable. The following conclusions are obtained:

1) The bearing capacity of BFRC-filled steel tube short columns is greater than that of CFST short columns by approximately 8.1% on average. The bridging effect of BF can inhibit crack development in the early stage of BFRC cracking, and the bearing capacity of short columns will be enhanced. When the load continues to increase, BFRC cracks will further develop. Meanwhile, BF is pulled off or pulled out, which causes the loss of the bridging effect. With the short column deformation increasing, the steel tube under the constraints of BFRC deformation plays a leading role gradually. Therefore, compared to the fiber length, the steel ratio of CFST has a greater effect on the mechanical properties of short columns.
2) BF has an effective influence on improving the ductility of CFST short columns, and the ductility coefficient of BFRC-filled steel tube short columns increases with an increase in the fiber ratio, while changing the fiber length affects the ductility coefficient insignificantly. After adding BF with a length of 12 mm, the ultimate bearing capacity of CFST short columns with wall thicknesses of 4 mm, 5 mm, and 6 mm increased by 10.3%, 9.5%, and 7.2%, respectively, higher than that of CFST.
3) When axially compressed under the same conditions, the plastic stage of BFRC-filled steel tube short columns appears later than that of CFST columns, resulting in large deformation at the peak load. The mixture with BF changes the plasticity of CFST. At the ultimate bearing capacity, all short columns are noted to have obviously bulged steel tubes and yield failure.
4) The bearing capacity of BFRC-filled steel tube short columns calculated using the finite element method is in good agreement with the test value, while the maximum difference between the calculation results based on the limit equilibrium method and test results is approximately 10%.
5) In this paper, the effect of BF on the behavior of CFST short columns under axial compression is studied. Different fiber lengths, fiber ratios, and steel tube wall thickness were taken as variables, while BF diameter, steel tube section shape, column slenderness ratio, and eccentricity were not considered. The effects of these variables on BFRC-filled steel tube columns will be further studied in the future. Meanwhile, considering the anisotropy of concrete, the discreteness of fiber, and the complex three-dimensional stress of CFST structures, the constitutive relationship of BFRC will be further studied.

Data availability statement

The raw data supporting the conclusion of this article will be made available by the authors without undue reservation.

Author contributions

XW: conceptualization, funding acquisition, supervision, validation, and writing–review and editing. LL: methodology, writing–original draft, and writing–review and editing. YX: methodology, writing–original draft, and writing–review and editing. YW: funding acquisition, methodology, and writing–review and editing. MW: supervision, validation, and writing–review and editing.

Funding

The author(s) declare that financial support was received for the research, authorship, and/or publication of this article. This research was funded by the Research Foundation of Education Bureau of Hunan Province, China (grant number 22A0561, 23A0559, and 23B0732), and the Natural Science Foundation of Hunan Province, China (grant number 2022JJ50267).

Conflict of interest

The authors declare that the research was conducted in the absence of any commercial or financial relationships that could be construed as a potential conflict of interest.

Publisher's note

References

Abushanab, A., Alnahhal, W., and Farraj, M. (2022). Experimental and finite element studies on the structural behavior of BFRC continuous beams reinforced with BFRP bars. *Compos. Struct.* 281, 114982. doi:10.1016/j.compstruct.2021.114982

Bian, H., Liu, Y., Guo, Y. D., Liu, Y., and Shi, W. J. (2023). Investigating stress–strain relationship and damage constitutive model of basalt fiber reinforced concrete under uniaxial compression. *J. Build. Eng.* 73, 106789. doi:10.1016/j.jobe.2023.106789

Chen, H. Y., Liao, F. Y., Yang, Y. X., and Ren, Y. (2023). Behavior of ultra-high-performance concrete (UHPC) encased concrete-filled steel tubular (CFST) stub columns under axial compression. *J. Constr. Steel Res.* 202, 107795. doi:10.1016/j.jcsr.2023.107795

Dong, J. F., Guan, Z. W., Chai, H. K., and Wang, Q. Y. (2023). High temperature behaviour of basalt fibre-steel tube reinforced concrete columns with recycled aggregates under monotonous and fatigue loading. *Constr. Build. Mater.* 389, 131737. doi:10.1016/j.conbuildmat.2023.131737

Dong, J. F., Wang, Q. Y., and Guan, Z. W. (2017). Material properties of basalt fibre reinforced concrete made with recycled earthquake waste. *Constr. Build. Mater.* 130, 241–251. doi:10.1016/j.conbuildmat.2016.08.118

Fang, Y., Liu, C. Y., Wang, Y. Y., and Zhang, S. M. (2019). Behavior of CSP-interlayer-steel tubular concrete short columns under axial compression. *J. Build. Struct.* 40, 126–133. (in Chinese). doi:10.14006/j.jzjgxb.2019.S1.016

Güneyisi, E. (2023). Axial compressive strength of square and rectangular CFST columns using recycled aggregate concrete with low to high recycled aggregate replacement ratios. *Constr. Build. Mater.* 367, 130319. doi:10.1016/j.conbuildmat.2023.130319

Han, L. H. (2016). *Concrete filled steel tubular structures-theory and practice*. Third Edition. Peking: Science Press. (in Chinese).

He, A., Cai, J., Chen, Q. J., Liu, X. P., Xue, H., and Yu, C. J. (2017). Axial compressive behaviour of steel-jacket retrofitted RC columns with recycled aggregate concrete. *Constr. Build. Mater.* 141, 501–516. doi:10.1016/j.conbuildmat.2017.03.013

Hu, H. S., Yang, Z. J., Xu, L., Zhang, Y. X., and Gao, Y. C. (2023). Axial compressive behavior of square concrete-filled steel tube columns with high-strength steel fiber-reinforced concrete. *Eng. Struct.* 285, 116047. doi:10.1016/j.engstruct.2023.116047

Lai, M. H., Lin, Y. H., Jin, Y. Y., Fei, Q., Wang, Z. C., and Ho, J. C. M. (2023). Uni-axial behaviour of steel slag concrete-filled-steel-tube columns with external confinement. *Thin-Walled Struct.* 185, 110562. doi:10.1016/j.tws.2023.110562

Lian, J., Yang, Y., Yang, M., and Zhao, Y. (2007). Experimental research on the mechanical behavior of chopped basalt fiber reinforced concrete. *Ind. Constr.* 137, 10–881. (in Chinese). doi:10.1007/s10870-007-9222-9

Lu, D., Jiang, X., Leng, Z., Huo, Y. L., Wang, D. Y., and Zhong, J. (2023a). Electrically conductive asphalt concrete for smart and sustainable pavement construction: a review. *Constr. Build. Mater.* 406, 133433. doi:10.1016/j.conbuildmat.2023.133433

Lu, D., Leng, Z., Lu, G. Y., Wang, D. Y., and Huo, Y. L. (2023b). A critical review of carbon materials engineered electrically conductive cement concrete and its potential applications. *Inter. J. smart. nano. Mater.* 14, 189–215. doi:10.1080/19475411.2023.2199703

Qi, J. N., Wang, J. Q., Zhou, K., Liu, J. Z., and Li, W. C. (2020). Experimental and theoretical investigations on shear strength of UHPC beams. *China J. Highw. transpo.* 33, 95–103. (in Chinese). doi:10.19721/j.cnki.1001-7372.2020.07.010

Sharif, A. M., Al-Mekhlafi, G. M., and Al-Osta, M. A. (2019). Structural performance of CFRP-strengthened concrete-filled stainless steel tubular short columns. *Eng. Struc* 183, 94–109. doi:10.1016/j.engstruct.2019.01.011

Wang, L., He, T. S., Zhou, Y. X., Tang, S. W., Tan, J. J., Liu, Z. T., et al. (2023). The influence of fiber type and length on the cracking resistance, durability and pore structure of face slab concrete. *Constr. Build. Mater.* 282, 122706. doi:10.1016/j.conbuildmat.2021.122706

Wang, L., Zhou, S. H., Shi, Y., and Chen, E. (2017). Effect of silica fume and PVA fiber on the abrasion resistance and volume stability of concrete. *Compos. Part B Eng.* 130, 28–37. doi:10.1016/j.compositesb.2017.07.058

Wang, X. Z., He, J., Mosallam, A. S., Li, C. X., and Xin, H. H. (2019). The effects of fiber length and volume on material properties and crack resistance of basalt fiber reinforced concrete (BFRC). *Adv. Mater. Sci. Eng.* 17. doi:10.1155/2019/7520549

Wang, X. Z., and Li, C. X. (2016). Experimental study on load-carrying capacity of basalt fiber reinforced concrete long columns under eccentric compression. *Bull. Chin. Ceram. Soci.* 35, 3242–3246. (in Chinese). doi:10.16552/j.cnki.issn1001-1625.2016.10.027

Wang, X. Z., Yang, Y. M., Yang, R. H., and Liu, P. (2022). Experimental analysis of bearing capacity of basalt fiber reinforced concrete short columns under axial compression. *Coatings* 12, 654. doi:10.3390/coatings12050654

Wen, Y. C., Hu, Z. J., Li, A. N. J., Li, Q. H., Li, X. P., and Xu, Y. (2021). Experimental study on CFRP-confined circularized concrete-filled square steel tube short columns. *Adv. Mater. Sci. Eng.* 2021, 1–13. doi:10.1155/2021/6620577

Xia, S., Ding, F. X., Wei, X. Y., Wei, X. Y., He, C., Wang, W. J., et al. (2023). Experimental study on stirrup-confined concrete-filled steel tubular stub columns under axial loading. *J. Railw. Sci. Eng.* 20. (in Chinese). doi:10.19713/j.cnki.43-1423/u.T20222433

Xiamuxi, A., Aosimanjiang, A., and Yang, B. (2023). Loading performance of reinforced and recycled aggregate concrete-filled circular steel tube short column with different steel ratios. *Constr. Build. Mater.* 399, 132486. doi:10.1016/j.conbuildmat.2023.132486

Yang, J., Chen, R., Zhang, Z. Y., Zou, Y., Zhou, J. T., and Xia, J. R. (2023). Experimental study on the ultimate bearing capacity of damaged RC arches strengthened with ultra-high performance concrete. *Eng. Struc.* 279, 115611. doi:10.1016/j.engstruct.2023.115611

Yu, M., Liao, W., Liu, S., Wang, T., Yu, C. L., and Cheng, S. S. (2023). Axial compressive performance of ultra-high performance concrete-filled steel tube stub columns at different concrete age. *Struct* 55, 664–676. doi:10.1016/j.istruc.2023.05.113

Zhang, Q., Yang, Q. C., Gu, X. L., and Jiang, Y. (2023b). Study on axial compression properties of concrete columns wrapped with basalt textile-reinforced fine concrete (BTRC) jackets. *Constr. Build. Mater.* 363, 129809. doi:10.1016/j.conbuildmat.2022.129809

Zhang, X. G., Gao, X., Wang, X. G., Meng, E. C., and Wang, F. (2020). Axial compression performance of basalt-fiber-reinforced recycled-concrete-filled square steel tubular stub column. *Adv. Concr. Constr.* 10, 559–571. doi:10.1002/suco.202100016

Zhang, Z., Abbas, E. M. A., Wang, Y., Yan, W. H., Cai, X. N., Yao, S., et al. (2021). Experimental study on flexural behavior of the BFRC-concrete composite beams. *Case Stud. Constr. Mater.* 15, e00738. doi:10.1016/j.cscm.2021.e00738

Zhang, Z. Y., Pang, K., Xu, L. H., Zou, Y., Yang, J., and Wang, C. B. (2023a). The bond properties between UHPC and stone under different interface treatment methods. *Constr. Build. Mater.* 365, 130092. doi:10.1016/j.conbuildmat.2022.130092

Zhen, W., Zhang, L., Ding, R., Sheng, P., and Fan, J. S. (2023). Application and experimental study of combined lateral resistant system in super high-rise steel structure with large aspect ratio and length-width ratio. *J. Build. Struct.* 44, 74. (in Chinese). doi:10.14006/j.jzjgxb.2022.0439

Zhou, Y., Wang, Y., Zhou, J. T., Huang, Z. H., Zhang, X. S., and Xiang, Z. F. (2022). Arch forming calculation theory and control method of 500m steel tube arch bridge. *China J. Highw. transpo.* 35, 60. (in Chinese). doi:10.19721/j.cnki.1001-7372.2022.05.006

Zong, S., Lu, Y. Y., Ma, W. T., Liu, Z. Z., and Li, P. (2023). Research on eccentric-compressive behaviour of steel-fiber-reinforced recycled concrete-filled square steel tube short columns. *J. Constr. Steel Res.* 206, 107910. doi:10.1016/j.jcsr.2023.107910

Zou, Y., Jiang, J. L., Yang, J., Zhang, Z. Y., and Guo, J. C. (2023). Enhancing the toughness of bonding interface in steel-UHPC composite structure through fiber bridging. *Cem. Concr. Compos.* 137, 104947. doi:10.1016/j.cemconcomp.2023.104947

frontiers | Frontiers in Materials

TYPE Original Research
PUBLISHED 08 February 2024
DOI 10.3389/fmats.2024.1361647

OPEN ACCESS

EDITED BY
Zhongya Zhang,
Chongqing Jiaotong University, China

REVIEWED BY
Yangxi Zhang,
Xi'an University of Architecture and Technology, China
Junlin Heng,
University of Birmingham, United Kingdom

*CORRESPONDENCE
Baojun Li,
jamberly2@163.com

RECEIVED 26 December 2023
ACCEPTED 24 January 2024
PUBLISHED 08 February 2024

CITATION
Song J, Li B, Kong L, Qin D, Zhu C, Kuang Y and Shan A (2024), Effect of interface treatment on the flexural performance of existing RC bridge beams strengthened with UHPC.
Front. Mater. 11:1361647.
doi: 10.3389/fmats.2024.1361647

Effect of interface treatment on the flexural performance of existing RC bridge beams strengthened with UHPC

Jianping Song[1], Baojun Li[1]*, Lingcai Kong[2], Dafan Qin[2], Chao Zhu[3], Yang Kuang[4] and Aicheng Shan[5]

[1]Guangxi Transportation Science and Technology Group Co., Ltd., Nanning, China, [2]Highway Development Center of Guixi, Guangxi Zhuang Autonomous Region, Nanning, China, [3]ChongQing Municipal Design and Research Institute Co., Ltd., Chongqing, China, [4]Planning and Technology Development Centre of Chongqing Fuling District, Chongqing, China, [5]ChongQing City Transportation Development & Investment Group Co., Ltd, Chongqing, China

As one of the most innovative cement-based materials, ultra-high performance concrete (UHPC), with excellent durability and mechanical properties, has been widely used in strengthening existing bridges. In this study, *in-situ* four-point bending tests were carried out to investigate the flexural behavior of precast reinforced concrete (RC) hollow slab beams in service for 15 years strengthened with UHPC. Among them, three hollow slab beams were strengthened with UHPC, and the interface treatment was chiseling, planting rebars, and a combination of chiseling and planting rebars, respectively. The remaining one without any strengthening treatment was used as the control specimen. To evaluate the enhancement effect of different interface treatments on UHPC-strengthened beams, the cracking load, ultimate load, crack development and failure modes of UHPC-strengthened beams were analyzed. Results indicated that the stiffness, deflection capacity and flexural capacity of UHPC-strengthened beams was significantly improved. Meanwhile, the stiffness of UHPC-strengthened beams in the pre-damage stage was increased by 49%–94%, when compared with the unstrengthened beam. Correspondingly, the ultimate flexural capacity was increased by 29%–38%. The interface chiseling treatment was more favorable to enhance the deformation capacity of UHPC-strengthened beams. The interface planting rebar treatment was more favorable to enhancing the ductility of UHPC-strengthened beams. The crack development was effectively suppressed by the interface chiseling and planting rebars together. This contributes to a higher load capacity reserve for UHPC-strengthened beams. The bearing capacity under serviceability limit state of the UHPC-strengthened beams was increased by 1.25, 2, and 2.5 times through the interface treatments of chiseling, planting rebars, and a combination of both, respectively.

KEYWORDS

bridge engineering, UHPC strengthening, hollow slab beam, flexural capacity, interface treatment

1 Introduction

Precast reinforced concrete (RC) hollow slab beam bridges are widely used in small and medium-span bridges in China. The reason is that it has many advantages such as simple manufacturing, convenient construction, low cost of engineering and easy large-scale factory production. However, with the increase of service life, as well as in the overloading, material aging, environmental erosion, natural disasters and other coupling effects (Zhang et al., 2019; Ren et al., 2023). The structural performance of a large number of existing hollow slab beam bridge declined significantly, extremely susceptible to safety accidents. Its safety performance is a priority concern for bridge management and maintenance departments (Zhou et al., 2023). Therefore, it is necessary to conduct an in-depth study on the service performance and strengthening measures of such bridge types.

Traditional strengthening methods of RC hollow slab beams all have certain limitations. For example, the enlarged section method reduces net clearance height and adds additional structural self-weight (Zhang et al., 2022). The maintenance tasks for the bonding steel plate strengthening method are heavy (Ciampa et al., 2023). The fiber composite material bonding strengthening method cannot overcome the brittle failure characteristics of the components (Xun et al., 2022). Finally, the external prestressed strengthening method has a complex construction process that significantly impacts traffic (Li et al., 2018). Therefore, the development of high-performance materials to strengthen existing RC hollow slab beams will be one of the effective ways to solve the above problems.

Based on compact microstructure and unique structural components, ultra-high performance concrete (UHPC) possesses outstanding mechanical properties, excellent toughness and ductility, as well as exceptional durability (Li et al., 2020; Du et al., 2021; Amran et al., 2022; Huang et al., 2022). Meanwhile, good bonding properties are exhibited at the interface between the UHPC and NC matrix (Feng et al., 2020; Tong et al., 2021; Yang et al., 2023; Zhang et al., 2023). Expansion of microcracks within the material can be significantly suppressed by the dispersed steel fibers within the UHPC, thereby giving the structure ultra-high toughness and ductility (Du et al., 2021; Zou et al., 2023a). Therefore, UHPC has a promising application for application in bridge repair and strengthening (Xue et al., 2020; Yang et al., 2022; Zou et al., 2023b; Leng et al., 2023).

At present, scholars have conducted in-depth research on the structural performance of beam bridges strengthening with UHPC (Zhu et al., 2020). summarized the current state of research on RC beams/slabs strengthened with UHPC, failure modes of UHPC-RC structures under bending action influenced by various parameters were identified (Zhang et al., 2022). proposed a prestressing-UHPC strengthening technique based on model tests, achieving efficient and durable strengthening protection of damaged RC beams (Hou et al., 2019). found that macro-cracks in concrete transformed into dense micro-cracks by using UHPC in the tensile zone. The interfacial cracks hardly cause delamination at the UHPC and RC interface (Prem et al., 2018; Li et al., 2021). and carried out a series of studies on the flexural characteristics of UHPC-NC composite beams under four-point bending by acoustic emission technique. Research indicated that UHPC exhibited high strength and plastic properties under bending, such as a significant increase in load carrying capacity, a reduction in the number and width of cracks, and a noticeable decrease in mid-span deflection. Based on experimental studies and numerical simulations (Zhu et al., 2021), discussed the effects of UHPC thickness and reinforcement ratio within the UHPC layer on the flexural response of pre-damaged RC beams. Results revealed that the cracking load and ultimate bearing capacity improved, with the increase of UHPC thickness and reinforcement ratio within the UHPC layer. Gradually, UHPC has become an attractive potential solution for enhancing the sustainability of existing RC beams.

In summary, a large number of studies on the strengthening measures of RC beams have been conducted by many scholars. Nevertheless, the above series of studies are usually based on indoor model tests or numerical simulations, failing to effectively and realistically reflect the service performance of actual RC beams. To overcome the shortcomings of existing research, the test beams in this paper originated from prefabricated RC hollow-core slab beams from a major highway in Heng County, Guangxi, China. The four-point bending field experiments were conducted with the interface treatment of chiseling, planting rebars and a combination of both as test variables. The effect of interface treatments on the flexural performance of existing RC beams strengthened with UHPC was investigated in this study. Comparative analyses of load capacity, load-displacement curves, stiffness and ductility coefficients of the test beams were performed. Finally, efficient flexural measures for actual RC beams strengthened with UHPC were proposed based on the field tests.

2 Experimental program

2.1 Overview of test beams

The test beams came from a highway bridge along route G324 within Heng County, Guangxi, China. This bridge was put into service in 2007 and has been in operation for 15 years. The total length of the bridge is 114.00 m, with a width of 12.00 m. The upper structure adopts prefab RC hollow slab beams of 15.98 m + 4 × 16.00 m + 15.98 m. The total span of the four test beams is 15.96 m, with a beam height of 0.90 m and a bottom plate width of 1.04 m. Notably, as the test beams were directly removed from the original bridge, the beam height includes a 15 cm-thick asphalt concrete paving layer. The mid-span section dimensions and strengthening details of the test beam are illustrated in Figure 1.

Carbonization depths of the test beams was found to be 0.5 mm–1.0 mm by the appearance and material property inspection of the original RC hollow slab beams. Multiple transverse cracks were present in the bottom plate of the test beam, with a small number of diagonal and vertical cracks on the web. The maximum crack length was 0.5 m, with a maximum width of 0.15 mm. Local concrete protection had peeled off, exposing and corroding rebar, bridge deck paving showed deformation, and expansion joints had failed due to blockage. Moreover, diseases such as inter-slab seepage and leakage were also observed. The load-bearing capacity and working performance of the bridge structure seriously deteriorated under

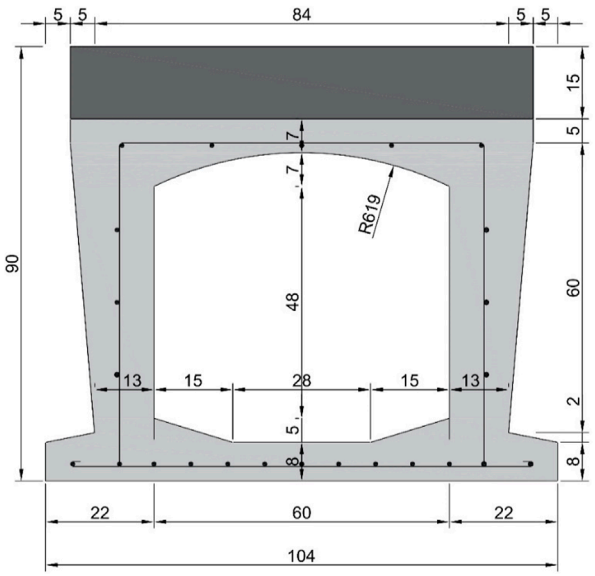

FIGURE 1
Mid-span section dimensions and strengthening details of the test beam (units: cm).

the influence of these diseases. Thus, the technical condition of the bridges was assessed at level 4.

2.2 Specimen description

To explore the flexural performance and crack distribution of RC hollow slab beam bottom plate strengthened with UHPC under load, four test beams were designed. Among them, one bare beam received no strengthening and served as the control group. The remaining three beams were strengthened with UHPC, all with a strengthening thickness of 5 cm. The numbering and influencing parameter settings of the test beams are shown in Table 1. To enhance the flexural performance of the UHPC-RC composite beams, the steel mesh was embedded into the UHPC layer. Details of the steel mesh, planting rebar size, and interface treatment are presented in Figure 2. The interface between UHPC and RC was treated by chiseling, planting rebars and a combination of both, respectively. Chiseling was done by means of manual chiseling, while planting rebars was done by locating the holes and subsequently fixing the rebars using a planting adhesive. In this case, the interface planting rebars are "L" type rebars and arranged in a plum blossom pattern. The spacing of each row of rebars was 330 mm. The implantation depth on the RC side was 6.5 cm, and on the UHPC side, it was 2.5 cm.

Notes:

(1) Explanation of specimen numbering: "B" represents the unstrengthened beam, "5"represents the thickness of the UHPC strengthening layer, "U" stands for strengthening using UHPC, "Ch" indicates that the interface treatment method is chiseling, and "Pr" signifies that the interface treatment method is planting rebars.
(2) Specifically, chiseling was carried out using a hand-held percussion drill to randomly and irregularly chisel the surface of the RC hollow slab bottom plate, with the roughness of the chiseled specimens maintained in the range of 2–3 mm. The outcome of the chiseling process is illustrated in Figure 2C.

2.3 Material properties

2.3.1 Normal concrete (NC)

Given that the test beam has been in service for 15 years, it is extremely difficult to directly strip regular standard specimens from the original girder bridge. Thus, after the flexural test was completed, considering factors such as the geometric dimensions of the test beam, the arrangement of rebar positions and maximum aggregate, the method of core drilling was used to sample from the web of the test beam at the beam end. Then, according to the "*Standard for test methods of concrete physical and mechanical properties*" (GB/T 50081–2019), material testing was conducted on the concrete. An overview of the material properties test of NC is shown in Figure 3A. The results of the mechanical properties are shown in Table 2.

2.3.2 UHPC

As the strengthening layer material, UHPC was a self-developed early-strength dry mix developed by the team. Rapid early strength development was observed, with an initial setting time of 6 h and a final setting time of 14 h. Compressive strength exceeding 70 MPa at 3 days and surpassing 120 MPa at 7 days was achieved. The slump value reached 850 mm, and a self-compacting performance rating of SF3 was attained, obviating the need for steam curing. The mix proportions of UHPC are shown in Table 3. Among them, the steel fiber in UHPC is 11 mm in length and 0.18 mm in diameter. It has a tensile strength of 2,870 MPa and a modulus of elasticity

TABLE 1 Impact parameters of the test beams.

Specimen number	Strengthening material	Interface treatment	Strengthening thickness
B	-	-	-
5UB-Ch	UHPC	Chiseling	5 cm
5UB-Pr	UHPC	Planting rebars	5 cm
5UB-Ch + Pr	UHPC	Chiseling + planting rebars	5 cm

10.3389/fmats.2024.1361647

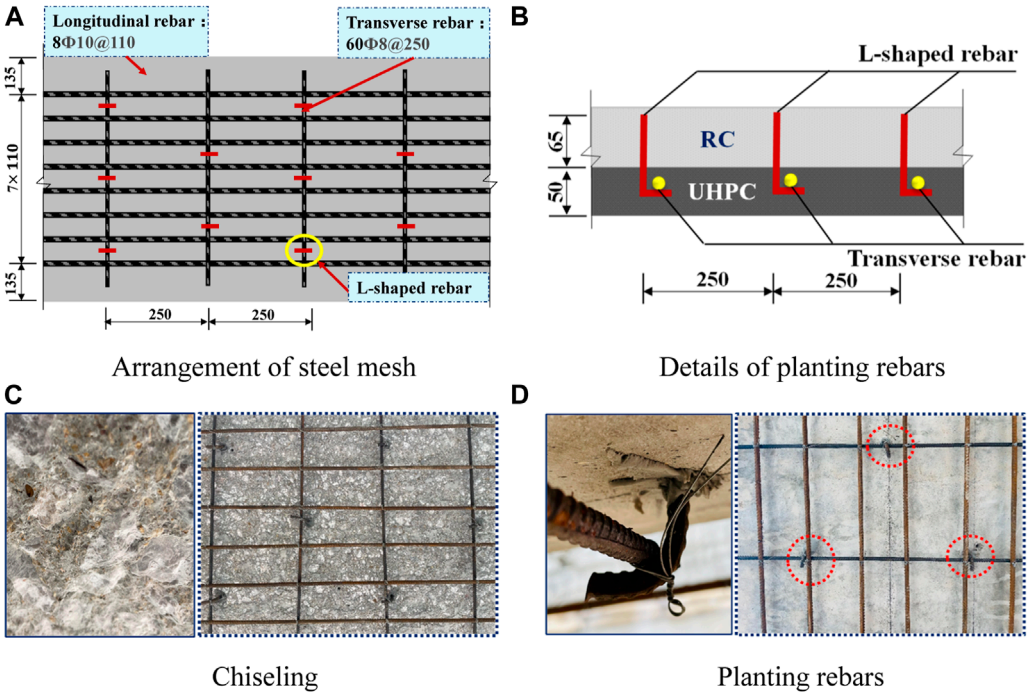

FIGURE 2
Details of steel mesh, planting rebars and interface treatment in test beams (units: mm).

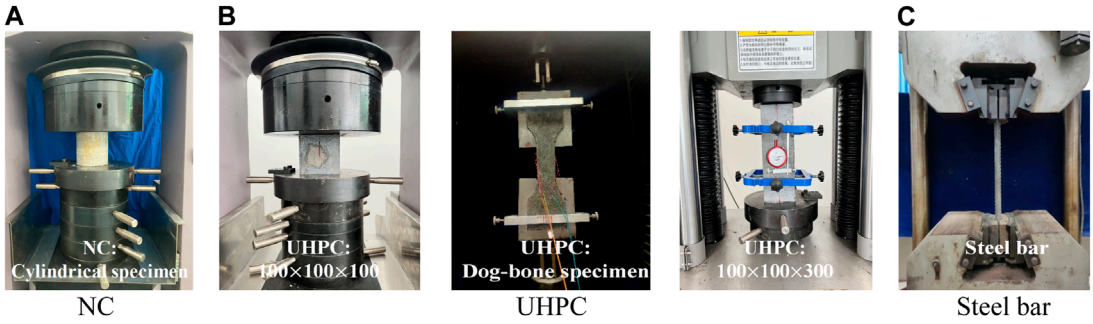

FIGURE 3
Mechanical properties test.

TABLE 2 Measured values of concrete material properties.

Material type	Cubic compressive strength (MPa)	Axial compressive strength (MPa)	Modulus of elasticity (MPa)
Hollow Slab Concrete (C30)	66.8	53.4	3.5×10^4

of 200 GPa. The mechanical properties of UHPC were determined according to the " *Reactive powder concrete*" (GB/T 31387–2015), standard. During the pouring of the UHPC strengthening layer, the compressive strength was obtained by six cubic specimens with dimensions of 100 × 100 × 100 mm for UHPC (Figure 3B). Six prism specimens with dimensions of 100 × 100 × 300 mm for UHPC was fabricated to obtain the axial compressive strength elastic modulus. Meanwhile, six dog-bone-shaped UHPC specimens were reserved for testing its tensile strength. The measured mechanical properties of UHPC are shown in Table 4.

TABLE 3 Mix proportions of UHPC.

Constituents	Amount (kg/m^3)
Cement	1,000
Silica fume	100
Fly ash	300
Basalt sand	1,100
Water	240
Superplasticizer	20
Steel fiber	170

2.3.3 Rebar

After the concrete in RC hollow slab beam cracked, the concrete quit working. At this point the tensile force in the cracked region of the RC hollow slab beam was mainly carried by the steel rebars. Therefore, the analysis of the structural performance of the flexural zone after cracking was closely related to the constitutive relationship of the steel rebars. Two types of steel rebars were used for RC hollow slab beams, namely, HRB300 and HRB335. After the four-point bending test and concrete specimen sampling were completed, the concrete in the bottom slab of the unstrengthened hollow slab beams was chiseled away. Taking into account the structural load characteristics, steel corrosion conditions and concrete cover conditions, steel specimens were selectively extracted from the least stressed locations at the ends of the beams for tensile testing.

The HRB400 hot-rolled ribbed steel rebars was used for UHPC strengthening layer of the test beams. The interface planting rebars were 8 mm in diameter. The transverse and longitudinal rebars in UHPC layer steel mesh were 8 mm and 10 mm in diameter, respectively. The mechanical properties of the steel rebars were tested in accordance with the standard " *Metallic materials - Tensile testing - Part 1: Method of test at room temperature*" (GB/T 228.1–2010). The mechanical performance indicators of the rebars are presented in Table 5.

2.4 UHPC strengthening

The entire fabrication process of the test beams is depicted in detail as shown in Figure 4. Firstly, as shown in Figure 4A, the test beam bottom plate was carefully levelled and dusted to ensure that the UHPC and RC interfaces were tighter and better bonded together. This was extremely important step, as a tight interfacial bond would substantially increase the durability and bearing capacity of the test beams. Subsequently, holes were drilled to locate the strengthened areas according to the predefined strengthening design scheme, as shown in Figures 4B, C. Next, the interface was treated as in Figure 4D, including chiseling, planting rebars, and a combination of chiseling and planting rebars. In this way, the bond between UHPC and RC was enhanced to further improve the strength and stability of the test beams.

After the above steps were completed, the erection of the steel mesh for the strengthening layer was installed as a means of providing additional support. Formwork was then installed to determine the thickness of the strengthening layer, as shown in Figures 4E, F. Finally, the pouring of the UHPC was carried out and the process and results are shown in Figures 4G, H. After the UHPC-RC combination test beams have been naturally maintained for a period of time, the four-point bending test can be carried out.

2.5 Loading and measurement

2.5.1 Loading scheme

The specific details of the experimental loading setup are illustrated in Figure 5. The experimental loading system primarily consists of anchor piles, a loading crossbeam, and hydraulic jacks, among other components. To facilitate the deformation measurement of the test beam, and adequately consider the space of the experimental equipment, concrete bearing platforms were designed at both ends of the beam. Rubber supports were placed between the top of the platform and the bottom of the test beam to simulate the effect of simple beam support.

The test beam was subjected to four-point bending loading, with two hydraulic jacks synchronized for incremental loading. To verify the proper functioning of the relevant measuring instruments

TABLE 4 Mechanical properties of UHPC.

Material type	Cubic compressive strength (MPa)	Tensile strength (MPa)	Modulus of elasticity (MPa)
UHPC	142.5	7.0	4.2×10^4

TABLE 5 Mechanical property indicators of steel rebar.

Material		Diameter/mm	Yield strength/MPa	Modulus of elasticity/MPa
Steel rebar	HRB300	14	335	2.0×10^4
	HRB335	25	376	2.1×10^5
	HRB400	8	435	2.2×10^4
	HRB400	10	437	2.2×10^4

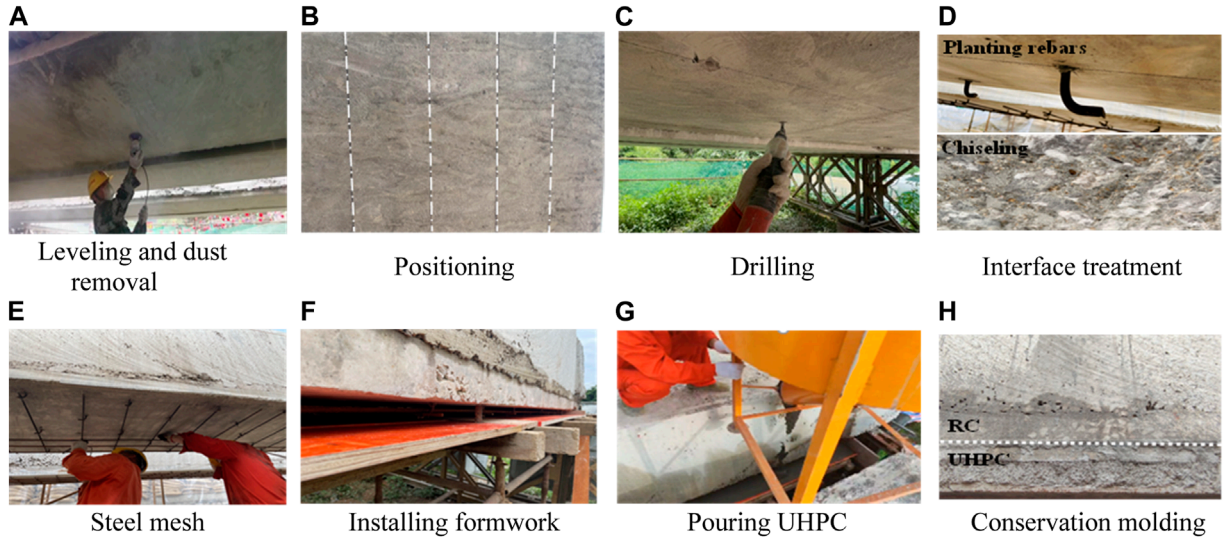

FIGURE 4
Fabrication process of UHPC-RC test beams.

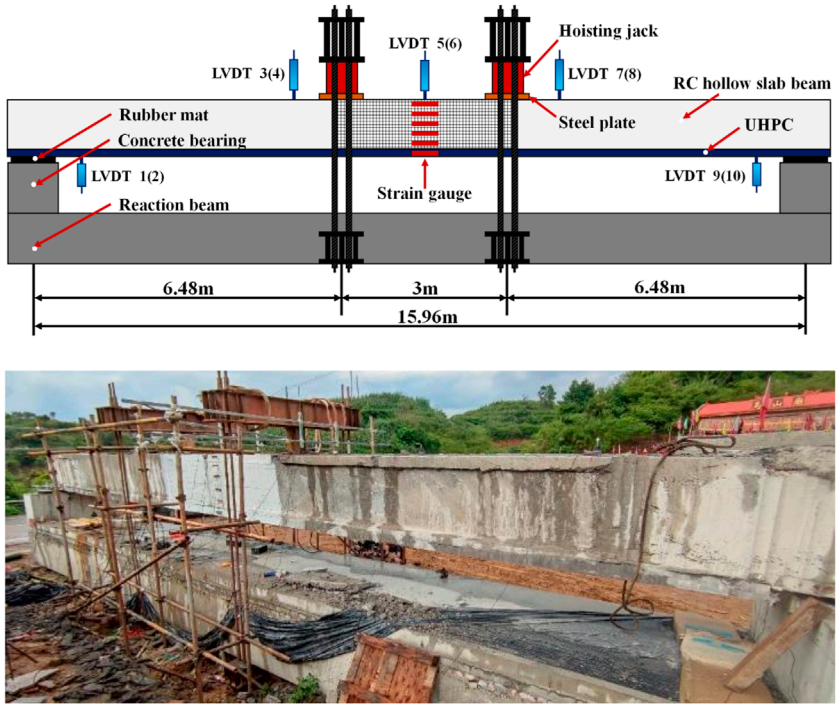

FIGURE 5
Loading device and measurement point arrangement.

and ensure good contact between different parts of the specimen, the test beam was initially subjected to preloading. Additionally, to ensure that the test beam experienced elastic loading, preventing cracking and any form of residual loading, the preloading load was approximately 20% of the ultimate load (Pu). After completing the preloading and unloading, formal loading of the test beam commenced. The formal loading was divided into two stages: i) The first stage involved force loading, with an approximate load increment of 40 kN for each level. Each level was held for 5 min to observe and record the test behavior. Loading proceeded to the next level once the readings stabilized. ii) The second stage was displacement loading, which was employed when the

specimen exhibited significant cracks or reached approximately 60%Pu. Loading was discontinued if the concrete in the compression zone of the test beam fractured, crushed, or if debonding occurred at the interface between UHPC and RC.

2.5.2 Measurement point arrangement

The arrangement of measurement points on the test beam is shown in Figure 5. i) Deflection measurements: A total of 10 linear variable differential transformers (LVDTs) were installed, located at the mid-span, at the loading point, and at the section corresponding to the beam end supports. The LVDTs were placed in a symmetrical manner along the span direction. Among these, LVDT displacement sensors with a 50 cm range were used for measurements at the mid-span and the two loading points, while LVDT displacement sensors with a 5 cm range were employed at the support points. ii) Strain measurements: In the vertical direction of the beam, 5 strain measurement points were evenly distributed along the height at the mid-span section of the precast RC hollow slab beam. Additionally, one strain measurement point was positioned at the center of the UHPC strengthening layer, resulting in a total of 6 strain measurement points. During the entire loading process, data from strain gauges and displacement sensors were recorded automatically. Simultaneously, the complete failure process of the specimen was documented using a camera.

To precisely measure crack width, crack distribution and strain conditions during the loading process, the concrete hinge joints on the side of the hollow slab beam were initially removed by chiseling. Subsequently, the pure bending segment (3 m) of the test beams was coated with white paint, a 10 cm × 10 cm grid was drawn. The crack observation instrument and marker pen were used to meticulously measure and record the positions, widths, and heights of cracks for each load level step.

3 Experimental phenomena

3.1 Unstrengthened beam B

The failure mode and crack distribution of the unstrengthened beam B) are illustrated in Figure 6. When loaded to 80 kN, microcracks appeared on the bottom surface of the mid-span section, with a crack width of 0.143 mm. Upon reaching 160 kN, multiple microcracks developed on the bottom surface, and microcracks at the mid-span section extended horizontally across the bottom plate. At this point, the maximum crack width on the bottom plate reached 0.211 mm, indicating the beam had reached its serviceability limit state. As the load increased to 240 kN, the bottom plate cracks gradually propagated upward along the web, with the maximum bottom plate crack width reaching 0.374 mm and the web's maximum crack width reaching 0.407 mm. With further load increments, the web cracks continued to propagate upward, both in width and in quantity. When the load reached 400 kN, the maximum crack width reached 1.073 mm. As the load increased to 560 kN, the primary crack at the bottom plate mid-span rapidly expanded and extended diagonally towards the web, forming multiple diagonal cracks with a maximum width of 1.886 mm. Upon reaching the yield load of 620 kN, the web cracks branched out in a dendritic pattern, gradually extending to the top plate of the test beam. The load increase slowed down, and at this point, the maximum crack width reached 2.13 mm. When the load reached the ultimate load of 680 kN, concrete spalling occurred at the

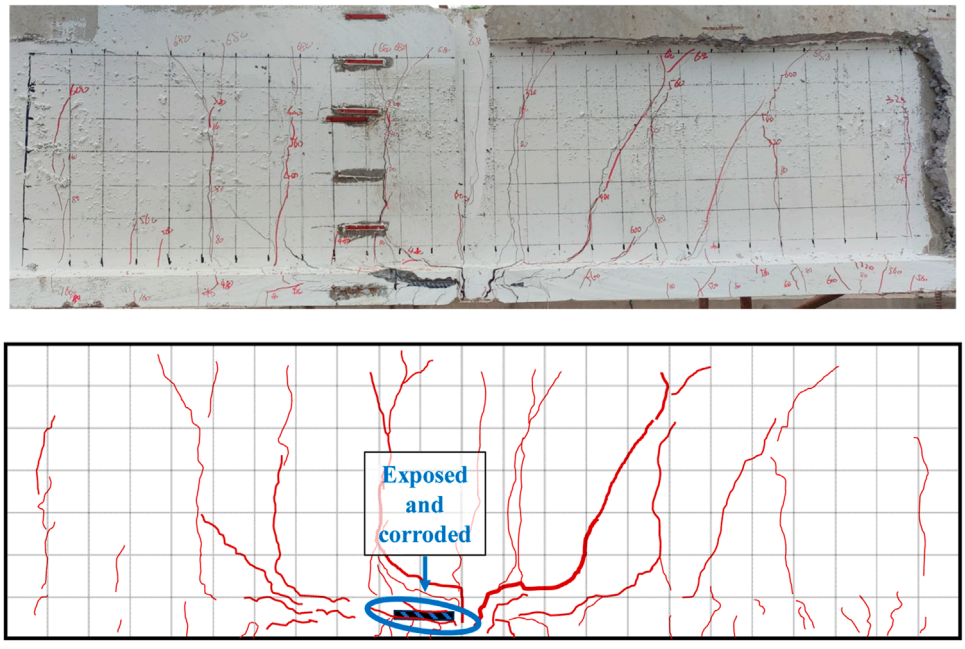

FIGURE 6
The failure mode of B beam.

mid-span of the bottom plate, exposing the reinforcement, and the test beam lost its load-bearing capacity. The compressed zone concrete remained uncracked.

3.2 Strengthening beam (5UB-Ch)

Compared to the B beam, the bottom plate of the 5UB-Ch beam was strengthened using 5 cm of UHPC, with chiseling treatment applied at the interface. After strengthening with UHPC, the flexural stiffness of the hollow slab beam increased. When loaded to 200 kN, a crack of 0.069 mm was found in the bottom plate of the mid-span section. When the load reached 240 kN, multiple micro-cracks appeared in the bottom plate and UHPC layer, with the maximum crack width being 0.167 mm. At the load of 480 kN, the cracks in the bottom plate extended to the web. The maximum crack widths in the bottom plate and UHPC layer were 0.194 mm, whereas, in the web, it measured up to 0.209 mm. At this point, the 5UB-Ch beam had reached its serviceability limit state.

As the load continued to increase, several vertical cracks appeared on the web, gradually extending to the top plate. The number and width of the cracks in the bottom plate increased, while evenly distributed micro-cracks developed in the UHPC layer. When the load reached the yield load of 720 kN, the maximum crack widths in the web and the bottom plate were 1.528 mm and 0.306 mm, respectively. Upon loading to 800 kN, the crack width in the bottom plate's mid-span section dramatically increased and quickly evolved into two main cracks, with the maximum crack width becoming 2.185 mm. When the load reached 840 kN, the structure lost its load-bearing capacity. No delamination was observed at the UHPC layer and RC interface. The failure mode and crack distribution of the 5UB-Ch beam are shown in Figure 7.

3.3 Strengthening beam (5UB-Pr)

The failure mode and crack distribution of the 5UB-Pr beam are shown in Figure 8. The 5UB-Pr beams had the same strengthening parameters as the 5UB-Ch beams, except that the interface treatment was planting rebars. Upon loading to 240 kN, three micro-cracks were observed in the bottom plate with a maximum crack width of 0.097 mm. When the load was increased to 320 kN, the number of cracks in the bottom plate grew and gradually extended to the web. Also some cracks were observed in the UHPC layer with a maximum crack width of 0.167 mm. At a load of 480 kN, the 5UB-Pr beam reached its serviceability limit state, with the maximum crack width of 0.203 mm.

As the load continued to increase, numerous evenly distributed minute cracks appeared in the UHPC layer, and several vertical cracks formed on the web and extended towards the top plate. When the load reached the yield load of 760 kN, the vertical cracks in the web developed in a tree-branch manner, extending upwards to the top of the test beam, with a maximum crack width of 0.986 mm. When the load reached 920 kN, the tension reinforcement of the 5UB-Pr beam yielded, and the structure lost its load-bearing capacity. However, the UHPC layer remained well-adhered to the RC beam, with no signs of separation.

3.4 Strengthening beam (5UB-Ch + Pr)

Figure 9 illustrates the failure mode of the 5UB-Ch + Pr beam under bending load. In the initial stage of loading, no cracks were visible on the surface of the test beam. Upon loading to 240 kN, three minor cracks appeared at the base of the hollow slab beam, with a maximum crack width of 0.083 mm. When the load reached

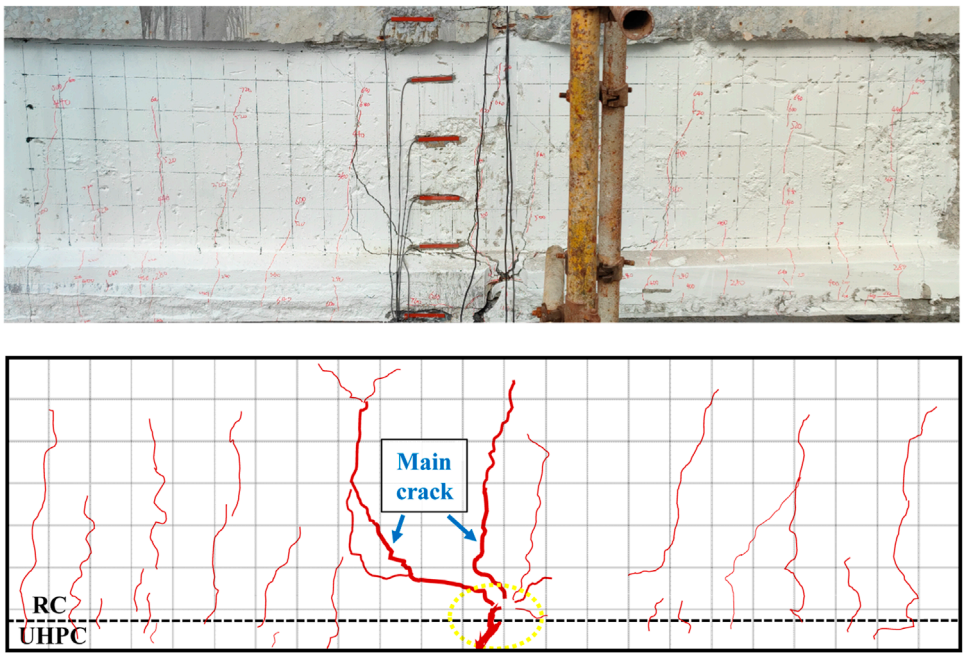

FIGURE 7
The failure mode of 5UB-Ch beam.

10.3389/fmats.2024.1361647

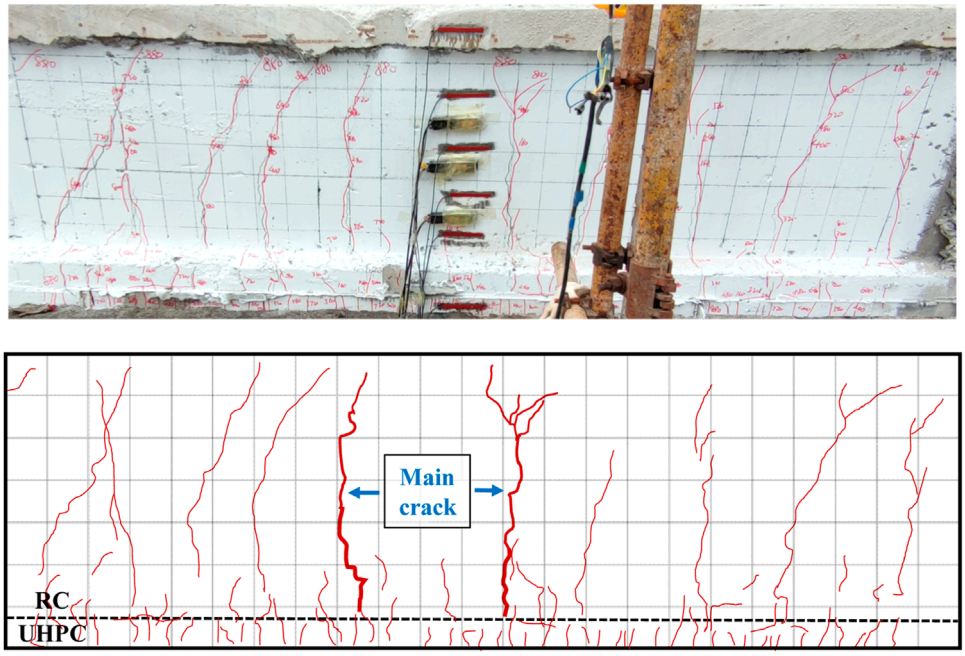

FIGURE 8
The failure mode of 5UB-Pr beam.

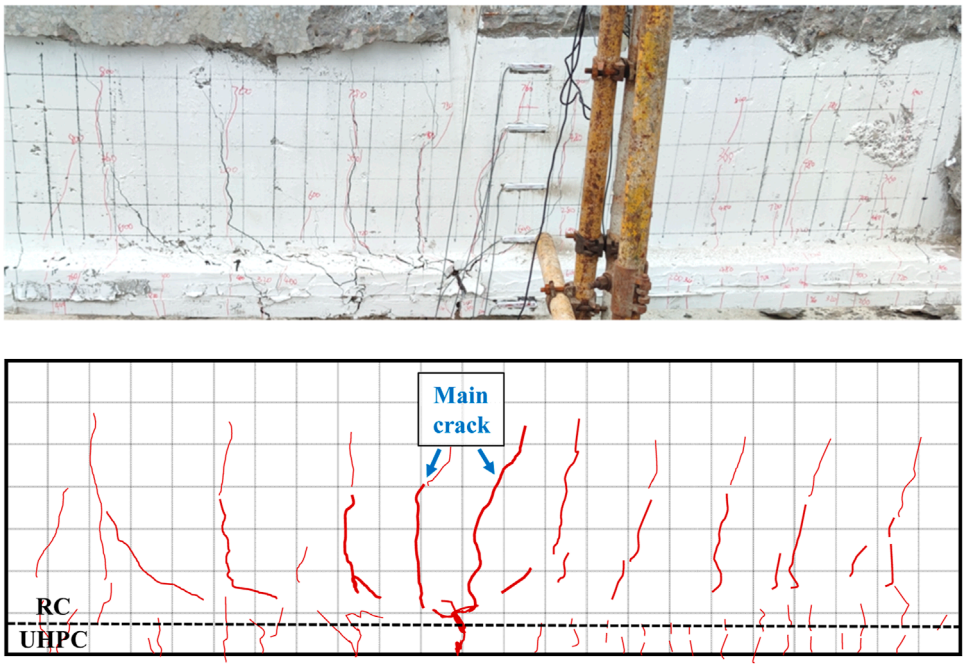

FIGURE 9
The failure mode of 5UB-Ch + Pr beam.

360 kN, the micro-cracks in the bottom plate of the hollow slab beam gradually extended upwards, and a few minor cracks emerged in the UHPC layer. At this point, the maximum crack widths were 0.111 mm in the web, 0.162 mm in the bottom plate. Upon loading to 600 kN, the cracks in the web continued to extend upwards, with maximum crack widths of 0.218 mm in the bottom plate, 0.181 mm in the web, and 0.132 mm in the UHPC layer. The 5UB-Ch + Pr test beam had reached its serviceability limit state.

10.3389/fmats.2024.1361647

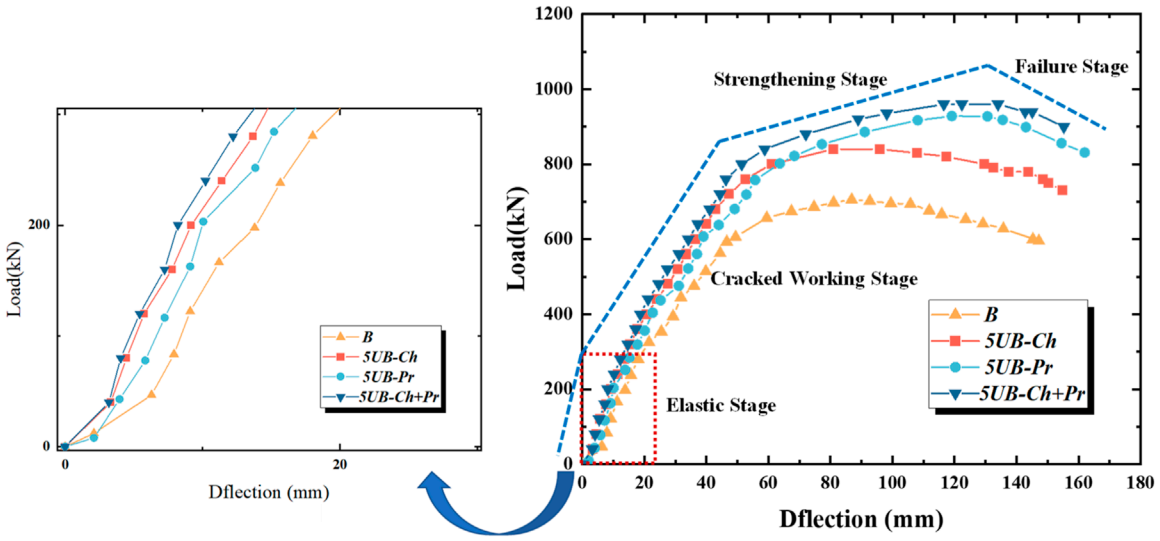

FIGURE 10
Load-displacement curves for mid-span sections.

As the load continued to increase, several vertical cracks developed on the web and extended gradually towards the top of the test beam in a tree-branch pattern. The number and width of the cracks in the bottom plate increased, while numerous evenly distributed micro-cracks appeared in the UHPC layer. Upon reaching the yield load of 820 kN, the maximum crack width was 0.958 mm for the web and 1.106 mm for the bottom plate, and the web cracks had developed to the top of the hollow slab beam. When the load reached 940 kN, the structure lost its load-bearing capacity. At this point, the UHPC layer was well-adhered to the bottom plate of the RC beam, with no signs of delamination detected.

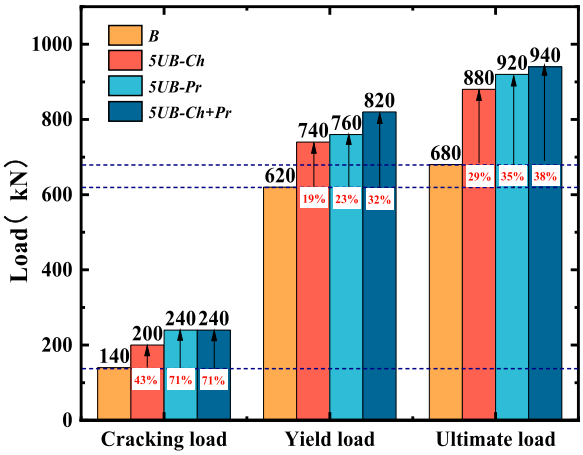

FIGURE 11
Bearing capacity index of test beams with different interface treatments.

4 Results and discussion

4.1 Load-displacement curves

The actual mid-span deflection of the test beam before and after strengthening was calculated based on the mid-span vertical displacement and support settlement. The load-deflection curve for the mid-span section of the unstrengthened beam and UHPC strengthened beams are shown in Figure 10. From Figure 10, it was evident that the failure process of the test beam under four-point bending was divided into four stages: i) Elastic stage: Initially, the behavior of the test beam was similar to that of a homogeneous elastic body. The mid-span deflection increased linearly with the increasing load. The load was shared by the tensioned concrete, tensioned steel rebar, and the UHPC strengthening layer. ii) Cracked working stage: After a decrease in the slope of the load-displacement curve, it stabilized. During this stage, cracks appeared on the bottom plate of the test beam and the UHPC strengthening layer. Some of the concrete in the tension zone stopped working and the stiffness of the member was decreased. The load was mainly supported by the tensioned steel rebar and the UHPC strengthening layer until the steel rebar yielded. iii) Strengthening stage: The load-displacement curve exhibited a nonlinear behavior, with the curvature accelerating with increasing deflection. As the tensioned steel rebar yielded, the load was primarily supported by the strengthening material UHPC and the steel mesh within the strengthening layer. iv) Failure stage: The UHPC layer strengthening failed and the stiffness of the test beams decreased significantly. The member lost its load-bearing capacity, and the load decreases as the deflection increased. The points of transition between these four stages (curve inflection points) are the cracking load (P_{cr}), yield load (P_y), and ultimate load (P_u) of the test beam.

10.3389/fmats.2024.1361647

TABLE 6 The magnitude of improvement in load capacity with different interface treatments.

Interface treatment	Cracking load (%)	Yield load (%)	Ultimate load (%)
Chiseling	43	19	29
Planting rebars	71	23	35
Chiseling + planting rebars	71	32	38

Throughout the loading process, the mid-span deflection of all four beams increased in response to the increasing load. It was evident that under equivalent load levels, significantly reduced mid-span deflection was exhibited by the UHPC-strengthened beam compared to the unstrengthened beam B). The effectiveness of UHPC strengthening in controlling the mid-span deflection of hollow slab beams has been confirmed by this observation.

4.2 Load capacity analysis

Due to the existence of pre-existing cracks in the in-service hollow slab beams, their cracking behavior is characterized by the appearance of new cracks and the extension of existing ones. Figure 11 displays various load-bearing indicators of the test beams, revealing different effects on the load-bearing capacity of the beams under various interface treatment methods. Compared with the unstrengthened beam, the performance of UHPC-strengthened beams was noticeable improved. These improvements in three different stages of loading were observed: cracking load, yield load, and ultimate load. The cracking load of UHPC-strengthened beams increased by 43%–71% as compared to the unstrengthened beam. Similarly, the yield load increased by 19%–32%, and the ultimate load increased by 29%–38%. Comparing and analyzing the load-bearing indicators of the four test beams, the interface treatment method has the most significant effect on the enhancement of the cracking resistance of the UHPC-strengthened beams. The enhancement occurred primarily due to two factors. The first factor was that larger moments of inertia were obtained by increasing the cross-section height. The second factor was that the strengthened beams were subjected to greater tensile stresses before cracking due to the high tensile strength of the UHPC. This phenomenon demonstrated the strengthening and toughening effect of UHPC.

The load-bearing capacity of 5UB-Ch + Pr beam was significantly increased as compared to 5UB-Ch and 5UB-Pr beams. The cracking load, yield load and ultimate load of 5UB-Ch + Pr beam were increased by 71%, 32% and 38%, respectively, compared to B beam. The formation of frictional interlocking at the UHPC-RC interface was facilitated by chiseling treatment, thereby enhancing the bond strength. Planting rebars provides an effective "bridging effect" for the interface through dowel action and drawing action. When there are small cracks in the material, the fibers act as a bridge, connecting the two sides of the crack, thus preventing the crack from progressing. Additionally, when the bottom of the test beam (in the tensile zone) was strengthened with UHPC, the concrete substrate was placed in the compressive zone. The full potential of the tensile strength of UHPC and the compressive strength of concrete can be utilized with this flexural load. It helps to seal existing cracks at the bottom of the concrete, increasing the durability of the beams. The magnitude of improvement in load capacity by UHPC strengthening with different interface treatments was compared in Table 6.

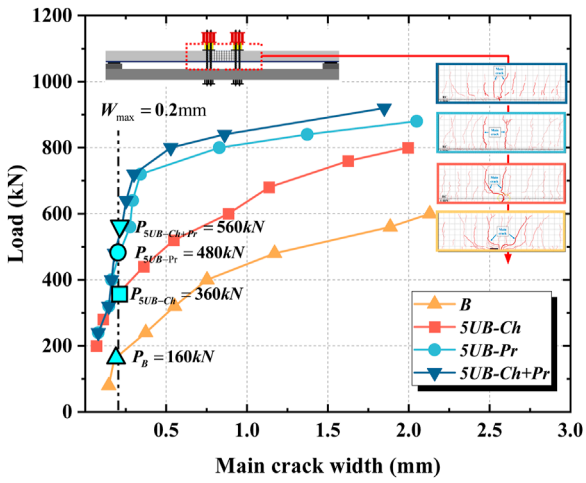

FIGURE 12
Test beam load-maximum crack width curve.

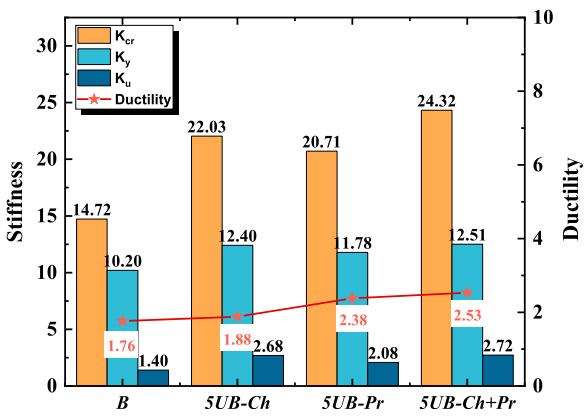

FIGURE 13
Stiffness and ductility coefficients of test beams with different interface treatments.

TABLE 7 The magnitude of improvement in stiffness and ductility with different interface treatments.

Interface treatment	Stiffness at pre-cracking stage (%)	Stiffness at pre-failure stage (%)	Structural ductility (%)
Chiseling	49	91	8
Planting rebars	41	49	35
Chiseling + planting rebars	65	94	44

4.3 Crack width analysis

Figure 12 presents the variation curve of the main crack width of the test beams under four-point bending. According to the "*Specifications for Design of Highway Reinforced Concrete and Prestressed Concrete Bridges and Culverts*" (JTG 3362–2018), the maximum allowable crack width for RC structures is limited to 0.2 mm. Under this crack width limitation, the load-bearing capacity of the unstrengthened beam was 160 kN. For the 5UB-Ch beam with chiseling treatment, the load capacity was 360 kN, which was increased 1.25 times in load-bearing capacity. The 5UB-Pr beam with interface treatment of planting rebars had a load of 480 kN, which was increased 2 times in load carrying capacity. The 5UB-Ch + Pr beam with interface treatment of planting rebars had a load of 560 kN, which was increased 2.5 times. Results showed that in case of smaller crack width, higher load-bearing capacity of UHPC strengthened beams was obtained as compared to unstrengthened beams. Additionally, at the same applied load, the crack widths of 5UB-Pr and 5UB-Ch + Pr beams were reduced compared to 5UB-Ch beam. The change in crack width became more evident as the load value increased. In comparison to 5UB-Ro beam, crack suppression was found to be more significant in 5UB-Pr and 5UB-Ro + Pr beams.

4.4 Stiffness and ductility analysis

In this study, the flexural stiffness of the test beams is defined by the slopes of the curves in three loading stages: the pre-cracking stage stiffness (K_{cr}), the pre-yield stage stiffness (K_y), and the pre-failure stage stiffness (K_u). Additionally, the displacement ductility coefficient is employed to assess the ductility performance of the test beams. This coefficient represents the ratio of the vertical displacement at the midspan under the yield load to the vertical displacement at the midspan under the ultimate load.

Figure 13 presents the stiffness and ductility coefficients of the test beams at different loading stages. It can be observed that the stiffness was highest in the pre-cracking stage. Compared to the B beam, the stiffness of the 5UB-Ch beam, 5UB-Pr beam, and 5UB-Ch + Pr beam increased by 50%, 41%, and 65%, respectively, in this stage. However, UHPC contributes significantly to the stiffness improvement of hollow slab beam in the failure stage. The stiffness of 5UB-Ch beam, 5UB-Pr beam, and 5UB-Ch + Pr beam increased by 91%, 49%, and 94%, respectively, compared to the B beam. The interface treatment methods have minimal impact on the stiffness of the test beams in the pre-yield stage. Additionally, using UHPC for strengthening significantly improved the ductility of the test beams. The ductility coefficients of 5UB-Ch beam, 5UB-Pr beam, and 5UB-Ch + Pr beam increased by 8%, 36%, and 44%, respectively, compared to the unstrengthened beam.

In addition, the stiffness of the 5UB-Ch beam is 6.4%, 5.2%, and 28.8% higher than that of the 5UB-Pr beam in the respective stages. However, the ductility index of the 5UB-Ch beam is lower than that of the 5UB-Pr beam. These results indicate that chiseling is more favorable for enhancing structural stiffness, while planting rebars is more advantageous for improving structural ductility. The effect of UHPC strengthening on stiffness and ductility with different interface treatments was compared in Table 7.

5 Conclusion

The following conclusions can be drawn from this research:

- The failure mode of the unstrengthened beam was characterized by concrete spalling in the tension zone and exposed of steel rebars. In contrast, the UHPC-strengthened beam exhibited a flexural failure mode. Throughout the loading process, the interface between the UHPC and the bottom plate of the RC hollow slab beam was well bonded and no peeling occurred. Uniformly distributed, dense and subtle cracks appeared in the UHPC strengthened layer. Vertical cracks with dendritic development extending to the top slab appeared in the web, and the crack width of the web cracks was larger than the cracks in the UHPC layer.
- Under different interface treatment methods, UHPC-RC beams exhibited various degrees of improvement in flexural load-carrying capacity. Compared to the unstrengthened beam, the cracking load of 5UB-Ch beam increased by 43%, 5UB-Pr beam by 71%, and 5UB-Ch + Pr beam by 71%. The yield load increased by 19% for 5UB-Ch, 23% for 5UB-Pr, and 32% for 5UB-Ch + Pr. The ultimate load increased by 29% for 5UB-Ch, 35% for 5UB-Pr, and 38% for 5UB-Ch + Pr.
- The concrete substrate was in the compression zone when UHPC was used to strengthen the service hollow slab beams in the tensile zone. This gave full potential to the super strong tensile strength of the UHPC and the compressive strength of the concrete, resulting in good crack control.
- The interface bond strength between the UHPC layer and the RC layer was strengthened by using three interfacial treatments: chiseling, planting rebars, and a combination of the two. Crack development in the test beams was effectively inhibited by a combination of chiseling and planting rebars. This measure allowed the interface to have an effective

"bridging effect", providing the structure with a higher bearing capacity reserve.

- Compared to the unstrengthened beams, the stiffness of UHPC-RC beams increased by 41%–65% and 49%–94% in the pre-cracking and pre-failure stages, respectively. During the pre-failure stage, UHPC played a significant role in increasing the stiffness, whereas a slight decrease in stiffness is observed during the pre-yield stage. At the same time, after UHPC strengthening, the structural ductility increased by 8%–44%.

To comprehensively assess the performance of structural strengthening, it is necessary to conduct further experimental and numerical analyses beyond the variables studied thus far. These additional analyses will explore the impact of critical parameters such as surface roughness, the depth of planting rebar, and the thickness of strengthening layers. Furthermore, environmental factors that can erode or age the strengthening must be taken into account. This requires in-depth scientific research to investigate these durability factors, ultimately ensuring the enduring effectiveness of the strengthening.

Data availability statement

The original contributions presented in the study are included in the article/Supplementary material, further inquiries can be directed to the corresponding author.

Author contributions

JS: Investigation, Writing–original draft. BL: Writing–review and editing. LK: Supervision, Writing–original draft. DQ: Investigation, Writing–original draft. CZ: Investigation, Writing–original draft. YK: Data curation, Writing–original draft. AS: Investigation, Writing–original draft.

Funding

The author(s) declare financial support was received for the research, authorship, and/or publication of this article. The authors highly appreciate the financial support from the Science and Technology Plan Projects of Chongzuo, China (Grant No. 2022ZC1206 and 2022ZC1217).

Conflict of interest

Authors JS and BL were employed by Guangxi Transportation Science and Technology Group Co., Ltd. Author CZ was employed by ChongQing Municipal Design and Research Institute Co., Ltd. Author AS was employed by ChongQing City Transportation Development & Investment Group Co., Ltd.

The remaining authors declare that the research was conducted in the absence of any commercial or financial relationships that could be construed as a potential conflict of interest.

Publisher's note

References

Amran, M., Huang, S. S., Onaizi, A. M., Makul, N., Abdelgader, H. S., and Ozbakkaloglu, T. (2022). Recent trends in ultra-high performance concrete (UHPC): current status, challenges, and future prospects. *Constr. Build. Mater.* 352, 129029. doi:10.1016/j.conbuildmat.2022.129029

Ciampa, E., Ceroni, F., De Angelis, A., and Pecce, M. R. (2023). Bond tests on concrete elements externally bonded with steel plates and assessment of bond strength models. *Eng. Struct.* 296, 116835. doi:10.1016/j.engstruct.2023.116835

Du, J., Meng, W., Khayat, K. H., Bao, Y., Guo, P., Lyu, Z., et al. (2021). New development of ultra-high-performance concrete (UHPC). *Compos. Part B Eng.* 224, 109220. doi:10.1016/j.compositesb.2021.109220

Feng, S., Xiao, H., and Li, H. (2020). Comparative studies of the effect of ultrahigh-performance concrete and normal concrete as repair materials on interfacial bond properties and microstructure. *Eng. Struct.* 222, 111122. doi:10.1016/j.engstruct.2020.111122

Hou, L., Zhou, B., Guo, S., Aslani, F., and Chen, D. (2019). Corrosion behavior and flexural performance of reinforced concrete/ultrahigh toughness cementitious composite (RC/UHTCC) beams under sustained loading and shrinkage cracking. *Constr. Build. Mater.* 198, 278–287. doi:10.1016/j.conbuildmat.2018.11.237

Huang, Y., Grünewald, S., Schlangen, E., and Luković, M. (2022). Strengthening of concrete structures with ultra high performance fiber reinforced concrete (UHPFRC): a critical review. *Constr. Build. Mater.* 336, 127398. doi:10.1016/j.conbuildmat.2022.127398

Leng, J., Yang, J., Zhang, Z., Zou, Y., Chen, J., and Zhou, J. (2023). Experimental and numerical investigations on force transfer mechanism of steel-concrete joint in hybrid girder bridges. *Structures* 54, 153–170. doi:10.1016/j.istruc.2023.04.104

Li, J., Wu, Z., Shi, C., Yuan, Q., and Zhang, Z. (2020). Durability of ultra-high performance concrete – a review. *Constr. Build. Mater.* 255, 119296. doi:10.1016/j.conbuildmat.2020.119296

Li, S., Zhang, L., Guo, P., Zhang, P., Wang, C., Sun, W., et al. (2021). Characteristic analysis of acoustic emission monitoring parameters for crack propagation in UHPC-NC composite beam under bending test. *Constr. Build. Mater.* 278, 122401. doi:10.1016/j.conbuildmat.2021.122401

Li, X., Wu, G., Shafiq Popal, M., and Jiang, J. (2018). Experimental and numerical study of hollow core slabs strengthened with mounted steel bars and prestressed steel wire ropes. *Constr. Build. Mater.* 188, 456–469. doi:10.1016/j.conbuildmat.2018.08.073

Prem, P. R., Murthy, A. R., and Verma, M. (2018). Theoretical modelling and acoustic emission monitoring of RC beams strengthened with UHPC. *Constr. Build. Mater.* 158, 670–682. doi:10.1016/j.conbuildmat.2017.10.063

Ren, J., Zhang, K., Xu, X., Xiao, Y., Ye, W., Deng, S., et al. (2023). Performance evolution of self-compacting concrete for ballastless track based on high-cycle fatigue damage constitutive model. *J. Cent. South Univ.* 30 (6), 2048–2063. doi:10.1007/s11771-023-5348-y

Tong, T., Yuan, S., Wang, J., and Liu, Z. (2021). The role of bond strength in structural behaviors of UHPC-NC composite beams: experimental investigation and finite element modeling. *Compos. Struct.* 255, 112914. doi:10.1016/j.compstruct.2020.112914

Xue, J., Briseghella, B., Huang, F., Nuti, C., Tabatabai, H., and Chen, B. (2020). Review of ultra-high performance concrete and its application in bridge engineering. *Constr. Build. Mater.* 260, 119844. doi:10.1016/j.conbuildmat.2020.119844

Xun, S., Shiping, Y., Yuhou, Y., Jian, F., and Litao, L. (2022). Comparative analysis of flexural performance of old full-scale hollow slab beams reinforced with

fiber composites. *Constr. Build. Mater.* 338, 127657. doi:10.1016/j.conbuildmat.2022.127657

Yang, J., Chen, R., Zhang, Z., Zou, Y., Zhou, J., and Xia, J. (2023). Experimental study on the ultimate bearing capacity of damaged RC arches strengthened with ultra-high performance concrete. *Eng. Struct.* 279, 115611. doi:10.1016/j.engstruct.2023.115611

Yang, J., Xia, J., Zhang, Z., Zou, Y., Wang, Z., and Zhou, J. (2022). Experimental and numerical investigations on the mechanical behavior of reinforced concrete arches strengthened with UHPC subjected to asymmetric load. *Structures* 39, 1158–1175. doi:10.1016/j.istruc.2022.03.087

Zhang, Y., Huang, S., Zhu, Y., Hussein, H. H., and Shao, X. (2022). Experimental validation of damaged reinforced concrete beam strengthened by pretensioned prestressed ultra-high-performance concrete layer. *Eng. Struct.* 260, 114251. doi:10.1016/j.engstruct.2022.114251

Zhang, Z., Jin, X., and Luo, W. (2019). Long-term behaviors of concrete under low-concentration sulfate attack subjected to natural variation of environmental climate conditions. *Cem. Concr. Res.* 116, 217–230. doi:10.1016/j.cemconres.2018.11.017

Zhang, Z., Pang, K., Xu, L., Zou, Y., Yang, J., and Wang, C. (2023). The bond properties between UHPC and stone under different interface treatment methods. *Constr. Build. Mater.* 365, 130092. doi:10.1016/j.conbuildmat.2022.130092

Zhou, G., Du, A., Wang, M., Fan, J., and Li, A. (2023). Performance degradation prediction of extra-wide concrete self-anchored suspension bridge under vehicle load considering time-dependent effects. *J. Cent. South Univ.* 30 (6), 1932–1947. doi:10.1007/s11771-023-5360-2

Zhu, Y., Zhang, Y., Hussein, H. H., and Chen, G. (2020). Flexural strengthening of reinforced concrete beams or slabs using ultra-high performance concrete (UHPC): a state of the art review. *Eng. Struct.* 205, 110035. doi:10.1016/j.engstruct.2019.110035

Zhu, Y., Zhang, Y., Li, X., and Chen, G. (2021). Finite element model to predict structural response of predamaged RC beams reinforced by toughness-improved UHPC under unloading status. *Eng. Struct.* 235, 112019. doi:10.1016/j.engstruct.2021.112019

Zou, Y., Jiang, J., Yang, J., Zhang, Z., and Guo, J. (2023a). Enhancing the toughness of bonding interface in steel-UHPC composite structure through fiber bridging. *Cem. Concr. Compos.* 137, 104947. doi:10.1016/j.cemconcomp.2023.104947

Zou, Y., Wu, C., Zhang, Z., Jiang, J., Yu, K., and Wang, X. (2023b). Investigation on flexural behavior of novel GFRP grid web-concrete hybrid beam. *Eng. Struct.* 278, 115489. doi:10.1016/j.engstruct.2022.115489

frontiers | Frontiers in Materials

TYPE Original Research
PUBLISHED 13 February 2024
DOI 10.3389/fmats.2024.1344760

OPEN ACCESS

EDITED BY
Zhongya Zhang,
Chongqing Jiaotong University, China

REVIEWED BY
Yundong Shou,
Wuhan University, China
Zhu Yunhua,
Qujing Normal University, China

*CORRESPONDENCE
Xin-Bao Gu,
✉ 15823405952@163.com

RECEIVED 26 November 2023
ACCEPTED 19 January 2024
PUBLISHED 13 February 2024

CITATION
Li W-W, Gu X-B, Yang C and Zhao C (2024), Level evaluation of concrete dam fractures based on game theory combination weighting-normal cloud model.
Front. Mater. 11:1344760.
doi: 10.3389/fmats.2024.1344760

Level evaluation of concrete dam fractures based on game theory combination weighting-normal cloud model

Wei-Wei Li[1], Xin-Bao Gu[1,2]*, Chao Yang[3] and Chao Zhao[3]

[1]School of Architecture, Nanyang Institute of Technology, Nanyang, China, [2]School of Civil Engineering, Nanyang Institute of Technology, Nanyang, China, [3]School of Civil Engineering, Sichuan University of Science and Engineering, Zigong, China

Hazard evaluation of concrete dam fractures is vital for safe operations. The width (S_1), length (S_2), and depth (S_3) of fractures are adopted as the assessment index, and the game theory combination weighting-normal cloud model is introduced. The normal cloud model of certain dam fractures is subsequently established. The weight coefficients of each index are calculated using game theory combination weighting, and the certainty degree of each index is determined using the cloud model. Finally, the hazard levels of the concrete dam fractures are judged. The proposed model solves the fuzziness and randomness of different indexes; the conclusions demonstrate that the model is feasible for the hazard assessment of concrete dam fractures, and its accuracy is very high; therefore, a new approach can be provided for future hazard-level assessments of concrete dam fractures.

KEYWORDS

level evaluation, concrete dam fracture, game theory, combination weighting method, normal cloud model

1 Introduction

Cracks are common in the operation of concrete dams, and their appearance has become a hidden danger to the safety of dam operations (Gu and Wu, 2019; Gu et al., 2021a). For timely action, the damage assessment of cracks investigates their influence on dam safety operations and engineering benefits. For example, the gravity arch dam in Longyangxia, China, has 35 cracks. Nine of the cracks are within the range of 10–30 m in length and 0.3–1.6 mm in surface width. These pose a safety hazard to the dam, so accurately assessing concrete dam fractures has great practical significance. As some uncertainties exist between the quantitative monitoring values and qualitative indicators, fracture evaluation is fuzzy and random (Gu et al., 2021b; Gu et al., 2021c). Therefore, accurately assessing concrete dam fractures has become a hot topic.

Many researchers have adopted methods to accurately assess the hazard grade of concrete dam fractures (Zhou et al., 2016; GuWu and Ma, 2022). For example, Zhang et al. considered the influence of cracks on the structure and durability of dams (ZHANG et al., 2022). The comprehensive evaluation of the entire serviceability of concrete dams was performed using evidence theory in conjunction with the displacement and stress conditions. Lu et al. (Lu et al., 2012) used variable fuzzy sets and extenics to verify damage from structural cracks in concrete dams. Zhang et al. (Zhang and Yang, 2018)

developed a cloud matter-element model for the fuzzy attribution of rank evaluation. The damage level of cracks is determined based on the maximum membership degree criterion. Feng et al. (Xue-hui, 2015) established the cloud-entropy weight model due to many factors, such as dam deformation and seepage. Zhou et al. (Zhou et al., 2008) analyzed the nature of the cloud model and discussed the comprehensive evaluation method for dam operational behaviors in conjunction with methods to determine the subjective, objective, and comprehensive weights of the evaluation indexes. Zhao et al. (Zhao and Liu, 2005) applied evidence theory to dam safety monitoring and proved the method's effectiveness. A dam surface crack detection algorithm based on adaptive region growth and local K-means clustering is proposed by Zou et al. (Zou et al., 2023); at present, CNN convolutional neural network method (Zhang et al., 2023) has also been applied in the field of concrete structure crack detection.

Although these methods promote the development of concrete dam fractures, they still require improvements (Gu et al., 2019; Gu et al., 2022a) due to complex calculation processes, low efficiency, etc. The game theory combination weighting method overcomes these insufficiencies by assessing the hazard grade of concrete dam fractures. The technique applies a game theory combination to determine the weights of each evaluation index. The normal cloud method then calculates the certainty and uncertainty degrees of each index. Finally, a fundamental synthetic matrix of a certain degree is constructed to determine the hazard level of concrete dam fractures.

The paper is organized as follows. Section 2 introduces the theory and methodology based on game theory combination weighting. Section 3 provides an engineering example of concrete dam fractures and analyzes the results. Section 4 draws conclusions.

2 Methodology

2.1 Combination weighting method

The standard weight calculation methods are divided into subjective, objective, and combination weights. Combination weighting is most common where two or three kinds of subjective and objective weights are combined to get the comprehensive weight. This process reduces errors caused by a single method (Klauer et al., 2012; Gu et al., 2022b). This study applies the entropy weight method and criteria importance through the inter-criteria correlation (CRITIC) method to calculate the index weights. The combination weights are obtained using game theory.

2.1.1 Entropy method

The entropy weight method is an objective approach to determining the weight coefficients based on the different degrees of information utility values for each evaluation index (Zhou et al., 2015; Chen and Zhou, 2019). This approach reflects the discreteness degree among index data. Its calculative process is given as follows:

① Construct the original matrix of the assessment index X

Assuming there are m evaluation indexes and n evaluation objects. Then, x_{ij} is the corresponding value of the ith assessment index at the jth assessment object. Its origin assessment matrix can be expressed as:

$$X = \left(x_{ij}\right)_{m\times n}(i = 1,2,...,m;j = 1,2,...,n) \tag{1}$$

② Normalization and forward processing

Various types of indicators and dimensional differences make it necessary to rule out the associated impacts, and dimensionless processing of each index is required. These are expressed as:

$$Y = \left(\mathrm{y}_{ij}\right)(i =)1,2,...,m,j = 1,2,....,n\Big) \tag{2}$$

The positive indicators are:

$$y_n = \frac{x_{ij} - \min\left(x_{ij}\right)}{\max\left(x_{ij}\right) - \min\left(x_{ij}\right)} \tag{3}$$

The negative indicators are:

$$y_n = \frac{\max\left(x_{ij}\right) - x_{ij}}{\max\left(x_{ij}\right) - \min\left(x_{ij}\right)} \tag{4}$$

where y_{ij} is the standard value of the ith assessment index at the jth assessment object.

③ Calculating information entropy of the ith assessment index (Gu and Wu, 2016)

$$h_i = \frac{1}{\ln n}\sum_{j=1}^{n} e_{ij}\ln e_{ij} \tag{5}$$

$$e_{ij} = \frac{y_{ij}}{\sum_{j=1}^{n} y_{ij}} \tag{6}$$

④ Calculation of weights $\omega_{1\mathrm{i}}$

$$\omega_{1\mathrm{i}} = \frac{1 - h_i}{m - \sum_{i=1}^{m} h_i} \tag{7}$$

where $0 < \omega_{i1i} \le 1, \sum_{i=1}^{m}\omega_{1i} = 1, i = 1,2,...,m.$

2.1.2 The CRITIC method

CRITIC is an objective weighting method proposed by Diakoulaki (ZHOU et al., 2017) that synthetically measures the index weight by calculating variability and conflicts of the index. Its calculative procedure is given as follows:

① There are m estimated objects and n assessment indexes assumed. These construct the matrix $A = \left(a_{ij}\right)_{m\times n}$, where $i = 1,2,...,m;j = 1,2,...,n$.

② The matrix A is standardized based on the Z-score method and is expressed as:

$$a_{ij}^{*} = \frac{a_{ij} - \overline{a}_j}{s_j}(i = 1,2,...,m;j = 1,2,...,b) \tag{8}$$

where $\overline{a}_j = \frac{1}{a}\sum_{i=1}^{m} a_{ij}$, $s_j = \sqrt{\frac{\sum_{i=1}^{m}\left(a_{ij} - \overline{a}_j\right)}{a-1}}$, and $\overline{a}_j$ and s_j are the mean value and standard deviation of the jth assessment index, respectively.

FIGURE 1
Location of the survey area.

FIGURE 2
Layout of the concrete dam.

TABLE 1 Information on the fractures.

Number	Dam block	State		
		S_1/mm	S_2/m	S_3/m
1	1#	0.175	8.7	1.2
2	2#	0.25	8	2.1
3	3#	0.15	4.4	0.5
4	4#	0.1	6	2.4
5	5#	0.15	11.5	0.6
6	6#	0.1	2	2.55
7	7#	0.2	3.2	1.52
8	8#	0.16	6.5	0.9
9	9#	0.25	7.1	1.2
10	10#	0.11	5.6	1.5

TABLE 2 Classification for fracture hazards.

Risk rank	I	II	III	IV
S_1/mm	[0 0.2]	[0.2 0.3]	[0.3 0.5]	[0.5 3]
S_2/m	[0 3]	[3 5]	[5 10]	[10 15]
S_3/m	[0 0.3]	[0.3 1]	Gu et al. (2022a)	[5 10]

③ Calculate the coefficient of variation for different indexes as:

$$BY_j = \frac{s_j}{a_j}(j = 1,2,...n) \tag{9}$$

where BY_j is the variation coefficient of the *jth* index.

④ The coefficients of the correlation are calculated based on the standardization matrix A^*. Their expressions are given as $X = (r_{kl})_{n\times n}(k = 1,2,...,n, l = 1,2,...,b)$, where r_{kl} are the coefficients of correlation between the *kth* and *lth* indexes, and:

$$r_{kl} = \frac{\sum_{i=1}^{m}(a_{ik} - \overline{a_k})(a_{il} - \overline{a_l})}{\sqrt{\sum_{i=1}^{m}(a_{ik} - \overline{a_k})^2}\sqrt{\sum_{l=1}^{m}(a_l - \overline{a_l})^2}}(r_{kl} = r_{lk}; k = 1,2,\cdots,m, l = 1,2,\cdots,m) \tag{10}$$

where a_{ik} and a_{il} are the standard value of measured values at the *kth* and *lth* indexes for the *ith* assessment object in the standardization matrix A^*, respectively. The $\overline{a_k}$ and $\overline{a_l}$ are the mean of the standard value of the measured values at the *kth* and *lth* indexes in the standardization matrix A^*, respectively.

⑤ Calculate the quantitative coefficient about the degree of independence for different assessment indexes. Its expression is (Zhao et al., 2021):

$$\eta_j = \sum_{k=1}^{n}\left(1 - \left|r_{kj}\right|\right)(j = 1,2,...,n) \tag{11}$$

⑥ Quantitative coefficients of the comprehensive information and the degree of independence of each index are solved as:

$$C_j = BY_j\sum_{k=1}^{n}\left(1 - r_{kj}\right)(j = 1,2,...,n) \tag{12}$$

⑦ Determination of the weight of each evaluation index can be expressed as:

$$\omega_j = \frac{C_j}{\sum_{j=1}^{n} C_j}(j = 1,2,...,n) \tag{13}$$

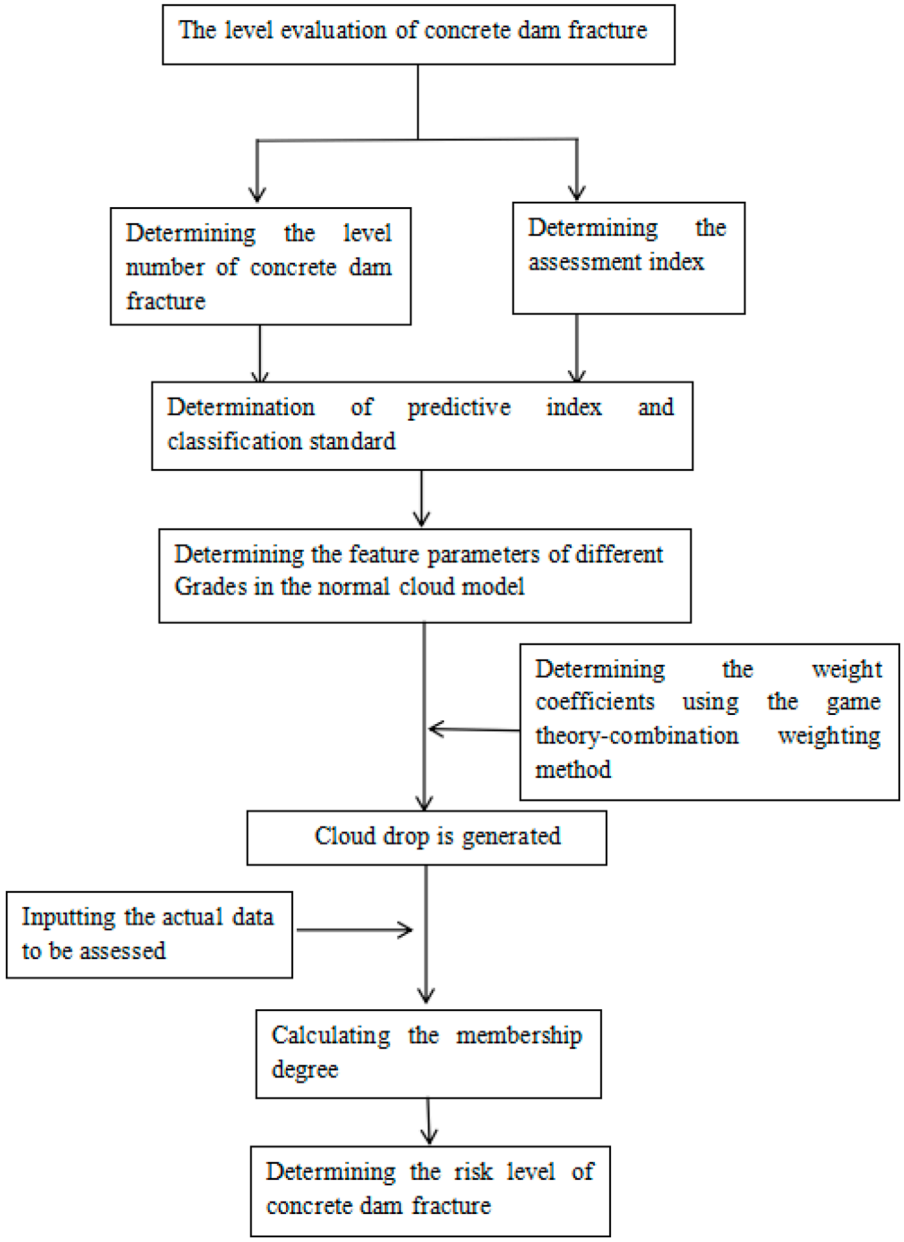

FIGURE 3
Flowchart of the assessment frame.

2.1.3 Combination weighting method of game theory

Based on game theory, the combination weight ω is obtained by combining the entropy weight and CRITIC methods. Its procedure is correlated as follows (B Zhang et al., 2018):

① The weight sets ω_1 and ω_2 are obtained by the entropy weight and CRITIC methods. It is assumed that a_1 and a_2 are the linear combination coefficients. Then, the weight sets ω_1 and ω_2 can be linearized as:

$$\omega = a_1\omega_1^T + a_2\omega_2^T \tag{14}$$

② According to game theory, the linear combination coefficients a_1 and a_2 in Formula (10) are optimized and expressed as:

$$\min \left\| a_k\omega_k^T - \omega_k \right\|^2 (k = 1, 2) \tag{15}$$

③ According to the differential properties of the matrix, the linear differential equation group for optimizing the first derivative condition of formula (15) is:

$$\begin{bmatrix} \omega_1\omega_1^T & \omega_1\omega_2^T \\ \omega_2\omega_1^T & \omega_2\omega_2^T \end{bmatrix} = \begin{bmatrix} \omega_1\omega_1^T \\ \omega_2\omega_2^T \end{bmatrix} \tag{16}$$

④ The optimal combination coefficients a_1 and a_2 are obtained via Formula (16). The normalization process

TABLE 3 Digital features of the cloud model.

Level	I			II			III			IV		
The digital feature	*Ex*	*En*	H_e	*Ex*	*En*	H_e	*Ex*	*En*	H_e	*Ex*	*En*	H_e
S_1	0.1	0.0333	0.01	0.25	0.0167	0.01	0.4	0.0333	0.01	1.75	0.4167	0.01
S_2	1.5	0.5	0.01	4	0.3333	0.01	7.5	0.8333	0.01	12.5	0.8333	0.01
S_3	0.15	0.05	0.01	0.65	0.1167	0.01	3	0.6667	0.01	7.5	0.8333	0.01

is obtained as $a_1^* = \frac{a_1}{(a_1+a_2)}$ and $a_2^* = \frac{a_2}{(a_1+a_2)}$. Then, based on game theory, the comprehensive weight ω can be obtained as:

$$\omega = a_1^* \omega_1^T + a_2^* \omega_2^T \tag{17}$$

2.2 Normal cloud model

The cloud model is defined as x, E, D, which is assumed to be a common quantitative set. The E is the domain, where $x \in E$, and D is the qualitative conception in the domain E. For the random research object x, a random number exists with a stable tendency $u(x) \in [0,1]$. Then, $u(x)$ is called the membership degree of x corresponding to D or the definitive degree. The distribution of the definitive degree in the domain E is called the membership cloud. If x meets $x \sim N(Ex, En'^2)$, and $En' \sim N(En, He^2)$, and $u(x)$ can be expressed as:

$$u(x) = \exp\left[-\frac{(x-Ex)^2}{2En'^2}\right] \tag{18}$$

where the distribution definitive degree $u(x)$ in the domain E is called the normal cloud or Gauss cloud. The expectation *Ex*, entropy *En*, and hyperentropy H_e are applied to represent digital features in the cloud model.

The *Ex* represents the point of a particular conception in the domain, *En* reflects the accepting range of the conception, and H_e demonstrates the uncertainty of the entropy with a magnitude reflecting the thickness of the cloud drop. These values are expressed as:

$$Ex = \frac{c^+ + c^-}{2} \tag{19}$$

$$En = \frac{c^+ - c^-}{6} \tag{20}$$

$$H_e = k_1 \tag{21}$$

where c^+ and c^- are the upper and lower bounds corresponding to the grade standard of the specific index, respectively. The hyperentropy H_e can select a proper constant k, set as 0.01 in the investigation.

3 Engineering example

3.1 Engineering background

The dam is located in Tianer County, Guangxi Province, China (Figure 1), and is a roller-compacted concrete gravity dam. All parts of the dam body with roller-compacted concrete conditions are roller-compacted concrete, while the others are standard concrete (Figure 2). The height of the dam body is 178 m, the maximum bottom width is 80 m, and the elevation of the dam top is 2160 m. As the dam began to operate, as many as 35 cracks appeared in the downstream surface. Most cracks are horizontal and distributed primarily at 2510–2570 m and few cracks or no obvious features are at other positions. The influence of these cracks on the dam's strength, stability, and safe operations is of great concern. So, 10 typical fractures were selected for evaluation. Their monitoring data are shown in Table 1.

4 Established assessment model

4.1 Constructed index system

Many factors affect the occurrence of concrete dam fractures; three evaluation indexes (width (S_1), length (S_2), and depth (S_3) of fracture) are selected as the assessments to simplify the calculations. According to the relevant references (Zhou et al., 2012), the three evaluation indexes are classified into four levels in Table 2. These are level I (slight), level II (common), level III (serious), and level IV (very serious).

4.2 Constructed evaluation frame

A flowchart of the assessment frame is plotted in Figure 3. Its calculative process is listed as follows:

1) Determining the evaluation index and corresponding classification.
2) Determining the weighting coefficients using the game method according to Eqs 1–17.
3) The characteristic parameters *Ex*, *En*, and H_e in the cloud model are calculated based on Eqs 19–21.

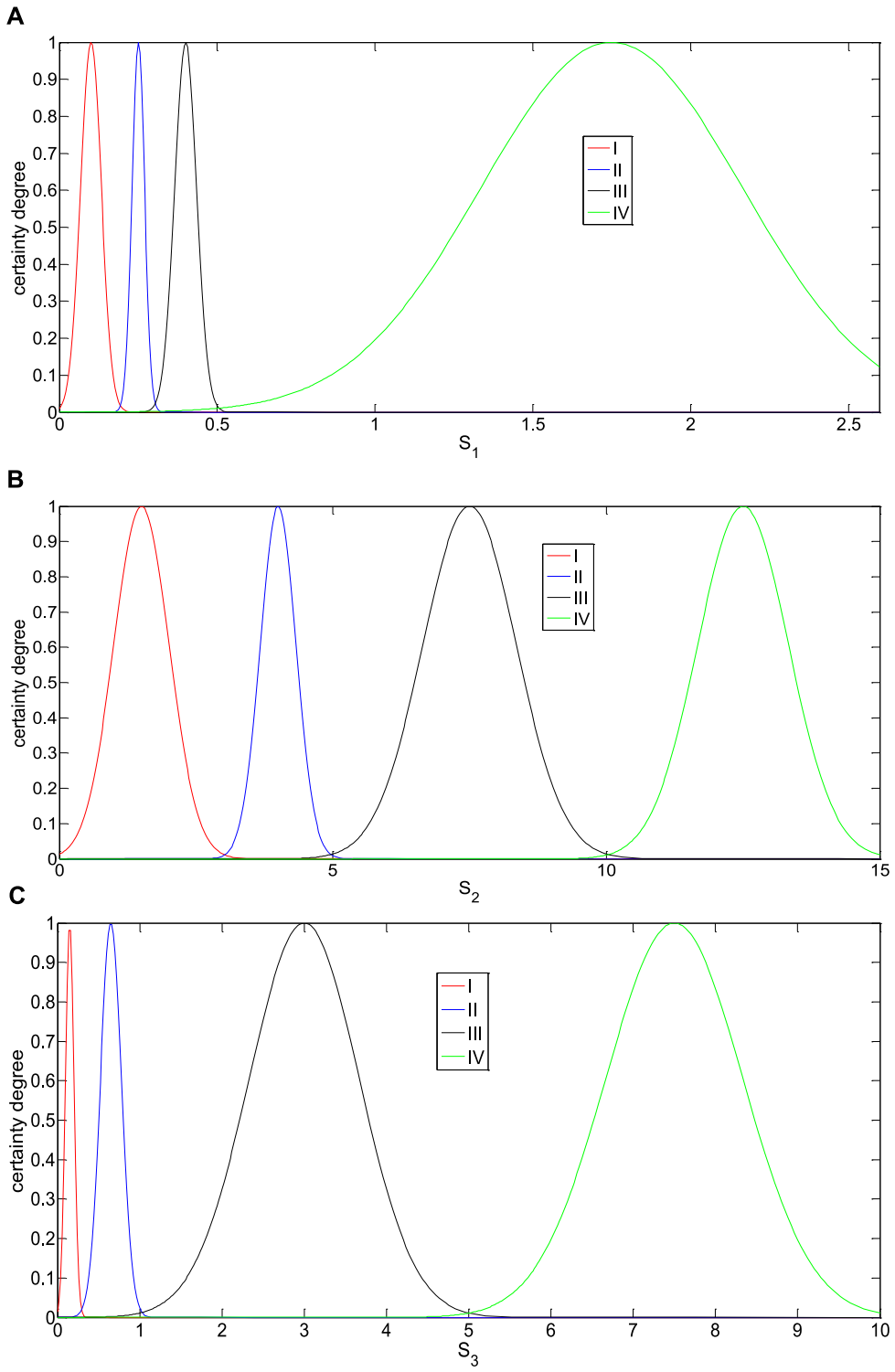

FIGURE 4
Cloud of each assessment index: **(A)** The width of fracture S1 **(B)** The length of fracture S2 **(C)** The depth of fracture S3.

4) Determining the membership degree of each assessment index when the characteristic parameters are instituted into Eq. 18.
5) The synthetic membership degree M of each level for different samples can be calculated according to Eq. 19.

$$M = \sum_{i=1}^{n} u_i \omega_i \tag{22}$$

6) The level corresponding to the maximum synthetic membership degree is determined as the final risk grade.

TABLE 4 Predicted results of the concrete dam fracture.

Sample No	The level of concrete dam fracture				Comprehensive assessment
	I	II	III	IV	
1	0.0209	0	0.1385	0	III
2	0	0.326	0.4375	0	III
3	0.0867	0.3385	0	0	II
4	0.2633	0	0.3385	0	III
5	0.0853	0.3747	0	0.1587	II
6	0.461	0	0.327	0	I
7	0.0029	0.0213	0.035	0	III
8	0.0519	0.0414	0.1587	0	III
9	0	0.2633	0.3013	0	III
10	0.2517	0	0.0569	0	I

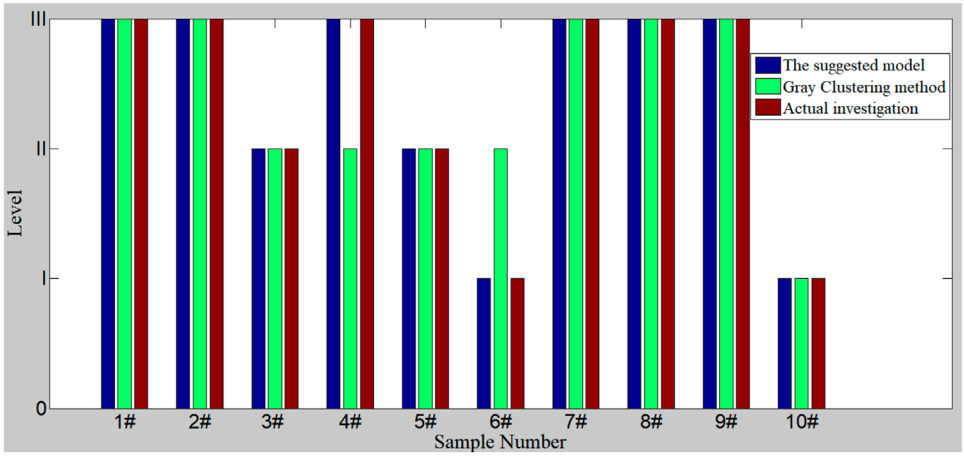

FIGURE 5
The comparison results of the three methods.

4.3 Determining index weight coefficients

1) Calculations of the weight coefficient ω_1 based on the entropy method.

According to Eqs 1–7 and in conjunction with Table 1, the corresponding weight coefficient can be calculated as:

$$\omega_1 = [0.1993 \quad 0.3561 \quad 0.4446]$$

2) Calculation of weight coefficient ω_2 based on the CRITIC method

Based on Eqs 8–10 and in conjunction with Table 1, the coefficients of correlation can be obtained as:

$$r = \begin{bmatrix} 1 & 0.3008 & 0.2026 \\ 0.3008 & 1 & 0.4328 \\ 0.2026 & 0.4328 & 1 \end{bmatrix}$$

According to Eq. 11, the standard deviation of different columns is obtained as:

$$\eta = (0.37 \quad 0.2907 \quad 0.3485)$$

Similarly, Eqs 12, 13 calculate the weights of each evaluation index as:

$$\omega_2 = (0.3962 \quad 0.2636 \quad 0.3403)$$

4) Calculation of combination weights.

Based on Eqs 14–17 and in conjunction with the weight sets ω_1 and ω_2, the combination weight ω is obtained as:

$$\omega = (0.2633 \quad 0.326 \quad 0.4107)$$

4.4 Determination of digital features in the normal cloud model

The classification standard of the normal cloud about seismic slopes is depicted in Table 3 based on Table 2 and in conjunction with Eqs 19–22. The characters of the cloud model corresponding to different indexes are calculated using the forward cloud generator, as plotted in Figure 4. The horizontal coordinates provide the magnitude of different variables. The vertical coordinates present the magnitude of the certainty degree. The sub-figure in Figure 4 includes four grades: I, II, III, and IV. The certainty degree of a given point at the state grade can be obtained when a certain variable is fixed.

The game theory combination weighting-normal cloud model is applied to evaluate the concrete dam fractures. The assessment results are depicted in Table 4. The hazard grade of the concrete dam fracture from Nos. 1–10 samples differ. The hazard level of concrete dam fractures at Nos. 1, 2, 4, 7, 8, and 9 samples is III and at Nos. 3s and 5 samples is I, and the remaining is I. Thus, the hazard level of the concrete dam fracture in most samples is significant, accounting for 60%. The remaining samples are light or common, accounting for 40%. So, necessary consolidation measurements should be taken for the Nos. 1, 2, 4, 7, 8, and 9 samples to prevent the concrete dam hazards. For example, grouting cracks could be performed. The other samples are considered safe.

The comparative results of the assessment model in Figure 5 indicate that the proposed method is consistent with the investigations for 10 different samples. Its accuracy reaches 100%, greater than the results from the Gray clustering method (80%) (LIANG et al., 2020). Therefore, estimating concrete dam fractures using the game theory combination weighting-normal cloud model is feasible. The proposed approach provides additional details for assessing concrete dam fractures. For example, the fracture length for the No. 5 sample is 11.5, belonging to level IV based on data in Table 2. In addition, the reliability distributions of the other indicators obtained using the proposed model belong to level III, indicating that the hazard level probability of the No. 5 sample at level III is greater than levels I, II, and IV. As a result, the hazard grade of the No. 5 sample is level III. Its hazard level is more likely to be level III than that of the No. 2 sample as the certain degree (0.3747) for level III is greater than the No. 2 sample (0.326). The results obtained using the proposed model accurately demonstrate the hazard level of concrete dam fractures and further determine the risk grade rankings for different samples at the same level.

5 Results and discussions

In comparison with the other traditional models, the fuzziness and randomness of evaluating the index are considered for the suggested model, and interval-oriented evaluation criteria are adopted. So, the suggested model improves the reliability of the assessment process and enhances the predictive accuracy of assessment results. So, in the future, it will have great application prospects in civil engineering.

However, some shortcomings still exist, for example, great calculative load and the neglected correlation among the indexes; these insufficiencies limit the development of the suggested method, but they still provide a new perspective for the hazard-level assessments of concrete dam fractures.

6 Conclusion

Considering the width (S_1), length (S_2), and depth (S_3) of fractures establishes a new evaluation method to assess the hazard level of concrete dam fractures based on the game theory combination weighting-normal cloud model. The weight coefficients for three different assessment indexes are first determined based on game theory combination weighting. Then, the certainty degrees for different indexes are calculated using the entropy normal cloud method. Finally, the comprehensive degree of concrete dam fractures is determined, and the hazard level is judged.

The proposed method assessed the hazard level of concrete dam fractures. The results obtained by the proposed method are consistent with actual investigations for 10 different samples. The method's accuracy reached 100%, which is greater than the results from the Gray clustering method (80%). The results give various hazard grades for the concrete dam fractures from Nos. 1–10 samples. The hazard level of concrete dam fracture at Nos. 1, 2, 4, 7, 8, and 9 samples is III, Nos. 3 and 5 samples is I, and the remaining is I. Thus, the hazard level of concrete dam fractures at most samples is significant, accounting for 60%. The remaining samples are considered light or common, accounting for 40%. So, the necessary consolidation measurements should be taken for Nos. 1, 2, 4, 7, 8, and 9 samples to reduce concrete dam risks. In addition, the reliability distributions of the other indicators obtained using the proposed model belong to level III, indicating that the hazard level probability of the No. 5 sample at level III is greater than levels I, II, and IV. The hazard grade of the No. 5 sample is level III, and its hazard level is more likely to be level III than that of the No. 2 sample as the certain degree (0.3747) for level III is greater than the No. 2 sample (0.326).

In total, the results from the proposed model accurately predict the hazard levels of concrete dam fractures and further determine the hazard grade ranking for different samples at the same level. The suggested method provides a new thought for the future of the hazard level of concrete dam fractures.

Data availability statement

The raw data supporting the conclusion of this article will be made available by the authors, without undue reservation.

Author contributions

W-WL: Data curation, Investigation, Writing–original draft. X-BG: Funding acquisition, Methodology, Writing–original draft. CY: Conceptualization, Supervision, Writing–review and editing. CZ: Formal Analysis, Validation, Writing–review and editing.

Funding

The author(s) declare financial support was received for the research, authorship, and/or publication of this article. This work is supported by the Opening Project of Sichuan Province University Key Laboratory of Bridge Non-destruction Detecting and Engineering Computing (2022QYJ02, 2022QYY02, and 2022QYJ02), Key scientific research projects of colleges and universities in Henan province (23B560019).

Conflict of interest

The authors declare that the research was conducted in the absence of any commercial or financial relationships that could be construed as a potential conflict of interest.

Publisher's note

All claims expressed in this article are solely those of the authors and do not necessarily represent those of their affiliated organizations, or those of the publisher, the editors and the reviewers. Any product that may be evaluated in this article, or claim that may be made by its manufacturer, is not guaranteed or endorsed by the publisher.

References

B Zhang, L., Wang, M. W., and Li., B. (2018). Pavement performance evaluation model based on intuitionistic fuzzy sets and TOPSIS decision theory. *J. Hefei Univ. Technol.* 41 (7), 934–938.

Chen, J. W., and Zhou, X. P. (2019). The enhanced extended finite element method for the propagation of complex branched cracks. *Eng. Analysis Bound. Elem.* 104, 46–62. doi:10.1016/j.enganabound.2019.03.028

Gu, X. B., Ma, Y., Wu, Q. H., Ji, X. J., and Bai, H. (2021a). The risk assessment of landslide hazards in Shiwangmiao based on intuitionistic fuzzy sets-Topsis model. *Nat. Hazards* 111, 283–303. doi:10.1007/s11069-021-05053-5

Gu, X. B., Shao, J. L., Wu, S. T., Wu, Q. H., and Bai, H. (2021b). The risk assessment of debris flow hazards in zhouqu based on the projection pursuit classification model. *Geotechnical Geol. Eng.* 8, 4–17.

Gu, X. B., Wang, L., and Wu, Q. H. (2022a). The risk assessment of debris flow in the duba river watershed using intuitionistic fuzzy sets: TOPSIS model. *Math. Problems Eng.* 2022, 1–12. Article ID 2031907. doi:10.1155/2022/2031907

Gu, X. B., Wang, L., and Wu, Q. H. (2022b). The risk assessment of debris flow in the duba river watershed using intuitionistic fuzzy sets: TOPSIS model. *Math. Problems Eng.* 2022, 12. Article ID 2031907. doi:10.1155/2022/2031907

Gu, X. B., and Wu, Q. H. (2016). The application of nonordinary, state-based peridynamic theory on the damage process of the Advances in Materials Science and Engineering rock-like materials. *Math. Problems Eng.* 3 (8), 1–9.

Gu, X. B., and Wu, Q. H. (2019). Seismic stability analysis of waterfront rock slopes using the modified pseudodynamic method. *Geotech. Geol. Eng.* 37 (3), 1743–1753. doi:10.1007/s10706-018-0718-1

Gu, X. B., Wu, Q. H., and Zhu, Y. H. (2019). The experimental investigation on the propagation process of crack for brittle rock similar material. *Geotechnical Geol. Eng.* 37 (6), 4731–4740. doi:10.1007/s10706-019-00934-w

Gu, X. B., Wu, S. T., Ji, X. J., and Zhu, Y. H. (2021c). The risk assessment of debris flow hazards in Banshanmen gully based on the entropy weight normal cloud method. *Adv. Civ. Eng.* 2021, 1–11. doi:10.1155/2021/8841310

GuWu, X.-B. Q.-H., and Ma, Y. (2022). Risk assessment of the rockburst intensity in a hydraulic tunnel using an intuitionistic fuzzy sets-TOPSIS model. *Adv. Mater. Sci. Eng.* 2022, 1–14. Article ID 4774978. doi:10.1155/2022/4774978

Klauer, S. G., Dingus, T. A., and Neale, V. L. (2012). *l. The impact of driver inattention on near-crash/crash risk: analysis using the 100-car naturalistic driving study data*. Washington: National Highway Traffic Safety.

Liang, J., Lan-ting, ZHOU, and Zhi-kun, L. I. U. (2020). Hazard assessment of concrete dam fracture based on the improved cloud-evidence theory. *J. Shandong Agric. Univ. (Nat. Sci. Ed.* 51 (3).

Lu, J., Fang, C., and Liuwei, W. U. (2012). The assessment on the crack danger of concrete. *Dam Based Theory Var. Fuzzy* 1 (2), 40–43. **(in Chinese)**.

Xue-hui, F. (2015). Evaluation of dam safety based on cloud model and entropy weight method. *Water Resour. Power* 33 (11), 57–60. **(in Chinese)**.

Zhang, J., and Yang, T. (2018). Study of a roof water inrush prediction model in shallow seam mining based on an analytic hierarchy process using a grey relational analysis method. *Arab. J. Geosci.* 11, 153. doi:10.1007/s12517-018-3498-2

Zhang, Z., Pang, K., Xu, L., Zou, Y., Yang, J., and Wang, C. (2023). The bond properties between UHPC and stone under different interface treatment methods. *Constr. Build. Mater.* 365, 130092. doi:10.1016/j.conbuildmat.2022.130092

Zhang, S., Dai, L., and Xiaohu, YUAN (2022). Fuzzy comprehensive prediction model of rock burst disaster in deep underground engineering. *J. Luoyang Inst. Sci. Technol.* 32 (3), 17–21.

Zhao, Y., Du, C., Bi, J., and Chaolin, W. (2021). Experimental investigation of triaxial compression and permeability of gritstone in geothermal environment. *Bull. Eng. Geol. Environ.* 80, 6971–6988. doi:10.1007/s10064-021-02370-8

Zhao, Y., and Liu, X. L. (2005). Application of ANN to risk assessment on debris flow. *J. Geol. Hazards Environ. Preserv.* 16 (2), 135–138.

Zhou, X. P., Bi, J., and Qian, Q. H. (2015). Numerical simulation of crack growth and coalescence in rock-like materials containing multiple pre-existing flaws. *Rock Mech. Rock Eng.* 48 (3), 1097–1114. doi:10.1007/s00603-014-0627-4

Zhou, X.-P., En-Ming, X., Yang, H.-Q., and Qi-Hu, Q. (2012). Different crack sizes analyzed for surrounding rock mass around underground caverns in Jinping I hydropower station. *Theor. Appl. Fract. Mech.* 57 (1), 19–30. doi:10.1016/j.tafmec.2011.12.004

Zhou, X. P., Gu, X. B., and Qian, Q. H. (2016). Seismic bearing capacity of shallow foundations resting on rock masses subjected to seismic loads. *KSCE J. Civ. Eng.* 20 (1), 216–228. doi:10.1007/s12205-015-0283-6

Zhou, X. P., Zhang, Y. X., Ha, Q. L., and Zhu, K. S. (2008). Micromechanical modelling of the complete stress-strain relationship for crack weakened rock subjected to compressive loading. *Rock Mech. Rock Eng.* 41 (5), 747–769. doi:10.1007/s00603-007-0130-2

Zhou, R., Wei, Z.-ying, Zhang, Y.-bin, and Shua, ZHANG (2017). A prediction of reference crop evapotranspiration based on generalized regression neural network and particle swarm optimization algorithm. *China Rural Water Hydropower* 6, 1–7.

Zou, Y., Jiang, J., Yang, J., Zhang, Z., and Guo, J. (2023). Enhancing the toughness of bonding interface in steel-UHPC composite structure through fiber bridging. *Cem. Concr. Compos.* 137, 104947. doi:10.1016/j.cemconcomp.2023.104947

frontiers | Frontiers in Materials

TYPE Original Research
PUBLISHED 19 March 2024
DOI 10.3389/fmats.2024.1379386

OPEN ACCESS

EDITED BY
Zhidong Zhang,
ETH Zürich, Switzerland

REVIEWED BY
Cong Zhou,
Hunan University of Science and Technology, China
Zhuangcheng Fang,
Guangdong University of Technology, China
Paolo Di Re,
Sapienza University of Rome, Italy

*CORRESPONDENCE
Jinlong Jiang,
jinlongjiang@mails.cqjtu.edu.cn

RECEIVED 31 January 2024
ACCEPTED 05 March 2024
PUBLISHED 19 March 2024

CITATION
Jiang H, Wang H, Deng X, Li Y, Zhou H, Wu C and Jiang J (2024), Shear performance of headless studs in ultra-high performance concrete bridge deck.
Front. Mater. 11:1379386.
doi: 10.3389/fmats.2024.1379386

Shear performance of headless studs in ultra-high performance concrete bridge deck

Haoting Jiang, Hongjie Wang, Xilei Deng, Yongguang Li, Heying Zhou, Chaolan Wu and Jinlong Jiang*

School of Civil Engineering, Chongqing Jiaotong University, Chongqing, China

Conventional stud connectors were proved to be inconvenient for the later disassembly and replacement in ultra-high performance concrete (UHPC) bridge decks. In this study, the headless studs which is a type of studs with their heads removed were employed as a substitute for conventional stud connectors, aiming to enhance the detachability of the bridge decks on the premise of ensuring the anti-lift bearing capacity of the decks. Three push-out specimens containing the headless studs with a diameter of 13 mm were carried out to study the mechanical properties of headless studs. In addition, the finite element model was developed to reveal the failure mechanism of headless studs in UHPC. Results indicated that the load-slip curve of headless stud connector can be divided into elastic stage, plastic stage and failure stage. The failure mode of headless studs was the shear fracture at the root of stud shank. Headless stud connections under cyclic loading can produce greater plastic deformation. The ultimate shear capacity and shear stiffness of headless studs were lower than those of conventional studs. Additionally, the UHPC slabs configured with headless studs have a small quantity of separation at the steel-UHPC interface, so it is suggested to use headless studs and conventional studs together in UHPC slabs to ensure the necessary anti-lift bearing capacity. Finite element analysis indicated that in the elastic stage, the bearing capacity of the push-specimen was dominated by the material properties of the headless stud. After entering the plastic stage, the bearing capacity of the push-specimen was mainly controlled by the UHPC below the headless stud.

KEYWORDS

steel-UHPC composite structure, shear connector, demountable, headless stud, shear performance

1 Introduction

Orthotropic steel bridge decks (OSD) are preferred for steel box girders or steel truss bridge decks due to their lower self-weight, lower material consumption, higher strength, and more convenient installation compared with concrete bridge decks (Luo et al., 2019; Zhu et al., 2022; Li et al., 2024). However, conventional orthotropic steel bridge decks exhibit lower local stiffness. Under the influence of wheel loads, the presence of welded residual stresses and stress concentration effects in the welded joint zone makes the decks more susceptible to fatigue damage (He et al., 2023; Zhu et al., 2021; van den Berg et al., 2021). Therefore, Shao et al. (Shao et al., 2013) proposed a composite material system composed of OSD and ultra-high performance concrete (UHPC)layers to enhance local stiffness. Dieng et al. (Dieng et al., 2013) pointed out that reinforcing the interaction

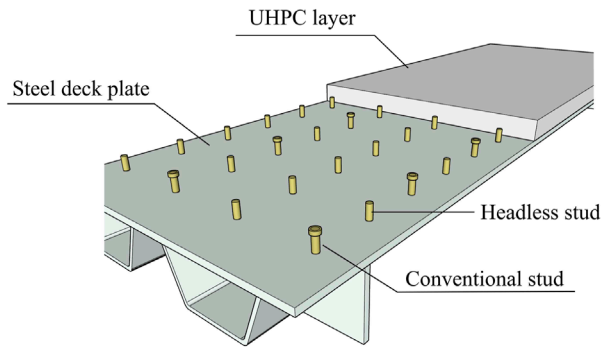

FIGURE 1
Headless studs in orthotropic steel-UHPC bridge deck.

between OSD and UHPC layers can significantly reduce stresses in both components. Conventional stud connectors welded to the steel plate are considered a reliable means to ensure a strong bonded interaction between OSD and UHPC layers (Cao et al., 2017; Jiang et al., 2022). Thus, conventional stud connectors play a vital role for the UHPC layer to assist the OSD in bearing the wheel loads of vehicles.

In the past few years, several studies investigated the shear behavior of the studs embedded in UHPC slabs. Kim et al. (Kim et al., 2015) conducted 15 push-out tests and found that when the aspect ratio of stud was reduced from 4 to 3.1 and the cover thickness over the stud head was decreased from 50 mm to 25 mm, the shear strength of stud would not be affected. A lower aspect ratio (2.7) and cover thickness (15 mm) were employed in the experiments conducted by Cao et al. (Cao et al., 2017), and the shear strength of stud could still be fully developed. Wang et al. (Wang et al., 2018; Wang et al., 2019) conducted experimental research on the static performance of large studs with diameter of 30 mm embedded in UHPC, it was found that UHPC could match the large studs very effectively, although the aspect ratio was reduced to 2.3. For demountable headed studs in UHPC, the minimum allowable aspect ratio was 1.5 (Wang et al., 2017). On the other hand, it was relatively conservative to arrange the studs in UHPC slabs using the minimum stud spacing in the longitudinal and transversal directions specified by current design codes (Hu et al., 2020). Kruszewski et al. (Kruszewski et al., 2018) and McMullen et al. (McMullen Kevin and Zaghi Arash, 2020) investigated the shear performance of the studs welded on corroded steel plates and embedded in UHPC. They discovered that the studs could reach their full strength even with stud spacing smaller than typically employed in practice. According to observations by Luo et al. (Luo et al., 2016a), a densely arranged longitudinal spacing of 3.5d could ensure the shear capacity of studs exceeding 0.9 times the full shear strength, while no strength reduction was observed with a transverse spacing of 2.3d.

UHPC is believed to have relatively great anchoring strength for conventional studs, which could be attributed to its excellent mechanical properties (Fang et al., 2024; Ding et al., 2021; Tian et al., 2022; Zhou et al., 2022; Zhang et al., 2023; Zhou et al., 2023; Fang et al., 2024; Leng et al., 2024; Ye et al., 2024). Lai et al. (Lai et al., 2023) experimentally investigated the pullout behavior of single studs and stud groups embedded in UHPC. The results showed that the single studs or stud groups embedded in UHPC had higher pullout strength and ductility than those embedded in NC. Lu et al. (Lu et al., 2021) conducted experimental research on the tensile performance of cast-in-place headed bolts embedded in high-strength concrete (HSC) and UHPC thin members of various embedment depths. They found that the anchorage performance of bolts in thin UHPC members was better than that in HSC. Additionally, according to the study by Choi et al. (Choi et al., 2015), the bearing capacity and displacement capacity of the anchors in ultra-high-performance fiber-reinforced concrete under tension and shear were significantly better than those in normal concrete. Li et al. (Li et al., 2022) studied the pull-out behavior of studs in UHPC with steel fibers. The results indicated that the UHPC specimens with steel fibers exhibited greater initial stiffness and better ductility than those without fibers. These findings further substantiate the feasibility of conventional studs which embedded in UHPC slabs.

Although conventional stud connectors are a viable option in OSD-UHPC composite bridge decks, they still have shortcomings. The head of conventional stud are firmly anchored within the UHPC, making the removal of damaged UHPC bridge deck units extremely challenging. Therefore, the use of conventional studs in UHPC is not conducive to the maintenance, replacement, and reusability for composite structures (Luo et al., 2012; Jurkiewiez et al., 2021; Zou et al., 2023). The conventional studs have excess anchored strength because of the exceptional performance of UHPC, this study attempts to release the constraint of conventional stud by removing its head (hereinafter called "headless studs"), as shown in Figure 1. The purpose of this approach is to enhance the efficiency of later removal and replacement of UHPC bridge deck units on the premise of ensuring the anti-lift bearing capacity. At present, research on the performance of headless studs has not been covered. To study the mechanical properties of headless studs embedded in UHPC, three push-out tests under monotonic and cyclic loads were carried out. In addition, the failure mechanism of headless studs was analyzed based on finite element model.

2 Experimental program

2.1 Test specimens

The push-out specimens are favored by many researchers because of their advantages such as small specimen size and low stress redistribution in studs (Cao et al., 2017; Fang et al., 2023a). In this study, there push-out specimen was used to study the shear behavior of headless studs. The specimens were designed with reference to Eurocode-4 (Anderson, 2023). The steel beam was made of two T-shaped steels made of Q345. The material of headless studs was M15, the diameter was 13 mm, and the height was 27 mm. The 12 headless studs were welded on the steel flanges on both sides of the specimen in three rows and two columns. The thickness of UHPC slab was 50 mm and the headless studs have a cover thickness of 15 mm. The reinforced steel bars in the UHPC slab were made of HRB400 and had a diameter of 10 mm. The structures of each push-out specimen were exactly the same, as shown in Figure 2. Among these three specimens, two were monotonically loaded specimens and one was cyclically loaded. They were distinguished by M and C and named DS-M1, DS-M2 and DS-C respectively.

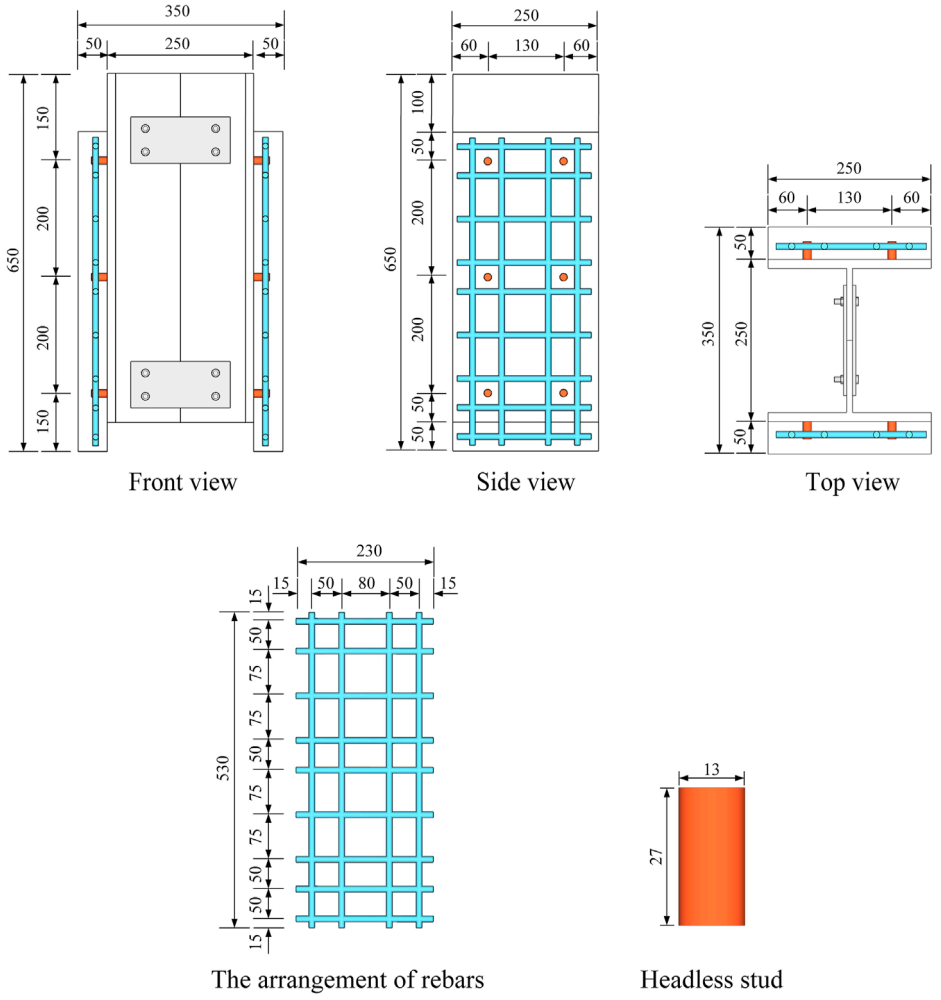

FIGURE 2
Dimensions of specimen (unit: mm).

The fabrication of push-out specimens was divided into 5 steps in total. (1) Welded the headless studs to the both sides of the steel flange according to the designated position. (2) Made formworks according to the size of the specimen and tied the steel bars. (3) Assembled the steel components and formworks. (4) Applied lubricating oil to the interface of steel plate and placed steel bars into formworks. (5) Poured UHPC. After the specimens were produced, they were watered and cured under natural conditions for 28 days. The fabrication steps of specimens are shown in Figure 3.

2.2 Material properties

In this study, the selected UHPC is formulated by mixing cement, silica fume, quartz sand, quartz flour, water reducing agent, water, and steel fibers. The dry material mix ratio of UHPC is listed in Table 1.

According to GB/T31387-2015 (General Administration of Quality Supervision, 2015), the compressive strength of UHPC was determined by conducting axial compression tests on cubic specimens, while the tensile strength was measured through axial tension tests on dog-bone-shaped specimens. Following the Chinese standard (China NTMC, 2010), the mechanical properties of the steel plate (Q345) and steel bar (HRB400) were measured through tension tests using the electronic universal testing machine (CMT2503). As shown in Figure 4, on the premise of ensuring the welding quality, the steel bars with a diameter greater than the diameter of the head of stud (22 mm) were welded at each end of the studs, and then the tensile tests were performed on these components to obtain the mechanical properties of studs. The specific performance parameters of the above materials are shown in Table 2.

2.3 Loading method and instrument layout

As shown in Figure 5A, the push-out specimens were tested in an electrohydraulic servo pressure testing machine with a capacity of 1,000 t. In order to ensure uniform force distribution on the studs on both sides of the specimen during the test, a small quantity of

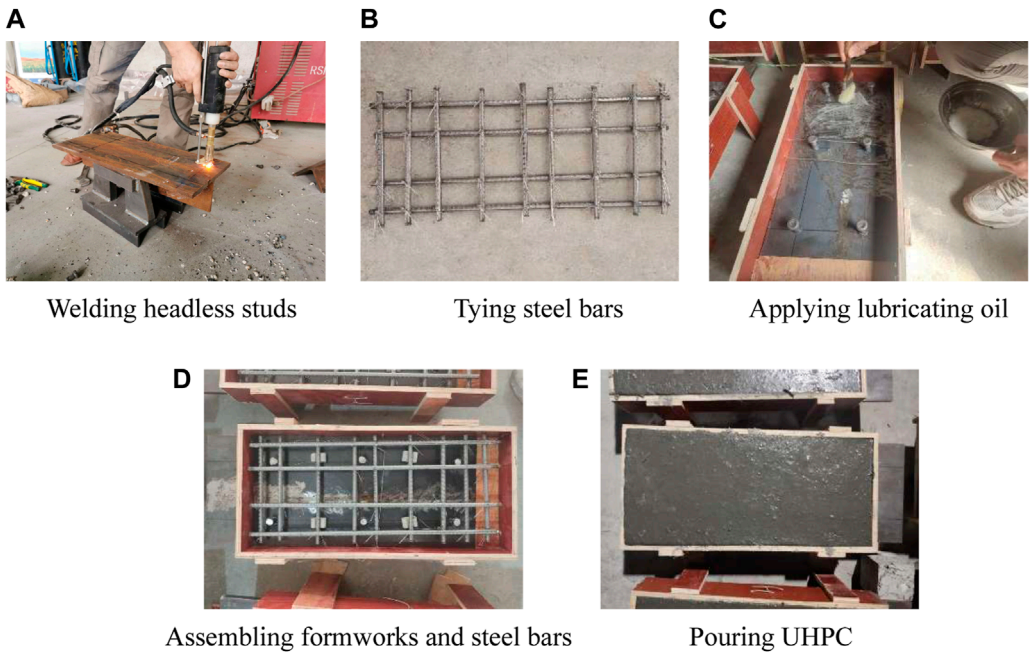

FIGURE 3
The manufacturing process of push-out specimens. **(A)** Welding headless studs. **(B)** Tying steel bars. **(C)** Applying lubricating oil. **(D)** Assembling formworks and steel bars. **(E)** Pouring UHPC.

TABLE 1 Dry material mix ratio of UHPC.

Component	Mass ratio	Volume dosage
Cement	1.000	—
Silica fume	0.250	—
Quartz sand	1.100	—
Quartz flour	0.300	—
Water reducing agent	0.019	—
Water	0.225	—
Steel fiber	—	2%

fine sand was placed at the bottom of the specimen and subsequently leveled using a balance ruler. The loading devices were arranged on top of the steel plate in the following order: spreading plate, circular cushion block, pressure transducer, and another circular cushion block. Six linear variable displacement transducers (LVDT) were used, as shown in Figure 5B, to measure the relative slip and relative separation between UHPC and steel plate, thereby obtaining the load-slip curve and load-separation curve. S1 and S2 in the figure are the tangential slip measuring points in the middle, while T1, T2 and B1, B2 are the normal separation measuring points at the top and bottom respectively. The thrust load during the test can be directly read from the digital display instrument on the pressure testing machine.

As shown in Figure 6, the loading procedure consists of monotonic and cyclic loading. Three preloading were performed before formal loading, and the force was set to 30% of the predicted ultimate load (P_u), the P_u here was determined through numerical simulation before loading, and its value was 720 kN. Monotonic loading means loading from zero load to failure of the specimen. Cyclic loading involves cycling between 0 P_u to 0.5 P_u and 0 P_u to 0.7 P_u ten times each and then loading beyond 0.7 P_u until failure of the specimen. During the elastic stage, loading was conducted in increments of 10 kN with a loading rate not exceeding 1 kN/s. During the elastic-plastic stage, loading was conducted in increments of 5 kN with a loading rate not exceeding 0.5 kN/s. The displacement control was utilized when the specimen entered the plastic stage or slip was observed, and a loading of 0.05 mm per level was applied.

3 Results and discussions

3.1 Failure mode

When each specimen was loaded to failure, the final shape of the specimen was recorded. As shown in Figure 7A, all three specimens showed that one side UHPC slab fell off from the steel beam. This is because it is difficult to ensure that the stress state of headless studs on both sides of specimen is exactly the same during the test, the headless studs on both sides did not fail at the same time. Among them, the left side slab of DS-M1 and DS-M2 specimens fell off, while the right slab of DS-C specimen fell off. Figure 7B shows the details of the interface between UHPC plate and steel flange. It can be seen from Figure 7B that the failure of the three specimens was

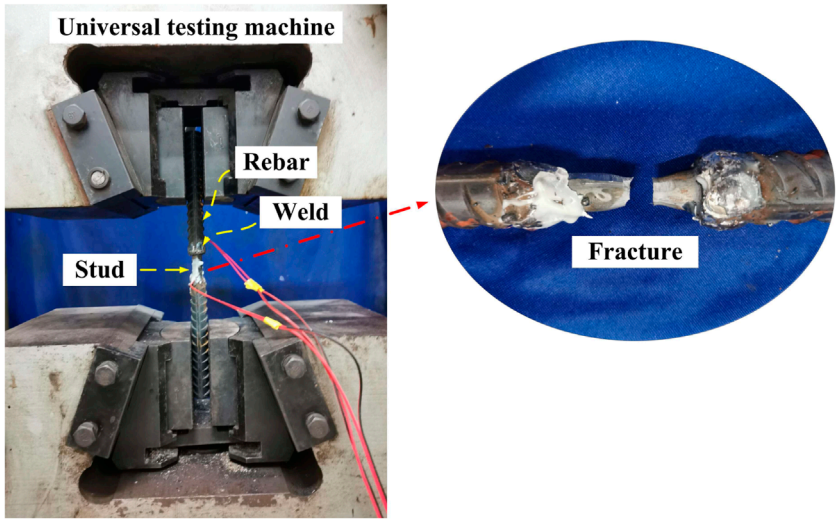

FIGURE 4
Mechanical property test of stud.

TABLE 2 Material properties of specimens.

Material name	E_c (GPa)	F_{cu} (MPa)	E_s (GPa)	F_y (MPa)	F_u (MPa)
UHPC	42.0	144.6	—	—	—
Q345	—	—	202.2	359.5	494.0
HRB400	—	—	210.0	439.3	577.1
Headless stud	—	—	206.0	355.0	530.0

Note: E_c is the elastic modulus of UHPC; F_{cu} is the cube compressive strength of UHPC; E_s is the elastic modulus of steel components; F_y is the yield strength of steel components; F_u is the tensile strength of steel components.

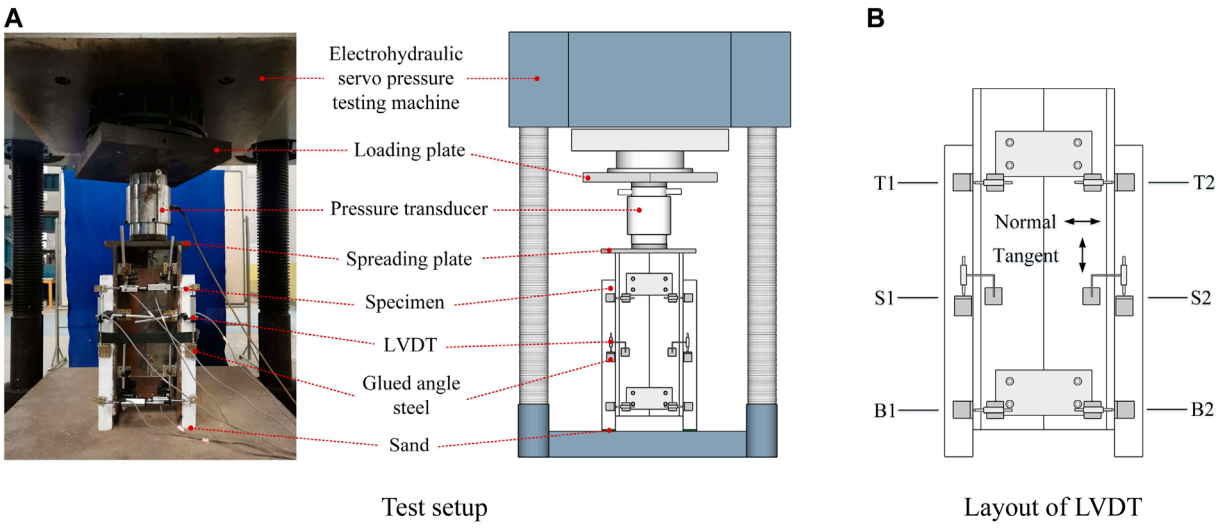

FIGURE 5
Test setup and layout of LVDTs. **(A)** Test setup. **(B)** Layout of LVDT.

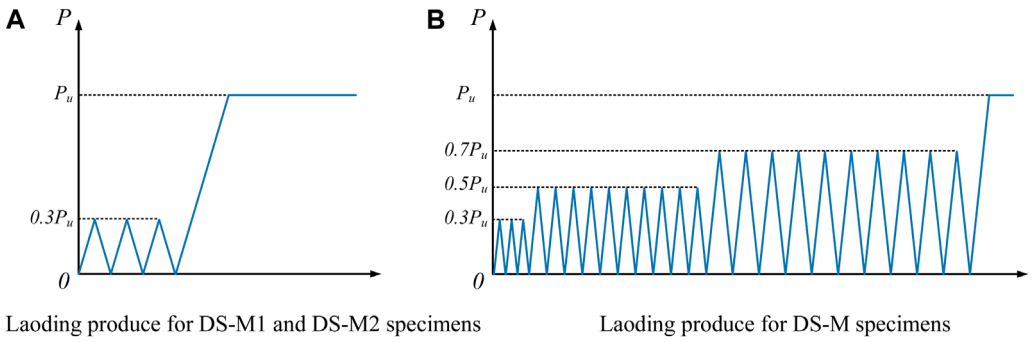

FIGURE 6
Loading produce for push-out tests. **(A)** Laoding produce for DS-M1 and DS-M2 specimens. **(B)** Laoding produce for DS-M specimens.

controlled by the fracture of stud shank near the root of the headless stud. The headless studs were still embedded in the UHPC and there was no obvious pull-out phenomenon. The welds on the steel flanges remain intact. In addition, except for the partial crushing at the root of headless stud, there was no damage in other areas on the inside of the UHPC slab, and there were no obvious cracks or damage on the outside. These phenomena were basically similar to the failure modes of the push-out specimens of conventional studs in UHPC (Kim et al., 2015; Cao et al., 2017; Tong et al., 2020).

3.2 Load-slip curves

Figure 8 shows the load-slip curves of all specimens, where the load represents the shear strength per headless stud (P_{stud}), which is calculated by dividing the shear capacity of specimen (P_u) by headless stud numbers. The interface slip is represented as the average of two vertical LVDTs (i.e., (S1+S2)/2, Figure 5B. For the DS-M1 and DS-M2 specimens under monotonic loading, the load slip curve can be divided into three stages. (1) Elastic stage (A1~B1): The load increases linearly with slip. (2) Plastic stage (B1~C1): As the slip increases, the UHPC under the root of headless stud was gradually crushed, the headless stud begins to undergo plastic deformation, and the load growth slows down. (3) Descending stage (After C1): After the load exceeded the ultimate bearing capacity, the headless studs were sheared off one after another, and the load dropped rapidly.

The DS-C specimen under cyclic loading can also be divided into the above three stages. When the cyclic load was 0.5 $P_{u,}$ the headless studs was basically in the elastic stage (A2~B2), the residual deformation after cyclic loading was small, and the loading and unloading curves basically coincide. After the 10th unloading of 0.5 P_u was completed, the residual slip was 0.041 mm. When the cyclic load was 0.7Pu, the headless studs had begun to undergo plastic deformation. The residual deformation after cyclic loading gradually increases with the number of loadings. The loading and unloading curves do not overlap. After the 10th 0.7 P_u unloading was completed, the residual slip reached 0.450 mm. It can be observed that the residual slip of the specimen under 0.7 P_u cyclic load is more obvious, which could be attributed to the gradual increase in cumulative deformation with the increase in the number of loadings after the headless studs yielded. However, the slip of the DS-C specimen under ultimate load was 22.15% and 19.07% higher than that of the DS-M1 and DS-M2 specimens respectively, and the ultimate bearing capacity was only 4.21% and 1.10% lower. It shows that cyclic loading has little effect on the bearing capacity of the headless studs, but it helps to improve the plastic deformation ability of the headless studs.

According to Eurocode 4 (Anderson, 2023), when the load of the connector reached the characteristic value (i.e., the load drops to 0.9 P_u), the interface slip is not less than 6 mm before it can be called a "plastic connector". As can be seen from Figure 8, the characteristic slip of three specimens was in the range of 3.41–3.65 mm. Therefore, the headless studs in UHPC do not meet the requirements of plastic connectors.

3.3 Load-separation curves

As shown in Figure 5B, the interfacial separation between steel plate and UHPC slab was measured using four transverse LVDTs. The top separation is represented as (T1+T2)/2, while the bottom separation is represented as (B1+B2)/2. Here, two specimens under monotonic loading were used for analysis, and the load-separation curves are shown in Figure 9. It can be seen that the trends of all load-separation curves are relatively similar to the trends of the load-slip curves. During the elastic phase, the bellow separation grew faster than the upper separation. After entering the plastic stage, the separation growth accelerated as the headless stud yielded. When the ultimate load was reached, the top separation and below separation of the DS-M1 specimen was 0.483 mm and 1.367 mm respectively, and top separation and below separation of the DS-M2 specimen was 0.814 mm and 0.935 mm respectively. Obviously, the below separation part was larger than the top separation, because the inevitable friction caused the transferred load to be applied eccentrically on the UHPC slab, thus causing the lateral deformation of the UHPC slab (Xu et al., 2012). Further, for the thin UHPC bridge deck with a thickness of 55 mm, a shear span length of 1,200 mm, and a conventional stud spacing of 200 mm, the interfacial separation between steel beam and UHPC slab was 1.17 mm under ultimate load (Xu, 2022). This result is 17% smaller than the maximum interfacial separation of the UHPC slab

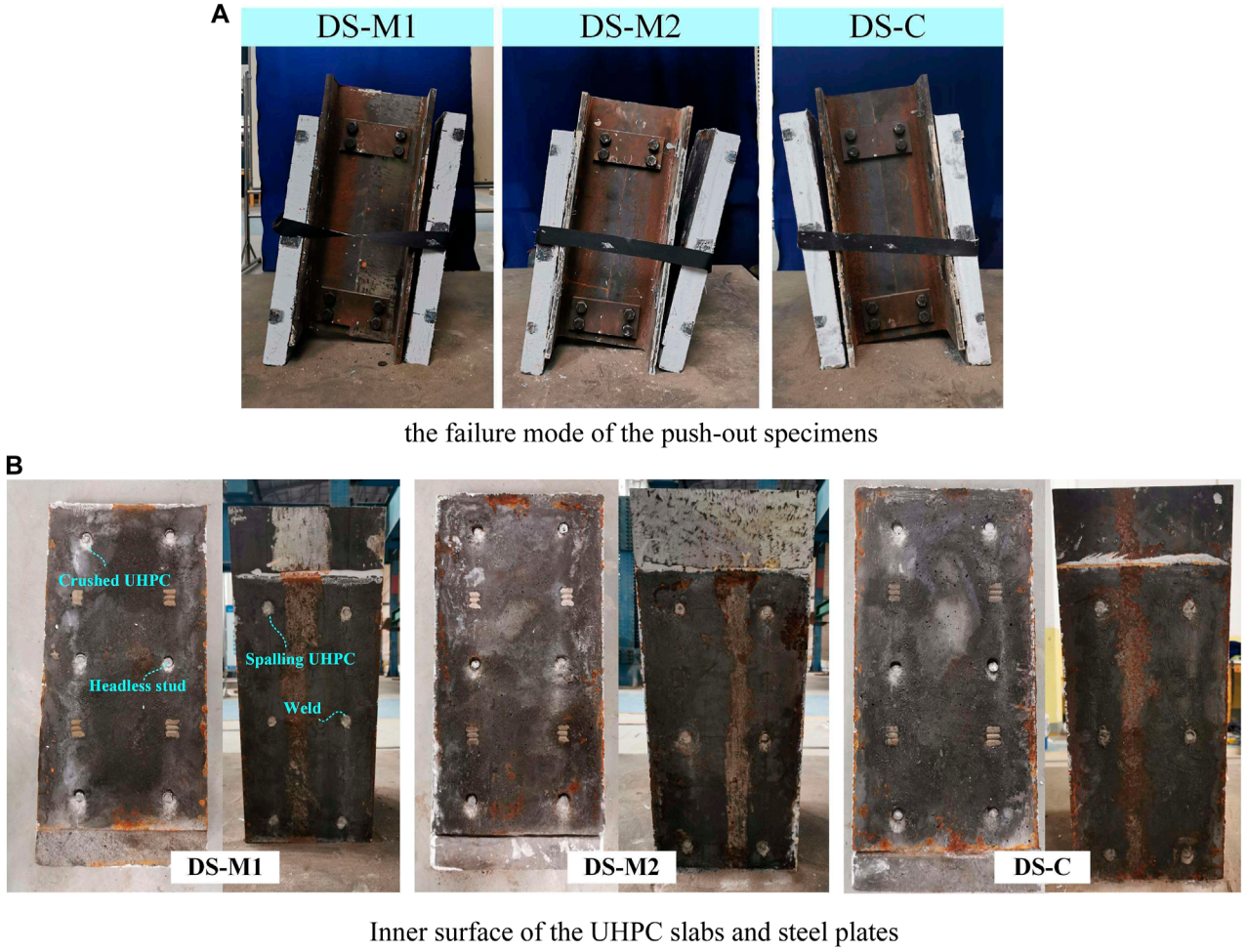

FIGURE 7
Failure modes of push-out specimens. **(A)** the failure mode of the push-out specimens. **(B)** Inner surface of the UHPC slabs and steel plates.

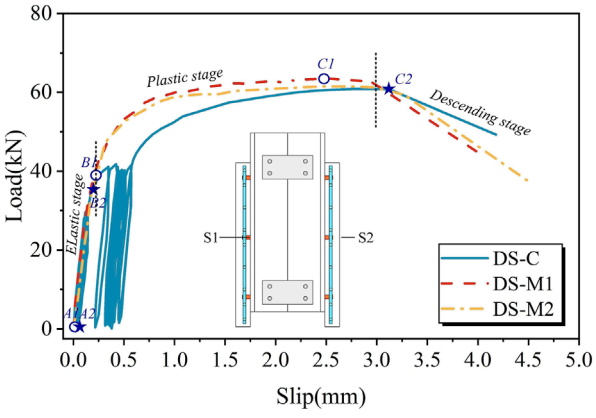

FIGURE 8
Load-slip curves.

configured with headless studs in this study. Therefore, it is suggested to use headless studs together with conventional studs in UHPC slabs to ensure sufficient anti-lifting bearing capacity.

3.4 Shear strength and shear stiffness

Since there have been some studies on the shear performance of conventional studs in UHPC (Kim et al., 2015; Wang et al., 2018; Ding et al., 2021; Fang et al., 2023b), in this study, we plan to use existing research results to compare with the experimental results of this paper. To ensure that the data comparison is valuable, existing data need to be screened. The filtering principles include the following four conditions: (1) The conventional stud diameter is 13 mm; (2) The UHPC compressive strength is greater than 120 MPa; (3) The group stud effect is not considered; (4) Specimens under monotonic loading.

Figure 10 shows the comparison of the shear capacity of selected conventional studs with the test results in this paper. It can be seen from Figure 10 that the test results in this paper are close to the results of the research by Cao et al. (Cao et al., 2017), and lower than the research results of Li et al. (Li et al., 2021) and Wu et al. (Wu et al., 2022) This is because in the study by Cao et al. (Cao et al., 2017), stud fractures were mostly caused by weld fracture, and there was almost no local damage of the UHPC slab. But in other studies, it was basically the shear failure of the stud shank. On average,

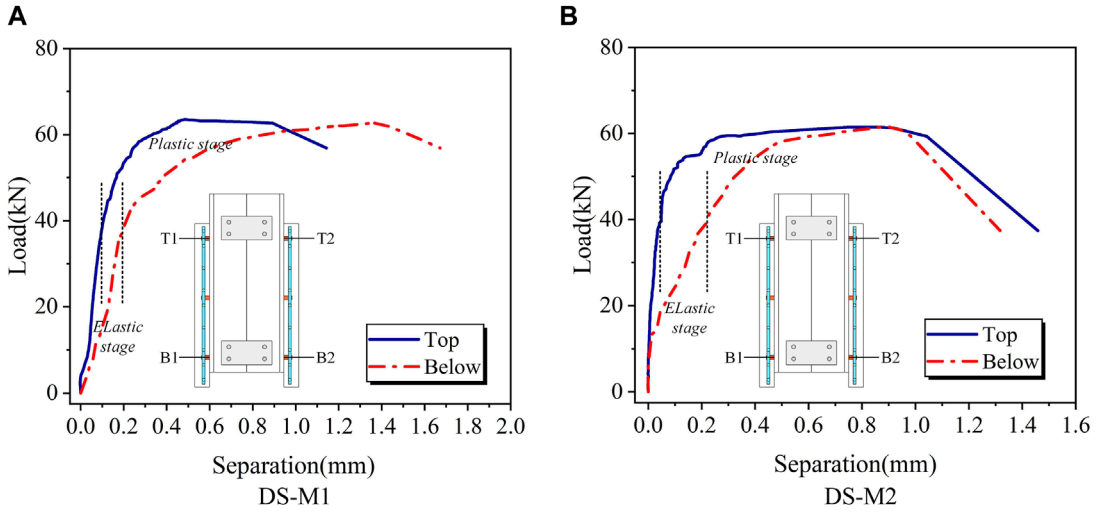

FIGURE 9
Load-separation curves. **(A)** DS-M1. **(B)** DS-M2.

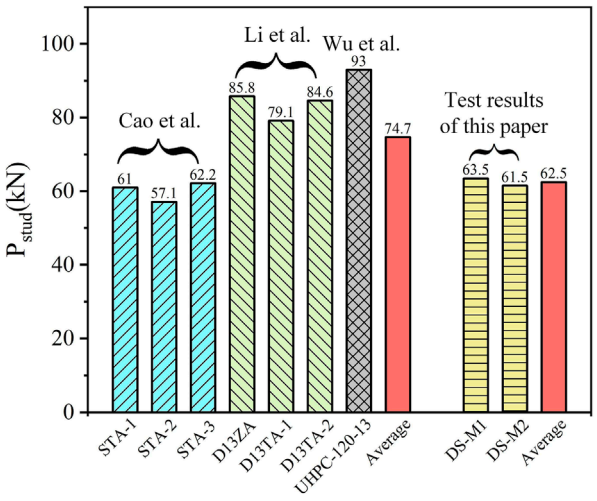

FIGURE 10
Comparison of shear strength (Cao et al., 2017; Li et al., 2021; Wu et al., 2022).

the shear capacity of headless studs is 16.3% lower than that of conventional studs. This may be because the headless stud loses the head restriction, and there may be a slight pull-out displacement in the normal direction, which leads to large plastic deformation at its root, an increase in stress level, and a decrease in bearing capacity.

Shear stiffness is an important indicator to measure whether the composite structure has good composite effect. The shear stiffness can be calculated based on the load-slip curve, which is defined as the slope of a secant line on the load-slip curve. Some researchers also use the slope of the secant line where the slip is 0.2 mm to express the shear stiffness (Tong et al., 2020; Zou et al., 2022). Cao et al. (Cao et al., 2017) used 3 methods to calculate the shear stiffness of conventional studs in UHPC. The results showed that the higher the point on the secant line, the lower the shear stiffness. For a single stud, the shear stiffness of stud obtained by the three methods varies between 266 and 396 kN/mm. However, since the slip of the stud in UHPC is relatively small, considering that the slip will have a greater impact on the shear stiffness, this paper adopted the method recommended in JSSC (2002) (JSSC Japan Society of Civil Engineers, 2002) to calculate the shear stiffness. JSSC (2002) (JSSC Japan Society of Civil Engineers, 2002) prefers to use points corresponding to 1/3 P_u. The shear stiffness calculated using selected data and test results is listed in Table 3. It can be seen from Table 3 that the shear stiffness of the headless studs is lower than that of the conventional studs. The average shear stiffness of conventional studs (STA-1 to UHPC-120–13) is 354.8, and the average shear stiffness of headless studs is 224.3. The average shear stiffness of headless studs is 36.8% lower than that of conventional studs. This may be attributed to the deformation of the headless studs during the elastic phase is larger than that of the conventional studs, resulting in lower shear stiffness.

4 Finite element analysis

4.1 General

The FE analysis was performed in the ABAQUS Explicit Module. The nonlinear contact as well as material damage and failure behavior can be powerfully simulated using the explicit central difference rule (Simulia, 2014; Guan et al., 2022; Xu et al., 2022). The FE models consisted of five components: H-section steel, UHPC layer, headless stud, weld, and steel bar. Considering the symmetry of geometry and loading, only a quarter of the push-out specimen was modeled to enhance computational efficiency.

As shown in Figure 11A, the UHPC layer, H-section steel, headless studs, and welds were simulated utilizing the C3D8R element type provided by the ABAQUS element library. C3D8R can prevent unexpected element shear locking, making it a suitable

TABLE 3 Shear stiffness for conventional studs and headless studs (Cao et al., 2017; Li et al., 2021; Wu et al., 2022).

Specimens	STA-1	STA-2	STA-3	D13TA-1	D13TA-2	UHPC-120–13	DS-M1	DS-M2
Shear stiffness k	369.9	397.8	421.6	299.3	270.8	369.1	255.3	193.2

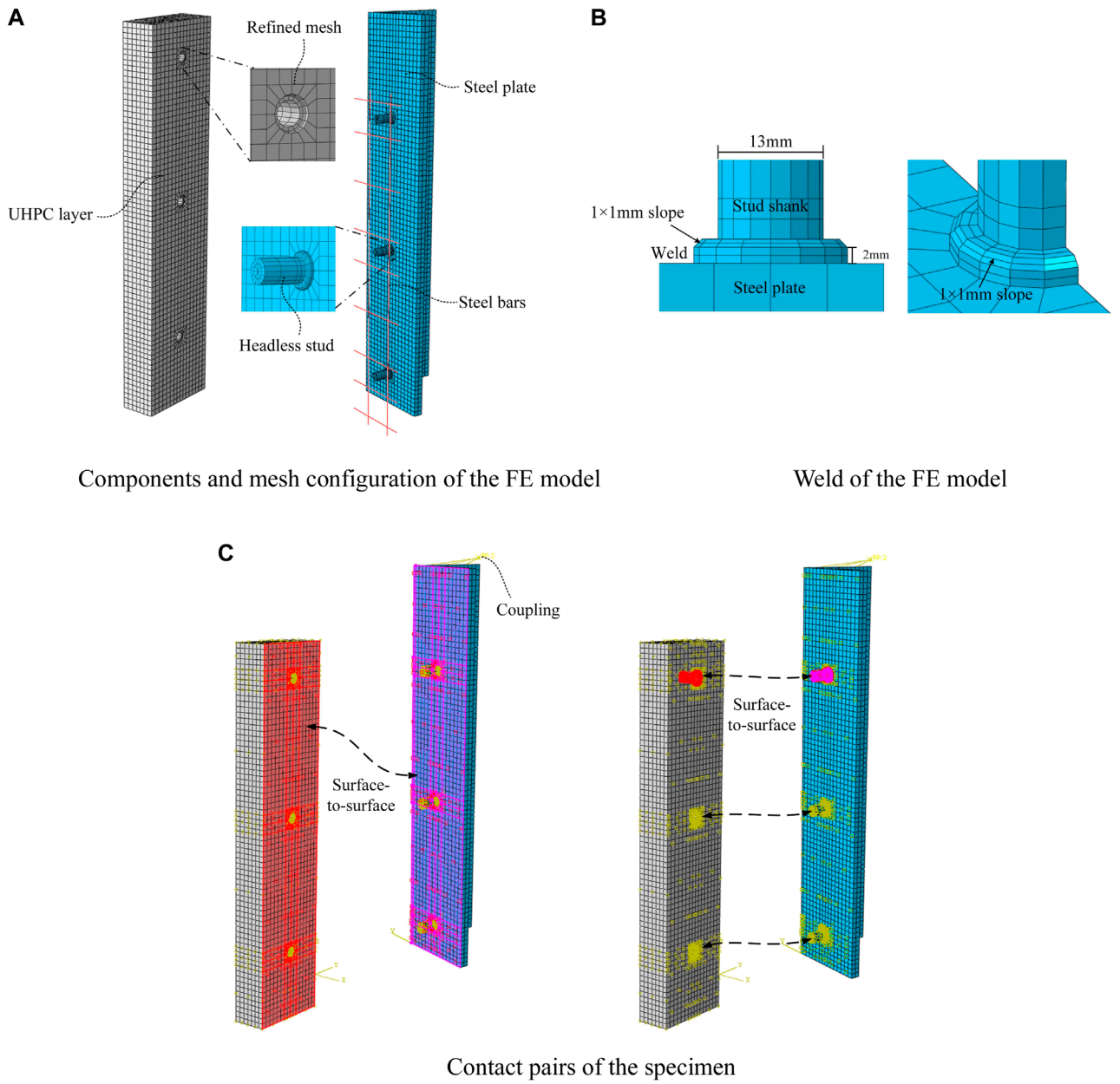

FIGURE 11
FE model of push-out specimen. **(A)** Components and mesh configuration of the FE model. **(B)** Weld of the FE model. **(C)** Contact pairs of the specimen.

method for nonlinear analysis with reasonable accuracy (Mia, 2017). The steel bars were constructed via B31 elements because they primarily acted as constraints on the concrete. It is worth noting that for studs embedded in UHPC, the welds should be modeled in the analysis considering their necessary contribution to the shear strength of studs (Cao et al., 2017; Cao and Shao, 2019; Tong et al., 2020; Huang et al., 2021). In this study, the modeling method for welds was referenced from the literature (Cao and Shao, 2019), where a 1 mm × 1 mm slope was simulated at the top corner of the weld, as shown in Figure 11B. To accurately

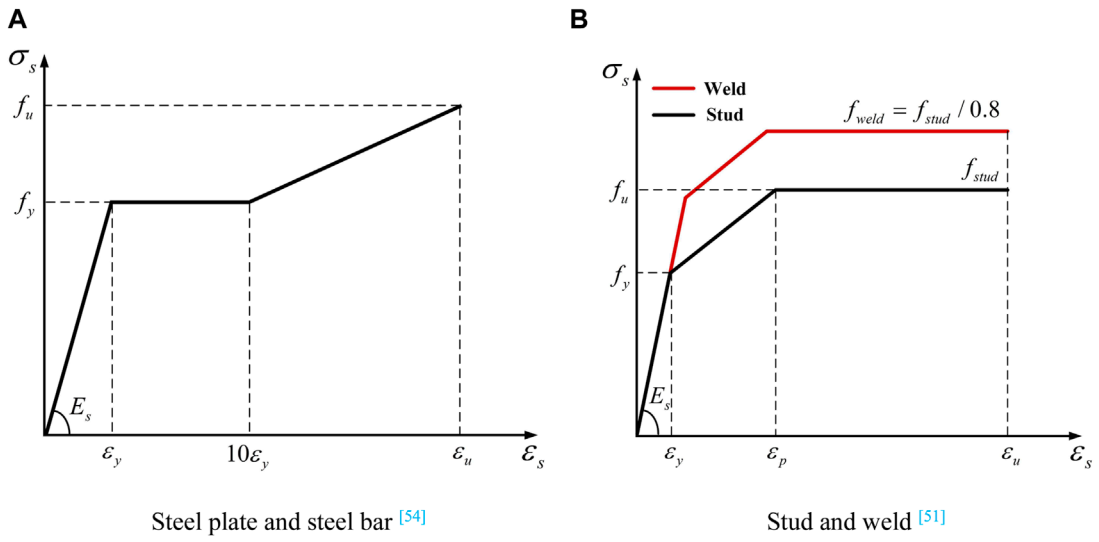

FIGURE 12
Material constitutive relations of steel (Cao and Shao, 2019; Zou et al., 2021). **(A)** Steel plate and steel bar Zou et al., 2021. **(B)** Stud and weld Cao and Shao, 2019.

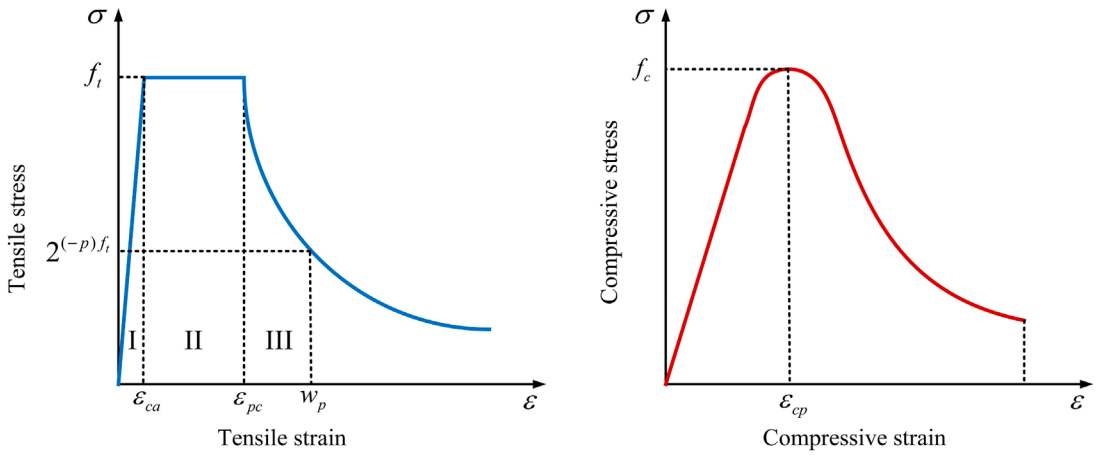

FIGURE 13
Stress-strain curves of UHPC (Cao and Shao, 2019).

simulate the severe distortion of the headless stud and the contact behavior between UHPC layer and steel plate, a refined mesh was essential in these specific zones. Thus, the size of the element representing the root of headless studs and the surrounding UHPC material was set to 2.5 mm, and other zones were set to 8 mm.

As shown in Figure 11C, the involved contact pairs were the steel-UHPC interface and the headless stud-UHPC interface. A surface-to-surface contact was applied on the above-mentioned contact pairs. In this contact model, the normal behavior between the two surfaces was defined as "hard contact" in the normal direction. For headless stud-UHPC interface, a "penalty function method" was utilized for the tangential direction, with a friction coefficient of 0.4 (Luo et al., 2016b; Huang et al., 2021; Guan et al., 2022). While the friction coefficient was not defined for the steel-UHPC interface.

Based on the symmetry of the specimens, the symmetric boundary conditions were applied to the surface along the symmetric plane of the model. While all degree of freedoms were restricted at the bottom of UHPC layer. Steel bars were embedded into the UHPC layer through the "embedded region constraints" available in ABAQUS. In addition, the top surface of the steel beam was coupled to a point, a 6 mm displacement was applied to this point, and a smoothing analysis step was set to prevent load fluctuations.

TABLE 4 Plasticity parameters of UHPC material.

Dilation angle ψ	Eccentricity λ	Yield stress ratio σ_{b0}/σ_{c0}	Constant stress ratio K_c	Viscosity coefficient
36°	0.1	1.16	0.6667	0.0005

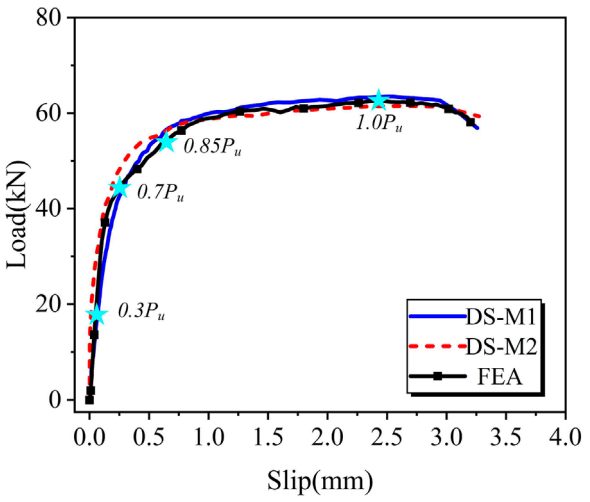

FIGURE 14
Comparison of load-slip curves from tests and FE analysis.

4.2 Material models

4.2.1 Steel components

The steel plate and steel bars were assumed to be ideal elastic-plastic materials. Their constitutive relationship was based on the tri-line stress-strain curve as shown in Figure 12A (Zou et al., 2021), and the mechanical properties are shown in Table 2.

Figure 12B illustrates the stress-strain curves of headless studs and welds. The main parameters of the headless stud constitutive obtained from the tensile test were as follows: f_y = 355 MPa, f_u = 530 MPa, ε_y = 0.003, ε_p = 0.04, ε_u = 0.12. It has been previously verified by Cao et al. (Cao and Shao, 2019) that the predicted load-slip curve generally agreed well with the test results when the weld strength (f_{weld}) was no less than that of the studs (i.e.,$f_{weld} = f_{stud}/0.8$). Consequently, the stress-strain relationship of the welds in FE model was defined as $f_{weld} = f_{stud}/0.8$.

4.2.2 UHPC

The CDP model in ABAQUS can simulate the damage and failure process of the UHPC layer (Lubliner et al., 1989; Lee and Fenves, 1998). For UHPC, its stress-strain curves for tension and compression behaviors need to be defined independently. Cao et al. (Cao and Shao, 2019) adopted the UHPC constitutive model that exhibited good agreement with the experimental results, including the stress-strain relationship in tension (Eq. 1) and the stress-strain relationship in compression (Eq. 2). Two types of stress-strain curves for UHPC are shown in Figure 13. The plasticity parameters of UHPC material are shown in Table 4.

$$\sigma = \begin{cases} \text{I} \quad \dfrac{f_t}{\varepsilon_{ca}}\varepsilon & 0 < \varepsilon \le \varepsilon_{ca} \\ \text{II} \quad f_t & \varepsilon_{ca} < \varepsilon \le \varepsilon_{pc} \\ \text{III} \quad \dfrac{f_t}{\left(1 + w/w_p\right)^p} & \varepsilon > \varepsilon_{pc} \end{cases} \tag{1}$$

$$\sigma = \begin{cases} f_c \dfrac{n\xi - \xi^2}{1 + (n-2)\xi} & 0 < \varepsilon \le \varepsilon_{cp} \\ f_c \dfrac{\xi}{2(\xi - 1)^2 + \xi} & \varepsilon > \varepsilon_{cp} \end{cases} \tag{2}$$

where, f_c is the compressive strength of UHPC, and its value is 144.6 MPa. f_t is the tensile strength of UHPC, and its value is 8.9 MPa. ξ is compressive strain ratio, defined as $\xi = \varepsilon/\varepsilon_{cp}$. ε_{cp} is the compressive strain corresponding to compressive strength, whose value is 0.0038. n is the elastic modulus ratio, defined as $n = E_c/E_t$. E_c is the initial elastic modulus, and its value is 42.0 GPa. E_t is the secant modulus at the compressive strength in the compressive stress-strain curve.

4.3 Validation of FE models

Figure 14 shows the comparison between the FE analysis results based on the load-slip curve and the test results. It can be seen from Figure 14 that the curve trend obtained by FE calculation was close to the test results. The ultimate bearing capacity per headless stud in the FE was 62.6 kN, and the ratios to the DS-M1 and DS-M2 specimens were 0.99 and 1.02 respectively. The slip corresponding to the ultimate bearing capacity of the FE model was 2.419 mm, and the slip corresponding to the ultimate bearing capacity of the DS-M1 and DS-M2 specimens was 2.553 mm and 2.619 mm respectively, i.e., the errors were 5.2% and 3.0% respectively. These results show that the load-slip curve calculated by FE model is in good agreement with the test results.

Figure 15 shows the comparison of the failure mode between test results and FE analysis results. The compressive and tensile damage coefficients of concrete (DAMAGC and DAMAGT), along with the equivalent plastic strain (PEEQ) were used to track the UHPC and headless stud failure zones, respectively. As can be seen from Figure 15A, the damage of UHPC in the FE results appeared in a very small zone around the headless studs. The compressive damage mainly occurred at the rear of headless studs, while the tensile damage was obvious at the front of headless studs. Figure 15B shows the PEEQ of the steel components in FE results. The zones in gray represent that the PEEQ exceeds 20%, and at this threshold, the stud fracture is assumed (Xu et al., 2022). It can be observed that the gray zones appeared at the junction of stud shank and weld,

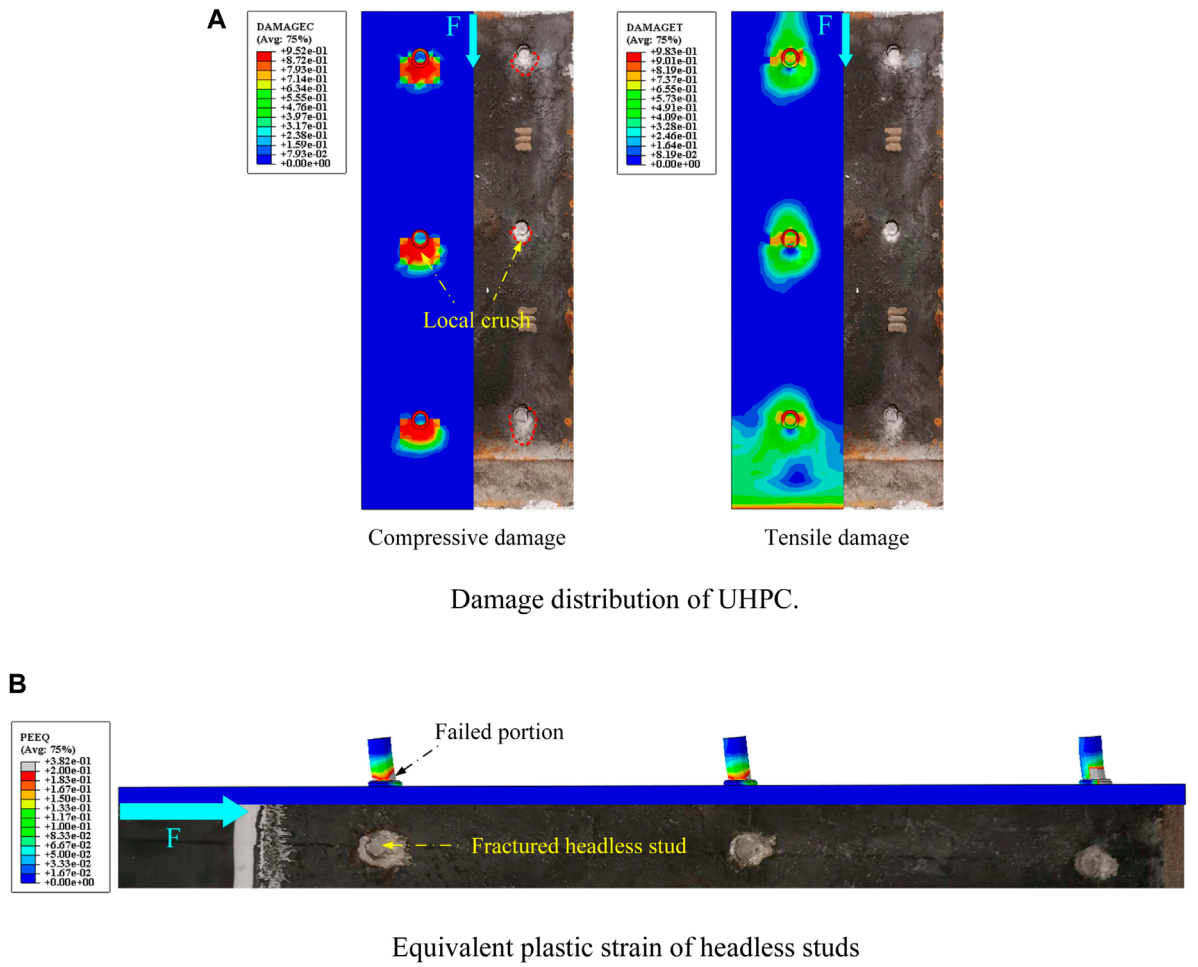

FIGURE 15
Comparison of experimental results and FE results. **(A)** Damage distribution of UHPC. **(B)** Equivalent plastic strain of headless studs.

indicating that the failure of headless studs is caused by the fracture at the root of stud shank. The results observed above are in good agreement with the test results.

4.4 Failure mechanism

Based on the stress slicing function in ABAQUS, the failure process of the headless stud in UHPC was observed, as shown in Figure 16. Here, q represents the resistance produced by UHPC to prevent headless stud from bending, and the red arrow corresponds to the maximum stress of headless stud and UHPC. The number of steps shown corresponds to the star markings in Figure 14. When the load was $0.3P_u$, the headless stud was in the elastic stage. The bearing capacity mainly comes from the material properties of headless stud, and the bearing capacity increases rapidly. When the bearing capacity reached $0.7P_u$, the headless stud begins to yield gradually, and the stress of the UHPC below the root of headless stud increased. At this time, the bearing capacity was mainly provided by UHPC, and the growth of bearing capacity was slower than before. In addition, a small amount of gap was observed at the rear end of the weld, which was caused by the downward movement of the steel beam. When the load was $0.85P_u$, the stress of the local UHPC below headless stud exceeded the ultimate compressive stress, indicating that it was crushed. The plastic deformation of the headless stud becomes larger and larger. This moment the bearing capacity continued to be provided by UHPC. However, there was a slight pull-out displacement on the top of the headless stud, and a small separation occurred at the interface between the steel beam and UHPC. When the load reached $1.0P_u$, the stress at the intersection between the root of headless stud and the weld was close to 530 MPa. The stress of the UHPC near headless stud continued to increase, and the bearing capacity was still mainly provided by UHPC. When the load exceeded $1.0P_u$, the headless stud was sheared along its root, and the bearing capacity decreases rapidly.

5 Conclusion

The following conclusions can be drawn from this research:

- A push-out test was conducted on the headless stud embedded in UHPC, and it was found that the load-slip curve of the headless stud can be divided into three stages, namely, elastic stage, plastic stage and failure stage.

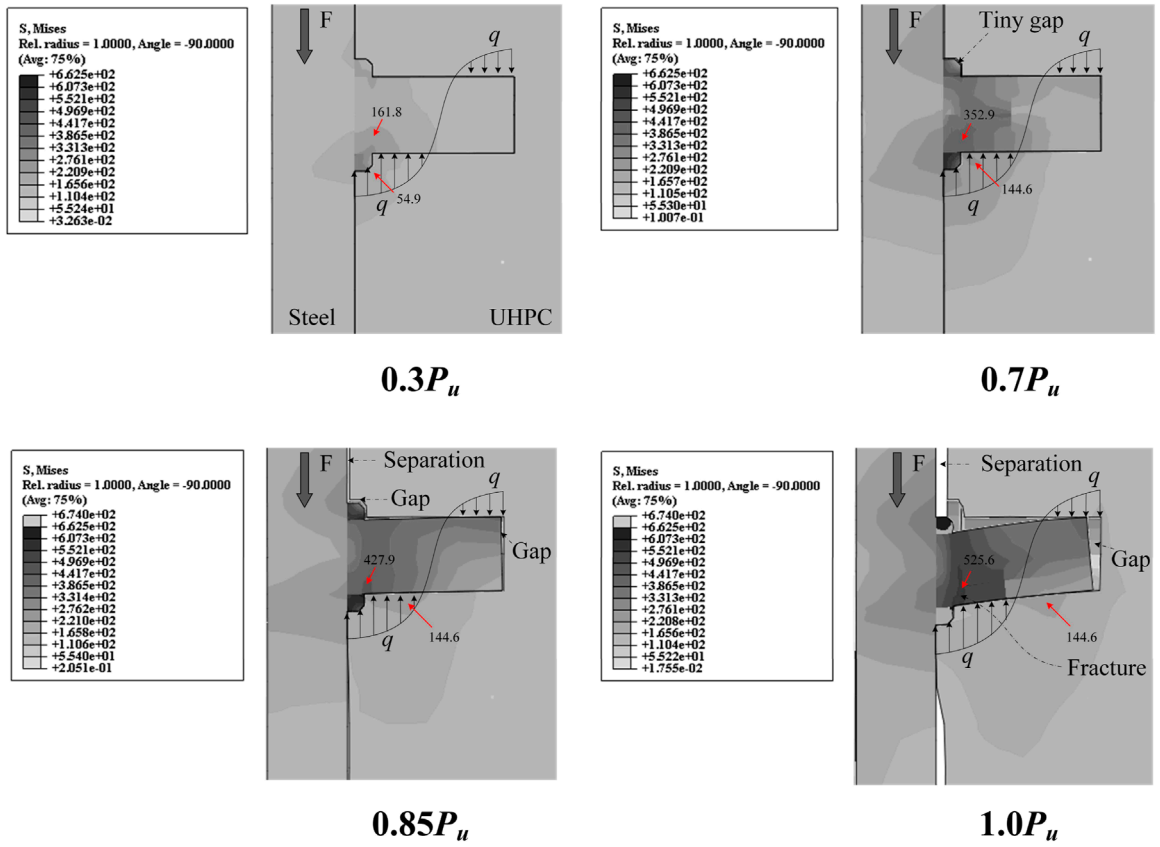

FIGURE 16
Failure process.

- The failure of the pushed-out specimen was dominated by the fracture of the root headless stud. There were signs of local crushing for the UHPC below the root of headless stud, but other than that, there was no obvious damage in other area.
- Under cyclic loading, the headless stud connector has greater plastic deformation capability. Compared with the specimens under monotonic loading (DS-M1, DS-M2), the slip of the specimen under cyclic loading (DS-M) at the ultimate bearing capacity increased by 22.15% and 19.07%, but the ultimate bearing capacity only decreased by 4.21% and 1.10%.
- Under the ultimate load, the maximum separation at the steel-UHPC interface of the UHPC slab configured with headless studs is 17% larger than that of the UHPC slab configured with conventional studs. Consequently, it is suggested to use headless studs together with conventional studs in UHPC slabs to ensure sufficient anti-lifting bearing capacity.
- Headless studs embedded in UHPC have lower load-bearing capacity and stiffness than conventional studs. Compared with conventional studs from which previous studies were collected, the average bearing capacity of per headless stud in this paper decreased by 16.3%, and the average shear stiffness decreased by 36.8%.
- The FE model well simulated the mechanical behavior of the headless stud in UHPC. The analysis results show that when the headless stud had not yielded, the bearing capacity of the push-out specimen mainly came from the material properties of the headless stud itself. After the headless stud produced plastic deformation, the bearing capacity of the push-out specimen was mainly provided by the UHPC below headless stud.

Data availability statement

The original contributions presented in the study are included in the article/Supplementary material, further inquiries can be directed to the corresponding author.

Author contributions

HJ: Conceptualization, Methodology, Writing–review and editing. HW: Formal Analysis, Software, Writing–original draft. XD: Data curation, Investigation, Writing–original draft. YL: Project administration, Resources, Validation, Writing–original draft. HZ: Data curation, Funding acquisition, Resources, Writing–original

draf. CW: Data curation, Supervision, Writing–original draft. JJ: Resources, Supervision, Writing–review and editing.

Funding

The author(s) declare that financial support was received for the research, authorship, and/or publication of this article. The authors express their sincere gratitude for the financial support provided by the National Natural Science Foundation of China (Grant No. 52278147, 52208302, 52278293), the Science and Technology Research Program of Chongqing Municipal Education Commission (KJZD-M202300706), the Natural Science Foundation of Chongqing, China (CSTB2023NSCQ-MSX0019), the Major Science and Technology Projects in Hainan (ZDKJ2021048).

Conflict of interest

The authors declare that the research was conducted in the absence of any commercial or financial relationships that could be construed as a potential conflict of interest.

Publisher's note

References

Anderson, D. (2023). *Eurocode 4 - design of composite steel and concrete structures*. Berlin, Germany: Springer.

Cao, J., and Shao, X. (2019). Finite element analysis of headed studs embedded in thin UHPC. *J. Constr. Steel Res.* 161, 355–368. doi:10.1016/j.jcsr.2019.03.016

Cao, J., Shao, X., Deng, L., and Gan, Y. (2017). Static and fatigue behavior of short-headed studs embedded in a thin ultrahigh-performance concrete layer. *J. Bridge Eng.* 22. doi:10.1061/(asce)be.1943-5592.0001031

China NTMC (2010). *National technical management committee of China. "Standard for metallic materials-tensile testing-Part 1: method of test at room temperature"*. (GB/T228-2010). Beijing: China NTMC.

Choi, S., Joh, C., and Chun, S.-C. (2015). Behavior and strengths of single cast-in anchors in Ultra-High-Performance Fiber-Reinforced Concrete (UHPFRC) subjected to a monotonic tension or shear. *KSCE J. Civ. Eng.* 19, 964–973. doi:10.1007/s12205-013-0246-8

Dieng, L., Marchand, P., Gomes, F., Tessier, C., and Toutlemonde, F. (2013). Use of UHPFRC overlay to reduce stresses in orthotropic steel decks. *J. Constr. Steel Res.* 89, 30–41. doi:10.1016/j.jcsr.2013.06.006

Ding, J., Zhu, J., Kang, J., and Wang, X. (2021). Experimental study on grouped stud shear connectors in precast steel- UHPC composite bridge. *Eng. Struct.*, 242. doi:10.1016/j.engstruct.2021.112479

Fang, S., Zhang, S., Cao, Z., Zhao, G., Fang, Z., Ma, Y., et al. (2023b). Effects of stud aspect ratio and cover thickness on push-out performance of thin full-depth precast UHPC slabs with grouped short studs: experimental evaluation and design considerations. *J. Build. Eng.*, 67. doi:10.1016/j.jobe.2023.105910

Fang, Z., Hu, L., Jiang, H., Fang, S., Zhao, G., and Ma, Y. (2023a). Shear performance of high-strength friction-grip bolted shear connector in prefabricated steel–UHPC composite beams: finite element modelling and parametric study. *Case Stud. Constr. Mater.* 18, e01860. doi:10.1016/j.cscm.2023.e01860

Fang, Z., Wu, J., Xu, X., Ma, Y., Fang, S., Zhao, G., et al. (2024). Grouped rubber-sleeved studs–UHPC pocket connections in prefabricated steel–UHPC composite beams: Shear performance under monotonic and cyclic loadings. *Eng Struct.* 305, 117781. doi:10.1016/j.engstruct.2024.117781

Fang, Z., Wu, J., Zhao, G., Fang, S., Ma, Y., and Jiang, H. (2024). Shear performance and design recommendations of single embedded nut bolted shear connectors in prefabricated steel–UHPC composite beams. *Steel Compos. Struct.* 50 (3), 319–336. doi:10.12989/scs.2024.50.3.319

General Administration of Quality Supervision (2015). *Inspection and Quarantine, beijing, China. Reactive powder concrete*. (GB/T 31387-2015). Beijing, China: General Administration of Quality Supervision. (in Chinese).

Guan, Y., Wu, J., Sun, R., Ge, Z., Bi, Y., and Zhu, D. (2022). Shear behavior of short headed studs in Steel-ECC composite structure. *Eng. Struct.*, 250. doi:10.1016/j.engstruct.2021.113423

He, X., Wu, C., Wang, R., Wei, L., and Jiang, C. (2023). Experimental study on buckling behavior of orthotropic steel deck with slender open ribs for large span suspension bridges. *J. Constr. Steel Res.* 201, 107681. doi:10.1016/j.jcsr.2022.107681

Hu, Y., Meloni, M., Cheng, Z., Wang, J., and Xiu, H. (2020). Flexural performance of steel-UHPC composite beams with shear pockets. *Structures* 27, 570–582. doi:10.1016/j.istruc.2020.05.039

Huang, Y., Chen, S., and Gu, P. (2021). Static and fatigue behavior of shear stud connection embedded in UHPC. *Structures* 34, 2777–2788. doi:10.1016/j.istruc.2021.09.043

Jiang, L., Nie, L., Zhou, W., Wu, X., and Liu, L. (2022). Distortional buckling analysis of steel-concrete composite box beams considering effect of stud rotational restraint under hogging moment. *J. Central South Univ.* 29, 3158–3170. doi:10.1007/s11771-022-5130-6

JSSC (Japan Society of Civil Engineers) (2002). *Guidelines for performance-based design of steel-concrete hybrid structures*. Tokyo: JSSC.

Jurkiewiez, B., Tout, F., and Ferrier, E. (2021). Push-out and bending tests of steel-concrete adhesively bonded composite elements. *Eng. Struct.*, 231. doi:10.1016/j.engstruct.2020.111717

Kim, J.-S., Kwark, J., Joh, C., Yoo, S.-W., and Lee, K.-C. (2015). Headed stud shear connector for thin ultrahigh-performance concrete bridge deck. *J. Constr. Steel Res.* 108, 23–30. doi:10.1016/j.jcsr.2015.02.001

Kruszewski, D., Wille, K., and Zaghi, A. E. (2018). Push-out behavior of headed shear studs welded on thin plates and embedded in UHPC. *Eng. Struct.* 173, 429–441. doi:10.1016/j.engstruct.2018.07.013

Lai, Z., Han, Y., Huang, J., and Yang, X. (2023). Pull-out behavior and design of headed studs in steel-UHPC composite structures. *Compos. Struct.*, 319. doi:10.1016/j.compstruct.2023.117135

Lee, J., and Fenves, G. L. (1998). Plastic-damage model for cyclic loading of concrete structures. *J. Eng. Mech.* 124, 892–900. doi:10.1061/(asce)0733-9399(1998)124:8(892)

Leng, J., Yang, J., Zhang, Z., Du, J., Zou, Y., and Zhou, J. (2024). Effect of vehicle-induced vibration on the strength, nano-mechanical properties, and microstructural characteristics of ultra-high-performance concrete during hardening process. *Cem. Concr. Compos.* 148, 105487. doi:10.1016/j.cemconcomp.2024.105487

Li, F., Tang, H., Wen, T., Li, J., Chen, Z., Jiang, Y., et al. (2022). Pullout behavior of studs in ultra-high performance concrete with steel fibers and novel structural fibers. *Structures* 44, 405–417. doi:10.1016/j.istruc.2022.08.017

Li, M., Shao, X., Cao, J., He, G., and Chen, Y. (2021). Performance of experimental and theoretical analysis on shear short headed studs embedded in UHPC. *China J. Highw. Transp.* 34, 191–204. (in Chinese). doi:10.19721/j.cnki.1001-7372.2021.08.016

Li, X., Lin, H., Zhao, A., Wang, R., Feng, Z., Zhang, S., et al. (2024). Experimental study on fatigue performance of double welded orthotropic steel bridge deck. *J. Constr. Steel Res.* 213, 108418. doi:10.1016/j.jcsr.2023.108418

Lu, K., Xu, Q., Wang, M., Yao, Y., and Wang, J. (2021). Anchorage performance of bolt connection embedded in thin UHPC members. *Structures* 34, 1253–1260. doi:10.1016/j.istruc.2021.08.060

Lubliner, J., Oliver, J., Oller, S., O?Ate E, (1989). A plastic-damage model for concrete. *Int. J. Solids Struct.* 25, 299–326. doi:10.1016/0020-7683(89)90050-4

Luo, P., Zhang, Q., Bao, Y., and Bu, Y. (2019). Fatigue performance of welded joint between thickened-edge U-rib and deck in orthotropic steel deck. *Eng. Struct.* 181, 699–710. doi:10.1016/j.engstruct.2018.10.030

Luo, Y., Hoki, K., Hayashi, K., and Nakashima, M. (2016a). Behavior and strength of headed stud–SFRCC shear connection. I: experimental study. *J. Struct. Eng.* 142, 142. doi:10.1061/(asce)st.1943-541x.0001363

Luo, Y., Hoki, K., Hayashi, K., and Nakashima, M. (2016b). Behavior and strength of headed stud–SFRCC shear connection. II: strength evaluation. *J. Struct. Eng.* 142, 142. doi:10.1061/(asce)st.1943-541x.0001372

Luo, Y., Li, A., and Kang, Z. (2012). Parametric study of bonded steel–concrete composite beams by using finite element analysis. *Eng. Struct.* 34, 40–51. doi:10.1016/j.engstruct.2011.08.036

McMullen Kevin, F., and Zaghi Arash, E. (2020). Experimental evaluation of full-scale corroded Steel Plate girders repaired with UHPC. *J. Bridge Eng.* 25, 04020011. doi:10.1061/(asce)be.1943-5592.0001535

Mia, M. (2017). *Investigation of load-slip behavior and fatigue life of headed shear stud connector*. https://core.ac.uk/download/pdf/211519869.pdf.

Shao, X., Yi, D., Huang, Z., Zhao, H., Chen, B., and Liu, M. (2013). Basic performance of the composite deck system composed of orthotropic steel deck and ultrathin RPC layer. *J. Bridge Eng.* 18, 417–428. doi:10.1061/(asce)be.1943-5592.0000348

Simulia, D. S. (2014). *ABAQUS analysis user's manual, version 6.14*. Rhode Island, USA: Dassault Systemes Simulia, Inc.

Tian, C., Wang, Y., Qiu, K., and Yang, Q. (2022). Effects of submicron-MgO and nano-MgO on the expansion and microscopic properties of high-performance concrete. *J. Central South Univ.* 29, 3186–3200. doi:10.1007/s11771-022-5090-x

Tong, L., Chen, L., Wen, M., and Xu, C. (2020). Static behavior of stud shear connectors in high-strength-steel–UHPC composite beams. *Eng. Struct.*, 218. doi:10.1016/j.engstruct.2020.110827

van den Berg, N., Xin, H., and Veljkovic, M. (2021). Effects of residual stresses on fatigue crack propagation of an orthotropic steel bridge deck. *Mater. Des.*, 198. doi:10.1016/j.matdes.2020.109294

Wang, J., Qi, J., Tong, T., Xu, Q., and Xiu, H. (2019). Static behavior of large stud shear connectors in steel-UHPC composite structures. *Eng. Struct.* 178, 534–542. doi:10.1016/j.engstruct.2018.07.058

Wang, J., Xu, Q., Yao, Y., Qi, J., and Xiu, H. (2018). Static behavior of grouped large headed stud-UHPC shear connectors in composite structures. *Compos. Struct.* 206, 202–214. doi:10.1016/j.compstruct.2018.08.038

Wang, J.-Y., Guo, J.-Y., Jia, L.-J., Chen, S.-M., and Dong, Y. (2017). Push-out tests of demountable headed stud shear connectors in steel-UHPC composite structures. *Compos. Struct.* 170, 69–79. doi:10.1016/j.compstruct.2017.03.004

Wu, F., Feng, Y., Dai, J., and Wang, G. (2022). Study on mechanical properties of stud shear connectors in steel-uhpc composite structures. *Eng. Mech.* 39 (2), 222–234. (in Chinese). doi:10.6052/j.issn.1000-4750.2021.05.0389

Xu, C., Sugiura, K., Wu, C., and Su, Q. (2012). Parametrical static analysis on group studs with typical push-out tests. *J. Constr. Steel Res.* 72, 84–96. doi:10.1016/j.jcsr.2011.10.029

Xu, Q. (2022). *Experimental study and refined analysis on new interfacial connections for steel-uhpc composite beam bridge 2022*. (in Chinese).

Xu, Q., Sebastian, W., Lu, K., Yao, Y., and Wang, J. (2022). Shear behaviour and calculation model for stud-UHPC connections: finite element and theoretical analyses. *Eng. Struct.* 254, 113838. doi:10.1016/j.engstruct.2022.113838

Ye, M., Li, L., Pei, B., Yoo, D.-Y., Li, H., and Zhou, C. (2024). A critical review on shear performance of joints in precast Ultra-High-Performance Concrete (UHPC) segmental bridges. *Eng. Struct.* 301, 117224. doi:10.1016/j.engstruct.2023.117224

Zhang, Z., Pang, K., Xu, L., Zou, Y., Yang, J., and Wang, C. (2023). The bond properties between UHPC and stone under different interface treatment methods. *Constr. Build. Mater.* 365, 130092. doi:10.1016/j.conbuildmat.2022.130092

Zhou, C., Wang, J., Jia, W., and Fang, Z. (2022). Torsional behavior of ultra-high performance concrete (UHPC) rectangular beams without steel reinforcement: experimental investigation and theoretical analysis. *Compos. Struct.* 299, 116022. doi:10.1016/j.compstruct.2022.116022

Zhou, C., Wang, J., Shao, X., Li, L., Sun, J., and Wang, X. (2023). The feasibility of using ultra-high performance concrete (UHPC) to strengthen RC beams in torsion. *J. Mater. Res. Technol.* 24, 9961–9983. doi:10.1016/j.jmrt.2023.05.185

Zhu, A., Ouyang, S., Chen, Y., and Sun, Y. (2022). Fatigue test and life evaluation of rib-to-deck connections in orthotropic steel bridge decks. *J. Constr. Steel Res.* 197, 107442. doi:10.1016/j.jcsr.2022.107442

Zhu, Z., Li, J., Huang, Y., and Carpinteri, A. (2021). Hot-spot stress models of cutout detail on orthotropic steel bridge decks. *J. Constr. Steel Res.* 183, 106762. doi:10.1016/j.jcsr.2021.106762

Zou, Y., Guo, J., Zhou, Z., Wang, X., Yu, Y., and Zheng, K. (2022). Evaluation of shear behavior of PCSC shear connection for the construction of composite bridges with prefabricated decks. *Eng. Struct.*, 257. doi:10.1016/j.engstruct.2022.113870

Zou, Y., Jiang, J., Yang, J., Zhang, Z., and Guo, J. (2023). Enhancing the toughness of bonding interface in steel-UHPC composite structure through fiber bridging. *Cem. Concr. Compos.* 137, 104947. doi:10.1016/j.cemconcomp.2023.104947

Zou, Y., Qin, F., Zhou, J., Zheng, Z., Huang, Z., and Zhang, Z. (2021). Shear behavior of a novel bearing-shear connector for prefabricated concrete decks. *Constr. Build. Mater.*, 268. doi:10.1016/j.conbuildmat.2020.121090

Frontiers in Materials

Investigates the discovery and design of materials for future application

A multidisciplinary journal that explores the breadth of materials science, engineering and mechanics - from carbon-based materials to smart materials.

Discover the latest Research Topics

See more →

Frontiers

Avenue du Tribunal-Fédéral 34
1005 Lausanne, Switzerland
frontiersin.org

Contact us

+41 (0)21 510 17 00
frontiersin.org/about/contact